THE ROLE OF LIPOXIDATION IN REGULATING PHOSPHATASE AND TENSIN HOMOLOG (PTEN) AND ITS DOWNSTREAM SIGNALLING

OPHÉLIE LANGLOIS

Doctor of Philosophy

ASTON UNIVERSITY

September 2024

The Role of Lipoxidation in Regulating Phosphatase and Tensin Homolog (PTEN) and its Downstream Signalling
Ophélie Langlois
Doctor of Philosophy
Aston University
2024

Thesis Abstract

Lipoxidation of proteins by lipid peroxidation products (LPPs) has emerged as an important mechanism regulating protein function, stability, and subcellular localization. Some LPPs can inhibit the crucial redox-sensitive tumour-suppressor Phosphatase and Tensin Homolog (PTEN). PTEN regulates metabolism, cell survival and proliferation, mainly by inhibition of the PI3K/Akt signalling pathway, and through non-canonical functions, depending on its subcellular localization. Nonetheless, the effects of only a few LPPs, including acrolein, 4-hydoxynonenal (HNE), and oxidized prostaglandins on PTEN and its downstream signalling have been reported and potential effects on its subcellular localization remain unknown.

The project therefore aimed to determine the effects of the LPPs 4-hydroxyhexenal (HHE) and 1-palmitoyl-2-(9-oxo-nonanoyl)-sn-glycero-3-phosphocholine (PONPC), a reactive truncated phospholipid, on PTEN function, localization and its downstream signalling. In this work, the *in vitro* assessment of human recombinant PTEN activity using 3-O-methylfluorescein phosphate (OMFP) showed a time- and concentration-dependent decrease in PTEN phosphatase activity, which correlated with PTEN aggregation. Although sites of adduction of PONPC could not be determined, tandem mass spectrometry (LC-MS/MS) analysis of HHE-treated human recombinant PTEN identified sixteen sites of adduction on PTEN cysteine, lysine, and histidine residues, suggesting that inhibition of PTEN activity could be the consequence of its lipoxidation. Immunofluorescence of PTEN in MCF-7 cells suggested that HHE and PONPC could lead to accumulation of PTEN in the nucleus and at the membrane, respectively. While preliminary data suggested that PTEN expression levels remained unchanged and that Akt expression levels were unchanged with HHE but decreased with PONPC, levels of phospho-Akt (Ser473 and Thr308) were generally elevated in a time- and concentration-dependent manner with HHE and PONPC treatments in HCT116 and MCF-7 cells, with a few exceptions. This suggested that HHE and PONPC could regulate cell signalling in an Akt-dependent manner and have important functional and biological effects, possibly via lipoxidation of PTEN.

PTEN; lipoxidation; redox biology; electrophilic lipids; HHE; PONPC; cell signalling

Acknowledgements

I would like to express my deepest gratitude to my supervisory team, Prof Corinne Spickett, Prof Andrew Pitt, Dr Cathy Slack, and Dr Philip Kitchen, for their invaluable guidance, patience, and support throughout this journey. Your insights have been instrumental in shaping this work.

A special thank you to all 2020-2024 members of the Oxidative Stress group. To (soon to be Dr) Yanis Pantoja, thank you for not only being a great friend but also a great lab partner. Dr Sarah Smith, thank you for sharing your knowledge and skills.

I am also grateful to Dr Charlotte Clarke-Bland and Dr Mariaelena Repici for their help in microscopy. I would also like to extend my heartfelt thanks to Prof Alan Goddard and Prof Roslyn Bill for their unwavering support. To Dr Alex Cheong and Dr Boubker Zaaimi, I deeply appreciate the moral support, having someone to talk to in your mother tongue is always appreciable. Dr Manoj Upadhya and Prof Zaid Al-Obaidi, your kindness and availability were much needed and appreciated.

I want to acknowledge the MemTrainees for making this experience more enjoyable, both morally and in the lab. Dr Alejandro Ronco-Campaña, you've been an amazing friend, thank you for always being there for me, for making me smile and for matching my crazy on all occasions. Dr Annaïg Rozo and Dr Alexis Lodé, my French companions, thank you for reminding me of home and always being incredible people.

A special shoutout to the Knitting Club for meeting almost without fault and helping me to relax and enjoy my hobby in such good company. To my dear friends back in France, thank you for still being there for me, even though we can very rarely see each other!

Finally, I want to express my deepest love and gratitude to my amazing partner, father and grandparents, whose endless support and love have carried me through every step of this journey. I would not be where I am without you. I love you immeasurably.

List of Contents

List of Abbreviations

15d-PGJ$_2$	15-deoxy-Δ12,14-prostaglandin J2
ACN	Acetonitrile
APC	Anaphase-promoting complex
APC/C	Anaphase-promoting complex/cyclosome
APS	Ammonium persulfate
ATM	Ataxia telangiectasia mutated kinase
BAD	Bcl2- associated agonist of cell death
Bcl-2	Anti-apoptotic B-cell lymphoma 2 protein
BLAST	Basic local alignment search tool
Bp	Base pairs
BSA	Bovine serum albumin
CATE	Catalase HPII
CDH1	APC/C activator protein
CFU	Colony-forming units
CID	Collision induced dissociation
CKD	Chronic kidney disease
CLS	Cytoplasmic localization sequence
CMV	Cytomegalovirus
CSTP1	Complete S transactivated protein 1
CV	Column volume
DAPI	4',6-diamino-2-phenylindole
DDA	Data-dependent analysis
ddH_2O	Double distilled water
dGTP	deoxyguanosine triphosphate
DGTP	Deoxyguanosinetriphosphate triphosphohydrolase
DIA	Data-independent analysis
DLS	Dynamic light scattering
DNA-PK	DNA-activated protein kinase
DNPH	2,4-dinitrophenylhydrazine
DSBs	Double-strand breaks
DTT	Dithiothreitol
ECD	Electron capture dissociation
ECL	Enhanced chemiluminescence
EDTA	Ethylenediaminetetraacetic acid
ELISA	Enzyme-linked immunosorbent assay
ER	Endoplasmic reticulum
ERK	Extracellular signal-regulated kinase
ERR-γ	Estrogen-related receptor γ
ESI	Electrospray ionization
ETD	Electron transfer dissociation
FAK	Focal adhesion kinase
FBS	Foetal bovine serum
FITC	Fluorescein isothiocyanate
FOXO	Forkhead box O
FRET	Fluorescence resonance energy transfer
GAPDH	Glyceraldehyde-3-phosphate dehydrogenase
GSH	Glutathione
GSK3	Glycogen synthase kinase-3
GST	Glutathione-S-transferase
HAUSP	Herpesvirus-associated ubiquitin protease

HBSS	Hank's balanced salt solution
HHE	4-hydroxy-2-hexenal
HIF	Hypoxia-induced factor
HILIC	Hydrophilic interaction liquid chromatography
His-tag	Polyhistidine tag
HNE	4-hydroxy-2-nonenal
HPLC	High performance liquid chromatography
HPLC-MS/MS	High performance liquid chromatography-coupled tandem mass spectrometry
HRP	Horseradish peroxidase
IAA	Iodoacetamide
IKK	Inhibitor of nuclear factor kappa-B kinase
IL-1	Interleukin-1
IMAC	Immobilized metal affinity chromatography
IPTG	Isopropyl β-D-1-thiogalactopyranoside
JACoP	Just Another Co-localization Plug-in
JNK	c-Jun-N-terminal kinase
Kb	kilobases
Keap1	Kelch-like ECH-associated protein 1
LB	Luria broth
LC	Liquid chromatography
LPPs	Lipid peroxidation products
IκBα	Nuclear factor of kappa light polypeptide gene enhancer in B-cells inhibitor alpha
MAGI	Membrane-associated guanylate kinase
MALDI	Matrix-assisted laser desorption/ionization
MAN2C1	α-mannosidase 2C1
MAPK	Mitogen-activated protein kinase
MAPKK	Mitogen-activated protein kinase kinase
MAPKKK	Mitogen-activated protein kinase kinase kinase
MDA	Malonaldehyde
MDM2	Mouse double minute 2 homolog
MESG	7-methyl-6-thioguanosine
MS	Mass spectrometry
MS/MS	Tandem mass spectrometry
MTM	Myotubularin
mTORC1	Mammalian target of rapamycin complex-1
mTORC2	Mammalian target of rapamycin complex-2
MTT	3-(4,5-Dimethylthiazol-2-yl)-2,5-diphenyltetrazolium bromide
murC	UDP-N-acetylmuramate-L-alanine
NADPH	Nicotinamide adenine dinucleotide phosphate
NES	Nuclear export signal
NF-κB	Nuclear factor kappa-light-chain-enhancer of activated B cells
NLS	Nuclear localization signal
NOS	Nitric oxide synthase
NOX	Nicotinamide adenine dinucleotide phosphate oxidases
Nrf2	Nuclear factor erythroid 2–related factor 2
NTA	Ni-nitrilotriacetic acid
NTPs	Nucleotide triphosphates
OMF	3-O-methylfluorescein
OMFP	3-O-methylfluorescein phosphate
ONE	4-oxo-2-nonenal
PBD	Phosphatidylinositol-(4,5)-bisphosphate-binding domain

PBS	Phosphate-buffered saline
PDB	Protein data bank
PDK1	Phosphoinositide-dependant kinase 1
PH	Pleckstrin homology
PHDs	Prolyl hydroxylases
PHLPP	PH domain leucine-rich repeat protein phosphatase
Pi	Inorganic phosphate
PI3K	Phosphatidylinositol-3-kinase
PIP2	Phosphatidylinositol-(4,5)-bisphosphate
PIP3	Phosphatidylinositol-(3,4,5)-triphosphate
PMSF	Phenylmethylsulfonyl fluoride
pNPP	Para-nitrophenyl phosphate
PONPC	1-palmitoyl-2-(9-oxo-nonanoyl)-sn-glycero-3-phosphocholine
POVPC	1-palmitoyl-2-(5′-oxo-valeroyl)-sn-glycero-3-phosphocholine
PP2A	Protein phosphatase 2A
PPARγ	Peroxisome proliferator activated receptor γ
PREX2a	Phosphatidylinositol-(3,4,5)-triphosphate Rac exchanger 2a
PtdIns	Phosphatidylinositides
PTEN	Tumour suppressor Phosphatase and Tensin Homolog Deleted on Chromosome 10
PTM	Post-translational modification
PTP	Protein tyrosine phosphatase
PUFAs	Polyunsaturated fatty acids
PVDF	Polyvinylidene fluoride
R^2	Coefficient of determination
RNS	Reactive nitrogen species
ROCK	RhoA-associated kinase
ROIs	Regions of interest
ROS	Reactive oxygen species
RT	Room temperature
SAS	Solvent accessibility surface
SDS	Sodium-dodecyl sulfate
SDS-PAGE	Sodium-dodecyl sulfate polyacrylamide gel electrophoresis
SEC	Size exclusion chromatography
SIPL1	Shank-interacting protein-like 1
SOC	Super optimal broth with catabolite repression
SUMO	Small ubiquitin-like modifier
TAE	Tris-acetate-ethylenediaminetetraacetic acid
TBS	Tris-buffered saline
TBS-T	Tris-buffered saline Tween 20
TE	Transformation efficiency
TEAB	Triethylammonium bicarbonate
TEMED	Tetramethylethylenediamine
TIC	Total ion chromatogram
TNFα	Tumour necrosis factor α
Trx	Thioredoxin
TSC1	Tuberous sclerosis complex 1
TSC2	Tuberous sclerosis complex 2
WGA	Wheat germ agglutinin
XIC	Extracted ion chromatogram
Δ12-PGJ_2	Delta-12-prostaglandin J2

List of Figures

List of Tables

Chapter 1 – General Introduction

1.1. Oxidative Stress Leads to Lipid Peroxidation

1.1.1. Origin of Oxidative Stress

Oxidative stress is a driver or mediator of various pathological conditions, particularly neurodegenerative diseases such as Alzheimer's disease, cardiovascular diseases, cancer and inflammation (Reuter et al., 2010, Bonda et al., 2010, Giustarini et al., 2009). It is characterized by an imbalance between oxidant species, such as reactive oxygen species (ROS) or reactive nitrogen species (RNS), and antioxidant defences. ROS are either free radicals, containing unpaired electrons on oxygen, or similar non-radical compounds. Superoxide anions ($O_2^{\cdot -}$) are the most common ROS found under physiological conditions (Burton and Jauniaux, 2011). They are formed through leakage of electrons on to molecular oxygen in the mitochondrial respiratory chain or the electron transport chain within the endoplasmic reticulum.

However, formation of ROS and RNS is also possible through enzymatic reactions (Burton and Jauniaux, 2011). For instance, the family of nicotinamide adenine dinucleotide phosphate (NADPH) oxidases (NOX), comprising seven members, serves as the primary enzymatic source of ROS in many cell types, each exhibiting distinct tissue distributions and activation mechanisms (Panday et al., 2015). They are responsible for the production of $O_2^{\cdot -}$ by transferring one electron from NADPH to oxygen. Additionally, the oxidase form of xanthine dehydrogenase generates $O_2^{\cdot -}$ during xanthine or hypoxanthine oxidation. Dismutation of $O_2^{\cdot -}$ forms hydrogen peroxide (H_2O_2), a non-radical ROS, either without catalysis or through the action of superoxide dismutase. Nitric oxide (·NO), a major RNS, emerges from the oxidation of L-arginine to form the intermediate N-hydroxy-L-arginine and further oxidation of this intermediate occurs to produce ·NO and L-citrulline, both of which oxidation steps are catalysed by the nitric oxide synthase (NOS) (Forman et al., 2002, Di Meo et al., 2016). Common ROS and RNS are listed in Table 1.1.

Table 1.1. Common reactive oxygen and nitrogen species.

ROS			RNS		
Name	**Chemical formula**	**Description**	**Name**	**Chemical formula**	**Description**
Superoxide	$O_2•^-$	Free radical	Nitric oxide	NO•	Free radical
Hydroxyl radical	•OH	Free radical	Nitrogen dioxide	$•NO_2$	Free radical
Peroxyl radical	ROO•	Free radical	Peroxynitrite	$ONOO^-$	Non-radical
Carbonate radical	$CO_3•^-$	Free radical	Dinitrogen dioxide	N_2O_2	Non-radical
Hydroperoxyl radical	$HO_2•$	Free radical	Dinitrogen tetraoxide	N_2O_4	Non-radical
Hypochlorous acid	HOCl	Non-radical			
Hydrogen peroxide	H_2O_2	Non-radical			

Based on Chiurchiù and Maccarrone, 2011.

Detoxification systems are in place in cells to remove these ROS and RNS. As discussed previously, superoxide dismutase catalyses the dismutation of $O_2•^-$ in H_2O_2, which can be removed by catalase in peroxisomes or glutathione (GSH) peroxidase and thioredoxin (Trx) peroxidase. Disulfide bonds are formed on GSH and Trx molecules, respectively, which can be reduced to thiols by GSH and Trx reductases at the expense of NADPH. Additionally, peroxiredoxins which, similarly to Trx peroxidase, utilise a reactive cysteine residue to reduce H_2O_2 and protect cells from oxidative stress. On the other hand, removal of RNS is not thought to be an enzymatic process, although peroxynitrite (ONOO-) was found to be a substrate for GSH peroxidase as well (Forman et al., 2002, Di Meo et al., 2016). Additionally, radicals can be scavenged by endogenous antioxidants such as glutathione, uric acid and pyruvate or antioxidants from nutritional sources such as ascorbic acid, tocopherols and carotenoids (Chiurchiù and Maccarrone, 2011).

1.1.2. Redox Signalling

Redox signalling is an essential process where ROS and RNS serve as signalling second messengers to regulate a variety of biological functions. It depends on the reaction between an oxidant (electrophile that attracts electrons such as ROS and RNS) and a nucleophile (that can share electrons). Cysteine, tyrosine (ionized), tryptophan, histidine and methionine residues in proteins are generally the nucleophiles involved in redox signalling. However, the thiolate form of cysteine residues is particularly targeted by oxidants as its pKa, typically around 8.3 for free cysteine, can be lowered by the specific environment allowing deprotonation to the thiolate ion, therefore enhancing its nucleophilic properties (Forman et al., 2014).

The Kelch-like ECH-associated protein 1 (Keap1)-nuclear factor erythroid 2–related factor 2 (Nrf2) plays a critical role in maintaining redox homeostasis in eukaryotic cells (Li et al., 2018a, Au et al., 2024, Sun et al., 2016, Tu et al., 2019). In physiological (unstressed)

conditions, a homodimer of Keap1 allows ubiquitination and proteasomal degradation of Nrf2 (Furukawa and Xiong, 2005, Zhang and Hannink, 2003). However, under oxidative stress, an intermolecular disulfide bond is formed between the two monomers, modifying the conformation of Keap1 (Wakabayashi et al., 2004, Dinkova-Kostova et al., 2002, Fourquet et al., 2010). Upon conformational change of Keap1, Nrf2 is freed, leading to its stabilization and accumulation in the nucleus where it regulates the expression of a variety of genes dependent on the antioxidant response element, thereby influencing the physiological and pathological effects of oxidant exposure (Zhang and Hannink, 2003, Ma, 2013). Another stress-induced pathway is the hypoxia-inducible factor (HIF) pathway. HIF-1α is hydroxylated by prolyl hydroxylases (PHDs) in normoxic (unstressed) conditions, leading to its degradation (Jaakkola et al., 2001). In hypoxic (stressed) conditions, mitochondrial dysfunction and ROS inhibit PHDs via alteration of PHDs' cofactor Fe^{2+} oxidation state, and HIF is stabilized, promoting its nuclear translocation (Koh et al., 2008) and regulation of genes that modulate metabolic pathways, bioenergetics and processes relevant to cancer onset and progression (Benita et al., 2009). Therefore, by adding this cellular signalling to the GSH and Trx/Trx reductase systems, cells are generally equipped to control redox homeostasis.

Although ROS play physiological roles via redox signalling as described above, an excessive generation of free radicals, mainly caused by environmental stressors and xenobiotics, can overpower these protective systems and cause oxidative damage within the cells by interacting with proteins, membranes and DNA. Such oxidative modifications of macromolecules are associated to the onset or progression of many diseases such as cardiovascular diseases, neurodegenerative diseases, cancer, inflammation, or ageing-related diseases (Rahal et al., 2014, Pizzino et al., 2017). Indeed, generation of ROS and RNS during oxidative stress impact essential signalling pathways such as the nuclear factor kappa-light-chain-enhancer of activated B cells (NF-κB) pathway, the mitogen-activated protein kinase (MAPK) pathway, the p53 pathway and phosphatidylinositol-3-kinase (PI3K)/Akt pathway (Lingappan, 2018, Rezatabar et al., 2019, Shi et al., 2021, Mukherjee et al., 2022), amongst others, linking oxidative stress to diseases.

1.1.3. Lipid Peroxidation and Formation of Lipid Peroxidation Products

By reacting with membranes, free radicals are able to oxidize lipids within the bilayer through a mechanism called lipid peroxidation. It is well established that non-enzymatic lipid peroxidation takes place in three stages: initiation, propagation, and termination (Mohd Fauzi and Spickett, 2015, Gueraud et al., 2010, Reis and Spickett, 2012, Sousa et al., 2017, Porter et al., 1995, Yin et al., 2011) (Figure 1.1). Initiation consists in the formation of a lipid radical

(R•) by loss of a hydrogen atom, caused by its abstraction by an initiator free radical. Phospholipids containing di-unsaturated or polyunsaturated fatty acids (PUFAs) are particularly vulnerable to radical attack, and one of the favoured oxidation targets for ROS, because of the low carbon-hydrogen bond energies exhibited by hydrogen atoms on methylene groups adjacent to double bonds. The formation of the lipid radical allows molecular oxygen to react with it to form a peroxyl radical (ROO•). The ROO• species formed is also a reactive radical which allows the second step in the peroxidation of lipids, the propagation. The newly formed peroxyl radical can abstract a hydrogen atom from another bis-allylic carbon-hydrogen bond to yield to a lipid hydroperoxide (ROOH) and a new lipid radical R•, thus propagating the radical chain reaction to multiple lipid molecules. The termination step is achieved either by combination of radical species forming non-radical phospholipid products, by intervention of antioxidants such as β-carotene or α-tocopherol or by formation of breakdown products, which are most often reactive electrophilic molecules.

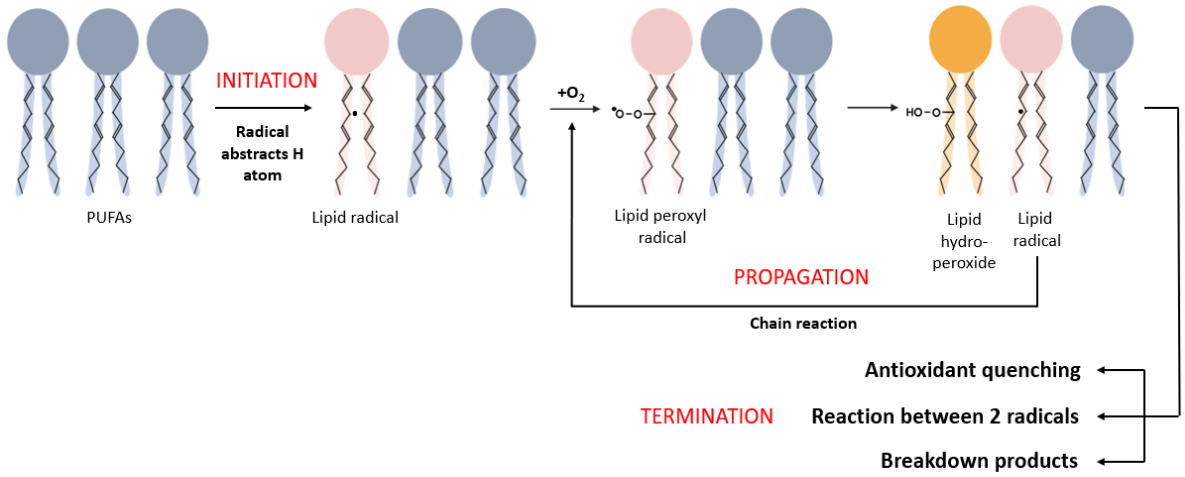

Figure 1.1. Non-enzymatic lipid peroxidation mechanism.
Adapted from Mohd Fauzi and Spickett, 2015.

1.1.4. The Diversity of Lipid Peroxidation Products

Cell membranes contain a variety of lipids that can be peroxidized including sphingolipids, glycerophospholipids, which can be esterified by an array of different PUFAs, and cholesterol (Harayama and Riezman, 2018). In addition to this diversity of targets, the mechanism of lipid peroxidation itself is complex, resulting in the formation of heterogeneous mixture of compounds. Peroxidation of ω-6-PUFAs (e.g. arachidonic acid and linoleic acid) and ω-3-PUFAs (e.g. α-linolenic acid, eicosapentenoic acid and docosahexenoic acid) esterified to phospholipids can be followed by rearrangement, fragmentation or cyclization, consequently giving rise to a plethora of oxidized lipids including intact oxidized phospholipids and short-chain or long-chain breakdown products, for which the reactivity will depend on their structure (Reis and Spickett, 2012, Sousa et al., 2017, Porter et al., 1995,

Yin et al., 2011, Porter, 1984). Well known short-chain lipid peroxidation products (LPPs) include α,β-unsaturated aldehydes such as 4-hydroxy-2-nonenal (HNE), 4-hydroxy-2-hexenal (HHE), acrolein and 4-oxo-2-nonenal (ONE), dialdehydes such as malonaldehyde (MDA), short alkanals, and ketones (Poli et al., 1985, Davies et al., 2020, Shibata et al., 2006). Long-chain peroxidation products are also diverse, including keto, hydroxy, epoxy, keto-hydroxy, hydroperoxide, di-hydroxy, ketohydroperoxide, keto-di-hydroxy, hydroxy-hydroperoxide and tri-hydroxy derivatives of fatty acyl chains (Reis et al., 2007).

Proposed mechanisms for fragmentation of lipid peroxidation intermediates are Hock cleavage involving protonation of the hydroperoxide and rearrangement of a C-C to C-O bond that leads to an unstable carbonium subsequently hydrolysed (Pryor and Porter, 1990, Spickett, 2013) and β-scission, in which an alkoxy radical readily breaks into an alkyl radical species and a carbonyl compound through cleavage of a C-C bond at the β-position (Loidl-Stahlhofen et al., 1994, Murakami and Ishida, 2017) (Figure 1.2).

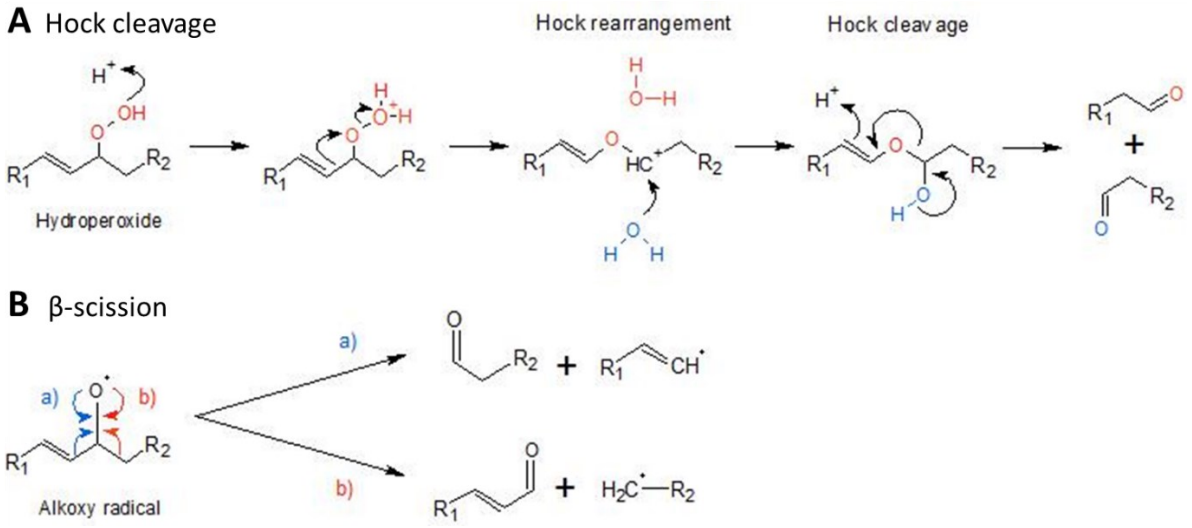

Figure 1.2. Hock cleavage and β-scission mechanisms.
(A) A hydroperoxide is protonated to yield an unstable carbonium by loss of water and subsequently undergoes rearrangement of a C-C bond to a C-O bond allowing Hock cleavage. (B) An alkoxy radical undergoes a radical rearrangement resulting in β-scission. Hock cleavage is energetically unfavourable compared to β-scission.

Peroxidation of arachidonic acid, either free or esterified to phospholipids can also lead to the formation of more complex products such as isoprostanes (Roberts and Morrow, 1997, Morrow et al., 1992), isoleukotrienes (Harrison and Murphy, 1995), and isolevuglandins (Davies et al., 2020, Salomon et al., 1997). Peroxyl radical derivatives of arachidonic acid undergo cyclization to a 5-membered ring and reduction after addition of O_2 to produce isoprostanes (Roberts and Morrow, 1997), while levuglandins are formed by cyclization of peroxyl radicals in an isoprostane-like pathway followed by cleavage of the resulting 5-membered ring (Salomon, 2005a). Cholesterol is an additional target of lipid peroxidation

and its oxidation by free radicals produces several biologically active products including 7α- and 7β-hydroperoxycholesterol, 7α-hydroxycholesterol and 7-ketocholesterol (Yoshida et al., 2007). Table 1.2 illustrates the diversity of structures of LPPs.

Importantly, modification of DNA and proteins can occur through reaction with these reactive electrophilic LPPs, leading to DNA carbonylation or covalently modified proteins in a process called protein lipoxidation.

Table 1.2. Type and structure of lipid peroxidation products.

Family	Name	Structure
Alkanals	Hexanal	
Dialdehydes	Malonaldehyde (MDA)	
	Glyoxal	
α,β-unsaturated aldehydes	Acrolein	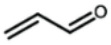
	4-hydroxy-2-nonenal (HNE)	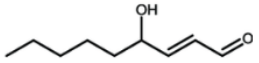
	4-hydroxy-2-hexenal (HHE)	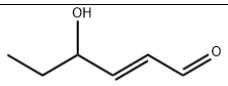
	4-oxo-2-nonenal (ONE)	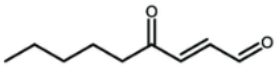
Fatty acid derivatives	5-Hydroxyeicosatetraenoic acid	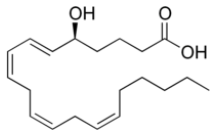
Oxidized phospholipids	1-palmitoyl-2-(5′-oxo-valeroyl)-sn-glycero-3-phosphocholine (POVPC)	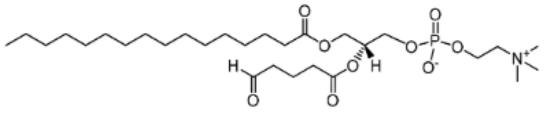
	1-palmitoyl-2-(9-oxo-nonanoyl)-sn-glycero-3-phosphocholine (PONPC)	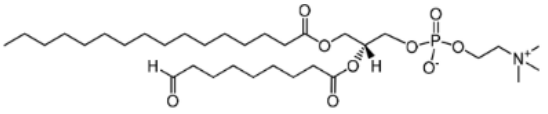
Isoleukotrienes	Leukotriene A_4	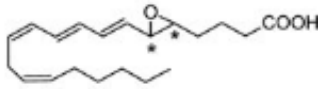
Isolevuglandins	Iso[10] Levuglandin D_2	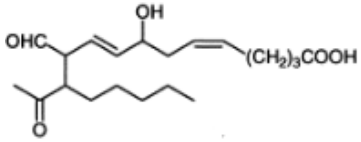
Isoprostanes	12 series F_2-isoprostane	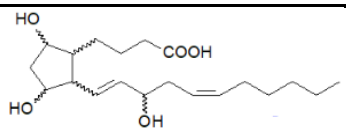
Prostaglandin derivatives	Δ12-prostaglandin J_2 (Δ12-PGJ_2)	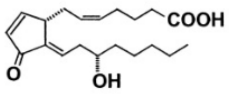
	15-deoxy- Δ12,14-prostaglandin J_2 (15d-PGJ_2)	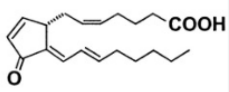
Oxidized cholesterol	7-ketocholesterol	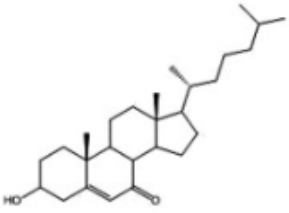

1.2. Protein Lipoxidation

1.2.1. Chemistry of Protein Lipoxidation

Protein lipoxidation has emerged as an oxidative post-translational modification (PTM). Aldehydic by-products of lipid peroxidation are electrophiles and can therefore react with nucleophiles (Shibata and Uchida, 2019). Electrophiles can act as potent modifying agents, with reaction rates comparable to or even exceeding those of oxidants like H_2O_2. They are often present at higher concentrations and are less effectively neutralized by protective systems compared to H_2O_2. As a result, electrophiles may cause similar or greater levels of nucleophilic modifications than highly reactive oxidants, particularly because oxidants are typically generated in very low concentrations in most *in vivo* environments (Sauerland and Davies, 2022). Side chains of cysteine, histidine and lysine residues in proteins are nucleophile sites where adduction can occur, with cysteine thiolates (side chain with a deprotonated sulfhydryl group) being the favoured target for reaction because of their high nucleophilicity (Vasil'ev et al., 2014), while reaction with an amine is favoured only when unprotonated (Skulj et al., 2019). To a lesser extent, the amino groups of N-terminal residues and the side chain of arginine residues can react with electrophiles but are less reactive than sulfhydryl thiolate groups of cysteine residues, the primary amine of lysine and the imidazole ring of histidine residues (Zhao et al., 2012).

Two main mechanisms lead to the formation of adducts: Schiff's base formation and Michael addition (Figure 1.3). Schiff's bases are formed by the condensation of a primary amine and an active carbonyl group by nucleophilic addition to yield a hemiaminal, and subsequent dehydration to generate an imine (Sani et al., 2018), while Michael additions involve a nucleophilic attack on the β-carbon of an α,β-unsaturated carbonyl followed by protonation of the α-carbon (Baker et al., 2007). Both reactions are reversible, and particularly Schiff's base formations which can be easily reversed in aqueous solutions (Lin et al., 2005b, Salomon, 2005b). Aldehydes and ketones can react with lysine's and arginine's side chains to form Schiff's base products, although only products of the reaction with the lysine's primary amine or the amine of the N-terminal residue of the protein are relatively stable (Spickett and Pitt, 2020). The arrangement of the three functions (aldehyde at C1, alkene at C2-C3 double bond and alcohol at C4 position) in substituted α,β-aldehydes makes the electrophilic carbon C3 particularly reactive (Gueraud et al., 2010, Sousa et al., 2017). Thus, α,β-unsaturated carbonyls can form Schiff's bases by reaction with the carbonyl group, but the β-carbon is more likely to be involved in the reaction with nucleophiles by Michael addition (Spickett and Pitt, 2020). In addition to the adduction of LPPs, proteins can undergo

cross-linking through reaction with bifunctional electrophiles (Perry et al., 2013, Sanchez-Gomez et al., 2010).

Although the nucleophilicity of the amino acid side chain and the reactivity of the electrophile, as stated previously, are major factors influencing the propensity of an adduct to form, the stability of the product, the surface accessibility of the nucleophile and the pH of the intracellular compartment will also impact the possibility of adduction (Vasil'ev et al., 2014, Spickett and Pitt, 2020).

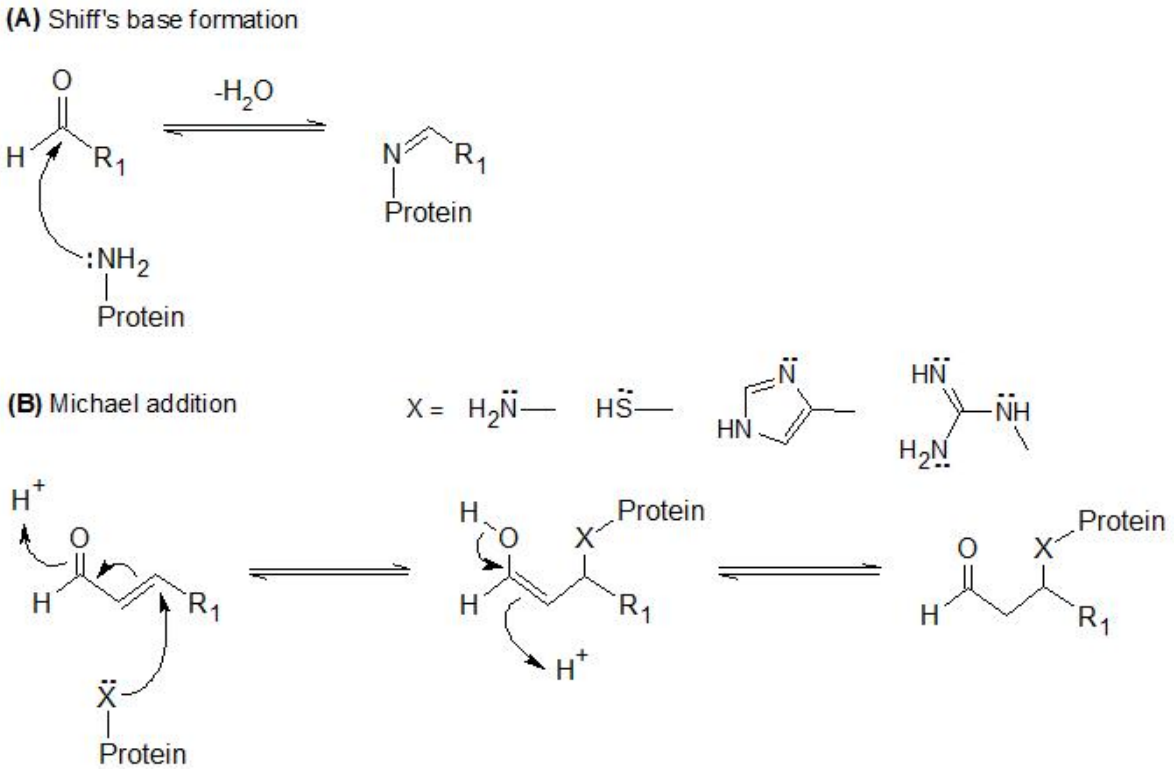

Figure 1.3. Mechanisms of formation of lipid peroxidation products.
(A) This depicts the Schiff's base formation with reaction between a primary amine (lysine or arginine side chains) and a carbonyl (here, an aldehyde). (B) This shows the Michael addition reaction between amino acid side chains (X = lysine, cysteine, histidine or arginine side chain) and an α,β-unsaturated aldehyde.

1.2.2. Detection Strategies of Protein-Oxidized Lipid Adducts

Colorimetric methods using reagents that react with aldehydes have been widely used to detect protein adducts such as derivatization of carbonyl groups formed by oxidative modifications with 2,4-dinitrophenylhydrazine (DNPH) or thiobarbituric acid reactive substances (TBArS). However, these reagents are not specific for lipoxidation as they can additionally detect direct oxidation of amino acid residues. Moreover, they will not detect all lipoxidation adducts but only the ones which have preserved carbonyl moieties after adduction (e.g. Michael adducts). Although the development of antibodies targeting specific

aldehydes, such as MDA, HNE, acrolein, HHE, 4-hydroperoxynonenal and 4-hydroxy-2E,6Z-dodecadienal, and protein-LPPs adducts have allowed a more specific recognition of proteins undergoing lipoxidation, the number of targets remains poor compared to the number of lipoxidation-derived adducts that can exist in complex samples and can have off-target binding (Afonso and Spickett, 2019). Direct labelling of protein adducts with reactive LPPs is also possible with the use of labelled analogues of oxidized or electrophilic lipid species. The conjugation of radioactive moieties, biotin or fluorescent labels to reactive species have made the visualization and separation of adducted proteins easier but the introduction of these moieties, which are usually bulky, can interfere with the reactivity of the conjugated electrophilic species (Aldini et al., 2015a). These methods are often not specific enough to understand the site-specificity of protein lipoxidation, which has led to the development of mass spectrometric strategies which are now the primary measurement technology for the detection and precise identification of lipoxidation products.

A wide variety of strategies have been used for mass spectrometry (MS) analysis of protein lipoxidation. Typically, MS analysis is based on the generation of ions from the molecules of interest using matrix-assisted laser desorption/ionization (MALDI) or electrospray ionization (ESI), and ESI is often coupled to liquid chromatography (LC) for the separation of molecules within a complex sample. Tandem mass spectrometry (MS/MS), commonly based on collision induced dissociation (CID), is performed to confirm the nature and the site of adduction. Modified peptides can be identified based on the mass shift compared to the unmodified peptide, which is directly related to the mass of the bound reactive lipid peroxidation product (Vasil'ev et al., 2014, Aldini et al., 2015a). MS approaches often follow bottom-up or top-down strategies, analysing peptide products of enzyme digestion or intact proteins respectively (Cassidy et al., 2021). Additionally, mass spectrometry can take advantage of non-MS methods to allow more specific and targeted analysis by enrichment of adducted proteins or peptides or derivatization of carbonyls. Derivatization with DNPH was shown to be a suitable tool in localizing the site of modification using mass spectrometry, especially where the DNPH reagent serves as a matrix in the MS analysis. Derivatization with biotin hydrazine tags, Girard’s P reagent (which introduces positive charges to the site of adduction) or solid phase hydrazine reagent, for instance, have been previously used for enrichment of lipoxidation products by avidin affinity chromatography, strong cation exchange chromatography and capture on hydrazide-coated glass beads, respectively (Colzani et al., 2013). Recently, an approach using click chemistry was found to be helpful in identifying the protein targets of covalent binding of reactive molecules. Chemically modified versions of electrophilic molecules containing an alkyne group can be used in cells to covalently modify their protein targets. The resulting adducted proteins can then be captured

using azide-derivatized agarose beads as azide compounds react with alkyne to form 1,2,3-triazole rings via copper-catalyzed click chemistry and subsequently analyzed by LC-MS (Sauerland et al., 2023).

1.2.3. Consequences of Protein Lipoxidation and Implication in Diseases

Lipoxidation can result in activation or inactivation of the targeted protein. There is much evidence of inhibition of protein activity by adduction of electrophiles, which is often time- and concentration-dependent, and may be either direct (binding to the catalytic residue) or indirect (conformational modification of the active site or binding pockets) (Sousa et al., 2019, Shearn et al., 2011b, Martyniuk et al., 2011, Fritz et al., 2011, Covey et al., 2010, Camarillo et al., 2016, Schopfer et al., 2010). In contrast, a few LPPs have also been shown to activate proteins, for instance, acting as ligands of the peroxisome proliferators-activated receptor γ (PPARγ), forming adducts with the cysteine located in the ligand binding pocket, thus activating the protein (Schopfer et al., 2010, Shiraki et al., 2005). In addition to participating in the inhibition of activity, conformational changes can lead to protein unfolding due to the exposure of hydrophobic residues that are normally buried (Scharf et al., 2013). This results in the activation of the unfolded protein response (Vladykovskaya et al., 2012). Another consequence of conformational changes is an increase in the level of β-sheets, well known for their involvement in protein aggregation, which inhibits the action of the 20S proteasome, hence preventing the degradation of aggregation products and leading to cell death (Shringarpure et al., 2000, Nieva et al., 2008, Kapphahn et al., 2007). Furthermore, the subcellular localization of proteins can be modified when subjected to lipoxidation, either through interplay with PTMs such as palmitoylation or by inhibition of protein-protein interactions necessary to determine the protein localization (Zorrilla et al., 2019). In fact, the interactome of the targeted protein might be affected by conformational changes following lipoxidation, modifying either protein-protein interactions (Mol et al., 2019) or protein-DNA interactions (Voitkun and Zhitkovich, 1999). Figure 1.4 provides a summary of the consequences of protein lipoxidation.

Despite the evidence of protein damage, the effects of protein lipoxidation on the system or disease are not always negative. Indeed, especially in the case of cancers, protein lipoxidation can not only result in increased malignancy, cancer progression and recurrence, and a compensatory cytoprotective response, but also antiproliferative effects and decreased metastatic activity (Martin-Sierra et al., 2019). This discrepancy in effect is believed to be related to the concentration of LPPs in cells; while low levels of LPPs would induce cell signalling and response to stress, high levels of LPPs would lead to pathological states or even cell death (Ayala et al., 2014). Protein lipoxidation is involved in regulating cell

signalling involved in stress responses. Notably, protein lipoxidation leads to the activation of the stress-induced Keap1-Nrf2 signalling pathway, which mediates the antioxidant transcriptional response to oxidative and electrophilic stress, as well as the heat shock response pathway, which protects cells from heat, oxidative and other forms of proteotoxic stress (Patinen et al., 2019). However, the redox-sensitive signalling pathways discussed previously, namely the NF-κB pathway, MAPK pathway, p53 pathway and the PI3K/Akt pathway were also found to be regulated by LPPs through protein lipoxidation. These pathways regulate essential cellular processes and their dysregulation is generally linked to diseases, particularly inflammation, ageing-related disorders and cancers (Barrera et al., 2018, Su et al., 2019).

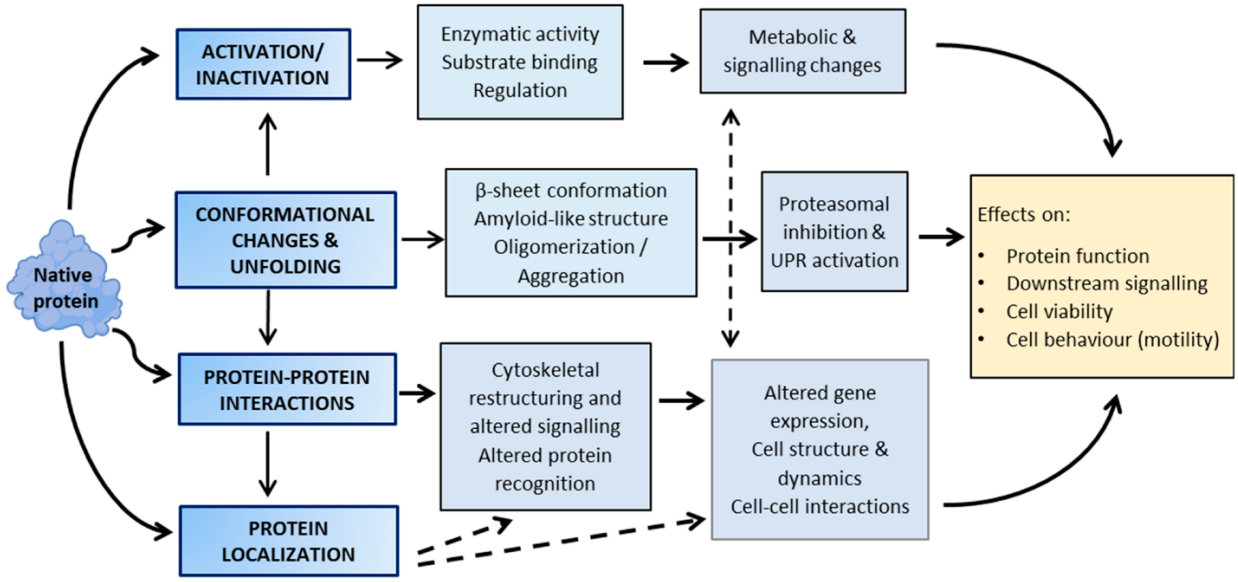

Figure 1.4. Consequences of protein lipoxidation.
Reproduced with permission from Viedma-Poyatos *et al.*, Protein Lipoxidation: Basic Concepts and Emerging Roles, Antioxidants, 2021.

In the canonical NF-κB signalling pathway, stimuli such as lipopolysaccharides, tumour necrosis factor α (TNFα), and interleukin-1 activate their receptors. This triggers a signalling cascade that leads to the activation of inhibitor of nuclear factor kappa-B kinase (IKK) subunit β within the IKK complex, which phosphorylates nuclear factor of kappa light polypeptide gene enhancer in B-cells inhibitor alpha (IκBα) at Ser32 and Ser36. This phosphorylation causes IκBα to be polyubiquitinated and degraded by the proteasome. As a result, NF-κB dimers (formed by RelA, or p65, and p50) are freed to translocate to the nucleus, where they activate the transcription of target genes (Hoesel and Schmid, 2013). In HeLa cells, 15-deoxy-Δ12,14-prostaglandin J2 (15d-PGJ_2) reduced NF-κB activity without affecting the degradation of IκBα or nuclear translocation, indicating a direct effect on NF-κB. 15d-PGJ_2 inhibited the DNA-binding ability of p50 (NF-κB subunit) by covalently binding to

Cys62 (Cernuda-Morollón et al., 2001, Straus et al., 2000). Additionally, HNE was found to lead to the same consequences but through a different mechanism: HNE could block phosphorylation and degradation of IκBα by inhibiting IKK activity through lipoxidation (Ji et al., 2001). However, multiple studies showed contradictory evidence. The contradictory effects of HNE on this pathway were extensively reviewed by Timucin and Basaga. In some cases, the NF-κB pathway was activated, in others it was inhibited. Although it is generally accepted that differential effects of LPPs are linked to their concentrations, the discrepancy in effects of HNE on the NF-κB pathway appeared at similar concentrations and it seemed to be rather cell type-dependent (Timucin and Basaga, 2017).

The mitogen-activated protein kinase (MAPK) pathway consists mainly of three separate MAP kinase cascades in mammalian cells, which all include signal initiation followed by a cascade of phosphorylation from MAPK kinase kinase (MAPKKK), to MAPK kinase (MAPKK), to MAPK. MAPK translocate to the nucleus to activate their substrates and lead to gene expression regulating proliferation, differentiation, inflammation, apoptosis and stress responses. These cascades are referred to as the extracellular-signal-regulated kinases (ERK) pathway, the c-Jun-N-terminal kinase (JNK) pathway and the p38 pathway, which are the MAPKs in these cascades (Zhang and Liu, 2002). In mouse embryonic fibroblasts (wild-type or lacking glutathione-S-transferase (GST)), HNE resulted in the activation of JNK, ERK 1/2 and p38 MAPKs, correlating with an increase in HNE-protein adducts, effects that were exacerbated in cells lacking GST, which showed it to play a protective role against LPP-induced stress (McElhanon et al., 2013). Additionally, H-Ras, which initiates the Raf-MEK-ERK pathway, was found to be activated by 15d-PGJ_2 following lipoxidation of the protein on Cys184 (Renedo et al., 2007, Oliva et al., 2003).

The p53 protein is one of the most renowned tumour suppressor proteins. It plays a crucial role in preventing cancer by interacting with multiple signalling pathways that regulate essential cellular processes like cell division, genomic stability, apoptosis, autophagy, immune responses, and tumour microenvironment regulation. When functioning normally, p53 binds to specific DNA sequences and induces the expression of genes that help prevent cancer. Under stress, p53 activates programmes such as cell cycle arrest, DNA repair, and apoptosis, suppressing tumour growth. However, inactivation of p53 function promotes cancer progression, invasion, and metastasis by allowing unchecked cell proliferation and survival (Marei et al., 2021). 15d-PGJ_2 could also form adducts on p53, at Cys277, resulting in accumulation of p53 in MCF-7 cells but the DNA binding and transcriptional activity of the adducted p53 were significantly reduced (Kim et al., 2010a). In contrast, HNE inhibited SK-N-BE cell proliferation by increasing the expression of p53, p53-like proteins (p63 and p73)

and p53 target proteins which modulate cell cycle progression and apoptosis (Laurora et al., 2005).

Most importantly in the context of this project, LPPs were proposed to be regulators of the PI3K/Akt pathway, which plays important roles in cell metabolism, growth, proliferation, and survival (Manning and Toker, 2017, Osaki et al., 2004, Hemmings and Restuccia, 2012). Most of the evidence suggests that the PI3K/Akt pathway can be activated by lipoxidation-induced inhibition of Phosphatase and Tensin Homolog (PTEN), an important tumour-suppressor negatively regulating this pathway by preventing Akt phosphorylation (Shearn et al., 2013, Shearn et al., 2011b, Covey et al., 2010, Covey et al., 2007, Smith, 2022, Suh et al., 2018). However, as often observed with LPPs, opposite effects have also been reported, where Akt signalling was decreased in response to HNE. HNE selectively led to phosphorylation of Akt2 (one of three isoforms of Akt) in insulin-dependent stimulation of the Akt2 pathway in HepG2 cells, but downstream signalling of Akt was inhibited. This inactivation of phosphorylated Akt was due to HNE-Akt2 covalent adducts, which were mapped to His196, His276 and Cys311 (Shearn et al., 2011a).

1.3. The Tumour Suppressor Phosphatase and Tensin Homolog Deleted on Chromosome 10 (PTEN)

1.3.1. The Structure and Isoforms of PTEN

PTEN (also named MMAC1/TEP1) is a dual specificity protein phosphatase that was discovered in 1997 and classified as a tumour suppressor because of its frequent loss of expression in cancer (Li and Sun, 1997, Li et al., 1997, Liaw et al., 1997, Myers et al., 1997, Steck et al., 1997). PTEN structure was first elucidated by Lee *et al*. in 1999. It consists of 403 amino acid residues and has 2 main domains (Figure 1.5): a N-terminal phosphatase domain (residues 15–185) containing the active site defined by the signature motif HCXXGXXR, including the catalytic Cys124, responsible for its phosphatase activity and a C-terminal C2 domain (residues 186–351) that allows membrane recruitment and binding (Lee et al., 1999). These two domains are flanked by disordered region that were not included in the original crystal structure of PTEN: a N-terminal sequence (residues 1-14) constituting the phosphatidylinositol-(4,5)-bisphosphate (PIP2)-binding domain (PBD) (Walker et al., 2004) and a C-terminal tail (residues 352-403) that contains PEST sequences (rich in proline (P), glutamic acid (E), serine (S) and threonine (T)) and a PDZ-binding motif (Georgescu et al., 1999).

The N-terminal PBD domain consists of a 14 residues-long sequence (MTAIIKEIVSRNKR) containing multiple basic residues that determine PTEN's binding to anionic lipids of the

membrane and its phosphatase activity through an allosteric mechanism (Campbell et al., 2003, Walker et al., 2004). It is a disordered region that folds upon binding to the membrane into an α-helix, facilitating the formation a lipid-binding pocket for its substrate (Wei et al., 2015, Redfern et al., 2008). Recently, it was suggested that the PBD exists in multiple conformations, including the α-helix conformation observed in previous studies, which can affect catalytic residues, suggesting a role in regulation of PTEN functions (Dawson et al., 2022).

The N-terminal phosphatase domain consists of a five-stranded β-sheet surrounded by two α-helices on one side and four on the other. The phosphatase active site pocket for phosphatidylinositol-(3,4,5)-triphosphate (PIP3) is surrounded by the “P” loop (residues 123–130), the “WPD” loop (residues 91–94) and the “TI” loop (residues 167–168), which form its walls. The “P” loop consists of a HCXXGXXR motif present in the active sites of protein tyrosine phosphatases (PTPs) and dual specificity protein phosphatases (Lee et al., 1999). In this motif, the catalytic cysteine Cys124, and Arg130 residues are essential for catalysis (Lee et al., 1999, Mighell et al., 2018) while His123 and Gly127 contribute to the “P” loop conformation (Lee et al., 1999). The Lys125 and Lys128 in this motif are basic residues and, together with the Lys93 in the “WDP” loop, they confer a highly basic character to the active site pocket, giving a favourable environment for binding of the negatively charged substrate PIP3 (Lee et al., 1999). The catalysis of PIP3 dephosphorylation by PTEN’s catalytic Cys124 involves two successive steps: the formation of a phosphoenzyme intermediate, where Cys124 in the active site becomes thiophosphorylated, followed by the hydrolysis of the phosphoenzyme intermediate through the action of Asp92 in the WPD loop (Xiao et al., 2007). Additionally, the phosphatase domain contains the "arginine loop", which spans residues 35–42. This loop creates a positively charged region on the phosphatase domain that is crucial for membrane binding and serves as contact point for the phosphatase domain's interaction with membranes (Masson et al., 2016).

The C-terminal C2 domain folds into a β-sandwich structure consisting of two antiparallel β-sheets with two short α-helices intervening between the strands. Two additional basic regions situated in the C2 domain, the CBR3 loop (residues 259–269), containing five lysine residues (conferring a net +5 positive charge to this sequence), and the solvent exposed Cα2 helix (residues 327–335), containing three lysine residues, are essential to membrane binding by electrostatic interactions with membrane anionic lipids (Lee et al., 1999, Shenoy et al., 2012, Yasui et al., 2014, Campbell et al., 2003). Interestingly, membrane binding increases the β-sheet content of the domain, suggesting that the interaction of these regions could lead to folding events (Redfern et al., 2008). These basic amino acids of the C2 domain face the same direction and are near the phosphatase active site (Lee et al., 1999).

They form a membrane-binding regulatory interface and interact with the inhibitory phosphorylated C-terminal tail, regulating PTEN function (Nguyen et al., 2014). It also has been proposed that a C2 domain-phosphatase domain association could facilitate PTEN positioning for catalysis of dephosphorylation of PIP3 (Das et al., 2003).

The C-terminal tail is considered intrinsically disordered (Malaney et al., 2013). It is essential to the tumour-suppressor role of PTEN as mutations in this region lead to loss of phosphatase activity. Two PEST sequences (residues 350–375 and 379–396) and a PDZ binding motif (residues 401-403, TKV) were identified in the C-terminal tail of PTEN (Georgescu et al., 1999). PEST sequences are polypeptides enriched in proline, glutamic acid, serine and threonine residues serving as proteolytic signals for rapid degradation of proteins exerting these sequences (Rechsteiner and Rogers, 1996). However, the PEST sequences in PTEN do not follow this rule as they are associated with enhanced PTEN stability and their deletion was shown to lead to decreased PTEN expression levels via rapid degradation (Georgescu et al., 1999). PDZ binding motives are short recognition modules for protein-protein interaction and organization of cell signalling assembly (Harris and Lim, 2001). This motif allows PTEN to interact with proteins. For instance, it was shown that the PTEN-microtubule-associated serine and threonine kinase 2 interaction was mediated by the PDZ binding motif of PTEN and the formation of this complex could modify PTEN subcellular localization (Terrien et al., 2012). The C-terminal tail has a critical role in regulating the conformation of PTEN: phosphorylation of the C-terminal tail causes a conformational change that masks the PDZ binding domain, reducing the ability of PTEN to bind to PDZ domain-containing proteins (Vazquez et al., 2001). In conjunction with the PBD, the C-terminal tail allows PTEN to switch from an “open” to “closed” conformation. This mechanism depends on the phosphorylation state of the C-terminal tail and regulates membrane association and full activation of PTEN (Malaney et al., 2013, Rahdar et al., 2009, Nussinov et al., 2021).

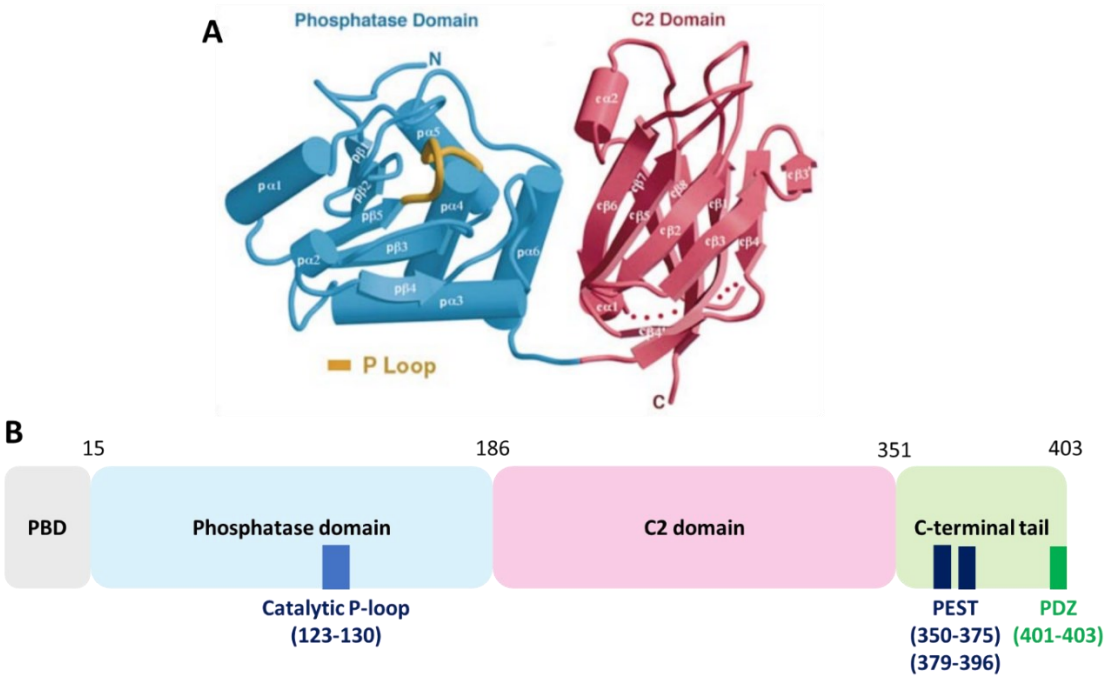

Figure 1.5. Structure and functional domains of PTEN.
(A) shows the crystal structure of PTEN, highlighting the N-terminal phosphatase domain in blue, the catalytic P-loop in yellow and the C-terminal C2 domain in red. This crystal structure does not represent the intrinsically disordered regions of PTEN (N-terminal PBD, sequence 286–309 and C-terminal tail). Reproduced with permission from Lee *at al.* (1999). (B) shows a schematic of PTEN domains. Numbers correspond to the position of residues.

PTEN has two isoforms that differ from the canonical form by extension of the N-terminus. The first discovered isoform, PTENα (also called PTEN-Long), is produced by alternative translation at the initiation codon CUG which is 5' of and in-frame with the canonical translation initiation codon AUG. PTENα extends canonical PTEN's N-terminus by 173 amino acids, leading to a 576 amino acid-long protein (Hopkins et al., 2013). PTENβ, the second isoform, is also translated from an alternative initiation codon 5' of and in-frame with the canonical initiation codon but only extends the N-terminus by 146 residues to canonical PTEN, leading to a 549 amino acid-long protein (Liang et al., 2017). Additionally, PTEN can form functional homodimers in solution, which are stabilized by its unphosphorylated C-terminal tails (Heinrich et al., 2015).

1.3.2. Subcellular Localization of PTEN and Associated Functions

Initially, PTEN was thought to localize exclusively in the cytoplasm and to associate transiently with the plasma membrane by electrostatic interactions with phosphatidylserines (Shenoy et al., 2012, Bononi and Pinton, 2015). However, several additional localizations of the protein have been reported more recently, including the nucleus and nucleolus, the mitochondria surface, mitochondria-associated-membranes and the endoplasmic reticulum. Additionally, PTEN can be secreted and enter neighbouring cells where it can be active (Bononi and Pinton, 2015). In different cell compartments, PTEN exerts different functions

(Figure 1.6). PTENα was found to be co-localized with the canonical PTEN at the mitochondria and also secreted, and PTENβ was predominantly found in the nucleus (Hopkins et al., 2013, Chow and Salmena, 2020).

In the cytoplasm, PTEN transiently associate with the plasma membrane. When associated with the membrane, PTEN dephosphorylates PIP3 to yield PIP2 (Maehama and Dixon, 1998, Ramaswamy et al., 1999). Through this lipid phosphatase activity, PTEN acts as an inhibitor of the phosphoinositide-3-kinase signalling pathway, which is involved in the oncogenic processes of cell survival, proliferation, migration and growth. Akt, the principal effector of the pathway, requires PIP3 for its activation by phosphorylation and PTEN down-regulates the abundance of PIP3, thereby down-regulating activation of Akt (Fumarola et al., 2014). This function corresponds to the canonical function of PTEN, categorizing it as a tumour suppressor. PTEN also exerts a non-canonical protein phosphatase activity against serine, threonine and tyrosine phosphoproteins (Besson et al., 1999). In the cytoplasm, PTEN can block cell migration by dephosphorylating the focal adhesion kinase (FAK) protein, stop the cell cycle in the G1 phase with a phosphatase-mediated down-regulation of cyclin D1 and directly dephosphorylate an array of proteins involved in cell motility and migration thereby inhibiting their function. Interestingly, PTEN may auto-dephosphorylate phosphorylation sites on its own C-terminal sequence to auto-regulate its activity (Chow and Salmena, 2020).

In the nucleus, the phosphatase shows additional functions that support its tumour suppressor role. PTEN can be associated with the centromere protein-C, a component of the kinetochore involved in centrosome separation, and regulates the expression of Rad51, which reduces DNA damage in order to maintain chromosomal stability and control DNA repair (Shen et al., 2007). Furthermore, PTEN enhances the tumour-suppressive activity of the anaphase-promoting complex (APC)-APC/C activator protein (CDH1) in a phosphatase-independent manner by directly interacting with anaphase-promoting complex/cyclosome (APC/C) and promoting its association with CDH1 (Song et al., 2011). Interestingly, recombinant PTEN harbouring a genetically-engineered nuclear localization signal (NLS), which artificially forced PTEN to adopt a nuclear localization, was able to dephosphorylate Akt as a pool of activated Akt exists in the nucleus; although to a lesser extent than wild-type PTEN, which can access both cytoplasmic and nuclear Akt (Trotman et al., 2007).

Nuclear PTEN mainly contributes to the maintenance of genome integrity and to the control of DNA replication, chromatin organization and cell cycle, functions that are relevant to its tumour-suppressor role. DNA instability is a consequence of various incidents including DNA replication errors, unequal chromosome segregation, natural decay of DNA and exposure to

genotoxic agents and cells have evolved to tackle this using a multitude of preventive mechanisms and damage responses to maintain genome integrity (Wang and Lindahl, 2016). PTEN was found to be essential to genome integrity by associating with centrometric protein C, a centromere-specific binding protein that allows linkage between centromere and kinetochore (Shen et al., 2007) and by dephosphorylating the mitotic kinesin motor EG5, promoting its interaction with microtubules and centrosomes to ensure proper chromosome segregation (He et al., 2016). PTEN seems to maintain chromatin structure by interacting with histones H1 and HP1α (Gong et al., 2015, Chen et al., 2014). It was also proposed that PTEN could play a role in DNA double-strand break (DSB) repair by regulating transcription levels and recruitment to DNA damage sites of Rad51, a major component of the homologous recombination-directed repair pathway (Shen et al., 2007, Bassi et al., 2013, Ma et al., 2019, Hou et al., 2019), although another report contradicted this and suggested it could be cell type-dependent (Sinha et al., 2020). In this context, Bassi *et al.* reported an impaired homologous recombination-directed DNA repair in PTEN-deficient cells and cells lacking a nuclear version of PTEN modified by small ubiquitin-like modifier (SUMO) at the lysine 254 (Lys254). This group found that the SUMO-PTEN was necessary for Rad51 recruitment to the DNA damage site and *foci* formation in response to DNA DSBs and this was negatively regulated by the protein kinase Ataxia telangiectasia mutated (ATM) which phosphorylates PTEN on serine 398 (Ser398) leading to its exclusion from the nucleus (Bassi et al., 2013). This phosphorylation of PTEN by ATM was more recently shown to promote PTEN interaction with the mediator of DNA damage checkpoint 1 (Zhang et al., 2019), which plays a critical role in DNA damage checkpoint response by working with histone H2AX to promote recruitment of repair proteins to the sites of DNA breaks (Stewart et al., 2003). DNA DSBs lead to di-methylation of PTEN at Lys349 by nuclear receptor binding SET domain protein 2, which allows recruitment of PTEN to DNA damage sites and repair of DSBs partly through dephosphorylation of γH2AX (Zhang et al., 2019).

The nucleus/cytoplasm partitioning of PTEN varies throughout the cell cycle, and nuclear PTEN levels are particularly high during the G0-G1 phase of the mitosis when cells are not actively dividing (Ginn-Pease and Eng, 2003). This was explained by the role of nuclear PTEN in cell cycle arrest where it down-regulates phosphorylation of MAPK to diminish nuclear levels of cyclin D1 (Radu et al., 2003, Chung and Eng, 2005), which, when accumulated in the nucleus during the G1 phase, promotes the transition to the S phase leading to cell cycle progression (Baldin et al., 1993). Nuclear PTEN directly enhances the activity of APC/C in a phosphatase-independent manner by promoting its association with CDH1 (Song et al., 2011). APC/C-CDH1 complex controls mitosis including mitotic exit and maintenance of the G1 phase (Li and Zhang, 2009), corroborating the role of PTEN in cell

cycle arrest. Aside from G0-G1, PTEN plays a role in decatenation of DNA in G2 and M phases through stabilization of TOP2A, a DNA topoisomerase (Kang et al., 2015), and controls the DNA replication process by dephosphorylating minichromosome maintenance complex component 2 at serine 41 (Ser41) and restricts replication fork progression under replicative stress (Feng et al., 2015).

PTEN localized in cell organelles shows additional functions. PTEN localized at the endoplasmic reticulum (ER) directly competes with F-box/LRR-repeat protein 2 for binding to the type 3 IP3 receptor (ER membrane channel), leading to the inactivation of Akt and transfer of Ca^{2+} from the ER to the mitochondria, resulting in Ca^{2+}-dependent apoptosis (Bononi et al., 2013). Finally, it was suggested that PTEN in mitochondria could regulate mitochondrial oxidative phosphorylation states and bioenergetics (Comelli et al., 2018). However, the role of PTEN in cell organelles is not yet well understood.

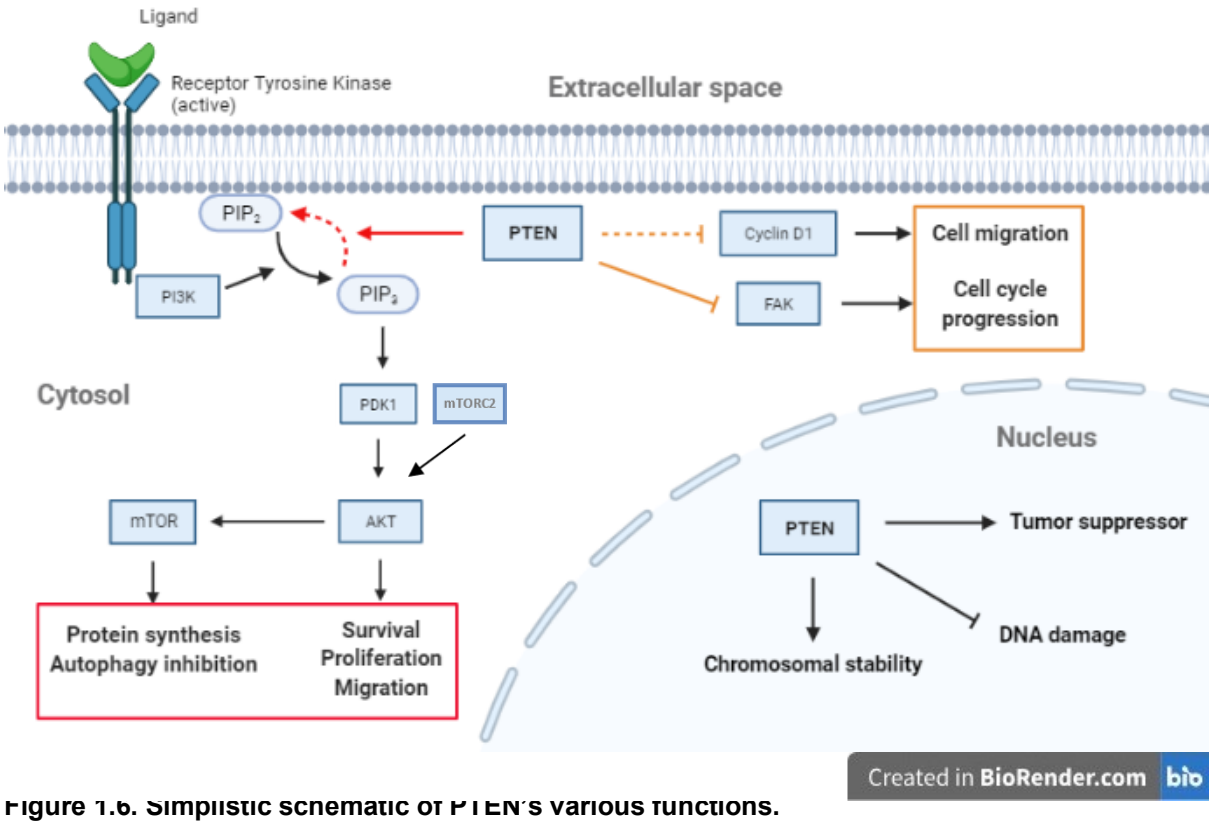

Figure 1.6. Simplistic schematic of PTEN's various functions.
Signalling in red shows the canonical function of PTEN via dephosphorylation of PIP3. Signalling in orange shows non-canonical functions of PTEN. Created with BioRender.com. PIP2: phosphatidylinositol-4,5-bisphosphate, PIP3; Phosphatidylinositol-3,4,5-trisphosphate; PI3K: Phosphoinositide 3-kinase; PDK1: phosphoinositide-dependant kinase 1; mTOR: mammalian target of rapamycin; Akt: protein kinase B; FAK: focal adhesion kinase.

1.3.3. Focus on the Role of PTEN in the PI3K/Akt Pathway

Phosphoinositide 3-kinases (PI3Ks) are plasma membrane-associated proteins that phosphorylate the 3′-hydroxyl group of phosphatidylinositides (PtdIns). They are divided into class I, II and III: class I PI3Ks are heterodimers constituted of a catalytic subunit p110 and a regulatory subunit p85; class II PI3Ks are monomeric proteins called PI3K-C2α, PI3K-C2β and PI3K-C2γ; and class III is a heterodimer of VPS34 with the myristoylated, membrane-associated VPS15. While the myotubularin (MTM) family phosphatases MTM1 and MTMR2 remove the 3′ phosphate from PtdIns(3)P phosphorylated by class II and class III PI3Ks, PTEN is responsible for the hydrolysis of the 3'-phosphate group phosphorylated by class I PI3Ks (Thorpe et al., 2015). In the absence of activating signals, p85 interacts with p110, inhibiting p110 kinase activity. Upon receptor tyrosine kinase or G-protein coupled receptor activation by insulin, growth factors, cytokine or hormones, class I PI3Ks are recruited to the plasma membrane, where p85 inhibition of p110 is relieved and p110 phosphorylates PIP2 to generate PIP3 (Thorpe et al., 2015, Hemmings and Restuccia, 2012, Osaki et al., 2004, Yang et al., 2019). PIP3 is a second messenger that recruits kinases with a pleckstrin homology domain (PH-domain) to the membrane. Therefore, PIP3 recruits the central effector of the pathway, Akt, and its activating kinase phosphoinositide-dependant kinase 1 (PDK1), allowing PDK1 and mammalian target of rapamycin complex 2 (mTORC2) to phosphorylate Akt on Thr308 and Ser473, respectively, leading to its activation (Denley et al., 2009, Manning and Toker, 2017, Guertin et al., 2006, Baffi et al., 2021). Additionally, Ser473 can be phosphorylated by DNA-activated protein kinase (DNA-PK), leading to its full activation (Feng et al., 2004).

Once active, Akt phosphorylates downstream signalling proteins to enable glycolysis, cell cycle progression, proliferation, cell growth and survival, processes involved in oncogenesis (Georgescu, 2010). It phosphorylates mouse double minute 2 homolog (MDM2) on serine 166 and 186, increasing the nuclear localization and stability of MDM2, which, in turn, decreases p53 levels and transcriptional activity to prevent cell senescence in stress conditions (Chibaya et al., 2021, Mayo and Donner, 2001). Akt also plays a role in the NF-κB signalling. Akt stimulates IKK activity by phosphorylation on Thr23 in the IKKα subunit. This leads to an IKK complex-mediated activation of the NF-κB transcription factor which stimulates oncogenic transformation induced by Akt (Bai et al., 2009). It was also shown that the mammalian target of rapamycin complex 1 (mTORC1)-associated protein Raptor is required for the ability of Akt to induce NF-κB activity (Dan et al., 2008). While mTORC1 is inhibited by tuberous sclerosis complex 1 and 2 (TSC1 and TSC2), activated Akt phosphorylates TSC2 to inhibit the TSC1/2 GAP activity toward the small GTPase Rheb, which is required to activate mTORC1. Therefore, Akt participates in the activation of mTORC1 (Bhaskar and Hay, 2007). The activated mTORC1 promotes cell growth primarily

through the activation of key anabolic processes: biosynthesis of macromolecules, including proteins, lipids, and nucleotides to build the biomass underlying cell, tissue, and organismal growth (Ben-Sahra and Manning, 2017). Activated Akt also inhibits three key downstream effectors: forkhead box O (FOXO); glycogen synthase kinase-3 (GSK3); and Bcl2-associated agonist of cell death (BAD). FOXO plays a key role in inhibiting cell growth and promoting apoptosis by triggering the expression of various pro-apoptotic proteins from the Bcl2 family, which target mitochondria, stimulating the production of death receptor ligands like Fas ligand and tumour necrosis factor-related apoptosis-inducing ligand, and increasing the levels of several cyclin-dependent kinase inhibitors. Through its interaction with p53, FOXO also acts as a significant tumour suppressor across different types of cancers. Phosphorylation of FOXO by Akt inhibits transcriptional functions of FOXO and therefore contributes to cell survival, growth and proliferation (Zhang et al., 2011). GSK3, a serine/threonine kinase, was first recognized for its role in regulating insulin-dependent glycogen synthesis. It has since been found to participate in various cellular processes such as differentiation, growth, motility, and apoptosis. Dysregulation of GSK-3 is associated with several human diseases, including Alzheimer's disease, type 2 diabetes, and cancer (Forde and Dale, 2007). Several kinases can phosphorylate GSK3. Amongst them, Akt phosphorylates GSK3 on Ser9 (for GSK3β) or Ser21 (for GSK3α) and inhibits its activity, leading to increased glycogen synthesis (Cross et al., 1995). BAD function, promoting cell death, is modulated by phosphorylation at two sites, serine 112 (Ser-112) and serine 136 (Ser-136). Akt phosphorylates BAD at Ser136, which correlates with cell survival (Datta et al., 1997).

PTEN acts as a negative regulator of this pathway and biological processes induced by activation of Akt. Indeed, PTEN dephosphorylates PIP3 into PIP2, blocking the signalling cascade by opposing the action of PI3K and negatively regulating the activation of Akt (Sun et al., 1999, Xiao et al., 2007, Stambolic et al., 1998, Maehama and Dixon, 1998), downregulating the above oncogenic processes. This is particularly important as studies have shown that cells lacking wild-type PTEN from PTEN-deficient mice (Stambolic et al., 1998), from gliomas (Haas-Kogan et al., 1998), or from patients with Cowden disease (Myers et al., 1998) have elevated levels of PIP3 associated with increased activity of Akt. This indicated that PTEN mainly exerts its tumour-suppressor function by negatively regulating the oncogenic PI3K/Akt pathway. Figure 1.7 shows a simplified PI3K/Akt signalling pathway, highlighting the role of PTEN. Considering the essential role of this pathway in protein synthesis, metabolism, cell growth, cell survival, cell proliferation and migration and cell cycle progression, PTEN dysfunction can contribute to the onset or development of multiple disorders such as Cowden syndrome, Proteus syndrome,

Bannayan–Riley–Ruvalcaba syndrome, and Lhermitte–Duclos disease (Blumenthal and Dennis, 2008) or various cancers (Ali et al., 1999, Alimonti et al., 2010, Ashrafizadeh et al., 2020, Lynch et al., 1997, Perren et al., 2000, Steck et al., 1997). Therefore, tuning of its functions is necessary to maintain cellular homeostasis.

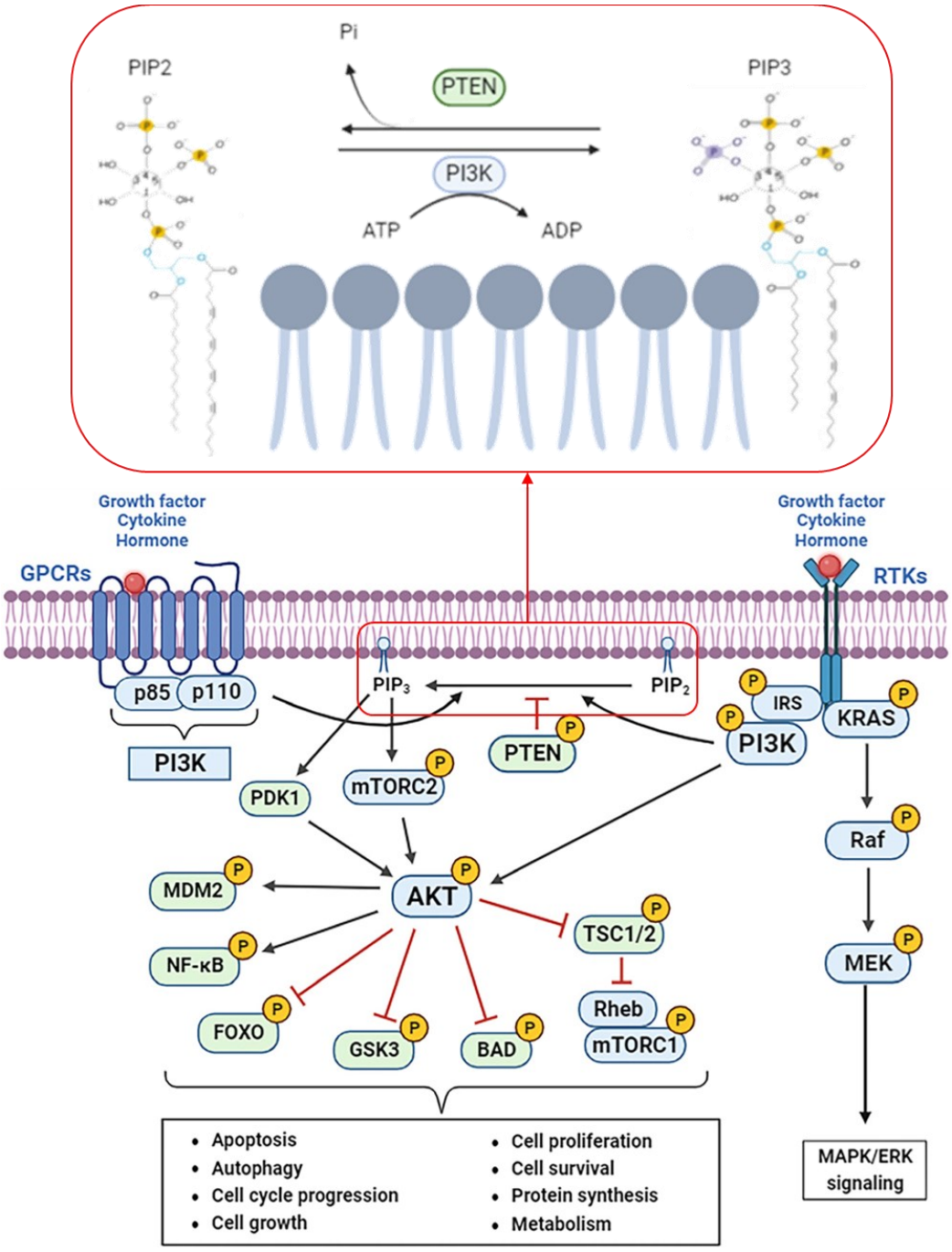

Figure 1.7. Schematic of the PI3K/Akt signalling pathway in which PTEN acts as a negative regulator.

Altered with permission from P.D. Leiphrakpam and C. Are (2024). PIP2: phosphatidylinositol-4,5-bisphosphate, PIP3; Phosphatidylinositol-3,4,5-trisphosphate; Akt: protein kinase B; BAD: Bcl2-associated agonist of cell death; ERK: extracellular signal-regulated kinase; FOXO: forkhead box O; GSK3: glycogen synthase kinase-3, KRAS: kirsten rat sarcoma virus; MAPK: mitogen-activated protein kinase; MEK: mitogen-activated protein kinase kinase: MDM2: mouse double minute 2

homolog; mTOR: mammalian target of rapamycin; mTORC1: mammalian target of rapamycin complex 1; mTORC2: mammalian target of rapamycin complex 2; NF-κB: nuclear factor-kappa B; PDK1: phosphoinositide-dependent kinase 1; PI3K: phosphatidylinositol 3-kinase; RAF, rapidly accelerated fibrosarcoma; TSC1/2: tuberous sclerosis proteins 1/2.

1.3.4. Regulation Mechanisms

1.3.4.1. Regulation of PTEN Subcellular Localization

PTEN subcellular localization is tightly regulated between the cytoplasmic and nuclear compartments. A short sequence at the N-terminal region of PTEN (residues 19–25) was found to build a cytoplasmic localization sequence (CLS) that is essential for cytoplasmic localization and retention. Mutations of residues within this sequence preserve lipid phosphatase activity and induce nuclear localization with a concomitant loss of growth-regulatory functions (Denning et al., 2007). Initially, it was believed that PTEN did not contain a NLS or nuclear export signal (NES) (Li et al., 1997, Trotman et al., 2007), sequences that direct proteins to or out of the nucleus through a nuclear pore complex (Lu et al., 2021), and was therefore thought to be a cytoplasmic protein that could enter the nucleus by diffusion (Liu et al., 2005a). However, although PTEN indeed lacks a traditional NLS, Chung *et al.* discovered four NLS-like sequences in PTEN. Amongst those, combinations of the sequences between residues 266-269 (KKDK) and 159-164 (RTRDKK) or 233-237 (RREDK) were fundamental for nuclear import of PTEN by major vault protein in MCF-7 cells (Chung et al., 2005). Soon after, nuclear exclusion motifs and a nuclear localization domain at the N-terminus of PTEN sequence were discovered: a sequence between residues 1-32 was found to lead to PTEN accumulation in the nucleus in human glioblastoma U87MG cells, which was mediated by an importin-related nuclear transport mechanism dependent on importin α proteins and the activity of the Ras-related nuclear protein Ran-GTPase (Gil et al., 2006). This combined evidence suggests that the nuclear import of PTEN is mediated via multiple pathways.

A few PTMs were found to regulate the nuclear localization of PTEN, including the addition of ubiquitin and SUMO. Indeed, monoubiquitination of the lysines at the 289th position (Lys289) and at the 13th position (Lys13) was found to be essential for PTEN nuclear import (Trotman et al., 2007). Additionally, SUMOylation of PTEN on Lys254, Lys266 and Lys289 also promotes its nuclear localization as SUMOylation-deficient PTEN mutants were excluded from the nucleus (Bassi et al., 2013, González-Santamaría et al., 2012), although Huang *et al.* showed that SUMOylation of Lys254 or Lys266 contributes to membrane binding (Huang et al., 2012). The nuclear import of ubiquitinated PTEN was found to be endosomal and dependent on Ras-related protein Rab5 and E3 ligase adaptor protein Ndfip1, where Ndfip1 binds to PTEN and regulates PTEN ubiquitination via the Nedd4 family

of E3 ubiquitin ligases (Li et al., 2014, Howitt et al., 2015, Howitt et al., 2012, Mund and Pelham, 2010). On the other hand, nuclear export of PTEN is regulated by the herpesvirus-associated ubiquitin protease (HAUSP, also called USP7), which induces de-ubiquitination of PTEN and results in exclusion of PTEN from the nucleus (Song et al., 2008) as well as ATM, as described previously. The exclusion of PTEN from the nucleus during the G1-S transition can also result from a feedback regulation by the PI3K/Akt/mTOR pathway via S6K1/2 (Liu et al., 2007).

The open/closed conformational state of PTEN is particularly important for its membrane and nuclear localization. Phosphorylation of serine/threonine clusters (residues Ser380, Thr382, Thr383, Ser385) in the C-terminal region of PTEN leads to a closed conformation with the C-terminal region associating with the core region at the surface. However, when this serine/threonine cluster is dephosphorylated, the C-terminal region dissociates from the core region, which leads to an open conformation of PTEN. In the open conformation, a membrane-binding regulatory interface, composed of the catalytic site, the calcium binding region 3 loop and the Cα2 loop, becomes accessible and stimulates the recruitment of PTEN to the plasma membrane (Nguyen et al., 2014, Nguyen et al., 2015, Vazquez et al., 2001, Das et al., 2003, Vazquez et al., 2000) and phosphorylation of Ser380 negatively regulates nuclear localization of PTEN (Chang et al., 2008). This, on the other hand, also makes Lys13 accessible for mono-ubiquitination, which promotes the transport of PTEN to the nucleus (Trotman et al., 2007, Kato et al., 2020). Interaction with the scaffold proteins MAGI-1b, MAGI-2, and MAGI-3 via the PDZ-binding motif leads to translocation to the membrane (Kotelevets et al., 2005, Subauste et al., 2005, Wu et al., 2000) and PTEN can also be translocated to the membrane by the RhoA-associated kinase (ROCK) through phosphorylation at Thr223, Ser229, Thr319 and Thr321 in the C2 domain (Li et al., 2005). The regulation of PTEN localization is correlated to the regulation of its functions, especially in the case of translocation to the membrane, which enhances its activity towards PIP3 and its contribution in inhibiting the PI3K/Akt pathway.

1.3.4.2. Regulation of PTEN Activity

PTEN activity can be regulated by its level of expression. Activation of the PI3K pathway by insulin and other growth factors regulates PTEN expression by controlling its mTOR-dependent translation. This negative feedback regulation is characterized by induction of PTEN expression, which limits the duration of the signal and prevents overactivation of the pathway (Mukherjee et al., 2021). PTEN gene expression is positively regulated by early growth response protein 1 (Virolle et al., 2001), PPARγ (Patel et al., 2001), Myc proto-oncogene (Kaur and Cole, 2013), p53 (Stambolic et al., 2001) and transcriptional factor

activating transcription factor-2 (Shen et al., 2006). On the other hand, it is negatively regulated by the NF-κB (Xia et al., 2007) and transforming growth factor β (Chow et al., 2010, Chow et al., 2008a, Chow et al., 2008b) signalling pathways and by c-Jun (Hettinger et al., 2007) and the hairy and enhancer of split-1 (Gao et al., 2015) transcription factors. Additionally, miRNAs (small non-coding single-stranded RNAs that modulate gene expression) affect PTEN expression through PTEN mRNA silencing and protein level reduction (Hong et al., 2010, Jin et al., 2013).

The open/closed model of PTEN described in section 1.3.4.1 is important for PTEN's function. Indeed, PTEN's action on PIP3 requires membrane binding. In the closed conformation, phosphorylation of PTEN's C-terminal tail causes it to bind to the phosphatase and C2 domains, preventing membrane binding and keeping PTEN inactive. Upon dephosphorylation, PTEN adopts an open conformation, releasing the tail and allowing membrane association through electrostatic interactions between the C2 domain and negatively charged lipids like phosphatidylserine and selective interactions with PIP2 via the N-terminal PBD. This open state activates the phosphatase domain and promotes PTEN's tumour-suppressive function, suggesting that phosphorylation-dependent intramolecular interactions tightly regulate PTEN activity (Rahdar et al., 2009, Vazquez et al., 2001, Vazquez et al., 2000, Georgescu et al., 1999). These residues are phosphorylated by the protein kinase CK2 (Torres and Pulido, 2001).

Other kinases including ROCK and GSK3β regulate phosphorylation levels of PTEN. GSK3β phosphorylates PTEN at Ser362 and Thr366 as part of a negative feedback loop of the PI3K/Akt signalling pathway (Al-Khouri et al., 2005, Jang et al., 2013). Phosphorylation was shown to generally be a PTM linked to the inactivation of PTEN in cancer cells (Silva et al., 2008, Nakahata et al., 2014). However, when PTEN is translocated to the membrane by the ROCK-induced phosphorylation at Thr223, Ser229, Thr319 and Thr321, its phosphatase activity is increased (Li et al., 2005). Phosphorylation is not the only PTM responsible for regulation of PTEN. In contrast to monoubiquitination, which directs PTEN to the nucleus, polyubiquitination of PTEN by the E3 ubiquitin-protein ligase NEDD4-1 triggers its degradation via the proteasome (Wang et al., 2007, Amodio et al., 2010, Hong et al., 2014). Additional E3 ligases were also proposed to fulfil this role: the NEDD4-like E3 ubiquitin-protein ligase (Maddika et al., 2011), X-linked inhibitor of apoptosis protein (Van Themsche et al., 2009) and E3 ubiquitin-protein ligase CHIP (Ahmed et al., 2012). On the other hand, deubiquitination stabilizes and actively regulate PTEN (Yuan et al., 2015, Zhang et al., 2013, Christine et al., 2022). Acetylation also plays a key role in regulating PTEN activity and function. The histone acetyltransferase PCAF interacts with PTEN and acetylates Lys125 and Lys128 in response to growth factor stimulation, which inhibits PTEN activity as these

sites are within the phosphatase domain (Okumura et al., 2006). Additionally, PTEN is acetylated by p300-CREB-binding protein at Lys402, located in the C-terminal PDZ domain-binding motif. This modification impacts PTEN's interactions with other proteins, further influencing its function (Ikenoue et al., 2008).

Finally, protein-protein interactions play a key role in regulating PTEN function. The formation of PTEN homodimers at the plasma membrane was found to lead to the full activation of its phosphatase activity towards PIP3 (Heinrich et al., 2015, Papa et al., 2014). The formation of complexes with membrane-associated guanylate kinase (MAGI)-1b, MAGI-2, and MAGI-3 that bind to PTEN's PDZ binding motif help stabilize and recruit PTEN to membrane complexes, where PTEN dephosphorylates PIP3, thus contributing to the negative regulation of the PI3K/Akt signalling pathway (Kotelevets et al., 2005, Subauste et al., 2005, Wu et al., 2000). The interaction between mammalian disks large homologue 1 and PTEN has been shown to enhance PTEN's tumour suppressor function and promote axonal myelination in Schwann cells. This interaction likely prevents PTEN degradation and increases its stability (Cotter et al., 2010). On the other hand, proteins such as PIP3 Rac exchanger 2a (PREX2a), shank-interacting protein-like 1 (SIPL1), and α-mannosidase 2C1 (MAN2C1) have been identified as negative regulators of PTEN. These proteins suppress PTEN's lipid phosphatase activity, leading to increased levels of phosphorylated Akt, thus activation of the PI3K/Akt pathway (Fine et al., 2009, He et al., 2010, He et al., 2011). PREX2a binds to PTEN on the C2 domain and C-terminal tail but not the PDZ-binding motif and PTEN inhibition is achieved via PREX2a's DHPH domain (Fine et al., 2009), SIPL1 was found to interact with the N-terminal portion of PTEN through its ubiquitin-like domain (He et al., 2010) and MAN2C1 binds to PTEN by means of multiple domains in the C-terminal portion of the protein but the binding site on PTEN was not identified (He et al., 2011).

1.3.4.3. Redox Sensitivity of PTEN

As described previously, PTEN contains several residues in domains important for its function, including the catalytic cysteine (Cys124) and the multiple lysines in the "P" loop and C2 domain that facilitate substrate binding and membrane association. The nucleophilic character of these residues makes them potential targets for oxidative damage and lipoxidation by electrophilic LPPs (Forman et al., 2014). Furthermore, the catalytic region of PTEN is homologous to that of PTPs. The catalytic cysteine of protein tyrosine phosphatases usually exhibits a low pKa, thus enhancing its nucleophilicity (Karisch and Neel, 2013) and making it a preferential target for oxidants and electrophilic lipids.

The first evidence of PTEN oxidative damage was shown by Lee *et al*. in 2002. In this study, they showed that PTEN could be inactivated *in vitro* by H_2O_2 through the formation of a

disulfide bond between the catalytic cysteine Cys124 and Cys71, and H_2O_2, in cells, could lead to a shift in PTEN electrophoretic mobility, as described *in vitro*, suggesting that this disulfide bond could form in cells as well. The inhibition of PTEN function was reversible by reduction of the oxidized PTEN, notably by Trx which directly interacted with PTEN to reduce the disulfide bond and restore PTEN's function (Lee et al., 2002). Oxidative inhibition of PTEN was later confirmed in cells; H_2O_2-treated Swiss 3T3 cells lost PTEN activity in a dose-dependent manner. Furthermore, the basal level of PIP3 increased after treatment with H_2O_2 in U87MG cells expressing PTEN, correlating with increased activation of Akt, while this was not true for cells lacking PTEN, suggesting that the accumulation of PIP3 was due to PTEN inhibition, making it unable to negatively regulate Akt activation (Leslie et al., 2003). RNS are also able to modify PTEN by S-nitrosylation. Nitric oxide (NO•) was found to suppress PTEN phosphatase activity and trigger its proteasomal degradation, effects that seemed to be the result of S-nitrosylation on Cys83 (Kwak et al., 2010, Numajiri et al., 2011). Although the subcellular localization of PTEN is tightly regulated by multiple factors as described previously, evidence showed that H_2O_2-induced oxidative stress leads to a nuclear accumulation of PTEN (Chang et al., 2008, Choi et al., 2013). Additionally, mRNA levels of the PTEN gene in HepG2 cells were found to be decreased in stress conditions (Kim et al., 2013), suggesting that oxidative stress could play a role in regulation of PTEN expression levels. However, this was true for treatments with superoxide radicals and serum deprivation but not for H_2O_2 treatments (Kim et al., 2013). It seems that the oxidative sensitivity of PTEN could be highly influenced by oxidative stress levels. Inactivation of Akt has previously been observed at low levels of oxidative stress, where PTEN did not undergo significant thiol oxidation, but a further increase in H_2O_2 levels led to oxidation and inhibition of PTEN and correlated activation of Akt (Tan et al., 2015). In fact, increased oxidative stress can either inhibit or enhance Akt phosphorylation. This differential response depends on a combination of effects on multiple proteins involved in the PI3K/Akt pathway: Akt, PTEN and protein phosphatase 2A (PP2A), a phosphatase that dephosphorylates Akt (Piguet and Dufour, 2011). At low levels, oxidation of Akt, but not the phosphatases PTEN or PP2A, caused a decline in Akt phosphorylation; whereas the thiol oxidation of Akt, PTEN and PP2A increased Akt phosphorylation at higher levels. (Tan et al., 2015). This was illustrated in a study by Yu *et al.* that contrasted with the effects of oxidative stress described previously. In this study, Parkinson's disease toxins-induced intracellular and mitochondrial H_2O_2 (which was most likely produced at lower concentrations than the H_2O_2 treatments administered in previous studies) activated PTEN and inactivated Akt, leading to apoptosis of neuronal cells (Yu et al., 2023).

Another aspect of PTEN regulation by oxidative stress emerged recently: the regulation of its interactome. Verrastro *et al.* compared the protein interactions of the reduced and oxidized forms of PTEN. In this study, fourteen interactors were over 2.5 times more abundantly bound to oxidized PTEN compared to its reduced form, including redox-sensitive and redox-insensitive proteins. Peroxiredoxin-1 and thioredoxin, proteins involved in protecting against oxidative damage, were interacting more with oxidized PTEN, suggesting a redox status-dependent interaction. Interestingly, multiple proteins involved in functioning of the actin cytoskeleton as well as DNA repair, chromosomal segregation and genomic stability were found to interact more strongly with oxidized PTEN (Verrastro et al., 2016). Although this study provided some insights into the modification of PTEN interactome in oxidative conditions, the interactors were identified from unstressed HCT116 cell lysates interacting with purified PTEN reduced or oxidized *in vitro* and the modification of PTEN's interactome could vary significantly in an oxidative context in cells.

The growing recognition of protein lipoxidation as a signalling mechanism increased the interest in such modifications in redox-sensitive proteins. Adduction of PTEN by HNE was previously reported (Shearn et al., 2013, Covey et al., 2010), as well as adduction of acrolein, 15d-PGJ_2 and Δ12-prostaglandin J2 (Δ12-PGJ_2) (Covey et al., 2010, Suh et al., 2018, Smith, 2022). Shearn *et al.* showed in 2011 that physiologically relevant concentrations of HNE could activate Akt (increased phosphorylation of Ser473 and Thr308) in a time- and concentration-dependent manner and through a PI3K-dependent mechanism in HepG2 cells and primary hepatocytes. Michael addition of HNE to PTEN, leading to its inhibition, was found to be the link between exposure to HNE and Akt activation (Shearn et al., 2011b). Two years later, the same group further examined PTEN lipoxidation and Akt activation in ethanol-fed mice. Redox balance was found to be impaired in this model, leading to PTEN lipoxidation and inhibition, and subsequent activation of Akt2 (one of the Akt isoforms) in liver. Treatment of a recombinant human PTEN with HNE led to the discovery of 9 sites of adduction on the protein (Cys71, Cys136, Lys147, Lys223, Cys250, Lys254, Lys313, Lys327 and Lys344). Among those, Cys71 and Lys327 were suggested to be particularly relevant to PTEN function as their modification may limit the substrate access to the active site or alter the association of PTEN with the membrane and thioredoxin-1, respectively. Interestingly, the catalytic cysteine could not be detected (Shearn et al., 2013). Acrolein, HNE, 15d-PGJ_2 and Δ12-PGJ_2 were also found to covalently modify and inactivate PTEN in MCF-7 cells, increasing Akt and/or β-catenin signalling and cell proliferation (Covey et al., 2010, Suh et al., 2018). The site of adduction of 15d-PGJ_2 on PTEN was identified *in vitro* and in MCF-7 cells to be Cys136, which correlated with the ROS-independent activation of Akt (Suh et al., 2018). Sites of adduction of acrolein on PTEN were also identified. Most of

them were similar to the ones observed with HNE. However, four additional residues were identified as adducted by acrolein: Lys6, Cys83, Cys296 and Cys304. Cys71, Cys136 and Cys327 appeared to mediate the loss of activity, suggesting similar mechanisms for inactivation of PTEN function (Smith, 2022). In the same study, modification of PTEN interactome upon acrolein treatments was investigated for the first time using the same method as Verrastro *et al*. Notably, E3 ubiquitin ligases were more abundantly bound to acrolein-modified PTEN, suggesting a possible role of the proteasome in regulating the existence of such LPP-modified PTEN (Smith, 2022).

1.4. Research Aims and Hypotheses

The identification of PTEN's redox-sensitivity initiated the investigation of the effects of lipid peroxidation products on PTEN's function and interactome and consequences on the PI3K/Akt pathway. However, only a small subset of LPPs, including the small reactive aldehydes HNE and acrolein and the cyclopentenones 15d-PGJ_2 and Δ12-PGJ_2, were investigated (Shearn et al., 2013, Shearn et al., 2011b, Covey et al., 2010, Suh et al., 2018, Smith, 2022) and the mechanisms underlying their effect on PTEN and its downstream signalling remain elusive.

This project therefore aimed to investigate the effects of HHE and PONPC on PTEN and its downstream signalling, broadening the range of type of LPPs studied in the context of PTEN lipoxidation by including an oxidized phospholipid for the first time. It was hypothesized that HHE and PONPC, like HNE, acrolein, 15d-PGJ_2 and Δ12-PGJ_2, could modulate PTEN activity and influence critical biological processes associated with PTEN, particularly the PI3K/Akt pathway. Notably, the structural similarity between HHE and HNE, both possessing α-β-unsaturated aldehyde functional groups, suggests a potential parallel impact on PTEN function. LPPs that can lead to PTEN lipoxidation were shown to interfere with PTEN's ability to regulate the activation of Akt kinase. Therefore, the effects of HHE and PONPC on PTEN's downstream signalling were evaluated in cancer cell lines using western blotting to determine the activation (phosphorylated) state of Akt with the hypothesis that like previously reported LPPs, HHE and PONPC could lead to activation of the pathway.

Additionally, PTEN is a protein that is localized in different cell compartments. Its functions depend on this subcellular localization and it was shown that oxidative stress could lead to a nuclear accumulation of PTEN (Chang et al., 2008). Surprisingly, the effects of LPPs on PTEN subcellular localization have never been studied and filling this knowledge gap is essential to understand how they can regulate PTEN functions. Treating cells with HHE and PONPC and analysing PTEN subcellular localization using confocal microscopy would allow determination of changes in PTEN distribution, with the hypothesis that HHE and PONPC

could modify PTEN localization through different mechanisms. PTEN localization could be modified by either direct interaction with key residues involved in PTEN's subcellular targeting or, in the case of PONPC, by trapping PTEN at the membrane by covalent binding as described by the "lipid whisker model" where the aldehydic function at the end of the truncated fatty acyl chain of oxidized lipids could protrude in the cytoplasm while the second fatty acyl chain of the lipid is anchored to the plasma membrane. This was performed in order to provide more insights into the molecular mechanisms underlying PTEN's localization changes in response to oxidative stress and lipid peroxidation products, which could correlate with the potential changes in the PI3K/Akt signalling pathway in cells exposed to HHE and PONPC with the hypothesis that altered PTEN localization due to HHE and PONPC exposure would affect its ability to regulate the PI3K/Akt pathway.

Finally, the identification of specific covalent modifications by LPPs is necessary to identify mechanisms regulating the biological effects observed under LPP exposure. Therefore, the last aim of this study was to map sites of adduction of HHE and PONPC on PTEN sequence, which could possibly identify essential residues involved in PTEN's function or localization regulation and explain the biological effects of these LPPs. Based on the structural similarity between HNE and HHE, it was expected that HHE would covalently modify similar residues to those discovered to be adducted by HNE in the study by Shearn *et al.* (Shearn et al., 2013). However, the adduction of PONPC onto PTEN could differ as its size and amphiphilic nature could limit its accessibility and interaction to some parts of the protein.

Chapter 2 – General Materials and Methods

2.1. Materials

All materials were purchased from ThermoFisher Scientific (UK) or Merck (UK), unless stated otherwise. JpExpress404 PTEN was a gift from Ramon Parsons (Addgene plasmid #49420; http://n2t.net/addgene:49420; RRID:Addgene_49420) (Hopkins et al., 2013). 809 pcDNA3 GFP PTEN was a gift from William Sellers (Addgene plasmid # 10759 ; http://n2t.net/addgene:10759 ; RRID:Addgene_10759) (Vazquez et al., 2001). The DNA maps and insert sequences of these plasmids encoding for a recombinant PTEN tagged with V5-tag and a polyhistidine (His)-tag or PTEN with a N-terminal GFP tag are detailed in Supplementary Figure 1 and Supplementary Figure 3, respectively. JpExpress404 PTEN was referred to as PTEN-V5-His plasmid DNA and pcDNA3 GFP PTEN was referred to as GFP-PTEN. HCT116 cells were obtained from Rudiger Woscholski's lab at Imperial College London (UK). MCF-7 cells were obtained from James Brown's lab at Aston University (UK). HHE was purchased from Cayman Chemical (USA) as a solution in ethanol and PONPC was purchased from Avanti® Polar Lipids (USA).

2.2. Plasmid DNA Purification

2.2.1. Bacterial Culture

TOP10 *E. coli* cells containing JpExpress404 PTEN (PTEN-V5-His) plasmid (referred to as PTEN-V5-His plasmid) and DH5α *E. coli* cells containing pcDNA3 GFP-PTEN expression plasmid were obtained as a stab culture and were previously grown to produce glycerol stocks by Sarah L. Smith (Aston University) (Smith, 2022). To expand the plasmid, TOP10 JpExpress404 PTEN and DH5α pcDNA3 GFP-PTEN cells were grown overnight (O/N) on Luria Broth (LB)-Agar plates containing 20 g/L LB and 12 g/L agar, supplemented with 100 µg/mL ampicillin, in a stationary incubator (Lenton Thermal Designs, UK) at 37˚C. Single colonies were individually inoculated into 5 mL of sterile LB media (20 g/L) supplemented with 100 µg/mL of ampicillin and incubated in a MaxQ 8000 orbital shaker (ThermoFisher Scientific, UK) O/N at 37˚C and 220 rpm. The next day, TOP10 JpExpress404 PTEN cells were processed for plasmid DNA isolation (section 2.2.2). DH5α pcDNA3 GFP-PTEN cells from the primary culture were inoculated in 250 mL of sterile LB medium supplemented with 100 µg/mL of ampicillin with a dilution of 1:200 to 1:500 and grown overnight in the orbital shaker at 37˚C, 200 rpm.

2.2.2. Plasmid DNA Isolation

Following overnight incubation, either 0.6 mL or 3 mL of the TOP10 JpExpress404 PTEN culture were collected. The 0.6 mL portion underwent centrifugation at 17,000 x g for 30 seconds at room temperature (RT), whereas a 1.5 mL aliquot of the 3 mL culture underwent initial centrifugation at 17,000 x g for 30 seconds at RT, the resulting supernatant was discarded, and the remaining culture was combined with the pellet for further centrifugation as above. Supernatants were then discarded, and cell pellets were resuspended in 600 µL of nuclease-free water (Promega, UK). Plasmid purification was carried out using the PureYield™ Mini Prep System (Promega, UK) according to the manufacturer's recommended protocol for DNA purification by centrifugation.

DH5α pcDNA3 GFP-PTEN cells from the secondary culture were pelleted by centrifugation at 4700 g for 10 minutes and purification of GFP-PTEN plasmid DNA was performed using the PureYield™ Plasmid Maxiprep System (Promega, UK) that provided all the solutions used in the procedure, excluding isopropanol and 95% ethanol. Cell pellets were resuspended in Cell Resuspension Solution, Cell Lysis Solution was added, mixed by inverting and incubated 3 minutes at RT. Neutralization solution was added directly after incubation, mixed by inverting and the flocculant mixture was centrifuged at 4700 g for 40 minutes (batch 1) or 14000 g for 20 minutes (batch 2). The lysate was filtered through a PureYield™ Clearing Column, then eluted through a PureYield™ Maxi Binding Column by centrifugation at 2000 g for 7 minutes (batch 1) or with a Vac-Mac™ vacuum manifold (Promega, UK) (batch 2). Endotoxin Removal Wash supplemented with isopropanol was added to the binding column and eluted by centrifugation at 2000 g for 6 minutes (batch 1) or using the Vac-Man™ vacuum manifold (batch 2). The column was washed with Column Wash supplemented with 95% ethanol solution by centrifugation at 2000 g for 5 minutes and left to dry for 30 minutes (batch 1) or under vacuum for 5 minutes using the Vac-Mac™ vacuum manifold. The bound plasmid DNA was eluted by centrifugating nuclease-free water through the column for 5 to 7 minutes at 2000 g. DNA concentration and purity were assessed by measuring the absorbance of the resulting solution at 260 nm and calculating the 260/230 and 260/280 (nm) ratios, respectively, using a NanoDrop 2000 (ThermoFisher Scientific, UK). The procedure given for GFP-PTEN plasmid batch 2 was also performed at +4˚C with all the solutions excluding the Cell Lysis Solution pre-cooled at +4˚C.

2.3. DNA Quantification

The quantification of the purified plasmid was conducted in triplicate using a NanoDrop 2000 (ThermoFisher Scientific, UK) by measuring absorbance at 230, 260, and 280 nm using the elution buffer included in the PureYield™ Mini Prep System (Promega, UK) kit as a blank. The Nanodrop 2000 software automatically converted absorbance values to DNA

concentration in ng/mL. This conversion involved normalizing the path length to 1 cm from 1 mm and modifying the Beer-Lambert equation C = (A × ε) / b with C = DNA concentration (ng/µL), A = absorbance at the measured wavelength (AU), ε = extinction coefficient of 50 ng-cm/µL for double-stranded DNA an b = pathlength (cm), as per the manufacturer's specifications.

2.4. Diagnostic Restriction Digestion

EcoRI and XbaI restriction sites were chosen for the digestion of the PTEN-V5-His plasmid and EcoRI and HindIII were chosen for the digestion of the GFP-PTEN plasmid. PTEN-V5-His plasmid DNA (0.2 µg/µL) was digested by EcoRI (0.2 U/µL) in 1X EcoRI+ buffer with bovine serum albumin (BSA) for linearization and a mixture of EcoRI (0.2 U/µL) and XbaI (0.2 U/µL) in 1X Tango buffer with BSA for double digestion O/N at 37˚C and subsequently set on ice. GFP-PTEN plasmid DNA (0.2 µg/µL) was digested by EcoRI (0.2 U/µL) in 1X EcoRI+ buffer with BSA and a mixture of EcoRI (0.2 U/µL) and Hind III (0.2 U/µL) in 1X Tango buffer with BSA for 90 minutes at 37˚C and subsequently set on ice. Gel electrophoresis was performed on a 1% agarose, tris-acetate-ethylenediaminetetraacetic acid (TAE) gel, loading 100 ng of plasmid DNA per well mixed with gel loading dye blue (6X) (New England BioLabs, UK) diluted to a final concentration of 1X with water. Electrophoresis was performed at 100 V for 60 to 90 minutes in TAE buffer (40 mM Tris, 20 mM acetate, 1 mM ethylenediaminetetraacetic acid (EDTA), pH 8.6). DNA was stained with a SYBR Safe DNA Gel stain solution in TAE buffer. The stained gel was imaged and processed using a G:Box XR5 and GeneSys software (Syngene, UK).

2.5. Expression of PTEN-V5-His in BL21 (DE3) *E. coli* Cells

2.5.1. Bacterial Culture

BL21 (DE3) *E. coli* cells containing PTEN-V5-His plasmid were streaked onto LB-agar plates supplemented with 100 µg/mL ampicillin and incubated O/N in a stationary incubator (Lenton Thermal Designs, UK) at 37˚C. Single colonies were individually inoculated into 10 mL of sterile LB media supplemented with 100 µg/mL ampicillin and incubated O/N in a MaxQ 8000 orbital shaker (ThermoFisher Scientific, UK) at 20˚C, 180 rpm until the OD_{600} reached 0.5-1.0. These primary cultures were used to inoculate secondary cultures with a 1:200 dilution (V:V) in sterile LB media supplemented with 100 µg/mL ampicillin (50 mL for small scale expression aiming to compare PTEN-V5-His expression levels and 10 x 400 mL for large scale expression of PTEN-V5-His for purification). The secondary cultures were incubated for 3-5 hours in a MaxQ 8000 orbital shaker (ThermoFisher Scientific, UK) at 37˚C, 220 rpm until an OD_{600} of 0.50-0.75 was reached.

2.5.2. Expression of PTEN-V5-His

When the desired OD_{600} was reached, isopropyl β-D-1-thiogalactopyranoside (IPTG) was added to a final concentration of 0.5 mM and cultures were further incubated O/N at 20˚C, 220 rpm in a MaxQ 8000 orbital shaker (ThermoFisher Scientific, UK), as optimized and described by Sarah L. Smith (Smith, 2022). The next day, cells were centrifuged at 4700 x g for 30 minutes at 4˚C. The supernatant was discarded, and cells were washed with ice cold 50 mM $NaPO_4$ pH 7.4, with 1 mM phenylmethylsulfonyl fluoride (PMSF). Cell pellets were obtained with centrifugation at 4700 x g for 30 minutes at 4˚C and stored at -20˚C until ready to be lysed.

2.5.3. BL21 (DE3) Cell Lysis

Pellets were thawed on ice for 1-2 hours and resuspended in 5 mL or 200 mL ice cold lysis buffer (50 mM sodium phosphate pH 8.0 with 500 mM NaCl, 0.1% Triton X-100, 1 mM PMSF, 1 mM dithiothreitol (DTT), 1 mg/ml lysozyme) for small scale (50 mL of culture) and large scale (2L of culture) PTEN-V5-His expression, respectively. The cell suspension was homogenized on ice using a Dounce homogenizer and incubated on a roller at 60 rpm, 4˚C for 2 hours. The lysate was sonicated on ice using a handheld sonicator with a MSF-7 probe at 50% amplitude in 10 second bursts with a 20 second rest in between, a total of 40 times, and centrifuged at 30,000 x g for 1 hour at 4˚C. The supernatant (whole lysate) was passed through a needle using a manual syringe to reduce its viscosity and filtered using a 0.45 µm syringe-filter (clarified lysate) on ice.

2.6. PTEN-V5-His Purification

2.6.1. Immobilized Metal Affinity Chromatography (IMAC)

A purification column was assembled by placing 0.5 mL of HIS-Select® Nickel Affinity Gel (Millipore, Sigma-Aldrich, UK) between two porous polyethylene discs at the base of an empty 5 mL gravity flow column (Pierce, ThermoFisher Scientific, UK). The binding buffer (25 mM $NaPO_4$ pH 8.0 with 500 mM NaCl, 0.1% Triton X-100, 1 mM PMSF, 1 mM DTT and imidazole), wash buffer (25 mM $NaPO_4$ pH 8.0 with 500 mM NaCl, 1 mM PMSF, 1 mM DTT and imidazole) and elution buffer (25 mM $NaPO_4$ pH 8.0 with 500 mM NaCl, 1 mM PMSF, 1 mM DTT and 250 mM imidazole) were freshly prepared and used within 24 hours. For purifications using 1 or 5 mM imidazole, the binding buffer as well as the wash buffer contained 1 or 5 mM imidazole, respectively. For purification with a step gradient of imidazole, the binding buffer contained 1 mM imidazole, and various wash buffers were prepared with 2, 5, 10, 25, and 50 mM imidazole. All purification steps were conducted at RT using ice-cold buffers and solutions, unless otherwise specified. The resin was conditioned

by rinsing with 10 column volumes (CV) (5 mL) of ddH_2O, followed by equilibration with 5 CV (2.5 mL) of elution buffer and 10 CV of binding buffer. To enhance lysate exposure to the nickel resin, the flow rate was adjusted to approximately 3 mL/min by partially obstructing the bottom of the gravity flow column with a 10 µL pipette tip.

Imidazole was added to the clarified lysate to a final concentration of 1 mM, which was subsequently poured through the column and the flow-through was collected on ice. For purifications using 1 or 5 mM imidazole, 20 CV (10 mL) of binding buffer and 10 CV of wash buffer were consecutively added and allowed to flow through to remove unbound proteins and detergent from the binding buffer. The bottom of the column was capped and 1 CV (0.5 mL) of wash buffer was added and incubated O/N at 4˚C. The following day, the wash buffer was allowed to flow through before adding 10 CV of elution buffer to elute PTEN-V5-His. This fraction was collected and set on ice. Post-elution buffer flow, the column underwent regeneration for subsequent applications as described below. For the purification involving a step gradient of imidazole, the same procedure was followed, with a modification in the wash step. Wash buffers containing 2, 5, 10, 25, and 50 mM imidazole were consecutively applied to the column as follows: 10 CV flowed through, and 1 CV was retained for a 30-minute incubation at 4˚C before being allowed to flow through. To address potential leached nickel and ensure complete reduction of the purified protein, EDTA and DTT were added to the elution fractions (purified PTEN-V5-His), reaching final concentrations of 1 mM and 10 mM, respectively.

During the purification process with 1 mM imidazole, fractions of the flow-through were systematically collected at intervals of 1-3 CV. In contrast, for the purification using 5 mM imidazole, the entire fraction was collected for each step without subdivision. In the case of the purification involving a step gradient of imidazole, fractions of the flow-through were collected at intervals of 1-2 CV, except for the elution fraction, which was collected without subdivision.

2.6.2. Column Regeneration and Recharging for Storage and Re-use

Column regeneration was performed after each use and involved sequential steps as follows: 10 CV of double distilled water H_2O were added and allowed to flow through for washing, followed by 5 CV of 6 M guanidine-HCl pH 7.5 to eliminate precipitated or denatured proteins. Subsequently, 2 CV of ddH_2O were applied for additional washing. If the column appeared grey or brown, recharging of the column was performed as per manufacturer's guidelines: 5 CV of 0.1 M EDTA pH 7.5 were used to remove reduced nickel from the resin, 2 CV of ddH_2O were used for washing, and 2 CV of 10 mg/mL nickel(II) sulfate were employed to recharge the column. Equilibration was achieved by adding 5 CV

of equilibration buffer A (25 mM $NaPO_4$ pH 8.0 with 500 mM NaCl and 250 mM imidazole) and 5 CV of equilibration buffer B (25 mM $NaPO_4$ pH 8.0 with 500 mM NaCl). To store the column, 10 CV of double distilled water (ddH_2O) were added and allowed to flow through, 10 CV of 20% ethanol were added and allowed to flow through until approximately 2 CV remained on top of the resin. The column was capped and stored at 4˚C.

2.6.3. Buffer-exchange and Concentration of the Elution Fraction

The elution fraction was subjected to buffer-exchange into either storage buffer (25 mM $NaPO_4$ pH 8.0 with 150 mM NaCl, 10 mM DTT and 1 mM EDTA) for short-term storage or reaction buffer (25 mM $NaPO_4$ pH 7.4 with 150 mM NaCl) for use in assays using a PD-10 desalting column (Cytiva, UK) following manufacturer's instructions. The resulting buffer-exchanged sample was concentrated using a 10 kDa molecular weight cut-off Pierce™ PES Protein Concentrator (ThermoFisher Scientific, UK). The concentrator was centrifuged at 4700 x g at 4˚C while the protein concentration was monitored (as per section 2.9.1) until a volume to achieve a protein concentration > 1 mg/mL was reached.

2.7. Mammalian Cell Culture

Human colorectal carcinoma cells (HCT116) and human breast cancer cells (MCF-7) were grown in McCoy's 5A (modified) medium or Dubecco's Modified Eagle Medium (DMEM), respectively, supplemented with 10% foetal bovine serum (FBS), penicillin (100 units (U)/mL) and streptomycin (100 µg/mL) at 37˚C in an atmosphere of 95% air and 5% CO_2. Confluent cells were subcultured every 2 to 3 days. For passages, cells were washed twice with phosphate-buffered saline (PBS) containing 137 mM NaCl, 2.7 mM KCl, 10 mM Na_2HPO_4 and 1.8 mM KH_2PO_4 (pH 7.4), incubated with prewarmed 0.25% trypsin-EDTA solution for 5 to 10 minutes at 37˚C, 5% CO_2, and seeded at a cell density of ~$2x10^4$ cells/cm^2 for HCT116 and ~$6x10^4$ cells/cm^2 in tissue culture-treated, non-pyrogenic, sterile flasks containing prewarmed fresh complete McCoy's 5A (modified) medium for HCT116 cells or DMEM for MCF-7 cells. All procedures were carried out under sterile conditions. For cell counting, cells were detached with 0.25% trypsin-EDTA as described previously and mixed with Trypan blue at a final concentration of 0.1–0.2%. Viable cells (unstained) and dead cells (blue) were manually counted on a haemocytometer under an inverted microscope to calculate cell density (cells/mL) and mortality (%).

2.8. Preparation of HHE and PONPC Working Solutions

HHE was purchased as a stock solution in ethanol at a concentration of 87.6 mM. PONPC was resuspended in ethanol for a 25 mM stock solution. For PTEN-V5-His treatments, 10X

solutions of HHE or PONPC were prepared in PTEN treatment buffer (25 mM sodium phosphate pH 7.4, 150 mM NaCl). For cell treatment, 10X solutions of HHE were prepared in PBS and used fresh or stored at -20˚C for short-term storage, while PONPC was prepared fresh, either at a 10X concentration in PBS for 3-(4,5-Dimethylthiazol-2-yl)-2,5-diphenyltetrazolium bromide (MTT) assays or in complete medium at a 2X concentration for western blotting sample preparation. As a control, vehicle solutions of ethanol in either PBS or complete medium (at final concentrations $\leq$ 0.2%, corresponding to the highest concentration of ethanol in HHE or PONPC treatments) were prepared as a 10X or 2X stock. H_2O_2 was used as a positive control for oxidative stress by preparing a 100X solution (100 mM) in PBS immediately before use.

2.9. Protein Concentration Assessment

2.9.1. Recombinant Protein Quantification

The purified, buffer-exchanged, and concentrated samples were quantified in triplicates with a NanoDrop 2000 (ThermoFisher Scientific, UK) using the elution buffer, storage buffer or reaction buffer as blank, accordingly. The theoretical molecular weight and molar extinction coefficient of PTEN-V5-His were calculated to be 52 kDa and 45,270 $M^{-1}.cm^{-1}$, respectively, using the ExPASy ProtParam tool (Swiss Institute of Bioinformatics, Switzerland). Assuming that the samples were 100% PTEN-V5-His, the NanoDrop 2000 was set using the above-mentioned parameters to calculate the protein concentration from the absorbance at 280 nm, using the method provided in section 2.3, after automatic conversion of the molar extinction coefficient to a percent extinction coefficient in ($g/100\ mL^{-1}.cm^{-1}$), as per manufacturer's specifications.

2.9.2. Cell Lysate Protein Concentration Assessment

The total protein concentration was determined by the BCA assay using Pierce™ BCA Protein Assay Kit (ThermoFisher Scientific, UK) in a 96-well plate: 25 µL of sample, blank and standard BSA with a concentration ranging from 0 to 2000 µg/mL) were mixed with 200 µL of reagent in triplicates. Plates were incubated 30 minutes at 37˚C and the absorbance was read at 562 nm after 10 minutes at RT. Average absorbance and standard deviation were calculated. A standard curve was constructed by applying linear regression to the plotted values of average absorbance of BSA. The linear regression was considered valid if the coefficient of determination (R^2) was above 0.95. The average absorbance of the blank was subtracted to average absorbances of samples and their concentration was calculated using the equation of the linear regression.

2.10. Sodium Dodecyl Sulfate Polyacrylamide Gel Electrophoresis (SDS-PAGE)

SDS-PAGE was performed with 8% or 10% acrylamide gels (resolving gel: 8% or 10% acrylamide, 375 mM Tris-HCl pH 8.8, 0.1% sodium-dodecyl-sulfate (SDS), 0.1% tetramethylethylenediamine (TEMED), 0.1% ammonium persulfate (APS); stacking gel: 4% acrylamide, 126 mM Tris-HCl pH 6.8, 0.1% SDS, 0.1% TEMED, 0.1% APS). Protein samples were mixed with water and 2X Laemmli buffer (125 mM Tris-HCl pH 6.8 with 4% SDS, 20% glycerol, 10% β-mercaptoethanol with 0.004% bromophenol blue) (Merck, UK) to give a final concentration of 1X, incubated at 95˚C for 5 minutes and cooled on ice. PageRuler Prestained protein ladder (ThermoFisher Scientific, UK) and samples were loaded into the wells of the gel and electrophoresis was performed using the Mini-PROTEAN™ electrophoresis system (Bio-Rad, UK) in running buffer (25 mM Tris, 192 mM glycine and 1% (w/v) SDS, pH 8.3) for 30 minutes at 50 V and at 120 V until the dye front reached the bottom of the gel. Gels were washed for 10 minutes 3 times in ddH_2O and incubated at least for 1 hour at RT in PageBlue Protein Staining Solution (ThermoFisher Scientific, UK) on a rocking shaker at 30 rpm. When protein bands were visible, gels were rinsed quickly with ddH_2O and distained in ddH_2O for at least 1 hour at RT on a rocking shaker at 30 rpm. Gels were imaged using a G:Box XR5 and GeneSys software (Syngene, UK). Images were processed with background subtraction using a rolling ball radius of 100 pixels and analysed with densitometry analysis using the ImageJ software (NIH, USA).

2.11. Mass Spectrometry Analysis

2.11.1. In-gel Digestion

Target bands from SDS-PAGE gels were excised and cut into pieces measuring 1-2 mm. For the analysis of endogenous PTEN from MCF-7 cells, bands at the expected molecular weight of migration of endogenous PTEN (55-60 kDa) into SDS-PAGE gels were excised and cut as previously described. The gel fragments underwent washing with 500 µl of 100 mM ammonium bicarbonate (NH_4HCO_3) for 1 hour on a shaker, followed by 500 µl of 50% acetonitrile (ACN) with 100 mM NH_4HCO_3 for an additional hour on a shaker. To these gel pieces, 150 µl of 100 mM NH_4HCO_3 and 10 µl of 45 mM DTT were added before incubation at 60°C for 30 minutes. Subsequently, the samples were allowed to cool to room temperature for 10-20 minutes, followed by the addition of 10 µl of 100 mM iodoacetamide (IAA) and incubation in the dark for 30 minutes at RT. The buffer was then removed, and the gel pieces were washed with 500 µl of 50% ACN with 100 mM NH_4HCO_3 for 1 hour on a shaker. For dehydration and shrinking of the gel pieces, 50 µl of ACN was added and left for

10 minutes. After removing the solvent, the gel pieces were dried in a vacuum centrifuge (VacuFuge Plus, Eppendorf, UK) for 10 minutes at 30°C. Each gel piece received between 10 and 40 µl of 20 µg/ml trypsin (prepared as per manufacturer's instructions) and was overlaid with 25 mM NH_4HCO_3 to cover the gel pieces. The digestion mix was incubated at 37°C O/N. After a brief centrifugation, all liquid samples were transferred to fresh microcentrifuge tubes. To enhance recovery of digested proteins, 20 µl of 5% formic acid was added to each gel piece and heated at 37°C for 20 minutes. This was followed by the addition of 40 µl of ACN to the gel pieces, heated at 37°C for another 20 minutes. The samples were subjected to vortex mixing between each of these steps. The solvent was pooled with the initial portion of the sample. Subsequently, the samples were dried in the vacuum centrifuge at 30°C, and the dried samples were stored at -20°C.

2.11.2. High Performance Liquid Chromatography Coupled with Tandem Mass Spectrometry (HPLC-MS/MS)

The dried peptides from either in-gel digestion or S-Trap™ sample processing were allowed to thaw at RT for 10 minutes before being re-suspended in 15-30 µL of liquid chromatography – mass spectrometry (LC-MS) grade H_2O with 0.1% formic acid (FA) through vigorous vortexing, followed by transfer to autosampler vials. Samples underwent analysis using an M-class LC system (Waters, UK) linked to a 5600 TripleTOF mass spectrometer (Sciex, UK). A 5 µl sample was loaded onto a nanoEase M/Z Symmetry C18 Trap column (180 µm x 20 mm) (Waters, UK) and washed at 15 µl/min for 4 minutes. The sample was then separated at 500 nl/min on a nanoEase M/Z Peptide C18 column (15 cm x 75 µm) (Waters, UK) or a NanoEase M/Z HSS C18 T3 column (Waters, UK) at 35°C. Peptides were eluted using a 45-minute gradient from 1% to 45% high-performance liquid chromatography (HPLC) Solvent B (99.9% ACN with 0.1% FA) in HPLC Solvent A (1% ACN, 0.1% FA in LC-MS H_2O). Following a 4-minute wash with 90% HPLC Solvent B, the column was re-equilibrated with 1% Solvent B for 8 minutes before the next sample run. Tandem mass spectrometry was applied to the resolved peptides based on the parameters detailed in Table 2.1.

Table 2.1. Tandem Mass spectrometry parameters.

Setting	Parameter used
Ion source	Nanospray
Spray Voltage	2.4 kV
Source Temperature	150˚C
Declustering Potential	100 V
Curtain Gas	25
TOF MS Survey Scan settings	
Mode	Positive Mode
Mass Range	350 – 1250 Da
Accumulation Time	200 ms
Sensitivity	High
MS/MS IDA Settings	
Number of ions selected	10
Charge	+2 to +5
Dynamic Exclusion Time	30 s
Energy Setting	Rolling Collision Energy

Chapter 3 – Expression and Purification of a Functional Recombinant PTEN

3.1. Introduction

Understanding the intricacies of cellular processes often hinges on the comprehensive study of proteins, typically requiring the expression and purification of recombinant proteins as a tool to investigate biological roles with precision. This is particularly useful for proteins with pivotal roles in cellular regulation such as PTEN, which is a key factor in cellular regulation, acting as a dual-specificity phosphatase and a tumour suppressor. Its role in modulating critical cellular processes, including cell cycle progression, apoptosis, and DNA repair, underscores its significance in maintaining cellular homeostasis (Shi et al., 2012). Since the first functional recombinant protein, somatostatin, was produced in 1977 using *Escherichia coli* cells (Itakura et al., 1977), the field has improved vastly to allow comprehensive study of proteins, from the use of different host organisms to the development of expression vectors with multiple combinations of replicons, promoters, selection markers, multiple cloning sites, and fusion protein or fusion protein removal strategies (Rosano and Ceccarelli, 2014).

Despite the prevalent use of *E. coli* as a protein expression system, the repertoire of host organisms has expanded to include other bacteria, yeasts, filamentous fungi, insect cells, mammalian cells, transgenic animals and plants, and, more recently, cell-free systems (Demain and Vaishnav, 2009). The selection of an expression system is determined by the characteristics of the target recombinant protein – its size, complexity, cellular localization and essential PTMs. Additionally, practical considerations, such as ease of use and cost-efficiency, contribute to the choice of the expression host. Although *E. coli* excels in the rapid and cost-effective expression of both prokaryotic and certain eukaryotic proteins, its limitations become apparent when dealing with complex proteins, such as those containing multiple disulfide bonds, eukaryotic membrane proteins, or large multi-domain assemblies and multi-subunit complexes, or containing crucial PTMs. Some glycosylated proteins can be active without the carbohydrate moiety and can therefore be produced in bacteria. However, if stability or proper folding requires proper glycosylation, this can often be provided by yeast, filamentous fungi, insect or mammalian cells. Additionally, the expression of proteins can be seen in the form of inclusion bodies in *E. coli*, resulting in incorrect folding and inactive proteins (Demain and Vaishnav, 2009, Schutz et al., 2023). Consequently, alternative hosts are often sought to overcome the constraints associated with *E. coli* expression, ensuring a more suitable expression system for the characteristics of the target

protein. Table 3.1 provides a comparison of the above-mentioned expression systems, with the exception of transgenic animals and plants, which are irrelevant for the small-scale protein expression discussed in this chapter (Rosano and Ceccarelli, 2014, Demain and Vaishnav, 2009, Chen, 2012, Terpe, 2006, Landeta et al., 2018, Schutz et al., 2023, Baghban et al., 2019, McKenzie and Abbott, 2018, Endo and Sawasaki, 2006).

Table 3.1. Comparison of characteristics of different protein expression systems for expression of human recombinant proteins

Expression system	E. coli	Other bacteria	Yeasts	Filamentous fungi	Insect cells	Mammalian cells	Cell-free systems
Speed	Fast	Moderate to Fast	Moderate	Moderate to Slow	Moderate to Slow	Moderate to Slow	Very fast
Ease of manipulation	Easy	Easy	Easy	Moderate (viscosity)	Intricate	Intricate	Easy
Cost	Inexpensive	Inexpensive	Inexpensive	Inexpensive	Expensive	Expensive	Expensive
Yields	High	High	High	High, but mostly after tedious optimization	High expression levels, but harder to scale up	Low	High expression levels but in low volumes
Protein size	Small	Small	Flexible	Flexible	Flexible	Flexible	Flexible
Processing of disulfide bonds / folding	Limited (enhanced in periplasm or specific strains)	Limited	Yes / generally good folding	Yes / proper folding	Yes / proper folding	Yes / proper folding	Yes / Difficult
Processing of post-translational modifications	Limited (notably glycosylation)	Limited (notably glycosylation)	Yes, but different from human	Yes, but different from human	Yes, but different from human	Yes, most similar to human	Depends on source of the extracts
Production in inclusion bodies	Yes	No	No	No	No	No	No
Compartment-alization	No	No	Yes	Yes	Yes	Yes	Possible
References	(Rosano and Ceccarelli, 2014, Demain and Vaishnav, 2009, Schutz et al., 2023, Chen, 2012, Terpe, 2006, Landeta et al., 2018)	(Demain and Vaishnav, 2009, Chen, 2012, Terpe, 2006, Landeta et al., 2018)	(Demain and Vaishnav, 2009, Schutz et al., 2023, Baghban et al., 2019)	(Demain and Vaishnav, 2009)	(Demain and Vaishnav, 2009, Schutz et al., 2023, McKenzie and Abbott, 2018)	(Demain and Vaishnav, 2009, Schutz et al., 2023, McKenzie and Abbott, 2018)	(Schutz et al., 2023, Endo and Sawasaki, 2006)

Recombinant wild-type PTEN and PTEN variants have been expressed extensively in *E. coli* (Das et al., 2003, Johnston and Raines, 2015b, Verrastro et al., 2016, Denning et al., 2007, Dey et al., 2008, Myers et al., 1998, Wang et al., 2007, Mehenni et al., 2005, Yim et al., 2009, Redfern et al., 2008, Campbell et al., 2003, Shearn et al., 2011b, Hodakoski et al., 2014, Myers et al., 1997, Johnston and Raines, 2015a, Arora and Ghosh, 2016, Zhang et al., 2022, Wei et al., 2015) and mammalian cells (Ramaswamy et al., 1999, Mosessian et al., 2009, Vazquez et al., 2001, Takahashi et al., 2006, Lee et al., 2015, Briercheck et al., 2015,

Choi et al., 2013, Gil et al., 2006, Gu et al., 1998, Kotelevets et al., 2001, Koul et al., 2002, Myers et al., 1998, Denning et al., 2007, Dey et al., 2008, Adey et al., 2000, Wang et al., 2007, Hodakoski et al., 2014, Mehenni et al., 2005, Yim et al., 2009, Zhang et al., 2022), but also successfully in yeasts (Fernandez-Acero et al., 2019, Rodriguez-Escudero et al., 2005, Andres-Pons et al., 2007, Kim et al., 2010b, Kim et al., 2011, Mehenni et al., 2005) and insect cells (Chen et al., 2016, Dempsey and Cole, 2018, Dempsey et al., 2021, Li et al., 2018b, Liang et al., 2017). Although expression of PTEN in eukaryotic systems allowed elucidation of its localization as well as identification of PTEN PTMs and roles in cellular processes, the production and purification of PTEN and variants in *E. coli* has been particularly useful in the specific study of its lipid and protein phosphatase activities (Denning et al., 2007, Dey et al., 2008, Johnston and Raines, 2015b, Myers et al., 1998, Verrastro et al., 2016, Hodakoski et al., 2014, Campbell et al., 2003, Shearn et al., 2011b, Myers et al., 1997, Johnston and Raines, 2015a). In these studies, PTEN was expressed as a fusion protein with polyhistidine (His)- or glutathione-S-transferase (GST)-tags. A multitude of other tags exist; for instance, Saraswat *et al.* (Saraswat et al., 2013) and Zhao *et al.* (Zhao et al., 2013) published comprehensive reviews about them – but they will not be discussed in this chapter as the His- and GST-tags have been the most commonly used for expression and purification of PTEN in bacterial systems.

These tags have been widely used for their ability to facilitate purification. Indeed, when placed either on the N- or C-terminus of the recombinant protein, they provide the opportunity to employ affinity chromatography techniques, offering a more straightforward purification process and greater purity of the isolated protein in a single step compared to general chromatography methods (Zhao et al., 2013, Jia and Jeon, 2016, Young et al., 2012, Saraswat et al., 2013). His-tags are affinity tags consisting of multiple histidine residues (usually 6 His residues). Histidine demonstrates robust interactions with transition metal ions (Co^{2+}, Ni^{2+}, Cu^{2+}, Zn^{2+}) due to the electron-donating properties of the histidine imidazole ring, facilitating the formation of coordination bonds with these metal ions. As a result, immobilized metal-affinity chromatography (IMAC) can be easily used for purifying His-tagged recombinant proteins. This technique employs solid resins which have a metal chelating group available for metal binding, and the remaining coordination sites on the metal bind His residues attached to the recombinant protein. Upon binding of the His-tagged protein to the matrix and subsequent washing, elution of the target proteins is achieved through either a pH shift or the addition of free imidazole (competitive reagent) to the matrix, conducted under native or denaturing conditions. Utilizing native conditions and imidazole as the eluent typically results in biologically active purification products, as the His-tag's relatively small size and charge minimally impact protein activity. However, a significant

drawback of employing this strategy for protein purification is the potential occurrence of nonspecific binding. Naturally occurring metal-binding proteins and histidine and cysteine-rich spots in proteins may exhibit affinity for the IMAC matrix, leading to their co-elution with the protein of interest. Additionally, non-specific hydrophobic interactions between proteins and the matrix can contribute to contamination of the recombinant protein. (Bornhorst and Falke, 2000, Saraswat et al., 2013). In contrast, GST-tags serve dual purposes in protein purification and enhancing the solubility of the recombinant protein (Young et al., 2012). GST is a cytoplasmic 26 kDa protein found in eukaryotic cells. While GST does not universally improve the solubility of proteins with intricate folding, it is anticipated that, owing to its considerable size, the solubility conferred by the GST moiety would extend to the fused recombinant protein. GST exhibits reversible, high-affinity but not specific binding to glutathione coupled to a sepharose matrix. Elution under mild, non-denaturing conditions is achieved by the introduction of reduced glutathione (competitive reagent) into the elution buffer, typically resulting in high yields and purity. However, the necessity of removing the GST moiety may arise depending on the application or properties of the target protein, which may be adversely affected by the inclusion of such a large tag, particularly its functionality. Consequently, this complicates the purification process, necessitating additional steps to cleave the GST from the protein and segregate the recombinant protein from the GST moiety (Harper and Speicher, 2011, Tossounian et al., 2024).

The degree of purity of the target protein is usually a determinant factor for the success of downstream experiments (Raynal et al., 2014). Despite the convenience of His- and GST-tags in streamlining protein purification, potential contamination by co-eluted proteins has been highlighted (Bornhorst and Falke, 2000, Harper and Speicher, 2011, Saraswat et al., 2013), indicating the need for quality control measures before downstream experiments. This typically involves evaluating the purity, integrity, homogeneity, and functionality of the protein sample. Purity and integrity assessment can be readily performed using sodium dodecyl sulfate polyacrylamide gel electrophoresis (SDS-PAGE), enabling the separation and detection of proteins in the sample and providing an initial indication of sample purity. Coupled with MS analysis, which allows precise identification of the target protein and potential contaminants, these techniques offer comprehensive insights into sample composition (Raynal et al., 2014). When purification of the target protein is unsuccessful or shows contamination, optimization of the affinity chromatography process can be necessary. To ensure optimal binding of the target protein to the matrix, it is recommended to (1) remove insoluble materials and to reduce the viscosity of the lysate applied to the chromatography matrix to avoid physical constraints on the matrix, (2) avoid too high concentration or dilution of the proteins as aggregates tend to form at high concentrations

and binding rates and capture efficiency can be reduced with diluted proteins and (3) optimize the amount of resin used and the flow rate to increase binding efficiency. Following initial binding, proteins bound by nonspecific interactions can be effectively removed through a series of washing steps where concentration of salts, pH, concentration of surfactants and concentration of the competitive reagent used for elution can be optimized (Urh et al., 2009). Analyzing protein homogeneity can also be crucial in control quality of the purified sample, as aggregated proteins are generally non-functional, and the oligomerization state of the target protein, if necessary for its function, can significantly impact downstream experiments. Dynamic light scattering (DLS) and size exclusion chromatography (SEC) are commonly employed methods for this purpose. DLS measures Brownian motion and correlates it with particle size, providing information on sample homogeneity, while SEC separates molecules based on their hydrodynamic properties, facilitating the separation and quantification of aggregates, contaminants, and potentially different molecular arrangements of the protein of interest. These are simple and generally available methods and can be complemented by other techniques. Once the purity, integrity and homogeneity of the sample have been assessed, the activity of the target protein can be measured to ensure that the purified protein is functional (Raynal et al., 2014).

PTEN phosphatase activity can be measured *in vitro* with purified PTEN using an array of different assays. The protein phosphatase activity of PTEN has been investigated numerous times in past studies. This can be achieved through the analysis of the phosphorylated state of artificially phosphorylated proteins or synthetic peptides (Dey et al., 2008, Zhang et al., 2012, Myers et al., 1997). Additionally, the release of radiolabelled phosphate from radiolabelled phosphorylated synthetic peptides (Spinelli and Leslie, 2015) after incubation with purified PTEN can also be measured. Nonetheless, the lipid phosphatase activity remains to date the most studied activity using purified PTEN. The phosphatidylinositol phosphate phosphatase assays described by Maehama *et al*. (Maehama and Dixon, 1998, Maehama et al., 2000) have become a standard practice for this and have been adapted by other groups over the years that followed (Spinelli and Leslie, 2015, Denning et al., 2007, Campbell et al., 2003, Shearn et al., 2011b, Koul et al., 2002, Dey et al., 2008). These allowed the assessment of PTEN lipid phosphatase activity by either measuring the release of inorganic phosphate (Pi) using malachite green (Geladopoulos et al., 1991) or by separating and quantifying lipid species on thin layer chromatography (Maehama and Dixon, 1998, Koul et al., 2002) after reaction of purified PTEN with water-soluble PIPs in a reducing environment. As an alternative to the measurement of released Pi by malachite green, which is highly toxic (Srivastava et al., 2004), the use of radiolabelled PIPs have also been reported (Myers et al., 1998), which were later on included in vesicles to assess PTEN lipid

phosphatase activity *in vitro* in a model mimicking the plasma membrane environment (Spinelli and Leslie, 2015). However, these assays rely on end-point measurements and efforts have been made to achieve continuous monitoring of PTEN activity *in vitro*. Johnston *et al.* proposed in 2015 an indirect and continuous measurement of PTEN catalytic activity based on the reaction of Pi and 7-methyl-6-thioguanosine (MESG) through the catalysis of bacterial nucleoside phosphorylase to form ribose-1-phosphate and 7-methyl-6-thioguanine, taking advantage of the large absorbance difference of MESG and 7-methyl-6-thioguanine. By adding purified PTEN with a soluble version of its natural substrate PIP3 in presence of MESG and bacterial nucleoside phosphorylase, the release of Pi by the reaction of PTEN with PIP3 can fuel the reaction catalysed by the bacterial nucleoside phosphorylase and the formation of 7-methyl-6-thioguanine can be measured (Johnston and Raines, 2015a). In contrast, the 3-O-methylfluorescein phosphate (OMFP) assay utilizing the conversion of non-fluorescent OMFP to fluorescent 3-O-methylfluorescein (OMF) by PTEN is a continuous and direct assay measuring PTEN phosphatase activity. Although OMFP is not a natural substrate of PTEN, it has been shown that, with a Km of 216 $\pm$ 14 µM, it was a suitable substrate for PTEN inhibition studies and PTEN drug screening (Mak and Woscholski, 2015).

The initial phase of this project focused on the generation of a purified PTEN protein, marking the foundational step toward addressing the impact of oxidized lipids HHE and PONPC on PTEN function and localization, along with identifying potential lipoxidation sites on PTEN. Recombinant PTEN not only offers a controlled experimental platform but also allows detailed biochemical and functional investigations. The objectives outlined in this chapter were to produce a functional recombinant human PTEN, PTEN-V5-His, using *E. coli* cells and refine the purification protocol to yield a product of adequate quantity and purity for subsequent analysis. The primary techniques involved in this endeavour included transformation of BL21(DE3) *E. coli* cells with a plasmid encoding for PTEN-V5-His and expression of the protein in these cells, followed by IMAC to purify PTEN-V5-His. Mass spectrometry analysis was performed to confirm the identification of human PTEN in the purified samples, followed by the assessment of phosphatase activity using the OMFP assay. While mass spectrometry demands relatively modest quantities of protein, the OMFP assay necessitates larger amounts, particularly when evaluating various treatment concentrations across multiple time points. Hence, ensuring sufficient protein yield for subsequent experimentation was critical. The successful production of active PTEN was imperative for assessing the impact of HHE and PONPC on PTEN's phosphatase activity in subsequent experiments. Moreover, the purity of the purified protein held significant importance, as contaminants could potentially interfere with PTEN's phosphatase activity,

providing misleading results. However, the risk of such interference could be mitigated through the identification of contaminants via mass spectrometry, thereby elucidating their identities and functions.

3.2. Materials and Methods

3.2.1. Materials

BL21 (DE3) *E. coli* competent cells were purchased from ThermoFisher Scientific. This strain carries the gene for T7 RNA polymerase under control of a lacUV5 promoter, allowing expression induction with IPTG. Mouse anti-PTEN (PTEN (26H9) Mouse mAb, #9556) and rabbit anti-PTEN (PTEN rabbit Ab, #9552) were purchased from Cell Signaling Technology (The Netherlands). The goat anti-mouse secondary antibody (goat anti-mouse IgG (H+L)-Horseradish Peroxidase (HRP) conjugate, #170-6516) was purchased from Bio-Rad (UK) and the goat anti-rabbit secondary antibody (Anti-Rabbit IgG (whole molecule)–Peroxidase antibody, #A6154) was purchased from Merck (UK).

3.2.2. Plasmid DNA Purification

PTEN-V5-His plasmid DNA was purified, quantified and checked for quality as described in General Materials and Methods, Sections 2.2 to 2.4.

3.2.3. Transformation of BL21 (DE3) *E. coli* Cells with PTEN-V5-His Plasmid

Competent cells of the *E. coli* protein expression strain BL21 (DE3) (Sigma-Aldrich, Merck, UK), underwent transformation with the JpExpress404 PTEN plasmid (PTEN-V5-His plasmid DNA) using the heat shock method. Thawed on ice, competent BL21 (DE3) cells were treated with 5, 20, or 80 ng of purified PTEN-V5-His plasmid DNA or nuclease-free water (Promega, UK) in a 50 µL volume. The BL21 (DE3) – plasmid DNA mixture was gently combined and incubated on ice for 30 minutes. The cells were subjected to heat shock at 42˚C for 30 seconds and then incubated on ice for 2 minutes. Following this, 250 µL of Super Optimal broth with Catabolite repression (SOC) media (Sigma-Aldrich, Merck, UK) was added. The cell suspension was incubated in a MaxQ 8000 orbital shaker (ThermoFisher Scientific, UK) at 37˚C, 225 rpm for 1 hour. After the initial outgrowth, 50 µL or 200 µL of the resulting cultures were plated on LB-agar plates supplemented with 100 µg/mL ampicillin and incubated for 15 hours in a stationary incubator (Lenton Thermal Designs, UK) at 37˚C. The colony-forming unit (CFU) was assessed the next day, and the transformation efficiency (TE) was calculated as follows:

$$\text{TE}\ (\text{CFU}/\mu\text{g}) = \frac{\text{CFU}}{\mu\text{g of DNA}} \times \frac{\text{culture volume (mL)}}{\text{volume plated (mL)}}$$

Single colonies from each plate of BL21 (DE3) transformed with 5 and 20 ng of plasmid DNA and plated with 50 µL of culture were inoculated into 5 mL of sterile LB medium supplemented with 100 µg/mL ampicillin in duplicate. This culture was incubated in a MaxQ

8000 orbital shaker (ThermoFisher Scientific, UK) at 37˚C, 220 rpm until the optical density at 600 nm (OD_{600}) reached 1, and glycerol stocks were produced by mixing the cultures 1:1 (V:V) with 50% sterile glycerol and frozen at -80˚C.

3.2.4. Expression of and Purification of PTEN-V5-His

Expression and purification of PTEN-V5-His was performed as described in General Materials and Methods, section 2.5 and 2.6, respectively. Protein samples were quantified as described in General Material and Methods, section 2.9.1.

3.2.5. Sodium-Dodecyl-Sulfate Polyacrylamide Gel Electrophoresis (SDS-PAGE)

SDS-PAGE was performed with 10% acrylamide gels as described in General Materials and Methods, section 2.10.

3.2.6. Western Blotting of PTEN

All steps were performed at RT on a rocking shaker at 30 rpm, unless stated otherwise. Proteins separated by SDS-PAGE were transferred onto a methanol-activated polyvinylidene fluoride (PVDF) membrane for 1 hour at 100 V on ice in transfer buffer (25 mM Tris, 190 mM glycine and 20% methanol) using the Mini Trans-Blot® Cell system (Bio-Rad, UK) after washing gel and membrane in ice-cold transfer buffer for 10 minutes. The membrane was subsequently reactivated with methanol. To check for transfer efficiency, the membrane was stained with Ponceau staining solution (0.2% (w/v) Ponceau Red in 5% (v/v) glacial acetic acid) and destained in ddH_2O for 1 minute. The membrane was completely destained by washing further with ddH_2O for 5 minutes and 3 times 5 minutes in Tris-buffered saline-Tween 20 (TBS-T) (20 mM Tris pH 7.5 with 150 mM NaCl and 0.1% (v/v) Tween-20).

The membrane was blocked in blocking solution (5% (m/v) skimmed milk powder in TBS-T) for 1 hour at RT and rinsed twice with TBS-T. The membrane was incubated with a solution of primary anti-PTEN antibody at a 1:1,000 dilution in blocking solution (for a mouse anti-PTEN antibody (Cell Signaling Technology, The Netherlands)) or 5% BSA in TBS-T (for a rabbit anti-PTEN antibody (Cell Signaling Technology, The Netherlands)) for 1h at RT or O/N at 4°C. The membrane was washed 3 x 5 minutes before incubation with an appropriate HRP-conjugated secondary antibody in blocking buffer at a dilution of 1:3,000 for the goat anti-mouse antibody (Bio-Rad, UK) and 1:10,000 for the goat anti-rabbit antibody (Merck, UK). Subsequently, the membrane was rinsed and washed 3 x 10 minutes in TBS-T and placed in Tris-buffered saline (TBS, 20 mM Tris pH 7.5 with 150 mM NaCl) before imaging.

To image the membrane, its surface was covered with SuperSignal™ West Pico Chemiluminescent Substrate (ThermoFisher Scientific, UK) or Clarity Western Enhanced Chemiluminescence (ECL) Substrate (BioRad, UK), prepared as per the corresponding manufacturer's instructions, and incubated in the dark at RT for 5 minutes. The excess substrate was removed and the membrane was placed between two acetate sheets to be imaged using a G:Box XR5 and GeneSys software (Syngene, UK). Images were processed and analysed with densitometry analysis using the ImageJ software (NIH, USA).

3.2.7. Mass Spectrometry Analysis of Purified PTEN-V5-His and Co-eluted Host Proteins

3.2.7.1. In-gel Digestion and High performance liquid chromatography coupled tandem mass spectrometry (HPLC-MS/MS)

In-gel digestion of target SDS-PAGE gel bands (contaminants or PTEN-V5-His) and HPLC-MS/MS were performed as described in General Materials and Methods, section 2.11.1 and section 2.11.2, respectively.

3.2.7.2. Protein Identification

Protein identification was performed using Mascot Daemon (Matrix Science, USA), using the settings in Table 3.2, after MS/MS data files were converted to mzML files using ProteoWizard. Data was filtered to provide protein matches with > 2 significant unique peptide sequences using a significance threshold of $p < 0.05$ and with a preferred taxonomy for *E. coli*. Protein outputs with a taxonomy other than *E. coli*, with the exception of PTEN, were excluded from relevant protein matches.

Table 3.2. Parameters chosen for Mascot searches.

Setting	Parameter used
Taxonomy	All entries
Database	SwissProt
Fixed Modifications	Carbamidomethyl (C)
Variable Modifications	Oxidation (M)
Enzyme	Trypsin
Maximum Missed Cleavages	1
Peptide Charge	2+, 3+ and 4+
Peptide Tolerance	0.5 Da
MS/MS Ions Search	Yes
Data Format	MzML
MS/MS Tolerance	0.5 Da
Instrument	ESI-QUAD-TOF

3.2.8. Protein Sequence Similarity Search

The protein sequence of human PTEN was searched for similarity against the protein sequences of identified contaminants using Basic Local Alignment Search Tool (BLAST, NIH, USA) with the Blast 2 sequences program (Altschul et al., 1997, Altschul et al., 2005) set to default parameters. Maximum number of target sequences was set to 100 and the word size was set to 3. The statistical significance threshold for reporting matches against PTEN sequence was 0.05. BLOSUM62 was used as a scoring matrix with existence gap costs of 11, extension gap costs of 1 and conditional compositional score matrix adjustment.

3.2.9. Phosphatase Activity Assay (OMFP Assay)

3-O-methylfluorescein phosphate (OMFP) was solubilised in DMSO to a stock concentration of 20 mM by sonication and stored in the dark at -20˚C in small aliquots to avoid repeated freeze-thaw cycles. Prior to the assay, the following reagents were prepared fresh and pre-warmed to 30°C: 10X assay buffer (250 mM sodium phosphate, 1.5 M NaCl, pH 8.0), ddH_2O, 100 mM DTT, and 10 mM EDTA. A standard curve for 3-O-methylfluorescein (OMF) was generated in triplicates at concentrations of 0, 0.1, 0.25, 0.5, 0.75, 1, 2.5, 5, 7.4, and 10 µM in 1X assay buffer, with a final volume of 200 µl for each replicate. In triplicates, 20 µg of PTEN-V5-His (used within 24 hours post-purification) was prepared in a black, flat-bottomed 96-well plate along with the OMF standards in 1X assay buffer with 10 mM DTT and 1 mM EDTA, reaching a final volume of 200 µl. The plate was manually mixed for 10 seconds and pre-warmed for 10-20 minutes at 30°C. Subsequently, 50 µl of OMFP reaction mix in 1X assay buffer was added to each well before measurement to reach either increasing concentrations of OMFP ranging from 1.3 µg/mL to 260 µg/mL or a fixed concentration of 130 µg/mL. A positive control with 10 units of alkaline phosphatase was prepared in the same way and two negative controls, one without PTEN-V5-His but with OMFP (PTEN-/OMFP+) and one with PTEN-V5-His but without OMFP (PTEN+/OMFP-) were used for background subtraction and control of PTEN-V5-His activity. Fluorescence measurements were performed using a FLUOstar Omega microplate reader and MARS Data Analysis Software (BMG Labtech, Germany). Gain adjustment was set to 90% of the fluorescence value of the highest standard concentration of OMF. The fluorescence was measured periodically for 20-35 minutes with 485 nm excitation (485BP1 filter) and 520 nm emission (EM520 filter) using, for each cycle, 20 flashes after shaking at 300 rpm for 3 seconds and settling for 0.5 seconds. Background hydrolysis of OMFP was eliminated from samples by subtracting fluorescence of the PTEN-/OMFP+ control at each time point and the increase in fluorescence through conversion of OMFP to OMF was calculated for each sample by subtracting the fluorescence at time 0 to the fluorescence at the last time of measurement. The increase in fluorescence was converted to the amount of OMF produced (in nmol) using the equation of the linear regression of the OMF standard curve and the specific activity of

PTEN-V5-His in each sample was calculated by dividing by the time of reaction (in minutes) and the amount of PTEN-V5-His (in mg).

3.2.10. Statistical Analysis

Data from multiple biological replicates, corresponding to independent purification batches, ($n \geq 3$) was analysed using GraphPad Prism 8.1.0 to perform one-way ANOVA analysis, correcting for multiple comparisons using the Tukey test with a 95% confidence interval. The P values were annotated as follows: $P > 0.05$ (ns), $P \leq 0.05$ (*), $P \leq 0.01$ (**), $P \leq 0.001$ (***), $P \leq 0.0001$ (****). Data is shown as mean values ± SEM unless stated otherwise.

3.3. Results

3.3.1. Purification of PTEN-V5-His plasmid DNA

The plasmid DNA JpExpress404 PTEN (PTEN-V5-His plasmid DNA) encoding for a recombinant PTEN tagged with both a V5 tag and a histidine tag (6xHis) (the map and insert sequence of the plasmid was provided in Supplementary Figure 1) was purified from TOP10 cells to allow transformation of BL21 (DE3) cells. Table 3.3. shows the DNA quantification in the purified PTEN-V5-His plasmid DNA purification samples, highlighting concentration, yield and purity. While the plasmid extraction from 0.6 mL of bacterial culture led to a DNA concentration of 31.0 ± 3.57 ng/µL (mean ± SEM), producing an average yield of 0.93 µg of DNA, extracting DNA from 3 mL of bacterial culture allowed a 5.8-fold increase in concentration with a final average DNA yield of 5.40 µg. The purity of the purified PTEN-V5-His plasmid DNA was also increased with the volume of culture used for the extraction. Indeed, values of 1.8 for the 260/280 (nm) ratio, mainly showing purity of the DNA against proteins, and 2 – 2.2 for the 260/230 (nm) ratio, which becomes appreciably lower than 2 in event of contamination with proteins, guanidine-HCl (used for DNA isolations), EDTA, carbohydrates, lipids, salts, or phenol, are desirable (Lucena-Aguilar et al., 2016). Although the absorbance ratios 260/280 (nm) of DNA extractions from 0.6 and 3 mL were both approaching 1.8, the 260/230 (nm) for these DNA extractions varied between volumes of culture used for DNA extraction and using 0.6 mL of culture did not lead to an acceptable 260/230 nm ratio compared to 3 mL of culture.

Table 3.3. Quantification of the purified PTEN-V5-His plasmid DNA

Volume of culture	Concentration (ng/µL)	Yield (µg)	A 260/280	A 260/230
0.6 mL	31.0 ± 3.57	0.93	1.72 ± 0.03	1.47 ± 0.10
3 mL	180 ± 3.63	5.40	1.88 ± 0.02	1.98 ± 0.17

Data shown as mean ± SEM.

To verify the identity of the purified DNA, a restriciton digestion analysis was performed using a single digestion with EcoRI and a double digestion with the combination of EcoRI and XbaI enzymes. The total length of the PTEN-V5-His plamid was 5.3 kilobases (kb). The double digestion of this plasmid with EcoRI and XbaI led in theory to a long fragment of 4571 base pairs and a short fragment of 763 base pairs, which was part of the sequence encoding the recombinant protein PTEN-V5-His (Supplementary Figure 1). In Figure 3.1, the linearized DNA obtained through a single digestion of the purified PTEN-V5-His plasmid DNA with EcoRI showed a single band at approximately 5.5 kb, while a double digestion with EcoRI and XbaI led to the formation of a long fragment at approximately 4.5 kb and a smaller one at approximately 750 bases, which corresponded to the expected bands.

Therefore, the purified DNA was identified as the JpExpress404 PTEN plasmid encoding for the recombinant protein PTEN-V5-His. However, the band of the uncut plasmid was found to migrate at a distance corresponding to a molecular weight of 8 – 9 kb, which was higher than the molecular weight of the linearized form of the plasmid DNA (5.3 kb). This implied that the purified plasmid DNA was not extracted under its supercoiled form but a more relaxed form, or even with an open-circular conformation.

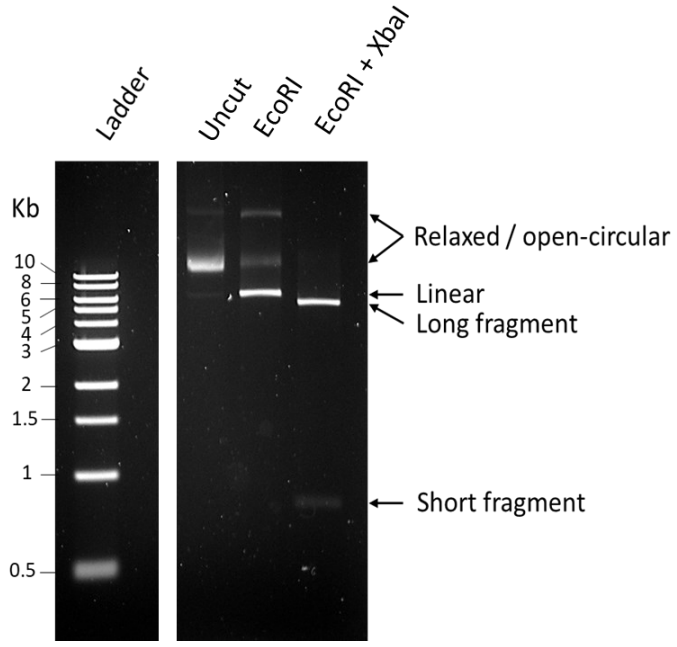

Figure 3.1. Representative restriction digest analysis of purified PTEN-V5-His plasmid DNA. Purified JpExpress404 PTEN plasmid DNA underwent digestion with either EcoRI (single digest) or a combination of EcoRI and XbaI (double digest). The uncut plasmid and digested DNA (from single and double digests) were separated by electrophoresis on a 1% SybrSafe-stained agarose gel. The theoretical lengths of the plasmid and digested fragments were 5.33 kb, 4.57 kb (long fragment), and 763 bases (short fragment). Middle lanes of the gel were cut out. Kb: kilobases.

Taken together, these data allowed the identification of the purified plasmid as JpExpress404 PTEN plasmid DNA (PTEN-V5-His plasmid DNA), which was extracted from TOP10 cells in sufficient quantities and purity for subsequent transformation of BL21 (DE3) cells for expression and purification of the recombinant PTEN, although the conformation of the purified plasmid was not supercoiled.

3.3.2. The Transformation of BL21 (DE3) *E. coli* Cells with PTEN-V5-His Plasmid DNA Led to Differential PTEN-V5-His Expression

To allow expression of PTEN-V5-His, BL21 (DE3) cells were transformed with purified plasmid A and plasmid B (PTEN-V5-His plasmid DNA from two distinct DNA extractions) using 5, 20, or 80 ng of DNA. The growth of colonies on selective LB-agar plates (containing ampicillin) was quantified post-transformation. All PTEN-V5-His plasmid DNA transformation

conditions supported colony growth (Table 3.4) with colonies of approximately 1-2 mm diameter, whilst the control with 0 ng of DNA used for transformation did not lead to bacterial growth, suggesting successful transformation and selection. Increasing the volume of bacterial culture from 50 µL to 200 µL led to a 4.8- and 4.4-fold increase in number of transformants for transformations with 5 ng of plasmid DNA and a 3.3- and 3.7-fold increase for transformations with 20 ng of plasmid DNA for plasmid A and plasmid B, respectively. However, transformation efficiencies (TE) were similar across volumes, plates and amount of DNA used for transformation but varied between plasmid A and B with near to a 2-fold decrease for plasmid B to the exception of transformations using 80 ng of DNA. Transformation with 80 ng of plasmid DNA resulted in highly confluent colonies, preventing the selection of single colonies, especially with a larger culture volume of 200 µL which showed fully confluent plates.

Table 3.4. Colony count and transformation efficiency of BL21 (DE3) with PTEN-V5-His plasmid DNA.

DNA (ng)	Streaked culture volume (µL)	Plasmid A		Plasmid B	
		Colony count	TE (CFU/µg)	Colony count	TE (CFU/µg)
0	200	No colony formed			
5	50	28	3.36×10^4	16	1.92×10^4
	200	134	4.02×10^4	71	2.13×10^4
20	50	178	5.34×10^4	90	2.70×10^4
	200	594$^{\$}$	4.46×10^4	332	2.49×10^4
80	50	670$^{\$}$	5.03×10^4	612$^{\$}$	4.59×10^4
	200	ND	ND	ND	ND

TE: transformation efficiency; $: confluent colonies; ND: not determined.

As single colonies were identified on plates streaked with 50 µL of transformed bacteria with both purified plasmids A and B, two single colonies on each plate were randomly selected for culture (C1 and C2) to check for PTEN-V5-His expression. After induction of the expression of PTEN-V5-His in these cultures, western botting of PTEN in the bacterial whole lysates showed that all cultures expressed PTEN-V5-His, identified by the bands at 60 kDa (Figure 3.2.B). Interestingly, the molecular weight at which PTEN-V5-His migrated was higher (approximatively 60 kDa) than the theoretical molecular weight of the protein (52 kDa) and all cultures presented a second band at a lower molecular weight, which was not present in the control (purified PTEN-V5-His) and could correspond to mistranslated PTEN-V5-His. The expression levels of PTEN-V5-His varied across the cultures; C1 of BL21 (DE3) transformed with 5 ng of the plasmid A (A-5-50-C1) and C2 of BL21 (DE3) transformed with 20 ng of plasmid B (B-20-50-C2) showed the most relative PTEN abundance over total proteins (Figure 3.2.A) whilst C1 and C2 of BL21 (DE3) transformed with 20 ng of plasmid A and C2 of BL21 (DE3) transformed with 5 ng of plasmid B showed approximately a 2-fold decrease in relative PTEN abundance (Figure 3.2.C) compared to the above mentioned.

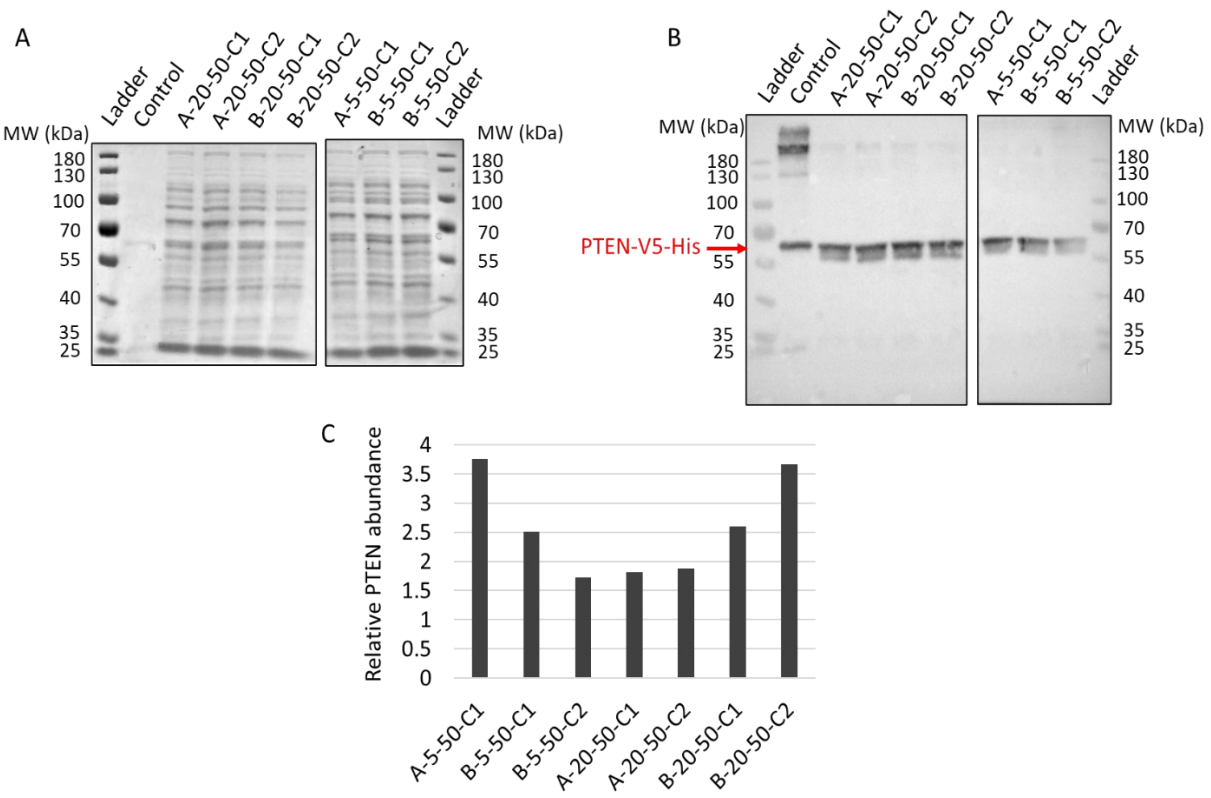

Figure 3.2. Quantification of PTEN-V5-His expression in transformed BL21 (DE3) cells.
(A) Five µg of protein from whole lysates of transformed BL21 (DE3) after expression of PTEN-V5-His were separated by SDS-PAGE. (B) Proteins from the SDS-PAGE gel (A) were subjected to western blotting of PTEN using anti-PTEN (mouse) and HRP-conjugated anti-mouse antibodies and detected with SuperSignal™ West Pico Chemiluminescent substrate (ThermoFisher Scientific). (C) PTEN-V5-His relative abundance to total proteins was quantified using a densitometry analysis (n=1).

This data suggested that bacteria from the A-5-50-C1 and B-20-50-C2 cultures were the most suitable for over-expression of PTEN-V5-His in BL21 (DE3) cells. These were therefore chosen for further expression and purification of PTEN-V5-His.

3.3.3. Optimization of PTEN-V5-His Purification Conditions

PTEN-V5-His purification was initially performed with 1 mM imidazole in either the BL21 (DE3) lysate and wash steps, followed by elution using 250 mM imidazole. The elution profile, depicted in Figure 3.3.A, revealed that the majority of proteins in the BL21 (DE3) lysate were eluted in the lysate flow-through, featuring the highest protein concentration of 5 mg/mL. This fraction primarily contained proteins unable to bind to the nickel resin employed for the His-tagged PTEN purification. The remaining unbound proteins, not eluted in the flow-through, were swiftly eluted with a binding buffer wash containing 0.1% Triton X-100 and 1 mM imidazole. This was demonstrated by decreased protein concentration in the first three fractions (column volume = 2, 3, and 4) of the binding buffer wash, stabilizing around 0 mg/mL for subsequent fractions. Washing with a buffer containing 1 mM imidazole without

Triton X-100 further depleted proteins from the purification column, reaching a maximum concentration of 0.96 mg/mL. Similar to the binding buffer wash elution profile, protein concentration in the next fraction stabilized around 0 mg/mL, indicating the absence of eluted proteins and suggesting that only bound proteins remained in the purification column.

Figure 3.3.B illustrates the protein content of fractions in Figure 3.3.A highlighted in red. Bands in the lysate flow-through and binding buffer wash fractions 1, 2, and 3 were similar, suggesting comparable protein content, albeit in decreasing concentrations as the purification column underwent washing. The wash fraction (corresponding to column volume 21 in Figure 3.3.A) displayed a predominant band at the expected molecular weight of PTEN-V5-His (~60 kDa), along with common bands from previous washes but with decreased intensity. This can be attributed to a proportional increase in PTEN-V5-His in this fraction, where the majority of unbound proteins had already been eluted. However, despite larger bands at the expected molecular weight of PTEN-V5-His in elution fractions 1, 2, and 3 (using 250 mM of imidazole) in Figure 3.3.B, suggesting successful elution and enrichment of the target protein, numerous bands above and below the expected molecular weight of PTEN-V5-His indicated co-elution of multiple proteins, showing poor sample purity. Additionally, a band at the expected molecular weight of PTEN-V5-His was also observed in the regeneration sample corresponding to the column volume 42 on Figure 3.3.A), suggesting that PTEN-V5-His was not fully recovered during the elution step.

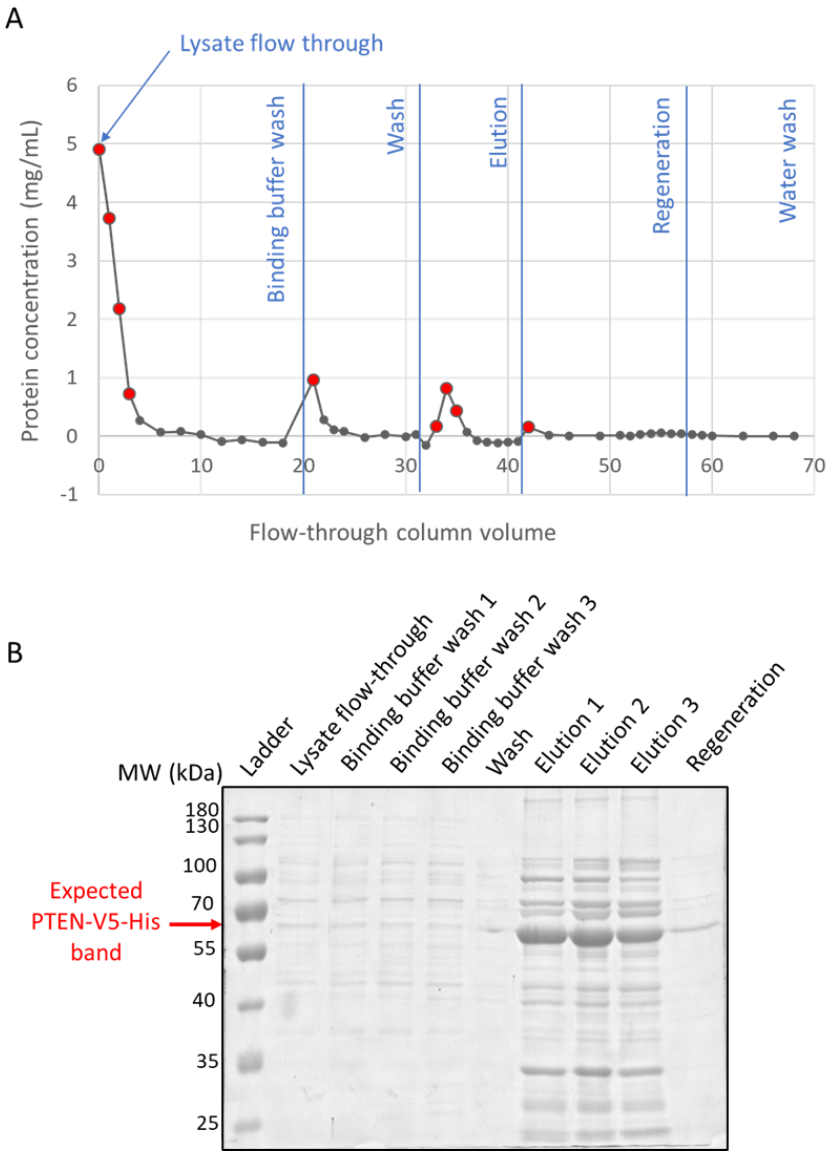

Figure 3.3. Purification of PTEN-V5-His using 1 mM of imidazole in washes and 250 mM of imidazole for PTEN-V5-His elution.

(A) Fractions of the flow-through were collected every 1-3 column volumes (0.5-1.5 mL) throughout the purification process. The protein concentration of each fraction was measured using a NanoDrop 2000 (ThermoFisher Scientific, UK) and (B) 5 µg of protein for selected fractions (highlighted in red on (A)) were separated by SDS-PAGE. MW: molecular weight. (n=1)

To reduce contamination of PTEN-V5-His with co-eluted proteins and optimize imidazole concentration in washes, a step-gradient from 2 mM to 50 mM imidazole was tested to elute proteins from a BL21 (DE3) lysate expressing PTEN-V5-His, followed by a final elution with 250 mM imidazole. Figure 3.4.A illustrates the elution profile of proteins from the BL21 (DE3) lysate expressing PTEN-V5-His. Similar to Figure 3.3.A, a majority of proteins were eluted in the lysate flow-through, reaching a concentration of 6.55 mg/mL, comprising proteins unable to bind to the nickel resin. The remaining unbound proteins were eluted within the first 6 column volumes of the binding buffer wash, stabilizing around 0 mg/mL for subsequent fractions. Washing with a buffer containing 2 mM of imidazole further depleted proteins from

the purification column, reaching a maximum concentration of 0.85 mg/mL and stabilizing between 0 and 0.1 mg/mL. Washes with 5 mM and 10 mM imidazole did not lead to increased protein elution, suggesting depletion of unbound proteins from the purification column. An increase in protein concentration was observed in all fractions of the wash using 25 mM imidazole (0.20 to 0.27 mg/mL), with another peak at 0.15 mg/mL for the wash using 50 mM imidazole. Elution with 250 mM imidazole resulted in a protein concentration of only 0.12 mg/mL, and the first fraction of column regeneration showed a concentration of 0.14 mg/mL, stabilizing around 0 mg/mL. This indicated partial elution of bound proteins with washes using 25 mM and 50 mM imidazole, resulting in low protein content in the elution fraction. Additionally, protein detection in the regeneration phase indicated incomplete recovery of bound proteins during elution.

To gain more insight in the protein content of these fractions, those exhibiting the highest protein concentration for each purification step (highlighted in red in Figure 3.4.A) were subjected to SDS-PAGE (Figure 3.4.B), and PTEN-V5-His was identified via western blotting (Figure 3.4.C). The protein content of the lysate flow-through and binding buffer wash looked similar to the whole lysate (clarified lysate) (Figure 3.4.B), showing that most of the proteins from the whole lysate were not able to bind to the nickel resin and were directly eluted. Faint bands in the clarified lysate and lysate flow-through identified PTEN, although the signal was insufficient for quantification of PTEN lost in the lysate flow-through. Washes with increasing imidazole concentrations showed distinct protein contents, with observed bands not necessarily at the same molecular weight. Only one band remained in the elution fraction at the expected molecular weight of PTEN-V5-His (Figure 3.4.B), indicating that proteins previously co-eluted with PTEN-V5-His were eluted at different imidazole concentrations, and all were eluted at 50 mM imidazole, leaving only PTEN-V5-His bound to the purification column for elution with 250 mM imidazole. PTEN-V5-His was identified in all washes from 10 mM imidazole (Figure 3.4.C), suggesting that using washes with imidazole concentrations higher than 5 mM would result in protein loss in the wash, leading to decreased yield, although contaminants were still visible in samples using 10 mM, 25 mM, and 50 mM imidazole (Figure 3.4.B). Bands below the molecular weight of PTEN-V5-His were also identified in Figure 3.4.C in the 25 mM wash, 50 mM wash and elution fractions but not in other fractions, possibly corresponding to degradation products of PTEN-V5-His or mis-translated protein still able to bind to the purification column.

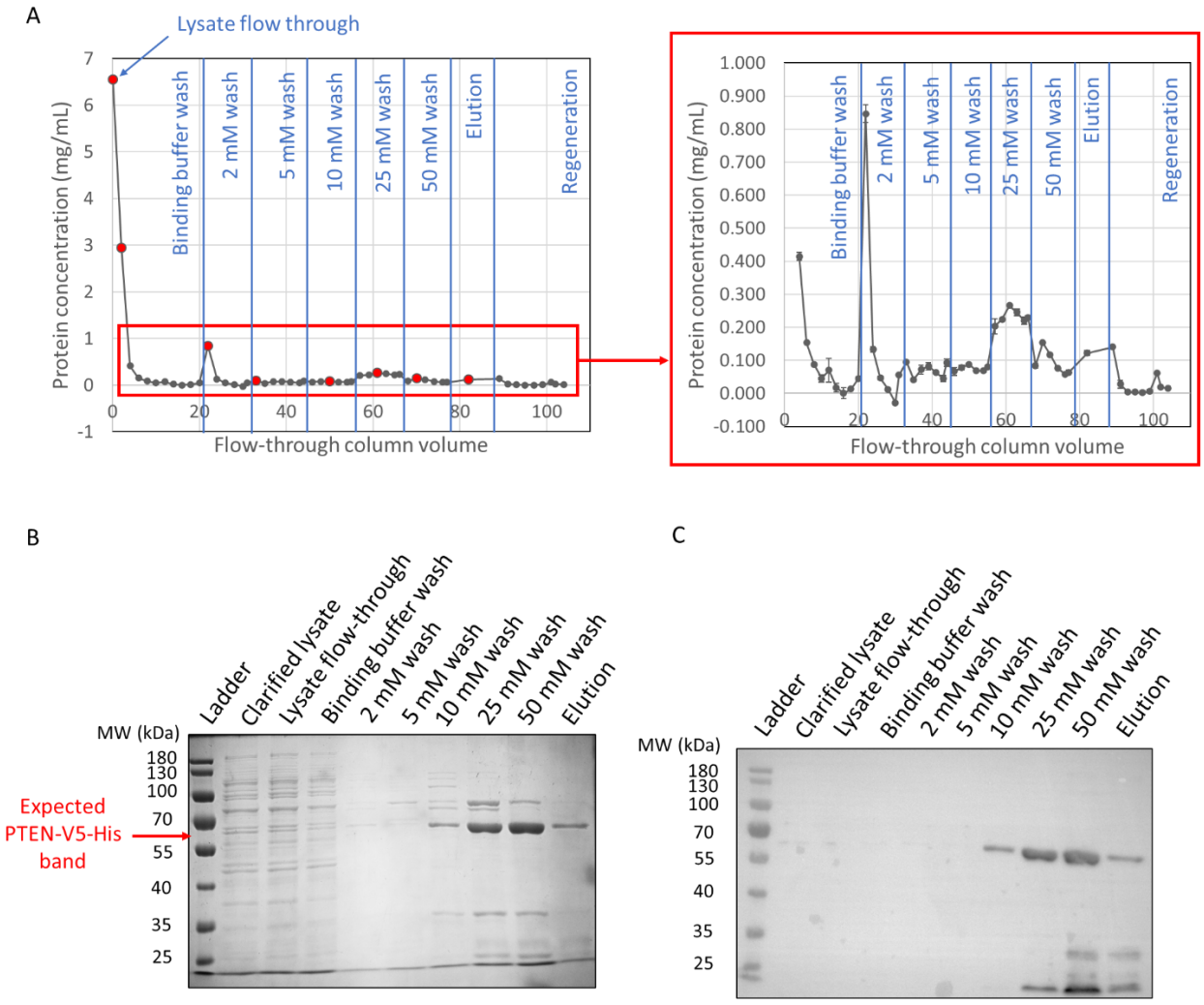

Figure 3.4. Protein elution of BL21 (DE3) – PTEN-V5-His whole lysate using a step gradient of imidazole.

(A) Elution profile of proteins from lysate of BL21 (DE3) expressing PTEN-V5-His. The proteins contained in the clarified lysate supplemented with 1 mM of imidazole were eluted of an IMAC column with washes containing from 1 mM (binding buffer wash) to 50 mM imidazole. Fractions of the flow-through were collected every 2 column volumes (1 mL), with the exception of the lysate flow-through and the elution fractions which were collected separately as a whole. The protein concentration of each fraction was measured in triplicates using a NanoDrop 2000 (ThermoFisher Scientific, UK). The curve between column volumes 4 and 104 was zoomed in for representation purposes. Values are mean ± SD (n=1). (B) Selected fractions (highlighted in red in (A)) were separated by SDS-PAGE. Five µg of protein were loaded for the clarified lysate, lysate flow through, binding buffer wash, and 2 mM wash, while 10 µL of the other samples were loaded into the gel. (C) Western blotting of PTEN was performed from (B) using anti-PTEN (mouse) and HRP-conjugated anti-mouse antibodies and detected with SuperSignal™ West Pico Chemiluminescent substrate (ThermoFisher Scientific, UK). MW: molecular weight.

Taken together, these data suggested that increasing the imidazole concentration in the washes would lead to higher purity of the purified PTEN-V5-His; however, loss of PTEN-V5-His was observed with concentrations higher than 5 mM. The purification protocol was therefore adapted to use 5 mM of imidazole in washes (including the binding buffer wash and subsequent washes), and the target protein was eluted using 250 mM imidazole.

Washing the purification column with 5 mM imidazole resulted in reduced contamination of the purified PTEN-V5-His compared to purification using 1 mM imidazole (Figure 3.3.B), as depicted in Figure 3.5.A. Specifically, eight bands at molecular weights different from the expected 60 kDa of PTEN-V5-His were identified in the purified PTEN-V5-His fraction. Among these, three were above and five were below 60 kDa. These bands were identified on the densitometry plot of the purified PTEN-V5-His lane (Figure 3.5.C). The same 60 kDa band and bands deemed contaminants, excluding the one at the highest molecular weight (above 180 kDa), were also present in the purified sample after buffer exchange and concentration (Figure 3.5.A). This was further supported by the densitometry plots of the buffer-exchanged and concentrated PTEN-V5-His lanes, which showed a similar profile compared to the purified PTEN-V5-His lane, with the exception of the peak on the left-hand side of the densitometry plot of the purified PTEN-V5-His lane, which was not identified in Figure 3.5.C. Figure 3.5.B confirmed the identity of PTEN-V5-His in the purified, buffer-exchanged, and concentrated PTEN-V5-His samples, where the 60 kDa band was labelled by the anti-PTEN antibody. The contaminant identified in the purified sample but not in the buffer-exchanged and concentrated samples was also labelled by the anti-PTEN antibody, suggesting it might have been an aggregated form of PTEN-V5-His formed during the purification process or misfolded during protein synthesis, eliminated during buffer exchange, likely due to its high molecular weight. However, the band at the expected molecular weight of PTEN-V5-His was also present in all washing fractions, implying that some protein was eluted in the washes. This indicated that not all PTEN-V5-His was recovered in the elution fraction (purified PTEN-V5-His).

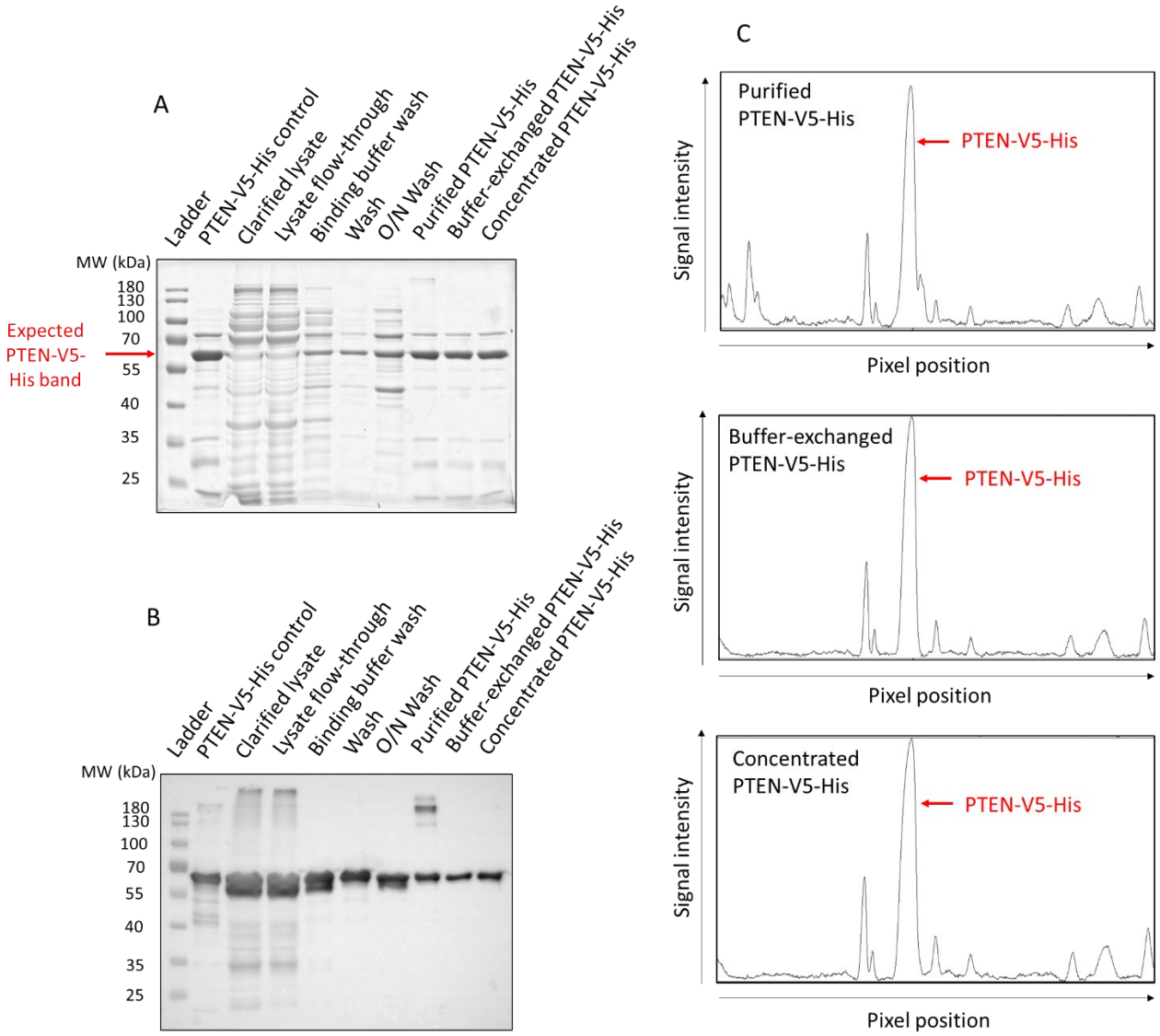

Figure 3.5. Purification of PTEN-V5-His using 5 mM of imidazole in washes and 250 mM of imidazole for PTEN-V5-His elution.

(A) Representative SDS-PAGE of proteins in fractions of steps of the purification of PTEN-V5-His and in samples after buffer-exchange and concentration of the purified PTEN-V5-His. Two µg of proteins were loaded into the gel for PTEN-V5-His control, purified, buffer-exchanged and concentrated PTEN-V5-His and 10 µL of the other samples were loaded into the gel. (B) Representative western blotting of PTEN using anti-PTEN (rabbit) and HRP-anti-rabbit antibodies after SDS-PAGE of the samples for which 0.2 µg of PTEN-V5-His control and purified, buffer-exchanged and concentrated PTEN-V5-His were loaded into the gel, while 10 µL of the other samples were loaded into the gel. (C) Representative densitometry plots of purified, buffer-exchanged, and concentrated PTEN-V5-His. Pixel position indicates the top to bottom lane from left to right.

The protein concentration and 260/280 nm ratio of purified, buffer-exchange and concentrated PTEN-V5-His was measured using a NanoDrop 2000 (ThermoFisher Scientific, UK) based on PTEN-V5-His molecular weight and extinction coefficient. An average loss of approximately 1 mg and 0.5 mg was observed between purified and buffer-exchange, and buffer-exchanged and concentrated samples (Table 3.5). As discussed previously, purified PTEN-V5-His displayed protein aggregation that was not found in buffer-

exchanged and concentrated samples, which would explain the decrease in yield between purified and buffer-exchanged samples, as aggregated protein would contribute to the measured protein concentration. The protein loss in the concentrated PTEN-V5-His, on the other hand, could be explained by retention of the protein in the filter unit. Despite this decrease in total yield after the post-purification steps, a satisfactory 4.582 ± 0.727 (mean ± SEM) mg of protein were still available for subsequent experiments (Table 3.5). Interestingly, the 260/280 nm absorbance ratio of purified PTEN-V5-His was > 1, suggesting contamination with DNA, whilst buffer-exchanged and concentrated samples showed 260/280 nm absorbance ratios of 0.581 ± 0.017 and 0.559 ± 0.005 (mean ± SEM), respectively (Table 3.5). This indicated that dialysis of purified PTEN-V5-His into the reaction buffer efficiently removed nucleic acids.

Table 3.5. Protein quantification of post-purification PTEN-V5-His samples.

	Purified	Buffer-exchanged	Concentrated
Concentration (mg/mL)	1.23 ± 0.16	0.73 ± 0.10	1.64 ± 0.20
Yield (mg)	6.16 ± 0.79	5.11 ± 0.70	4.58 ± 0.73
A 260/280	1.29 ± 0.11	0.58 ± 0.02	0.56 ± 0.01

Data shown as mean ± SEM based on measurements in triplicates of 5 biological replicates.

The densitometry plots (illustrated in Figure 3.5.C) were used to determine the percentage of PTEN-V5-His in the purified, buffer-exchanged, and concentrated PTEN-V5-His samples as well as in the elution samples resulting of the purification of PTEN-V5-His using 1 mM imidazole in the washes (Figure 3.3.B). The purification using 1 mM imidazole in washes resulted in elution fractions containing on average 31.1% of PTEN-V5-His, whereas the percentage of PTEN-V5-His in the purified, buffer-exchanged and concentrated PTEN-V5-His samples was almost 2-fold higher with 57.8%, 61.0% and 58.3%, respectively, representing a significant difference in purity between the purified PTEN-V5-His samples obtained using 1 mM and 5 mM imidazole in the washes (Figure 3.6).

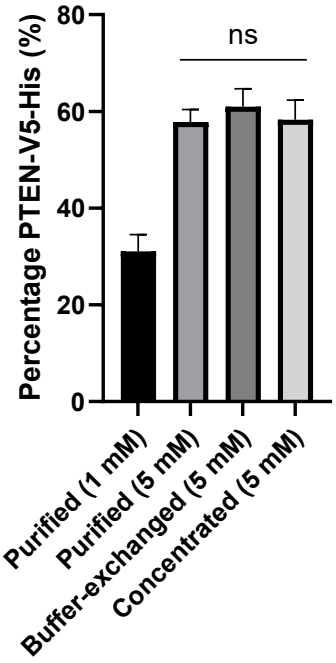

Figure 3.6. Percentage of PTEN-V5-His in post-purification samples.
A densitometry analysis of the purified PTEN-V5-His resulting from washes with 1 mM imidazole was performed on Elution 1, 2 and 3 of Figure 3.3.B (technical replicates of one biological replicate: n=1), while the analysis of the purified, buffer-exchanged, and concentrated PTEN-V5-His samples using 5 mM imidazole was performed on three biological replicates (n=3). Data represents the mean ± SEM (n=1 for 1 mM imidazole purification; n=3 for 5 mM imidazole purification). Statistical analysis was performed using one-way ANOVA with Turkey's post-test, $P > 0.05$ (ns).

In conclusion, although purification of PTEN-V5-His using 5 mM imidazole in the washes and 250 mM imidazole in the elution buffer did lead to approximatively 60% PTEN-V5-His in the purified samples, purity was highly improved compared to the purification using 1 mM imidazole in the washes. The protein was not fully recovered as some of it was eluted with the washes, but sufficient amounts of protein were obtained for further use in experimental procedures.

3.3.4. Identification of Proteins in Purified PTEN-V5-His Samples

To confirm the purification of the target recombinant PTEN and the absence of proteins that could interfere with subsequent activity assays, the proteins that were present in the 60 kDa band previously referred as PTEN-V5-His and bands referred as contaminants were identified using a HPLC-MS/MS analysis of the peptides resulting from in-gel digestion of each band presented in Figure 3.7.

Band A (> 180 kDa) was previously identified as potential aggregates in the purified samples that were not identifiable in buffer-exchanged and concentrated PTEN-V5-His samples (Figure 3.5). As previously discussed, these potential aggregates may have been partly eliminated during buffer exchange. However, they were visible in the concentrated sample

with higher amount of protein (5 µg in SDS-PAGE of Figure 3.7 vs 2 µg in SDS-PAGE of Figure 3.5). Band C represented the ~60 kDa band associated with PTEN-V5-His. Bands B (~70-80 kDa), D (~40-45 kDa), E (~33-35 kDa), and F (~27 kDa) appeared to correspond to co-eluted host proteins, referred to as contaminants. These bands appeared as multiple bands, suggesting the existence of several proteins around the same molecular weight that were co-eluted with PTEN-V5-His. Due to the challenges associated with manually cutting closely located gel bands, these multiple bands were treated as a single entity. Additionally, a faint band between bands A and B appeared in the SDS-PAGE of the concentrated sample but was too faint for manual identification and cutting for LC-MS/MS analysis.

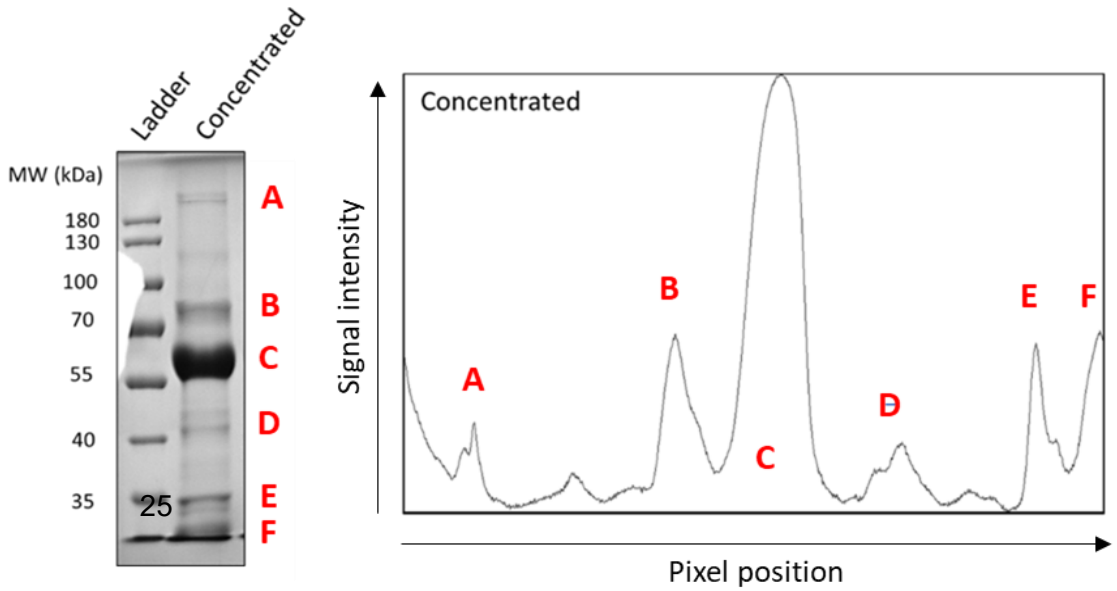

Figure 3.7. Band selection for LC-MS/MS analysis of proteins in concentrated PTEN-V5-His sample.
Concentrated PTEN-V5-His (5 µg) was resolved on a 10% acrylamide gel through reducing and denaturing SDS-PAGE and stained with PageBlue staining solution (ThermoFisher Scientific, UK) before imaging using a G:Box XR5 and GeneSys software (Syngene, UK). Images were processed and bands were identified using densitometry analysis with the ImageJ software (NIH, USA). Pixel position indicates the top to bottom lane from left to right.

Proteins in the excised gel bands A – F were subjected to in-gel digestion with trypsin and the resulting peptides were analysed by LC-MS/MS. The identification of proteins in each band was performed using Mascot Daemon (Matrix Science, USA) search engine and were reported in Table 3.6.

As anticipated, the protein in band C (~60 kDa) was primarily identified as human PTEN, exhibiting a high confidence score of 3896 and a sequence coverage of 45% with 230 peptide matches spanning 20 different unique peptide sequences. However, it should be noted that the full PTEN-V5-His, including the linker, V5-tag, and His-tag, can only be assumed to be expressed based on its apparent molecular weight in SDS-PAGE gels.

Indeed, the Mascot search, utilized for identification, could only match proteins from the SwissProt database, where PTEN is included but not the sequences of the tags.

Based on data filtering, a total of 22 host proteins were identified alongside human PTEN in the concentrated PTEN-V5-His samples (Table 3.6). The presence in bands A and B of only proteins that did not match the apparent molecular weight of these bands strongly suggested that they represented protein aggregates, as expected. Interestingly, catalase HPII (CATE) was found in band A without being present as a single protein in other bands. No clear band was identified at its apparent molecular weight (84 kDa) on the SDS-PAGE gel (Figure 3.7) and it was not identified in band B (~70-80 kDa). This could indicate that CATE had a higher potential for aggregation compared to PTEN and the bifunctional polymyxin resistance protein ArnA, another host protein identified in band B.

As described previously, PTEN was the most confident protein match in band C, indicating that it was the most abundant protein in the gel band. It seemed, however, that host proteins with similar molecular weights were co-eluted as unique sequences from alkyl hydroperoxide reductase subunit F (56 kDa), chaperonin GroEL (57 kDa), L-aspartate oxidase (61 kDa), UDP-N-acetylmuramate-L-alanine ligase (murC) (54 kDa) and deoxyguanosinetriphosphate triphosphohydrolase (DGTP) (60 kDa) were also detected in band C. While 230 peptide matched PTEN sequence, only a maximum of 13 peptide matches were found for these host proteins, which implied that they were present in small amounts compared to PTEN-V5-His. To a lesser extent, this also related to ArnA and DnaK for band B and large ribosomal subunit protein uL2 for band E, which could therefore be considered as the major contaminants in PTEN-V5-His samples.

Surprisingly, PTEN was also detected in bands B, D, E and F; however, the number of peptide matches was markedly lower (> 25-fold decrease) compared to band C. This raises the possibility of cross-contamination between samples. A similar observation was made for GroEL and RL2 which were found in bands corresponding to higher molecular weights (band B and band C, respectively) but were confidently identified in bands matching their expected molecular weights. The presence of only a few sequences of these proteins in bands of higher molecular weights suggested a potential for cross-contamination, further supported by the presence of PTEN in all bands. However, the possibility of existence of multimeric states or for a potential migration issue in the SDS-PAGE gel, where traces of proteins of lower molecular weights could have been found along the migration path, could not be excluded for GroEL and uL2. In contrast, ribosomal small subunit pseudouridine synthase A and DNA-binding transcriptional dual regulator CRP were identified in band E (~30-35 kDa) despite their expected molecular weight of 26 and 24 kDa, respectively, but were not found in band

F of approximately 27 kDa. Alike PTEN-V5-His, these proteins could migrate in SDS-PAGE gels to higher apparent molecular weights, which would explain their presence in band E but not F.

The function of each of the identified proteins was searched on the protein database UniProtKB to identify potential phosphatases that could interfere with PTEN phosphatase activity *in vitro* (Table 3.6). Amongst the host proteins, 5 that exhibit exclusively an ATPase activity (hydrolysis of adenosine triphosphate) were reported: the chaperone proteins GroEL (Fenton and Horwich, 1997), DnaK (McCarty and Walker, 1991) and HtpG (Nadeau et al., 1993), involved in protein folding and stabilization; the protein involved in replication and PriA (Tanaka et al., 2007); and murC, involved in bacterial cell wall synthesis (Liger et al., 2005). Similarly, DGTP is a triphosphohydrolase that can dephosphorylate nucleotide triphosphates (NTPs) with a preference for deoxyguanosine triphosphate (dGTP) (Seto et al., 1988a). RapZ was found to have both ATPase and GTPase activities and has been shown to dephosphorylate para-nitrophenyl phosphate (pNPP) *in vitro* (Luciano et al., 2009). With the exception of the chaperone proteins GroEL and DnaK, only a few sequences (< 10) were identified for these proteins, which implies that their relative abundance was low, suggesting that the risk of contribution to the phosphatase activity in the concentrated PTEN-V5-His sample was low. Additionally, RapZ was the sole protein found to be able to dephosphorylate other substrates than NTPs. As both OMFP and pNPP are non-proteinaceous, non-specific substrates for phosphatases, this represented a risk for interference with the subsequent OMFP assays to assess PTEN-V5-His phosphatase activity. However, only 3 sequences of RapZ were identified, which suggested a low relative abundance of RapZ in the sample and, therefore, a small possibility of contribution to the phosphatase activity in the sample.

Multiple proteins were identified in the SDS-PAGE gel band containing PTEN-V5-His (band C). This raised another problem relating to subsequent LC-MS/MS analysis of PTEN-V5-His in order to identify potential lipoxidation sites on the protein as common sequences between PTEN-V5-His and these host proteins could lead to misidentification of adduction sites. The sequence alignment of PTEN with these host proteins showed that they did not share any common sequence with PTEN (data not shown) as there was no significant similarity found, which ruled out the possibility of misidentification of adduction sites on PTEN.

Table 3.6. LC-MS/MS identification of proteins in concentrated PTEN-V5-His bands.

Band (Apparent MW)	Identified protein	Accession	MW (Da)	Score	Sequence coverage (%)	Num. of peptide matches (Num. of significant unique sequences)	Phosphatase activity [$]
A (>180 kDa)	PTEN	PTEN_HUMAN	47706[#]	522	23	28 (10)	✓
	Catalase HPII	CATE_ECOLI	84224	706	22	23 (15)	×
	Bifunctional polymyxin resistance protein ArnA	ARNA_ECOBW	74869	402	26	17 (9)	×
B (~70-80 kDa)	**Bifunctional polymyxin resistance protein ArnA**	**ARNA_ECOBW**	**74869**	**1878**	**44**	**77 (15)**	**×**
	Chaperone protein DnaK	**DNAK_ECOHS**	**69146**	**1633**	**39**	**63 (7)**	**✓**
	PTEN	PTEN_HUMAN	47706[#]	201	13	9 (5)	✓
	Chaperone protein HtpG	**HTPG_ECOHS**	**71378**	**185**	**12**	**6 (6)**	**✓**
	Primosomal protein N'	**PRIA_ECOLI**	**82231**	**124**	**8**	**5 (5)**	**✓**
	Chaperonin GroEL	CH60_ECO24	57464	95	9	5 (5)	✓
	Threonine-tRNA ligase	**SYT_ECO5E**	**74722**	**87**	**6**	**4 (4)**	**×**
	Succinate dehydrogenase flavoprotein subunit	**SDHA_ECOLI**	**65008**	**130**	**6**	**3 (3)**	**×**
C (~60 kDa)	**PTEN**	**PTEN_HUMAN**	**47706[#]**	**3896**	**45**	**230 (20)**	**✓**
	Alkyl hydroperoxide reductase subunit F	**AHPF_ECOLI**	**56484**	**351**	**29**	**13 (13)**	**×**
	Chaperonin GroEL	**CH60_ECO24**	**57464**	**275**	**22**	**12 (12)**	**✓**
	Large ribosomal subunit protein uL2	RL2_ECO24	29956	167	26	6 (6)	×
	L-aspartate oxidase	**NADB_ECO57**	**60854**	**164**	**11**	**6 (6)**	**×**
	UDP-N-acetylmuramate--L-alanine ligase	**MURC_ECOBW**	**53706**	**109**	**8**	**4 (4)**	✓
	Deoxyguanosinetriphosphate triphosphohydrolase	**DGTP_ECOBW**	**59688**	**74**	**6**	**3 (3)**	✓
D (~40-45 kDa)	**Succinylornithine transaminase**	**ASTC_ECOBW**	**43980**	**622**	**28**	**17 (9)**	**×**
	Bifunctional chorismate mutase/prephenate dehydratase	**CMPDT_ECOLI**	**43312**	**315**	**18**	**13 (8)**	**×**

	Chaperone protein DnaJ	**DNAJ_ECOHS**	**41589**	**288**	**14**	**9 (5)**	**×**
	Histidine biosynthesis bifunctional protein HisB	**HIS7_ECO57**	**40606**	**135**	**10**	**4 (4)**	**×**
	PTEN	PTEN_HUMAN	47706[#]	104	9	4 (4)	✓
E (~30-35 kDa)	**Large ribosomal subunit protein uL2**	**RL2_ECO24**	**29956**	**1405**	**51**	**62 (12)**	**×**
	Uncharacterized HTH-type transcriptional regulator YeiE	**YEIE_ECOLI**	**32874**	**190**	**15**	**6 (4)**	**×**
	Ribosomal small subunit pseudouridine synthase A	RSUA_ECOLI	25963	159	25	6 (4)	×
	Nase adapter protein RapZ	**RAPZ_ECOBW**	**32586**	**140**	**12**	**3 (3)**	**✓**
	DNA-binding transcriptional dual regulator CRP	CRP_ECOLI	23796	99	15	3 (3)	×
	PTEN	PTEN_HUMAN	47706[#]	57	6	3 (3)	✓
F (~27 kDa)	PTEN	PTEN_HUMAN	47706[#]	191	17	4 (4)	✓
	Small ribosomal subunit protein uS3	**RS3_ECO24**	**25967**	**185**	**13**	**4 (3)**	**×**

For each band, protein match outputs were ranked (from top to bottom) by the number of peptide matches (high to low) and score (high to low). Data represents values for one experiment.
Protein matches in bold had molecular weights closely matching to the apparent molecular weight of the corresponding SDS-PAGE gel band.
$: Accessions were searched on UniProtKB database to identify functions.
#: Molecular weight of endogenous PTEN; molecular weight of PTEN-V5-His = 52018 Da.

3.3.5. Post-purification PTEN-V5-His Samples Exhibited Phosphatase Activity

Prior to quantifying PTEN-V5-His activity, a range of OMFP concentrations were tested with concentrated PTEN-V5-His to assess the optimal concentration to be used for the study and confirm that PTEN-V5-His was active after purification, buffer-exchange, and concentration. Figure 3.8 illustrates the dephosphorylation kinetics of OMFP by concentrated PTEN-V5-His across concentrations ranging from 1.3 µM to 260 µM OMFP. Except for 260 µM, all concentrations exhibited linear kinetics with a positive slope, indicating active PTEN-V5-His capable of dephosphorylating this substrate. The slope increased with OMFP concentrations, particularly at 65, 130, and 260 µM, demonstrating a concentration-dependent enhancement in the rate of OMFP to OMF conversion. However, 260 µM OMFP resulted in assay saturation and high variability, shown by the plateau from 30 minutes of reaction and the increased errors, respectively, precluding its use for further experiments despite its elevated conversion rate. At 34 minutes and 10 seconds, the fluorescence value for 130 µM OMFP was twice that of 65 µM OMFP, leading to the selection of 130 µM OMFP for quantifying PTEN-V5-His phosphatase activity in purified, buffer-exchanged, and concentrated samples.

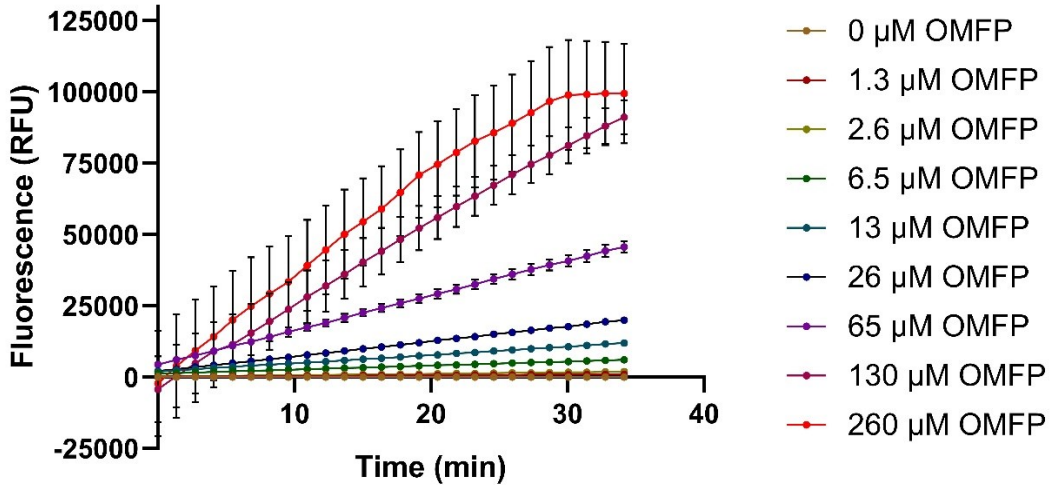

Figure 3.8. OMFP dephosphorylation by concentrated PTEN-V5-His.
Increasing concentrations of OMFP with 20 µg of concentrated PTEN-V5-His in triplicates were incubated at 30˚C for 34 minutes and 10 seconds. Fluorescence (520 nm) of the product of dephosphorylation of OMFP (OMF) was recorded over time and the values were corrected using a blank containing the corresponding concentration of OMFP without enzyme. Data points represent mean ± SEM of technical triplicates of one independent experiment (n=1).

Using the concentration of 130 µM OMFP, the specific phosphatase activity (given in nmol OMF/min/mg PTEN-V5-His) of the purified, buffer-exchanged, and concentrated PTEN-V5-His was quantified to assess the functionality and stability of PTEN-V5-His throughout the process post-purification. As previously described, PTEN-V5-His was found to be active in

the concentrated sample. In Figure 3.9, the specific phosphatase activity was measured to be 1.270 ± 0.141 (mean ± SEM) nmol OMF/min/mg in concentrated PTEN-V5-His samples, which was not found to be significantly different from the purified and buffer-exchanged PTEN-V5-His samples which showed specific phosphatase activities of 1.437 ± 0.255 (mean ± SEM) and 1.165 ± 0.125 (mean ± SEM) nmol OMF/min/mg, respectively.

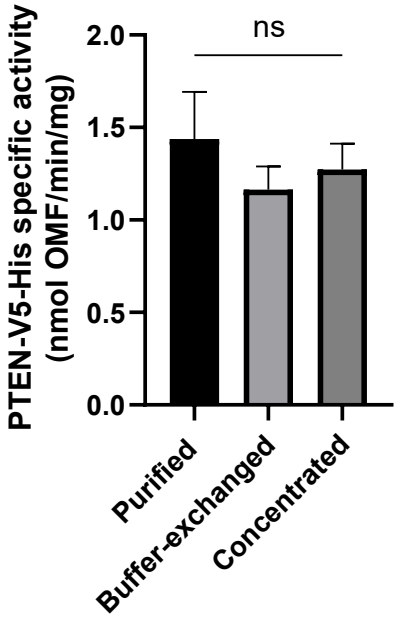

Figure 3.9. Specific phosphatase activity of PTEN-V5-His in post-purification samples.
Twenty µg of either purified, buffer-exchanged or concentrated PTEN-V5-His samples were loaded in triplicates with 130 µM OMFP and the fluorescence at 520 nm was measured during incubation for 20 minutes at 30˚C. The amount of OMF produced was calculated using the equation of the regression line of an OMF standard curve (Supplementary Figure 2), and the mean specific activity was calculated in 4 biological replicates. Values represent mean ± SEM (n=4). Statistical analysis was performed using one-way ANOVA with Turkey's post-test, P > 0.05 (ns).

In conclusion, PTEN-V5-His was purified as an active recombinant protein, able to dephosphorylate the OMFP substrate and the specific activity was not modified throughout the post-purification process to lead to concentrated PTEN-V5-His, which could be utilized to assess the effects of oxidized lipids on PTEN activity *in vitro*.

3.4. Discussion

The project aimed to purify a functional human PTEN to study its response to oxidized lipids *in vitro*. In this chapter, a recombinant PTEN, PTEN-V5-His, was produced in *E. coli* and purified using IMAC with satisfactory yields of approximately 3 mg/L of culture. Mass spectrometry confirmed PTEN's identity, and its phosphatase activity was confirmed with the OMFP assay. PTEN-V5-His specific activity was measured to be between 1.2 and 1.4 nmol OMF/min/mg protein in post-purification samples (purified, buffer-exchanged, and concentrated PTEN-V5-His samples). Optimizing purification was crucial for adequate protein yield and purity. Although the percentage of PTEN in the sample only reached approximately 60% and contaminants were still identified in the post-purification PTEN-V5-His samples after optimisation, this represented a substantial increase in purity compared to the first trial using 1 mM of imidazole. Furthermore, LC-MS/MS analysis of the remaining contaminants suggested that they would not interfere with the OMFP assay to analyse PTEN activity *in vitro* after treatment with oxidized lipids nor with the analysis of PTEN sequence to identify potential lipoxidation products of PTEN.

PTEN-V5-His was successfully expressed in BL21 (DE3) *E. coli* cells following transformation, despite a lower than optimal TE which usually ranges between 10^5 and 2 x 10^9 CFU/µg DNA with chemical transformation (Aune and Aachmann, 2010). The experimental TE obtained after transformation of BL21 (DE3) cells with the PTEN-V5-His plasmid DNA was quite low (between 2 x 10^4 and 5 x 10^4) using chemical transformation with the heat-shock method, compared to what has been reported previously (Rahimzadeh et al., 2016, Aune and Aachmann, 2010). Multiple factors can trigger low TE, including the quality of the competent cells or the size and quality of the plasmid DNA (Aune and Aachmann, 2010, Yoshida and Sato, 2009). In this case the latter was most likely responsible, as the conformation of the plasmid was not supercoiled. It has previously been shown that DNA topology could be an important factor influencing TE, supercoiled plasmid DNA resulting in higher TE than relaxed circular conformations (Ohse et al., 1997). This could have been counteracted by purification of plasmids at low temperature, for instance, which has been shown to yield to the extraction of higher proportions of the supercoiled conformation of plasmids (Carbone et al., 2012). However, selection of transformants for comparison of expression levels of PTEN-V5-His was not restricted by the low TE as a large number of single colonies could be identified, therefore no further optimization was performed to obtain a supercoiled form of the PTEN-V5-His plasmid DNA to test this hypothesis.

LC-MS/MS analysis of the band presumed to be PTEN-V5-His definitively confirmed the presence of PTEN in the samples, validating the successful isolation and purification of PTEN-V5-His from *E. coli*. Previous reports have indicated typical yields of recombinant PTEN from *E. coli* expression ranging between 1.5 and 5 mg/L of culture (Johnston and Raines, 2015a, Smith, 2022, Arora and Ghosh, 2016, Spinelli and Leslie, 2015). Here, the one-step purification process utilizing immobilized nickel-affinity chromatography with the His-tagged PTEN resulted in satisfactory yields falling within the range of typical yields found in previous studies, despite a slight protein loss after buffer-exchange and concentration. However, even with a significant increase in PTEN purity after optimization of the imidazole concentration in the purification buffers, contaminants remained. Co-elution of host proteins in IMAC purifications occurs frequently (Bolanos-Garcia and Davies, 2006). However, characterisation data, including the degree of purity, of recombinant PTEN expressed in *E. coli* and purified is generally scarce in published studies. His-tagged PTEN purifications described by Wei *et al.* (Wei et al., 2015) and Das *et al.* (Das et al., 2003) reported a > 90% pure His-tagged PTEN after a one-step purification both using a Ni-nitrilotriacetic acid (NTA) agarose column from Qiagen, which contrasts with our findings. The use of a different affinity resin and procedure could explain the discrepancy in PTEN purity. Additionally, Johnston *et al.* reported obtaining a pure His-tagged PTEN after a multi-step purification involving Ni-affinity and gel-filtration chromatography, along with anion exchange chromatography, although quantitative data was not provided as the purity of PTEN was reported with exclusively a cropped image of the SDS-PAGE of their purified samples (Johnston and Raines, 2015a). Redfern *et al.* also utilized a multi-step purification process to achieve a purified His-tagged PTEN with purity exceeding 95% (Redfern et al., 2008). In fact, multi-step purification processes often seem to be used to purify PTEN (Johnston and Raines, 2015b, Johnston and Raines, 2015a, Wang et al., 2007, Redfern et al., 2008, Zhang et al., 2022), reflecting the challenges in achieving high purity with a one-step purification approach, as observed in this chapter. Consequently, it is important to note that the calculated yield was based on total protein yield and not specific to PTEN-V5-His. The actual yield of PTEN-V5-His would therefore be 60% of 3 mg/L: 1.8 mg/L of culture. Contamination of PTEN-V5-His samples also impacted the amount of protein utilized in phosphatase activity assays, as the assay's protein amount was correlated with total proteins, thereby influencing the calculation of PTEN-V5-His specific activity.

According to Bolanos-Garcia and Davies, *E. coli* stress responsive proteins are the main host proteins that co-purify with recombinant proteins in IMAC purifications and they could be classified based on the concentration of imidazole required to elute them, which were 30 to 50 mM, 55 to 80 mM and concentrations exceeding 80 mM (Bolanos-Garcia and Davies,

2006). With 5 mM imidazole used to wash proteins off the resin and 250 mM imidazole to elute PTEN-V5-His, the concentration of imidazole in wash steps was far below the required concentrations to wash these proteins away in order to get a pure PTEN-V5-His, but such concentrations could not be used prior to elution as major PTEN-V5-His loss was identified in washes containing imidazole concentrations ≥ 25 mM (Figure 3.4). With almost 20% of the co-eluted protein being chaperone proteins (4/22), and proteins involved in antioxidant defence (CATE and alkyl hydroperoxide reductase subunit F), stress responsive proteins were indeed well represented in purified PTEN-V5-His samples. Identification of the PTEN-V5-His contaminants by mass spectrometry showed that some of the co-eluted host proteins, such as ArnA (also called YfbG), GroEL and CRP, were also reported by Bolanos-Garcia and Davies as commonly co-eluted host proteins. They also showed that native *E. coli* proteins that are co-purified by IMAC exhibit a wide diversity of folds and oligomerisation states (Bolanos-Garcia and Davies, 2006), which could explain the presence of GroEL and CRP in bands of higher molecular weight. Additionally, ArnA, succinylornithine transaminase, and large ribosomal subunit protein uL2 were previously found to be co-eluted with His-tagged PTEN (Smith, 2022). Although most of the identified contaminants were detected with fewer than 10 peptide matches compared to 230 for PTEN, which suggested that they were present in relatively low abundance, the LC-MS/MS analysis was performed from different gel bands, making comparisons unreliable. Quantitative LC-MS/MS with direct in-solution digestion of the proteins would have given more insights into the relative abundance of host proteins found in the PTEN-V5-His samples.

Ensuring that potential contaminants did not interfere with the assessment of PTEN-V5-His activity or the identification of sites of adduction by HHE and PONPC was a crucial preliminary step before conducting experiments with the purified PTEN-V5-His samples. BLAST analysis revealed no sequence similarity between the host proteins co-eluted in the same band as PTEN-V5-His and PTEN. Thus, even if HHE or PONPC were to covalently bind to these bacterial proteins, the adduction sites would not be attributed to any PTEN sequence. While seven of the identified contaminants (GroEL, DnaK, HtpG, PriA, MurC, DGTP, and RapZ) have known phosphatase activities, most of them being NTPases (Fenton and Horwich, 1997, McCarty and Walker, 1991, Nadeau et al., 1993, Tanaka et al., 2007, Liger et al., 2005, Seto et al., 1988a, Luciano et al., 2009), there was no evidence in the literature that they could dephosphorylate OMFP. Nevertheless, the use of pNPP, which (like OMFP) is an unnatural substrate to assess phosphatase activity, suggested that RapZ, for instance, could be active against other substrates than its natural substrate.

GroEL is a chaperone protein that can hydrolyse ATP but this activity is dependent on complex formation of GroEL with GroES (Madan et al., 2008) which has not been identified

in the contaminants of PTEN-V5-His. Additionally, in a study of Virmani *et al*. aiming to show that GroEL is involved in the folding of a *B. anthracis* Serine/Threonine kinase to active form, a mixture of GroEL and GroES in presence of pNPP did not lead to dephosphorylation of pNPP (Virmani et al., 2018). Similarly, DnaK and HtpG are chaperone proteins carrying an ATPase activity (McCarty and Walker, 1991, Nadeau et al., 1993). DnaK ATPase activity has been shown to be weak but was stimulated by the presence of DnaJ and GrpE. These two proteins were found to stimulate the ATPase activity of DnaK slightly individually with DnaK and greatly stimulate it when together, possibly in a sequential manner (Liberek et al., 1991). DnaJ was also part of the co-eluted host proteins found in PTEN-V5-His samples, but not GrpE, implying that DnaK ATPase activity could be slightly stimulated *in vitro*. Like GroEL, DnaK was used in a pNPP assay aiming to evaluate DnaK binding to HspR. Bandyopadhyay *et al*. incubated denatured or renatured his-tagged HspR with native DnaK and performed an enzyme-linked immunosorbent assay (ELISA) where the his-tagged HspR could bind to the plate surface (Ni-NTA) and alkaline phosphatase-conjugated anti-HspR or anti-DnaK antibodies were added to measure pNPP dephosphorylation (Bandyopadhyay et al., 2012). In this experiment, binding of anti-DnaK showed an approximate 5-fold increase in the abundance of DnaK in denatured HspR samples compared to renatured HspR samples but the dephosphorylation of pNPP was comparable between denatured and renatured HspR samples when probing with anti-HspR sera. This implied that DnaK, although highly abundant in the denatured HspR samples, did not contribute to pNPP dephosphorylation. HtpG is a metal-dependent ATPase which exhibits chaperonin activity towards denatured proteins in coordination with the DnaK/DnaJ/GrpE chaperone system. HtpG is most active in presence of calcium or magnesium but loses its activity in absence of metal (Mangla et al., 2023) and buffers used in the OMFP assay did not contain such metals.

There was no evidence of activity against substrates other than natural substrates for PriA, DGTP and murC. Furthermore, the ATPase activity of primosomal protein N' is dependent on the presence of DNA (Tanaka et al., 2003), DGTP catalyses the hydrolysis of dGTP to deoxyguanosine and triphosphate in a Mg^{2+}-dependent manner (Seto et al., 1988b, Beauchamp and Richardson, 1988) and murC only hydrolyses ATP if L-alanine is absent but uridine diphosphate-N-acetylmuramate is present with the divalent cations Mg^{2+}, Mn^{2+} or Co^{2+} (Emanuele Jr et al., 1996). Concentrated PTEN-V5-His samples and OMFP assay buffers being exempt of DNA and metals, PriA, DGTP and murC did not seem to represent a risk of interference with the assessment of PTEN-V5-His phosphatase activity.

Because the phosphatase activities of these six proteins are regulated by interaction with other proteins, DNA or the presence of metals and, most importantly, they do not seem to

act on non-natural substrates, it was unlikely that they could exhibit phosphatase activity against OMFP *in vitro.*

RapZ is a protein that modulates the synthesis of GlmS, by affecting the processing and stability of GlmZ (Kalamorz et al., 2007). Contrasting with the above-mentioned proteins, RapZ was found to be able to catalyze dephosphorylation of ATP, GTP but also pNPP with a specific activity of 1.75 mol of pNPP/min/mol of enzyme and a Km of 8.65 mM in a study by Luciano *et al*. (Luciano et al., 2009), implying that RapZ was not selective of NTPs. Although RapZ seemed to be present in concentrated PTEN-V5-His samples in relatively low abundance with only 3 peptide matches identified, this represented the main limitation in the study of the phosphatase activity of PTEN-V5-His, which could have been mitigated by adding a control with a selective PTEN inhibitor to rule out contribution of other proteins to the dephosphorylation of OMFP.

Although PTEN exhibits the highest affinity for PIP3, followed by IP4, OMFP serves as a suitable alternative substrate, with a Km of 216 µM (Mak and Woscholski, 2015). In contrast, PTEN's activity against pNPP is notably lower (Mak and Woscholski, 2015, Maehama et al., 2001). However, assays using PIP3 or IP4 are end-point assays, while OMFP allows continuous monitoring of PTEN phosphatase activity, which ensures that measurements are taken during the linear phase of the reaction. Mak *et al*. and Verrastro *et al*. reported specific activities between approximately 0.4 and 0.7 nmol OMF/min/mg protein (Verrastro et al., 2018, Verrastro et al., 2016, Mak and Woscholski, 2015). Their evaluation of PTEN phosphatase activity was conducted using PTEN-GST rather than PTEN-V5-His, and with buffers that differed in composition from the experimental conditions described here. This variation in experimental procedure could potentially account for the differences observed in PTEN specific activity values as PTEN-V5-His specific phosphatase activity against OMFP was measured to be approximately 1.4, 1.2 and 1.3 nmol OMF/min/mg protein in purified, buffer-exchanged and concentrated PTEN-V5-His samples, respectively. This was similar to the specific activity of up to ~1.3 nmol OMF/min/mg of protein reported by Smith using the same recombinant PTEN and conditions in the same laboratory (Smith, 2022). The similarity between the values obtained in this study and in the study by Smith also suggested that the contaminants of PTEN-V5-His samples were not contributing to OMFP dephosphorylation, which confirmed the suitability of the purified PTEN-V5-His samples to assess the effects of HHE and PONPC on PTEN phosphatase activity. Potential contribution of contaminants to phosphatase activity could have been investigated using a selective inhibitor of PTEN phosphatase activity, which would suppress hydrolysis of OMFP by PTEN-V5-His. Notably, the buffer-exchange and concentration processes applied to PTEN-V5-His did not result in any alteration of PTEN activity *in vitro*, indicating its stability in the designated buffer for

subsequent treatment and activity assays. This provided confidence that the purified PTEN-V5-His would be suitable for measuring PTEN activity accurately using the OMFP assay, which allowed investigation of the effects of oxidized lipids on PTEN function described in the next chapter.

Chapter 4 – Functional Consequences of HHE and PONPC on PTEN and its Downstream Signalling

4.1. Introduction

As described previously, PTEN is a redox-sensitive protein that has been shown to be inhibited by a few oxidized lipids through the process of lipoxidation (Shearn et al., 2013, Shearn et al., 2011b, Covey et al., 2010), which consists in the adduction of proteins by oxidized (and electrophilic) lipids (Viedma-Poyatos et al., 2021). In fact, adduction of HNE was previously reported (Shearn et al., 2013, Shearn et al., 2011a), as well as adduction by acrolein and Δ12-PGJ_2 (Covey et al., 2010). Shearn *et al.* showed in 2011 that physiologically relevant concentrations of HNE could activate Akt (increased phosphorylation of Ser473 and Thr308) in a time- and concentration-dependant manner and through a PI3K-dependant mechanism in HepG2 cells and primary hepatocytes. Michael addition of HNE to PTEN, leading to its inhibition, was suggested to be the link between exposure to HNE and Akt activation (Shearn et al., 2011b, Shearn et al., 2011a). Two years later, the same group further examined PTEN lipoxidation and Akt activation in ethanol-fed mice. Redox balance was found to be impaired in this model, leading to PTEN lipoxidation and inhibition, and subsequent activation of Akt2 (one of the Akt isoforms) in liver. Treatment of a recombinant human PTEN with HNE led to the discovery of 9 sites of adduction on the protein. Among those, it was suggested that Cys71 and Lys327 were particularly relevant to PTEN function as their modification may limit the substrate access to the active site or alter the association of PTEN with the membrane and thioredoxin-1, respectively. Interestingly, adduction of the catalytic cysteine (Cys124) was not detected (Shearn et al., 2013). Acrolein, HNE and Δ12-PGJ_2 were also found to covalently modify and inactivate PTEN in MCF-7 cells, increasing Akt and β-catenin signalling and cell proliferation (Covey et al., 2010). The site of adduction of 15d-PGJ_2 on PTEN was identified *in vitro* and in MCF-7 cells to be Cys136, which correlated with the ROS-independent activation of Akt and an oncogenic phenotype in xenograft models (Suh et al., 2018). Table 4.1 summarizes the effects of acrolein, HNE, 15d-PGJ_2 and Δ12-PGJ_2 on PTEN. Moreover, it seems that the oxidative sensitivity of PTEN could be highly influenced by oxidative stress levels. Inactivation of Akt has previously been observed at low levels of oxidative stress, where PTEN did not undergo significant thiol oxidation, but a further increase in H_2O_2 levels led to oxidation and inhibition of PTEN and correlated activation of Akt (Tan et al., 2015).

Table 4.1. Experimental evidence of PTEN lipoxidation and its biological effects.

Lipid peroxidation product	Treatment target	Concentration (μM) or molar ratio (MR)	Exposure time	Biological effects	Modified residues	Reference
HNE	HepG2 cells	12.5 to 100	0 to 120 min	Akt activation (with 25 to 100 μM HNE for 1 h, from 30 min with 100 μM HNE) via a PI3K-dependent mechanism and independent of Akt-specific phosphatases inhibition	NR	(Shearn et al., 2011b)
		12.5 to 250	120 min	Decreased intracellular levels of reactive oxygen species up to 100 μM		
		100	60 min	Increased cellular PIP3 concentration Increased levels of PTEN presenting carbonyls		
		100	0 to 120 min	Time-dependent decrease in PTEN phosphorylation on S380/T382/383 (activating dephosphorylation)		
		25 and 100	60 min	Inhibition of PTEN phosphatase activity to 40-50% (independent from activating dephosphorylation)		
		100	60 min (+24h recovery)	Increased lipid accumulation		
	Primary rat hepatocytes	12.5 to 100	60 min	Akt activation (at 50 and 100 μM)		
	Recombinant human PTEN	0.1:1 to 20:1	30 min	Inhibition of PTEN phosphatase activity in a concentration-dependent manner from 1:1 molar ratio	Michael addition (unknown site)	
	Recombinant human PTEN	1:1 to 10:1	30 min	Formation of multimeric forms of PTEN	Cys(71,136,250) Lys(147,223,254, 313,327,334)	(Shearn et al., 2013)
	MCF-7 cells	10	30 min	Increased levels of PTEN presenting carbonyls	NR	(Covey et al., 2010)
	HEK 293 cells	6	0 to 16 h	Time-dependent increase of cellular phospho-(S473) Akt (active), phospho-(S9) GSK3β (inactive) and β-catenin levels		
	STF3A cells	2 to 20	24 h	Increased β-catenin signalling		

	Isolated PTEN	10 (unknown MR)	NP	57% inhibition of PTEN activity		
Δ12-PGJ_2	MCF-7 cells	10	30 min	Increased levels of PTEN presenting carbonyls	NR	(Covey et al., 2010)
		2 to 20	30 min	Concentration-dependent increase in Akt phosphorylation on T308		
		20	0 to 120 min	Time-dependent increase in Akt phosphorylation on T308		
	MCF-7 cells	20	30	Akt activation without modification of PTEN expression levels and activation of PDK1		
		1 and 10	NR	Akt-dependent increase in cell proliferation		
	HEK 293 cells	6	0 to 16 h	Time-dependent increase of cellular phospho-(S473) Akt (active), phospho-(S9) GSK3β (inactive) and β-catenin levels	NR	
	STF3A cells	2 to 20	24 h	Increased β-catenin signalling		
	Isolated PTEN	1 (unknown MR)	NR	56% inhibition of PTEN activity		
Acrolein	MCF-7 cells	20	10 min	Increased levels of PTEN presenting carbonyls	NR	
	HEK 293 cells	20	0 to 6 h	Time-dependent increase of cellular phospho-(S473) Akt (active), phospho-(S9) GSK3β (inactive) and β-catenin levels		
	STF3A cells	2 to 20	24 h	Increased β-catenin signalling		
	Isolated PTEN	10 (unknown MR)	NR	40% inhibition of PTEN activity		
15d-PGJ_2	MCF-7 cells	10	3 to 48 h	Time-dependent increase in Akt phosphorylation (unspecified phosphorylation site) Increased migration Time-dependent adduction of endogenous PTEN Adduction of transfected PTEN Increased cell colony formation	Cys136	(Suh et al., 2018)

	MDA-MB-231 cells	10	3 to 12 h	Time-dependent increase in Akt phosphorylation (unspecified phosphorylation site) Time-dependent adduction of endogenous PTEN	NR	
	Recombinant PTEN	30 (unknown MR)	1 h	PTEN adduction	Cys136	
	Balb/c nude mice xenograft model	2 mg/kg	Bi-weekly for 3 weeks	Increased tumour growth Increased Akt phosphorylation in tumour tissues (unspecified phosphorylation site)	NR	

HNE: 4-hydoxy-2-nonenal; Δ12-PGJ_2: delta-12-prostaglandin J2; 15d-PGJ_2: 15-deoxy-Δ12,14-prostaglandin J2; PIP3: phosphatidylinositol-(3,4,5)-triphosphate; NR: not reported.
Molar ratios were expressed as mol of lipid peroxidation product to mol of PTEN (lipid peroxidation product:PTEN).
Akt activation signifies increased phosphorylation at both Akt Ser473 and Thr308 residues.

Investigation of the effects of lipid peroxidation products (LPPs) on PTEN have been restricted to the above-mentioned LPPs (acrolein, HNE and Δ12-PGJ_2). This study aimed to gain more insights into the effects of oxidized lipids on the function and downstream signalling of PTEN by investigating two other biologically relevant oxidized lipids: 4-hydroxy-2-hexenal (HHE) and palmitoyl-oxononanoyl phosphatidylcholine (PONPC). The α-β-unsaturated aldehyde HHE and the truncated phospholipid PONPC are LPPs originating from ω-3 polyunsaturated fatty acids (α-linolenic, eicosapentaenoic or docosahexaenoic acid) and phosphatidylcholine esterified-ω-6 polyunsaturated fatty acids (γ-linolenic or arachidonic acid), respectively. As such, they can form adducts on macromolecules including proteins, which is referred to as protein lipoxidation, and impact biological processes (Viedma-Poyatos et al., 2021).

Although it has been suggested that HHE mediates the anti-inflammatory and antioxidant effects of ω-3 polyunsaturated lipids at low concentrations by activation of Nrf2/heme oxygenase 1 system (Ishikado et al., 2010, Nakagawa et al., 2014, Ishikado et al., 2013, Yang et al., 2018a), it was found to be cytotoxic at high concentrations (Brambilla et al., 1986, Sousa et al., 2019, Lovell et al., 2012, Bae et al., 2011). In 1986, HHE effects on DNA were discovered: after exposure to HHE at a cytotoxic concentration (170 μM), HHE could induce a significant amount of DNA fragmentation and an increase in sister-chromatid exchange frequency (Brambilla et al., 1986), as well as alkylation of deoxyguanosine via Michael addition (Winter et al., 1986). These suggested possible mechanisms for genotoxicity. Furthermore, HHE was also found to induce cell apoptosis by modulation of the levels of anti-apoptotic B-cell lymphoma 2 protein (Bcl-2) and pro-apoptotic Bcl-2 associated X protein through reactive oxygen and free radical species accumulation (Bae et al., 2011, Lee et al., 2004b). Interest in HHE-induced protein lipoxidation and impact on biological processes grew. In a study by Awada *et al*., increased HHE-protein adducts were observed in a concentration-dependent manner. These HHE-protein adducts were correlated with upregulation of glutathione peroxidase 2 and the endoplasmic reticulum chaperone immunoglobulin heavy chain-binding protein, which could represent a mechanism to counteract HHE-induced inflammation and oxidative stress (Awada et al., 2012). Detection of HHE-bound proteins also suggested a role of lipoxidation by HHE in disease progression, such as progression of Alzheimer's disease. Levels of free and protein-bound HHE were increased in multiple cerebral regions in the progression of Alzheimer's disease (Bradley et al., 2012). Treatment of primary cortical cultures with HHE to simulate these findings led to a time- and concentration-dependent decrease in cell survival and a concentration-dependent decrease in glucose uptake in treated cells (Bradley et al., 2012) and subtoxic (2.5 μM) HHE concentrations significantly impaired glutamate uptake in primary rat astrocytes (Lovell et al.,

2012). The impaired glutamate uptake was directly related to an increase in HHE-bound excitatory amino acid transporter-2, the main glutamate transporter in the brain (Lovell et al., 2012). HHE level also correlated with chronic kidney disease (CKD) as HHE plasma concentrations and amounts of HHE-bound proteins in plasma of CKD patients were found to increase compared to healthy individuals (Soulage et al., 2020). Metabolic processes could also be affected by HHE as it decreased glyceraldehyde-3-phosphate dehydrogenase (GAPDH) activity and protein level in time- and dose-dependent manners (Tsuchiya et al., 2005) and pyruvate kinase could be inhibited by HHE-induced lipoxidation *in vitro* and in MCF-7 cells (Sousa et al., 2019). The implication of protein lipoxidation by HHE in cell signalling particularly illustrates the importance of this LPP in biological processes. For instance, the nuclear protein estrogen-related receptor γ (ERR-γ) was found to be modified by HHE in the obese state. *In vitro* lipoxidation decreased the DNA-binding capacity of ERR-γ and correlated with the obesity-linked down-regulation of many key genes promoting mitochondrial bioenergetics (Hauck et al., 2018). Additionally, HHE plays a role in NF-κB signalling and is, therefore, associated with inflammatory responses. HHE induced NF-κB activation by inhibitor of κB phosphorylation, accompanied by stimulation of iNOS, which can lead to activation of various proinflammatory genes (Lee et al., 2004a). An increase in the activity of p38 MAPK and extracellular signal-regulated kinase (ERK) was also found in parallel, indicating that p38 MAPK and ERK are involved in HHE-induced NF-κB activation (Je et al., 2004). Most importantly in the context of this chapter, HHE was capable of covalently modifying insulin and disrupted its biological activity and related signalling pathways, contributing to diabetic status. HHE-adducted insulin was less effective than native insulin in reducing glycemia in mice and had a decreased capacity to stimulate glucose uptake in adipocytes and skeletal muscle cells, showing increased insulin-resistance (Pillon et al., 2011, Soulage et al., 2018). Impaired insulin-induced phosphorylation of Akt was also observed at concentrations ranging from 10 to 100 µM (Soulage et al., 2018), which contrasted with the findings on the investigation of PTEN with HNE previously discussed, where Akt phosphorylation was found to be increased, suggesting that HHE and HNE could have different effects on this signalling pathway. Similarly, HHE reduced insulin-induced IRS1 phosphorylation, and limited its interaction with the p85 regulatory subunit of PI3K (Soulage et al., 2018). Thus, is it evident that HHE has a wide variety of effects on enzyme activities and metabolic pathways.

Although it has been demonstrated that not all oxidized phospholipids have the same biological activity and that the active group at the sn-2 position is mainly responsible for it (Subbanagounder et al., 2000), investigation of biological effects related to protein lipoxidation by PONPC is scarce in the literature, as opposed to the study of the biological

effects of mixtures of oxidized phospholipids. Increased levels of oxidized phospholipids, including PONPC specifically, were related to lung injury (Ke et al., 2019), periodontitis (Ademowo et al., 2020) and myocardial ischaemia-reperfusion injury (Yeang et al., 2019). Ke *et al.* showed in early work that basal levels of PONPC in lungs increased in a two-fold manner between young (2 to 4 months old) and old (18 to 24 months old) mice (Ke et al., 2019). This was put in the context of respiratory infections, to which the elderly population was more susceptible. In this context, they demonstrated that PONPC (amongst other truncated oxidized phospholipids) had low proinflammatory potential alone but could lead to endothelial permeability and exacerbate infection-induced lung injury, particularly in old mice, which could be the result of over-expression of the inflammatory markers TNFα, IL-6, KC, and IL-1β (Ke et al., 2019, Ke et al., 2023, Karki et al., 2023). PONPC has also been found to increase in cardiomyocytes (*in vitro* and *in vivo* in rats) following ischaemia and reperfusion, along with other oxidized phospholipids, and was the most abundant of the detected oxidized phospholipids in another study (Yeang et al., 2019). This was further confirmed in patients presenting with ST-elevation myocardial infarction who presented increased concentrations of PONPC in plasma after reperfusion, with PONPC being the most abundant of the 15 truncated oxidized phospholipids detected (Solati et al., 2021). PONPC could induce cell death of cardiomyocytes *in vitro* and it was found to be located mainly in the mitochondria, where it could increase mitochondria permeability (Yeang et al., 2019). The role of PONPC in cardiomyocyte cell death was further examined by Stamenkovic et al., who showed that PONPC could lead to ferroptosis (Stamenkovic et al., 2021). These data support the concept that PONPC formation is closely related to cardiovascular diseases and may contribute to some pathological effects.

Despite the evident bioactivity of both of these oxidized lipids, a limited understanding exists regarding their specific effects. Given that the redox-sensitive protein PTEN plays a pivotal role in cellular signalling, it is reasonable to hypothesize that HHE and PONPC, like HNE, acrolein, 15d-PGJ_2 and Δ12-PGJ_2, could modulate PTEN activity and influence critical biological processes associated with PTEN. Notably, the structural similarity between HHE and HNE, both possessing α-β-unsaturated aldehyde functional groups, suggests a potential parallel impact on PTEN function. Most importantly, PONPC is part of truncated oxidized phospholipids, a type of oxidized lipids that remains unexplored in their effects on PTEN despite their known biological activity. Therefore, investigating the effects of HHE and PONPC on PTEN and its downstream signalling could provide valuable insights into the interplay between inflammation, oxidative stress, and PTEN-related disorders including cancer. As described in Chapter 3, the OMFP assay was successful in assaying PTEN phosphatase activity. The effects of HHE and PONPC on PTEN phosphatase activity were

therefore measured using this method. PIP3 recruits Akt kinase to the cell membrane where PDK1 and mTORC2 phosphorylate Akt on a threonine residue at the 308th position (Thr308) and a serine residue at the 473rd position (Ser473), respectively (Manning and Toker, 2017), and PTEN acts as a negative regulator of Akt activation by converting PIP3 to PIP2 (Maehama and Dixon, 1998). LPPs that can lead to PTEN lipoxidation may interfere with PTEN's ability to regulate the activation of Akt kinase. Therefore, after identifying the sublethal concentrations of HHE and PONPC using MTT assays to assess metabolic activity of two different cancer cell lines (HCT116 and MCF-7 cells), the effects of HHE and PONPC on PTEN's downstream signalling were evaluated in these cells using western blotting to determine the activation (phosphorylated) state of Akt with the hypothesis that, alike HNE, HHE could lead to activation of the pathway.

4.2. Materials and Methods

4.2.1. Materials

3-O-methylfluorescein (OMF) was purchased from Apollo Scientific (UK) and 3-O-methylfluorescein phosphate (OMFP) was purchased from Merck (UK) as 3-O-methylfluorescein phosphate cyclohexylammonium salt. Most primary antibodies were purchased from Cell Signaling Technology (The Netherlands): rabbit anti-p-Akt (S473) (Phospho-Akt (Ser473) Antibody, #9271), rabbit anti-p-Akt (T308) (Phospho-Akt (Thr308) (D25E6) XP® Rabbit mAb, #13038) and rabbit anti-PTEN (PTEN rabbit Ab, #9552). Rabbit anti-β-actin (Anti-beta Actin antibody, #ab227387) was purchased from Abcam (UK). HRP-conjugated goat anti-rabbit secondary antibody (Anti-Rabbit IgG (whole molecule) – Peroxidase antibody, #A6154) was purchased from Merck (UK).

4.2.2. Expression and Purification of PTEN-V5-His

PTEN-V5-His was expressed and purified from BL21 (DE3) cells as described in General Materials and Methods, section 2.5 and 2.6, respectively, using binding buffer and wash buffer containing 5 mM imidazole and elution buffer containing 250 mM imidazole. The purified protein was quantified as described in General Materials and Methods, section 2.9.1.

4.2.3. Treatment of PTEN-V5-His with HHE and PONPC

Concentrated PTEN-V5-His at a final concentration of 1 mg/mL (19.2 µM) was treated with HHE or PONPC at treatment:PTEN-V5-His molar ratios of 0:1, 0.1:1, 0.5:1, 1:1, 5:1, 10:1 and 20:1 (0, 1.92, 9.6, 19.2, 96, 192 and 384 µM, respectively) for 30 min or 2 hours at 37˚C. To prepare the samples, a 10X stock for each concentration of treatment was prepared in PTEN treatment buffer (25 mM sodium phosphate pH 7.4, 150 mM NaCl) and added to 100 µg of concentrated PTEN-V5-His in a final volume of 100 µL. The samples were incubated on a heating block at 37˚C for 30 minutes or 2 hours. Shortly before the end of the incubation, a 50 mM sodium borohydride ($NaBH_4$) solution was prepared in PTEN treatment buffer, which was added to samples to a final concentration of 5 mM and incubated at RT for 30 min for complete reduction of the protein and free aldehydes.

4.2.4. PTEN-V5-His Phosphatase Activity Assay (OMFP Assay)

4.2.4.1. OMF Standard Curve

A 10 µM OMF stock solution was prepared from a 20 mM OMF solution (in DMSO) in pre-warmed OMFP assay buffer (25 mM sodium phosphate pH 8, 150 mM NaCl) at 30˚C. An OMF standard curve was prepared in triplicates in a black 96-well plate by diluting the 10 µM

OMF stock solution in OMFP assay buffer to obtain concentrations of 0.1, 0.25, 0.5, 0.75, 1, 2.5, 5, 7.5 and 10 µM in 200 µL final volume per well and a triplicate of 200 µL per well of OMFP assay buffer without OMF was added to the plate as a blank.

4.2.4.2. OMFP Assay of HHE- and PONPC-treated PTEN-V5-His

OMFP assay of HHE- and PONPC-treated PTEN-V5-His was conducted as described in Chapter 3, section 3.2.9, using a final concentration of 130 µM OMFP. Before addition of the OMFP mix, two controls were added by duplicating PTEN-/OMFP+ and PTEN+/OMFP- controls, which were supplemented with $NaBH_4$ to a final concentration of 0.5 mM. These were used for background OMFP hydrolysis subtraction and control of the activity of HHE- and PONPC-treated PTEN-V5-His samples.

4.2.5. Cell Viability Assessment

4.2.5.1. Seeding of HCT116 and MCF-7 for MTT Standard Curve

Serial two-fold dilutions of HCT116 and MCF-7 cells were seeded into a non-pyrogenic, tissue culture-treated, sterile 96-well plate in triplicates in 100 µL of complete medium (McCoy's 5A (modified) medium for HCT116 cells or DMEM for MCF-7 cells, complemented with 10% (v/v) FBS, 100 U/mL penicillin and 100 µg/mL streptomycin), starting with 100,000 cells per well. As a blank, one triplicate was left cell-free. The plate was incubated at 37˚C, 5% CO_2. After 24 hours, the MTT assay was performed as described below.

4.2.5.2. Seeding and Treatment of HCT116 and MCF-7 with HHE and PONPC

Aliquots of $1x10^4$ HCT116 or MCF-7 cells were seeded in a sterile 96-well plate in a final volume of 180 µL of complete medium and incubated for 24 hours at 37˚C, 5% CO_2. As a blank, a triplicate for each cell line was left cell-free. For HHE treatments, 20 µL of a 10X HHE stock solution were added in triplicates for each concentration. For PONPC treatments, the medium was removed from all wells, 200 µL of a 10X PONPC stock solution were added in tubes to complete medium to obtain the desired concentrations, thoroughly mixed, and 200 µL were added to cells in triplicates for each concentration. Previously prepared vehicle solutions were similarly added. As a positive control for cell death, 1 mM H_2O_2 was added in triplicates, either by preparing a 10X solution in PBS for HHE treatment control, or by directly diluting H_2O_2 in complete medium for PONPC treatment control. Plates were then incubated for 2, 4 or 24 hours at 37˚C, 5% CO_2 and the MTT assay was performed.

4.2.5.3. The 3-(4,5-Dimethylthiazol-2-yl)-2,5-diphenyltetrazolium bromide (MTT) Assay

After incubation, the medium was removed, and the wells were washed with PBS. An aliquot of 90 µL of phenol red-free empty medium (McCoy's 5A for HCT116 and DMEM for MCF-7, without FBS, penicillin and streptomycin) as well as 10 µL of MTT solution (5 mg/mL MTT in PBS) were added in each well. Plates were manually shaken for 15 seconds and incubated at 37˚C, 5% CO_2 for 3 hours. Viable cells with active mitochondria convert MTT into insoluble purple formazan crystals via enzymatic reduction. Dead or non-metabolically active cells do not perform this conversion (Ghasemi et al., 2021). Formazan crystals were solubilized by resuspension in 100 µL of 40 mM HCl, 0.1% Triton X-100 in isopropanol and shaking on a plate shaker at 1050 rpm for 30 min at room temperature. The absorbance at 570 nm was measured using a Multiskan GO plate reader (ThermoFisher Scientific, UK) and data was processed using the GraphPad Prism 8.1.0 software (GraphPad, USA).

4.2.6. Insulin Stimulation of HCT116 and MCF-7 Cells

Sterile 6-well plates were seeded with $1x10^6$ HCT116 or MCF-7 cells per well and incubated for 18 to 20 h at 37˚C, 5% CO_2. The media was removed, and cells were washed twice with PBS and starved in FBS-free media (McCoy's 5A (modified) medium for HCT116 cells or DMEM for MCF-7 cells, supplemented with 100 U/mL penicillin and 100 µg/mL streptomycin) for 2 h at 37˚C, 5% CO_2. Control cells (unstimulated) were directly lysed while the media for insulin-stimulated cells was replaced with complete media (McCoy's 5A (modified) medium for HCT116 cells or DMEM for MCF-7 cells, supplemented with 10% FBS, 100 U/mL penicillin and 100 µg/mL streptomycin) supplemented with 10 nM or 50 nM insulin. After 5, 10, 20, 30 or 60 min incubation at 37˚C, 5% CO_2, cells were harvested and lysed.

4.2.7. Treatment with HHE and PONPC of Insulin-Stimulated HCT116 and MCF-7 cells

Sterile clear 6-well plates were seeded with $1x10^6$ HCT116 or MCF-7 cells per well and incubated for 18 to 20 hours at 37˚C, 5% CO_2. Cells were treated, accordingly to General Materials and Methods, section 2.8, with 5, 10, 25 or 50 µM HHE or PONPC for 30 min, 2 h or 4 h at 37˚C, 5% CO_2 or untreated by adding an equal amount of PBS for HHE controls or complete media for PONPC controls (Ctrl), or ethanol (Vehicle) and incubated for 30 min, 2 h or 4 h at 37˚C, 5% CO_2. All HHE- and PONPC-treated cells as well as controls were stimulated with 10 nM insulin for 60 min prior to cell lysis.

4.2.8. Cell Lysis

HCT116 and MCF-7 cells were washed twice with ice-cold PBS on ice and scraped in 100 µL/well of lysis buffer (50 mM Tris-HCl pH 7.5, 1 mM EDTA, 150 mM NaCl and 1% Triton X-100) supplemented with 1 mM PMSF, cOmplete™ EDTA-free protease inhibitor cocktail

(Merck, UK) and Pierce phosphatase inhibitor (ThermoFisher Scientific, UK) as per manufacturer's instructions. Cell suspensions were transferred to microcentrifuge tubes and agitated at 4˚C for 30 min. Protein lysates (supernatants) were harvested after centrifugation at 14,000 x g for 10 min. Total protein concentration of each sample was assessed as described in General Materials and Methods, section 2.9.2.

4.2.9. SDS-PAGE

SDS-PAGE was performed with 10% acrylamide gels and 20 µg of protein per well as described in General Materials and Methods, section 2.10.

4.2.10. Western Blotting of PTEN/Akt Signalling Proteins

4.2.10.1. Protein Transfer

Proteins separated by SDS-PAGE were transferred onto methanol-activated PVDF membranes at 30 V overnight in transfer buffer (25 mM Tris, 190 mM glycine and 20% methanol) at 4˚C using the Mini Trans-Blot® Cell system (Bio-Rad, UK). The membranes were subsequently reactivated with methanol, stained with a Ponceau S staining solution (0.2% (w/v) Ponceau S/5% (v/v) glacial acetic acid) to check for transfer efficiency and destained in water for 5 min and 3 times 5 min in TBS-T.

4.2.10.2. Immunoblotting

P-Akt (S473), p-Akt (T308), total Akt (t-Akt), PTEN and β-actin (loading control) were successively probed with specific primary antibodies. The PVDF membranes were blocked in blocking solution (5% milk powder in TBS-T) for 1 hour at RT, incubated with anti-p-Akt primary antibodies in 5% BSA in TBS-T at the working dilution of 1:1,000 overnight at 4˚C, washed in TBS-T (3 washes of 5 minutes each), incubated with HRP-conjugated anti-rabbit secondary antibodies in blocking solution at the working concentration of 1:5,000 for 1 hour at RT and imaged. Membranes were stripped of antibodies with stripping buffer (200 mM glycine, 3.5 mM SDS and 1% Tween-20, pH 2.2) for 10 minutes twice on a rocking shaker at maximum speed, washed twice in TBS (2 mM Tris, 150 mM NaCl) for 10 minutes and twice in TBS-T for 5 minutes. Following another blocking step as previously described, t-Akt probing followed the same steps with the anti-Akt primary antibody and same secondary antibody in blocking solution at a 1:10,000 dilution and the membranes were stripped as previously described. For PTEN and β-actin, the PVDF membranes were blocked as previously described, incubated with anti-PTEN primary antibodies in blocking solution at the working dilution of 1:1000 overnight at 4˚C and washed in TBS-T (3 washes of 5 minutes each). The membranes were then incubated with anti-β-actin primary antibodies in blocking

solution at the working dilution of 1:5000 for 1 hour at RT, washed in TBS-T (3 washes of 5 minutes each), incubated with HRP-conjugated anti-rabbit secondary antibodies in blocking solution at the working concentration of 1:10,000 for 1 hour at RT and imaged. PTEN and β-actin were initially probed separately to ensure proper labelling.

4.2.10.3. Imaging

After each incubation with HRP-conjugated secondary antibodies, membranes were washed intensively (3 washes of 10 minutes each) in TBS-T, rinsed in TBS and incubated with either SuperSignal™ West Atto Ultimate substrate (TheroFisher scientific, UK), Clarity Western ECL Substrate (Bio-Rad, UK) or EZ-ECL (Biological Industries, Israel) as per manufacturer's instructions. Membranes were placed between two acetate sheets and imaged using a G:Box XR5 with GeneSys software (Syngene, UK) or a ChemiDoc MP (Bio-Rad, UK). Images were processed using the software ImageJ. The density of the signal for each band was determined after light background subtraction using a rolling ball radius of 100 and either normalized to t-Akt intensity for p-Akt or to β-actin for PTEN using the Excel software (Microsoft, USA). The normalized density values were subsequently normalized to the vehicle control on GraphPad Prism 8.1.0. (GraphPad, USA).

4.2.11. Statistical Analysis

Statistical analysis was performed on GraphPad Prism 8.1.0. (GraphPad, USA). Data from three or more biological replicates with one variable was analysed using one-way ANOVA analysis, correcting for multiple comparisons using the Tukey post-test. Data from three or more biological replicates with two variables was analysed using two-way ANOVA analysis, correcting for multiple comparisons using Dunnett's post-test when comparing to untreated control or using Sidak's post-test for comparisons within a variable. In the event of missing replicates in a two-variable analysis, statistical analysis was performed using a mixed-effects analysis with correction for multiple comparisons as previously described. Statistical significance was defined as $P < 0.05$. The P values were annotated as follows: $P > 0.05$ (ns), $P \leq 0.05$ (*), $P \leq 0.01$ (**), $P \leq 0.001$ (***), $P \leq 0.0001$ (****). Data is shown as mean values ± SEM unless stated otherwise.

4.3. Results

4.3.1. Effects of Conditions for PTEN Treatment with Oxidized Lipids on PTEN-V5-His Phosphatase Activity

To uncover the scope of parameters influencing PTEN-V5-His specific activity in these experiments, the specific activity of untreated samples subjected to the same conditions as HHE- or PONPC-treated samples (reduction with 5 mM $NaBH_4$ for 30 minutes at RT and incubation for 30 minutes or 2 hours at 37˚C) were compared with concentrated PTEN-V5-His (not reduced by $NaBH_4$ and not incubated at 37˚C). The specific activity of PTEN-V5-His after incubation for 2 hours at 37˚C was significantly lower than the non-incubated PTEN-V5-His (Figure 4.1). This suggests that activity is partially lost over time, possibly due to oxidation of PTEN-V5-His or degradation by proteases. However, the specific activity of PTEN-V5-His was not significantly different between samples incubated at 37˚C for 30 minutes and not incubated, which showed that reduction of the protein had no significant impact on its specific activity.

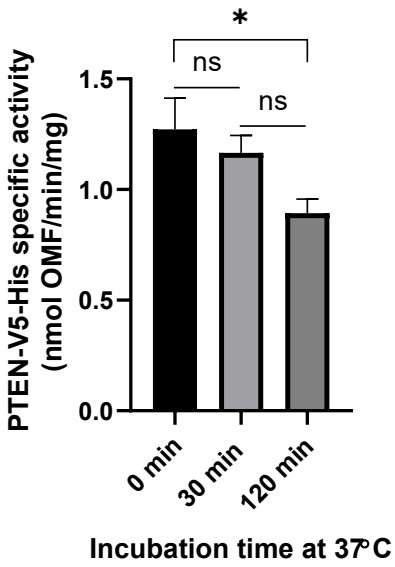

Figure 4.1. Effect of incubation at 37˚C of PTEN-V5-His on its specific phosphatase activity.
Twenty µg of either untreated and not incubated concentrated PTEN-V5-His or $NaBH_4$-treated (5 mM for 30 min at RT) and incubated for 30 or 120 min at 37˚C were loaded in triplicates with 130 µM OMFP and the fluorescence at 520 nm was measured during incubation for 20 minutes at 30˚C. The amount of OMF produced was calculated using the equation of the regression line of an OMF standard curve (Supplementary Figure 2), and the mean specific activity was calculated for each biological replicate. Data represents mean ± SEM of 4 biological replicates (n=4) for 0 min incubation and 6 biological replicates (n=6) for 30 and 120 min incubation. Statistical analysis was performed using one-way ANOVA with Turkey's post-test; $P > 0.05$ (ns), $P \leq 0.05$ (*).

As incubation times influenced PTEN-V5-His specific activity, normalization of data to untreated samples was used in subsequent measurements to compare 30 minutes and 2 hours treatments.

4.3.2. HHE and PONPC Inhibited PTEN-V5-His Phosphatase Activity in a Concentration- and Time-Dependent Manner

To identify the effects of HHE and PONPC on PTEN phosphatase activity, the specific activity against OMFP of PTEN-V5-His was measured after treatment with increasing concentrations of HHE or PONPC (0.1:1, 0.5:1, 1:1, 5:1, 10:1 and 20:1 treatment:PTEN-V5-His molar ratios corresponding to treatment concentrations of 1.92, 9.6, 19.2, 96, 192 and 384 µM, respectively) for 30 minutes and 2 hours *in vitro*. This was normalized to the untreated control to account for the contribution of incubation times at 37˚C to the modification of PTEN-V5-His specific phosphatase activity.

In Figure 4.2, a significant decrease in specific phosphatase activity was observed for PTEN-V5-His treated with HHE and PONPC for 30 minutes and 2 hours. HHE led to a significant inhibition of PTEN-V5-His phosphatase activity from 10:1 and 5:1 HHE:PTEN-V5-His molar ratios after treatment for 30 minutes and 2 hours, respectively. At a 20:1 HHE:PTEN-V5-His molar ratio, only 32.7±2.9% and 8.9±1.0% (mean ± SEM) of the specific phosphatase activity of PTEN-V5-His remained after treatment for 30 minutes and 2 hours, respectively (Figure 4.2.A). PONPC showed a similar effect on PTEN-V5-His but at lower treatment concentrations, with a PTEN-V5-His specific phosphatase activity significantly lower from 1:1 PONPC:PTEN-V5-His molar ratios for both 30 minutes and 2 hours treatments (Figure 4.2.B). Surprisingly, the percentage of PTEN-V5-His activity in samples treated with a 1:1 HHE:PTEN-V5-His molar ratio for 2 hours was not found to be significantly different from the control although it led to a value of 88.1±11.2% activity (mean±SEM) (Figure 4.2.A), which was comparable to the values obtained with PONPC in the corresponding conditions (86.7±2.4% and 87.1±4.0% (mean±SEM) for 30 minute- and 2 hour-treatments, respectively) (Figure 4.2.B). This was possibly due to the higher variance obtained with the HHE treatment. At a PONPC:PTEN-V5-His molar ratio of 20:1, the remaining fraction of active PTEN-V5-His was comparable to HHE, with 28.3±1.3% and 7.7±3.8% (mean±SEM) for 30 minutes and 2 hours treatments, respectively (Figure 4.2.B).

At concentrations of HHE and PONPC inhibiting PTEN-V5-His, the decrease in specific phosphatase activity was generally higher after 2 hours than after 30 minutes of treatment, suggesting that the inhibitions of PTEN-V5-His by HHE and PONPC was also time-dependent. As Figure 4.2.A showed, HHE significantly decreased PTEN-V5-His phosphatase activity at a HHE:PTEN-V5-His molar ratio of 5:1 after 2 hours treatment, but

not after 30 min treatment, and this was highlighted with a P value of 0.0108 and a 30.6% mean difference in percentage activity between the 30 minutes- and 2 hours-treatments. Similarly, at a molar ratio of 10:1, the inhibition of PTEN-V5-His by HHE was stronger after 2 hours than after 30 minutes of treatment with a percentage activity of 72.9±6.7% and 24.18±1.5% (mean±SEM), respectively, leading to difference of 48.7% percentage activity and a P value of 0.0002. In contrast, the difference of resulting PTEN-V5-His activity between 30 minutes and 2 hours treatments with a 20:1 HHE:PTEN-V5-His molar ratio did not lead to a significant difference, although the mean difference was 23.8%. For PONPC, the difference in percentage activity of PTEN-V5-His between 30 minutes- and 2 hours-treatments was significant with P values ≤ 0.0001 for PONPC:PTEN-V5-His molar ratios of 5:1, 10:1 and 20:1, but not for a molar ratio of 1:1. This suggested that an equimolar presence of PONPC with PTEN-V5-His could lead to the inhibition of PTEN-V5-His but that time of exposure to PONPC was enhancing PTEN-V5-His inhibition with higher concentrations only. However, it cannot be excluded that enhancement of the inhibition of PTEN-V5-His could be observed for longer treatment durations.

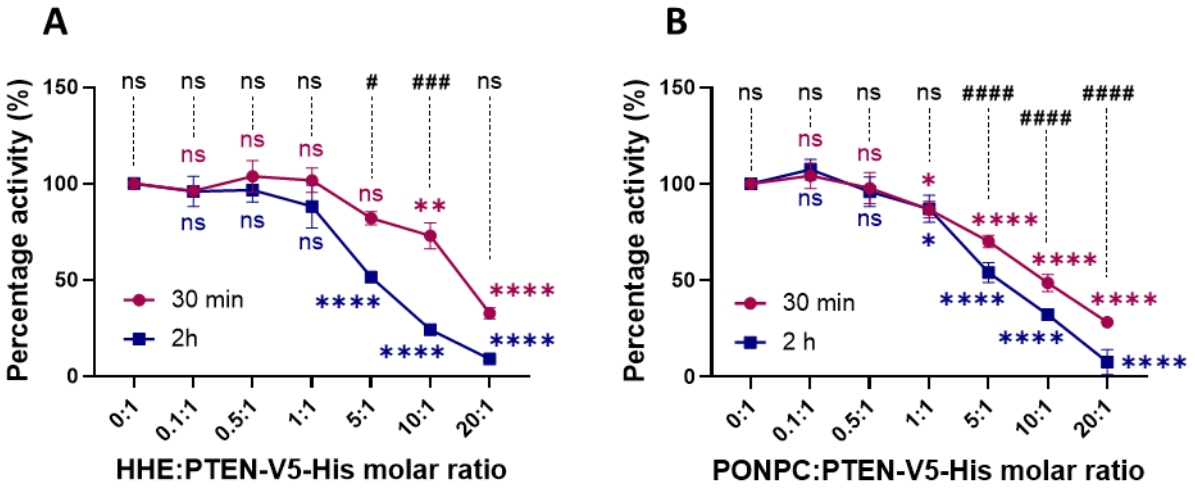

Figure 4.2. HHE and PONPC inhibited PTEN-V5-His in a time- and concentration-dependent manner.

Concentrated PTEN-V5-His was untreated or treated with increasing molar ratios of HHE (A) or PONPC (B) for 30 min and 2 h at 37˚C, followed by reduction with 5 mM $NaBH_4$ for 30 min at RT. Twenty µg of untreated or treated samples were loaded in triplicates in a black 96-well plate with 130 µM OMFP for 20 min at 30˚C, while fluorescence at 520 nm was measured periodically. PTEN-V5-His specific phosphatase activity was calculated based on the linear regression of an OMF standard curve (Supplementary Figure 2) and normalized to the untreated control. Data represents mean ± SEM of 3 biological replicates measured in triplicates (n=3). Statistical analysis was performed using two-way ANOVA with multiple comparisons to the untreated control using Dunnett's post-test to test the effect of treatment concentrations (P > 0.5 (ns), P ≤ 0.05 (*), P ≤ 0.01 (**), P ≤ 0.001 (***), P ≤ 0.0001 (****)) or with Sidak's post-test to test the effect of time of exposure at a fixed treatment concentration (P > 0.5 (ns), P ≤ 0.05 (#), P ≤ 0.01 (##), P ≤ 0.001 (###), P ≤ 0.0001 (####)).

4.3.3. Toxicity of HHE and PONPC on HCT116 and MCF-7 Cells

The effects of HHE and PONPC on HCT116 and MCF-7 cell viability were investigated to identify sublethal concentrations. Prior to assaying HHE and PONPC, it was essential to identify the optimal seeding cell density for MTT assays (in a 96-well plate format). This was determined by seeding HCT116 and MCF-7 cells in a two-fold dilution series from 100,000 cells per well and performing MTT assays after 24 hours incubation at 37˚C. The aim was to identify a seeding cell density with a resulting absorbance value at 570 nm from solubilized formazan that was falling within a linear range and exhibiting minimal variance to be able to accurately detect variation of cell viability when assaying HHE and PONPC. A linear correlation between cell number and MTT-induced absorbance ($R^2 \geq 0.98$) was obtained up to 50,000 cells per well for HCT116 cells and 12,500 cells per well for MCF-7 cells (Figure 4.3). However, although a linear correlation could be identified up to 50,000 cells per well for HCT116 cells, the intersection at the Y axis increased with the seeding density (Figure 4.3.C). A seeding cell density of 10,000 cells per well was therefore chosen for MTT assays using HCT116 and MCF-7 cells as a compromise between resulting absorbance, acceptable regression coefficient, and limited variance.

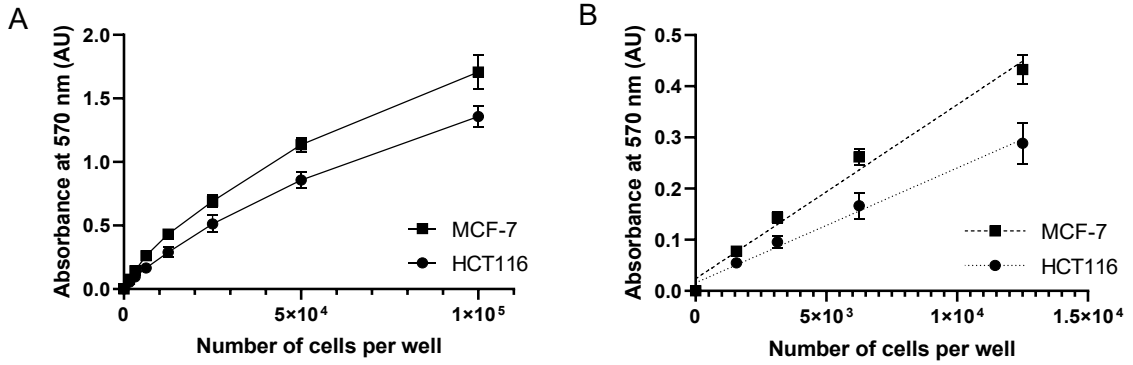

C

	HCT116		MCF-7	
Maximum cell density	**R^2**	**Y axis intersection**	**R^2**	**Y axis intersection**
3,125	0.9929	0.0023	0.9979	0.001917
6,250	0.9892	0.0089	0.9960	0.0086
12,500	0.9895	0.0132	0.9855	0.0236
25,000	0.9928	0.0249	0.9759	0.0499
50,000	0.9881	0.0444	0.9782	0.0805
100,000	0.9773	0.0810	0.9634	0.1373

Figure 4.3. MTT assay standard curve of HCT116 and MCF-7 cells and linearity of the assay. HCT116 and MCF-7 cells were seeded in triplicates in a 96-well plate at densities shown. After incubation at 37˚C for 24 h, the MTT assay was performed and the absorbance at 570 nm was measured using a Multiskan Go plate reader (ThermoFisher Scientific, UK). The results are expressed as mean ± SEM of three biological replicates measured in triplicates (n=3). (A) shows the viability of HCT116 and MCF-7 cells. (B) is a representation of the linearity of the MTT assay with HCT116 cells and MCF-7 cells using seeding cell densities up to 12,500 cells/well. Linearity was

determined by a linear regression analysis (dotted lines) in Graphpad Prism 8.0. (C) presents the regression coefficients and intersection to Y axis of the linear regression lines plotted with different maximum seeding cell densities.

To assess the impact of HHE and PONPC on cell viability and determine suitable working concentrations for experimental use without inducing cell death, MTT assays were conducted on HCT116 and MCF-7 cells following treatment with varying concentrations of HHE and PONPC for 2, 4, and 24 hours. HCT116 cells seemed to be more sensitive to HHE and PONPC than MCF-7 cells, with generally lower viability with treatment concentrations and time of exposure, which was particularly visible for HHE (Figure 4.4). HHE showed a time- and concentration-dependent effect on cell viability of both HCT116 and MCF-7 cells, with a significant decrease of HCT116 cell viability (up to ~20%) from 100 µM, 50 µM and 25 µM after 2 hours, 4 hours and 24 hours of treatment, respectively (Figure 4.4.A), while MCF-7 cell viability was only found to be significantly decreased (up to ~50%) at a concentration of 100 µM after 4 and 24 hours of exposure (Figure 4.4.B). In contrast, PONPC only showed a similar effect after treatment of HCT116 cells for 4 hours, where a significant decrease in cell viability was observed with increasing concentrations of PONPC, ultimately reaching 60% viability (Figure 4.4.C). Interestingly, the viability of HCT116 cells treated with PONPC for 2 and 24 hours seemed to decrease slightly (from 100% to 80%) for concentrations up to 10 µM and to increase to basal levels at higher concentrations (Figure 4.4.C). This was not observed in MCF-7 cells. In the latter, PONPC did not seem to affect cell viability with PONPC at concentrations up to 50 µM after 2 and 4 hours of exposure (Figure 4.4.D). However, although only treatment of MCF-7 cells with 50 µM PONPC for 24 hours led to a statistical difference in cell viability, it seemed that 24 hours of exposure of MCF-7 cells to PONPC could affect cell viability at lower concentrations with cell viabilities ranging between 89.8% and 84.3% (Figure 4.4.D). These results suggested that HHE exhibits greater toxicity compared to PONPC, particularly evident in HCT116 cells.

As 24 hours of treatment showed generally more effects on HCT116 (except for PONPC treatments) and MCF-7 cells viability, further investigation of the biological effects of HHE and PONPC were performed at lower time points to avoid cell toxicity. This is important to note as this study would relate to acute effects of exposure to these oxidized lipids, rather than chronic exposure to low concentrations of HHE and PONPC. When considering 2 and 4 hours of treatment with HHE and PONPC, with the exception of PONPC treatment of HCT116 cells which raised a concern of cell toxicity with an average value of 60% cell viability at 50 µM PONPC, 50 µM of both HHE and PONPC seemed to be the critical concentration where significant decrease in cell viability could be observed in both cell lines with cell viabilities ranging from 85.9% to 101.7%. Therefore, this concentration was chosen as maximal concentration for biological assays.

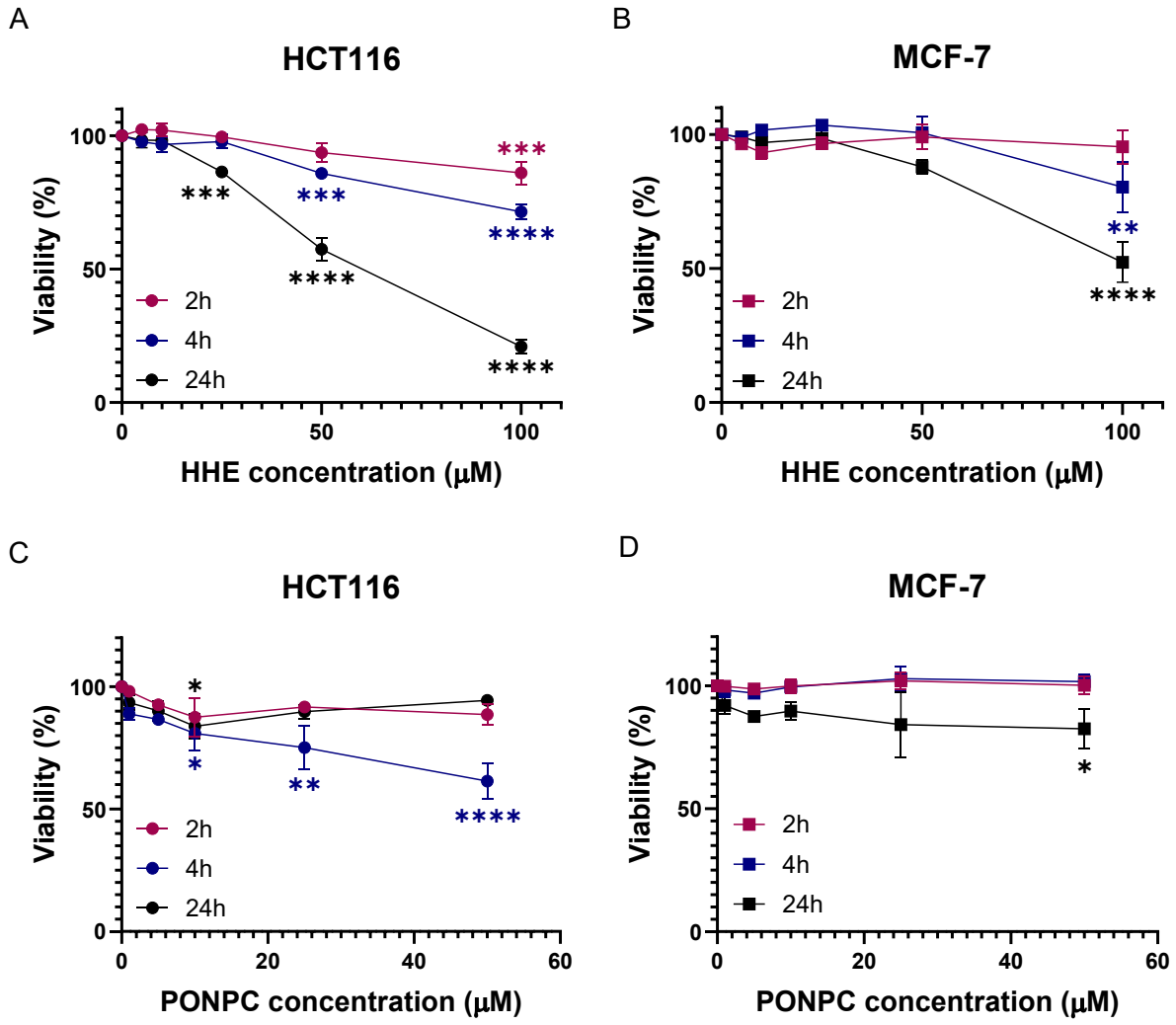

Figure 4.4. Effects of HHE and PONPC on HCT116 and MCF-7 cell viability.
(A) Cell viability of HCT116 cells in response to HHE. (B) Cell viability of MCF-7 cells in response to HHE. (C) Cell viability of HCT116 cells in response to PONPC. (D) Cell viability of MCF-7 cells in response to PONPC. HCT116 and MCF-7 cells were untreated or treated with HHE or PONPC at various concentrations for 2, 4 and 24 h, and cell viability was determined using MTT assays. The control (untreated, in vehicle) group corresponds to 100% of viable cells. Data is presented as the mean percentage of viability compared to the untreated control ± SEM (n=6 and n=5 for HCT116 cells treated with HHE and MCF-7 cells treated with HHE, respectively, and n=3 for PONPC treatments on HCT116 and MCF-7 cells). Statistical analysis was performed using two-way ANOVA with Dunnett's post-test for multiple comparisons to the untreated control; absence of annotation represents $P > 0.05$ (ns), $P \leq 0.05$ (*), $P \leq 0.01$ (**), $P \leq 0.001$ (***), $P \leq 0.0001$ (****).

The MTT assays conducted provided insight into the broader cellular context of these human cancer cells following exposure to HHE and PONPC. It is evident that HHE and PONPC, rather than specifically targeting PTEN, would influence multiple cellular components and various biological processes simultaneously as an array of different biomolecules can be affected by such molecules, including components of the PI3K/PTEN/Akt pathway. Indeed, while PTEN limits proliferation and survival, viability was lost, which suggested that multiple

components were affected, as inhibition of PTEN alone would be expected to lead to increased proliferation.

4.3.4. Insulin Reversibly Stimulated Phosphorylation of Akt in HCT116 and MCF-7 Cells

In a cellular context, PTEN is particularly known for its role in negatively regulating the PI3K/Akt signalling pathway. As dephosphorylation of PIP3 occurs via PTEN catalysis, PTEN indirectly inhibits Akt, which is naturally activated in the presence of PIP3 by phosphorylation of two different sites: serine at the 473rd position (Ser473) and threonine at the 308th position (Thr308). Activation of Akt is dependent on the interaction of tyrosine kinase receptors with their ligand, like the insulin receptor with insulin, for instance. When PTEN lipid phosphatase activity is inhibited or lost, Akt phosphorylation is enhanced as cellular PIP3 abundance increases. To investigate if HHE and PONPC could affect PTEN lipid phosphatase activity *in cellulo*, the phosphorylation state of Akt was examined in insulin-stimulated cells.

The kinetics of insulin-induced Akt phosphorylation were first investigated in HCT116 and MCF-7 cells by subjecting serum-deprived cells to 10 nM or 50 nM insulin in complete media for durations ranging from 5 to 60 minutes. Immunoblotting for phospho(p)-Akt (S473) and p-Akt (T308) (Figure 4.5) revealed notable phosphorylation of Akt at both sites 30 minutes following insulin stimulation. However, this phosphorylation state appeared to diminish partially at 60 minutes, as indicated by lower levels of p-Akt (S473) and p-Akt (T308) compared to the 30-minute time point. Nonetheless, these levels were mostly higher than those observed for stimulation durations less than 30 minutes, during which low or negligible Akt phosphorylation was detected. In the absence of insulin stimulation (unstimulated control), p-Akt (S473) and p-Akt (T308) were not detected, although the band for t-Akt on the membranes for p-Akt (T308) detection was of low intensity. This could be due to a down-regulation of the expression of Akt in the unstimulated samples. However, an uneven loading of protein from lysates in the SDS-PAGE gel was more likely but no detection of loading control (housekeeping gene, for instance) was performed to confirm this. These findings suggested that prior to the peak of Akt phosphorylation observed at 30 minutes, there was a modest activation of Akt in HCT116 cells, though not in MCF-7 cells. Specifically, in HCT116 cells, slight but detectable levels of p-Akt (S473) and p-Akt (T308) were observed between 5 and 20 minutes post-insulin stimulation, while only minimal traces of p-Akt (T308) were noted in MCF-7 cells at 5, 15, and 20 minutes post-insulin induction.

As the primary aim of this investigation was to evaluate the impact of HHE and PONPC on Akt activation in HCT116 and MCF-7 cells, an intermediate level of Akt phosphorylation was

deemed optimal. If Akt were fully activated, detecting any further positive regulation of Akt phosphorylation would have been challenging. Conversely, observing negative regulation of Akt phosphorylation at very low levels of basal Akt phosphorylation would also have been difficult. Given these considerations, examining the effects of HHE and PONPC on Akt activation could not be reliably achieved in unstimulated cells or cells stimulated for less than 30 minutes, as p-Akt levels were either undetectable or minimal under these conditions. Additionally, a 30-minute insulin stimulation resulted in high levels of Akt phosphorylation, potentially masking any potential increases in Akt phosphorylation induced by HHE and PONPC treatments. Therefore, to ensure an appropriate window for observing alterations in Akt phosphorylation, a 60-minute insulin stimulation was performed alongside HHE and PONPC treatments in HCT116 and MCF-7 cells. However, it is important to note that there were variations in levels of total Akt across some of the western blot membranes; verification of protein loading with housekeeping gene labelling would have been useful to determine whether these variations were the result of modification of Akt expression levels or technical error.

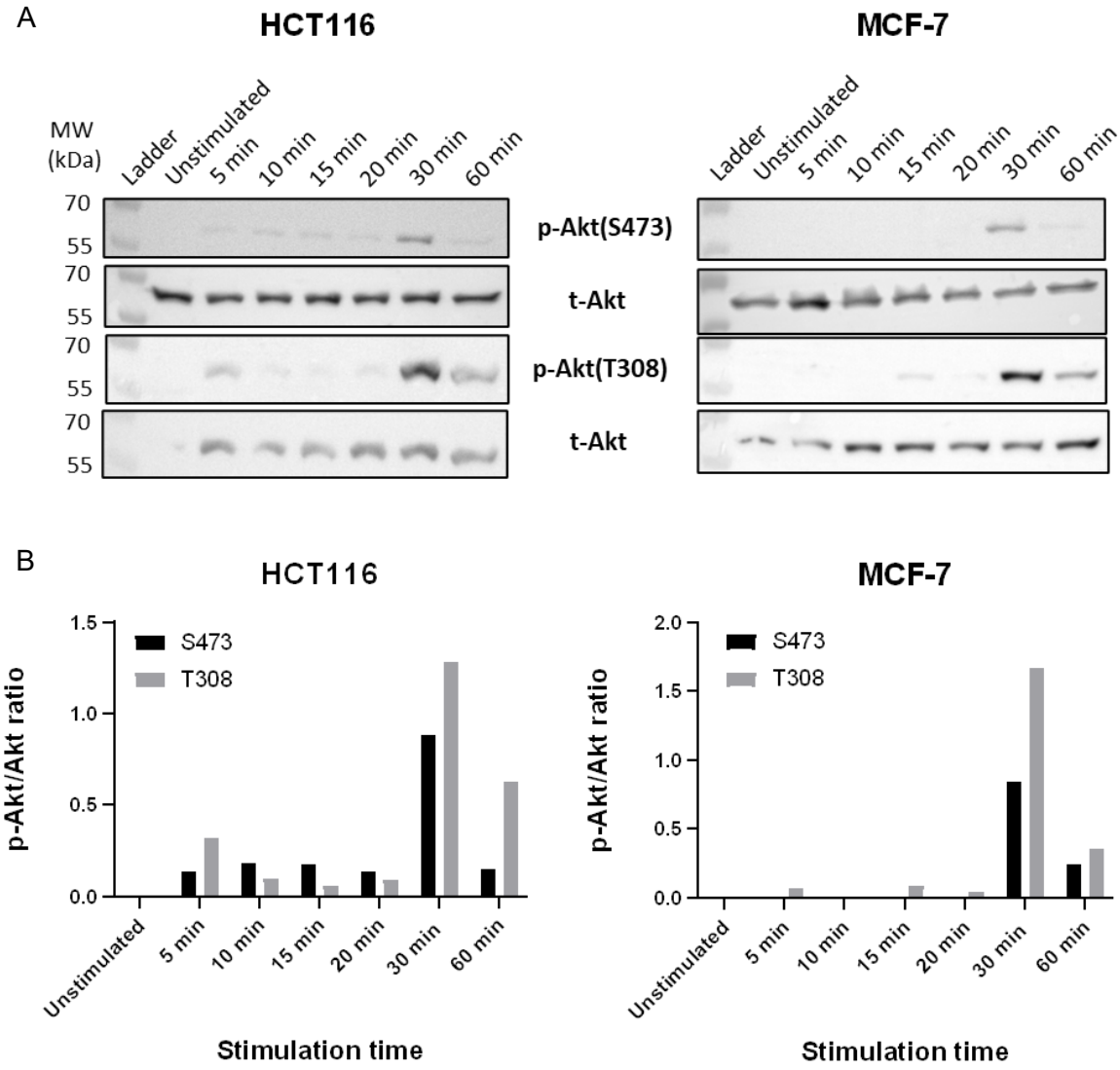

Figure 4.5. Timecourse of activation of Akt by insulin in HCT116 and MCF-7 cells.
(A) Western blot of p-Akt and total Akt (t-Akt) in HCT116 and MCF-7 cells after insulin stimulation. After 2 hours of starvation, HCT116 and MCF-7 cells were incubated in complete media supplemented with insulin at 37˚C for 5 to 60 minutes. Cells were lysed with protease and phosphatase inhibitors and proteins were resolved by SDS-PAGE with 20 µg per well. Immunoblotting for p-Akt (S473) and p-Akt (T308) was performed separately. The membranes were stripped and t-Akt was subsequently probed. Membranes were imaged using Clarity ECL substrate (Bio-Rad, UK) and a G:Box XR5 with GeneSys software (Syngene, UK). Western blots of p-Akt (S473) and p-Akt (T308) were obtained after stimulation with 10 nM and 50 nM insulin, respectively. (B) shows the densitometry analysis of the p-Akt/t-Akt ratio of HCT116 and MCF-7 cells stimulated for 5 to 60 min with insulin, performed using ImageJ software. Data represents values for one biological replicate (n=1).

4.3.5. Effects of HHE and PONPC on Akt Phosphorylation State in HCT116 and MCF-7 Cells

To determine if HHE and PONPC could affect the PI3K/PTEN/Akt pathway in HCT116 and MCF-7 cells, both cell lines were treated with HHE or PONPC at concentrations ranging from 5 to 50 µM for 30 minutes, 2 hours or 4 hours in parallel with stimulation with 10 nM insulin

for 1 hour and western blotting of p-Akt (S473), p-Akt (T308) and total Akt (t-Akt) were performed to measure p-Akt/t-Akt ratios in all conditions. These data are shown in Figures 4.7- 4.10, with the western blot images in panels A and B and p-Akt/t-Akt ratios in panels C and D.

In HCT116 cells, treatment with HHE at concentrations ≥ 25 µM led to an increase of phosphorylation on Ser473 after 2 h and 4 h of treatment, particularly for 50 µM HHE which showed a significant difference in relative levels of p-Akt (S473) compared to the vehicle control at both time points, while treating with HHE for 30 min did not modify levels of p-Akt (S473) (Figure 4.6.A and 4.6.C). An increase in relative p-Akt (T308) seemed to occur in HCT116 cells treated with 50 µM HHE for 30 min but this was not significant compared to the vehicle control. However, treatments for 2 h did not seem to modify p-Akt (T308) levels and treatments for 4 h seemed to lead to decreased phosphorylation of Thr308 with ≥ 25 µM HHE, although all variations were not significantly different from the vehicle control (Figure 4.6.B and 4.6.D). The lack of significance is most likely to be due to the high variation between biological replicates.

Interestingly, HHE seemed to affect phosphorylation of Thr308 on Akt in MCF-7 cells differently. Although results were less clear than with HCT116 cells as the variation between replicates seemed to be generally higher, HHE seemed to increase phosphorylation levels of Ser473 in MCF-7 cells after 2 h and 4 h treatment as well (Figure 4.7.A and 4.7.C). However, there was no significant modification of relative phosphorylation of Ser473 in MCF-7 cells treated with HHE for 30 min (Figure 4.7.C). The same effects seemed to occur on Thr308 in MCF-7 cells, although only treatment for 4 h with 50 µM HHE was found to lead to a significant increase in relative phosphorylation of Thr308 (Figure 4.7.B and 4.7.D).

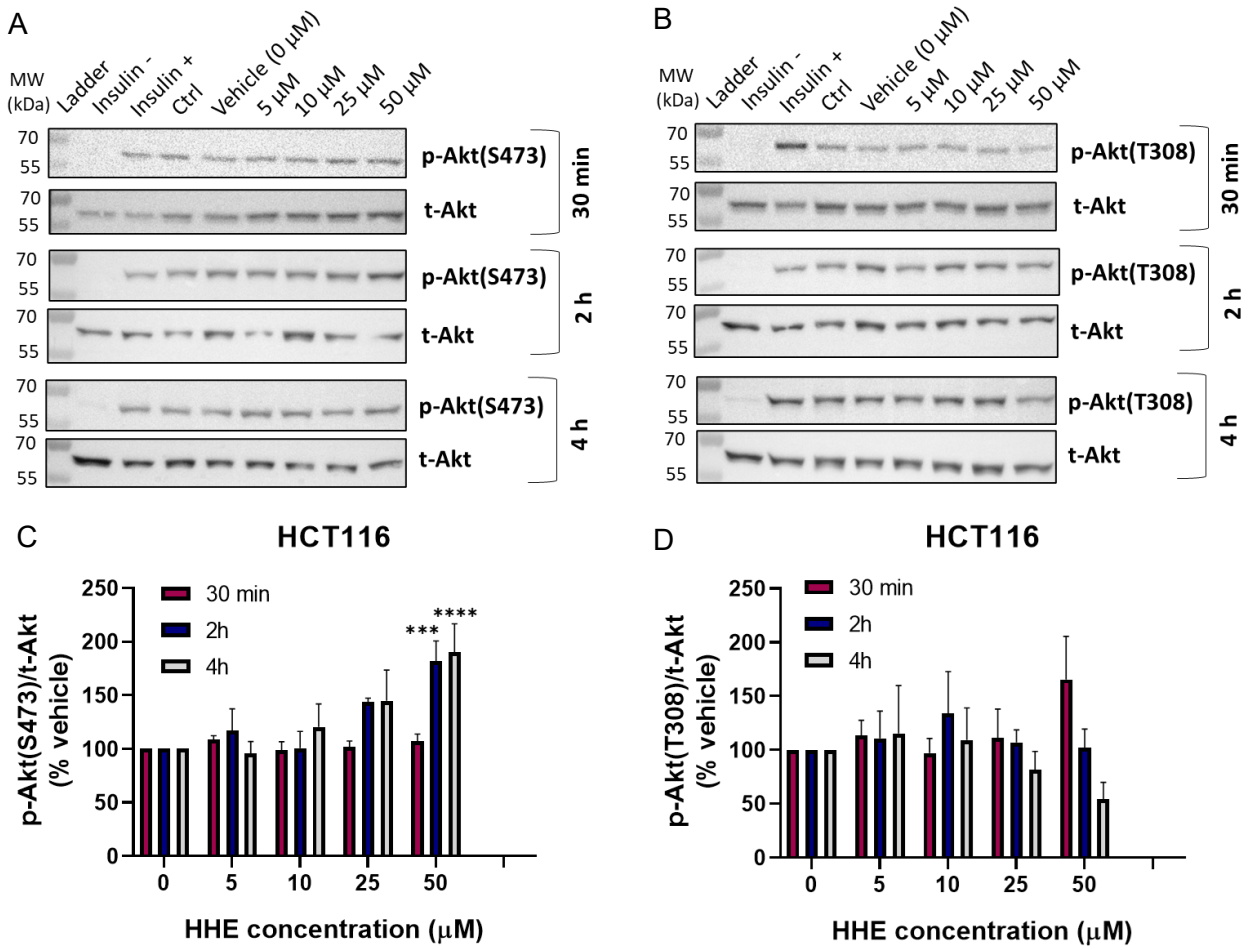

Figure 4.6. Effects of HHE on Akt phosphorylation in HCT116 cells.

(A and B) Representative western blotting of p-Akt (S473) (A), p-Akt (T308) (B) and t-Akt in insulin-stimulated HCT116 cells treated with increasing concentrations of HHE. HCT116 cells were treated with 5, 10, 25 or 50 µM HHE for 30 min, 2 h or 4 h at 37˚C or untreated by adding PBS (Ctrl) or ethanol in PBS (Vehicle). Cells were stimulated with 10 nM insulin 1 h prior to cell lysis in presence of protease and phosphatase inhibitors. Lysates of unstimulated HCT116 cells and HCT116 cells stimulated with 50 nM insulin for 30 min prior to cell lysis were used as controls for Akt phosphorylation. Twenty µg of each lysate were resolved by SDS-PAGE and proteins were transferred onto PVDF membranes. Immunoblotting of p-Akt (S473) and p-Akt (T308) was performed on separate membranes, followed by stripping and immunoblotting of total Akt (t-Akt) for both membranes. P-Akt (S473), p-Akt (T308) and t-Akt were imaged using a G:Box XR5 with GeneSys software (Syngene, UK). (C and D) Relative p-Akt (S473)/t-Akt (C) and p-Akt (T308)/t-Akt (D) ratios in insulin-stimulated HCT116 cells treated with increasing concentrations of HHE. Densitometry analysis was performed using ImageJ software. P-Akt band intensities were normalized to the corresponding t-Akt intensities and ratios were normalized to the vehicle control. Data represents mean ± SEM of 3 or 4 biological replicates (p-Akt (S473) – HHE 30 min (n=4), HHE 2 h (n=3), HHE 4 h (n=3); p-Akt (T308) – HHE 30 min (n=4), HHE 2 h (n=3), HHE 4 h (n=4)). Statistical analysis was performed using two-way ANOVA with Dunnett's post-test for multiple comparisons to the vehicle control; absence of annotation represents P >0.05 (ns), P ≤ 0.05 (*), P ≤ 0.01 (**), P ≤ 0.001 (***), P ≤ 0.0001 (****).

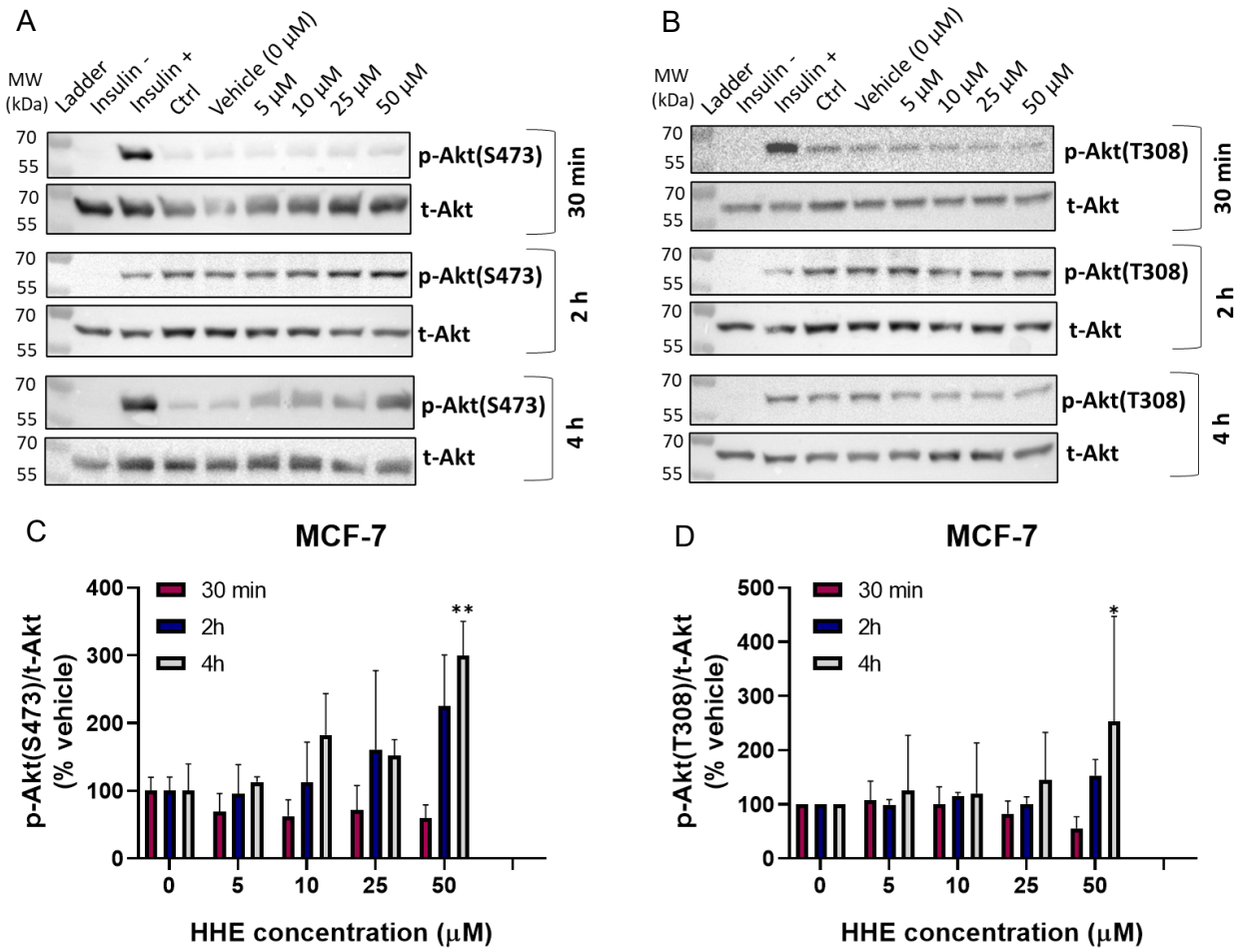

Figure 4.7. Effects of HHE on Akt phosphorylation in MCF-7 cells.
(A and B) Representative western blotting of p-Akt (S473) (A), p-Akt (T308) (B) and t-Akt in insulin-stimulated MCF-7 cells treated with increasing concentrations of HHE. Western blotting was performed on MCF-7 cells as described in Figure 4.6. (C and D) Relative p-Akt (S473)/t-Akt (C) and p-Akt (T308)/t-Akt (D) ratios in insulin-stimulated MCF-7 cells treated with increasing concentrations of HHE. Densitometry analysis was performed as described in Figure 4.6. Data represents mean ± SEM of 2 or 3 biological replicates (p-Akt (S473) and p-Akt (T308) – HHE 30 min (n=3), HHE 2 h (n=2), HHE 4 h (n=3)). Statistical analysis was performed using two-way ANOVA with Dunnett's post-test for multiple comparisons to the vehicle control; absence of annotation represents $P > 0.05$ (ns), $P \leq 0.05$ (*), $P \leq 0.01$ (**), $P \leq 0.001$ (***), $P \leq 0.0001$ (****).

In HCT116 cells, it seemed that Akt phosphorylation increased in a time- and concentration-dependent manner with PONPC treatments (Figure 4.8). The most significant increase was observed at 50 µM PONPC after 2 and 4 hours of treatment, suggesting prolongued activation of the Akt signaling pathway in response to PONPC (Figure 4.8.C and 4.8.D). It is important to note that none of these modifications in phosphorylation levels were found to be statistically significant, reflecting the reduced number of biological replicates and high variability between replicates.

In MCF-7 cells, the effects of PONPC were less clear as only two biological replicates were performed and, as previously discussed, reproducibility between replicates seemed lower than in HCT116 cells. Putting 30 min treatments aside because of their high variability,

relative p-Akt (S473) levels seemed to be stable up to 25 µM PONPC after 2 h and 4 h treatments, while they seemed to increase after 2 h of treatment using 50 µM PONPC and decrease after 4 h of treatment using 50 µM PONPC (Figure 4.9.C). The effects of PONPC on relative p-Akt (T308) levels were similar (Figure 4.9.D).

Taken all together, the measurements of Akt phosphorylation at both sites suggested that HHE and PONPC could generally be involved in Akt activation in cells at high concentrations and prolonged periods of time. This was particularly evident in HCT116 cells, although an opposite trend was observed for Thr308 in HHE-treated HCT116 cells and PONPC-treated MCF-7 cells and high variations between replicates made it, in some cases, unclear. The appearance of different effects on the PI3K/Akt pathway after 2 and 4 hours of treatment compared to 30 minutes also suggested that the cell response to HHE was dynamic, with different adaptation to short- and long-term expositions to HHE. As PTEN was found to be inhibited *in vitro* by both HHE and PONPC, it is possible to hypothesize that the increase in Akt phosphorylation could be related to an inhibition of PTEN in cells. However, Akt phosphorylation is regulated through different mechanisms, and the increase in Akt phosphorylation could also be related to effects of HHE and PONPC on other components of the PI3K/Akt pathway as well as the levels of expression of PTEN.

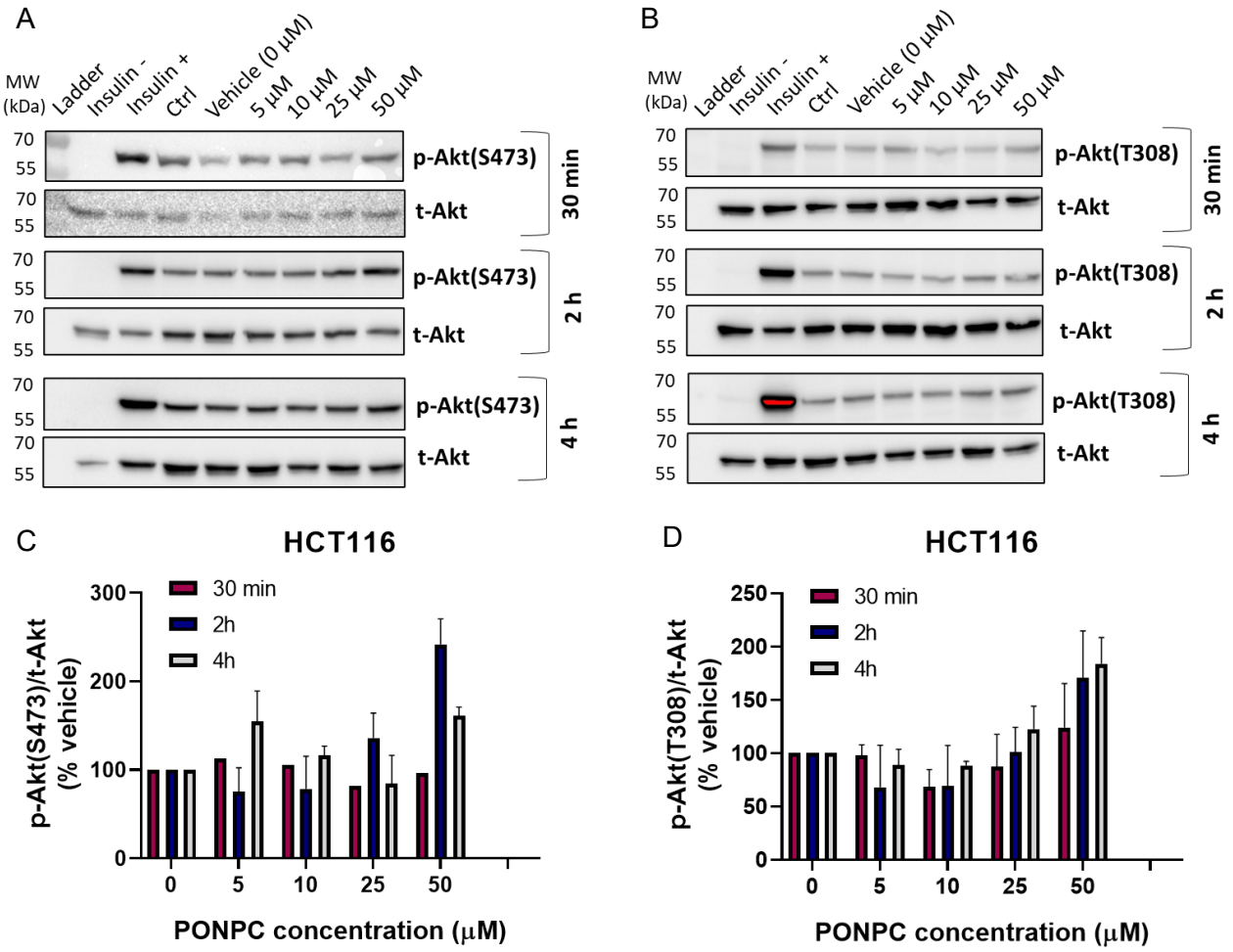

Figure 4.8. Effects of PONPC on Akt phosphorylation in HCT116 cells.
(A and B) Representative western blotting of p-Akt (S473) (A), p-Akt (T308) (B) and t-Akt in insulin-stimulated HCT116 cells treated with increasing concentrations of PONPC. HCT116 cells were untreated (Ctrl), untreated in presence of ethanol (Vehicle) or treated with 5, 10, 25 or 50 µM PONPC for 30 min, 2 h or 4 h at 37˚C. Cells were stimulated with 10 nM insulin 1 h prior to cell lysis in presence of protease and phosphatase inhibitors. Lysates of unstimulated HCT116 cells and HCT116 cells stimulated with 50 nM insulin for 30 min prior to cell lysis were used as controls for Akt phosphorylation. Twenty µg of each lysate were resolved by SDS-PAGE and proteins were transferred onto PVDF membranes. Immunoblotting of p-Akt (S473) and p-Akt (T308) was performed on separate membranes, followed by stripping and immunoblotting of total Akt (t-Akt) for both membranes. P-Akt (S473), p-Akt (T308) and t-Akt were imaged using a G:Box XR5 with GeneSys software (Syngene, UK) or a ChemiDoc MP (Bio-Rad, UK). (C and D) Relative p-Akt (S473)/t-Akt (C) and p-Akt (T308)/t-Akt (D) ratios in insulin-stimulated HCT116 cells treated with increasing concentrations of PONPC. Densitometry analysis was performed using ImageJ software. P-Akt band intensities were normalized to the corresponding t-Akt intensities and ratios were normalized to the vehicle control. Data represents mean ± SEM of 1, 2 or 3 biological replicates (p-Akt (S473) – PONPC 30 min (n=1), PONPC 2 h (n=3), PONPC 4 h (n=3); p-Akt (T308) – PONPC 30 min (n=3), PONPC 2 h (n=3), PONPC 4 h (n=2)). Statistical analysis was performed using a mixed-effects analysis with Dunnett's post-test for multiple comparisons to the vehicle control; absence of annotation represents P >0.05 (ns), P ≤ 0.05 (*), P ≤ 0.01 (**), P ≤ 0.001 (***), P ≤ 0.0001 (****).

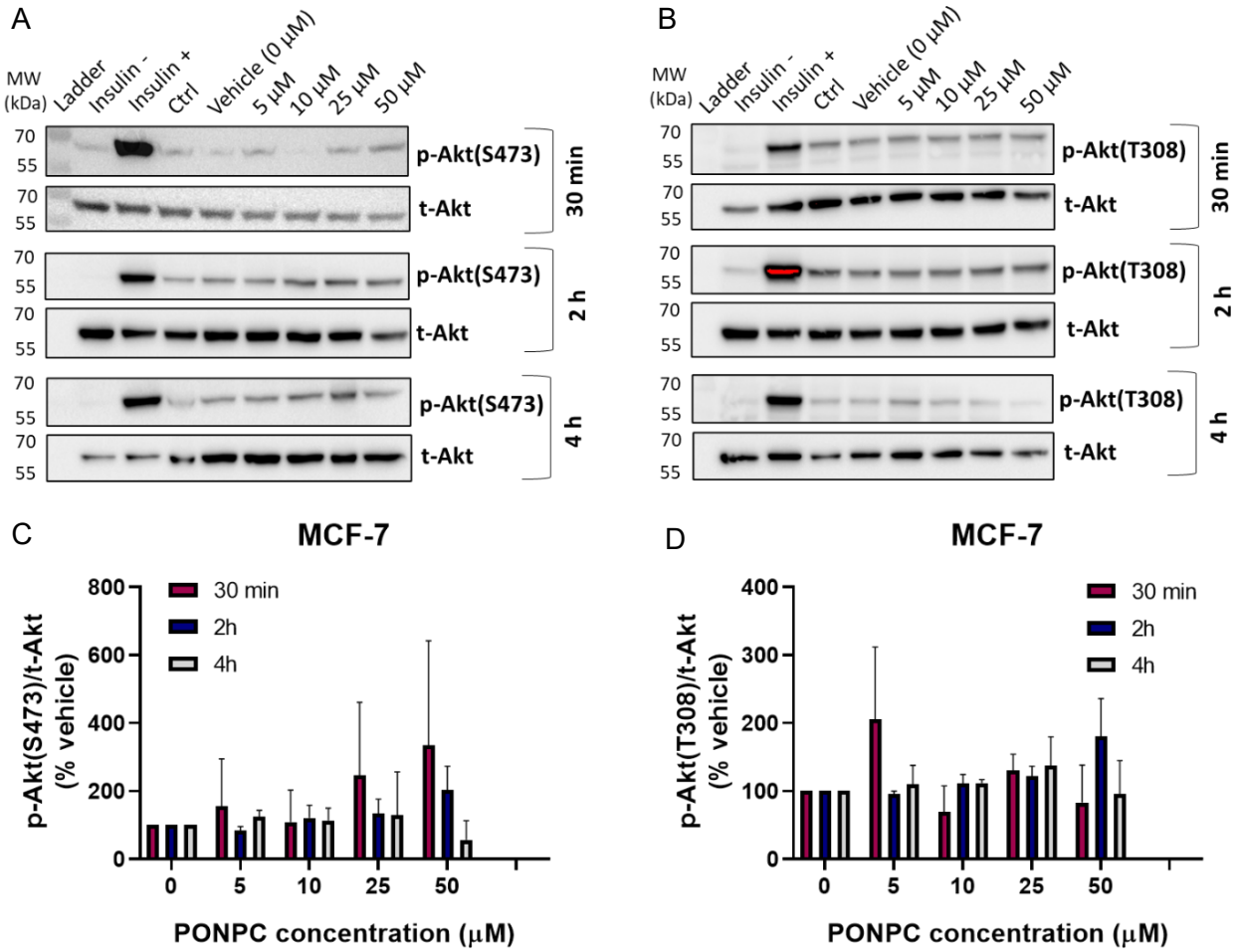

Figure 4.9. Effects of PONPC on Akt phosphorylation in MCF-7 cells.
(A and B) Representative western blotting of p-Akt (S473) (A), p-Akt (T308) (B) and t-Akt in insulin-stimulated MCF-7 cells treated with increasing concentrations of PONPC. Western blotting was performed on MCF-7 cells as described in Figure 4.8. (C and D) Relative p-Akt (S473)/t-Akt (C) and p-Akt (T308)/t-Akt (D) ratios in insulin-stimulated MCF-7 cells treated with increasing concentrations of PONPC. Densitometry analysis was performed as described in Figure 4.8. Data represents mean ± SEM of 2 biological replicates (n=2).

To understand if the observed modifications of the phosphorylation state of Akt could be related to a modification of the activation of the PI3K/Akt pathway, the levels of expression of Akt were measured. Indeed, activation or inhibition of the pathway would be true only if an increased or decreased phosphorylation of Akt was observed with unchanged levels of expression of Akt, or with an increase or decrease of Akt levels, respectively.

In the case of HHE-treated HCT116 and MCF-7 cells, the level of expression of Akt seemed unchanged across treatment concentrations (Figure 4.10). Indeed, the levels of expression of Akt in HCT116 cells treated with HHE for 30 minutes (Figure 4.10.B) and MCF-7 cells treated with HHE for 30 minutes and 4 hours (Figure 4.10.D) did not show significant differences compared to the untreated control. However, only 2 biological replicates were investigated for HCT116 cells treated with HHE for 2 and 4 hours and MCF-7 cells treated

with HHE for 2 hours. Hence, although the levels of Akt seemed unchanged with HHE concentrations, replicating this experiment would be necessary to draw firm conclusions.

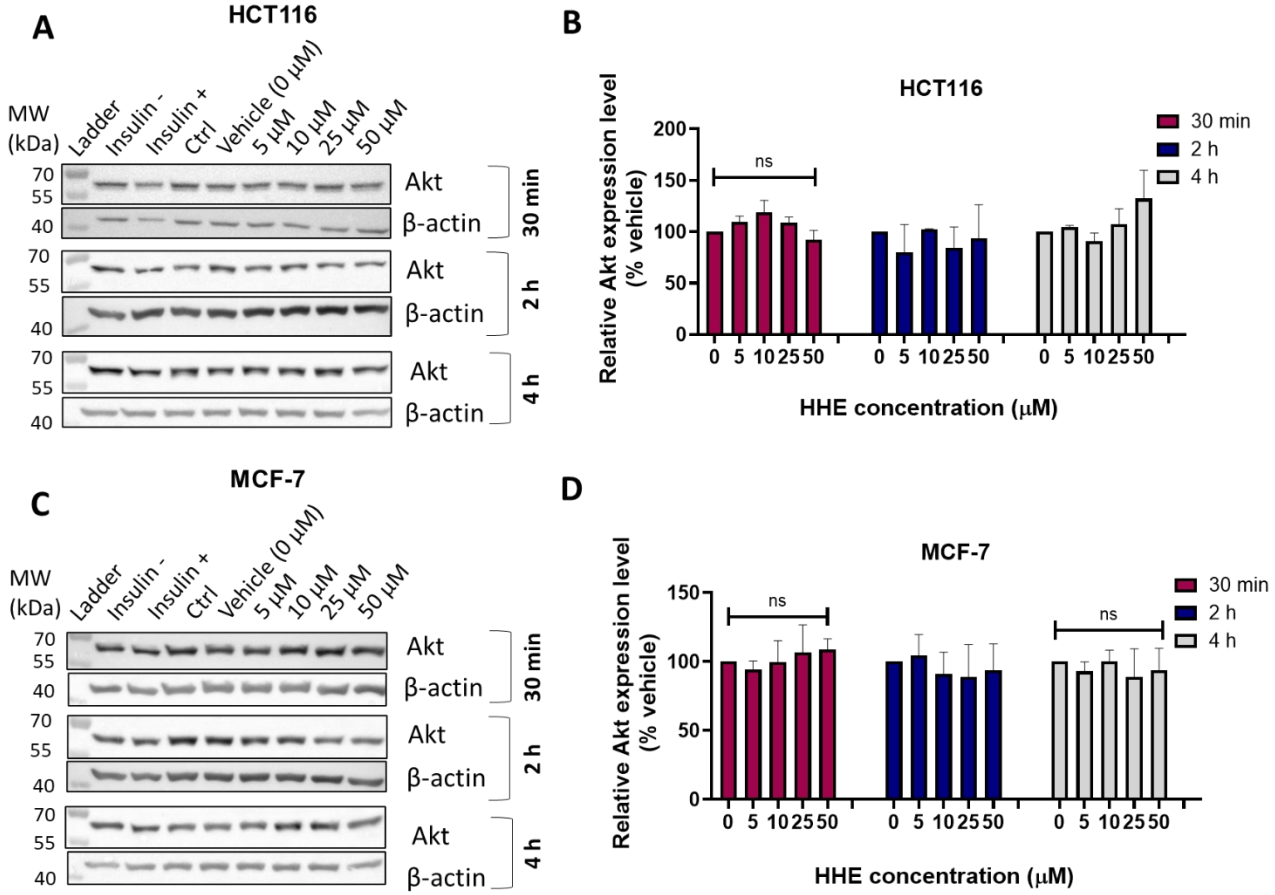

Figure 4.10. Effects of HHE on Akt expression levels in HCT116 and MCF-7 cells.
Representative western blotting of total Akt and β-actin in untreated or HHE-treated (for 30 minutes, 2 hours or 4 hours) HCT116 (A) and MCF-7 (C) cell lysates. Western blotting was performed on MCF-7 cells as described in Figure 4.6, followed by stripping of the membranes and probing of β-actin. Images of total Akt and β-actin were analysed by densitometry and total Akt was normalised to β-actin. (B) and (D) show normalized levels of expression in untreated and HHE-treated HCT116 cells and MCF-7 cells, respectively. Data represents mean ± SEM of 2 biological replicates (n=2) for HCT116 cells treated with HHE for 2 and 4 hours and MCF-7 cells treated with HHE for 2 hours or 3 biological replicates (n=3) for HCT116 cells treated with HHE for 30 minutes and MCF-7 cells treated with HHE for 30 minutes and 4 hours. Statistical analysis was performed using a mixed-effects analysis with Turkey's post-test for multiple comparisons; $P > 0.05$ (ns).

On the other hand, a trend towards lower Akt levels appeared with increased concentrations of PONPC in HCT116 and MCF-7 cells treated for 2 hours and 4 hours (Figure 4.11). Although only 2 biological replicates were investigated, which made statistical analysis unreliable, the common trend across the two cell lines as well as the relatively low standard error to the means increased the confidence in accuracy of these data. This suggested that PONPC could lead to degradation of Akt in cells. This trend was not observed in treatments with PONPC for 30 minutes (Figure 4.11), suggesting that this Akt degradation process would happen after this first time point.

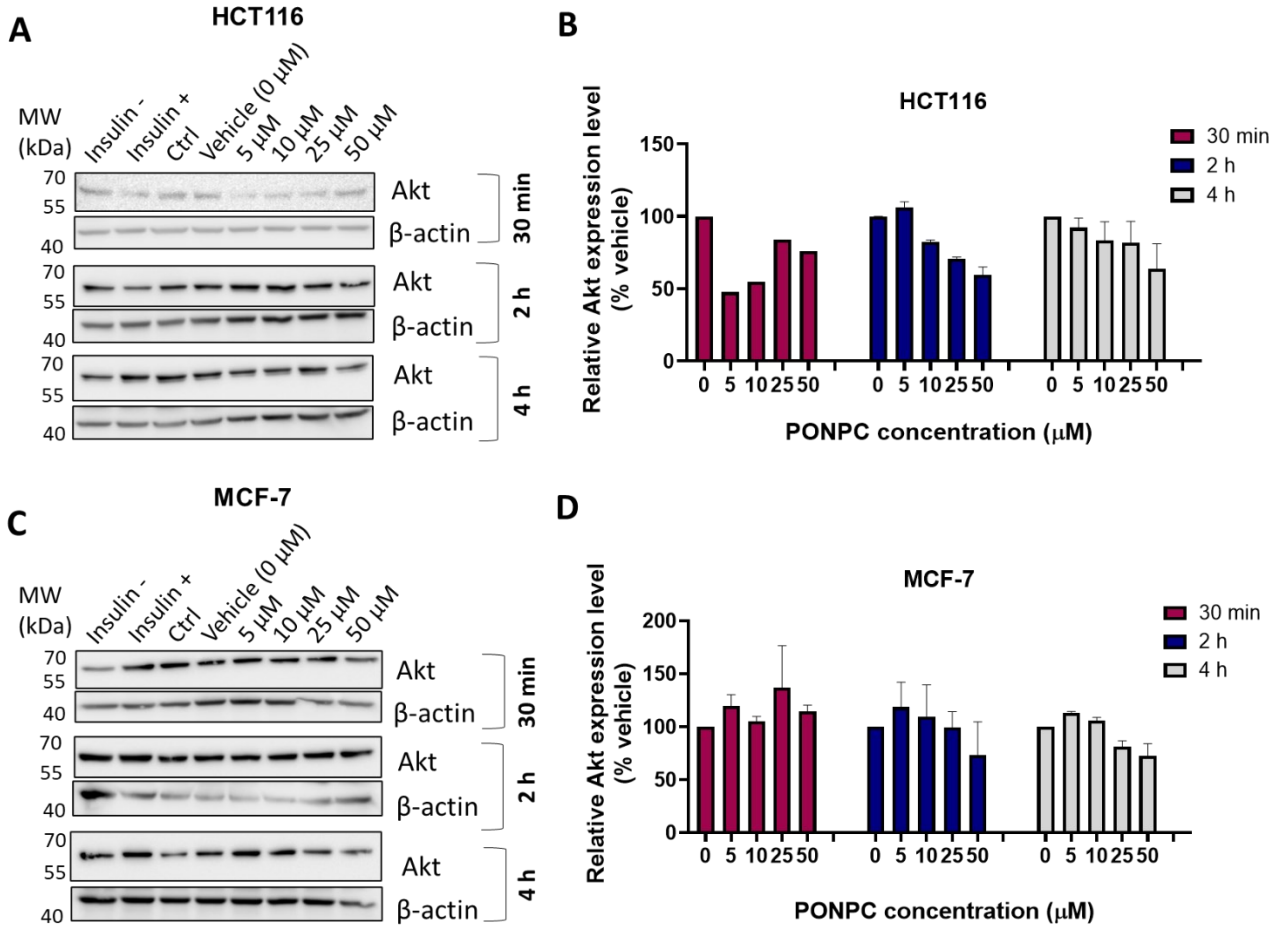

Figure 4.11. Effects of PONPC on Akt expression levels in HCT116 and MCF-7 cells.
Representative western blotting of total Akt and β-actin in untreated or PONPC-treated (for 30 minutes, 2 hours or 4 hours) HCT116 (A) and MCF-7 (C) cell lysates. Western blotting was performed on MCF-7 cells as described in Figure 4.8, followed by stripping of the membranes and probing of β-actin. Images of total Akt and β-actin were analysed by densitometry and total Akt was normalised to β-actin. (B) and (D) show normalized levels of expression in untreated and PONPC-treated HCT116 cells and MCF-7 cells, respectively. Data represents the value for 1 biological replicate for HCT116 cells treated with PONPC for 30 min or the mean ± SEM of 2 biological replicates (n=2) for all other conditions.

Considering the unmodified levels of expression of Akt in HCT116 and MCF-7 cells after HHE treatments, the modifications of levels of phosphorylation of Akt would be associated with modifications of the activation state of the PI3K/Akt pathway. In contrast, the effects of PONPC could be more complex as a potential decrease in Akt levels with treatments for 2 and 4 hours would need to be accounted for to understand the variations of p-Akt levels in these conditions.

4.3.6. Effects of HHE and PONPC on PTEN Expression Levels in HCT116 and MCF-7 Cells

It is known that protein lipoxidation can influence protein levels *in cellulo* by affecting degradation of the adducted protein or by affecting transcription levels of target genes,

particularly in the case of proteins involved in antioxidant responses (Viedma-Poyatos et al., 2021). Modification of PTEN levels would influence the activation state of Akt (Alimonti et al., 2010). The potential influence of HHE and PONPC on PTEN levels was therefore investigated by western blotting of PTEN on the membranes used for Akt immunoblotting after stripping, allowing quantification of PTEN in HHE- (Figure 4.12.A and 4.12.C) and PONPC-treated (Figure 4.13.A and 4.13.C) HCT116 and MCF-7 cells.

After 30 minutes of treatment, PTEN levels appeared to decrease in HCT116 cells with increasing concentrations of HHE, reaching 69.3% after treatment with 50 µM HHE (Figure 4.12.B). Conversely, PTEN levels seemed to remain relatively stable in MCF-7 cells across HHE concentrations (Figure 4.12.D). However, due to the variability observed between only two biological replicates, the statistical significance of these changes in PTEN levels in HCT116 and MCF-7 cells could not be determined. On the other hand, the analysis of PTEN levels after 2 hours and 4 hours of treatment with HHE in HCT116 and MCF-7 cells was conducted using three biological replicates, ensuring a more robust dataset. With some exceptions, deviations in PTEN levels did not exceed 15% (Figure 4.12). Additionally, no statistically significant differences in PTEN levels were observed across all conditions. Although there was a possible trend appearing for HCT116 cells treated with HHE for 30 minutes to decrease PTEN with high treatment concentrations, the opposite was true for 4 hours of treatment. However, the use of additional higher concentrations would be required to confirm this, which would not be physiologically relevant. This suggested that HHE could not lead to significant up-regulation or down-regulation of PTEN expression in HCT116 and MCF-7 cells. This could also be dependent on cell type, as response to HHE from HCT116 and MCF-7 cells seemed different for each time point between the two cell lines.

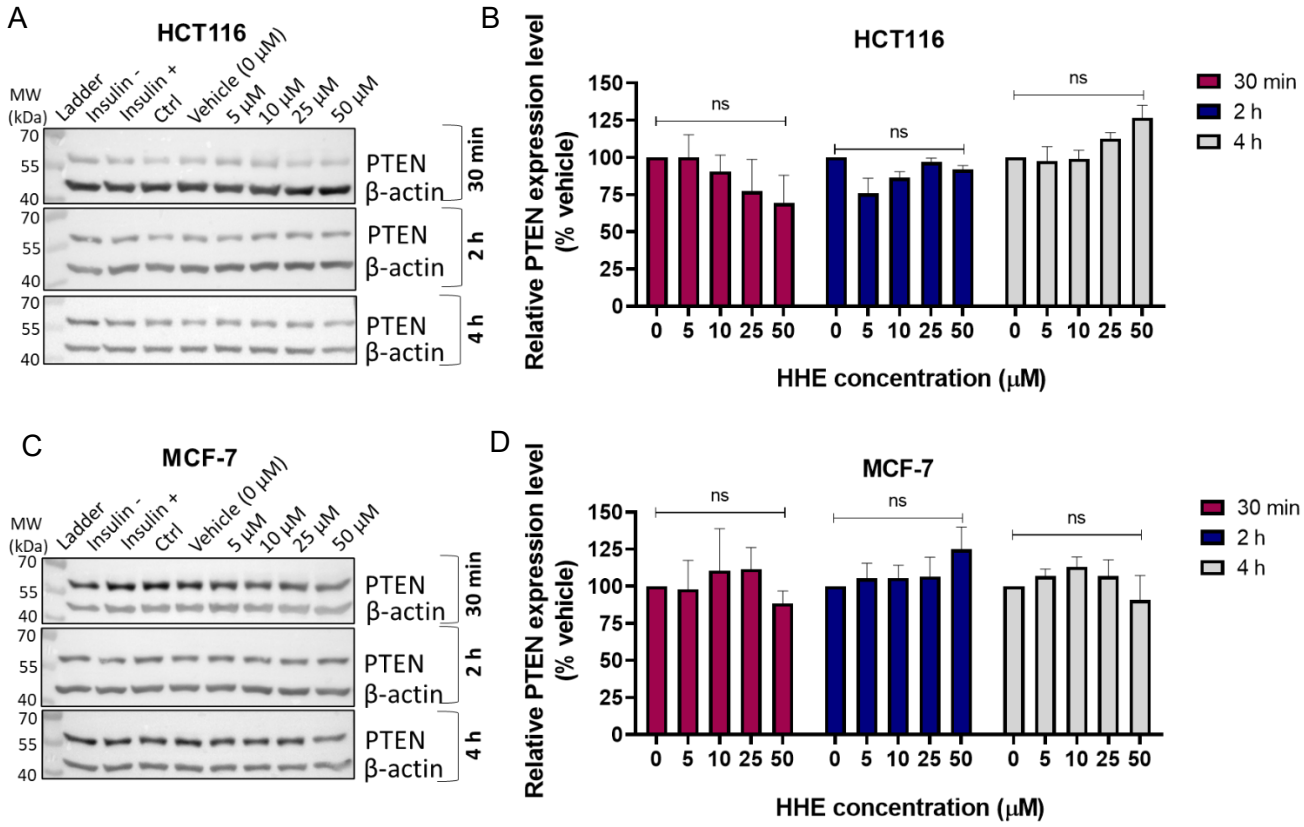

Figure 4.12. Effects of HHE on PTEN expression levels in HCT116 and MCF-7 cells.
(A and C) Representative western blots of PTEN and β-actin in HCT116 (A) and MCF-7 (C) cells. HCT116 cells were untreated (Crtl), untreated in presence of ethanol (Vehicle) or treated with 5, 10, 25 or 50 µM HHE for 30 min, 2 h or 4 h at 37˚C. Cells were stimulated with 10 nM insulin 1 h prior to cell lysis in presence of protease and phosphatase inhibitors. Twenty µg of each lysate were resolved by SDS-PAGE and proteins were transferred onto PVDF membranes. After immunoprobing of p-Akt and t-Akt, membranes were stripped. Immunoprobing of PTEN and β-actin was sequentially performed and signal from both proteins was imaged using a G:Box XR5 with GeneSys software (Syngene, UK). (B and D) Relative PTEN expression levels in insulin-stimulated HCT116 (B) and MCF-7 (D) cells treated with HHE. Densitometry analysis was performed using ImageJ software. PTEN signal was normalized to β-actin and values were represented as % of vehicle. Data represents mean ± SEM of 2 or 3 biological replicates (HHE 30 min: n=2; HHE 2 h: n=3; HHE 4 h: n=3). Statistical analysis was performed using a mixed-effects analysis with Turkey's post-test; $P > 0.05$ (ns).

Although only one or two biological replicates have been investigated for PONPC, data seemed to show a trend to decreased PTEN expression levels correlating with the concentration of PONPC for HCT116 cells treated for 2 hours (Figure 4.13.B). At 30 min and 4 hours post-treatment in HCT116 cells, PTEN levels seemed to be relatively stable across PONPC concentrations (Figure 4.13.B). In MCF-7 cells, there was considerable variation across the concentration range. Although there appeared to be a trend to lower PTEN levels at higher treatment concentrations with the longer time courses, more replicates would be necessary to draw conclusions (Figure 4.13.D). Indeed, the number of replicates investigated did not allow statistical analysis and bands corresponding to Akt, which could be

observed most likely because of a lack of stripping of the membranes, were observed and close enough to PTEN bands to, in some cases, almost merge into one (Figure 4.13.C).

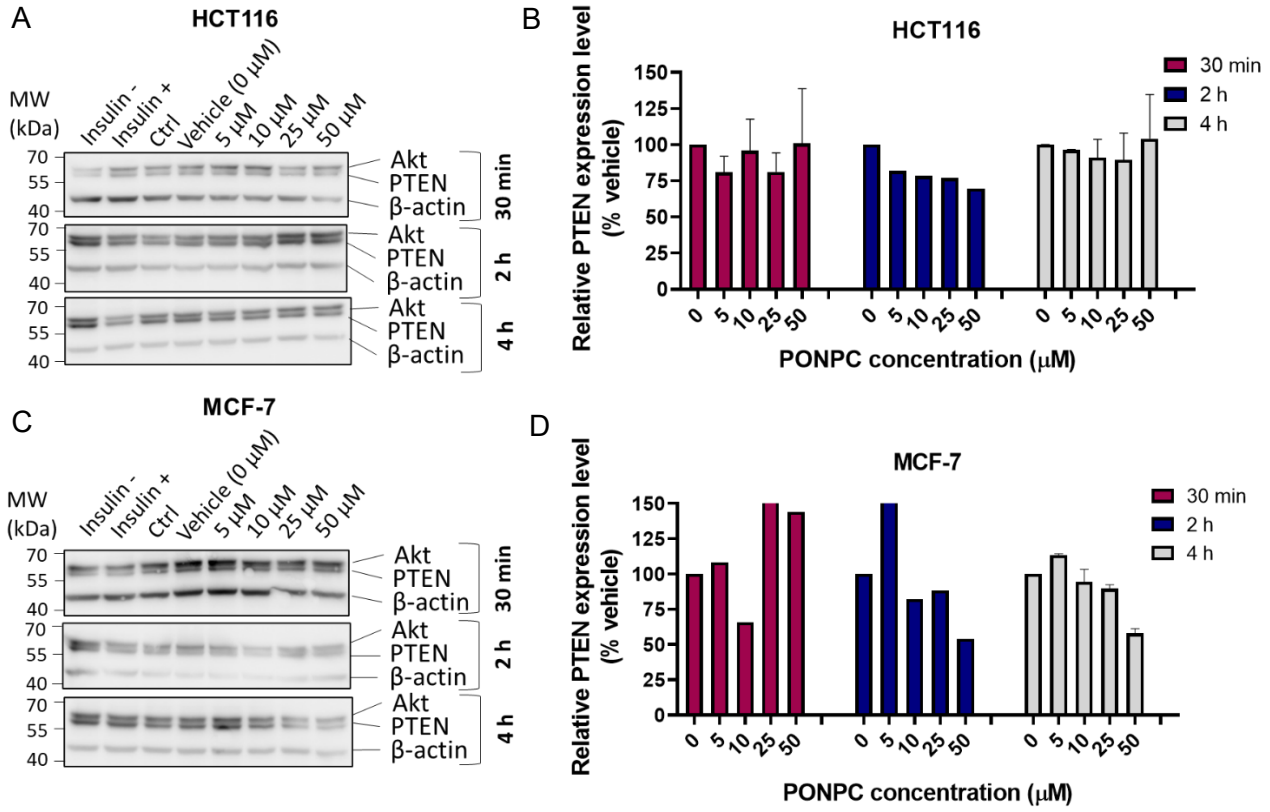

Figure 4.13. Effects of PONPC on PTEN expression levels in HCT116 and MCF-7 cells.
(A and C) Representative western blots of PTEN and β-actin in HCT116 (A) and MCF-7 (C) cells. Western blotting was performed as described in Figure 4.12 using PONPC as treatment. (B and D) Relative PTEN expression levels in insulin-stimulated HCT116 (B) and MCF-7 (D) cells treated with PONPC. Densitometry analysis was performed as described in Figure 4.12. Data represents the value of normalized PTEN expression level relative to the untreated control (vehicle) of one biological replicate (n=1) for HCT116 PONPC 2h, MCF-7 PONPC 30 min and MCF-7 PONPC 2 h or the mean normalized PTEN expression level relative to the untreated control (vehicle) ± SEM of 2 biological replicates (n=2) for HCT116 PONPC 30 min, HCT116 PONPC 4 h and MCF-7 PONPC 4 h.

4.4. Discussion

The current investigation found that HHE was toxic in HCT116 and MCF-7 cells in a time- and concentration-dependent manner, particularly at concentrations of 50 μM and higher, but PONPC seemed less toxic up to 50 μM. Following exposure to HHE and PONPC, Akt phosphorylation at both activating sites, Ser473 and Thr308, could be increased in most cases in a concentration- and time-dependent manner in HCT116 and MCF-7 cells, suggesting that HHE and PONPC could play a role in activating the PI3K/Akt pathway, leading to cell survival, migration, and proliferation. As this was not reflected in the effects of HHE and PONPC on cell viability of HCT116 and MCF-7 cells, it may be the case that HHE and PONPC also acted on other biological processes, leading to cell death. However, the activation of Akt correlated with the observed inhibition of PTEN *in vitro*, which was also concentration- and time-dependent, but no significant difference in PTEN expression levels were observed, suggesting an action of these LPPs on the PI3K/Akt pathway via PTEN inhibition.

The findings regarding cell viability generally agreed with previously reported concentration- and time-dependent cell toxicity of HHE (Bradley et al., 2012, Lovell et al., 2012, Bae et al., 2011). However, HHE seemed to be toxic at higher concentrations than previously reported (25 μM after 4 hours of treatment on primary astrocytes (Lovell et al., 2012) or 16 hours of treatment on cortical neurons (Bradley et al., 2012) and even 10 μM after 24 hours of treatment on HK-2 cells (Bae et al., 2011)). On the other hand, treatment of L6 muscle cells with 10 to 100 μM HHE for 30 min surprisingly led to a concentration-dependent increase in cell viability (Soulage et al., 2018), possibility reflecting activation of Akt. Most importantly, treatment of MCF-7 cells with 2 to 200 μM HHE for 2 and 24 hours in a study by Sousa *et al.* led to only a slight decrease in cell viability (up to ~20%) for concentrations ≥ 20 μM (Sousa et al., 2019), which correlated with data presented in this chapter, with the exception of 24 hours of treatment, which led to higher toxicity in MCF-7 cells. This would suggest a cell type-dependent sensitivity to HHE, which has been observed between HCT116 and MCF-7 cells after treatment for 24 hours, HHE being less toxic in MCF-7 cells. The toxicity of HHE could result from its propensity to increase reactive radical species in cells (Bae et al., 2011, Lee et al., 2004a, Lee et al., 2004b), further increasing oxidative damage, and its genotoxicity (Brambilla et al., 1986, Winter et al., 1986) rather than solely its ability to covalently modify proteins. On the other hand, PONPC has not shown significant cell toxicity in HCT116 and MCF-7 cells for concentrations up to 50 μM, which contrasts with previously reported low cell viability of cardiomyocytes exposed to 10 μM PONPC for 1 hour or 4 hours (<20% compared to control cardiomyocytes treated with a non-oxidized phosphatidylcholine)

(Yeang et al., 2019, Stamenkovic et al., 2021). This discrepancy could potentially be explained by a cell type-dependent sensitivity to PONPC, as with HHE, or by the different methods employed to assess cell viability, mainly the absence of serum in culture media during treatment of cardiomyocytes, compared to the presence of 10% foetal bovine serum in media used to culture and treat HCT116 and MCF-7 cells. Indeed, serum contains proteins, hormones, growth factors, cytokines, fatty acids and other lipids, carbohydrates and a plethora of other molecules (Lee et al., 2022), which could alter PONPC interaction with cells. However, the presence of serum better reflects physiological conditions where oxidized phospholipids increase in circulation during oxidant stress events (Liu et al., 2013). Additionally, Yeang *et al.* and Stamenkovic *et al.* treated cells with PONPC prepared as liposomal vesicles, which could highly impact the interaction of PONPC with cell membranes and lead to different results when assessing the toxicity of this oxidized phospholipid.

Short-term exposure (2 and 4 hours) of HCT116 and MCF-7 cells to HHE and PONPC, even at high concentrations, did not lead to a significant reduction in cell viability. This does not reflect, however, the subtle modifications in biological processes that cells could undergo after HHE and PONPC exposure. This chapter set out with the aim of assessing the effects of HHE and PONPC on PTEN and its downstream signalling as it has been shown that a few LPPs (HNE, acrolein, 15d-PGJ_2 and Δ12-PGJ_2) could inhibit PTEN activity and lead to activation of the PI3K/Akt and/or β-catenin pathways (Shearn et al., 2011b, Covey et al., 2010, Suh et al., 2018). The ability of HHE and PONPC to inhibit PTEN phosphatase activity *in vitro* in a concentration- and time-dependent manner was reported for the first time in this chapter. This finding was consistent with studies by Suh *et al*., Shearn *et al.* and Covey *et al.* and provides further support for the hypothesis that PTEN is generally a target of LPPs that act as inhibitors of its function. Furthermore, HHE and PONPC significantly reduced PTEN activity at molar ratios of 5:1 and 1:1, respectively, while HNE was found to be efficient in inhibiting PTEN from a molar ratio of 1:1 (Shearn et al., 2011b). This suggested that the reactivity of PONPC and HNE could be similar, while HHE may be less reactive towards PTEN. Comparison of HHE and HNE reactivity is rather confusing in the literature. HHE- and HNE-bound proteins were identified in similar amounts amongst mitochondrial proteins that underwent lipoxidation with various LPPs (Chavez et al., 2011), suggesting a comparable reactivity. On the other hand, although both HHE and HNE plasma concentrations increased in chronic kidney disease patients, only covalent adducts of HHE but not HNE on plasma proteins were observed in these patients (Soulage et al., 2020), suggesting a higher reactivity of HHE compared to HNE, but it was also showed that HNE is approximately 30% more reactive than HHE in forming adducts with PE-containing phospholipids (Bacot et al., 2003) and 50% more reactive than HNE in forming adducts with bovine serum albumin

(Pillon et al., 2010). This suggests a specificity in the reactivity of LPPs depending on the target of adduction. PTEN might, accordingly, be a better target for HNE and PONPC than for HHE. However, the mechanism by which LPPs could inhibit PTEN remains to be investigated. For instance, mass spectrometric evidence of PTEN adduction by HNE did not directly prove alteration of PTEN active site but rather suggested a limitation in substrate access to the active site or alteration of the association of PTEN with the membrane (Shearn et al., 2011b). Regulation of PTEN also occurs via phosphorylation of C-terminal residues Ser380/Thr382/383, leading to an inactive state (Vazquez et al., 2001). Lipoxidation of these residues could therefore lead to modification of PTEN phosphatase activity. Nonetheless, formation of multimeric states of PTEN via cross-linking after HNE treatments was also reported (Shearn et al., 2013) and inhibition of PTEN activity could be the result of such structural changes. Therefore, it will be necessary to investigate this further for HHE and PONPC in order to understand whether this is a possible mechanism.

The ability of HHE and PONPC to inhibit PTEN *in vitro* suggested that they could participate in the activation of the PI3K/Akt pathway if PTEN could also be inhibited *in cellulo*. Previous studies evaluating the effects of HNE, acrolein, 15d-PGJ_2 and Δ12-PGJ_2 on the PI3K/Akt pathway all pointed to a propensity of these LPPs to increase phosphorylation of Akt on Ser473 and Thr308 *in cellulo*, correlating with an inhibition of PTEN *in vitro*, which implies a role of LPPs in enhancing activation of the PI3K/Akt pathway in hepatocellular carcinoma cells, MCF-7 cells or HEK 293 cells (Shearn et al., 2011b, Shearn et al., 2013, Covey et al., 2010). However, insulin-focused investigations demonstrated an impaired phosphorylation of Akt in L6 muscle cells treated with HHE for 30 min at concentrations ranging from 10 to 100 µM (Soulage et al., 2018), a discrepancy that could result from a different reactivity of HHE compared to HNE or to a cell type-dependent sensitivity to these LPPs. No data on the association of PONPC with the PI3K/Akt pathway has been reported so far. Here, effects of HHE and PONPC on the activation state of Akt were investigated in HCT116 and MCF-7 cells, the latter being one of the cell lines used to report effects of HNE, acrolein and Δ12-PGJ_2 (Covey et al., 2010). Interestingly, treating insulin-stimulated HCT116 and MCF-7 cells with sub-lethal concentrations (up to 50 µM) of HHE and PONPC at different time points suggested that the effects on Akt phosphorylation status of both these LPPs were more complex than what has been reported in the literature, as they would differ between both cell lines and between HHE and PONPC. Corroborating the findings of Soulage *et al*. in L6 muscle cells previously discussed (Soulage et al., 2018), the results of the current study showed that HHE could lead to decreased phosphorylation of Akt on both activating sites after 30 min of treatment with HHE, representing an early event that could be dependent on the inhibition of insulin action. However, this was not true for longer exposure times as 2 and

4 hours of treatment led to a concentration-dependent increase in p-Akt (S473) and p-Akt (T308) levels in MCF-7 cells, corroborating the findings on HNE, acrolein and Δ12-PGJ_2 effects (Shearn et al., 2011b, Covey et al., 2010). Strikingly, the same pattern could not be observed for Thr308 phosphorylation levels in HCT116 cells, and findings were also contradictory between HCT116 and MCF-7 for PONPC treatments, supporting the hypothesis that effects of HHE and PONPC, and possibly other LPPs, could be cell type-dependent. The modifications observed in Akt phosphorylation after exposure to HHE were not related to a significant modification of PTEN expression levels, which further supports the findings of Covey *et al.* in which Akt was activated without modification of PTEN expression levels nor the activation of PDK1 (Covey et al., 2010), suggesting more strongly a link between PTEN inhibition and Akt activation in cells exposed to LPPs. Similarly, the effects of PONPC on Akt phosphorylation status, which are reported for the first time here, leaned towards an increase in phosphorylation of Akt as well, although it seemed to appear at earlier time points and be reversible in MCF-7 cells compared to HCT116 cells. However, a note of caution is due here since the evaluation of PONPC effects on Akt phosphorylation status in MCF-7 cells was incomplete with only a maximum of two biological replicates and, notably, the analysis of Akt levels seemed to suggest that PONPC could lead to degradation of Akt, making the increase of p-Akt not necessarily related to an activation of the PI3K/Akt pathway; repeating this experiment would be necessary to draw firm conclusions on effects of PONPC on Akt activation kinetics in MCF-7 cells. This also applies to the effects of PONPC on PTEN expression levels. What is most interesting about these results is that, although the modification of the phosphorylation state of Akt were similar between Ser473 and Thr308 sites in most cases, modification of the phosphorylation on Ser473 and Thr308 phosphorylation sites in HCT116 cells exposed to HHE differed widely. Akt phosphorylated at Thr308 primarily leads to protein synthesis, while Akt phosphorylated at Ser473 mainly promotes anti apoptotic and cell survival pathways (Vadlakonda et al., 2013). Hence, it could be inferred that HHE could differentially alter specific axes of the PI3K/Akt pathway in certain cell types, specifically regulating biological processes; in this case, preferentially promoting cell survival rather than cell growth.

Despite these promising results potentially linking PTEN inhibition by LPPs to modification of the activation of the PI3K/Akt pathway, questions remain. Most importantly, ROS have been shown to activate Akt via PTEN oxidation (Leslie et al., 2003, Connor et al., 2005). Increased ROS generation could be linked to HHE exposure (Bae et al., 2011, Bae et al., 2016) in certain cell types but not all, and HHE could even have protective effects against lipopolysaccharide-induced production of ROS in microglial cells (Yang et al., 2018a). Oxidized phospholipids are also known to be involved in the generation of ROS in

endothelial cells (Karki and Birukov, 2020), although it has not be specifically demonstrated in regards to PONPC yet. Therefore, it is important to note that the observed activation of Akt in HCT116 and MCF-7 cells could be an indirect result of the generation of ROS following HHE and PONPC exposure. It is possible that it could be a direct effect on one or even several components of the PI3K/Akt pathway regulating Akt phosphorylation, including PH domain leucine-rich repeat protein phosphatase (PHLPP) and complete S transactivated protein 1 (CSTP1), phosphatases dephosphorylating p-Akt (S473) (Gao et al., 2005, Zhuo et al., 2013), as well as PP2A, a phosphatase dephosphorylating p-Akt Thr308 (Kuo et al., 2008). Measurement of ROS production using common specific fluorescent probes in parallel of identifying potential inhibiting covalent modifications on PTEN would provide more insights into the mechanism of Akt activation by LPPs. However, potential effects of LPPs on other components of the pathway, notably direct regulators of Akt, cannot be ruled out. To develop a full picture of the role of HHE and PONPC in the activation (or, in some cases, the inhibition) of Akt, additional studies will therefore be needed to better understand the effects of LPPs on all the components of the PI3K/Akt pathway that could lead to modification of Akt phosphorylation state, which could potentially strengthen the link between PTEN sensitivity to LPPs and activation of the pathway. Amongst these, the investigation of PTEN subcellular localization, which is important to determine its function, and, ultimately, the evidence that HHE and PONPC can covalently modify PTEN are essential.

Chapter 5 – Effects of HHE and PONPC on PTEN Subcellular Localization

5.1. Introduction

PTEN is known to be mainly a cytoplasmic protein, transiently interacting with the plasma membrane (Gil et al., 2016, Leslie et al., 2016, Matsuoka et al., 2013). However, it also localizes to the nucleus (Chung and Eng, 2005, Gil et al., 2006) and nuclear localization can be dominant in some cases (in follicular thyroid and pancreatic islet cells, for instance) (Trotman et al., 2007, Gimm et al., 2000, Perren et al., 2000). More recently, PTEN was additionally found to be associated with endosomes as well as the endoplasmic reticulum, mitochondria and mitochondria-associated membranes, and distributed along microtubules (Bononi et al., 2013, Leslie et al., 2016, Bononi and Pinton, 2015). The various functions of PTEN within different cellular compartments and the mechanisms regulating its localization were described in Chapter 1. In the context of this chapter, it is crucial to emphasize that PTEN's subcellular localization is highly likely to determine its biological functions. These include its canonical role as a lipid-phosphatase for PIP3 when associated with the membrane, facilitating the negative regulation of the PI3K/Akt signalling pathway, while PTEN's interactions with regulatory and effector proteins in specific subcellular compartments, such as the cytoplasm or nucleus, are essential for its non-canonical activities (Gil et al., 2016, Nguyen et al., 2015). Evidence of modification of Akt activation state without noticeable modification of PTEN expression levels was reported in the previous chapter in HCT116 and MCF-7 cells exposed to HHE and PONPC. Although this could be the result of a direct effect on PTEN phosphatase activity, which was inhibited *in vitro* by HHE and PONPC, it could also be explained by a modification of PTEN interaction with the plasma membrane. In fact, Liu *et al.* demonstrated that a recombinant PTEN that is strictly localized in the nucleus and unable to reach the plasma membrane had a diminished ability to inhibit Akt phosphorylation in U251MG cells (Liu et al., 2005b). This therefore led to the necessity of exploring the potential modification of PTEN subcellular localization which could interfere with its role in regulating the PI3K/Akt pathway and other non-canonical functions.

Oxidative stress has not only been shown to regulate PTEN activity but has also notably been identified as a mechanism regulating PTEN subcellular localization, leading to PTEN nuclear accumulation (Chang et al., 2008, Hou et al., 2019, Kato et al., 2020). It has also been shown that reduction of nuclear PTEN results in accumulation of ROS, leading to cellular damage (Wu et al., 2014). Under hydrogen peroxide (H_2O_2)-induced stress following

treatment of mouse embryonic fibroblast cells with 1 mM H_2O_2 for 1 hour, nuclear PTEN increased p53 levels, enhancing p53-mediated cell cycle arrest and ROS reduction to protect cells from further DNA damage and tumorigenesis (Chang et al., 2008) and led to a reduction of H_2O_2-induced micronuclei formation in HeLa cells treated with 0.5 mM H_2O_2 for 2 hours (Hou et al., 2019). The translocation to the nucleus following exposure to H_2O_2 seemed to be dependent on Grb2, which could translocate PTEN to the nucleus and interact with PTEN and Rad51 to help DNA repair (Hou et al., 2019) and required ubiquitination of Lys13 (Kato et al., 2020). Additionally, nuclear accumulation was found to be a consequence of an altered nuclear export of PTEN in cells subjected to treatment with H_2O_2 (Chang et al., 2008, Kato et al., 2020). More specifically, the rate of nuclear import of PTEN after exposure of DU145 cells to 0.5 mM H_2O_2 for 30 min was similar to untreated cells, while the nuclear export was almost completely abrogated during this time (Kato et al., 2020). Although it seems that the retention of PTEN in the nucleus during oxidative stress results from a need for maintenance of genome integrity, the mechanisms regulating this process have yet to be understood. The possibility that stressors directly modify PTEN to regulate its localization cannot be excluded. This has been shown for GAPDH, for instance, where oxidative S-nitrosylation and S-thiolation of Cys152 on GAPDH leads to the formation of a complex between GAPDH and the E3-ubiquitin-ligase Saih1, which can be translocated to the nucleus (Gerszon and Rodacka, 2018).

Although there is no evidence that HHE or PONPC, specifically, can modify protein localization, lipoxidation by LPPs can alter subcellular localization of proteins by modification of residues involved in subcellular targeting, alteration of the transport mechanism or modification of a specific chemical environment on the protein necessary for its interaction with the trafficking machinery or cell compartments (Viedma-Poyatos et al., 2021). Taking GADPH as an example again, it was shown that not only oxidatively-modified GADPH but also acrolein-lipoxidized GADPH was relocated to the nucleus (Nakamura et al., 2013). Particularly relevant for PONPC, the “lipid whisker model” has been proposed for truncated phospholipids resulting from lipid peroxidation within membranes. This model describes a particular arrangement of the fatty acyl chains where the addition of a polar oxygen atom following peroxidation of phospholipids reorients the polar acyl chain; instead of remaining buried within the membrane bilayer, it protrudes into the aqueous compartment (Greenberg et al., 2008). This arrangement makes the electrophilic carbonyl group accessible to macromolecules surrounding it. As the other fatty acyl chain of the phospholipid remains anchored to the membrane, this creates an environment for anchorage of cytoplasmic proteins to membranes. Most importantly, residues involved in the regulation of PTEN localization, including K13 and K289, which are essential to PTEN nuclear import when

mono-ubiquinated (Trotman et al., 2007), and the N-terminal PIP2-binding motif (residues 6-15), which mainly drives membrane binding (Walker et al., 2004, Campbell et al., 2003), are generally basic residues. PTEN membrane localization is indeed favoured by the interaction of key basic residues (Arg and Lys) within the N-terminal PIP2-binding motif, the pβ2-pα1 loop in the phosphatase domain, and the CBR3 loop in the C2 domain (Jang et al., 2021). These basic residues are nucleophilic residues that can be covalently modified by electrophilic LPPs. Hence, LPPs could influence PTEN localization, but this has never been investigated for any LPP, including HHE and PONPC.

This chapter therefore aimed to understand the effects of HHE and PONPC on PTEN subcellular localization. To identify the subcellular localization of a protein, two main methods are usually employed: cell fractionation or cellular imaging (Bononi and Pinton, 2015). Cell fractionation consists of gentle breakage of cells during which subcellular components such as nuclei, mitochondria, the Golgi apparatus, lysosomes and peroxisomes remain intact. These components can then be separated by consecutive centrifugation steps at increasing speeds as they display different sedimentation coefficients depending on their mass, size and shape. However, obtaining good purity in this type of separation is challenging; it can be improved by using sucrose gradients, which allow the different cell components to separate into distinct bands that can be collected individually (Alberts et al., 2002). Several techniques can be used following cell fractionation to detect and quantify the protein of interest, including western blotting (Meftahi et al., 2021) and ELISA (Iha et al., 2022), for which the main limitations are related to the existence, quality and specificity of antibodies targeting the protein of interest (Ghosh et al., 2014, Sakamoto et al., 2018). Mass spectrometry is an antibody-free approach that is used to detect proteins from cell fractionation samples and, although it mainly is utilized for organellar proteomics (the description of protein contents in subcellular compartments), it can detect and enable quantification of a protein of interest (Gauthier and Lazure, 2008, Cox and Emili, 2006, Yan et al., 2008). The numerous steps required to perform cell fractionation and process the different samples to obtain qualitative and quantitative information about the target protein makes cell fractionation generally less convenient than cellular imaging through fluorescence microscopy, which is a more direct method for assessing protein localization. Fluorescence microscopy takes advantage of the ability of fluorescent molecules to absorb photons and re-emit lower-energy photons a few nanoseconds later, resulting in a longer wavelength of emitted light compared to the absorbed light (Stokes shift) (Sanderson et al., 2014). It enables the selective and specific detection of molecules at low concentrations while maintaining a favourable signal-to-background ratio. Traditional epifluorescence microscopy excels at detecting fluorophores in thin samples; however, its application to thick or living

samples is limited by the indiscriminate excitation of the entire sample, resulting in a significant proportion of fluorescent photons emanating from out-of-focus regions. This limitation has been addressed by confocal microscopy, which restricts photodetection to light originating from the focal plane, thereby significantly improving the clarity and specificity of fluorescence imaging (Yuste, 2005, Elliott, 2020). The detection of the protein of interest relies either on the existence of an antibody highly specific to the targeted protein (directly conjugated to a fluorophore for direct immunofluorescence or that can be detected by a secondary antibody conjugated to a fluorophore for indirect immunofluorescence) or on the expression of the protein of interest fused to a fluorophore, such as the widely used green fluorescence protein (GFP). Multiple proteins can be detected simultaneously with different fluorophores, a process called multiplexing (Farre et al., 2007, Im et al., 2019). Both immunofluorescence and fluorescent protein-tagging are reliable techniques to determine protein subcellular localization as demonstrated by Stadler *et al.* as, amongst >500 proteins analysed, 80% yielded the same subcellular localization between the two methods (Stadler et al., 2013). Although direct immunofluorescence is quicker, indirect immunofluorescence provides high sensitivity and signal amplification. These methods are limited by the risk of off-target binding by antibodies, the sensitivity of fluorophores to photobleaching and spectral overlap of different fluorophores that are used simultaneously (Im et al., 2019). These limitations can be mitigated by blocking of the sample and careful choice of fluorophores and detection method for acquisition of images. By fluorescently labelling organelles with fluorescent probes and dyes, such as 4’,6-diamino-2-phenylindole (DAPI) for the nucleus, MitoTracker dyes for mitochondria, or wheat germ agglutinin (WGA) conjugated to a fluorophore for the plasma membrane, it is possible to analyse co-localization of the protein of interest with cell compartments (Farre et al., 2007, Chazotte, 2011).

To investigate the effects of HHE and PONPC on PTEN subcellular localization, the co-localization of endogenous PTEN with the nucleus and plasma membrane in MCF-7 cells was analysed and a model for the expression of GFP-PTEN in HCT116 cells was developed. Specifically, endogenous PTEN's subcellular localization in MCF-7 cells were analysed and quantified, focusing on its presence in the nucleus and at the plasma membrane, using confocal fluorescence microscopy and specific organelle markers (DAPI for the nucleus and WGA for the plasma membrane). To facilitate real-time visualization of PTEN localization, a model of HCT116 cells expressing PTEN fused to GFP was established. Indeed, GFP-PTEN expression in HCT116 cells could allow visualization of PTEN with lower background, higher resolution, avoidance of possible fixative artefacts (Michaelson and Philips, 2006) and, most importantly, would provide the possibility for live-cell imaging to investigate the dynamics of cells response to HHE and PONPC in terms of

PTEN localization. This involved transfecting HCT116 cells with a GFP-PTEN construct and validating expression via western blotting and fluorescence microscopy. Treating cells with HHE and PONPC and analysing PTEN subcellular localization using confocal microscopy would allow determination of changes in PTEN distribution, with the hypothesis that HHE and PONPC could modify PTEN localization through either direct interaction with key residues involved in PTEN's subcellular targeting or, in the case of PONPC, by trapping PTEN at the membrane by covalent binding as described by the lipid whisker model. This was performed in order to provide more insights into the molecular mechanisms underlying PTEN's localization changes in response to oxidative stress and lipid peroxidation products, which could correlate with the observed changes in the PI3K/Akt signalling pathway in MCF-7 and HCT116 cells exposed to HHE and PONPC with the hypothesis that altered PTEN localization due to HHE and PONPC exposure would affect its ability to regulate the PI3K/Akt pathway. The choice of confocal fluorescence microscopy over other methods, such as cell fractionation and mass spectrometry, was driven by its advantages in providing direct and specific visualization of PTEN's subcellular localization in cells, preserving cellular context and dynamics with high-resolution imaging and the ability to analyse multiple fluorophores simultaneously.

5.2. Materials and Methods

5.2.1. Materials

CF®594-conjugated wheat germ agglutinin (WGA) was purchased from Biotium (USA), prepared as per manufacturer's instructions and stored in aliquots protected from the light at -20˚C. The rabbit anti-PTEN primary antibody (PTEN (138G6) rabbit Ab, #9559), validated for immunohistochemistry, was purchased from Cell Signaling Technology (The Netherlands) and the goat fluorescein isothiocyanate (FITC)-conjugated anti-rabbit secondary antibody (Anti-Rabbit IgG (whole molecule)–FITC antibody produced in goat, #F0382) was purchased from Merck (UK); these were used for in the immunostaining procedure (section 5.2.3.2). Mouse anti-PTEN primary antibody (PTEN (26H9) Mouse mAb, #9556) and rabbit anti-α,β-tubulin primary antibody (α/β-Tubulin Antibody, #2148) were used for western blotting and purchased from Cell Signaling Technology (The Netherlands). The goat anti-mouse secondary antibody (goat anti-mouse IgG (H+L)- HRP conjugate, #170-6516) was purchased from Bio-Rad (UK) and the goat anti-rabbit secondary antibody (Anti-Rabbit IgG (whole molecule)–Peroxidase antibody, #A6154) was purchased from Merck (UK), both were conjugated with HRP and used for western blotting (section 5.2.8.2). The ECL (SuperSignal West PICO chemiluminescence substrate) was purchased from ThermoFisher Scientific (UK) and EZ-ECL (Enhanced Chemiluminescence Detection Kit for HRP) was purchased from Biological Industries (USA). 809 pcDNA3 GFP PTEN was a gift from William Sellers (Addgene plasmid #10759) (Vazquez et al., 2001). 809 pcDNA3 GFP PTEN expression plasmid was sent by Addgene in an *E. coli* (DH5α strain) agar stab. This plasmid is referred as "GFP-PTEN plasmid DNA". Enzymes (EcoRI and HindIII) were purchased from Fermentas (UK). EcoRI+ buffer with BSA was purchased from Fermentas (UK) and Tango buffer with BSA was purchased from ThermoFisher Scientific (UK).

5.2.2. Membrane Staining Optimization

MCF-7 cells were seeded on poly-L-Lysine-treated round coverslips in 12-well plates at a cell density of 4 x 10^5 cells/well and a final volume of 1 mL of complete medium. Plates were incubated at 37˚C overnight. After 24 h of incubation, coverslips were washed twice with pre-warmed PBS. A solution of 4% formaldehyde in PBS was added in the wells and incubated for 15 minutes at 37˚C. Wells were washed with pre-warmed Hank's balanced salt solution (HBSS; 140 mM NaCl, 5 mM KCl, 1 mM $CaCl_2$, 0.4 mM $MgSO_4$, 0.5 mM $MgCl_2$, 0.3 mM Na_2HPO_4, 0.4 mM KH_2PO_4, 6 mM glucose and 4 mM $NaHCO_3$, pH 7.4) twice and 500 µL of a CF594-conjugated WGA solution at increasing concentrations (0, 1, 2.5, 5, 7.5 and 10 µg/mL in HBSS) were added. Plates were incubated at 37˚C for 10 minutes, the membrane

staining solution was discarded and wells were washed three times 5 min with HBSS. The coverslips were mounted on a microslide using Fluoroshield mounting media containing DAPI (Merck, UK), sealed with nail varnish and stored at 4˚C until imaged. Images were acquired using a TCS SP8 laser scanning confocal microscope (Leica Microsystems, UK) with a 63X oil objective (HC PL APO CS2 63x/1.40 OIL), available at the imaging facility of Aston University. The numerical aperture of the objective lens was 1.40 and the software used for data acquisition was LAS X (Leica Microsystems, UK). DAPI and CF®594 were excited at 405 nm and 592 nm, respectively. HyD SMD 2 and HyD SMD 4 detectors were used for DAPI and CF594, respectively, and emission of each fluorophore was respectively detected between 410-500 nm and 597-750 nm in separate sequences, recorded between frames. DAPI and CF594 spectra are presented in Figure 5.1. All images were obtained at a speed of 100 Hz and a size of 1024 x 1024 pixels. Overlay images of DAPI and CF®594 channels were analysed on ImageJ where channels were split to measure the fluorescence of WGA-CF®594 and allow a cell count using DAPI staining separately. For the analysis of the intensity of the CF®594 fluorescence, the total fluorescence intensity of images was corrected to the background fluorescence of the unstained control by subtracting the intensity value of the control to the value of each image. The resulting CF-594® fluorescence intensity was normalized to the number of cells in the corresponding image for all WGA-CF®594 concentrations based on the nuclei count using the DAPI staining.

5.2.3. Immunofluorescence of Endogenous PTEN

5.2.3.1. Cell Seeding and Treatment

MCF-7 cells were seeded on poly-L-Lysine-treated round coverslips in 12-well plates at a cell density of 4 x 10^5 cells/well and a final volume of 1 mL of complete medium. Plates were incubated at 37˚C overnight. The next day, cells were treated with 5 µM or 50 µM of HHE or PONPC in a final volume of 1 mL of complete medium. HHE or PONPC was added by removing 100 µL or 500 µL of medium from the wells for the 10X HHE and 2X PONPC stock solutions, respectively, and replacing it by the treatment stock solution. Following the same procedure, the vehicle solution was added to one well as a negative control. One well was left untreated without vehicle as a supplementary negative control. Plates were manually shaken for 10 seconds and incubated for 2 hours at 37˚C, 5% CO_2. One hour prior to the end of the treatments, 1 mM H_2O_2 was added in a separate well by removing 10 µL of medium from the well and replacing it by 10 µL of the 100X H_2O_2 stock solution as a positive control for nuclear localization of PTEN.

5.2.3.2. Staining and Slide Preparation

After 2 h of treatment with HHE or PONPC, the medium was removed, and coverslips were washed twice with pre-warmed PBS. 4% formaldehyde in PBS was added to the wells and incubated for 15 minutes at 37˚C. Wells were washed with pre-warmed HBSS twice and 500 µL of a CF594-conjugated WGA solution (5 µg/mL in HBSS) were added. Plates were incubated at 37˚C for 10 minutes, the membrane staining solution was discarded and wells were washed twice with HBSS. Cells were permeabilized with 0.2% Triton X-100 in HBSS for 10 minutes at room temperature on a rocking shaker and wells were washed twice with HBSS. Cells were then incubated in blocking solution (1% BSA in HBSS) for 30 minutes at room temperature on a rocking shaker and wells were washed twice with HBSS. Humidified chambers were created by placing a distilled water-soaked paper towel in a petri dish. 50 µL of either blocking solution (to provide an unstained control) or anti-PTEN primary antibody in blocking solution at a 1:200 dilution for each coverslip were added onto a piece of parafilm placed in the humidified chamber. Coverslips were placed cell-side down on each drop and were incubated overnight at 4˚C in the dark. The next day, the coverslips were placed cell-side up in a clean 12-well plate and washed three times for 5 minutes with ice-cold HBSS on a rocking shaker. The same steps were repeated for the FITC-conjugated secondary antibody at a 1:80 dilution in blocking solution and, after the washes, the coverslips were mounted on a microslide using Fluoroshield mounting media containing DAPI (Merck, UK), sealed with nail varnish and stored at 4˚C until imaged.

5.2.3.3. Confocal Microscopy Imaging

Images were acquired using a TCS SP8 laser scanning confocal microscope (Leica Microsystems, UK) with a 63X oil objective (HC PL APO CS2 63x/1.40 OIL), available at the imaging facility of Aston University. The numerical aperture of the objective lens was 1.40 and the software used for data acquisition was LAS X (Leica Microsystems, UK). DAPI, FITC and CF594 were excited at 405 nm, 495 nm and 592 nm, respectively. HyD 1, HyD SMD 2 and HyD SMD 4 detectors were used for DAPI, FITC and CF594, respectively, and emission of each fluorophore was respectively detected between 410-500 nm, 511-600 nm, and 597-750 nm in separate sequences, recorded between frames, allowing absence of crosstalk between fluorophores. DAPI, FITC and CF594 spectra are presented in Figure 5.1. All images were obtained at a speed of 100 Hz for a size of 1024 x 1024 pixels. The imaging parameters (gain and pixel values) were manually set so that the FITC channel did not give fluorescent signal on unstained samples with antibodies and that all channels did not lead to saturation in all samples. The parameters remained unchanged between the different samples but differed between each biological replicate to accommodate variations in sample preparation.

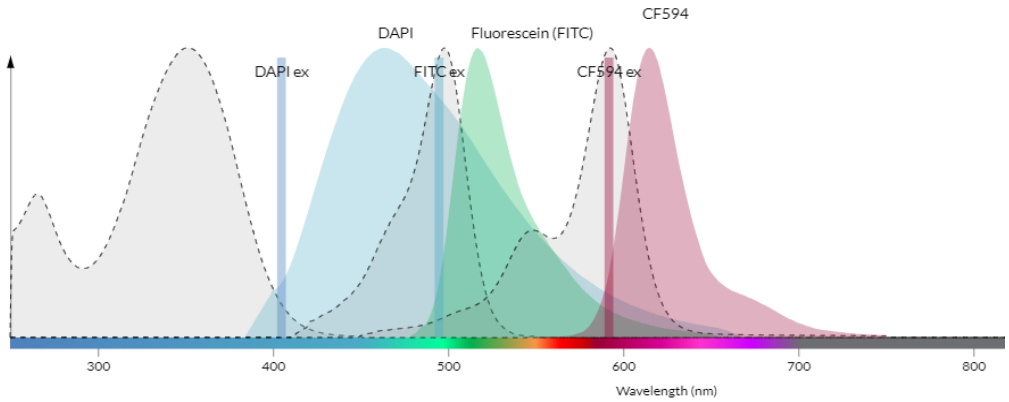

Figure 5.1. Spectra visualization of DAPI, FITC and CF®594 fluorophores.
The blue, green and red spectra show the emission spectra of DAPI, FITC and CF®594, respectively. The grey spectra on the left-hand side of each emission spectra show the excitation spectra of the corresponding fluorophore. The vertical lines at 405, 495, and 592 nm represent the excitation wavelengths used for DAPI, FITC, and CF®594, respectively. (Built on and extracted from www.biotium.com).

5.2.3.4. Co-localization Analysis

The analysis of the co-localization of PTEN-FITC with DAPI or WGA-CF594 was performed using the software ImageJ. Ten regions of interest (ROIs) were created by selecting single cells on overlay images (merged FITC, DAPI and CF®594 channels) for each condition in each of 3 biological replicates. ROIs were unmerged to provide single channel images and the Manders' coefficients (Manders et al., 1993) M1 (fraction of PTEN-FITC overlapping with DAPI of WGA-CF594) and M2 (fraction of DAPI or WGA-CF594 overlapping with PTEN-FITC) were calculated using the Just Another Co-localization Plug-in (JACoP) plugin (Bolte and Cordelieres, 2006) after defining pixel intensity thresholds for each channel. Coefficient values were calculated as follows with Ri and Gi representing the fluorescence of two different channels (Dunn et al., 2011):

$$M_1 = \frac{\sum_i R_{i,\text{colocal}}}{\sum_i R_i} \text{ where } R_{i,\text{colocal}} = R_i \text{ if } G_i > 0 \text{ and } R_{i,\text{colocal}} = 0 \text{ if } G_i = 0 \text{ and } M_2 = \frac{\sum_i G_{i,\text{colocal}}}{\sum_i G_i} \text{ where } G_{i,\text{colocal}} = G_i \text{ if } R_i > 0 \text{ and } G_{i,\text{colocal}} = 0 \text{ if } R_i = 0$$

The mean and standard error of the mean (SEM) of M1 and M2 of three biological replicates were calculated using the GraphPad Prism 8.1.0 software (GraphPad, USA).

5.2.3.5. Analysis of PTEN Cellular Partitioning

Using the ImageJ software, channels (FITC, DAPI and WGA-CF®594 channels) were split on each overlay image. Areas of fluorescence of DAPI and WGA-CF®594 channels were selected after manually thresholding intensity values to remove any background fluorescence and reported as a selection onto the image of the fluorescence of the FITC channel. The total fluorescence of PTEN-FITC and the fluorescence of PTEN-FITC within

the selected areas were measured to obtain intensity values of total cellular PTEN-FITC, nuclear PTEN-FITC and membranous PTEN-FITC. The fluorescence intensity values of PTEN-FITC in the cytoplasm were calculated by subtracting the intensity values of nuclear PTEN-FITC and membranous PTEN-FITC to the intensity values of total cellular PTEN-FITC. Nuclear, membranous and cytoplasmic PTEN-FITC fluorescence intensity values were expressed as a percentage of the total cellular PTEN-FITC fluorescence intensity. Calculations were performed on the Excel software (Microsoft, USA) and results of three biological replicates were analysed on GraphPad Prism 8.1.0 (GraphPad, USA) for statistical analysis.

5.2.4. Plasmid DNA Purification

GFP-PTEN plasmid DNA was purified, quantified and checked for quality as described in General Materials and Methods, Sections 2.2 to 2.4.

5.2.5. Transient Transfection of HCT116 Cells and Epifluorescence Microscopy of Transfected Cells

HCT116 cells were seeded ($1x10^5$ to $6x10^5$ cells/well) in 12-well plates and incubated at 37˚C, 5% CO_2. Cells grown to 50% to 80% confluency were transfected with the purified GFP-PTEN plasmid DNA (batch 1 or batch 2) using lipofectamine 2000 (ThermoFisher Scientific, UK). Different plasmid DNA to lipofectamine 2000 ratios were added to the cells (1:2; 1:3 and 1:4 DNA:lipofectamine 2000 (v/v)), using a fixed amount of 1.6 µg or 3.2 µg of GFP-PTEN plasmid DNA per well. Plasmid DNA and lipofectamine 2000 were first mixed separately with serum-free and antibiotics-free McCoy's 5A (modified) medium. After 5 minutes of incubation at RT, plasmid DNA and lipofectamine 2000 were mixed together, incubated 20 minutes at RT and 200 µL of the solution was added to the wells. 200 µL of serum- and antibiotic-free medium was added to the control wells. Plates were incubated at 37˚C in an atmosphere of 95% air and 5% CO_2 overnight and the medium was changed the next day. Epifluorescence microscopy imaging was performed using brightfield and the GFP filter cube and HC PL FLUOTAR 10.0x0.30 dry objective (Leica Microsystems, UK) at the imaging facility of Aston University. The integrated density of the fluorescence of GFP-PTEN was measured using the ImageJ software after setting the colour threshold to hue = 65-110 (green colour only), saturation = 100-255 and brightness = 0-255. Results were analysed using the Excel software (Microsoft, USA) by correcting the integrated density of images of transfected cells by subtracting the integrated density value of the unstained control.

5.2.6. Cell Harvesting and Lysis

At 24 or 48 hours post-transfection, HCT116 cells were washed twice with PBS and incubated with trypsin-EDTA for 5 minutes at 37˚C, 5% CO_2. Trypsin was inactivated with McCoy's (modied) 5A medium, FBS 10%, penicillin-streptomycin 1% and harvested in 1.5 mL Eppendorf tubes subsequently put on ice. Tubes were centrifuged at 1000 x g for 5 minutes at 4 ˚C. Pellets were resuspended twice in PBS and centrifuged at 1000 x g for 5 minutes at 4˚C, discarding the supernatant after each centrifugation step. Resulting pellets were then resuspended in lysis buffer (50 mM Tris-HCl pH 7.5, 1 mM EDTA, 150 mM NaCl and 1% Triton X-100) supplemented with 1 mM PMSF, with or without phosphatase inhibitors (PhosSTOP™, Roche, UK) and set on ice for 15 to 30 minutes. Tubes were centrifuged at 21000 x g for 2 minutes at 4˚C and the supernatants (protein lysates) were stored at -80˚C. Total protein concentration was assessed as described in General Materials and Methods, section 2.9.2.

5.2.7. SDS-PAGE

SDS-PAGE was performed with 10% acrylamide gels and 5 to 20 µg of protein per well as described in General Materials and Methods, section 2.10.

5.2.8. Western Blotting of Endogenous PTEN and GFP-PTEN

5.2.8.1. Protein Transfer

Proteins separated by SDS-PAGE were transferred onto a methanol-activated PVDF membrane for 1 hour at 100 V in transfer buffer (25 mM Tris, 190 mM glycine and 20% methanol, pH 8.3) using the Mini Trans-Blot® Cell system (Bio-Rad). The membrane was subsequently reactivated with methanol, stained with a Ponceau S staining solution (0.2% (w/v) Ponceau S/5% (v/v) glacial acetic acid) to check for transfer efficiency and destained in water for 5 minutes and 3 times 5 minutes in Tris buffered saline (TBS)-Tween (2 mM Tris, 150 mM NaCl and 0.1% (v/v) Tween-20, pH 7.4).

5.2.8.2. Immunoblotting

PTEN and α/β tubulin (loading control) were probed with specific primary antibodies. The PVDF membrane was blocked in blocking solution (5% milk powder in TBS-T) for 1 hour at RT, incubated with anti-PTEN primary antibody in blocking solution at the working dilution of 1:1000 for 1 hour at RT and washed in TBS-T (3 washes of 5 minutes each). The membrane was then incubated with anti-α,β-tubulin primary antibodies in blocking solution at the working dilution of 1:1000 for 1 hour at RT, washed in TBS-T (3 washes of 5 minutes each), incubated with a mixture of HRP-conjugated anti-rabbit and anti-mouse secondary antibodies in blocking solution at the working concentration of 1:10000 and 1:3000,

respectively, for 1 hour at RT and imaged (section 5.2.8.3). Immunoblotting of PTEN and α,β-tubulin were done separately prior to using both antibodies together to ensure specificity of the antibody binding, and to ensure correct band identification.

5.2.8.3. Imaging

After incubation with HRP-conjugated secondary antibodies, the membrane was washed 3 times 10 minutes in TBS-T, rinsed in TBS (2 mM Tris, 150 mM NaCl, pH 7.4) and incubated 5 minutes with ECL or 1 minute with EZ-ECL. The membrane was placed between two acetate sheets and imaged using a G:Box (GBox XR5, Syngene, UK), selecting sample area on the membrane for auto-exposure time calculation. Images were processed using the software ImageJ. The density of the signal for each band was determined and background signal was subtracted from the density values, which were subsequently divided by the density values of the corresponding loading control (α,β-tubulin) for normalization. When replicates were analysed, the average of normalized density values and the standard deviation were calculated using the Excel software (Microsoft, USA).

5.2.9. Statistical Analysis

Statistical analysis was performed on GraphPad Prism 8.1.0. (GraphPad, USA). Data from three biological replicates was analysed using one-way ANOVA in analysis comprising one variable and two-way ANOVA in analysis comprising two variables, correcting in both cases for multiple comparisons using the Tukey post-test. Statistical significance was defined as $P < 0.05$. The P values were annotated as follows: $P > 0.05$ (ns), $P \leq 0.05$ (*), $P \leq 0.01$ (**), $P \leq 0.001$ (***), $P \leq 0.0001$ (****). Data are shown as mean values ± SEM unless stated otherwise.

5.3. Results

5.3.1. Optimization of the Membrane Staining of MCF-7 Cells

To evaluate the optimal concentration of WGA-CF®594 meeded to obtain an even staining of the plasma membrane, MCF-7 cells were stained with increasing concentrations ranging from 1 to 10 µg/mL. Coverslips were mounted with Fluoroshield mounting medium containing DAPI to stain nuclei in order to provide information about cell count in fluorescence images (for normalization purposes). Interestingly, the intensity of the DAPI staining was inconsistent across samples (Figure 5.2.A). This could result from different factors such as inconsistency of staining of different areas on the coverslips (which can occur if the amount of mounting media in contact with cells in different areas was different because of the orientation of the coverslip during application or the presence of water droplets diluting the mounting media) or photobleaching of the stain. Care was taken to obtain consistent nuclear staining in PTEN co-localization analysis but could differ between images, possibly due to the use of different focal planes. As shown in Figure 5.2.A, a minimum of 2.5 µg/mL WGA-CF®594 was required to stain membranes in MCF-7 cells. However, staining appeared inconsistent at this concentration, whereas cells appeared to be consistently stained with concentrations ≥ 5 µg/mL. This was further confirmed by the quantification of the intensity of WGA staining per cell (Figure 5.2.B), which increased in a concentration-dependent manner up to 5 µg/mL. Surprisingly, the fluorescence intensity per cell at higher concentrations did not increase or plateau but decreased slightly. This decrease in staining could be the result of a poor access to the membranes forming cell junctions which are generally not accessible to macromolecules. As monomers of WGA are 17.1 kDa, its access to this kind of structure may be restricted. This is important to note as it implies that confluence of cells in samples investigating PTEN subcellular localization should be limited to avoid uneven staining of the plasma membrane and could influence the analysis of PTEN co-localization with WGA-CF®594. A concentration of 5 µg/mL WHA-CF®594 was therefore used for membrane staining in all subsequent microscopy experiments.

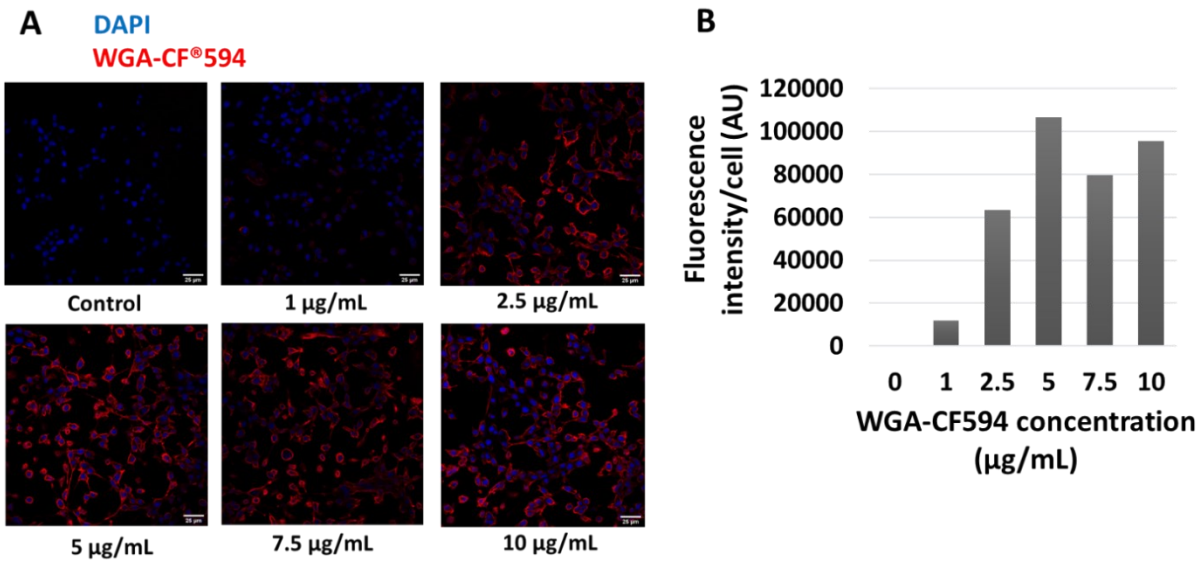

Figure 5.2. Membrane staining of MCF-7 cells using increasing concentrations of WGA-CF®594.
MCF-7 cells were cultured on poly-L-lysine-coated coverslips overnight, fixed and stained with concentrations of WGA CF594 ranging from 1 µg/mL to 10 µg/mL. Coverslips were then mounted onto microslides using Fluoroshield mounting medium containing DAPI (Merck, UK) to stain nuclei and imaged using a TCS SP8 confocal microscope (Leica Microsystems, UK). (A) shows representative merged images of dual staining with DAPI (blue) and WGA-CF®594 (red). Scale bar = 25 µm. (B) shows the corrected (to the control) mean fluorescence intensity for each concentration of WGA normalized to the number of cells from 2 replicate images of 1 biological replicate (n=1).

5.3.2. Effects of HHE and PONPC on Endogenous PTEN Localization in MCF-7 Cells

Indirect immunofluorescence was used to visualize endogenous PTEN in MCF-7 cells. Nuclei as well as plasma membranes were additionally stained using DAPI and WGA-CF594, respectively, to analyse co-localization of PTEN-FITC fluorescence (fluorescence of the FITC-conjugated secondary antibody targeting the anti-PTEN primary antibody) with these cell compartments.

MCF-7 cells were used to investigate subcellular localization of endogenous PTEN because of their higher PTEN expression levels compared to HCT116 cells, the latter showing only ~30% of the PTEN expression levels observed in MCF-7 cells (Figure 5.3). In fact, immunofluorescence of endogenous PTEN in HCT116 cells led to a low fluorescence intensity and a high background (data not shown), while MCF-7 cells allowed successful detection of PTEN (Figure 5.4).

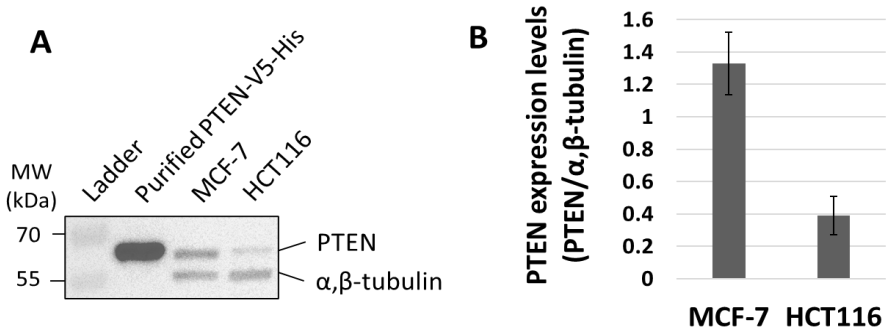

Figure 5.3. Endogenous PTEN expression levels in HCT116 and MCF-7 cells.
(A) Representative western blot of PTEN and α,β-tubulin in HCT116 and MCF-7 cells. HCT116 and MCF-7 cell lysates (10 µg protein) were resolved using SDS-PAGE followed by immunoblotting of PTEN and α,β-tubulin, imaged using a G:Box XR5 (Syngene, UK). Purified PTEN-V5-His was used as a positive control for PTEN immunoblotting and negative control for α,β-tubulin immunoblotting. (B) Densitometry analysis of PTEN expression levels in HCT116 and MCF-7 cells normalized to α,β-tubulin. The densitometry analysis was performed using ImageJ on one biological replicate (n=1) measured on 3 independent western blots. Data is shown as the mean normalized PTEN expression with error bars representing the SD of a technical triplicate.

Staining of nuclei with DAPI and membranes with WGA-CF®594 were also successful. Surprisingly, WGA-CF®594 led to staining of intracellular membranes as well (Figure 5.4). This could be due to internalization of WGA leading to staining of the Golgi apparatus and trans-Golgi network (Pavelka et al., 2008, Allen et al., 1989). However, this intracellular staining was not observed in MCF-7 cells that did not undergo immunostaining (fixed but not permeabilized) (Figure 5.2), suggesting that this could instead be the consequence of remaining WGA molecules during immunostaining steps possibly allowing WGA molecules to enter and interact with intracellular membranes.

As it has been reported previously that H_2O_2-induced oxidative stress led to accumulation of nuclear PTEN in cells by inhibiting the nuclear export of the protein (Chang et al., 2008, Kato et al., 2020), MCF-7 cells were, in parallel, treated with H_2O_2 (1 mM for 1 hour) to provide a positive control for oxidative stress-induced nuclear localization of PTEN. Superficially, the images suggested that PTEN was mainly located in the cytoplasm in control MCF-7 cells and MCF-7 cells treated with vehicle, while it was either diffuse in the cell or even sequestered in the nucleus after treatment with 1 mM H_2O_2 for 1 hour. This seemed to correlate with a more important membrane localization of PTEN in control and vehicle-treated MCF-7 cells, as shown by the colour shift from red to orange in merged images, compared to H_2O_2-treated MCF-7 cells, which seemed to remain red in merged images. Treating with HHE seemed to have similar effects to H_2O_2 on co-localization of PTEN with the nucleus, particularly for treatments using 50 µM HHE, although membrane localization did not seem to differ compared to the vehicle. The same observation could be made for the membrane localization of PTEN in PONPC-treated cells. However, the images of PTEN

localization compared to DAPI staining suggested that PONPC did not lead to nuclear relocalization (Figure 5.4). To obtain more conclusive results on PTEN subcellular localization, a quantitative analysis was performed, showing co-localization of PTEN with the nucleus or the membrane in Figure 5.5 and 5.6, respectively, and the percentage of PTEN in each compartment in Figure 5.7.

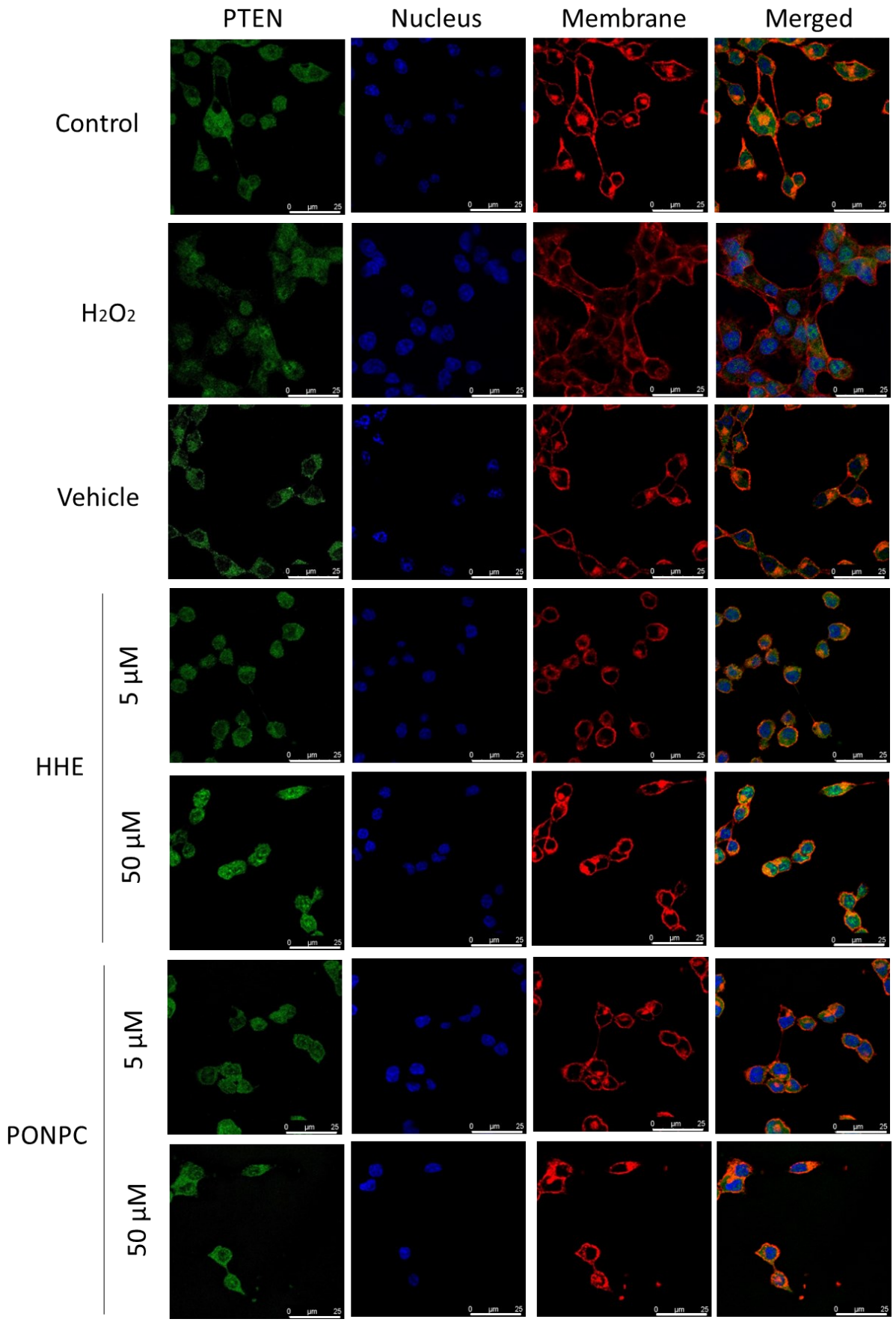

Figure 5.4. Representative confocal microscopy images of PTEN, nucleus and cell membranes in MCF-7 cells untreated or treated with oxidative stressors.

MCF-7 cells were cultured on coverslips and untreated (Control) or treated with 1 mM H_2O_2 for 1 h, 0.2% ethanol (Vehicle), or 5 µM and 50 µM of HHE or PONPC for 2 h. After treatment, cells were fixed with 4% paraformaldehyde, the membranes were stained using CF®594-WGA (red) and immunostaining of PTEN was performed using a primary anti-PTEN antibody and a FITC-conjugated secondary antibody (green). Coverslips were mounted onto microslides using Fluoroshield mounting medium containing DAPI (Merck, UK) (blue) to stain nuclei. Samples were imaged using a TCS SP8 confocal microscope (Leica Microsystems, UK). Scale bar = 25 µm. This is representative of images obtained in 3 biological replicates (n=3).

The analysis of Manders' coefficients (M1 and M2) between PTEN-FITC and DAPI or WGA-CF®594 showed that treatment for 2 hours of MCF-7 cells with 50 µM of HHE led to a significant increase of both M1 (PTEN-DAPI) and M2 (DAPI-PTEN) compared to the vehicle with P values of 0.0024 and 0.013, respectively (Figure 5.5.A). Treating with 5 µM of HHE also seemed to increase nuclear PTEN, although to a lesser extent as the increase in M1 (PTEN-DAPI) was not significant (P = 0.1328) but M2 (DAPI-PTEN) was with a P value of 0.0108 (Figure 5.5.A). This provided evidence that HHE could lead to relocalization of PTEN to the nucleus, although not as efficiently as H_2O_2 which, as expected, showed a 2-fold and 3-fold increase in M1 (PTEN-DAPI) and M2 (DAPI-PTEN), respectively (Figure 5.5.A). No accumulation nor depletion of PTEN at the membrane was observed as M1 (PTEN-WGA) and M2 (WGA-PTEN) were not statistically different from the vehicle after treatment with 5 and 50 µM of HHE for 2 hours (Figure 5.5.B).

On the other hand, M1 (PTEN-DAPI) and M2 (DAPI-PTEN) of MCF-7 cells treated with 5 µM or 50 µM PONPC for 2 hours showed that PONPC did not lead to accumulation nor depletion of PTEN in the nucleus (Figure 5.6.A). Indeed, M1 (fraction of PTEN-FITC fluorescence overlapping with DAPI) and M2 (fraction of DAPI overlapping with PTEN-FITC fluorescence) did not differ statistically between the vehicle and the treatments with PONPC. In contrast, although the modification of membrane localization of PTEN following PONPC treatment was subtle, both fractions of PTEN-FITC fluorescence overlapping with WGA-CF®594 fluorescence (M1 (PTEN-WGA)) and the fraction of WGA-CF®594 fluorescence overlapping with PTEN-FITC fluorescence (M2 (WGA-PTEN)) significantly increased in MCF-7 cells treated with 50 µM PONPC (P=0.002 and P=0.0075, respectively), but not with 5 µM PONPC (Figure 5.6.B). This suggested that PONPC could partially sequester PTEN at the membranes in MCF-7 cells at a high concentration.

Taken together, these results suggest that there is an association between PTEN subcellular localization and exposure of cells to LPPs, as HHE could relocate PTEN in the nucleus, even at low concentration, but not the plasma membrane or intracellular membranes, while PONPC could not relocate PTEN in the nucleus but could increase PTEN membrane localization at high concentration.

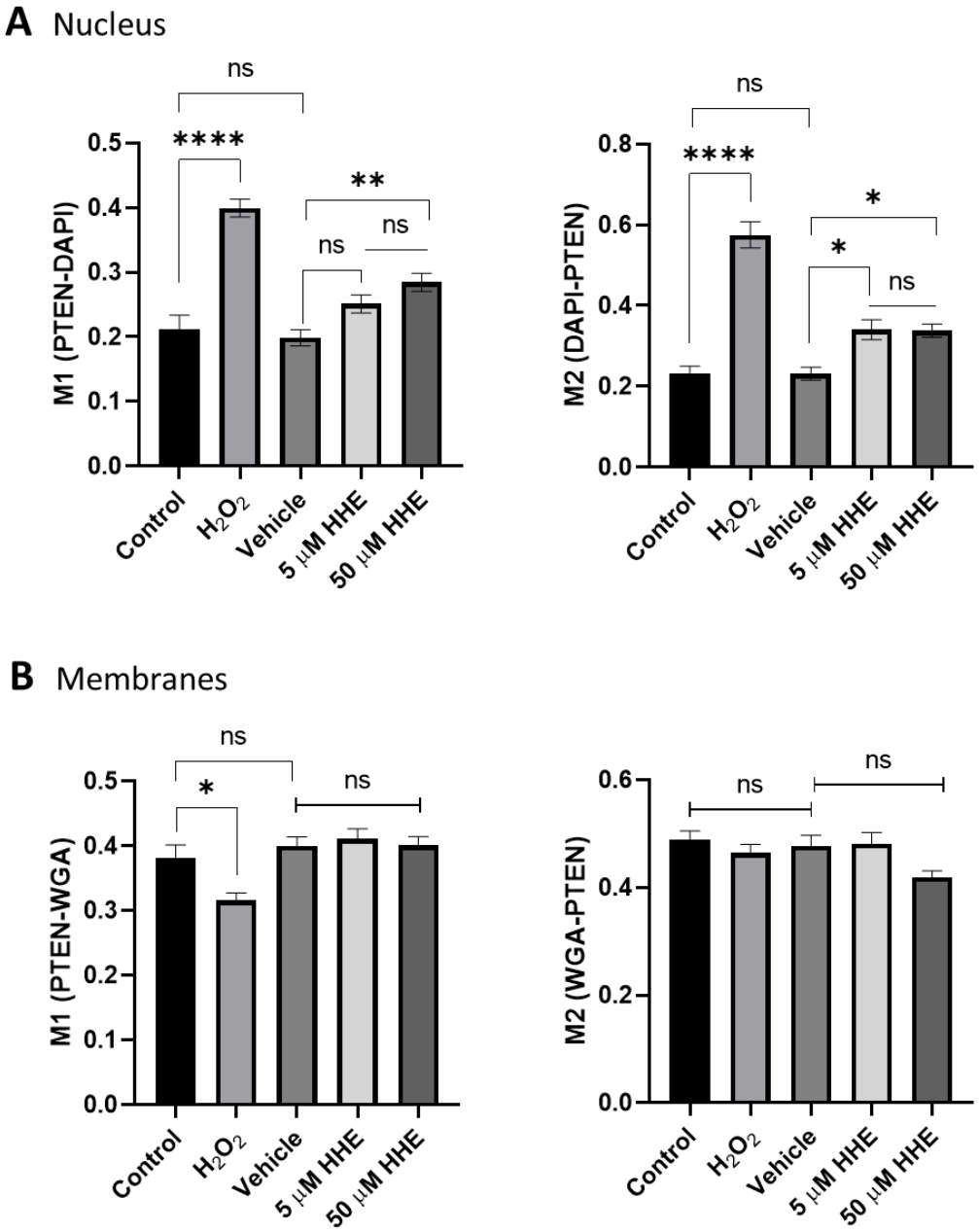

Figure 5.5. Effects of HHE on PTEN co-localization with nucleus and membranes in MCF-7 cells.

Co-localization analysis of PTEN (immunostained with FITC) with DAPI staining nuclei (A) and WGA-CF®594 staining cell membranes (B). MCF-7 cell were untreated (Control) or treated with 1 mM H_2O_2 for 1 h, 0.057% ethanol (Vehicle), or 5 μM and 50 μM of HHE for 2 h and prepared as described in Figure 5.2. Ten cells in each condition of each biological replicate were analysed using the JaCoP plugin of the ImageJ software. M1 represents the fraction of FITC (PTEN) in DAPI (nuclei) or WGA-CF®594 (membranes) and M2 represents the fraction of DAPI (nuclei) or WGA-CF®594 (membranes) in FITC (PTEN). Data represents mean ± SEM of 3 biological replicates (n=3), each including 10 technical replicates. Statistical analysis was performed using one-way ANOVA with Turkey's post-test; $P > 0.05$ (ns), $P \leq 0.05$ (*), $P \leq 0.01$ (**), $P \leq 0.001$ (***), $P \leq 0.0001$ (****).

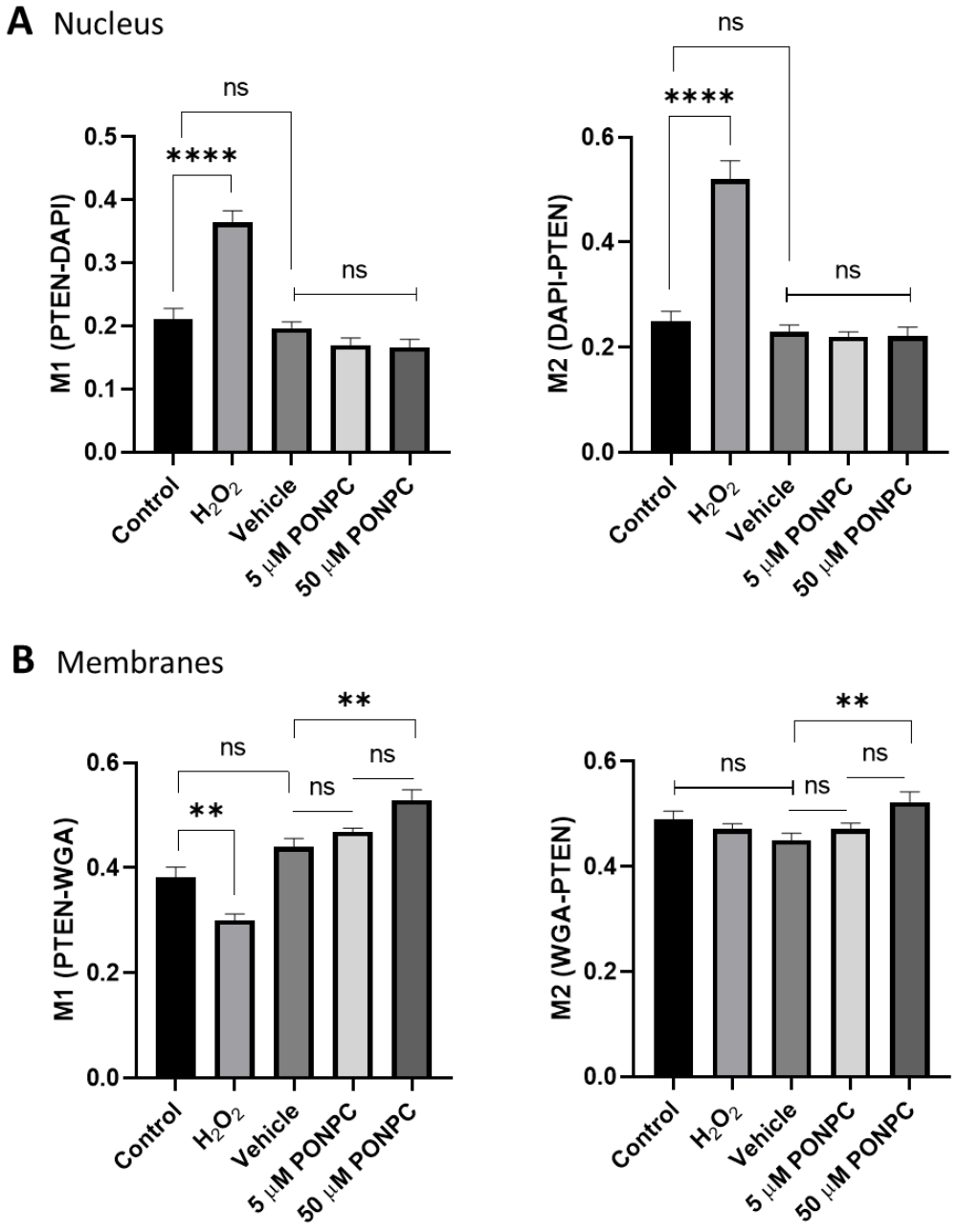

Figure 5.6. Effects of PONPC on PTEN co-localization with nucleus and membranes in MCF-7 cells.

Co-localization analysis of PTEN (immunostained with FITC) with DAPI staining nuclei (A) and WGA-CF®594 staining cell membranes (B). MCF-7 cell were untreated (Control) or treated with 1 mM H_2O_2 for 1 h, 0.2% ethanol (Vehicle), or 5 μM and 50 μM of PONPC for 2 h and prepared as described in Figure 5.2. Ten cells in each condition of each biological replicate were analysed using the JaCoP plugin of the ImageJ software as described in Materials and Methods. M1 represents the fraction of FITC (PTEN) in DAPI (nuclei) or WGA-CF®594 (membranes) and M2 represents the fraction of DAPI (nuclei) or WGA-CF®594 (membranes) in FITC (PTEN). Data represents mean ± SEM of 3 biological replicates (n=3) for 10 cells per replicate. Statistical analysis was performed using one-way ANOVA with Turkey's post-test; $P > 0.05$ (ns), $P \leq 0.05$ (*), $P \leq 0.01$ (**), $P \leq 0.001$ (***), $P \leq 0.0001$ (****).

The fluorescence of FITC was measured in areas stained by either DAPI, WGA-CF®594 or unstained areas of the confocal microscopy images of MCF-7 cells treated with HHE or PONPC for 2 hours to give more insights into the fraction of PTEN in the nucleus, membranes or cytoplasm, respectively. Although no significant differences were found with this analysis, the results showed trends corroborating those of Manders' coefficients. As shown in Figure 5.7.A, the percentage of PTEN localized at the membranes was not modified by HHE treatments, as previously demonstrated by M1 (PTEN-WGA) in Figure 5.5.B, and was stable at ~45% of the total PTEN-FITC fluorescence. As the percentage of PTEN at the membranes was unchanged in these conditions, the increase in PTEN fraction in the nucleus was ultimately compensated with a decrease in cytoplasmic PTEN. This further confirmed that HHE could increase nuclear PTEN without altering the membranous pool of PTEN, but by rather leading to translocation of cytoplasmic PTEN into the nucleus. However, because WGA-CF®594 stained both the plasma membrane and Golgi apparatus, these results cannot confirm PTEN localization to the plasma membrane *per se*. The percentage of PTEN associated with the Golgi apparatus could indeed increase proportionally to a decrease in plasma membrane-associated PTEN, and vice-versa. The analysis of the fraction of PTEN localizing at the membranes, in the nucleus or cytoplasm after exposure of MCF-7 cells to PONPC also corroborated the findings using Manders' coefficients (Figure 5.6); the percentage of nuclear PTEN (~30%) was not modified by PONPC after treatment of the cells. As described for the increase in nuclear PTEN after HHE treatments, the increase in membrane-associated PTEN was accommodated by the cytoplasmic pool of PTEN as the fraction of PTEN in the cytoplasm following treatment with 50 µM PONPC seemed to decrease accordingly. As noted above, these data cannot support the specific association of PTEN to the plasma membrane or Golgi apparatus. It is also important to note that the staining of intracellular membranes led to high intensities of fluorescence of WGA-CF®594 and did not enable clear identifications of the structures, which implied that the PTEN-FITC signal obtained at the intracellular membranes could also be partly cytoplasmic PTEN, which would explain the low percentage of cytoplasmic PTEN found in this analysis. This therefore represents the main limitation of this study and ensuring a specific staining of the plasma membrane would be necessary to draw firm conclusions on PTEN membrane association.

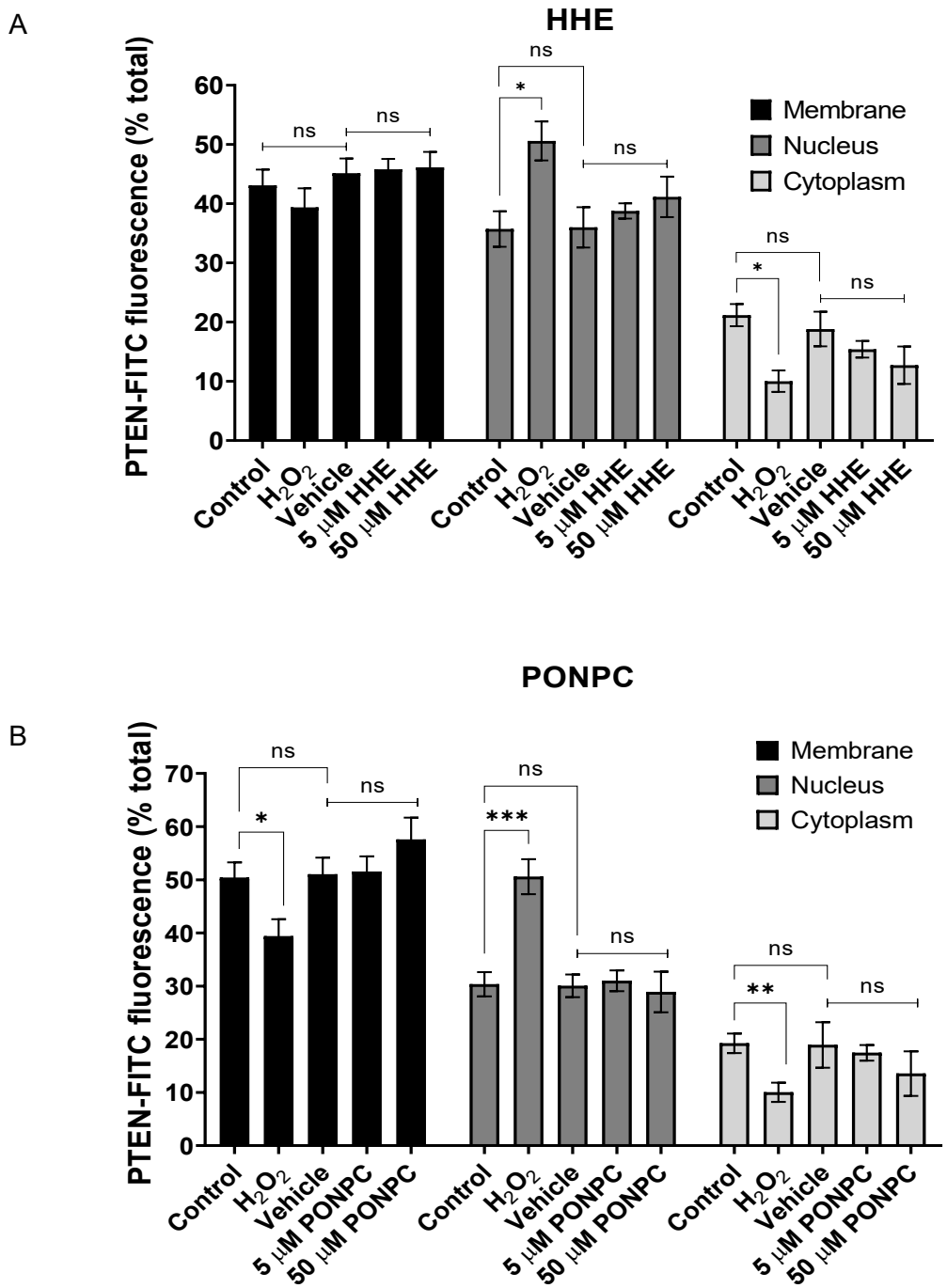

Figure 5.7. Effects of HHE and PONPC on PTEN partitioning in MCF-7 cells.

Analysis of PTEN (immunostained with FITC) fraction associated with membranes, in the nucleus or in the cytoplasm of MCF-7 cells. MCF-7 cell were untreated (Control) or treated with 1 mM H_2O_2 for 1 h, 0.2% ethanol (Vehicle), or 5 μM and 50 μM of HHE (A) or PONPC (B) for 2 h and prepared as described in Figure 5.2. Confocal images were analysed using the ImageJ software as described in Materials and Methods. Data represents mean ± SEM of 3 biological replicates (n=3); one to four images per condition in each biological replicate were analysed, with >20 cells per image. Statistical analysis was performed using one-way ANOVA with Turkey's post-test; $P > 0.05$ (ns), $P \leq 0.05$ (*), $P \leq 0.01$ (**), $P \leq 0.001$ (***).

5.3.3. Optimization of Transfection of HCT116 Cells with GFP-PTEN plasmid DNA

5.3.3.1. Purification of pcDNA3 GFP-PTEN

In an attempt to confirm the results obtained with endogenous PTEN in MCF-7 cells using another model, a recombinant PTEN tagged with GFP was overexpressed in HCT116 cells. Purification of an expression plasmid encoding for a GFP-PTEN fusion protein was primarily needed for expression of the protein in mammalian cells. The map and insert sequence of the plasmid is shown in Supplementary Figure 3. It is a 7336 base pairs (bp) long plasmid containing a cytomegalovirus (CMV) promoter that allows the transcription of the mRNA encoding for a GFP-PTEN fusion protein in mammalian cells, the GFP sequence being placed at the 5' end of the PTEN sequence. The full open reading frame for the GFP-PTEN protein is characterized by 1944 bp encoding for a 647 amino acids long protein containing the GFP at its N-terminus and the canonical PTEN at its C-terminus, separated by a linker of 6 amino acids. The plasmid also contains the sequence of an ampicillin resistance gene allowing bacterial selection for amplification of the plasmid *in vitro.*

The first purification of the plasmid (batch 1) resulted in a DNA concentration of 764 ng/µL. The 260/280 nm and 260/230 nm ratios were 1.88 and 2.2, respectively. The second purification (batch 2) yielded 847 ng/µL of GFP-PTEN plasmid DNA, with 1.9 and 2.29 260/280 nm and 260/230 nm ratios, respectively, showing a good purity of DNA against proteins and chemicals.

The restriction analysis of this plasmid, using EcoRI and HindIII restriction sites, was expected to yield the linearized plasmid for the single digestion with EcoRI and two fragments for the combined digestion of EcoRI and HindIII: a short fragment of 1956 bp and a long fragment of 5380 bp. The agarose gel showed the expected fragmentation pattern for both batch 1 and batch 2 (Figure 5.8). One band for control plasmids corresponding to the full-size plasmid and one band for the single restriction digestion by EcoRI at approximately 7 kbp were obtained. Although the double restriction digestions yielded two major bands corresponding to the long (between 5 and 6 kbp) and short (approximately 2 kbp) fragments, a small band of the same size of the single digestion product could be seen in batch 1 and batch 2 double digestions, indicating that the double digestion was not complete. This band corresponds to a linearized form of the plasmid, hence the result of a single digestion either by EcoRI or HindIII. No other band was detected; thus, the plasmid was successfully purified. However, the apparent size of the control GFP-PTEN plasmid DNA was higher than expected, showing at an apparent molecular weight above 10 kbp, migrating less into the gel than its linearized form, which suggested that it was in an open-circular conformation. Batch

1 was first observed in an open-circular conformation and the purification of batch 2 was in fact an attempt to obtain the supercoiled plasmid. Indeed, transfection of mammalian cells are generally favoured by a compact plasmid conformation which corresponds to the supercoiled conformation (Carbone et al., 2012). This was tried by modification of various points in the procedure, including quality and sterility of solutions as well as consumables, but no supercoiled plasmid was detected in batch 2 either.

To rule out the possible contribution of DNAse contaminations to the conformation of the plasmid, the purification was performed entirely in a cold room at +4˚C to inhibit any potential enzyme activity with pre-cooled buffers, excluding the lysis buffer. A plasmid at a concentration of 694 ng/µL was obtained and showed a good purity with 260/280 and 260/230 ratios of 1.92 and 2.44, respectively. The restriction digestion analysis of this plasmid with EcoRI and HindIII showed, similarly to the plasmids obtained by purification at room temperature, a band at approximately 7 kbp for the digestion with EcoRI only, two bands of approximately 5.5 and 2 kbp for the double digestion with EcoRI and HindIII and the band corresponding to the uncut control plasmid was found above 10 kbp (Figure 5.8), indicating that the purified plasmid was indeed the GFP-PTEN plasmid but that its conformation, even when purified at low temperature, was open-circular. This indicates that DNAse contaminations are likely not to be the cause of the open-circular conformation of the purified plasmid.

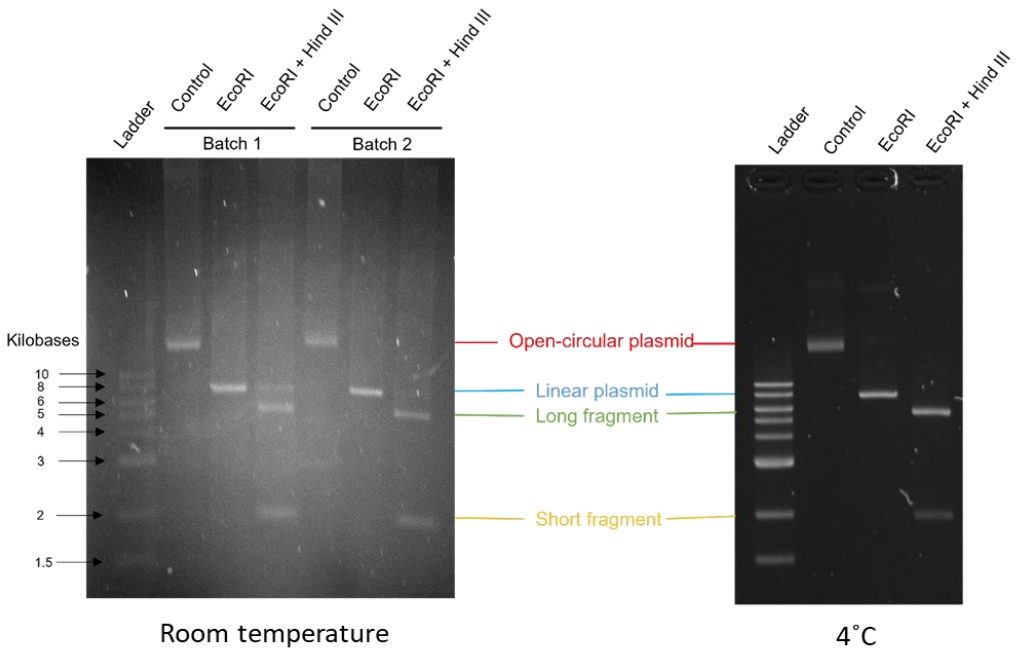

Figure 5.8. Restriction analysis of purified GFP-PTEN plasmid DNA.
A hundred ng of uncut (Control) purified GFP-PTEN plasmid DNA or purified GFP-PTEN plasmid DNA digested with EcoRI alone or EcoRI and HindIII were loaded in wells of a 1% agarose gel and

migrated at 100 V for 90 minutes. DNA bands were detected with SYBR Safe staining (ThermoFisher Scientific, UK).

5.3.3.2. Effects of Transfection on Cell Viability

First, two GFP-PTEN plasmid DNA (batch 1) concentrations were tested for transfection of HCT116 cells: 1.6 µg of DNA were used per well, as recommended by the manufacturer of lipofectamine 2000, and a double amount of DNA (3.2 µg) was tested in the same conditions. Increasing DNA to lipofectamine 2000 ratios (1:2, 1:3 and 1:4) were tested. Lipofectamine 2000 is used in ratios with DNA, thus it is important to note that lipofectamine 2000 concentrations increased proportionately with the amount of DNA. This reagent is toxic at high concentrations for mammalian cells. Therefore, the cell density and cell mortality were assessed 48 hours after transfection. This was performed only once for optimization of the experimental conditions.

Overall, the cell density after 48 hours was higher for lower amounts of DNA and lipofectamine 2000 than for higher amounts. In fact, for 1.6 µg, the cell density of cells transfected when 80% confluent did not vary compared to the control (HCT116 cells for which serum-free medium was added instead of the transfection complex), while cells transfected at lower confluency showed a small decrease in cell density but remained stable across the different DNA to lipofectamine 2000 ratios, except for the 1:4 ratio with 50% confluent cells which almost decreased by half (Figure 5.9.B). For doubled amounts of DNA and lipofectamine 2000, a large drop in cell densities was observed for all percentages of confluency and all DNA to lipofectamine 2000 ratios, particularly for 1:3 and 1:4 (Figure 5.9.D). The mortality was indeed increased in cell populations transfected with higher amounts of DNA and lipofectamine (Figure 5.9.A and Figure 5.9.C). However, an increased mortality in control cells was also observed, questioning the significance of the increase in transfected populations.

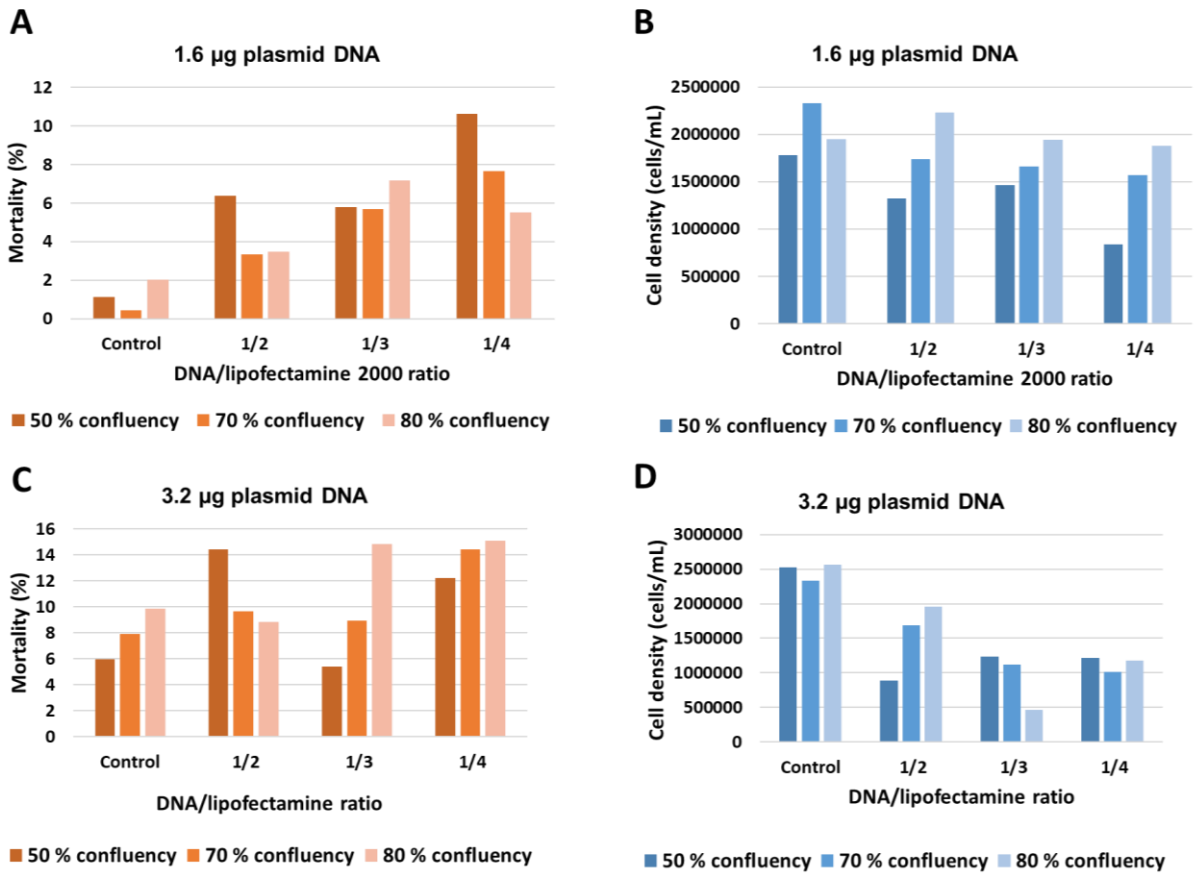

Figure 5.9. Cell density and mortality of transfected HCT116 cells at 48 hours post-transfection with 1.6 or 3.2 µg of GFP-PTEN plasmid DNA.
HCT116 cells at 50%, 70% and 80% confluency were transfected in 12-well plates using 3 ratios of DNA to lipofectamine 2000 (1/2, 1/3 and 1/4) and cell count was performed 48 hours post-transfection. No lipofectamine 2000 or DNA was added to controls. Data is shown for one biological replicate (n=1) and represents the average of 4 counts per condition. (A) and (C) show cell mortality of cells after transfection with 1.6 and 3.2 µg of plasmid DNA (per well), respectively. (B) and (D) show cell density of cells after transfection with 1.6 and 3.2 µg of plasmid DNA (per well), respectively.

Considering these results, further transfections were performed only with 1.6 µg of GFP-PTEN plasmid DNA, keeping the same DNA to lipofectamine 2000 ratios.

The analysis of cell viability was then performed on HCT116 cells undergoing transfection using 1.6 µg of plasmid DNA for 24 hours to gain more insights into the time-dependent effects of transfection on viability. Using the same DNA to lipofectamine 2000 ratios, cells showed low mortality ($\leq 4\%$) for ratios of 1:2 and 1:3 (Figure 5.10.A), which was also generally lower compared to 48 hours post-transfection (Figure 5.9.A). A 2-fold and 3-fold increase in cell mortality was observed at a ratio of 1:4 for cell transfected at a confluency of 70% and 80%, respectively (Figure 5.10.A). This contrasted with the resulting mortality of HCT116 cells at this DNA:lipofectamine 2000 ratio after 48 hours of transfection (Figure 5.9.A), which showed an inversed trend with decreasing mortality correlating with increasing

cell confluency at the time of transfection. In both cases, however, transfection with DNA:lipofectamine 2000 ratios of 1:2 or 1:3 seemed to lead to less cell mortality than with a 1:4 ratio. However, cell density seemed to decrease in all conditions compared to control HCT116 cells (Figure 5.10.B) to a higher extent than what was observed 48 hours post-transfection (Figure 5.9.B), particularly for cell transfected at 50% confluency which showed a minimum of a 2-fold reduction in cell density in all conditions compared to control HCT116 cells (Figure 5.10.B).

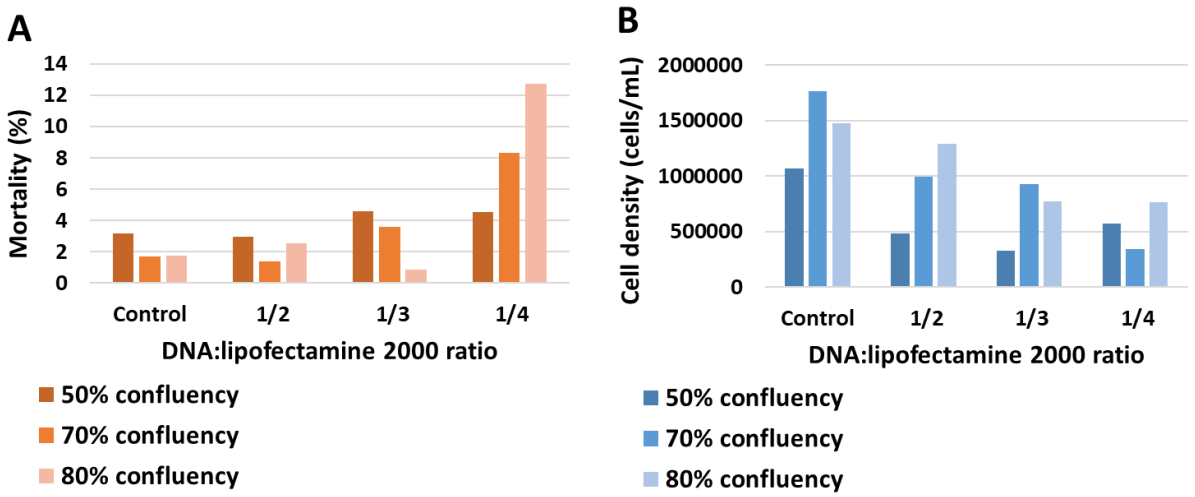

Figure 5.10. Cell density and mortality of transfected HCT116 cells at 24 hours post-transfection with 1.6 of GFP-PTEN plasmid DNA.
HCT116 cells at 50%, 70% and 80% confluency were transfected in 12-well plates using 3 ratios of DNA to lipofectamine 2000 (1/2, 1/3 and 1/4) and 1.6 µg of plasmid DNA per well. Cell count was performed 24 hours post-transfection. No lipofectamine 2000 or DNA was added to controls. Data represents the mean mortality (A) or cell density (B) of two biological replicate (n=2). Cell count was performed 4 times per condition in each biological replicate.

Therefore, for an analysis of GFP-PTEN expression in HCT116 cells following transfection with 1.6 µg of GFP-PTEN plasmid DNA, 1:2 or 1:3 DNA:lipofectamine 2000 ratios used on cells at 70% or 80% confluency for both 24 hours and 48 hours of transfection seemed to be the optimal conditions to obtain minimal cell mortality with resulting cell density close to control cells.

5.3.3.3. Effects of Confluency at Transfection, DNA to Lipofectamine 2000 Ratio and Time on GFP-PTEN Expression Levels in Transfected HCT116 Cells

In order to investigate the transfection efficiency of the transient transfection of HCT116 cells with GFP-PTEN plasmid DNA (batch 1), time of expression, confluency at the time of transfection and DNA to lipofectamine 2000 ratios were considered. HCT116 cells in 12-well plates were transfected using 1.6 µg of GFP-PTEN plasmid DNA per well and 1:2, 1:3 and

1:4 DNA to lipofectamine 2000 ratios. Transfection was performed on 50%, 70% and 80% confluent cells, and one well (for each confluency) was left without transfection as a control. Medium was changed the next day, cells were imaged, harvested and lysis of cells was performed 24 hours or 48 hours after transfection.

For 24 hours of expression, all transfected samples showed GFP-PTEN expression (bands between 70 and 100 kDa), with a higher signal than for native PTEN (approximately 60 kDa), but not equivalent across all samples. There appeared to be a trend of decreasing signal correlated to increasing cell confluency at transfection time (Figure 5.11.A). Although the western blot showing GFP-PTEN expression 48 hours after transfection does not show as good a resolution, most likely due to an insufficient exposure of the membrane (native PTEN was not detectable), it seems to show the same results as for 24 hours post-transfection; the expression of GFP-PTEN decreased with the increase of cell confluency at transfection time (Figure 5.11.B). This trend was supported by densitometry analysis (normalized to α,β tubulin) where level of expression of GFP-PTEN for each DNA to lipofectamine 2000 ratio decreased with increased cell confluency, either for 24 hours of protein expression and 48 hours of protein expression (Figure 5.11.C and Figure 5.11.D, respectively. GFP-PTEN expression after 48 hours was particularly increased for transfection at 50% confluency and 1:3 DNA:lipofectamine 2000 ratio compared to other conditions (2.24 compared to a maximum value of 1.32 for transfection at 50% confluency with a 1:2 DNA to lipofectamine 2000 ratio) (Figure 5.11.D). In contrast, GFP-PTEN expression after 24 hours did not vary for same cell confluency across the different DNA to lipofectamine 2000 ratios, except for 80% cell confluency at transfection time where 1:3 and 1:4 DNA to lipofectamine 2000 ratios show a better expression of the protein than with the 1:2 ratio (Figure 5.11.C).

Overall, these data suggest that transfection of GFP-PTEN plasmid DNA (batch 1) in HCT116 cells is most efficient with low cell confluency at transfection, although it was shown previously that 50% confluency could lead to low cell proliferation after transfection. However, because this analysis was performed across multiple gels separating 1:2 and 1:3 DNA:lipofectamine 2000 ratio to 1:4 DNA:lipofectamine 2000 ratios, the comparison of the efficiency in transfection of the different ratios was not possible.

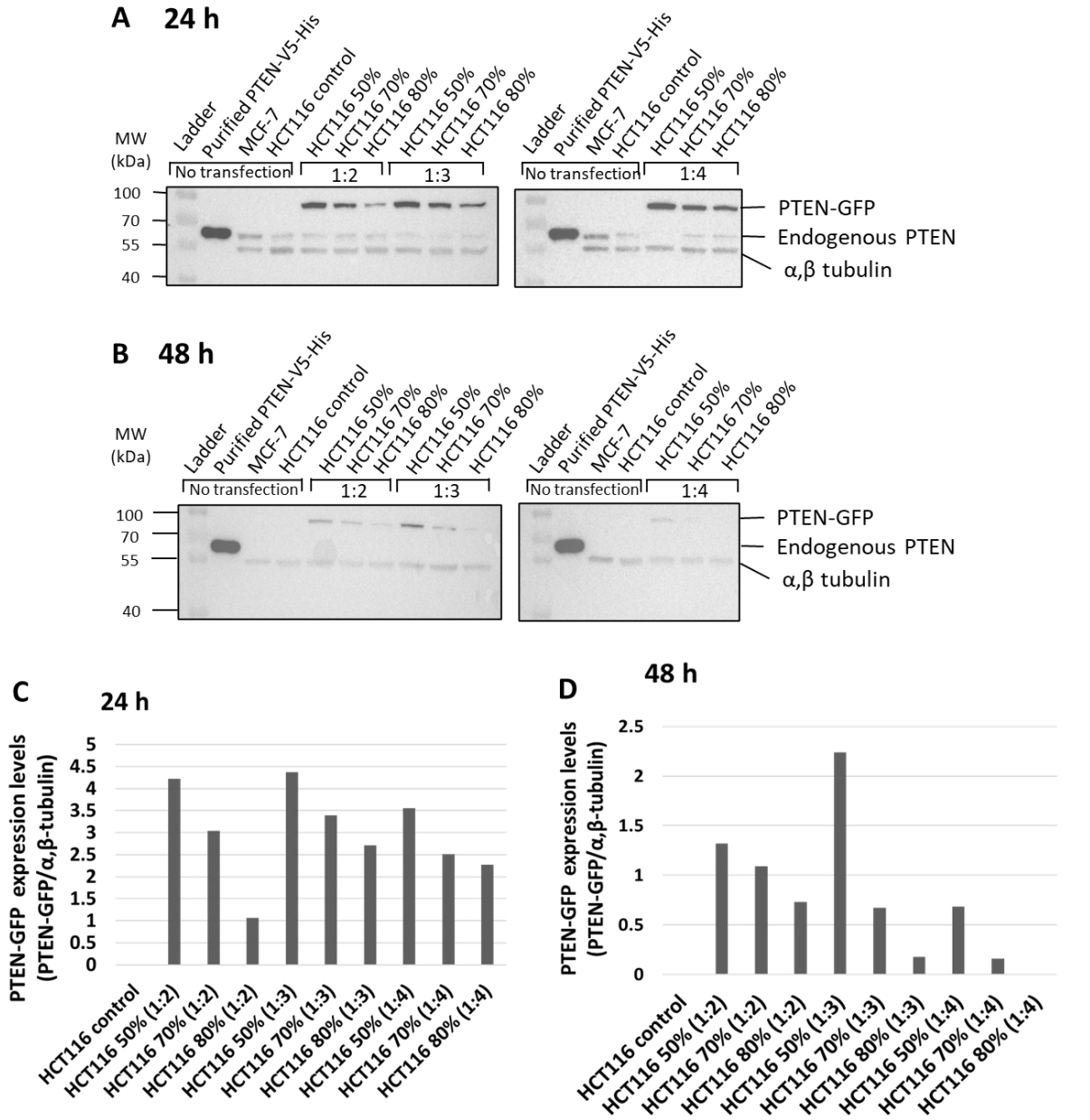

Figure 5.11. GFP-PTEN expression in HCT116 cells 24 and 48 hours post-transfection with GFP-PTEN plasmid DNA (batch 1).

(A) and (B) show representative western blots of GFP-PTEN, endogenous PTEN and α,β-tubulin in transfected HCT116 for different confluency at time of transfection and increasing DNA:lipofectamine 2000 ratios (1:2, 1:3 and 1:4). HCT116 control represents not transfected HCT116 cells. MCF 7 is a negative control for transfection and positive control for endogenous PTEN expression. An additional positive control for PTEN was added (Purified PTEN-V5-His). Cells were harvested and lysed 24 hours post-transfection, 10 µg of total protein were loaded and the membranes were imaged after incubation with ECL (A) or 48 hours post-transfection, 15 µg of total proteins were loaded and the membranes were imaged after incubation with ECL (B) on a G:Box XR5 (syngene, UK). (C) and (D) show quantification of GFP-PTEN expression (normalized to α,β-tubulin) in western blots (A) and (B), respectively. Data represents values for one biological replicate (n=1).

To investigate further the influence of the DNA to lipofectamine 2000 ratio on transfection efficiency, 70% confluent cells were transfected with 1.6 µg of GFP-PTEN plasmid DNA

(batch 1 and batch 2) at previously reported DNA to lipofectamine 2000 ratios and cells were harvested and lysed 48 hours post-transfection. The expression of GFP-PTEN was observed by western blotting. GFP-PTEN appeared to be expressed to a lesser extent than endogenous PTEN in this experiment (Figure 5.12.A) indicating limited transfection of HCT116 cells. The level of GFP-PTEN expressed by transfected HCT116 cells was increased from the 1:2 to 1:4 ratio (Figure 5.12.B); the average expression for a 1:2 ratio was 6 times lower than that for a 1:3 ratio and 9 times lower than for a 1:4 ratio.

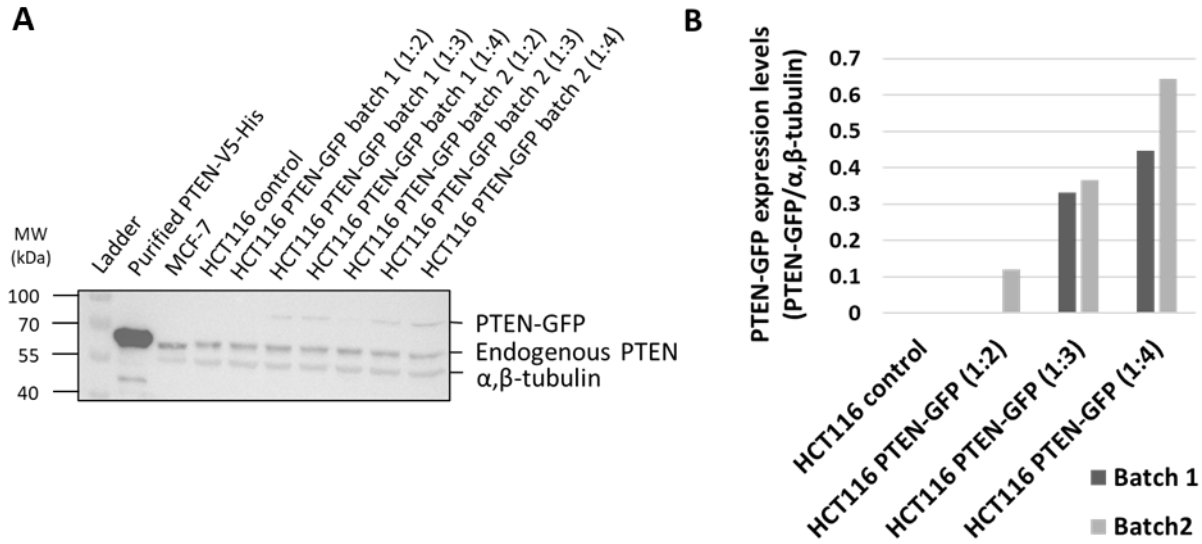

Figure 5.12. Comparison of GFP-PTEN expression in HCT116 transfected with GFP-PTEN plasmid DNA (batch 1 and batch 2) using increasing ratios of DNA to lipofectamine 2000.
(A) Western blot of GFP-PTEN, endogenous PTEN and α,β-tubulin in HCT116 cells transfected at 70% confluency at time of transfection with increasing DNA (batch 1 or batch 2):lipofectamine 2000 ratios (1:2, 1:3 and 1:4). HCT116 control represents not transfected HCT116 cells. MCF-7 cells was used a negative control for transfection and positive control for endogenous PTEN expression. An additional positive control for PTEN was added (Purified PTEN-V5-His). Cells were harvested and lysed 48 hours post-transfection, 10 µg of total protein were resolved by SDS-PAGE and transferred onto a PVDF membrane for immunoblotting. The membrane was imaged after incubation with ECL. (B) Densitometry analysis of the expression of GFP-PTEN (normalized to α,β tubulin) with GFP-PTEN plasmid batch 1 and batch 2 at 1:2, 1:3 and 1:4 DNA to lipofectamine 2000 ratios. Data represents values of one biological replicate (n=1).

The time-dependence of expression of GFP-PTEN following transfection could not be assessed by the western blot analysis as probing and processing of membranes differed between membranes for samples harvested at 24 hours and 48 hours after transfection. To address this, fluorescence imaging of the wells for each condition was performed. Images were taken for all conditions at similar cell densities to allow comparison of GFP-PTEN expression levels considering the absence of nuclear staining for normalization. Transfection of HCT116 cells at 50% or 70% confluence with a DNA:lipofectamine 2000 ratio of 1: or 1:4 seemed to be the conditions leading to highest expression of GFP-PTEN after 24 hours of protein expression (Figure 5.13.A), whilst it was restricted to 70% confluent cells at the time

of transfection with the same DNA:lipofectamine 2000 ratios for cells allowed to express GFP-PTEN for 48 hours (Figure 5.13.B). The transfection efficiency of the samples expressing GFP-PTEN the most at both 24 hours and 48 hours post-transfection seemed to be similar (Figure 5.13.A and 5.13.B).

Quantification of GFP-PTEN fluorescence in these images allowed more accurate representation of the levels of expression of GFP-PTEN in these samples. This analysis confirmed the results of the western blotting of GFP-PTEN: expression of GFP-PTEN generally increased with the DNA:lipofectamine 2000 ratios but decreased with the cell confluency at the time of transfection (Figure 5.14). The expression levels of GFP-PTEN were very similar between 24 hours and 48 hours post-transfection for HCT116 cells transfected at 70% and 80% confluency at the same DNA:lipofectamine 2000 ratios. This was, however, not true for HCT116 cells transfected at 50% confluency, for which levels of GFP-PTEN were ~2-fold higher at 24 hours post-transfection compared to 48 hours post-transfection for transfections using a 1:2 DNA:lipofectamine 2000 ratio and ~30% lower at 24 hours post-transfection compared to 48 hours post-transfection for transfections using a 1:3 DNA:lipofectamine 2000 ratio, while GFP-PTEN levels were similar at a 1:4 ratio (Figure 5.14). As the nuclei were not stained in these experiments and cell were generally fully confluent, it was not possible to count cells to provide the transfection efficiency calculated as Number of GFP-PTEN Expressing Cells ÷ Total Number of Cells. Nuclear staining would therefore be necessary for a definitive evaluation of the transfection efficiency of HCT116 in these experiments.

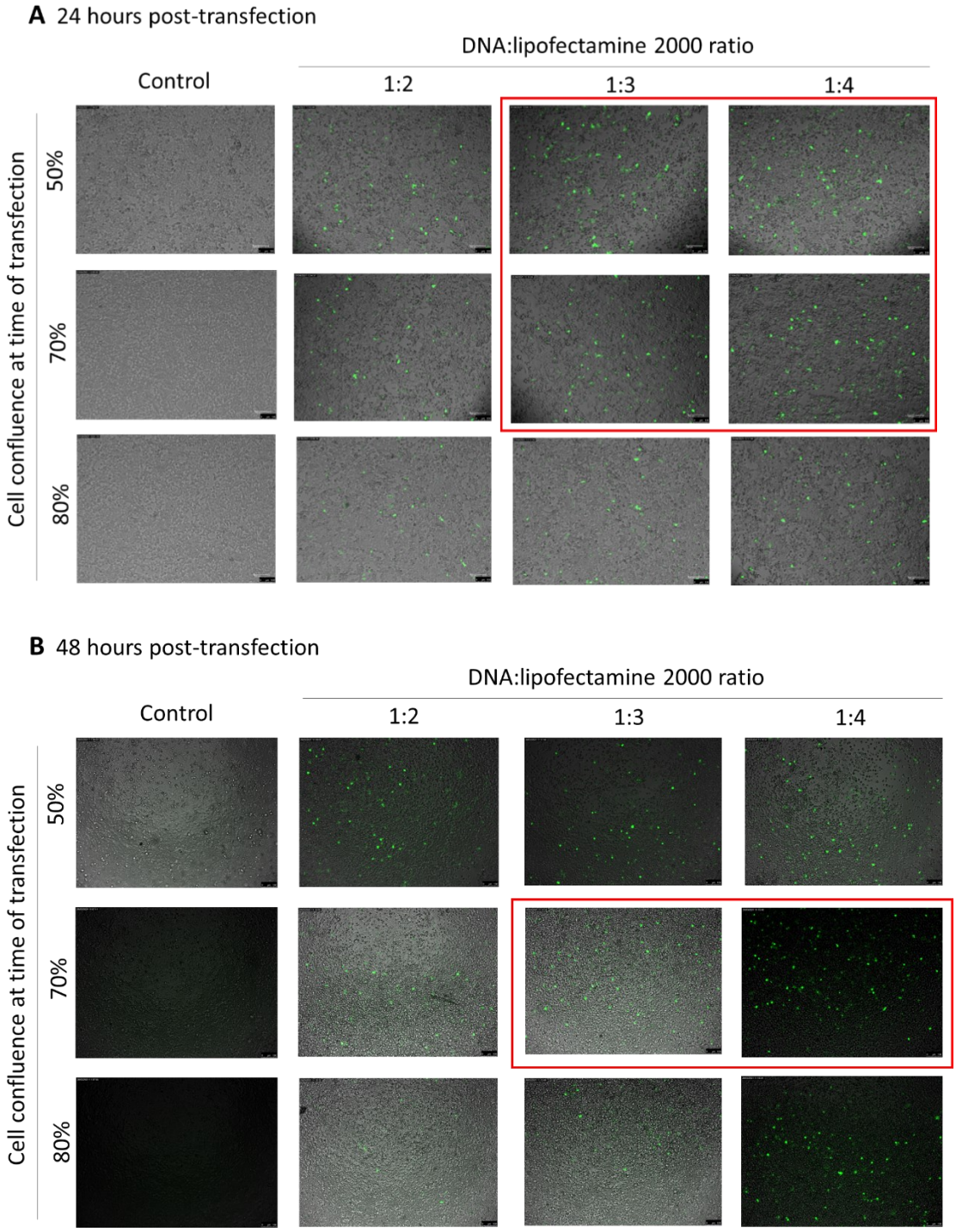

Figure 5.13. Epifluorescence microscope images of GFP-PTEN fluorescence in HCT116 cells transfected with GFP-PTEN plasmid DNA (batch 1) after 24 or 48 hours of protein expression.
This shows representative images of the fluorescence of GFP-PTEN (green) in transfected HCT116 at 24h (A) or 48h (B) post-transfection. Transfection was performed on HCT116 cells grown in 12-well plates at different confluency and using increasing DNA:lipofectamine 2000 ratios with 1.6 µg DNA/well. Cell imaging was performed using brightfield epifluorescence and a GFP filter cube with HC PL FLUOTAR 10.0x0.30 dry objective (Leica Microsystems, UK) either 24 hours or 48 hours post-transfection. The scale bar indicates 100 µm. The images with apparent highest fluorescence emission are squared in red.

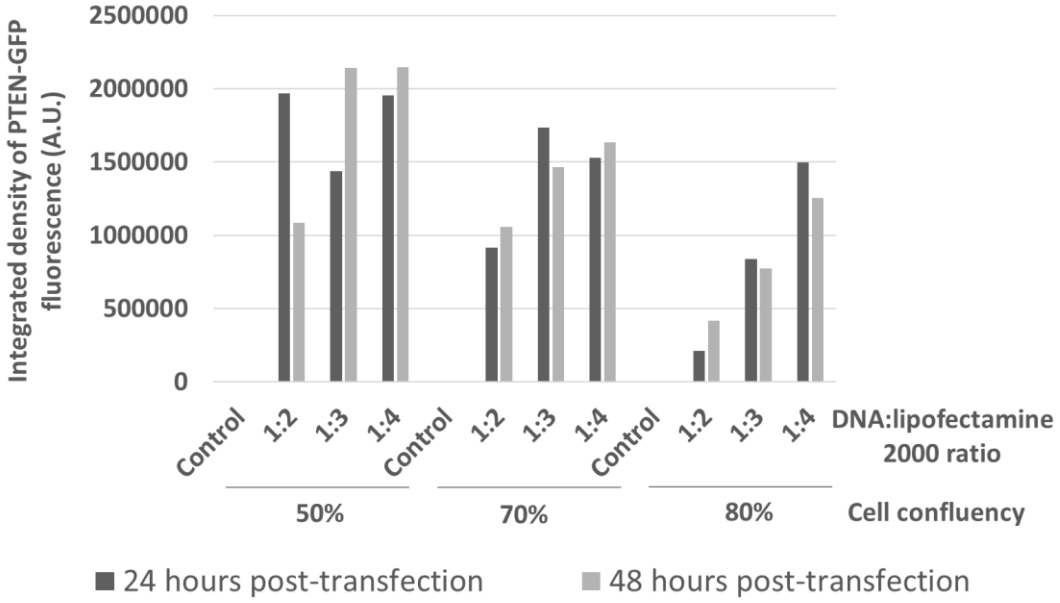

Figure 5.14. Semi-quantitative analysis of GFP-PTEN expression at 24 hours and 48 hours post-transfection of HCT116 cells at different confluency and DNA:lipofectamine 2000 ratios.
HCT116 cells were transfected and imaged as described in Figure 5.12. Fluorescence of GFP-PTEN in images (at similar confluency) was measured using the ImageJ software. Data represents the values of integrated density of GFP-PTEN fluorescence of one biological replicate (n=1) measured once for 48 hours post-transfection samples or the mean integrated density of GFP-PTEN fluorescence of one biological replicate (n=1) measured in technical duplicate for the 24 hours post-transfection samples.

Taken together, these results showed that transfection of HCT116 cells at a low confluency (Figure 5.11 and 5.14) with a 1:4 ratio of DNA to lipofectamine 2000 (Figure 5.12 and 5.14) allow the highest expression of GFP-PTEN. However, it was observed that high concentrations of lipofectamine 2000 in culture media is detrimental for cells (Figure 5.9 and 5.10), while a DNA to lipofectamine 2000 ratio of 1:3 did not show high cell mortality (Figure 5.9 and 5.10) but an increased expression of GFP-PTEN compared to 1:2 ratios (Figure 5.12). Therefore, transfection at a 1:3 ratio seems to be a good compromise to balance the mortality induced by higher amounts of lipofectamine 2000. From the fluorescence imaging (Figure 5.13 and 5.14), it appeared that expression of the protein would be similar between 24 hours post-transfection and 48 hours post-transfection. Although further investigation is necessary to fully optimize this model, this provided insights into the conditions necessary to obtain overexpression of GFP-PTEN in HCT116 cells, which would allow to investigate the effects of HHE and PONPC on PTEN localization in another model, providing more robust evidence when added to the investigation on endogenous PTEN in MCF-7 cells.

5.4. Discussion

For the first time, effects of LPPs on PTEN localization were investigated. The analysis of the co-localization of PTEN with DAPI suggested that PTEN could accumulate in the nucleus of MCF-7 cells in response to HHE treatments, similarly but to a lesser extent than the H_2O_2-induced PTEN translocation in the nucleus. This is in line with evidence that HHE-modified proteins tend to be located more in the nucleus and perinuclear regions of retinal cells after light exposure of rat retina that increased the HHE- and HNE-modified protein content in these cells (Tanito et al., 2005). However, previous studies provided evidence that H_2O_2 induces accumulation of PTEN in the nucleus by inhibiting PTEN nuclear export in response to DNA damage (Kato et al., 2020, Chang et al., 2008) and HHE was found to induce DNA damage from concentrations of 10 µM in hepatocytes (Eckl et al., 1993). Hence, it is questionable whether the translocation of PTEN to the nucleus after exposure of cells to HHE is related to a response to potential DNA damage induced by HHE like the H_2O_2-induced PTEN translocation in the nucleus, especially as the concentrations tested are close to the concentrations found to induce DNA damage in hepatocytes, or if it is a direct consequence of PTEN modification by adduction of reactive HHE. Evaluation of DNA damage after HHE treatment in parallel to evidence of endogenous PTEN adduction by HHE would provide more insights into the molecular mechanism of PTEN accumulation in the nucleus following HHE exposure.

In contrast to what was observed with HHE, PONPC did not modify PTEN co-localization with the nucleus, but showed a significant modification of membrane association of PTEN in MCF-7 cells treated with 50 µM PONPC but not 5 µM PONPC. This suggested that PTEN localization could be influenced by PONPC but at high concentrations only. Information on the behaviour of PONPC in cells in the literature is limited. However, it was shown for POVPC, another truncated phospholipid that has been studied more widely, that fluorescent POVPC analogues are inserted rapidly into the plasma membrane of vascular smooth muscle cells during their first contact with the cell surface, resides there as a consequence of their association with amine-containing lipids and proteins, and are subsequently partially transferred to perinuclear regions (Moumtzi et al., 2007). PONPC, which has a very similar structure, is most likely to act in a similar manner and could therefore covalently modify membrane-associated PTEN, trapping it at the membrane whilst residing in the bilayer, and relocating it to perinuclear regions, which was measured by the co-localization analysis of PTEN with the membranes as intracellular membranes were stained by WGA-CF®594. This also means that the modification of PTEN membrane localization at high concentrations of PONPC could be due to trafficking of PONPC to intracellular membranes rather than increase in plasma membrane association of PTEN. There is, however, no evidence of

cellular uptake of PONPC (nor HHE) in our experimental procedures. This is particularly important as the localization of the oxidized lipids would give essential information on their potential biological consequences and this can be addressed similarly to the POVPC analogues by synthesizing PONPC or HHE analogues with conjugation to different fluorophores.

Surprisingly, although the analysis of colocalization of PTEN with the nuclei and membranes and the analysis of PTEN partitioning in MCF-7 cells led to the same conclusions, the significant differences observed in the co-localization analysis were correlated to rather small changes in percentage of endogenous PTEN localized at the nucleus (following HHE treatment) or at the cell membranes (following PONPC treatment). This could be the result of different values used as thresholds of the fluorescence of PTEN-FITC for the two analytical methods. Indeed, whilst the analysis of the percentage of PTEN in the different MCF-7 cell compartments required to threshold the fluorescence intensities of PTEN-FITC to values covering the entire surface of the cell (grey value = 2-255), thresholds were set to higher intensities for the analysis of Manders' coefficients to avoid accounting for autofluorescence and off-target effects (Dunn et al., 2011). This meant that low intensity pixels of PTEN-FITC fluorescence were accounted for in the analysis of the partitioning of PTEN in MCF-7 cells but not in the colocalization analysis using Manders' coefficients. As low-intensity pixels are often a representation of cellular background, the colocalization analysis would reflect more accurately the actual localization of PTEN compared to the analysis of PTEN partitioning. However, an additional method to visualize PTEN subcellular localization would reinforce this data to provide stronger evidence of the changes that PTEN undergoes following treatment with HHE or PONPC and the intention was to address this by cellular imaging of GFP-PTEN in transfected HCT116 cells.

The objectives of the project were to purify a plasmid encoding a GFP-PTEN fusion protein in order to express the protein in mammalian cells (HCT116 cells) to provide a model for confirmation of the results obtained with endogenous PTEN in MCF-7 cells. It has previously been shown to be effective for the expression of GFP-PTEN in mammalian cells, having been transfected into several cell lines - 16HBE and CFBE, PC3, SK-MEL-24 or 786-O and U2-OS cells - using different methods (Riquelme et al., Kimbrough-Allah et al., Lin et al., Vazquez et al., 2001). Kato *et al.* managed to express a fusion GFP-PTEN protein in HCT116 cells in 2020 and showed that GFP had no effect on PTEN localization or ability to translocate to the nucleus as the analysis of GFP-PTEN localization in transfected DU145 cells rendered the same results than with endogenous PTEN in the same cell line (Kato et al., 2020). This provided evidence that the GFP-PTEN-expressing HCT116 cells model would be suitable for this project. Transfection of HCT116 cells would allow monitoring of

possible changes in the localization of the protein after treatment with HHE and PONPC. The plasmid encoding GFP-PTEN was purified and allowed transfection of HCT116 cells. However, the transfection efficiency was found to be low. One explanation for this may be the conformation of the plasmid after purification. Indeed, transfections are favoured by a compact plasmid conformation which corresponds to the supercoiled conformation. Purification of plasmids at low temperature was shown to yield to the extraction of higher proportions of the supercoiled conformation of the plasmid (Carbone et al., 2012). Therefore, purification at +4˚C was performed but did not lead to an increased purification of the supercoiled plasmid. It is also possible that the simple variation in cell line results in lower efficiency, as transfection is highly dependent on the cell line and reagent employed, in addition to factors intrinsic to the plasmid. For instance, a comparative analysis of the efficiency of transfection of plasmids encoding for luciferase and β-galactosidase using multiple reagents, including lipofectamine 2000, in 10 different cell types was previously performed (Yamano et al., 2010). This study showed that, for HCT116 cells, the transfection efficiency of the luciferase plasmid was one of the highest across all cell lines using lipofectamine 2000 but one of the lowest across all reagents used in HCT116, while transfections of the β-galactosidase plasmid were efficient with all reagents in HCT116 and lipofectamine 2000 worked better with HCT116 than with most of the other cell lines. For this reason, polyethylenimine was also tested as a transfection reagent but was unsuccessful in transfecting HCT116 cells with GFP-PTEN plasmid DNA (data not shown). Addressing all factors influencing transfection efficiency would therefore be necessary in the future, considering the difficulty of analysing results for GFP-PTEN localization when it is expressed in few cells. Best conditions for transfection of GFP-PTEN plasmid DNA in HCT116 were determined as a low cell confluency at time of transfection (50%) and a 1:3 ratio of DNA to lipofectamine 2000. The different incubation times (24 hours and 48 hours) did not seem to lead to different levels of expression of GFP-PTEN, although it was demonstrated previously that 48 hours generally led to higher expression in experimental procedures using the same plasmid for transfecting mammalian cells (Kimbrough-Allah et al., Lin et al.). It was shown that high lipofectamine 2000 concentrations induce a decreased density of HCT116 cells. Using 5 µL of lipofectamine 2000 in 2 mL transfection volume to transfect Capan-2 cells, Zhong *et al.* showed that cell growth was slowed by the transfection reagent and that prolonged culture (after 48 hours) of transfected cells caused increases in early apoptotic cells and damaged cells or necrotic cells and modification of the cell cycle, resulting in a reduced viability (Zhong et al., 2008). This could therefore explain the observed decreased cell density of HCT116 after transfection.

Most importantly, the consequences of HHE and PONPC on PTEN subcellular localization need to be in the context of reaction between PTEN and the oxidized lipids. So far, it has not been demonstrated that PTEN can be modified by HHE or PONPC. Such investigation involves the purification of PTEN in order to treat the protein directly *in vitro* with HHE and PONPC and detect potential adducts formed with the protein using mass spectrometry. Expression of His-tagged PTEN in bacteria has allowed purification of the protein as described in Chapter 3, which could be treated *in vitro* with HHE and PONPC and analysed by MS/MS. This work to provide evidence of lipoxidation of PTEN by HHE and PONPC is at the centre of the next chapter and this allowed the previously observed consequences of treatments on PTEN localization to be linked with its potential adduction by these oxidized lipids.

Chapter 6 – Characterization of HHE and PONPC Adducts on PTEN

6.1. Introduction

The consequences of HHE and PONPC on purified PTEN-V5-His phosphatase activity, HCT116 and MCF-7 cell viability, phosphorylation state of Akt as well as PTEN's expression levels and subcellular localization in HCT116 and/or MCF-7 cells were investigated in previous chapters. The hypothesis was that PTEN could be a target of adduction by oxidized lipids such as HHE and PONPC and that such modification of PTEN could lead to disruption in associated pathways. Although modification of the activation state of the PI3K/Akt pathway was observed in response to HHE and PONPC treatments in HCT116 and MCF-7 cells without upregulation or down regulation of PTEN and modification of PTEN localization was observed in MCF-7 cells, the capability of HHE and PONPC to form covalent adducts on PTEN remained to be confirmed in order to link these cellular effects to PTEN lipoxidation by HHE and PONPC.

As discussed throughout this thesis, PTEN is a redox-sensitive protein susceptible to lipoxidation by oxidized lipids such as HHE and PONPC. This susceptibility is primarily due to the presence of nucleophilic residues in the PTEN sequence, which can react with these reactive aldehydes to form covalent adducts (Stemmer and Hermetter, 2012, Viedma-Poyatos et al., 2021). These nucleophilic residues are cysteine (Cys), histidine (His), lysine (Lys) and arginine (Arg) residues, which represent 2.48% (10/403 residues), 3.23% (13/403 residues), 8.44% (34/403 residues) and 4.96% (20/403 residues) of PTEN sequence, respectively. N-terminal residues can also be adducted by electrophilic species as the primary amine is not involved in a peptide bond and available for reaction (Viedma-Poyatos et al., 2021). As described in the General Introduction (section 1.2.1), oxidized lipids can covalently bind to side chains of nucleophilic residues through two mechanisms: Schiff base formation or Michael addition. Schiff bases are formed by the condensation of a primary amine and an active carbonyl group by nucleophilic addition to yield a hemiaminal, and subsequent dehydration to generate an imine (Sani et al., 2018) and Michael additions involve a nucleophilic attack on the β-carbon of an α,β-unsaturated carbonyl followed by protonation of the α-carbon (Baker et al., 2007). HHE is an α,β-unsaturated aldehyde, similar to HNE and acrolein, which contains an electronegative carbonyl oxygen atom that can promote the withdrawal of mobile electron density from the beta-carbon atom (involved in the double bond), causing regional electron deficiency. These characteristics make HHE a soft

electrophile which preferentially forms Michael adducts with soft nucleophiles. Therefore, cysteine sulfhydryl groups are the primary nucleophilic targets of HHE, in contrast to nitrogen-containing groups or harder biological nucleophiles such as lysine, arginine or histidine residues (LoPachin et al., 2009, Esterbauer et al., 1991). Michael adduct formation is reversible, and the HHE Michael adducts can gain in stability by rearranging into cyclic hemiacetals by reaction between the hydroxyl and aldehyde groups (Milic et al., 2015b, Skulj et al., 2019). Alternatively, the carbonyl carbon atom of HHE could form adducts with primary amines such as lysine or arginine side chains, forming a Schiff base. Based on these two possible mechanisms of adduction for HHE, it is also able to cross-link proteins by reacting via both mechanisms on two different macromolecules (LoPachin et al., 2009, Esterbauer et al., 1991). On the other hand, PONPC is only able to adduct proteins via Schiff base formation on primary amines (Ravandi et al., 1997, Milic et al., 2015a, Afonso et al., 2018) as it contains an aldehyde group but no unsaturation to participate in the Michael addition reaction. Figure 6.1 shows a representation of the possibilities of adduction by HHE and PONPC on nucleophilic residue side chains.

As discussed in section 1.2.2, both antibody-based methods and MS are targeted approaches for detecting and quantifying protein adducts formed by specific oxidized lipids. MS technology has the potential to identify and quantify these compounds, offering precise, sensitive, and high-throughput analysis. A key advantage of MS over antibody-based and other non-MS methods is its ability to pinpoint the exact site of adduction and elucidate the mechanism by which oxidized lipids form adducts with proteins (Aldini et al., 2015b, Maier et al., 2010, Shibata et al., 2017, Milic et al., 2015a, Vasil'ev et al., 2014). As defining the specific residues in PTEN sequence that could undergo adduction by HHE and PONPC was the ultimate aim, antibody-based methods will not be discussed in this chapter; further information on antibody-based methods and other non-MS methods can be found in a review by Aldini et *al.* (Aldini et al., 2015b).

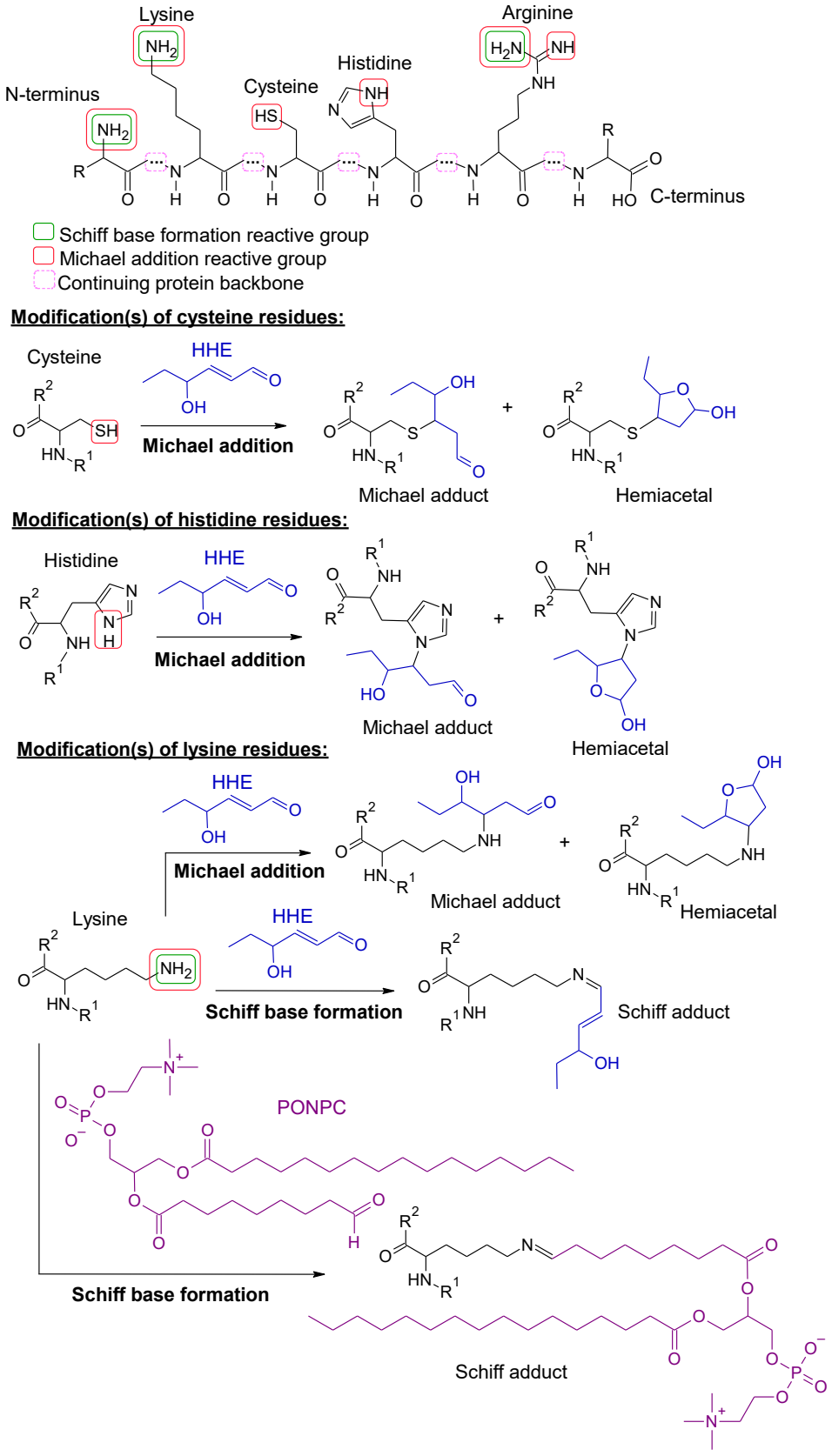

Figure 6.1. Representation of Michael and Schiff adduction of HHE and PONPC on nucleophilic residues.

Based on Viedma-Poyatos *et al*., 2021 and Škulj and Vazdar, 2019. Adduction of arginine's -NH_2 and -NH groups follow the same mechanisms than of lysine and histidine residues, respectively.

Top-down, middle-down, and bottom-up proteomics are three mass spectrometry-based approaches used for protein analysis, each providing unique insights into protein structure, modifications, and function. Top-down proteomics involves the direct analysis of intact proteins, allowing comprehensive characterization of proteoforms, including PTMs, sequence variants, and truncations. This approach uses techniques such as electron capture dissociation (ECD) and electron transfer dissociation (ETD) to fragment whole proteins, thereby retaining complete structural information (Toby et al., 2016). Top-down proteomics is highly valuable for studying complex protein isoforms and is increasingly applied in clinical settings due to its ability to reveal the full complexity of proteoforms (Garcia, 2010). However, it requires high-resolution mass spectrometry and is more challenging for large proteins due to the difficulty in ionizing and fragmenting whole proteins (Zhang and Ge, 2011). Middle-down proteomics serves as a compromise between top-down and bottom-up approaches by analysing large peptides (typically 3-15 kDa) produced from proteins through limited proteolysis. This method preserves more structural context than bottom-up while being easier to handle than intact proteins, making it suitable for mapping PTMs and analyzing protein-protein interactions (Cristobal et al., 2017). Middle-down proteomics is particularly effective for studying complex protein systems, such as monoclonal antibodies, where it allows the identification and characterization of PTMs in specific regions (Fornelli et al., 2014). In contrast, bottom-up proteomics is the most widely used approach for protein analysis, involving the digestion of proteins into smaller peptides (usually <3 kDa) before mass spectrometric analysis (Sidoli et al., 2015). Digestion can be achieved by using specific proteases such as trypsin, chymotrypsin, Lys-C or Glu-C (Miller et al., 2021). This method is highly efficient for large-scale proteomics, enabling the identification and quantification of numerous proteins in complex samples. Bottom-up proteomics, although suitable to find the exact site of modification on proteins for PTMs, often loses information about the intact protein sequence (Sidoli et al., 2015). It relies on liquid chromatography coupled with mass spectrometry (LC-MS) for peptide separation and identification, making it suitable for high-throughput protein identification and quantification (Wu et al., 2012).

In the context of protein lipoxidation, the bottom-up approach is generally used and has proved to be a powerful tool to identify sites of adduction (Afonso et al., 2018). Karpievitch *et al.* reviewed liquid chromatography mass spectrometry-based proteomics methods (Karpievitch et al., 2010). Briefly, in LC-MS/MS analysis following protein digestion, the resulting peptides are initially separated by liquid chromatography, typically utilizing a high-performance liquid chromatography (HPLC) system. The peptides are introduced into an HPLC column that contains a non-polar (hydrophobic) stationary phase. The interaction

between peptides and this stationary phase is proportional to the hydrophobic regions of the peptides. As a polar mobile phase flows through the column, it facilitates the separation of peptides by allowing hydrophilic peptides to elute more rapidly than hydrophobic ones. A gradient is applied to progressively decrease the polarity of the mobile phase, thereby eluting peptides with increasing hydrophobic content. The retention time of each eluted peptide is recorded by the detector, generating a chromatogram that provides information on the elution times of peptide precursors. In LC-MS, subsequent to chromatographic separation, the peptide precursors are ionized, commonly through electrospray ionization (ESI). In ESI, the sample is introduced into a fine needle under high voltage, causing electrostatic repulsion that disperses the solvent into a fine spray of highly charged droplets. As these droplets evaporate, they leave behind highly charged ions that are directed into the mass spectrometer. ESI is particularly suited for LC-MS applications as it naturally accommodates peptides in a liquid state. Once the precursor peptides enter the mass spectrometer, tandem mass spectrometry (MS/MS) is employed to perform data-dependent analysis (DDA). The mass spectrometer measures the mass-to-charge ratio (m/z) of the ionized molecules. Typically, several of the most intense (high-abundance) peaks from an initial MS (MS1) scan are selected, and the corresponding ions (precursor ions) are subjected to further fragmentation, providing detailed fragmentation data for each highly intense peptide detected. However, this approach may overlook low-intensity ions, which are less likely to be selected for MS/MS analysis. To mitigate this limitation, data-independent analysis (DIA) can be employed, which does not preferentially select the most intense peaks, providing more comprehensive peptide detection. Protein identification is based on the identification of specific fragmentation patterns which allow sequencing of the peptides and, by comparing to sequences in a protein database, the sequenced peptides can be assigned to a specific protein with good accuracy.

For the detection of modification of proteins by oxidized lipids, the assignment of the peptides to specific proteins has also to allow for a mass shift corresponding to the mass of the modification. In the case of Michael adducts and Schiff base formation, it is important to note that stabilization of adducts is beneficial prior to analysis by LC-MS/MS (Afonso et al., 2018). Michael and Schiff adducts are often unstable as they are reversible reactions, leading to the loss of the modified product during sample preparation or analysis. Both of these adducts can be stabilized by reduction, which is often achieved using sodium borohydride ($NaBH_4$) or sodium cyanoborohydride ($NaBH_3CN$). These reducing agents allow reduction of the carbonyl group to an hydroxyl group for Michael adducts or the reduction of the imine group of Schiff bases to a secondary amine (Fritz et al., 2012, Billman and Diesing, 1957) without reducing other functional groups. An important downfall of the bottom-up

strategy is the necessity for the proteins to be digested by a protease leading to the formation of peptides that can be successfully detected by the chosen LC-MS/MS method. Typically, trypsin is used for protein digestion due to its robustness, reproducibility and the beneficial properties of the resultant peptides. Trypsin cleaves at the carboxyl side of lysine or arginine, unless followed by a proline as per Keil rule (Keil, 1992), producing peptides that ionize efficiently. However, using a protease other than trypsin can sometimes enhance the identification of key peptides and employing multiple proteases in parallel can lead to better outcomes, increasing the number of proteins and PTMs identified by providing broader proteome coverage (Miller et al., 2021, Keil, 1992). For instance, it has been shown that trypsin, which typically cleaves after lysine and arginine residues, usually fails to cleave after these residues when they are chemically modified. Modifications such as ubiquitination significantly reduce or block trypsin cleavage at lysine residues, leading to incomplete digestion and the presence of uncleaved peptides in the analysis (Sun et al., 2023). Additionally, studies have shown that trypsin has difficulty cleaving at modified arginine residues, such as when modified with cyclohexanedione, which further demonstrates that chemical modifications can prevent trypsin from recognizing and cleaving these residues (Samy et al., 1980).

Thus far, three studies aimed to identify adducts by oxidized lipids on PTEN using a bottom-up approach (Shearn et al., 2013, Smith, 2022, Suh et al., 2018). Shearn *et al.* used trypsin as a digestion enzyme to form peptides to be analysed by LC-MS/MS in positive ion mode. In-gel digestion (digestion of proteins in SDS-PAGE gel) was performed on a commercial recombinant human PTEN treated with HNE for 30 min at increasing molar ratios (Shearn et al., 2013). The LC-MS/MS analysis of the resulting tryptic peptides allowed detection of nine sites of adduction of HNE on PTEN sequence, including cysteine and lysine residues only (Shearn et al., 2013). On the other hand, Smith investigated the modification of PTEN by acrolein, another small reactive aldehyde, in the same laboratory as the current study. PTEN-V5-His was purified and treated with increasing molar ratios of acrolein and the reaction was stopped by reduction using $NaBH_4$ at different time points (10 min, 1 hour or 4 hours). Digestion of PTEN was either performed using in-gel digestion or in-solution digestion and multiple proteases were tried. The combination of these different approaches allowed detection of a total of twelve sites of adduction of acrolein on PTEN, including eight of the nine sites of modification identified by Shearn *et al.* (Smith, 2022). Suh *et al*. treated a recombinant PTEN with 15d-PGJ_2 (30 µM, unknown molar ratio) for 1 hour or MCF-7 cells, transiently transfected with PTEN for overexpression, with 10 µM 15d-PGJ_2 for 6 hours and performed in-gel digestion of treated PTEN using trypsin. LC-MS/MS analysis allowed

identification of Cys136 as an important site of adduction of 15d-PGJ_2 in PTEN treated *in vitro* and *in cellulo*. Table 6.1. summarizes the findings of these three studies.

Table 6.1. Summary of findings on PTEN adduction by oxidized lipids (Smith, 2022, Shearn et al., 2013, Suh et al., 2018).

Study design	**Reference**	(Shearn et al., 2013)	(Smith, 2022)			(Suh et al., 2018)
	Treatment	HNE	Acrolein			15d-PGJ_2
	Conditions	1:1-10:1 molar ratio (HNE:PTEN), 30 min at 37˚C	0.2:1-20:1 molar ratio (acrolein:PTEN), 10 min, 1 h, 4 h at 37˚C			30 µM, 1 h at RT (rPTEN) 10 µM, 6 h at 37˚C (MCF-7 cells)
	Protease	Trypsin	Trypsin	Chymotrypsin	Trypsin/Glu-C	Trypsin
Modified residues	K6		✓			
	C71	✓	✓	✓	✓	
	C83			✓		
	C136	✓	✓			✓
	K147	✓	✓	✓		
	K223	✓	✓			
	C250	✓	✓		✓	
	K254	✓				
	C296				✓	
	C304				✓	
	K313	✓	✓			
	K327	✓		✓		
	K344	✓		✓		

The evidence provided by Shearn *et al.,* Suh *et al.* and Smith on the possibility of adduction of oxidized lipids on PTEN led to the hypothesis that covalent modification of PTEN by HHE and PONPC could cause the biological effects observed in HCT116 and MCF-7 cells in previous chapters. To confirm the latter, the aim of this chapter was to identify protein modification by HHE and PONPC and potentially identify critical residues that can be modified leading to alteration of PTEN structure, function and/or localization. This was firstly investigated on the purified functional PTEN-V5-His. Although derivatization of retained carbonyl groups on protein adducts formed by reactive electrophilic lipids or use of tagged derivatives of electrophilic lipids have widely been used to identify targets of protein lipoxidation, identification of the nature of adducts and sites of adduction requires high resolution MS approaches (Aldini et al., 2015b). Bottom-up approaches followed by MS/MS analysis are the favoured methods to specifically detect protein adducts (Vasil'ev et al., 2014, Aldini et al., 2015b). Therefore, a bottom-up approach, digesting PTEN-V5-His with

trypsin, was used in conjunction with LC-MS/MS analysis of the resulting peptides to allow identification of both the nature of the adduct formed and the precise site of adduction, i.e. the residue with which HHE or PONPC can react. Additionally, the structural integrity of PTEN-V5-His after HHE or PONPC treatment was investigated by SDS-PAGE and western blotting to determine if cross-linking or aggregation could occur and, if so, if it could be related to the observed inhibition of PTEN-V5-His function *in vitro* detailed in Chapter 4. However, using *in vitro* treatments of proteins does not necessarily reflect the actual reaction in cells, as regulatory mechanisms exist *in vivo* to control lipid and oxidized lipid fate (Liu and Czaja, 2012, Ding et al., 2021, Karasawa, 2006, Chakraborti, 2003). Therefore, efforts were made to detect protein adducts with HHE and PONPC on endogenous PTEN from MCF-7 cells, using LC-MS/MS to analyse treated-cell lysates in order to show that PTEN could in fact be modified by such entities *in cellulo*.

6.2. Materials and Methods

6.2.1. Materials

The rabbit anti-PTEN (PTEN rabbit Ab, #9552) primary antibody was purchased from Cell Signaling Technology (The Netherlands). The goat anti-rabbit secondary antibody (Anti-Rabbit IgG (whole molecule)–Peroxidase antibody, #A6154) was purchased from Merck (UK). HHE was purchased from Cayman Chemical (USA) as a solution in ethanol and PONPC was purchased from Avanti® Polar Lipids (USA). Trypsin Gold and Trypsin/Lys-C were mass spectrometry grade protein digestion enzymes purchased from Promega (UK). Trypsin Gold was reconstituted as per manufacturer's instructions. Trypsin/Lys-C mix was reconstituted in 50 mM triethylammonium bicarbonate (TEAB) to a final concentration of 1 µg/µL. S-Trap™ spin columns were purchased from ProtiFi (USA).

6.2.2. Expression and Purification of PTEN-V5-His

Expression and purification of PTEN-V5-His was performed as described in General Materials and Methods, section 2.5 and 2.6, using binding buffer and wash buffer containing 5 mM imidazole and elution buffer containing 250 mM imidazole. The purified protein was quantified as described in General Materials and Methods, section 2.9.1.

6.2.3. Treatment of PTEN-V5-His with HHE and PONPC

Concentrated PTEN-V5-His at a final concentration of 1 mg/mL (19.2 µM) was treated with HHE or PONPC at treatment:PTEN-V5-His (52 kDa) molar ratios of 0:1, 0.1:1, 0.5:1, 1:1, 5:1, 10:1 and 20:1 (0, 1.92, 9.6, 19.2, 96, 192 and 384 µM, respectively) for 30 min or 2 hours at 37˚C. To prepare the samples, a 10X stock for each concentration of treatment was prepared in PTEN treatment buffer (25 mM sodium phosphate pH 7.4, 150 mM NaCl) and added to 100 µg of concentrated PTEN-V5-His in a final volume of 100 µL. The samples were incubated on a heating block at 37˚C for 30 minutes or 2 hours. Shortly before the end of the incubation, a 50 mM sodium borohydride ($NaBH_4$) solution was prepared in PTEN treatment buffer, which was added to samples to a final concentration of 5 mM and incubated at RT for 30 min for complete reduction of the protein and free aldehydes.

6.2.4. Seeding and Treatment of MCF-7 cells with HHE and PONPC

Sterile 6-well plates were seeded with $1x10^6$ MCF-7 cells per well and incubated overnight at 37˚C, 5% CO_2. Cells were treated, accordingly to General Materials and Methods, section 2.8, with 5 or 50 µM HHE or PONPC or untreated by adding a solution of ethanol in PBS or complete DMEM (Vehicle) at a final concentration $\leq 0.2\%$ in a final volume of 1.5 mL/well and incubated for 4 hours at 37˚C, 5% CO_2. Cells were washed twice with ice-cold PBS on

ice and harvested by scraping in ice-cold PBS on ice followed by centrifugation at 1000 x g for 5 min at 4˚C to collect cell pellets. Cell pellets were stored at -80˚C until ready to be processed as described in section 6.2.5.

6.2.5. S-Trap™ Sample Processing

Cell pellets were thawed on ice and lysed in 50 µL lysis buffer composed of 5% sodium dodecyl sulfate (SDS) in 50 mM TEAB, pH 8.5, by thoroughly vortexing. DNA was sheered by sonication for 15 min in a bath sonicator, addition of benzonase endonuclease (Merck, UK) and further sonication until the cell lysates were clear. Cell lysates were centrifuged at 13,000 x g for 8 min at RT. The supernatants were harvested and dried in a Vacufuge Plus Concentrator (Eppendorf, UK) for 2 hours at 45˚C. The dried extracts were resuspended in lysis buffer. Tris(2-carboxyethyl)phosphine was added to a final concentration of 5 mM and samples were incubated at 55˚C for 15 min on a heating block to fully reduce proteins, then cooled to RT. IAA was added to a final concentration of 20 mM and samples were incubated for 1 hour at RT protected from light for protein alkylation. Phosphoric acid was added to a final concentration of 2.5% (v/v) to completely denature proteins and the samples were thoroughly mixed by vortexing. Six times the volume of the samples of binding/wash buffer (100 mM TEAB in 90% methanol) was added and samples were mixed by vortexing. Twenty µL of the samples (corresponding to 40 µg of protein) were loaded onto S-Trap™ spin columns and the proteins were trapped into the column matrix by centrifugation at 4,000 x g for 30 seconds. The remainder of the samples were stored at -20˚C for in-gel digestion analysis. Columns were washed with 150 µL of binding/wash buffer and centrifugation at 4,000 x g for 30 seconds 3 times with rotation of the columns by 180˚ between each wash. After the last wash, an additional centrifugation step at 4,000 x g for 1 min was added to ensure the absence of binding/wash buffer in the columns. Columns were placed in clean 2 mL low protein bind tubes (Eppendorf, UK). For protein digestion, 4 µg of Trypsin/Lys-C mix (1 µg of protease for 10 µg of protein) were added onto the surface of the column matrix and the columns were incubated at 37˚C on a heating block for 18 hours. To elute the peptides, 40 µL of 50 mM TEAB, 0.2% (v/v) formic acid and 50% (v/v) ACN were consecutively applied to the columns with centrifugation at 4,000 x g for 1 min after addition of each solution. The peptides were dried using a Vacufuge Plus Concentrator (Eppendorf, UK) at RT for 3 hours and stored at -20˚C until ready to be analysed by tandem mass spectrometry as described in section 6.2.8.

6.2.6. SDS-PAGE

SDS-PAGE was performed with 8% or 10% acrylamide gels as described in General Materials and Methods, section 2.10. For the PTEN-V5-His samples, 5 or 2 µg of protein per

well were resolved. For protein extracts from S-Trap™ sample preparation (precipitated in methanol), proteins were resolubilized with a 1:1 (v:v) ratio of 10% SDS and ~100 µg protein per well (estimated based on cell count at harvest) were resolved.

6.2.7. Western Blotting of PTEN

Proteins separated by SDS-PAGE were transferred onto methanol-activated PVDF membranes at 100 V for 1 hour at RT in transfer buffer (25 mM Tris, 190 mM glycine and 20% methanol) cooled with ice using the Mini Trans-Blot® Cell system (Bio-Rad, UK). The membranes were subsequently reactivated with methanol for 1 min, stained with a Ponceau S staining solution (0.2% (w/v) Ponceau S/5% (v/v) glacial acetic acid) to check for transfer efficiency and destained in water for 5 min and 3 times 5 min in TBST-T. The PVDF membranes were blocked in blocking solution (5% milk powder in TBS-T) for 1 hour and rinsed with TBS-T. Membranes were incubated with the rabbit anti-PTEN primary antibody in 5% BSA in TBS-T at a dilution of 1:1000 for 1 hour and washed 3 times for 5 min with TBS-T. Subsequently, membranes were incubated with HRP-conjugated anti-rabbit secondary antibody in blocking solution at a dilution of 1:10,000 for 1 hour, washed 3 times 10 min with TBS-T and rinsed in TBS. Washing and probing steps were performed at RT on a rocking shaker at 30 and 15 rpm, respectively. Membranes were incubated in Clarity Western ECL Substrate (Bio-Rad, UK) as per manufacturer's instructions, placed between two acetate sheets and imaged using a G:Box XR5 with GeneSys software (Syngene, UK). Densitometry analysis was performed using the software ImageJ. Data was analysed using the Excel software (Microsoft, USA) and GraphPad Prism 8.1.0. (GraphPad, USA).

6.2.8. Mass Spectrometry Analysis

6.2.8.1. In-gel Digestion and HPLC-MS/MS

In-gel digestion of target SDS-PAGE gel bands (PTEN-V5-His, protein aggregates or endogenous PTEN from MCF-7 cell lysates) was performed as described in Materials and Methods, section 2.11.1. HPLC-MS/MS was performed as described in General Materials and Methods, section 2.11.2.

6.2.8.2. Mascot Search Parameters for Protein Identification and Modification Mapping

Protein identification and modification mapping was performed using Mascot (Matrix Science, USA), using the settings in Table 6.2, after MS/MS data files were converted to mzML files using ProteoWizard. Data was filtered to provide protein matches with > 2 significant unique peptide sequences using a significance threshold of $P < 0.05$.

Table 6.2. Parameters chosen for Mascot Searches.

Setting	Parameter Used
Taxonomy	Homo Sapiens or All Entries
Database	SwissProt
Fixed Modifications	None
Variable Modifications	Oxidation (M) Carbamidomethyl (C) Modifications described in Table 6.3.
Enzyme	Trypsin
Maximum Missed Cleavages	2
Peptide Charge	2+, 3+ and 4+
Peptide Tolerance	0.5 Da
MS/MS Ions Search	Yes
Data Format	MzML
MS/MS Tolerance	0.5 Da
Instrument	ESI-QUAD-TOF

"*Homo Sapiens*" taxonomy was used to analyse both monomeric and aggregated PTEN-V5-His while "All Entries" was used to analyse aggregates separately to identify possible host co-eluted proteins involved in formation of protein aggregates. Protein matches from taxonomy other than *E. coli* apart from PTEN were excluded from the analysis as considered to be contaminants from sample preparation.

Data from HHE- and PONPC-treated PTEN-V5-His were analysed separately with variable modifications set as described in Table 6.3. Modification hits (Michael adducts or Schiff base with HHE and Schiff base with PONPC) that were identified by the Mascot search were manually validated based on b and y ions coverage and on the identification of y^0 ions where applicable.

Table 6.3. Parameters of variable modifications for detection of HHE- and PONPC-modified PTEN-V5-His.

Samples	HHE-treated		PONPC-treated
Modification	HHE Michael (reduced)	HHE Schiff (reduced)	PONPC (reduced)
Residue(s)	C, H, K, R	K, R	K
Composition	C(6) H(12) O(2)	C(6) H(8) O	C(33) H(64) N O(8) P
Monoisotopic Delta (Da)	+116.083730	+96.057515	+633.436955
Average Delta (Da)	116.1583	96.1271	633.8369

6.2.9. *De Novo* Sequencing

De novo sequencing was performed using the PeakView software (SCIEX, U.S.A) after extraction of MS/MS spectra of 184.0733 ± 0.1 Da ions. The MS/MS spectrum extracted from each of the peaks on the extracted ion chromatogram (XIC) for 184.0733 ± 0.1 Da ions were investigated based on the existence of mass difference between peaks corresponding

to the monoisotopic mass of residues as provided in Supplementary Table 1. The identified peptide sequences (≥ 4 residues) were compared to PTEN sequence to determine possible matches. In the event of a match, the full sequence of the peptide was determined based on the mass of the first identified fragment and the mass and theoretical charge of the precursor ion.

6.2.10. Protein Visualization

For the structural analysis of PTEN, the 3D coordinates were obtained from the Protein Data Bank (PDB) under the accession code 7JUL. Visualization and analysis were performed using Discovery Studio (Biovia, Dassault Systèmes, France). The PDB file was imported into the software, and the structure was visualized, highlighting specific regions of interest using the software's built-in tools. Solvent accessibility surface (SAS) was calculated using built-in tools with 240 grid points per atom and a probe radius of 1.4 Å. Residues with a SAS >25% or <10% were considered exposed or buried, respectively. Images of the structure were captured for documentation and presentation purposes.

6.2.11. Statistical Analysis

Statistical analysis was performed on GraphPad Prism 8.1.0. (GraphPad, USA). Data from three biological replicates was analysed using two-way ANOVA analysis, correcting for multiple comparisons to the untreated control using the Tukey post-test. Statistical significance was defined as $P < 0.05$. The P values were annotated as follows: $P > 0.05$ (ns), $P \leq 0.05$ (*), $P \leq 0.01$ (**), $P \leq 0.001$ (***), $P \leq 0.0001$ (****). Data is shown as mean values ± SEM unless stated otherwise.

6.3. Results

6.3.1. HHE and PONPC Led to PTEN-V5-His Aggregation *In Vitro,* Correlating with Inhibition of PTEN-V5-His Phosphatase Activity

To verify whether HHE and PONPC could modify PTEN-V5-His *in vitro*, PTEN-V5-His purified from *E. coli* was treated with increasing molar ratios of HHE or PONPC for 30 min or 2 h at 37˚C and samples were analysed by SDS-PAGE analysis and western blotting to provide general insights into potential molecular modifications such as alteration of the apparent molecular weight of the protein or structural modification. Indeed, as oxidized lipids form adducts on proteins, their weight is added to the weight of the protein, leading to a shift in migration towards higher apparent molecular weights. This could be easily visualized with PONPC modifications as adduction by one molecule of PONPC would add 633 Da to the initial molecular weight of the protein; the more molecules that adduct one molecule of PTEN-V5-His, the higher the apparent molecular weight would be. Additionally, PONPC carries a constitutive positive charge, enhancing the decrease in migration in SDS-PAGE analysis. As HHE is a smaller and uncharged molecule (adding 96 Da or 116 Da, depending on the type of adduct formed), this would be more difficult to observe on an SDS-PAGE gel. SDS-PAGE could also allow the detection of potential SDS-resistant aggregates that could be formed as lipoxidation can lead to modification of the structure. These can be observed as a result of exposure of hydrophobic parts that tend to form aggregates to increase their stability in aqueous solution or formation of interprotein crosslinks (Montine et al., 2002, Spickett and Pitt, 2020).

The SDS-PAGE analysis most importantly revealed that both HHE and PONPC treatment could lead to the formation of protein aggregates as shown by bands appearing at apparent molecular weights above 180 kDa (Figure 6.2). HHE particularly led to such aggregates from HHE:PTEN-V5-His molar ratios of 5:1 and 0.5:1 after treatment for 30 min and 2 h, respectively. It is important to note that where aggregates formed in HHE-treated PTEN-V5-His samples, some of the aggregates remained at the bottom of the well, possibly because their molecular weight was too high to enter even the stacking gel (Figure 6.2.A and 6.2.B). This could explain the apparent diminished number of aggregates forming the band >180 kDa in the PTEN-V5-His sample treated with HHE at a molar ratio of 20:1 (HHE:PTEN-V5-His) (Figure 6.2.B). For PONPC, these aggregates were particularly visible for PONPC:PTEN-V5-His molar ratios 5:1 at both time points but seemed to be in higher amounts after 2 h of treatment (Figure 6.2.C and 6.2.D). This data suggested that aggregation of PTEN-V5-His resulted from treatment with HHE or PONPC that occurred in a concentration- and time-dependent manner. Surprisingly, after HHE treatments, the bands

corresponding to monomeric PTEN-V5-His seemed to migrate slightly further, suggesting a lower molecular weight, at the molar ratios where aggregation was observed and seemed to lose intensity with increasing molar ratios, which was particularly visible after 2 h of treatment (Figure 6.2.A and 6.2.B). The decreased intensity of the bands is most likely due to the contribution of PTEN in the formation of aggregates, leading to less protein in a monomeric form. The effects of PONPC on monomeric PTEN-V5-His followed an opposite trend as monomeric PTEN-V5-His formed a smear towards higher molecular weights with increasing concentrations of PONPC at the molar ratios where aggregates were observed at both time points (Figure 6.2.C and 6.2.D). This perfectly reflects the addition of several molecules of PONPC per molecule of PTEN-V5-His as described previously, strongly suggesting that PONPC can form covalent adducts with PTEN.

Interestingly, HHE, but not PONPC, seemed to affect one of the contaminants present in PTEN-V5-His samples as the bands between 25 and 35 kDa migrated towards higher molecular weights from a molar ratio of 5:1 (Figure 6.2.A and 6.2.B). Not all contaminants were visibly affected, which suggested that HHE could modify a range of proteins but could have a certain specificity. However, this was not investigated further as it was out of the scope of this study.

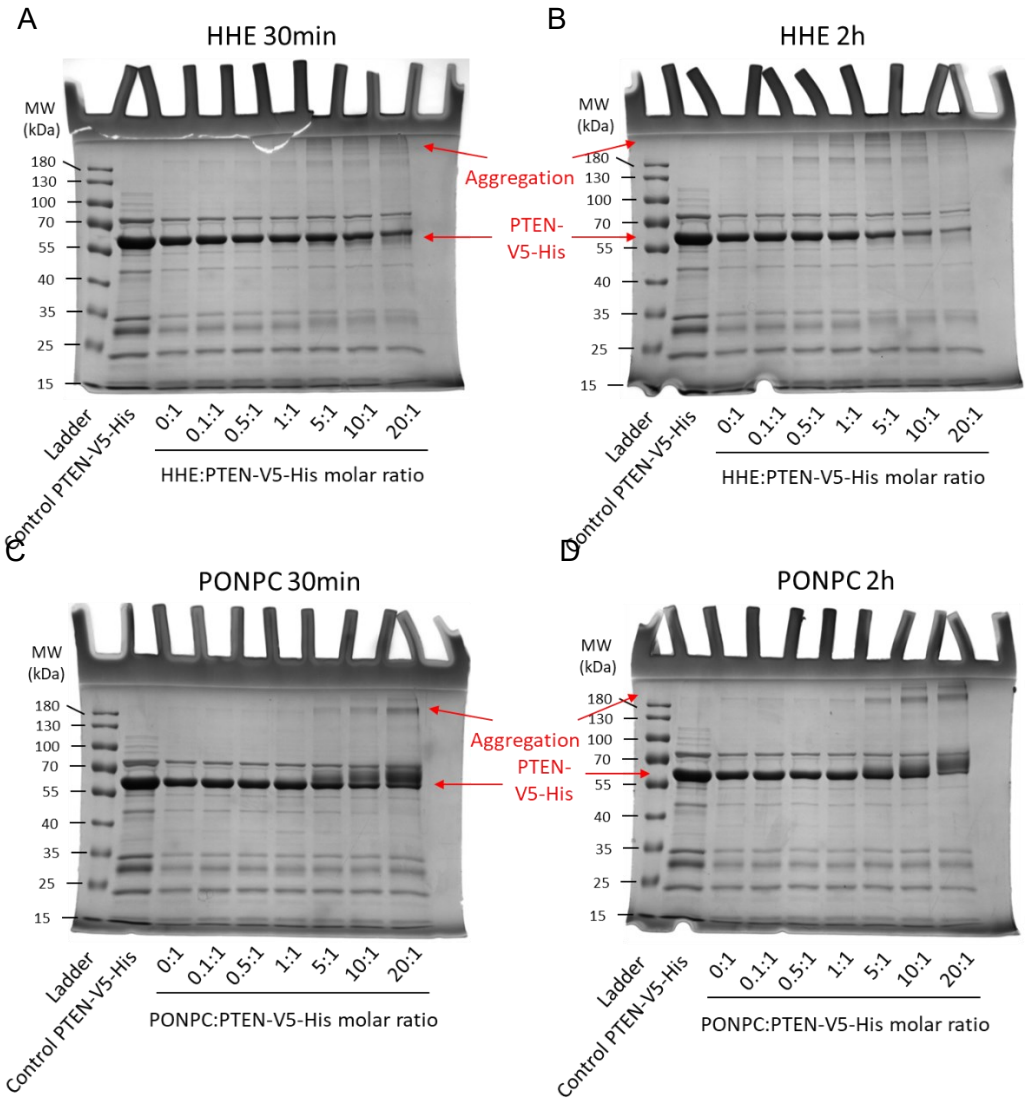

Figure 6.2. Representative reducing SDS-PAGE of untreated or treated PTEN-V5-His with HHE or PONPC for 30 minutes or 2 hours.

Purified PTEN-V5-His was untreated or treated for 30 min or 2 hours at 37˚C with HHE or PONPC at increasing molar ratios. Treatments were ended by reduction by adding $NaBH_4$ to a final concentration of 5 mM. Control PTEN-V5-His represents untreated PTEN-V5-His without reduction with $NaBH_4$. Proteins (5 µg/well) were resolved on 8% acrylamide gels by reducing SDS-PAGE, stained with PageBlue Staining solution (ThermoFisher Scientific, UK) and imaged using a G:Box XR5 and GeneSys software (Syngene, UK). Representative SDS-PAGE of PTEN-V5-His treated with HHE for 30 min (A), HHE for 2 h (B), PONPC for 30 min (C) and PONPC for 2h (D).

To confirm the presence of PTEN in protein aggregates and quantify the degree of aggregation of PTEN-V5-His in HHE- and PONPC-treated PTEN-V5-His samples, SDS-PAGE gels were subjected to western blotting against PTEN and PTEN bands were analysed by densitometry analysis.

Figure 6.3.A, 6.3.D, 6.4.A and 6.4.D all show that the degree of aggregation of PTEN-V5-His increased with the concentration of HHE or PONPC and exposure time. HHE (Figure 6.3) generally led to more aggregation of PTEN-V5-His compared to PONPC (Figure 6.4). Interestingly, increasing the time of exposure of PTEN-V5-His to HHE led to aggregation at

lower HHE:PTEN-V5-His molar ratios (from 5:1 after 30 min of treatment (Figure 6.3.A) and from 0.5:1 after 2 hours of treatment (Figure 6.3.D)), while increasing the time of exposure of PTEN-V5-His to PONPC did not lead to aggregation at lower molar ratios but only seemed to increase the amount of aggregation at the same molar ratios (Figure 6.4.A and 6.4.D).

Most importantly, the concentration- and time-dependent decrease in the percentage of monomeric PTEN-V5-His and the concentration- and time-dependent loss of PTEN-V5-His activity were found to correlate. Although the coefficients of determination (R^2) between monomeric PTEN-V5-His (% of total PTEN-V5-His) and specific activity (% of untreated control) after HHE treatments (30 min and 2 hours) were < 0.95 (Figure 6.3.C and 6.3.F), Figure 6.3.B and 6.3.E showed that the percentage of monomeric PTEN-V5-His in the HHE-treated PTEN-V5-His samples matched closely the decreasing percentage of specific activity up to high molar ratios of HHE to PTEN-V5-His. This difference at high molar ratios could be explained by the portion of aggregates that remained in the wells of the gels at these molar ratios, which could not be detected by western blotting as only the resolving gels were analysed. On the other hand, the coefficients of determination between monomeric PTEN-V5-His (% of total PTEN-V5-His) and specific activity (% of untreated control) after PONPC treatments (30 min and 2 hours) were > 0.95 (Figure 6.4.C and 6.4.F), suggesting a strong correlation between these variables. However, unlike HHE treatments, PONPC treatments did not lead to a close match of the percentage of monomeric PTEN-V5-His with the percentage of specific activity of PTEN-V5-His (Figure 6.4.B and 6.4.E), but rather a decreasing trend that correlated. This suggested that HHE could induce a loss of function by causing PTEN-V5-His aggregation, but PONPC could rather cause a partial loss of function by aggregation coupled with a direct inhibition of the phosphatase activity of PTEN-V5-His.

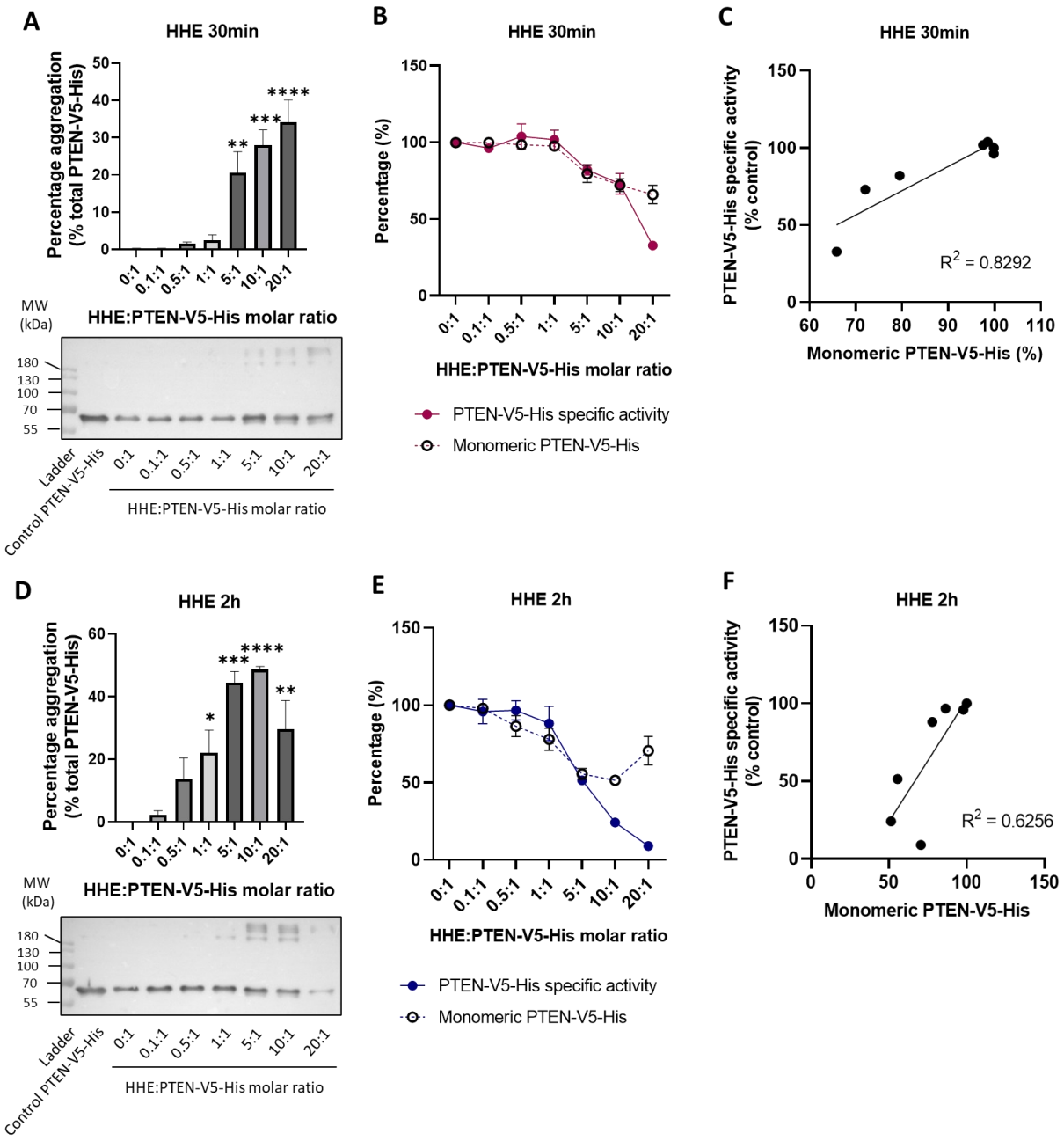

Figure 6.3. Quantification of PTEN-V5-His aggregation and correlation with inhibition of PTEN-V5-His phosphatase activity after HHE treatment.

(A) and (D) show representative western blots of PTEN in PTEN-V5-His samples treated with HHE for 30 min or 2 hours, respectively, at increasing HHE:PTEN-V5-His molar ratios and quantification by densitometry analysis of the percentage of aggregation (normalized to total PTEN-V5-His). Samples were prepared as described in Figure 6.2. and 200 ng of protein per well were resolved by SDS-PAGE on 10% acrylamide gels. Proteins were transferred onto PVDF membranes and PTEN was labelled using a rabbit anti-PTEN primary antibody and an HRP-conjugated anti-rabbit IgG secondary antibody. Membranes were imaged after incubation in Clarity ECL substrate (Bio-Rad, UK) using a G:Box XR5 with GeneSys software (Syngene, UK) and images were analysed with the ImageJ software (Fiji, USA. (B) and (E) represent the percentage of monomeric PTEN-V5-His (% total PTEN-V5-His, measured by densitometry analysis) and the percentage of specific activity (% untreated control) after 30 min or 2 h treatment, respectively, with HHE at increasing molar ratios. The specific activity of PTEN-V5-His was measured as described in Chapter 4, Section 4.2.4 and data was processed as described in Chapter 4, Figure 4.2. (C) and (F) show the correlation between PTEN-V5-His specific activity and % monomeric PTEN-V5-His with an XY plot of these variables and linear

regression built using GraphPad Prism 8.1.0 (GraphPad, USA). Data shown as mean ± SEM of 3 biological replicates (n=3). Statistical analysis was performed using one-way ANOVA with Turkey's post-test for multiple comparisons to the untreated control (0:1); P > 0.05 (unlabelled), P ≤ 0.05 (*), P ≤ 0.01 (**), P ≤ 0.001 (***), P ≤ 0.0001 (****).

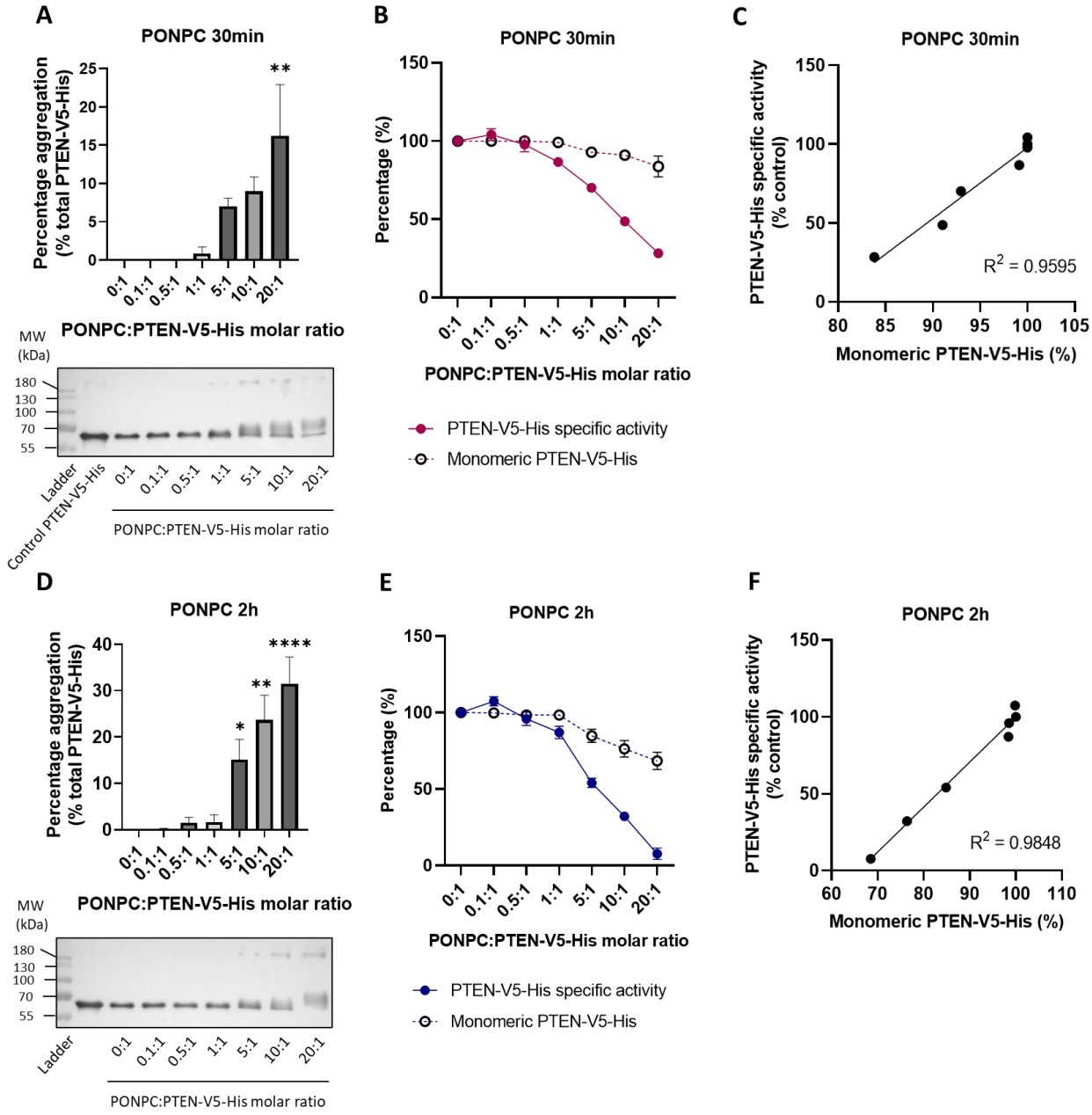

Figure 6.4. Quantification of PTEN-V5-His aggregation and correlation with inhibition of PTEN-V5-His phosphatase activity after PONPC treatment.
Data was collected and processed as described in Figure 6.3 for treatments of PTEN-V5-His with PONPC for 30 min (A, B, C) and 2 h (D, E, F) at increasing PONPC:PTEN-V5-His molar ratios.

6.3.2. Composition of HHE- and PONPC-induced Protein Aggregates

To gain more insight into the composition of the protein aggregates, the SDS-PAGE gel bands corresponding to protein aggregates (of an apparent molecular weight > 180 kDa) were excised and subjected to in-gel digestion with trypsin to identify proteins by LC-MS/MS.

The increase in percentage of aggregation with the increase in concentration of treatment and/or exposure time was accompanied with an increase in the number of host proteins detected in the protein aggregates for both HHE- and PONPC-treated samples (Table 6.4). Generally, HHE-induced protein aggregates were composed of a higher number of distinct proteins with a 3- to 4-fold increase in the number of protein hits at corresponding molar ratios compared to PONPC-induced protein aggregates (Table 6.4). However, this could be the result of a better peptide recovery for HHE-treated samples compared to PONPC-treated samples as suggested by the number of peptides matching with PTEN sequence that were generally higher in HHE-induced aggregates, particularly for one the biological replicates, compared to PONPC-induced aggregates (Supplementary Table 2).

Table 6.4. Number of proteins identified in HHE- and PONPC-induced protein aggregates.

Treatment	Exposure time (min)	Molar ratio (treatment:PTEN-V5-His)				
		0.5:1	1:1	5:1	10:1	20:1
HHE	30	N/A	N/A	8±4	10±3	12±2
	120	4±1	5±1	11±7	9/19	7/24
PONPC	30	N/A	N/A	3±1	3±1	3±1
	120	N/A	N/A	4±0	5±1	4±2

Data shown as mean±SD based of 3 biological replicates (n=3) with the exception of HHE treatments for 2 h at 10:1 and 20:1 molar ratios (HHE:PTEN-V5-His), representative of 2 biological replicates (n=2).
N/A: not applicable; no band corresponding to protein aggregates was observed in the SDS-PAGE gels.

PTEN was the identified protein with the most peptide matches and highest emPAI (Table 6.5) for all samples except for protein aggregates in one replicate of PTEN-V5-His samples treated with HHE for 2 hours at a 0.5:1 molar ratio or PONPC for 30 min at a 5:1 molar ratio, suggesting that protein aggregates were mainly formed by aggregation of PTEN-V5-His. Although this could be due to a particular tendency of PTEN to form aggregates in response to exposure to oxidized lipids compared to the other components of the samples, it is most likely to be correlated to the relative abundance of the different proteins in the samples, PTEN-V5-His representing ~60% of total proteins.

A total of 28 host proteins were identified in HHE-induced and PONPC-induced aggregates, the most frequent ones that appeared in >90% of samples were Bifunctional polymyxin resistance protein ArnA, Large ribosomal subunit protein uL2 and Chaperonin GroEL (Table 6.5). Amongst those 28 proteins, 9 were common to the identified contaminants in concentrated PTEN-V5-His samples (Chapter 3, section 3.3.4), representing 41% of the initially identified host proteins that were co-eluted with PTEN-V5-His. Unexpectedly, 19 additional host proteins that were not identified in the initial screening of contaminants were identified in HHE- and PONPC-induced protein aggregates. However, the emPAI of these host proteins was generally lower than the host proteins identified in the initial contaminants screening (data not shown), suggesting that they were in relatively low abundance. This

could explain the lack of detection of these proteins in the initial contaminant screening as many showed molecular weights where no bands were apparent on the SDS-PAGE gels used for in-gel digestion and LC-MS/MS identification of the proteins in the samples. As discussed in Chapter 3, an in-solution digestion would have been more suitable to detect all contaminants in the samples by LC-MS/MS, which could have led to the identification of these additional proteins in protein aggregates. However, some of the additional host proteins were only detected in one biological replicate, such as FKBP-type peptidyl-prolyl cis-trans isomerase SlyD, Tyrosine recombinase XerD, Glycerol-3-phosphate regulon repressor, Protein RecA, Blue light- and temperature-regulated antirepressor BluF, Aminoalkylphosphonate N-acetyltransferase and 2-oxoglutarate dehydrogenase E1 component, which were only detected in the replicate showing the most peptide counts, therefore the best peptide recovery. However, DNA-directed RNA polymerase subunit beta was only detected in a replicate that showed relatively poor peptide counts, suggesting that the co-eluted host proteins could also vary from one purification batch (replicate) to another. It is important to note that this identification was based on protein matches for which a minimum of 3 significant unique sequences were found to avoid false positive results; the proteins that were identified with a low number of peptide matches in some samples and not detected in other samples may have been detected using a lower threshold of significant unique sequences. This is also applicable to the detection of host proteins in the initial screening of contaminants (Chapter 3, section 3.3.4) as the protein identification was based on the same parameters; a lower threshold of significant unique sequences could have provided protein matches corresponding to the additional host proteins observed in the HHE- and PONPC-induced protein aggregates.

Table 6.5. LC-MS/MS identification of proteins forming aggregates in HHE- or PONPC-treated PTEN-V5-His samples.

Identified protein	Accession	MW (Da)	Identified in:		Score		Sequence coverage (%)		Num. of peptide matches (Num. of significant unique sequences)		emPAI	
			HHE-treated	PONPC-treated	HHE-treated	PONPC-treated	HHE-treated	PONPC-treated	HHE-treated	PONPC-treated	HHE-treated	PONPC-treated
PTEN	***PTEN_HUMAN***	***47136***	***Yes £***	***Yes £***	***3137***	***1516***	***66***	***48***	***129 (21)***	***44 (15)***	***27.27***	***3.25***
Succinylornithine transaminase	***ASTC_ECOBW***	***43980***	***Yes***	***Yes***	***1268***	***337***	***54***	***27***	***36 (13)***	***9 (8)***	***7.56***	***1.19***
Bifunctional polymyxin resistance protein ArnA	***ARNA_ECOBW***	***74869***	***Yes £***	***Yes £***	***1597***	***665***	***54***	***28***	***69 (6)***	***26 (15)***	***6.50***	***1.38***
Large ribosomal subunit protein uL2	***RL2_ECO24***	***29956***	***Yes £***	***Yes***	***346***	***141***	***40***	***20***	***21 (8)***	***6 (5)***	***3.76***	***1.36***
DNA-binding transcriptional dual regulator CRP	***CRP_ECOLI***	***23796***	***Yes***	***Yes***	***234***	***142***	***33***	***20***	***9 (6)***	***4 (4)***	***3.17***	***1.05***
Ribosomal RNA small subunit methyltransferase	RSMI_ECOLI	31329	Yes	No	273	ND	52	ND	10 (10)	ND	2.88	ND
Chaperonin GroEL	***CH60_ECO24***	***57464***	***Yes £***	***Yes***	***854***	***222***	***49***	***14***	***22 (17)***	***5 (4)***	***2.55***	***0.35***
Chaperone protein DnaK	***DNAK_ECOHS***	***69088***	***Yes***	***No***	***986***	***ND***	***47***	***ND***	***28 (20)***	***ND***	***2.45***	***ND***
Small ribosomal subunit protein uS3	***RS3_ECO24***	***25967***	***Yes***	***No***	***251***	***ND***	***39***	***ND***	***11 (6)***	***ND***	***2.13***	***ND***
Glycogen synthase	GLGA_ECOBW	52789	Yes	No	483	ND	30	ND	19 (10)	ND	1.86	ND
Glutamine--fructose-6-phosphate aminotransferase	GLMS_ECOLI	67081	Yes	Yes	567	77	36	3	20 (15)	2 (2)	1.78	0.14
FKBP-type peptidyl-prolyl cis-trans isomerase SlyD	SLYD_ECOLI	20840	Yes	No	255	ND	41	ND	8 (4)	ND	1.74	ND
Ribosomal small subunit pseudouridine synthase A	***RSUA_ECOLI***	***25849***	***Yes***	***No***	***140***	***ND***	***45***	***ND***	***6 (6)***	***ND***	***1.67***	***ND***
Elongation factor Tu 1	EFTU1_ECO24	43256	Yes	No	192	ND	27	ND	8 (8)	ND	1.2	ND
Large ribosomal subunit protein uL13	RL13_ECO24	16009	Yes	No	47	ND	27	ND	3 (3)	ND	1.19	ND
Small ribosomal subunit protein uS5	RS5_ECO24	17592	Yes	No	95	ND	20	ND	3 (3)	ND	1.05	ND
Tyrosine recombinase	XERD_ECOLI	34225	Yes	No	222	ND	23	ND	8 (5)	ND	0.86	ND

XerD												
Glycerol-3-phosphate regulon repressor	GLPR_ECOLI	28030	Yes	No	144	ND	24	ND	4 (4)	ND	0.83	ND
Large ribosomal subunit protein uL15	RL15_ECO24	14957	Yes	No	N/A	ND	N/A	ND	N/A	ND	N/A	ND
Protein RecA	RECA_ECOBW	37950	Yes	No	151	ND	14	ND	4 (4)	ND	0.57	ND
Protein YdcF	YDCF_ECOLI	29687	Yes	No	81	ND	13	ND	3 (3)	ND	0.54	ND
Chaperone protein DnaJ	***DNAJ_ECOHS***	***41018***	***Yes***	***No***	***105***	***ND***	***12***	***ND***	***4 (4)***	***ND***	***0.51***	***ND***
Blue light- and temperature-regulated antirepressor BluF	BLUF_ECOLI	45266	Yes	No	61	ND	7	ND	3 (3)	ND	0.33	ND
Cell division protein FtsZ	FTSZ_ECOLI	10299	Yes	No	ND	ND	ND	ND	ND	ND	ND	ND
Bifunctional uridylyltransferase/uridylyl-removing enzyme	GLND_ECOBW	102326	Yes	No	81	ND	4	ND	4 (4)	ND	0.18	ND
2-oxoglutarate dehydrogenase E1 component	ODO1_ECO57	104996	Yes	No	114	ND	4	ND	3 (3)	ND	0.13	ND
Bifunctional aspartokinase/homoserine dehydrogenase 2	AK2H_ECOLI	88833	Yes	Yes	ND	ND	ND	ND	ND	ND	ND	ND
Aminoalkylphosphonate N-acetyltransferase	PHNO_ECOLI	16559	Yes	No	ND	ND	ND	ND	N ND	ND	ND	ND
DNA-directed RNA polymerase subunit beta	RPOB_ECOBW	150538	Yes	Yes	ND	ND	ND	ND	ND	ND	ND	ND

This table is representative of 3 biological replicates (n=3) with the exception of 2 h treatments with HHE at a 10:1 and 20:1 molar ratio (HHE:PTEN-V5-His), which are represented by 2 biological replicates (n=2). It shows data for HHE- or PONPC-induced protein aggregates for the sample with the highest number of identified proteins. Data was ordered by decreasing emPAI (most abundant to least abundant) from top to bottom based on HHE-treated samples results.
emPAI: The Exponentially Modified Protein Abundance Index (emPAI) offers approximate, label-free, relative quantitation of the proteins in a mixture based on protein coverage by the peptide matches in a database search result (Ishihama et al., 2005).
£: proteins that were identified in >90% of HHE- or PONPC-induced protein aggregates.
ND: not detected.
Protein hits in ***bold and italic*** represent proteins identified in the initial identification of contaminants in concentrated PTEN-V5-His samples (Chapter 3, section 3.3.4).

HHE adducts were confidently identified on only 5 proteins forming aggregates: PTEN, ArnA, Succinylornithine transaminase, Large ribosomal subunit protein uL2 and DNA-binding transcriptional dual regulator CRP (data not shown). The generally higher sequence coverage obtained for these proteins could explain the identification of HHE adducts, which are a rare occurrence given the relative number of residues that can be subjected to modification within one protein sequence. However, other proteins identified with high sequence coverage (for instance, GroEL and DnaK) were not found to be covalently modified by HHE, suggesting that the protein adduction of HHE could be selective. On the other hand, no modification by PONPC could be identified on any of the proteins forming aggregates, including PTEN (data not shown).

The potential adduction of PTEN by HHE or PONPC was essential in understanding the effects of these oxidized lipids on the structure, function and localization of PTEN. Indeed, if essential residues involved in the regulation of PTEN function or localization could be covalently modified, this would provide valuable insights into the mechanisms by which HHE or PONPC could influence PTEN and its downstream signalling. Therefore, this was investigated further in both monomeric PTEN-V5-His and aggregated PTEN-V5-His.

6.3.3. Identification of HHE- and PONPC-adducts on PTEN-V5-His *In Vitro*

6.3.3.1. Increasing PTEN Sequence Coverage to Maximise Adduct Detection Capabilities

In order to detect HHE or PONPC adducts and identify precisely the site of adduction on PTEN sequence, it is important to obtain good sequence coverage (% of PTEN sequence detected by the LC-MS/MS analysis). Work was therefore carried out to optimize the protein concentration loaded on the gel. Initially, 2 µg of protein per well (untreated or treated PTEN-V5-His with increasing molar ratios of HHE or PONPC) were loaded onto 10% acrylamide SDS-PAGE gels. In-gel digestion of monomeric PTEN-V5-His bands resulted in low sequence coverage (Table 6.6). Indeed, a limited number of peptides were detected as matching with PTEN sequence in the LC-MS/MS analysis, suggesting that either the amount of material was insufficient, and/or the peptide recovery was limited. Increasing the amount of protein loaded to 5 µg per well and decreasing the percentage of acrylamide from 10% to 8% (to facilitate recovery of large peptides) resulted in a 1.7- to 2-fold increased average PTEN sequence coverage (Table 6.6) with up to 84% and 71% sequence coverage in monomeric PTEN-V5-His samples and protein aggregates, respectively. The sequence coverage of aggregated proteins was found to be generally lower than for monomeric PTEN-V5-His (Table 6.6), potentially due to the limited amount of aggregated protein available in

the samples (particularly for aggregates at the lowest molar ratios, which were ≤20% of total protein (Figure 6.3 and 6.4)).

Table 6.6. Summary of the PTEN sequence coverage and number of peptide matches identified by Mascot search in HHE- and PONPC-treated PTEN-V5-His samples processed in different conditions.

Condition	Treatment	Sequence coverage (%)		Number of significant matches	
		Monomeric PTEN-V5-His	Aggregates	Monomeric PTEN-V5-His	Aggregates
2 µg; 10% acrylamide	HHE	29.7±12.4	N/A	26.9±21.2	N/A
	PONPC	37.6±5.8	N/A	41.9±12.1	N/A
5 µg; 8% acrylamide	HHE	58.3±12.2	39.5±16.5	119.6±46.6	55.3±42.1
	PONPC	64.0±8.1	38.4±10.5	137.5±53.9	31.9±13.3

Data shows mean±SD based on all samples (molar ratios) of 2 or 3 biological replicates (independent PTEN-V5-His purification batches) for samples prepared from 2 µg protein in 10% acrylamide gels (n=2) and 5 µg protein in 8% acrylamide gels (n=3), respectively.
N/A: not applicable; protein aggregate bands were not analysed.

Figure 6.5 presents a comparative analysis of the PTEN sequence coverage for both monomeric PTEN-V5-His and protein aggregates with samples prepared using either 2 µg of protein per well in 10% acrylamide SDS-PAGE gels or 5 µg of protein per well in 8% acrylamide SDS-PAGE gels. The highest observed sequence coverage across all samples was 84% (Figure 6.5). Notably, the C-terminal portion of PTEN exhibited greater sequence coverage compared to the N-terminal portion in most samples. Specific regions, namely residues 12-15 (NKRR), 56-62 (FLDSKHK), 160-163 (TRDK), 261-267 (QNKMLKK), and 328-335 (ANKDKANR), consistently showed an absence of coverage. This lack of detection can partly be explained by the high frequency of Lys and Arg residues within these regions. Since trypsin cleaves peptide bonds following Lys and Arg residues (except when succeeded by a proline, as per Keil rule (Keil, 1992)), digestion of PTEN-V5-His with this enzyme results in the formation of short peptides. Given the mass/charge (m/z) range of 350-1250 Da set for the MS/MS data acquisition, these small peptides may have fallen outside the detectable m/z range, especially if they contained additional positively charged residues, which further reduces the m/z ratio for each additional charge. Ultimately, it was impossible to identify potential modifications by HHE on the Cys, His, Lys and Arg residues in these undetected peptides. Unexpectedly, the 41 amino acid-long sequence containing the catalytic cysteine (Cys124) could be detected, although only in one PONPC-treated sample with one peptide detected. The poor detection of this peptide could also be explained by its size, which, in contrast to the above-mentioned peptides, was most likely too high. Indeed, the sequence 85-125 only contains one residue that could be recognised by trypsin as a cleavage site, Lys102, but this is followed by a proline. As mentioned previously, trypsin is unable to cleave after a Lys residue or Arg residue followed by a proline, making the resulting peptide 41 amino acid long, which was most likely difficult to recover during sample preparation and of a high m/z value. Figure 6.6 illustrates the theoretical sites of

cleavage by trypsin on PTEN sequence as well as the localisation of potential targets of HHE (C, H, K, R) and PONPC (K, R) and the sequence coverage across all samples with the exception of peptide 85-125 containing the catalytic Cys124, only identified once.

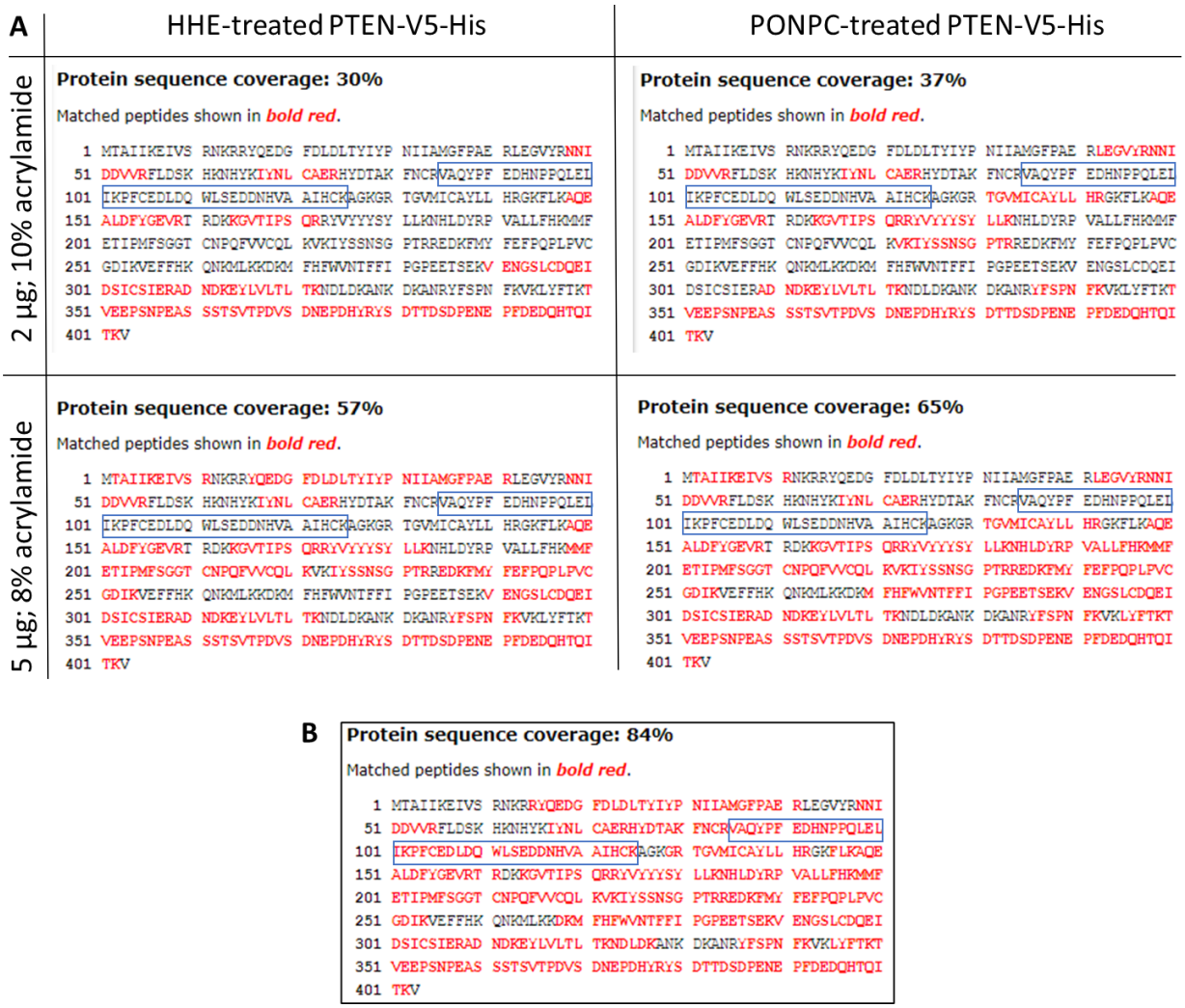

Figure 6.5. Representative PTEN sequence coverage.
(A) shows the representative average PTEN sequence coverage in HHE- or PONPC-treated PTEN-V5-His after in-gel digestion (using trypsin) of SDS-PAGE gel bands corresponding to monomeric PTEN-V5-His in 10% acrylamide gels loaded with 2 µg of protein/well or in 8% acrylamide gels loaded with 5 µg of protein/well. (B) shows the maximal PTEN sequence coverage across all samples after in-gel digestion (using trypsin) of SDS-PAGE gel bands corresponding to monomeric PTEN-V5-His or protein aggregates. The 41 amino acid-long peptide containing the catalytic cysteine (C124) is shown circled in blue.

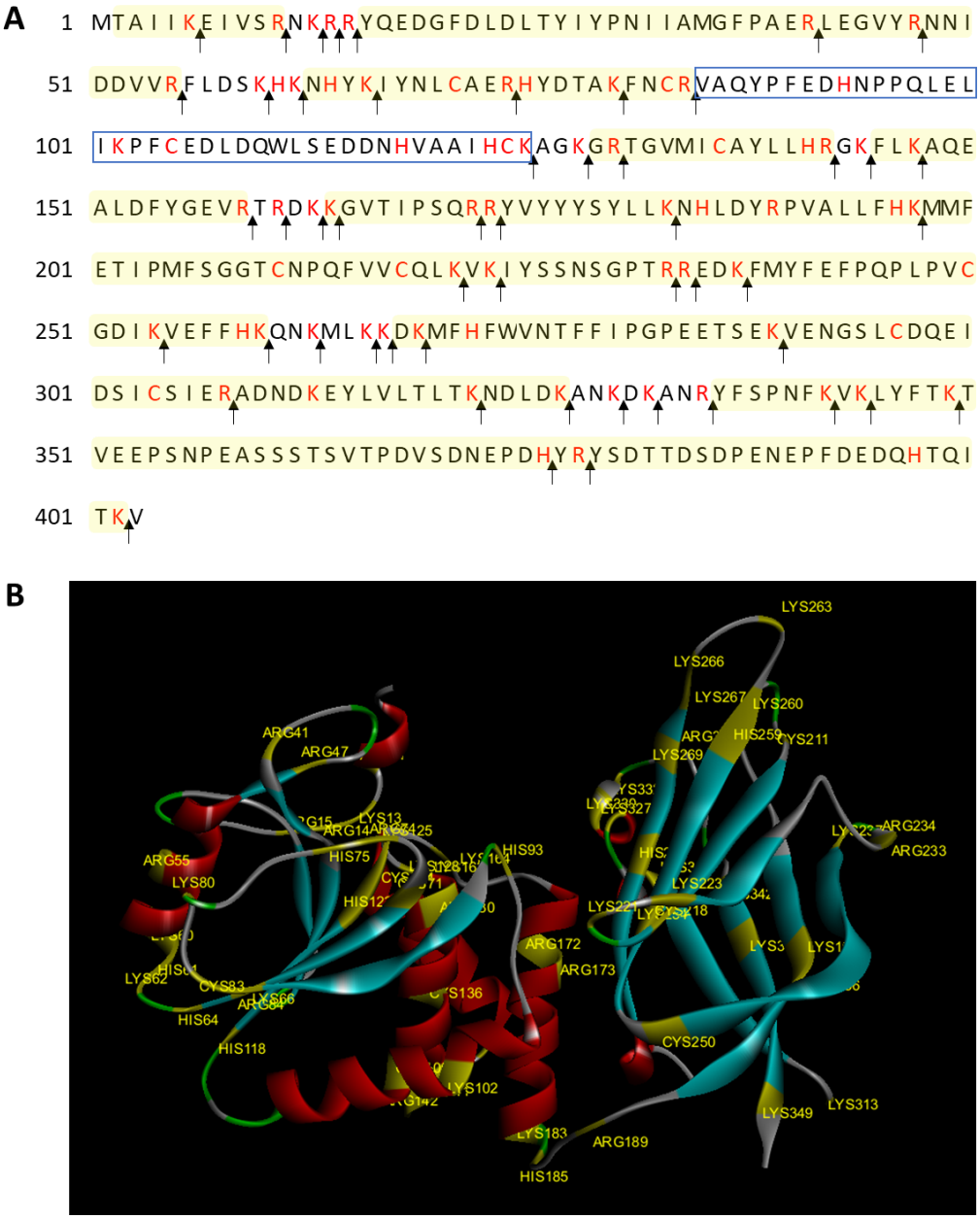

Figure 6.6. Localisation of possible HHE targets and tryptic peptides in PTEN sequence.
(A) PTEN sequence was annotated with arrows indicating theoretical cleavage sites by trypsin, potential HHE targets (C, H, K and R residues) in red, detected peptides highlighted in yellow (cumulative sequence coverage for all HHE- and PONPC-treated PTEN-V5-His samples analysed by LC-MS/MS after in-gel digestion of monomeric PTEN-V5-His and protein aggregate bands using trypsin), and the 41 amino acid-long peptide containing the catalytic C124 circled in blue. (B) highlights (yellow) the position of potential targets of HHE on PTEN structure (PDB: 7JUL, 349/403 residues (Dempsey et al., 2021)). This excluded the unresolved peptides 1-6 (MTAIIK), 282-312 (GPEETSEKVENGSLCDQEIDSI CSIERADND) and 352-403 (EEPSNPEASSSTSVTPDVSDNEPD HYRYSDTTDSDPENEPFDEDQHTQITKV).

6.3.3.2. Sites and Mechanism of Adduction by HHE on Monomeric and Aggregated PTEN-V5-His

SDS-PAGE gel bands (from 8% acrylamide gels with 5 µg protein per lane) corresponding to monomeric or aggregated PTEN-V5-His proteins in samples treated with increasing molar

ratios of HHE for either 30 or 120 minutes at 37°C were excised and subjected to LC-MS/MS analysis, as previously described. The Mascot search engine was employed to identify mass differences between the theoretical mass of the unmodified peptide and modifications introduced by HHE. Specifically, two types of modifications were considered: Michael addition (monoisotopic mass shift = +116.0837 Da) and Schiff base formation (monoisotopic mass shift = +96.057515 Da), both in reduced form, as samples were fully reduced after treatment with sodium borohydride and using DTT during LC-MS/MS preparation. Samples with PTEN sequence coverage below 15% were excluded from further analysis.

The majority of the modifications detected through Mascot were attributed to Michael addition of HHE on PTEN residues. Table 6.7 summarizes the residues that underwent Michael addition of HHE, highlighting the corresponding peptides identified by the Mascot search and the frequency of HHE adducts. After manual validation, 16 PTEN residues were confidently identified as being covalently modified by HHE. Notably, Cys, Lys and His residues were modified by HHE, while Arg residues were not. Furthermore, modified Lys residues resulted in missed trypsin cleavage sites, as trypsin was unable to cleave after a modified Lys residue. In contrast, unmodified peptides were generally cleaved after their corresponding Lys residues (data not shown), further supporting the accurate identification of modified Lys residues where missed cleavage occurred.

The propensity for HHE modification seemed to vary between different residues. Several residues (Cys71, Lys147, Cys250, Cys296, Cys304) showed consistent modification across both monomeric and aggregated PTEN-V5-His, suggesting that these residues may be particularly prone to HHE modification. Other residues, such as Lys164, Lys313, Lys349, and His397**,** were only modified at higher HHE ratios (5:1 or 10:1), indicating that these residues were less reactive or less accessible at lower concentrations of HHE. Additionally, the consistency of modification increased with higher molar ratios of HHE, as modifications were observed across all biological replicates in a concentration-dependent manner. With increasing concentrations of HHE, the frequency of modification seemed to generally increase as well. This supported the hypothesis that the extent of HHE modification is concentration-dependent.

Evidence indicated that Cys71, Cys211, Cys250, and Cys296 were the most frequently modified residues in aggregated PTEN-V5-His. Notably, residues such as Cys136, Cys211, Lys349, and His376 exhibited modifications primarily in the aggregated form rather than in the monomeric form. This observation suggested that these residues may either become more exposed or reactive during aggregation, or their modification could potentially drive the

aggregation of PTEN-V5-His. Unfortunately, it was not possible to draw definitive conclusions regarding the mechanism by which HHE might induce PTEN aggregation.

In certain cases, the limited detection of peptides constrained the analysis of HHE Michael adduct frequency and its correlation with increasing HHE concentrations. For example, the peptide 145-167 (FLKAQEALDFYGEVR), which included Lys147, was identified in only a small number of samples, and only a maximum of twice per sample. As previously discussed, modifications on lysine residues can hinder trypsin cleavage. Consistent with this, peptides spanning 148-167 were frequently detected, indicating that Lys147 served as a well-recognized cleavage site. This observation suggested that Michael adduction of HHE at Lys147 was a relatively rare event. If Lys147 were modified, the abundance of the 145-167 peptide would be expected to increase, leading to more frequent detection. Furthermore, peptide identification was lower in samples from SDS-PAGE gels bands corresponding to aggregated proteins compared to monomeric PTEN-V5-His. This discrepancy could be attributed to the generally lower sequence coverage observed in aggregated samples. It is also important to note that the abundance of PTEN-V5-His in the aggregated protein bands on SDS-PAGE gels was lower than in the monomeric PTEN-V5-His bands. This difference in protein abundance was particularly relevant because lower protein amounts were likely to result in reduced peptide recovery, as demonstrated by the sequence coverage optimization presented in the previous section.

Interestingly, HHE modifications at Lys147, Cys218, and Cys296 were detected in the untreated PTEN-V5-His control samples. Although manual validation suggested that the modifications at Lys147 and Cys218 were false positives, the modification at Cys296 appeared to be a true positive. This finding was explored in greater detail later in this chapter.

Table 6.7. Summary of the Mascot identification of sites of adduction of HHE on PTEN through Michael addition.

Modified residue	Peptide	Exposure time (min)	Monomeric PTEN-V5-His (per molar ratio HHE:PTEN-V5-His)							Aggregated PTEN-V5-His (per molar ratio HHE:PTEN-V5-His)				
			0:1	0.1:1	0.5:1	1:1	5:1	10:1	20:1	0.5:1	1:1	5:1	10:1	20:1
K6	TAII**K#**EIVSR	30	0/4	0/3	0/11	0/6	0/5	0/3	1/5	N/A	N/A	0/1	0/1	0/6
		120	0/3	0/4	0/1*	0/5	0/3	0/3		0/1*	0/2	0/3	0/3	1/2*
C71	IYNL**C#**AER	30	0/24	4/24£	4/19£	6/17£	8/23£	9/27£	8/22£	N/A	N/A	5/12£	9/17£	8/14£
		120	0/20	2/18	3/15£*	5/24£	6/20£	7/17£	6/10£	3/8£*	3/11£	8/21£	6/15£	7/12£*
C136	TGVMI**C#**AYLLHR	30	0/10	0/9	0/7	0/9	0/6	0/5	0/1	N/A	N/A			
		120	0/15	0/7	0/8*	0/9	0/10	0/2	0/1			0/1	1/2	1/1*
K147	FL**K#**AQEALDFYG EVR	30	1/1				0/1	0/1		N/A	N/A			1/1
		120		0/1	1/2*		0/1		1/1			1/1	2/2	1/1*
K164	**K#**GVTIPSQR	30	0/1	0/2	0/1	0/3	0/3	0/3	1/4	N/A	N/A	0/1	0/1	0/2
		120	0/3	0/3	0/2*	0/2	0/3	0/3	0/1		0/1	0/2	1/2	1/3*
H185	N**H#**LDYRPVALLFH K	30	0/5	0/2	0/3	0/1	0/1	0/3	1/2	N/A	N/A	0/1	0/2	
		120	0/3	0/1	0/3*	0/6	0/3				0/2		0/3	1/4*
C211	MMFETIPMFSGGT **C#**NPQFVVCQLK	30	0/33	0/43	0/19	0/22	0/23	1/11	0/5	N/A	N/A	1/2	1/1	1/1
		120	0/33	0/18	0/12*	0/25	0/8	2/7		0/1*	1/5	5/12	3/7	3/4*
C218	MMFETIPMFSGGT CNPQFVV**C#**QLK	30	1/33	0/43	0/19	2/22	4/23	4/11	2/5	N/A	N/A	0/2	0/1	0/1
		120	0/33	0/18	0/12*	2/25	2/8	3/7		0/1*	0/5	0/12	2/7	1/4*
K223	V**K#**IYSSNSGPTR	30	0/2	0/3	0/2	0/3	1/4	1/3	2/3	N/A	N/A			1/1
		120	0/3	0/3	0/2*	0/4	0/2	1/2	2/2			0/2	1/2	2/2£*
C250	EDKFMYFEFPQPL PB**C#**GDIK	30	0/34	1/49	1/23	1/29	1/28	4/18	1/12	N/A	N/A	1/5	1/3	2/4
		120	0/49	1/19	2/29*	0/33	2/28	3/15	0/4	1/3*	1/6	1/9	2/10	2/10*
C296	VENGSL**C#**DQEIDS ICSIER	30	1/9	1/14	1/7	3/9£	6/12£	9/20£	7/11£	N/A	N/A	1/1	2/2	2/2
		120	1/13	0/8	1/6*	4/14£	7/13£	3/11		0/2*	1/3	8/13	1/3	4/7*
C304	VENGSLCDQEIDSI **C#**SIER	30	0/9	0/14	1/7	1/9	5/12£	7/20	6/11	N/A	N/A	0/1	1/2	1/2
		120	0/13	0/8	0/6*	1/14	6/13	3/11		0/2*	0/3	6/13	1/3	4/7*
K313	ADND**K#**EYLVLTLT K	30	0/13	0/9	0/9	0/9	0/9	0/13	1/7	N/A	N/A	0/3	0/4	0/4
		120	0/11	0/8	0/7*	0/15	0/8	1/8	0/3	0/2*	0/4	0/6	0/8	5/10
K349	LYFT**K#**TVEEPSNP EASSSTSVTPDVS DNEPDHYR	30	0/2	0/1	0/1	0/2	0/2	0/1	0/1	N/A	N/A			
		120	0/2	0/1	0/2*	0/2	0/1							1/1*
H376 H376	TVEEPSNPEASSS TSVTPDVSDNEPD **H#**YR	30	0/82	0/82	0/47	0/29	1/37	8/32£	4/29£	N/A	N/A	0/20	0/25	1/18
		120	0/60	0/39	0/21*	0/25	5/52£	7/29£	8/24£	0/4*	0/14	1/17	8/31	3/24*

H397	YSDTTDSDPENEP	30	0/51	0/52	0/37	0/37	**1/43**	**1/22**	**4/44£**	N/A	N/A	0/6	0/15	**1/24**
	FDEDQ**H#**TQITK	120	0/36	0/32	0/26*	**1/43**	**2/48**	**3/32**	**3/18£**	0/6	0/12	0/23	**3/24**	**5/14***

Data is representative of 3 biological replicates (3 independent PTEN-V5-His production batches) except for the conditions labelled with *, for which data is representative of 2 biological replicates.
Results are shown as follows: HHE-modified peptide(s)/total peptide(s), with HHE-modified peptides defined as the total number of peptides assigned with a Michael addition of HHE in all biological replicates for the corresponding condition and total peptide(s) defined as the total number of identified peptides (unmodified and modified by HHE) in all biological replicates for the corresponding condition.
#: Residue identified with HHE Michael adduct.
£: adduct(s) identified in all biological replicates for the corresponding conditions.
Greyed-out boxes show samples for which no peptide was detected across all biological replicates.

The peptide output from the Mascot search containing Cys71 was a good example of accurate Mascot identification of HHE Michael adducts on PTEN. Figure 6.7 shows the fragmentation spectra and sequence analysis for three different identification of the peptide 67-74 (IYNLCAER) containing Cys71: one with an unmodified Cys71 (Figure 6.7.A), one with an alkylated Cys71 (carbamidomethyl C71, Figure 6.7.B) and one where Cys71 was identified with a reduced HHE Michael adduct (Figure 6.7.C). Typically, a Mascot sequence analysis provides the observed b and y ions generated from peptide fragmentation (shown in red) as well as the theoretical b and y ions (shown in black), the b ions representing fragments starting from the N-terminus of the peptide and the y ions representing fragments starting from the C-terminus of the peptide. The Mascot sequence analysis also provides additional b and y ions with specific characteristics such as additional charge and neutral loss. Symbols are used to define these characteristics: "++", "*" and "0", representing doubly charged ions, the loss of ammonia (NH_3: Δmass = -17 Da) and the loss of water (H_2O: Δmass = -18 Da), respectively.

The Mascot identification of the peptide 67-74 (IYNLCAER) was successful with 100% y ion coverage up to the last residue (I) of the sequence for the peptides including an alkylated (Figure 6.7.B) or HHE-modified (Figure 6.7.C) Cys71. In comparison, only the y(2) ion (ER) was not identified in the fragmentation data from the unmodified peptide (Figure 6.7.A). The y ions picked for sequencing corresponded to peaks of the highest intensities on the fragmentation spectra (Figure 6.7, upper panes), which further increased the confidence in an accurate assignment of the peptide sequence, as well as modifications. Indeed, while the y(1) to y(3) ions (corresponding to the C-terminal fragments up to Cys71) were the same mass in all three peptide identifications, a mass shift of the following y ion peaks was observed for the peptides with a modified Cys71 (Figure 6.7.B and 6.7.C) compared to the unmodified peptide (Figure 6.7.A). A mass difference of +57.0215 Da, corresponding to the mass of a carbamidomethyl group, and a mass difference of +116.0838 Da, corresponding to the adduction of HHE via Michael addition, were consistently applied to y(4) to y(7) ions (fragments including Cys71) in Figure 6.7.B and 6.7.C, respectively, compared to the unmodified peptide (Figure 6.7.A). This allowed the correct assignment of carbamidomethylation of Cys71, which was to be expected from the alkylation step in the MS sample preparation process, and provided evidence that HHE could covalently modify PTEN residues and that a Mascot search could confidently and precisely identify the site of these modifications. Numerous y^0 ions were detected in the fragmentation data from the HHE-modified peptide but not from the unmodified or carbamidomethylated peptides (Figure 6.7). This was particularly surprising as y^0 ions, which result from the loss of water, are generally restricted to fragments containing residues with hydroxyl groups (OH) such as

serine (Ser), threonine (Thr) and tyrosine (Tyr), carboxyl groups (COOH) such as aspartic acid (Asp) and glutamic acid (Glu) or glutamine (Gln) with its amide group, and are a rare occurrence as the side chains must be exposed to high energies to induce cleavage of specific bonds and eliminate water (Harrison, 2012, O'Hair and Reid, 1998, Savitski et al., 2007). The y^0 ions were consistently detected for y(4) to y(7) ions, all of which included the HHE-modified Cys71, but not for fragments lacking the HHE-modified Cys71 (y(1) to y(3) ions). Notably, only the y(7) ion contained a residue (Tyr) that was prone to forming y^0 ions, and the intensity of these peaks was relatively high compared to the corresponding y ions (Figure 6.7.C). This suggested that the identification of the y^0 ions was accurate and likely resulted from the loss of water from the bound HHE molecule, rather than from side chains of the residues. Since HHE contains a hydroxyl group and the Michael addition of HHE to residues does not mask its aldehyde group, reduction of the aldehyde during borohydride treatment gives rise to an additional primary alcohol group, and elimination of this (observed as water loss) is favourable as it gives rise to a conjugated diene. Moreover, this pattern was also observed for peptides with HHE Michael adducts on Cys211, Cys250, and Cys304 (data not shown), suggesting that the unusually high y^0 ion signal could serve as a marker for the presence of HHE Michael adducts on cysteine residues.

A Unmodified C71

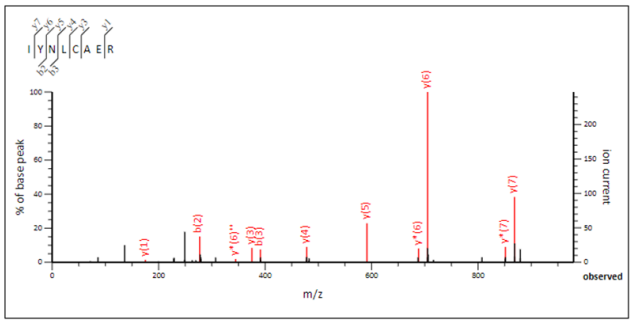

#	b	b^{++}	b*	b^{*++}	b^{0}	b^{0++}	Seq.	y	y^{++}	y*	y^{*++}	y^{0}	y^{0++}	#
1	114.0913	57.5493					I							8
2	***277.1547***	139.0810					Y	***868.3982***	434.7027	851.3716	426.1894	850.3876	425.6974	7
3	**391.1976**	196.1024	374.1710	187.5892			N	***705.3348***	353.1711	688.3083	344.6578	687.3243	344.1658	6
4	504.2817	252.6445	487.2551	244.1312			L	***591.2919***	296.1496	574.2654	287.6363	573.2813	287.1443	5
5	607.2908	304.1491	590.2643	295.6358			C	***478.2078***	239.6076	461.1813	231.0943	460.1973	230.6023	4
6	678.3280	339.6676	661.3014	331.1543			A	***375.1987***	188.1030	358.1721	179.5897	357.1881	179.0977	3
7	807.3706	404.1889	790.3440	395.6756	789.3600	395.1836	E	304.1615	152.5844	287.1350	144.0711	286.1510	143.5791	2
8							R	***175.1190***	88.0631	158.0924	79.5498			1

B Carbamidomethyl C71

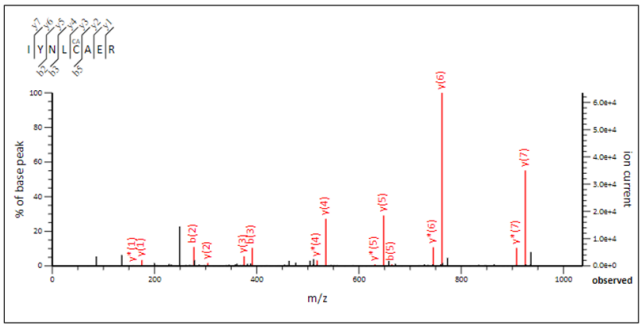

#	b	b^{++}	b*	b^{*++}	b^{0}	b^{0++}	Seq.	y	y^{++}	y*	y^{*++}	y^{0}	y^{0++}	#
1	114.0913	57.5493					I							8
2	**277.1547**	139.0810					Y	***925.4196***	463.2135	908.3931	454.7002	907.4091	454.2082	7
3	**391.1976**	196.1024	374.1710	187.5892			N	***762.3563***	381.6818	745.3297	373.1685	744.3457	372.6765	6
4	504.2817	252.6445	487.2551	244.1312			L	***648.3134***	324.6603	631.2868	316.1470	630.3028	315.6550	5
5	**664.3123**	332.6598	647.2858	324.1465			C	***535.2293***	268.1183	518.2028	259.6050	517.2187	259.1130	4
6	735.3494	368.1783	718.3229	359.6651			A	***375.1987***	188.1030	358.1721	179.5897	357.1881	179.0977	3
7	864.3920	432.6996	847.3655	424.1864	846.3815	423.6944	E	***304.1615***	152.5844	287.1350	144.0711	286.1510	143.5791	2
8							R	***175.1190***	88.0631	158.0924	79.5498			1

C HHE Michael adduct C71

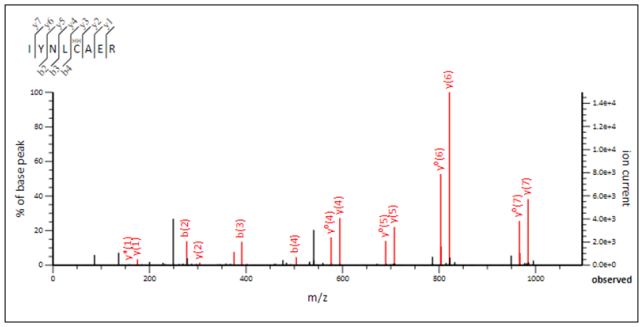

#	b	b^{++}	b*	b^{*++}	b^{0}	b^{0++}	Seq.	y	y^{++}	y*	y^{*++}	y^{0}	y^{0++}	#
1	114.0913	57.5493					I							8
2	**277.1547**	139.0810					Y	***984.4819***	492.7446	967.4553	484.2313	966.4713	483.7393	7
3	**391.1976**	196.1024	374.1710	187.5892			N	***821.4186***	411.2129	804.3920	402.6996	803.4080	402.2076	6
4	**504.2817**	252.6445	487.2551	244.1312			L	***707.3756***	354.1915	690.3491	345.6782	689.3651	345.1862	5
5	723.3746	362.1909	706.3480	353.6777			C	***594.2916***	297.6494	577.2650	289.1362	576.2810	288.6441	4
6	794.4117	397.7095	777.3851	389.1962			A	***375.1987***	188.1030	358.1721	179.5897	357.1881	179.0977	3
7	923.4543	462.2308	906.4277	453.7175	905.4437	453.2255	E	***304.1615***	152.5844	287.1350	144.0711	286.1510	143.5791	2
8							R	***175.1190***	88.0631	158.0924	79.5498			1

Figure 6.7. Representative Mascot peptide identification of the unmodified, alkylated or HHE-modified Cys71.

(A) Mascot search identified peptide 67-74 (IYNLCAER) as unmodified (A), carbamidomethylated on residue C71 (B) or with a reduced Michael addition of HHE on residue C71 (C). Each of the panels displays an upper pane with the fragmentation spectrum showing identified ions as peaks marked in red. The lower table presents the matched b and y ion coverage, with the matching ions shown in red. Bold italic red: the ion series contributed to the score of the peptide; bold red: the number of matches in the ion series is greater than would be expected by chance; non-bold red: the number of matches in the ion series is no greater than would be expected by chance.

While the Mascot search engine effectively identified peptide modifications, it could also erroneously assign modifications to identified peptides (false positives), making manual validation essential to the correct assignment of HHE adducts. This was particularly important to determine if the HHE adducts identified in untreated PTEN-V5-His samples were false or true positives. A comparative analysis of the Mascot output from the fragmentation data of peptides with HHE modifications on Lys147, Cys218 and Cys296 in

untreated PTEN-V5-His samples and HHE-treated PTEN-V5-His samples (considered as true positives) is shown in Figure 6.8, Supplementary Figure 4 and Figure 6.9, respectively.

For HHE-modified Lys147 (Figure 6.8), the Mascot search assigned the HHE modification from identification of the peptide 145-159 (FLKAQEALDFYGEVR). Although the y ion coverage was similar between the untreated (Figure 6.8.A) and HHE-treated PTEN-V5-His samples (Figure 6.8.B), it did not cover Lys147 in either case, which means that the y ions cannot be used to confirm modification of Lys147 by HHE. Although the y ion coverage provided strong confidence in the sequencing of the peptide for the HHE-treated PTEN-V5-His sample with a generally high intensity of assigned y ion peaks (Figure 6.8.B), the intensity of these peaks in the untreated PTEN-V5-His sample was consistently low (Figure 6.8.A). The low intensity of the peaks that were matched by Mascot may indicate an incorrect identification, especially in cases where the software might attempt to fit noise to known ion series in the absence of strong signal. On the other hand, the higher intensity peaks in the HHE-treated PTEN-V5-His sample reflected genuine peptide fragments, indicating accurate peptide sequencing. Although Lys147 was not covered by b ions in both cases, reducing the confidence of accurate assignment of the HHE modification, the presence of the b(5) to b(10) ions in the HHE-treated PTEN-V5-His sample (Figure 6.8.B) suggested that Lys147 was covalently bound by HHE. Indeed, these 6 fragment ions corresponded to the mass of the N-terminal part of the peptide with a delta mass of +116.0838 Da (Figure 6.8.B), mass of an HHE Michael adduct. On the other hand, no b ion was assigned by the Mascot search engine for the HHE-modified peptide 145-159 (FLKAQEALDFYGEVR) in the untreated PTEN-V5-His sample (Figure 6.8.A), which constituted further evidence that this HHE Michael addition on Lys147 was falsely assigned. Therefore, based on the low intensity of the peaks, the lack of high intensity y^0 ions and the lack of b ions, the modification of Lys147 in the untreated PTEN-V5-His sample was classified as a false positive.

A HHE-modified K147: False positive (untreated PTEN-V5-His)

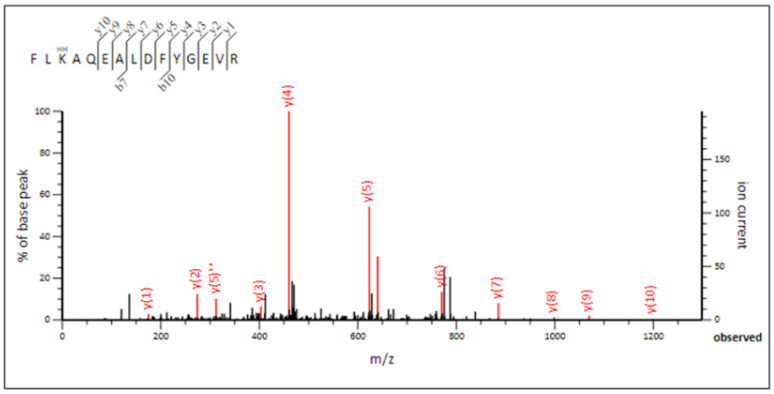

#	b	b^{++}	b*	b^{*++}	b^0	b^{0++}	Seq.	y	y^{++}	y*	y^{*++}	y^0	y^{0++}	#
1	148.0757	74.5415					F							15
2	261.1598	131.0835					L	1754.9323	877.9698	1737.9058	869.4565	1736.9218	868.9645	14
3	505.3384	253.1729	488.3119	244.6596			K	1641.8483	821.4278	1624.8217	812.9145	1623.8377	812.4225	13
4	576.3756	288.6914	559.3490	280.1781			A	1397.6696	699.3384	1380.6430	690.8251	1379.6590	690.3331	12
5	704.4341	352.7207	687.4076	344.2074			Q	1326.6325	663.8199	1309.6059	655.3066	1308.6219	654.8146	11
6	833.4767	417.2420	816.4502	408.7287	815.4662	408.2367	E	*1198.5739*	599.7906	1181.5473	591.2773	1180.5633	590.7853	10
7	904.5138	452.7606	887.4873	444.2473	886.5033	443.7553	A	*1069.5313*	535.2693	1052.5047	526.7560	1051.5207	526.2640	9
8	1017.5979	509.3026	1000.5714	500.7893	999.5873	500.2973	L	*998.4942*	499.7507	981.4676	491.2374	980.4836	490.7454	8
9	1132.6249	566.8161	1115.5983	558.3028	1114.6143	557.8108	D	*885.4101*	443.2087	868.3836	434.6954	867.3995	434.2034	7
10	1279.6933	640.3503	1262.6667	631.8370	1261.6827	631.3450	F	*770.3832*	385.6952	753.3566	377.1819	752.3726	376.6899	6
11	1442.7566	721.8819	1425.7300	713.3687	1424.7460	712.8767	Y	*623.3148*	312.1610	606.2882	303.6477	605.3042	303.1557	5
12	1499.7781	750.3927	1482.7515	741.8794	1481.7675	741.3874	G	*460.2514*	230.6293	443.2249	222.1161	442.2409	221.6241	4
13	1628.8207	814.9140	1611.7941	806.4007	1610.8101	805.9087	E	*403.2300*	202.1186	386.2034	193.6053	385.2194	193.1133	3
14	1727.8891	864.4482	1710.8625	855.9349	1709.8785	855.4429	V	*274.1874*	137.5973	257.1608	129.0840			2
15							R	*175.1190*	88.0631	158.0924	79.5498			1

B HHE-modified K147: True positive (HHE-treated PTEN-V5-His)

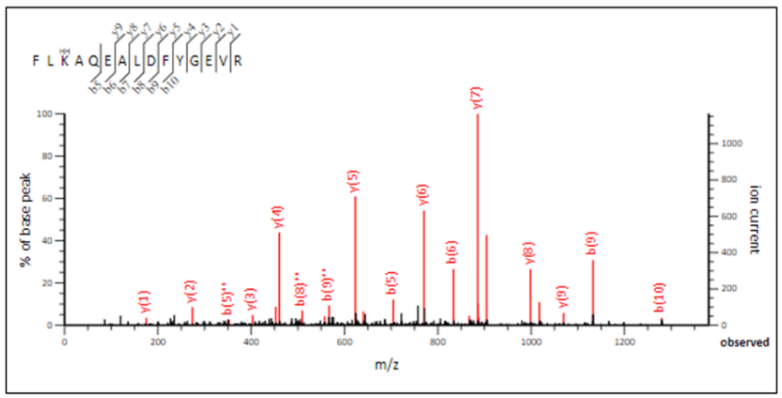

#	b	b^{++}	b*	b^{*++}	b^0	b^{0++}	Seq.	y	y^{++}	y*	y^{*++}	y^0	y^{0++}	#
1	148.0757	74.5415					F							15
2	261.1598	131.0835					L	1754.9323	877.9698	1737.9058	869.4565	1736.9218	868.9645	14
3	505.3384	253.1729	488.3119	244.6596			K	1641.8483	821.4278	1624.8217	812.9145	1623.8377	812.4225	13
4	576.3756	288.6914	559.3490	280.1781			A	1397.6696	699.3384	1380.6430	690.8251	1379.6590	690.3331	12
5	704.4341	352.7207	687.4076	344.2074			Q	1326.6325	663.8199	1309.6059	655.3066	1308.6219	654.8146	11
6	833.4767	417.2420	816.4502	408.7287	815.4662	408.2367	E	1198.5739	599.7906	1181.5473	591.2773	1180.5633	590.7853	10
7	904.5138	452.7606	887.4873	444.2473	886.5033	443.7553	A	*1069.5313*	535.2693	1052.5047	526.7560	1051.5207	526.2640	9
8	1017.5979	509.3026	1000.5714	500.7893	999.5873	500.2973	L	*998.4942*	499.7507	981.4676	491.2374	980.4836	490.7454	8
9	1132.6249	566.8161	1115.5983	558.3028	1114.6143	557.8108	D	*885.4101*	443.2087	868.3836	434.6954	867.3995	434.2034	7
10	1279.6933	640.3503	1262.6667	631.8370	1261.6827	631.3450	F	*770.3832*	385.6952	753.3566	377.1819	752.3726	376.6899	6
11	1442.7566	721.8819	1425.7300	713.3687	1424.7460	712.8767	Y	*623.3148*	312.1610	606.2882	303.6477	605.3042	303.1557	5
12	1499.7781	750.3927	1482.7515	741.8794	1481.7675	741.3874	G	*460.2514*	230.6293	443.2249	222.1161	442.2409	221.6241	4
13	1628.8207	814.9140	1611.7941	806.4007	1610.8101	805.9087	E	*403.2300*	202.1186	386.2034	193.6053	385.2194	193.1133	3
14	1727.8891	864.4482	1710.8625	855.9349	1709.8785	855.4429	V	*274.1874*	137.5973	257.1608	129.0840			2
15							R	*175.1190*	88.0631	158.0924	79.5498			1

Figure 6.8. Representative Mascot peptide identification for false and true positive HHE modification of Lys147 in untreated-PTEN-V5-His and HHE-treated PTEN-V5-His samples.

A Mascot search identified peptide 145-159 (FLKAQEALDFYGEVR) with an HHE Michael adduct on K147 in an untreated PTEN-V5-His sample (A) and an HHE-treated PTEN-V5-His sample (B). Panel (A) and (B) both display an upper pane with the fragmentation spectrum showing matched ions as red peaks. The lower table presents the matched b and y ion coverage, with the matching ions shown in

red. Bold italic red: the ion series contributed to the score of the peptide; bold red: the number of matches in the ion series is greater than would be expected by chance; non-bold red: the number of matches in the ion series is no greater than would be expected by chance.

A similar case was observed for C218, which was identified as modified by HHE through Michael addition in the peptide 198-221 (MMFETIPMFSGGTCNPQRVVCQLK) in the untreated PTEN-V5-His sample (Supplementary Figure 4). The Mascot software identified peaks for the HHE Michael adduct that were not the highest intensity peaks in the fragmentation spectrum, unlike those identified in the HHE-treated PTEN-V5-His sample. Many peaks were assigned to b ions with neutral losses from oxidized methionine (M199), but their intensities matched those of other b and y ions, suggesting random assignment. Although the b ion coverage was better in the untreated PTEN-V5-His sample, the accuracy of this assignment is questionable. The absence of the y(4) ion, which included the putative HHE-modified Cys218, further indicated potential misidentification. Reduced y ion coverage between Cys211 and Cys218 in untreated samples contrasts with the more complete detection in treated samples, implying that if an HHE modification occurred, it was more likely on Cys211 than Cys218.

On the other hand, despite the lack of direct identification of the b(7) or y(13) ions corresponding to the first N-terminal or C-terminal fragments including Cys296, respectively, the identification of Cys296 as modified by HHE in the 290-308 peptide (VENGSLCDQEIDSI CSIER) in the untreated PTEN-V5-His sample seemed accurate. Indeed, the pattern of detected b and y ions to sequence the peptide and identify the HHE modification on Cys296 was similar between the untreated and HHE-treated samples (Figure 6.9.A and 6.9.B). In both cases, the most intense peaks were picked for assignment of the sequence, suggesting accurate sequencing. Despite the lack of identification of b(7) and y(13) and the absence of y ion coverage from Cys296, multiple b ions with a shift in mass corresponding to the weight of an HHE Michael adduct (b(10)-b(12) and b(14) for the untreated PTEN-V5-His sample, Figure 6.9.A, and b(10)-b(11) and b(13) for the HHE-treated sample, Figure 6.9.B) were detected. Additionally, the only two residues in the identified peptide that could be considered as potential targets for HHE were Cys296 and Cys304 as trypsin successfully cleaved after Lys308. If Lys308 was modified, trypsin would most likely have not been able to recognise the cleavage site (Chauvet and Acher, 1971, Samy et al., 1980), leading to an extended peptide at the C-terminus with a missed cleavage at Lys308. Considering that, in both cases, the y ion coverage around Cys304 was good for masses of unmodified fragments and the y(5) ion (corresponding to the first fragment containing Cys304) was the second most intense peak in the fragmentation data (Figure 6.9.A and 6.9.B), Cys296 was the only confident match for HHE adduction. However, the intensity of the peaks assigned to the b ions corresponding to fragments containing Cys296 was relatively low compared to

other peaks that were not picked for sequencing of the peptide, suggesting that the assignment could be incorrect. Although this could imply that Cys296 was not modified by HHE in either untreated and HHE-treated samples, the Mascot assignment of two coexisting HHE Michael adducts on Cys296 and Cys304 on the same peptide (290-308, MMFETIPMFSGGTCNPQFVVCQLK) (Figure 6.9.C) suggested that Cys296 could indeed be modified by HHE. The good y and b ion coverage of the doubly-modified sequence as well as the consistent signals for y^0 and b^0 ions provided confidence in accurate assignment of HHE modifications of this peptide (Figure 6.9.C). This strongly suggested that the modification on Cys296 was assigned correctly.

A HHE-modified C296 (untreated PTEN-V5-His)

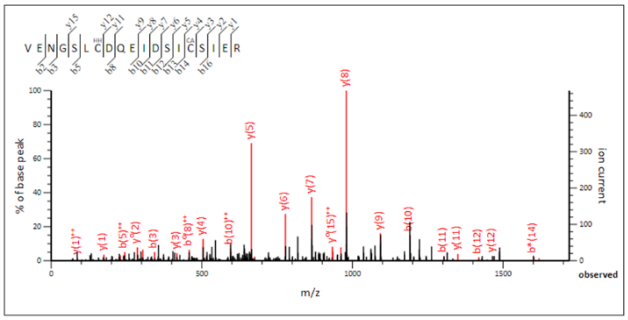

#	b	b++	b*	b*++	b0	b0++	Seq.	y	y++	y*	y*++	y0	y0++	#
1	100.0757	50.5415					V							19
2	229.1183	115.0628			211.1077	106.0575	E	2183.9795	1092.4934	2166.9529	1083.9801	2165.9689	1083.4881	18
3	343.1612	172.0842	326.1347	163.5710	325.1506	163.0790	N	2054.9369	1027.9721	2037.9103	1019.4588	2036.9263	1018.9668	17
4	400.1827	200.5950	383.1561	192.0817	382.1721	191.5897	G	1940.8940	970.9506	1923.8674	962.4373	1922.8834	961.9453	16
5	487.2147	244.1110	470.1882	235.5977	469.2041	235.1057	S	1883.8725	942.4399	1866.8460	933.9266	1865.8619	933.4346	15
6	600.2988	300.6530	583.2722	292.1397	582.2882	291.6477	L	1796.8405	898.9239	1779.8139	890.4106	1778.8299	889.9186	14
7	819.3917	410.1995	802.3651	401.6862	801.3811	401.1942	C	1683.7564	842.3818	1666.7299	833.8686	1665.7458	833.3766	13
8	934.4186	467.7130	917.3921	459.1997	916.4081	458.7077	D	1464.6635	732.8354	1447.6369	724.3221	1446.6529	723.8301	12
9	1062.4772	531.7422	1045.4507	523.2290	1044.4666	522.7370	Q	1349.6366	675.3219	1332.6100	666.8086	1331.6260	666.3166	11
10	1191.5198	596.2635	1174.4932	587.7503	1173.5092	587.2583	E	1221.5780	611.2926	1204.5514	602.7794	1203.5674	602.2873	10
11	1304.6039	652.8056	1287.5773	644.2923	1286.5933	643.8003	I	1092.5354	546.7713	1075.5088	538.2581	1074.5248	537.7660	9
12	1419.6308	710.3190	1402.6043	701.8058	1401.6202	701.3138	D	979.4513	490.2293	962.4248	481.7160	961.4408	481.2240	8
13	1506.6628	753.8351	1489.6363	745.3218	1488.6523	744.8298	S	864.4244	432.7158	847.3978	424.2026	846.4138	423.7105	7
14	1619.7469	810.3771	1602.7203	801.8638	1601.7363	801.3718	I	777.3923	389.1998	760.3658	380.6865	759.3818	380.1945	6
15	1779.7775	890.3924	1762.7510	881.8791	1761.7670	881.3871	C	664.3083	332.6578	647.2817	324.1445	646.2977	323.6525	5
16	1866.8096	933.9084	1849.7830	925.3951	1848.7990	924.9031	S	564.2776	282.6425	487.2511	244.1292	486.2671	243.6372	4
17	1979.8936	990.4505	1962.8671	981.9372	1961.8831	981.4452	I	417.2456	209.1264	400.2191	200.6132	399.2350	200.1212	3
18	2108.9362	1054.9718	2091.9097	1046.4585	2090.9257	1045.9665	E	304.1615	152.5844	287.1350	144.0711	286.1510	143.5791	2
19							R	175.1190	88.0631	158.0924	79.5498			1

B HHE-modified C296 (HHE-treated PTEN-V5-His)

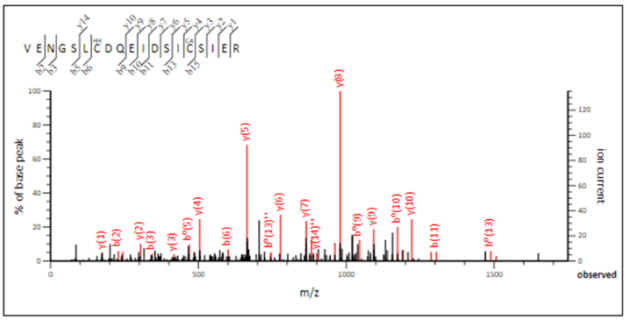

#	b	b++	b*	b*++	b0	b0++	Seq.	y	y++	y*	y*++	y0	y0++	#
1	100.0757	50.5415					V							19
2	229.1183	115.0628			211.1077	106.0575	E	2183.9795	1092.4934	2166.9529	1083.9801	2165.9689	1083.4881	18
3	343.1612	172.0842	326.1347	163.5710	325.1506	163.0790	N	2054.9369	1027.9721	2037.9103	1019.4588	2036.9263	1018.9668	17
4	400.1827	200.5950	383.1561	192.0817	382.1721	191.5897	G	1940.8940	970.9506	1923.8674	962.4373	1922.8834	961.9453	16
5	487.2147	244.1110	470.1882	235.5977	469.2041	235.1057	S	1883.8725	942.4399	1866.8460	933.9266	1865.8619	933.4346	15
6	600.2988	300.6530	583.2722	292.1397	582.2882	291.6477	L	1796.8405	898.9239	1779.8139	890.4106	1778.8299	889.9186	14
7	819.3917	410.1995	802.3651	401.6862	801.3811	401.1942	C	1683.7564	842.3818	1666.7299	833.8686	1665.7458	833.3766	13
8	934.4186	467.7130	917.3921	459.1997	916.4081	458.7077	D	1464.6635	732.8354	1447.6369	724.3221	1446.6529	723.8301	12
9	1062.4772	531.7422	1045.4507	523.2290	1044.4666	522.7370	Q	1349.6366	675.3219	1332.6100	666.8086	1331.6260	666.3166	11
10	1191.5198	596.2635	1174.4932	587.7503	1173.5092	587.2583	E	1221.5780	611.2926	1204.5514	602.7794	1203.5674	602.2873	10
11	1304.6039	652.8056	1287.5773	644.2923	1286.5933	643.8003	I	1092.5354	546.7713	1075.5088	538.2581	1074.5248	537.7660	9
12	1419.6308	710.3190	1402.6043	701.8058	1401.6202	701.3138	D	979.4513	490.2293	962.4248	481.7160	961.4408	481.2240	8
13	1506.6628	753.8351	1489.6363	745.3218	1488.6523	744.8298	S	864.4244	432.7158	847.3978	424.2026	846.4138	423.7105	7
14	1619.7469	810.3771	1602.7203	801.8638	1601.7363	801.3718	I	777.3923	389.1998	760.3658	380.6865	759.3818	380.1945	6
15	1779.7775	890.3924	1762.7510	881.8791	1761.7670	881.3871	C	664.3083	332.6578	647.2817	324.1445	646.2977	323.6525	5
16	1866.8096	933.9084	1849.7830	925.3951	1848.7990	924.9031	S	564.2776	282.6425	487.2511	244.1292	486.2671	243.6372	4
17	1979.8936	990.4505	1962.8671	981.9372	1961.8831	981.4452	I	417.2456	209.1264	400.2191	200.6132	399.2350	200.1212	3
18	2108.9362	1054.9718	2091.9097	1046.4585	2090.9257	1045.9665	E	304.1615	152.5844	287.1350	144.0711	286.1510	143.5791	2
19							R	175.1190	88.0631	158.0924	79.5498			1

C HHE-modified C296 and C304 (HHE-treated PTEN-V5-His)

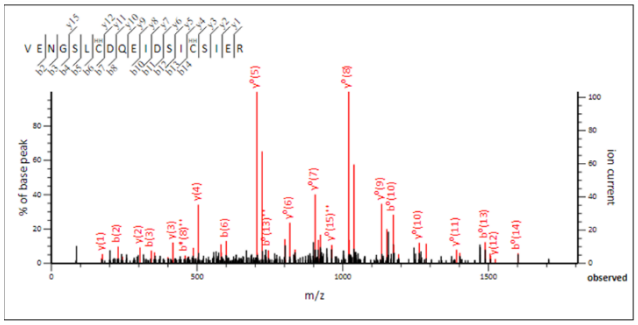

#	b	b++	b*	b*++	b0	b0++	Seq.	y	y++	y*	y*++	y0	y0++	#
1	100.0757	50.5415					V							19
2	229.1183	115.0628			211.1077	106.0575	E	2243.0418	1122.0245	2226.0152	1113.5112	2225.0312	1113.0192	18
3	343.1612	172.0842	326.1347	163.5710	325.1506	163.0790	N	2113.9992	1057.5032	2096.9726	1048.9899	2095.9886	1048.4979	17
4	400.1827	200.5950	383.1561	192.0817	382.1721	191.5897	G	1999.9562	1000.4818	1982.9297	991.9685	1981.9457	991.4765	16
5	487.2147	244.1110	470.1882	235.5977	469.2041	235.1057	S	1942.9348	971.9710	1925.9082	963.4577	1924.9242	962.9657	15
6	600.2988	300.6530	583.2722	292.1397	582.2882	291.6477	L	1855.9027	928.4550	1838.8762	919.9417	1837.8922	919.4497	14
7	819.3917	410.1995	802.3651	401.6862	801.3811	401.1942	C	1742.8187	871.9130	1725.7921	863.3997	1724.8081	862.9077	13
8	934.4186	467.7130	917.3921	459.1997	916.4081	458.7077	D	1523.7258	762.3665	1506.6992	753.8532	1505.7152	753.3612	12
9	1062.4772	531.7422	1045.4507	523.2290	1044.4666	522.7370	Q	1408.6988	704.8530	1391.6723	696.3398	1390.6883	695.8478	11
10	1191.5198	596.2635	1174.4932	587.7503	1173.5092	587.2583	E	1280.6402	640.8238	1263.6137	632.3105	1262.6297	631.8185	10
11	1304.6039	652.8056	1287.5773	644.2923	1286.5933	643.8003	I	1151.5977	576.3025	1134.5711	567.7892	1133.5871	567.2972	9
12	1419.6308	710.3190	1402.6043	701.8058	1401.6202	701.3138	D	1038.5136	519.7604	1021.4870	511.2472	1020.5030	510.7551	8
13	1506.6628	753.8351	1489.6363	745.3218	1488.6523	744.8298	S	923.4866	462.2470	906.4601	453.7337	905.4761	453.2417	7
14	1619.7469	810.3771	1602.7203	801.8638	1601.7363	801.3718	I	836.4546	418.7309	819.4281	410.2177	818.4441	409.7257	6
15	1838.8398	919.9235	1821.8133	911.4103	1820.8292	910.9183	C	723.3706	362.1889	706.3440	353.6756	705.3600	353.1836	5
16	1925.8718	963.4396	1908.8453	954.9263	1907.8613	954.4343	S	564.2776	282.6425	487.2511	244.1292	486.2671	243.6372	4
17	2038.9559	1019.9816	2021.9294	1011.4683	2020.9453	1010.9763	I	417.2456	209.1264	400.2191	200.6132	399.2350	200.1212	3
18	2167.9985	1084.5029	2150.9719	1075.9896	2149.9879	1075.4976	E	304.1615	152.5844	287.1350	144.0711	286.1510	143.5791	2
19							R	175.1190	88.0631	158.0924	79.5498			1

Figure 6.9. Representative Mascot peptide identification of peptide 290-308 (VENGSLCDQEIDSICSIER) with HHE modifications on Cys296 and Cys304.

A Mascot search identified peptide 290-308 (VENGSLCDQEIDSICSIER) with an HHE Michael adduct on C296 in an untreated PTEN-V5-His sample (A) and an HHE-treated PTEN-V5-His sample (B) as well as double HHE Michael adducts on both C296 and C304 (C). All panels display an upper pane with the fragmentation spectrum showing identified ions as peaks marked in red. The lower table presents the matched b and y ion coverage, with the matching ions shown in red. Bold italic red: the ion series contributed to the score of the peptide; bold red: the number of matches in the ion series is greater than would be expected by chance; non-bold red: the number of matches in the ion series is no greater than would be expected by chance.

Peptides 198-221 (MMFETIPMFSGGTCNPQFVVCQLK), 238-254 (FMYFEFPQPLPVCGDIK) and 350-378 (TVEEPSNPEASSSTSVTPDVSDNEPDHYR) were identified by Mascot as modified by HHE on their C-terminal Lys or Arg residues.

For instance, in the peptide 238-254 (FMYFEFPQPLPVCGDIK), Lys254 was identified as modified by an HHE Michael adduct (Figure 6.10). This was particularly surprising as modified Lys and Arg residues generally result in missed cleavages by trypsin, which is not able to recognise the cleavage site, as discussed previously (Chauvet and Acher, 1971, Samy et al., 1980). The peptide seemed to be confidently sequenced by Mascot with a high coverage by y ions from y(5) to y(15), covering most of the peptide sequence with the exception of the C-terminal region following Cys250 (Figure 6.10). This lack of coverage explained the possible misassignment of the HHE modification on this peptide. Indeed, as fragments with a mass shift of +116.0837 Da, corresponding to an HHE Michael adduct, were only detected from the fragment including Cys250 (y(5)) (Figure 6.10), Mascot most likely misassigned an HHE Michael adduct on Cys250 to Lys254.

This observation also applied to the peptide 350-378 (TVEEPSNPEASSSTSVTPDVSDNEPDHYR), where Mascot identified Arg378 as being modified by HHE. However, the y(1) and y(2) ions, which are C-terminal fragments that do not include His376 (R and YR, respectively), did not exhibit the expected +116.0837 Da mass shift. In contrast, fragments containing His376 did show this shift, suggesting that the HHE Michael adduct was incorrectly assigned to Arg378 and that His376 was the more likely site of modification (Supplementary Figure 5). Similarly, the peptide 198-221 (MMFETIPMFSGGTCNPQFVVCQLK) was identified by Mascot as having an HHE modification on Lys221, but the lack of C-terminal fragments suggested that Cys218 could be the actual site of modification. In this case, two fragments that did not include Cys218 (y(1) and y(2) for K and LK, respectively) showed a +116.0837 Da mass shift, although one of these fragments (y(2) corresponding to the LK fragment) was also detected without the mass shift, making it difficult to determine conclusively the exact site of HHE modification (Supplementary Figure 6).

HHE-modified K254: False positive (C-terminal K)

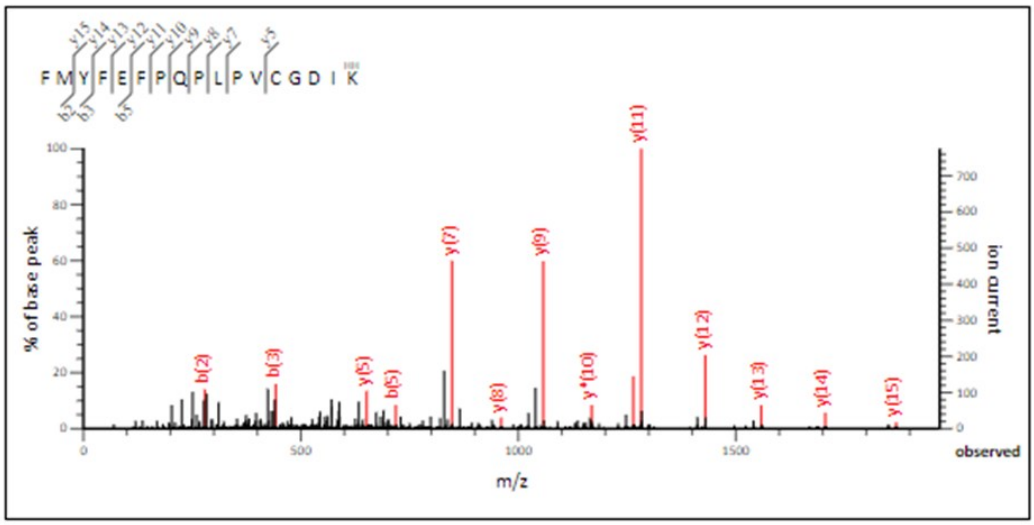

#	b	b^{++}	b*	b^{*++}	b^0	b^{0++}	Seq.	y	y^{++}	y*	y^{*++}	y^0	y^{0++}	#
1	148.0757	74.5415					F							17
2	**279.1162**	140.0617					M	1999.9908	1000.4990	1982.9642	991.9857	1981.9802	991.4937	16
3	**442.1795**	221.5934					Y	***1868.9503***	934.9788	1851.9237	926.4655	1850.9397	925.9735	15
4	589.2479	295.1276					F	***1705.8870***	853.4471	1688.8604	844.9338	1687.8764	844.4418	14
5	**718.2905**	359.6489			700.2799	350.6436	E	***1558.8185***	779.9129	1541.7920	771.3996	1540.8080	770.9076	13
6	865.3589	433.1831			**847.3484**	424.1778	F	***1429.7760***	715.3916	1412.7494	706.8783	1411.7654	706.3863	12
7	962.4117	481.7095			944.4011	472.7042	P	***1282.7075***	641.8574	1265.6810	633.3441	**1264.6970**	632.8521	11
8	1090.4703	545.7388	1073.4437	537.2255	1072.4597	536.7335	Q	1185.6548	593.3310	**1168.6282**	584.8178	1167.6442	584.3257	10
9	1187.5230	594.2652	1170.4965	585.7519	1169.5125	585.2599	P	***1057.5962***	529.3017	1040.5696	520.7885	1039.5856	520.2965	9
10	1300.6071	650.8072	1283.5805	642.2939	**1282.5965**	641.8019	L	***960.5434***	480.7754	943.5169	472.2621	942.5329	471.7701	8
11	1397.6599	699.3336	1380.6333	690.8203	1379.6493	690.3283	P	***847.4594***	424.2333	830.4328	415.7200	829.4488	415.2280	7
12	1496.7283	748.8678	1479.7017	740.3545	1478.7177	739.8625	V	750.4066	375.7069	733.3801	367.1937	732.3960	366.7017	6
13	1599.7375	800.3724	1582.7109	791.8591	1581.7269	791.3671	C	***651.3382***	326.1727	634.3116	317.6595	633.3276	317.1675	5
14	1656.7589	828.8831	1639.7324	820.3698	1638.7484	819.8778	G	548.3290	274.6681	531.3025	266.1549	530.3184	265.6629	4
15	1771.7859	886.3966	1754.7593	877.8833	1753.7753	877.3913	D	491.3075	246.1574	474.2810	237.6441	473.2970	237.1521	3
16	1884.8699	942.9386	1867.8434	934.4253	1866.8594	933.9333	I	376.2806	188.6439	359.2540	180.1307			2
17							K	263.1965	132.1019	246.1700	123.5886			1

Figure 6.10. Representative Mascot output for false positive identification of HHE modification on C-terminal K residue of the identified peptide 238-254 (FMYFEFPQPLPVCGDIK).
A Mascot search identified the peptide 238-254 (FMYFEFPQPLPVCGDIK) with an HHE Michael adduct on K254 in an HHE-treated PTEN-V5-His sample. An upper pane with the fragmentation spectrum showing identified ions as peaks marked in red and a lower table with the matched b and y ion coverage, with the matching ions shown in red are presented. Bold italic red: the ion series contributed to the score of the peptide; bold red: the number of matches in the ion series is greater than would be expected by chance; non-bold red: the number of matches in the ion series is no greater than would be expected by chance.

In addition to Michael adducts, modification of PTEN by HHE through Schiff base formation was assigned on 3 peptides: 143-159 (GKFLKAQLDFYGEVR) for which the HHE modification was assigned to Lys147; 173-123 (RYVYYYSYLLK) with a modification on Arg173; and 238-254/260 (FMYFEFPQPLPVCGDIK/VEFFHK) for which addition of HHE by Schiff base formation was assigned to either Lys254 alone or Lys254 and Lys260, along with His259 identified as a Michael addition of HHE. However, none of these assigned modifications were confidently identified as true positives following manual validation. It is also important to note that, across all samples and biological replicates, the modification of

Lys147, Arg173 and Lys254 (alone) via Schiff base formation were only identified on one peptide each. As an example, Figure 6.11 shows the Mascot peptide match leading to the identification of an HHE Schiff adduct on Lys147. The y-ion series showed strong peaks for y(4) to y(7) ions, indicating high-confidence matches for the C-terminal RVEGYFD peptide sequencing. However, there was no coverage of the sequence by b ions. Indeed, only one b ion (b(8), corresponding to the N-terminal sequence GKFLKAQE) was identified in the fragmentation spectrum. The putative modification on Lys147 was therefore not covered, suggesting a false positive identification of an HHE Schiff adduct. Furthermore, although the mass of the precursor suggested addition of HHE, another lysine residue was part of that sequence, Lys144, and no data allowed discrimination between Lys144 and Lys147 for HHE modification.

The case of Arg173 (Supplementary Figure 7) was very similar: a good coverage of y ions was identified, leading to confidence in the peptide identification, but there was no coverage of the fragments containing the putative modification. The HHE Schiff adduct on Lys254 was also classified as false positive based on the lack of assignment of peaks of highest intensity in the fragmentation data and the fact that Lys254 was the C-terminal residue which trypsin cleaved successfully after and was not covered by y ions. In fact, the y ions coverage was limited to the identification of three fragment ions which were of low intensity and could have been noise rather than true fragment ions (Supplementary Figure 8). The assignment of two distinct HHE Schiff adducts (on Lys254 and Lys260) and one HHE Michael adduct (on His259) on a single peptide was surprising. In fact, the peaks that were selected by Mascot for sequencing of the peptide 238-260 (FMYFEFPQPLPVCGDIKVEFFHK) were exclusively corresponding to fragments with a loss of ammonium (-64 Da) and limited to 6 b ions and 2 y ions for a 23 amino acid-long peptide, which strongly suggested that this was a misidentification (Supplementary Figure 9).

HHE-modified K147 (Schiff)

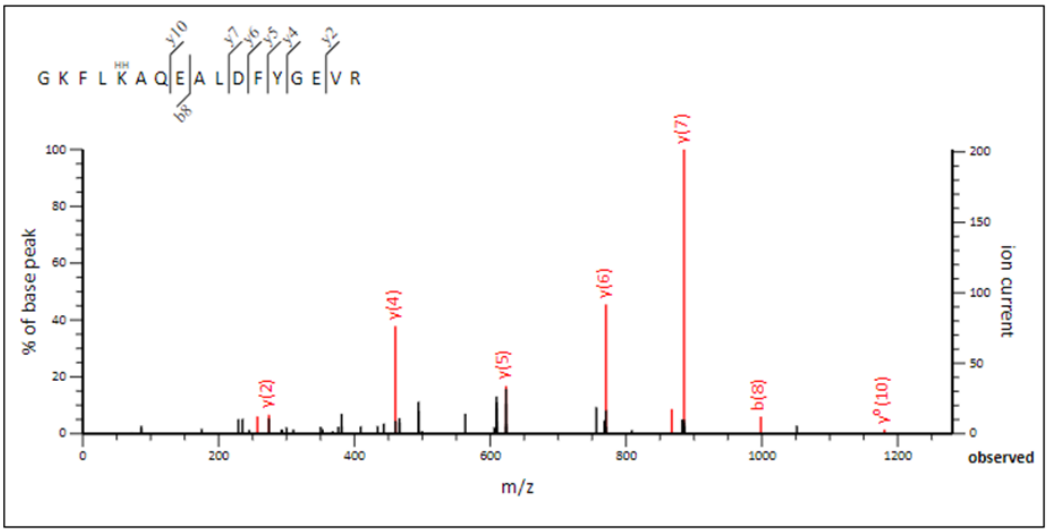

#	b	b^{++}	b*	b*$^{++}$	b^{0}	b^{0++}	Seq.	y	y^{++}	y*	y*$^{++}$	y^{0}	y^{0++}	#
1	58.0287	29.5180					G							17
2	186.1237	93.5655	169.0972	85.0522			K	2010.0695	1005.5384	1993.0429	997.0251	1992.0589	996.5331	16
3	333.1921	167.0997	316.1656	158.5864			F	1881.9745	941.4909	1864.9480	932.9776	1863.9640	932.4856	15
4	446.2762	223.6417	429.2496	215.1285			L	1734.9061	867.9567	1717.8796	859.4434	1716.8955	858.9514	14
5	670.4287	335.7180	653.4021	327.2047			K	1621.8220	811.4147	1604.7955	802.9014	1603.8115	802.4094	13
6	741.4658	371.2365	724.4392	362.7232			A	1397.6696	699.3384	1380.6430	690.8251	1379.6590	690.3331	12
7	869.5244	435.2658	852.4978	426.7525			Q	1326.6325	663.8199	1309.6059	655.3066	1308.6219	654.8146	11
8	998.5669	499.7871	981.5404	491.2738	980.5564	490.7818	E	1198.5739	599.7906	1181.5473	591.2773	1180.5633	590.7853	10
9	1069.6041	535.3057	1052.5775	526.7924	1051.5935	526.3004	A	1069.5313	535.2693	1052.5047	526.7560	1051.5207	526.2640	9
10	1182.6881	591.8477	1165.6616	583.3344	1164.6776	582.8424	L	***998.4942***	499.7507	981.4676	491.2374	980.4836	490.7454	8
11	1297.7151	649.3612	1280.6885	640.8479	1279.7045	640.3559	D	***885.4101***	443.2087	868.3836	434.6954	867.3995	434.2034	7
12	1444.7835	722.8954	1427.7569	714.3821	1426.7729	713.8901	F	***770.3832***	385.6952	753.3566	377.1819	752.3726	376.6899	6
13	1607.8468	804.4270	1590.8203	795.9138	1589.8362	795.4218	Y	***623.3148***	312.1610	606.2882	303.6477	605.3042	303.1557	5
14	1664.8683	832.9378	1647.8417	824.4245	1646.8577	823.9325	G	***460.2514***	230.6293	443.2249	222.1161	442.2409	221.6241	4
15	1793.9109	897.4591	1776.8843	888.9458	1775.9003	888.4538	E	403.2300	202.1186	386.2034	193.6053	385.2194	193.1133	3
16	1892.9793	946.9933	1875.9527	938.4800	1874.9687	937.9880	V	***274.1874***	137.5973	257.1608	129.0840			2
17							R	175.1190	88.0631	158.0924	79.5498			1

Figure 6.11. Mascot peptide identification of Lys147 modified by HHE through Schiff base formation was classified as a false positive result.
A Mascot search identified the peptide 143-159 (GKFLKAQLDFYGEVR) with an HHE Schiff adduct on K147 in an HHE-treated PTEN-V5-His sample. An upper pane with the fragmentation spectrum showing identified ions as peaks marked in red and a lower table with the matched b and y ion coverage, with the matching ions shown in red, are presented. Bold italic red: the ion series contributed to the score of the peptide; bold red: the number of matches in the ion series is greater than would be expected by chance; non-bold red: the number of matches in the ion series is no greater than would be expected by chance.

When localising the identified HHE-modified residues on PTEN sequence, one was located in the N-terminal PIP2 binding domain, five were located in the phosphatase domain, eight in the C2 domain and two were in the C-terminal tail (Figure 6.12.A). Strikingly, all cysteine residues, with the exception of Cys124 (which was not detected in HHE-treated PTEN-V5-His samples) and Cys83, were found to be modified by HHE in at least one sample. In contrast, multiple histidine, lysine and arginine residues were not identified as modified by

HHE (Figure 6.12.A). This suggested that cysteine residues were the primary targets for HHE.

HHE was observed to modify not only solvent-accessible residues but also Cys71, Cys136, and Cys211, which are typically considered buried within PTEN's three-dimensional structure, exhibiting a solvent accessibility surface (SAS) of less than 10% as determined by Discovery Studio's built-in SAS calculation tools (Figure 6.12.B). With such low SAS values, these cysteine residues were generally assumed to be shielded from solvent interaction, making them less susceptible to chemical modification. Notably, while HHE-modified Cys136 and Cys211 were predominantly detected in aggregated forms, suggesting that PTEN may undergo conformational changes upon aggregation allowing these residues to become accessible, Cys71 was consistently modified in all HHE-treated PTEN-V5-His samples, even at low HHE ratios (Table 6.7). The consistent modification of Cys71 by HHE implied that PTEN possessed inherent flexibility or dynamic regions that permitted the transient exposure of this residue, typically buried. This structural flexibility might be essential for PTEN's functional or regulatory mechanisms. Consequently, modification of Cys71 could potentially impair PTEN's function.

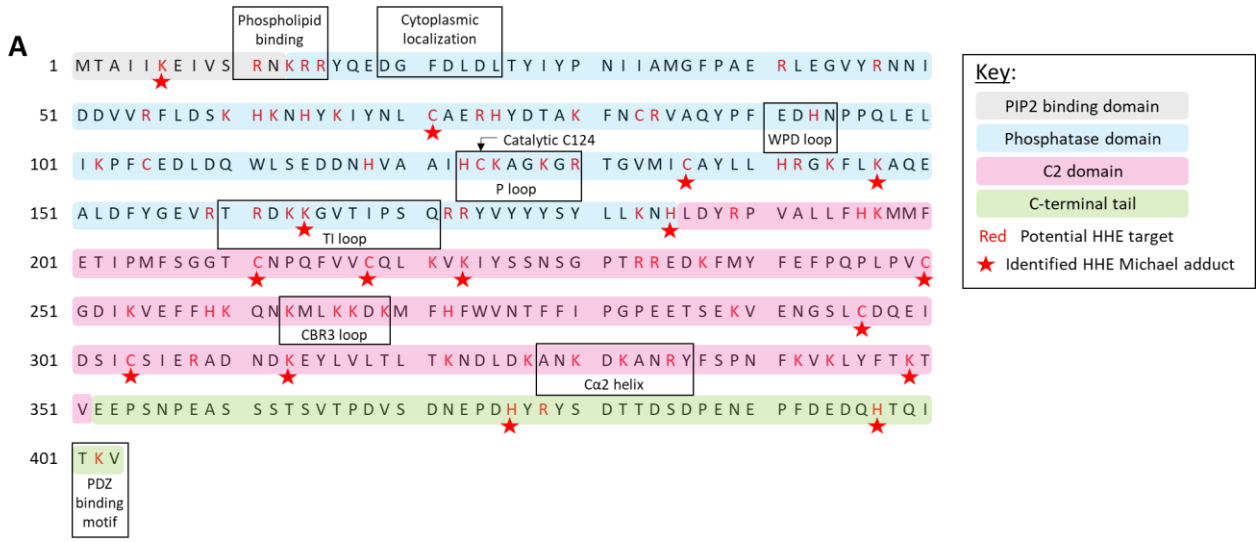

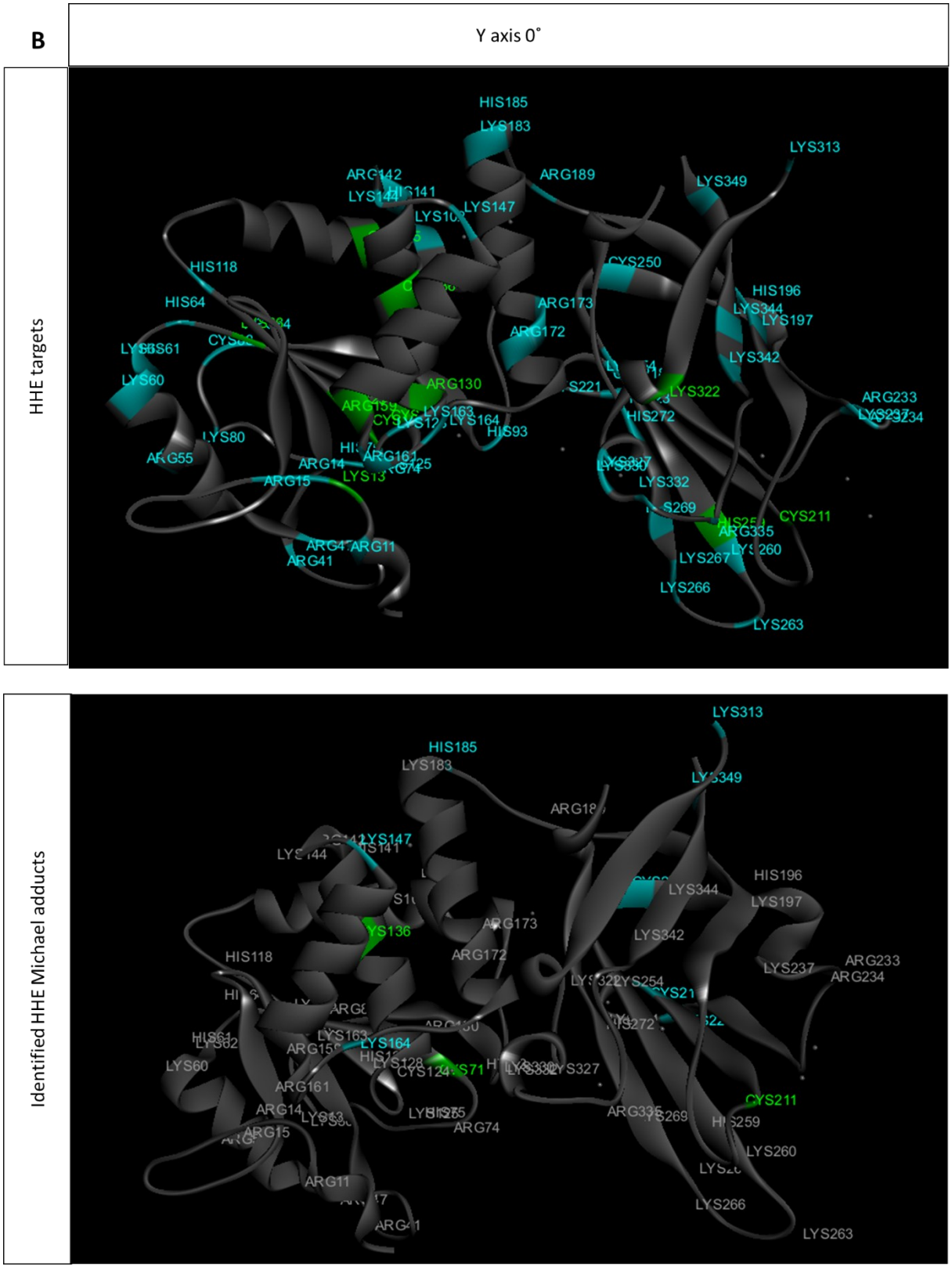
B
Y axis 0˚
HHE targets
HIS185
LYS183
LYS313
ARG142
ARG189
LYS349
LYS147
HIS118
CYS250
HIS64
HIS196
ARG173
LYS344
LYS197
ARG172
LYS342
LYS60
ARG130
LYS322
ARG233
HIS272
LYS80
ARG55
ARG161
LYS332
LYS269
CYS211
ARG335
LYS267
LYS266
LYS263
Identified HHE Michael adducts
LYS313
HIS185
LYS183
LYS349
LYS147
HIS196
LYS344
LYS197
ARG173
LYS342
LYS136
HIS118
ARG172
LYS237
ARG233
ARG234
LYS254
CYS211
LYS164
LYS60
ARG161
ARG14
ARG74
CYS211
ARG15
LYS260
ARG11
LYS266
LYS263

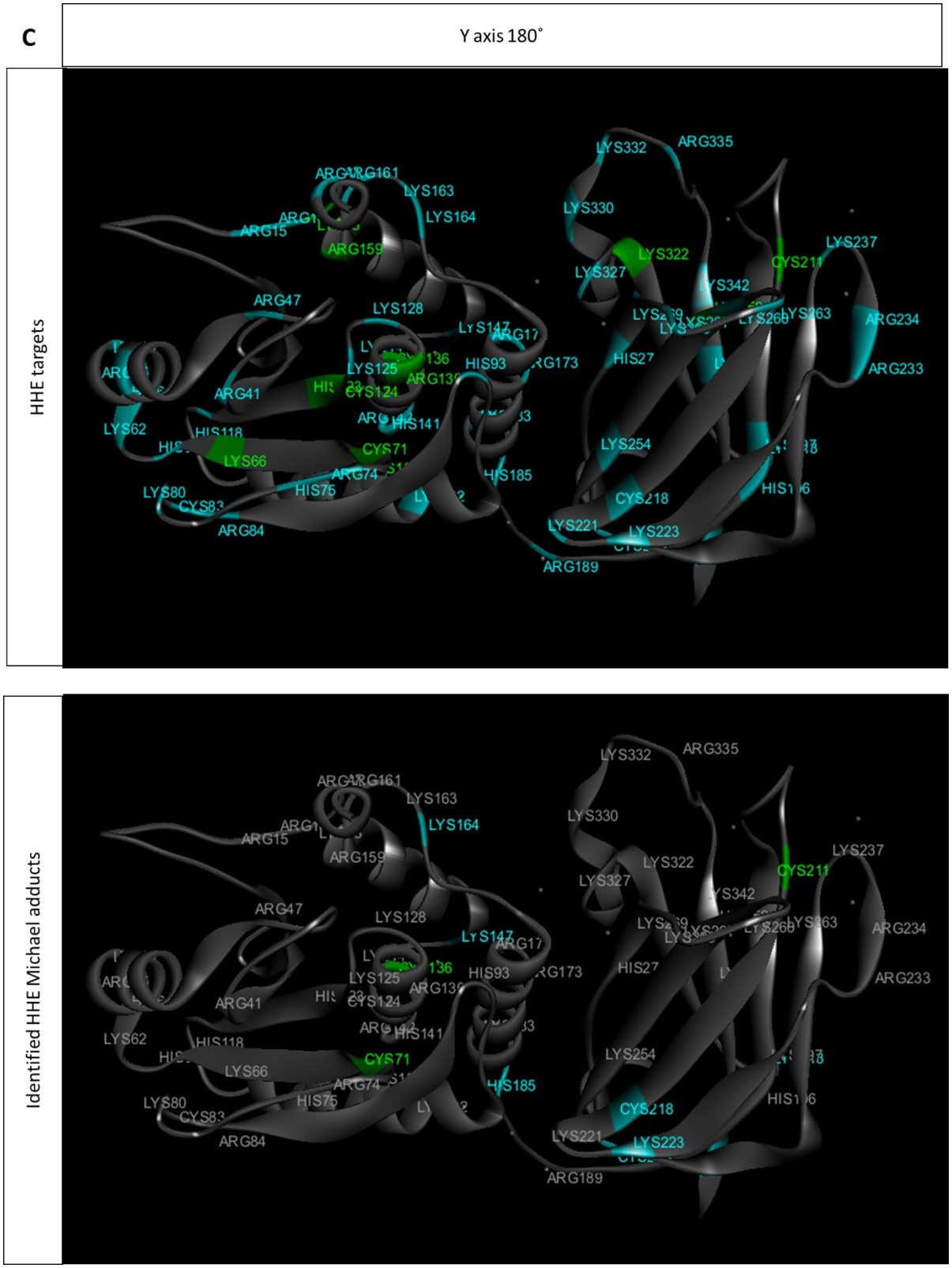

Figure 6.12. Localisation and solvent accessibility of HHE-modified PTEN residues.
Identified residues that underwent HHE Michael addition were highlighted on the annotated sequence (A) and structure (B,C) of PTEN. (A) shows the identified HHE Michael adducts (highlighted with a red star) compared to all HHE potential targets (in red). Sequence annotations are based on literature (Lee et al., 1999, Campbell et al., 2003, Walker et al., 2004, Denning et al., 2007). (B and C) shows the localisation of HHE potential targets (upper panes) and identified HHE Michael adducts (lower panes) on PTEN structure as well as their SAS (cyan: SAS>25%, green: SAS<10%). Residues that

did not correspond to HHE potential targets (upper panes) or identified HHE Michael adducts (lower panes) are shown in grey. This excluded the unresolved peptides 1-6 (MTAIIK), 282-312 (GPEETSE KVENGSLCDQEIDSICSIERADND) and 352-403 (EEPSNPEASSSTSVTPDVSDNEPDHYRYSDTTD SDPENEPFDEDQHTQITKV), therefore, the HHE-modified K6, C296, C304, H376 and H397 were not visible.

6.3.3.3. Sites of Adduction by PONPC on Monomeric and Aggregated PTEN-V5-His: a Challenging Identification

Similar experiments were carried out to investigate the formation of PONPC adducts on PTEN-V5-His. The Mascot search engine was employed to identify potential mass differences indicative of PONPC modification. The expected modification involved the formation of a Schiff base between PONPC and specific lysine or arginine residues on PTEN, resulting in a predictable monoisotopic mass shift. Given that the samples were fully reduced post-treatment using sodium borohydride, and DTT was employed during LC-MS/MS preparation, the anticipated mass shift for PONPC-modified peptides was +633.436955 Da, reflective of the reduction state. However, the Mascot search did not detect any PTEN residues modified by PONPC, even though overall sequence coverage was satisfactory, as detailed in section 6.3.3.1. This suggested that, under the conditions tested, PONPC modification did not occur or was not detectable at the expected sites. Unexpectedly, the Mascot search identified potential modifications corresponding to a monoisotopic mass shift of +631.4213 Da on lysine residues Lys147, Lys254, and Lys269. This shift was 2 Da less than the expected +633.436955 Da, corresponding to unreduced Schiff base modifications. However, given that the samples were fully reduced during preparation, these findings raised concerns about the validity of these identifications, suggesting that they might not represent true PONPC modifications but rather artifacts of the analytical process.

For Lys147, the identification of the peptide was primarily based on y ions, which generally provided good sequence coverage up to the residue thought to be modified. However, no y ion directly corresponding to the modified Lys147 was detected. The intensity of the detected peaks, with the exception of y(12), was low, which diminished the confidence in this identification (Figure 6.13.A). Moreover, the detection of the b ion corresponding to the first fragment containing Lys147 was limited to a number of matches not exceeding random expectation, implying potential misidentification. The absence of other b ions and lack of 184.1 Da fragment to corroborate the presence of the modification further supported the hypothesis that Lys147 was not genuinely modified by PONPC. This identification of unreduced PONPC modification was therefore classified as a false positive. The evidence for Lys269 PONPC modification was similar. The peptide spanning residues 268-289 (DKMFHFWVNTFFIPGPEETSEK) showed good y ion coverage between y(3) and y(12),

which partially covered the sequence (FFIPGPEETS). However, the peaks assigned to these y ions were not the dominant peaks in the spectrum, questioning the reliability of these assignments. The lack of detected b ions meant that there was no confirmation of sequence coverage around Lys269, thereby strongly suggesting a false positive for the identification of the PONPC Schiff adduct at this position (Supplementary Figure 10).

Regarding Lys254, the assignment of a PONPC Schiff adduct was classified as a false positive for several reasons. The peptide sequence 238-254 (FMYFEFPQPLPVCGDIK) identified Lys254 as the C-terminal residue, which would be unlikely if this residue were modified (Figure 6.13.B). This discrepancy alone suggested an anomalous identification. Although some b ions were detected, indicating partial sequencing of the peptide, the coverage did not extend to the C-terminus but was limited to residue Leu247, covering the 238-247 sequence with only about 60% b ion coverage. Furthermore, the absence of y ions provided no supporting evidence for the existence of the PONPC adduct, thereby confirming the false positive nature of this identification.

A Unreduced PONPC Schiff adduct K147: False positive

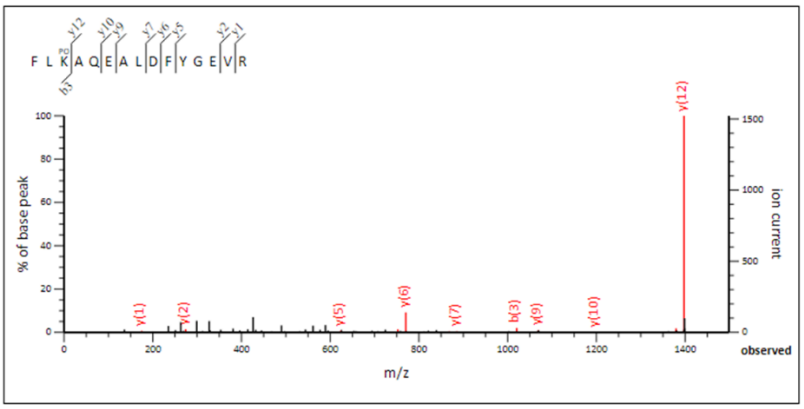

#	b	b^{++}	b*	b^{*++}	b^0	b^{0++}	Seq.	y	y^{++}	y*	y^{*++}	y^0	y^{0++}	#
1	148.0757	74.5415					F							15
2	261.1598	131.0835					L	2270.2699	1135.6386	2253.2434	1127.1253	2252.2593	1126.6333	14
3	1020.6760	510.8416	1003.6495	502.3284			K	2157.1858	1079.0966	2140.1593	1070.5833	2139.1753	1070.0913	13
4	1091.7131	546.3602	1074.6866	537.8469			A	*1397.6696*	699.3384	1380.6430	690.8251	1379.6590	690.3331	12
5	1219.7717	610.3895	1202.7452	601.8762			Q	1326.6325	663.8199	1309.6059	655.3066	1308.6219	654.8146	11
6	1348.8143	674.9108	1331.7878	666.3975	1330.8037	665.9055	E	*1198.5739*	599.7906	1181.5473	591.2773	1180.5633	590.7853	10
7	1419.8514	710.4293	1402.8249	701.9161	1401.8409	701.4241	A	*1069.5313*	535.2693	1052.5047	526.7560	1051.5207	526.2640	9
8	1532.9355	766.9714	1515.9089	758.4581	1514.9249	757.9661	L	998.4942	499.7507	981.4676	491.2374	980.4836	490.7454	8
9	1647.9624	824.4849	1630.9359	815.9716	1629.9519	815.4796	D	*885.4101*	443.2087	868.3836	434.6954	867.3995	434.2034	7
10	1795.0308	898.0191	1778.0043	889.5058	1777.0203	889.0138	F	*770.3832*	385.6952	753.3566	377.1819	752.3726	376.6899	6
11	1958.0942	979.5507	1941.0676	971.0374	1940.0836	970.5454	Y	*623.3148*	312.1610	606.2882	303.6477	605.3042	303.1557	5
12	2015.1156	1008.0615	1998.0891	999.5482	1997.1051	999.0562	G	460.2514	230.6293	443.2249	222.1161	442.2409	221.6241	4
13	2144.1582	1072.5828	2127.1317	1064.0695	2126.1477	1063.5775	E	403.2300	202.1186	386.2034	193.6053	385.2194	193.1133	3
14	2243.2266	1122.1170	2226.2001	1113.6037	2225.2161	1113.1117	V	*274.1874*	137.5973	257.1608	129.0840			2
15							R	*175.1190*	88.0631	158.0924	79.5498			1

B Unreduced PONPC Schiff adduct K254: False positive

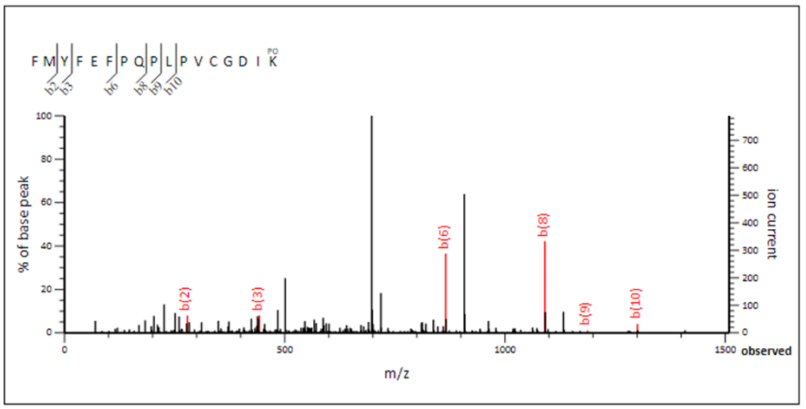

#	b	b^{++}	b*	b^{*++}	b^0	b^{0++}	Seq.	y	y^{++}	y*	y^{*++}	y^0	y^{0++}	#
1	148.0757	74.5415					F							17
2	*279.1162*	140.0617					M	2515.3283	1258.1678	2498.3018	1249.6545	2497.3178	1249.1625	16
3	*442.1795*	221.5934					Y	2384.2879	1192.6476	2367.2613	1184.1343	2366.2773	1183.6423	15
4	589.2479	295.1276					F	2221.2245	1111.1159	2204.1980	1102.6026	2203.2140	1102.1106	14
5	718.2905	359.6489			700.2799	350.6436	E	2074.1561	1037.5817	2057.1296	1029.0684	2056.1456	1028.5764	13
6	*865.3589*	433.1831			847.3484	424.1778	F	1945.1135	973.0604	1928.0870	964.5471	1927.1030	964.0551	12
7	962.4117	481.7095			944.4011	472.7042	P	1798.0451	899.5262	1781.0186	891.0129	1780.0345	890.5209	11
8	*1090.4703*	545.7388	1073.4437	537.2255	1072.4597	536.7335	Q	1700.9923	850.9998	1683.9658	842.4865	1682.9818	841.9945	10
9	*1187.5230*	594.2652	1170.4965	585.7519	1169.5125	585.2599	P	1572.9338	786.9705	1555.9072	778.4572	1554.9232	777.9652	9
10	*1300.6071*	650.8072	1283.5805	642.2939	1282.5965	641.8019	L	1475.8810	738.4441	1458.8545	729.9309	1457.8704	729.4389	8
11	1397.6599	699.3336	1380.6333	690.8203	1379.6493	690.3283	P	1362.7969	681.9021	1345.7704	673.3888	1344.7864	672.8968	7
12	1496.7283	748.8678	1479.7017	740.3545	1478.7177	739.8625	V	1265.7442	633.3757	1248.7176	624.8625	1247.7336	624.3704	6
13	1599.7375	800.3724	1582.7109	791.8591	1581.7269	791.3671	C	1166.6758	583.8415	1149.6492	575.3282	1148.6652	574.8362	5
14	1656.7589	828.8831	1639.7324	820.3698	1638.7484	819.8778	G	1063.6666	532.3369	1046.6400	523.8237	1045.6560	523.3316	4
15	1771.7859	886.3966	1754.7593	877.8833	1753.7753	877.3913	D	1006.6451	503.8262	989.6186	495.3129	988.6346	494.8209	3
16	1884.8699	942.9386	1867.8434	934.4253	1866.8594	933.9333	I	891.6182	446.3127	874.5916	437.7994			2
17							K	778.5341	389.7707	761.5076	381.2574			1

Figure 6.13. Representative false positive Mascot peptide identification of residues modified by PONPC through Schiff base formation.

A Mascot search identified the peptide 145-159 (FLKAQLDFYGEVR) with a PONPC Schiff adduct on K147 (A) and the peptide 238-254 (FMYFEFPQPLPVCGDIK) with a PONPC Schiff adduct on K254 (B). In both panels, an upper pane with the fragmentation spectrum showing identified ions as peaks

marked in red and a lower table with the matched b and y ion coverage, with the matching ions shown in red, are presented. Bold italic red: the ion series contributed to the score of the peptide; bold red: the number of matches in the ion series is greater than would be expected by chance; non-bold red: the number of matches in the ion series is no greater than would be expected by chance.

In summary, while the LC-MS/MS analysis aimed to detect PONPC modifications in PTEN-V5-His, the evidence did not support the presence of true PONPC modifications. Mascot failed to identify reduced PONPC Schiff adducts and only led to identification of unreduced adducts. For the latter, the observed mass shifts were inconsistent with the expected outcomes of the experimental design and likely represent artifacts or erroneous assignments rather than genuine modifications.

These findings highlighted the challenges in obtaining meaningful LC-MS/MS data and interpreting it. Indeed, evidence of PONPC adduction onto PTEN-V5-His was suggested by the SDS-PAGE gels where bands corresponding to monomeric PTEN-V5-His in samples treated with a 5:1, 10:1 and 20:1 molar ratio of PONPC:PTEN-V5-His clearly shifted towards higher molecular weights (Figure 6.2). This suggested that PONPC modifications existed in the samples but that the LC-MS/MS analysis and Mascot detection did not enable them to be identified. Several hypotheses were drawn from this to explain the difficult detection of PONPC modification: 1) Schiff base formation is a reversible mechanism and could be less stable than Michael addition (Rauniyar and Prokai, 2009, Ishii et al., 2007), making detection of Schiff adducts more difficult. This could also explain why Mascot could identify multiple HHE Michael adducts but failed to confidently identify HHE Schiff adducts; Schiff adducts could be too labile to remain intact during LC-MS/MS analysis. 2) The size of the resulting peptides could be too high to be detected. Indeed, as PONPC could only react with lysine and arginine residues, modification would have led to missed cleavage by trypsin, leading to longer peptides. Furthermore, PONPC is a relatively large molecule, adding 633 Da to a modified peptide, which further adds to the final mass of the peptide. This important additional mass could lead to a peptide that fails to be detected by LC-MS/MS with a m/z detectable range set to 350-1250 Da. 3) Phosphate ester bonds of phosphocholines easily fragment in MS/MS analyses, leading to the formation of a diagnostic ion with a m/z of 184.0733 Da corresponding to the phosphocholine headgroup of phosphatidylcholines (Hsu and Turk, 2001, Hsu and Turk, 2003). In the event of PONPC modification, the fragmentation of the ester bond of PONPC's phosphocholine by, for example, in source fragmentation, would lead to a change in the mass shift for the identified peptides, making the Mascot search unable to detect modifications, as well as a less efficient fragmentation of the peptide, ultimately leading to low quality sequencing.

To address the latter, a manual analysis of the fragmentation data was performed (Sousa et al., 2017). Using the PeakView software (SCIEX, U.S.A.), the MS/MS data was searched for

the presence of the diagnostic ion for the phosphocholine head group of PONPC (184.0733 Da) generating extracted ion chromatograms (XIC) from all of the MS/MS total ion chromatograms (TIC) of PONPC-treated samples where PONPC adducts were expected (5:1, 10:1, 20:1 molar ratios of PONPC:PTEN-V5-His) with a ± 0.1 Da mass tolerance. MS/MS spectra containing the 184.0733 ± 0.1 Da peaks were selected and *de novo* sequencing was performed, comparing identified peptide sequences to PTEN sequence.

Figure 6.14 shows an example of such *de novo* sequencing of PTEN peptides from a fragmentation spectrum extracted from the XIC of the 184.0733 ± 0.1 Da ions. It originated from a 184.077 Da ion that was present in the fragmentation data from a molecule eluted after 27.069 min, which was potentially a peptide (Figure 6.14.A). The MS/MS spectrum (Figure 6.14.B) shows the full fragmentation spectrum for this precursor of 1049.9 Da. A five amino acid-long peptide (VTPDV) was identified based on the delta mass between peaks at m/z values of 1132.4474, 1231.5253, 1346.5424, 1443.5943, 1544.6504 and 1643.7114 Da. As this peptide matched with a peptide in PTEN sequence (365-VTPDV-369), the presence of a high intensity peak at 184.077 Da suggested the presence of a PONPC adduct on PTEN. However, the identified sequence did not contain any residue that could be a target of PONPC (Lys or Arg). Therefore, identifying the full sequence of the precursor was essential to assess the possibility of PONPC modification.

Without missed cleavage, the sequence of the precursor ion would have been TVEEPSNPEASSSTSVTPDVSDNEPDHYR (peptide 350-378). Considering that the mass of the fragment ion at the C-terminal of the identified peptide was 1132.4474 Da, it was expected that the sequence downstream of the identified peptide corresponded to this mass if no missed cleavage occurred. This was validated by calculating the theoretical mass of the peptide 370-378 (SDNEPDHYR), which was 1132.4475 Da (sum of the mass of the residues composing peptide 370-378 + 19 Da corresponding to the additional -OH group on the C-terminal residue). This further confirmed that the identification of the peptide was accurate and provided evidence that there was no missed cleavage following Arg378. This also suggested that Arg378 was not adducted by PONPC. Therefore, if PONPC modification occurred, it would have been on the N-terminal part of the sequence. To identify if a missed cleavage could have occurred at Lys349, therefore suggesting that Lys349 could have undergone adduction by PONPC, the mass of possible peptides was calculated. The theoretical mass of the peptide 350-378 (TVEEPSNPEASSSTSVTPDVSDNEPDHYR) without missed cleavage was 3147.3490 Da. With a triply charged peptide, the m/z value of this peptide equalled 1049.12 Da, closely matching the mass of the precursor detected by the LC-MS/MS analysis (1049.9 Da) (Figure 6.14.B). This meant that the identified peptide

was most likely not modified by PONPC, despite the high intensity of the ion corresponding to the m/z of the phosphocholine fragment ion at 184.0766 Da.

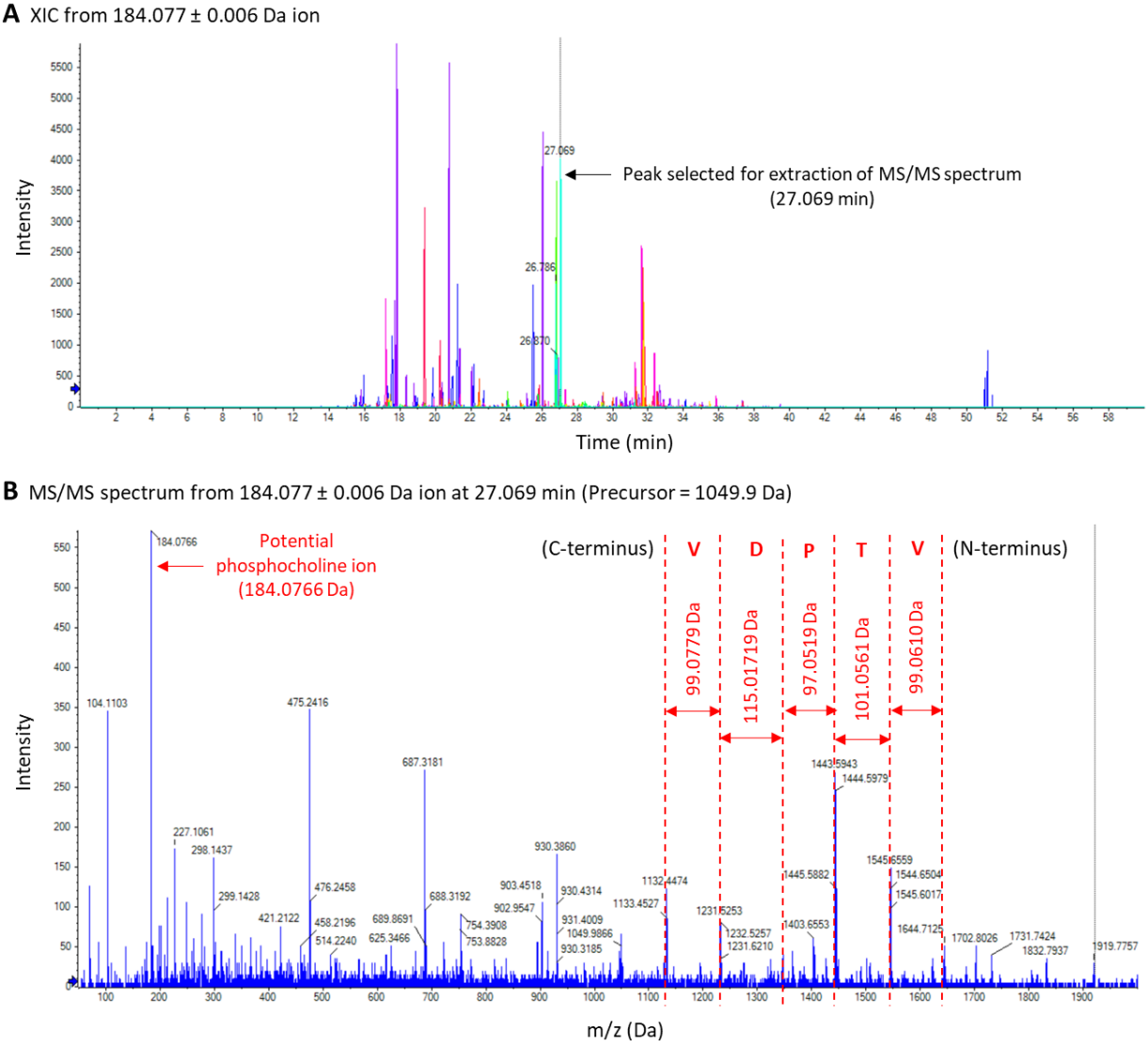

Figure 6.14. Representative *de novo* sequencing of PTEN peptides suspected to be modified by PONPC based on the identification of 184.07 Da ions corresponding to the mass of fragmented PONPC's phosphocholine group.

PTEN-V5-His was treated with PONPC at increasing molar ratios for 30 or 120 min at 37˚C. Resulting monomeric PTEN-V5-His and protein aggregates were analysed by LC-MS/MS following in-gel digestion using trypsin. Data from samples in which PTEN-V5-His was believed to be covalently modified by PONPC were manually analysed using the PeakView software (SCIEX, U.S.A.). (A) shows the XIC of 184.077 Da ions in monomeric PTEN-V5-His sample from the sample treated with a 20:1 PONPC:PTEN-V5-His ratio for 120 min, highlighting the peak selected for extraction of the MS/MS spectrum associated to the presence of the 184.0766 Da ion. (B) shows the MS/MS spectrum of the ion at m/z 1049.9 Da, identified as a peptide originating from PTEN-V5-His (peptide 365-369, VTPDV). The details of the *de novo* sequencing are shown as delta masses associated to the corresponding residue in red.

Six additional peptides were identified using the same method: peptides 34-40 (AMGFPAE), 49-54 (NIDDVV), 89-95 (PFEDHNP), 167-171 (TIPSQ), 213-217 (PQFVV), and 337-340

(FSPN) (Supplementary Figure 11). However, none of these peptides exhibited a high-intensity peak at 184.077 Da, indicating a low likelihood of modification by PONPC. Moreover, the precursor masses did not suggest any missed trypsin cleavage, further supporting that these peptides, like peptide 350-378 (VTPDV), were likely not covalently modified by PONPC. This finding invalidated the hypothesis that the Mascot search failed to detect PONPC adducts due to the loss of the phosphocholine group from PONPC. Despite SDS-PAGE gels strongly suggesting the presence of PONPC adducts in PTEN-V5-His samples treated with PONPC at molar ratios ≥ 5:1 (PONPC:PTEN-V5-His), no evidence of PONPC modification on PTEN was observed in the MS/MS data. This discrepancy suggested that the method used in this study might be inadequate. It is possible that the resulting peptides were too large, indicating that the use of an alternative digestion enzyme might be necessary to reveal potentially modified lysine and arginine residues. Alternatively, if the lack of PONPC adduct identification was due to the instability of Schiff bases, a different method would be required to identify adduction sites, potentially by stabilizing the adducts further, for instance.

6.3.4. Trials to Detect Adduction of Endogenous PTEN in MCF-7 Cells

Although LC-MS/MS analysis of HHE-treated PTEN-V5-His samples provided strong evidence for the modification of PTEN by HHE, including the identification of specific adduction sites, and despite the SDS-PAGE gels of PONPC-treated PTEN-V5-His samples suggesting that PONPC could potentially modify PTEN (despite lacking concrete evidence of PONPC modifications), the ultimate objective was to identify modifications on endogenous PTEN. This was essential to correlate the observed biological effects of HHE and PONPC on cells.

MCF-7 cells were specifically chosen for this study due to their relatively high expression of PTEN compared to HCT116 cells (Chapter 5, Figure 5.3). Given that PTEN is a low-abundance protein, it was hypothesized that utilizing the S-Trap™ system would enable the recovery of PTEN peptides, even in low abundance, as this system has been shown to be more effective in recovering peptides and identifying proteins than traditional in-solution or in-gel digestion methods (Ding et al., 2020, Ludwig et al., 2018, Yang et al., 2018b). Unfortunately, a Mascot search for human proteins did not detect PTEN among the 525 to 616 protein matches identified in lysates from untreated-, HHE- or PONPC-treated MCF-7 cells, as no peptide matches for PTEN were found using this method. In fact, the majority of proteins identified with high confidence were high abuhndance cytoskeletal proteins and metabolic enzymes (data not shown). This suggested that, despite the enhanced peptide

recovery and increased protein identification capabilities of the S-Trap™ system, the abundance of PTEN was still too low to be detected.

To address the difficulty in detecting PTEN using LC-MS/MS analysis, which may be due to its low abundance, an alternative method was employed to enrich PTEN during the sample preparation for LC-MS/MS. This method was similar to the one used for PTEN-V5-His samples. In this process, cell lysates were first separated using 8% acrylamide SDS-PAGE gels. Gel bands at the position where PTEN was expected to migrate (surrounding 50 kDa) were then excised for further analysis by LC-MS/MS after in-gel digestion with trypsin. A Mascot search was conducted to identify human proteins within these bands, which revealed between 352 and 458 proteins in the regions where PTEN would likely migrate (data not shown). PTEN was identified in almost all samples, except for one (specifically, the cell lysate of MCF-7 cells treated with 50 µM HHE). Despite this, only up to three peptide matches corresponding to PTEN were found across all samples, covering a maximum of 12% of the PTEN sequence (Table 6.8 and Figure 6.15). No HHE or PONPC modification was observed in the identified peptides.

Table 6.8. Summary of Mascot peptide identification for endogenous PTEN in HHE- and PONPC-treated MCF-7 cells.

Sample	PTEN detection	Score	Number of peptide matches (significant)	Number of peptide sequences (significant)	Sequence coverage (%)	Sequence(s)
Control	✓	32	3 (3)	3 (3)	12	YVYYYSYLLK FMYFEFPQPLPVCGDIK MMFETIPMFSGGTCNPQFVVCQLK
HHE 5 µM	✓	35	1 (1)	1 (1)	4	FMYFEFPQPLPVCGDIK
HHE 50 µM	X	N/A	N/A	N/A	N/A	N/A
PONPC 5 µM	✓	35	2 (2)	2 (2)	7	IYNLCAER MMFETIPMFSGGTCNPQFVVCQLK
PONPC 50 µM	✓	47	1 (1)	1 (1)	1	IYNLCAER

Data is representative of one biological replicate (n=1).
N/A: not applicable.

Control

Protein sequence coverage: 12%

Matched peptides shown in ***bold red***.

```
  1 MTAIIKEIVS RNKRRYQEDG FDLDLTYIYP NIIAMGFPAE RLEGVYRNNI
 51 DDVVRFLDSK HKNHYKIYNL CAERHYDTAK FNCRVAQYPF EDHNPPQLEL
101 IKPFCEDLDQ WLSEDDNHVA AIHCKAGKGR TGVMICAYLL HRGKFLKAQE
151 ALDFYGEVRT RDKKGVTIPS QRRYVYYYSY LLKNHLDYRP VALLFHKMMF
201 ETIPMFSGGT CNPQFVVCQL KVKIYSSNSG PTRREDKFMY FEFPQPLPVC
251 GDIKVEFFHK QNKMLKKDKM FHFWVNTFFI PGPEETSEKV ENGSLCDQEI
301 DSICSIERAD NDKEYLVLTL TKNDLDKANK DKANRYFSPN FKVKLYFTKT
351 VEEPSNPEAS SSTSVTPDVS DNEPDHYRYS DTTDSDPENE PFDEDQHTQI
401 TKV
```

HHE 5 µM

Protein sequence coverage: 4%

Matched peptides shown in ***bold red***.

```
  1 MTAIIKEIVS RNKRRYQEDG FDLDLTYIYP NIIAMGFPAE RLEGVYRNNI
 51 DDVVRFLDSK HKNHYKIYNL CAERHYDTAK FNCRVAQYPF EDHNPPQLEL
101 IKPFCEDLDQ WLSEDDNHVA AIHCKAGKGR TGVMICAYLL HRGKFLKAQE
151 ALDFYGEVRT RDKKGVTIPS QRRYVYYYSY LLKNHLDYRP VALLFHKMMF
201 ETIPMFSGGT CNPQFVVCQL KVKIYSSNSG PTRREDKFMY FEFPQPLPVC
251 GDIKVEFFHK QNKMLKKDKM FHFWVNTFFI PGPEETSEKV ENGSLCDQEI
301 DSICSIERAD NDKEYLVLTL TKNDLDKANK DKANRYFSPN FKVKLYFTKT
351 VEEPSNPEAS SSTSVTPDVS DNEPDHYRYS DTTDSDPENE PFDEDQHTQI
401 TKV
```

PONPC 5 µM

Protein sequence coverage: 7%

Matched peptides shown in ***bold red***.

```
  1 MTAIIKEIVS RNKRRYQEDG FDLDLTYIYP NIIAMGFPAE RLEGVYRNNI
 51 DDVVRFLDSK HKNHYKIYNL CAERHYDTAK FNCRVAQYPF EDHNPPQLEL
101 IKPFCEDLDQ WLSEDDNHVA AIHCKAGKGR TGVMICAYLL HRGKFLKAQE
151 ALDFYGEVRT RDKKGVTIPS QRRYVYYYSY LLKNHLDYRP VALLFHKMMF
201 ETIPMFSGGT CNPQFVVCQL KVKIYSSNSG PTRREDKFMY FEFPQPLPVC
251 GDIKVEFFHK QNKMLKKDKM FHFWVNTFFI PGPEETSEKV ENGSLCDQEI
301 DSICSIERAD NDKEYLVLTL TKNDLDKANK DKANRYFSPN FKVKLYFTKT
351 VEEPSNPEAS SSTSVTPDVS DNEPDHYRYS DTTDSDPENE PFDEDQHTQI
401 TKV
```

PONPC 50 µM

Protein sequence coverage: 1%

Matched peptides shown in ***bold red***.

```
  1 MTAIIKEIVS RNKRRYQEDG FDLDLTYIYP NIIAMGFPAE RLEGVYRNNI
 51 DDVVRFLDSK HKNHYKIYNL CAERHYDTAK FNCRVAQYPF EDHNPPQLEL
101 IKPFCEDLDQ WLSEDDNHVA AIHCKAGKGR TGVMICAYLL HRGKFLKAQE
151 ALDFYGEVRT RDKKGVTIPS QRRYVYYYSY LLKNHLDYRP VALLFHKMMF
201 ETIPMFSGGT CNPQFVVCQL KVKIYSSNSG PTRREDKFMY FEFPQPLPVC
251 GDIKVEFFHK QNKMLKKDKM FHFWVNTFFI PGPEETSEKV ENGSLCDQEI
301 DSICSIERAD NDKEYLVLTL TKNDLDKANK DKANRYFSPN FKVKLYFTKT
351 VEEPSNPEAS SSTSVTPDVS DNEPDHYRYS DTTDSDPENE PFDEDQHTQI
401 TKV
```

Figure 6.15. PTEN sequence coverage obtained from detection of endogenous PTEN in HHE- and PONPC-treated MCF-7 cells.

MCF-7 cells were treated with 5 or 50 µM of HHE or PONPC for 4 hours. Control MCF-7 cells were treated with vehicle (0.2% ethanol in PBS). Cell lysates were prepared as described in Materials and Methods (section 6.2.4) and kept as precipitates in methanol. Precipitated proteins were resolubilised in SDS and the protein extracts were resolved onto 8% acrylamide SDS-PAGE gels for in-gel digestion using trypsin of the band corresponding to PTEN molecular weight (~50 kDa). Samples were analysed by LC-MS/MS and sequence coverage was obtained using Mascot Deamon (Matrix Science, U.S.A.). Data is representative of one biological replicate (n=1).

6.4. Discussion

The current study attempted, for the first time, to provide evidence of lipoxidation of PTEN by HHE and PONPC. It was hypothesized that these oxidized lipids could covalently modify nucleophilic residues within PTEN's sequence, potentially disrupting its function and, in the case of HHE, its localization, as observed in previous chapters. Mass spectrometric analysis of HHE or PONPC-treated purified recombinant PTEN-V5-His identified multiple cysteine, lysine and histidine residues that were modified by HHE through Michael addition; a total of 16 residues were confidently identified as targets of HHE and the extent of the modifications were generally dependent on the HHE concentration. On the other hand, PONPC modifications were more challenging to identify. No site of adduction could be determined and only potential artifacts of PONPC modification could be detected. However, the increasing shift in PTEN-V5-His migration and the apparition of protein aggregation with increasing PONPC concentration in the SDS-PAGE and western blot analysis of PONPC-treated PTEN-V5-His strongly suggested that, similarly to HHE, PONPC could covalently modify PTEN. Both HHE and PONPC could lead to concentration- and time-dependent protein aggregation, for which levels correlated with the inhibition of PTEN phosphatase activity *in vitro*. This suggested that modification by HHE, and potentially PONPC, could have functional effects. Therefore, detecting lipoxidation of PTEN *in cellulo* was essential to firmly conclude on the importance of HHE and PONPC adduction in the cellular effects observed in previous chapters. This was attempted using two different LC-MS/MS-based methods but no evidence of HHE or PONPC covalent modification of PTEN could be found due to the lack of detection or sequence coverage of the low-abundance endogenous PTEN in the MCF-7 cell lysates for which only more abundant proteins were identified.

An important outcome of the current study was the identification of multiple sites of adduction of HHE on PTEN sequence. Being an α,β-unsaturated aldehyde like HNE and acrolein, HHE was expected to form adducts with similar residues on PTEN sequence to those identified by Shearn *et al.* and Smith (Shearn et al., 2013, Smith, 2022), which were amongst the only three studies reporting mass spectrometric analysis of PTEN lipoxidation to date. A comparative summary is presented in Table 6.9. The similarity in modified residues between HHE and HNE and acrolein was confirmed, with 9/13 sites of modifications in common with these studies. Specifically, all sites of adduction of HNE but Lys254, Lys327 and Lys344 (6/9) (Shearn et al., 2013) were also identified as sites of adduction of HHE and 9/12 residues, with the exception of Cys83, Lys327 and Lys344, identified as modified by acrolein (Smith, 2022) were also identified as modified by HHE. Interestingly, HHE-modified Lys254 was identified by Mascot Daemon but was determined to be a false positive following manual validation as the sequence coverage between Cys250

and Lys254 did not allow discrimination between the two residues and it was unlikely that trypsin could have cleaved after a modified residue (Figure 6.10), assigning the HHE modification to Cys250 instead. As Shearn *et al.* identified both Cys250 and Lys254 as modified by HNE, the modification by HHE on Lys254 could be a true positive. In the case of Cys83, this residue was only identified as modified by acrolein following digestion with chymotrypsin but not trypsin in the same study (Smith, 2022). Potentially, the yield in the peptide containing Cys83 was higher with chymotrypsin than with trypsin, implying difficulty of identification of possible modifications by HHE in the current study. Strikingly, additional sites of adduction were identified for HHE: Lys(164, 349), His(185, 376, 397) and Cys(211, 218). Amongst these new identifications of modified residues, Lys164, His185 and Lys349 were rare events only occurring at the highest molar ratios of HHE to PTEN-V5-His, suggesting that they could easily have been missed in other studies and it could not be excluded that these could also be targets of acrolein and HNE. The low frequency of detection also provided less confidence about these modifications. The same was true for Cys211, although many peptides were found to be modified by HHE on this residue in aggregated PTEN-V5-His samples. It was surprising to see that Cys218, His376 and His397 were identified as modified by HHE in multiple peptides and in various conditions while it was not detected in other studies. Taken with the lack of identification of HHE-modified Lys327 and Lys344, this suggested selectivity of different, yet similar, small reactive oxidized lipids towards PTEN residues. Apart from the selectivity, different oxidized lipids also have different reactivity. It is believed that alkenals and hydroxy- or oxo-alkenals, such as HHE, are the most reactive oxidized lipids (Viedma-Poyatos et al., 2021). This agreed with the appearance of aggregated PTEN-V5-His at concentrations of HHE generally lower than those of PONPC and the observed increase in aggregation of PTEN-V5-His with time at low ratios for HHE but not PONPC.

Similarly to the current study, the catalytic cysteine Cys124 could not be detected in either Shearn *et al*. or Smith's investigations using trypsin for protein digestion (Smith, 2022, Shearn et al., 2013). However, Smith's study used chymotrypsin as an alternative digestion enzyme in an attempt to detect this residue and it was found to be successful. Nonetheless, no modification by acrolein was found on this critical residue (Smith, 2022). Considering the possible different selectivity of acrolein and HHE, digestion using chymotrypsin might have allowed peptides containing the catalytic Cys124 to be detected and determined if HHE could modify this residue. This would have provided more insights into the mechanism by which adduction of PTEN by HHE could lead to inhibition of PTEN phosphatase activity.

Cys71, Cys250 and Cys296 were the residues undergoing HHE modification to the highest extent, suggesting that HHE had a certain selectivity towards different residues. Cysteine

residues seemed to be the preferred targets of HHE as they were generally detected more frequently than lysine or histidine residues. Generally, a low pKa, the presence of neighbouring positively charged, aromatic or H-bond donor residues, solvent accessibility and steric hindrance can influence cysteine reactivity (Weerapana et al., 2010, Gambardella et al., 2020, Kwak et al., 2010, Marino, 2014, Ramachandran et al., 2000).The presence of such abundant modification of Cys71 was very interesting. As discussed by Shearn *et al*., the analysis of the conformation of Cys71 and Cys124 (the catalytic cysteine which forms a disulfide bond with Cys71 as part of a mechanism of redox regulation) suggested that these two residues were spatially next to each other in the inactive state (Shearn et al., 2013). This ultimately implied that if Cys71 could be modified by HHE to this extent, is was likely that Cys124 could be modified as well, notably because of its low pKa (~4.5), which would make it a preferential target for reactive electrophiles (Kwak et al., 2010, Cho et al., 2004).

Table 6.9. Comparative analysis of modified PTEN by HNE, acrolein, 15d-PGJ$_2$ and HHE identified by LC-MS/MS analysis.

Study design	**Reference**	(Shearn et al., 2013)	(Smith, 2022)			(Suh et al., 2018)	Current study
	Treatment	HNE 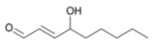	Acrolein 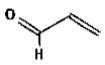			15d-PGJ$_2$ 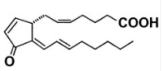	HHE 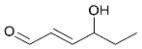
	Conditions	1:1-10:1 molar ratio (HNE:PTEN) 30 min at 37˚C	0.2:1-20:1 molar ratio (acrolein:PTEN) 10 min, 1 h, 4 h at 37˚C			30 µM, 1 h at RT (rPTEN) 10 µM, 6 h at 37˚C (MCF-7 cells)	0.1:1-20:1 molar ratio (HHE:PTEN) 30 min, 2h at 37 ˚C
	Protease	Trypsin	Trypsin	Chymotrypsin	Trypsin/Glu-C	Trypsin	Trypsin
	Digestion	In-gel	In-gel	In-gel	In-solution	In-gel	In-gel
Modified residues	K6		✓				✓
	C71	✓	✓	✓	✓		✓
	C83			✓			
	C136	✓	✓			✓	✓
	K147	✓	✓	✓			✓
	K164						✓
	H185						✓
	C211						✓
	C218						✓
	K223	✓	✓				✓
	C250	✓	✓		✓		✓
	K254	✓					
	C296				✓		✓
	C304				✓		✓
	K313	✓	✓				✓
	K327	✓		✓			
	K344	✓		✓			
	K349						✓
	H376						✓
	H397						✓

The extent of PTEN modification by HHE and PONPC seemed to be concentration- and time-dependent. This was also true for the amount of protein aggregation found in samples and, for HHE, the aggregation levels seemed to very closely match the pattern of inhibition of PTEN phosphatase activity *in vitro* up to high molar ratios of HHE to PTEN-V5-His. This suggested that the inhibition of phosphatase activity observed could rather be a loss of function due to structural changes and that HHE could act as an inhibitor of PTEN phosphatase activity at higher concentrations, although it appeared that the quantification of monomeric or aggregated PTEN-V5-His was biased by the aggregates retained in the wells of the gel for high molar ratios of treatment, which could not be quantified. In contrast,

PONPC seemed to exhibit different mechanisms of regulation of PTEN function as the inhibition of phosphatase activity appeared to be only partially linked to PTEN-V5-His aggregation, suggesting that PONPC acted as an inhibitor of PTEN activity. The observation of PTEN-V5-His aggregates was important as, according to Palumbo *et al*., computational tools revealed that PTEN mutants, involved in various pathologies, demonstrated an increased propensity for aggregation, which may contribute to disease phenotypes (Palumbo et al., 2020). This was confirmed by Claes *et al*. who showed that, under stress conditions, PTEN readily undergoes amyloid-like aggregation as a result of mutation in tumour cells and aggregation of wild-type PTEN could be observed following disruption of protein homeostasis. PTEN aggregation status was correlated with poor clinical outcome, suggesting that PTEN aggregation might be an important component of cancer cell biology (Claes et al., 2020). Aggregation of PTEN was observed following treatment with HNE and acrolein as well (Shearn et al., 2013, Smith, 2022) and the current study provided, for the first time, evidence that the same outcome could come from a much more complex molecule, the oxidized phospholipid PONPC. Unlike acrolein, HNE and HHE, PONPC cannot lead to protein cross-linking as it can only covalently modify proteins by forming Schiff bases via a single aldehyde group. The observed protein aggregates might be the result of a modification of the chemical environment of the modified proteins, possibly leading to either hydrophobic interactions between PONPC fatty acyl chains or unfolding events that expose hydrophobic regions of the proteins. However, the former seemed unlikely as PONPC aggregates in micelle-like formation (Pande et al., 2010). Considering the ability of SDS to solubilise lipids (Tan et al., 2002), micelles would be solubilized in the SDS-PAGE gel analysis and protein aggregates would not be visible if they were the result of PONPC fatty acyl chains interactions only. The ability of these reactive aldehydes to induce aggregation of PTEN *in vitro* questioned the relationship between oxidative stress and cancer, and potentially other diseases related to PTEN defects. However, no evidence was found on the ability of these oxidized lipids to induce aggregation of PTEN *in cellulo*.

In the case of HHE, it was difficult to pinpoint the origin of such aggregation based on the LC-MS/MS results as most of the identified target residues were modified by HHE in both monomeric and aggregated PTEN-V5-His samples. Moreover, PTEN-V5-His aggregates were generally identified from fewer peptide matches than monomeric PTEN-V5-His. This could be the result of the reduced amount of protein found in the gel bands corresponding to protein aggregates and increasing the load could lead to identification of more peptide matches. However, it was shown that aggregation-resulting structural changes can prevent trypsin from cleaving proteins (Zhang et al., 2023). The minimal identification of peptides in aggregates compared to monomeric form of PTEN could potentially be inevitable without

attempting to disrupt the interactions leading to aggregation. Nonetheless, modification of Cys211 stood out as a potential factor in inducing PTEN aggregation. HHE adducts on this residue were primarily identified in aggregated PTEN-V5-His samples, although more peptides including Cys211 (unmodified) could be detected in the monomeric PTEN-V5-His samples. In the study by Palumbo *et al.*, which aimed to curate known PTEN protein mutations from clinically relevant patient databases including patients with PTEN-related diseases for modification of PTEN's propensity to aggregate, it was found that PTEN's propensity to aggregate was increased with mutation of a polar or charged residue to a more hydrophobic residue within or adjacent to aggregation-prone regions (identified as residues 133–140, 174-182, 191-195, 271-280 and 315-321), or highly hydrophobic regions (Palumbo et al., 2020). Modification of polar cysteine residues (and other nucleophilic targets) by oxidized lipids would tend to increase the hydrophobicity of the residue due to the lipidic nature of the modifying molecule. Although Cys211 was not part of the aggregation-prone regions, it was flagged as a "buried" residue in PTEN crystal structure 7JUL, suggesting that its surroundings might be hydrophobic. Therefore, modification of Cys211 by HHE could lead to aggregation of PTEN. Because the LC-MS/MS analysis could not provide information on co-existing modifications of individual proteoforms of HHE-modified PTEN, it was not possible to determine the causal relationship between lipoxidation of Cys211 and PTEN aggregation, as this is most likely to result from a synergic effect of multiple co-existing modifications. Lys6, Cys71, Cys136 and Lys223 could be involved in increasing the propensity of PTEN for aggregation as it was found to be the result of missense mutations of these residues (Palumbo et al., 2020).

All identified HHE modifications were found to be through a Michael addition mechanism and no modification via Schiff base formation was confidently detected. This was in accordance with the previous reports that could not detect Schiff adducts with HNE or acrolein (Smith, 2022, Shearn et al., 2013); evidence of such adducts on PTEN remains non-existent. Although it is believed that the reaction is possible, it was shown that different oxidized lipids have different reactivity characteristics. For instance, a comparative analysis of ONE and HNE reactivity towards proteins showed that ONE could form fast Schiff bases with lysine residues while HNE-Schiff bases were not observed and only Michael adducts were detected for the latter (Lin et al., 2005a). It could not be excluded that HHE was unable to form Schiff bases with PTEN although there is evidence of HHE Schiff adducts on other proteins such as pyruvate kinase and metal-deficient Cu,Zn-superoxide dismutase (Sousa et al., 2019, Dantas et al., 2020). Therefore, a lack of stability of the Schiff adducts seemed more likely. The unstable nature of Schiff adducts could also explain why, although the structural changes observed in the SDS-PAGE and western blot analysis of PONPC-treated

PTEN-V5-His strongly suggested that PONPC could covalently bind PTEN, PONPC adducts were not detected. Furthermore, while there is extensive evidence of lipoxidation of proteins by small reactive aldehydes such as HNE, ONE, malonaldehyde or acrolein (Sousa et al., 2019, Camarillo et al., 2016, Zhao et al., 2012, Chavez et al., 2011, Smith, 2022, Dantas et al., 2020), the study of lipoxidation by truncated phospholipids is much more limited (Reis et al., 2006, Milic et al., 2012, Hoff et al., 2003), potentially because of the difficulty in detecting such modifications. Indeed, aside from the high reversibility of Schiff base formation, the mixed chemical nature of truncated oxidized phospholipid-peptide species (polar peptide and hydrophobic lipid) challenges their detection using the usual reversed phase LC-MS/MS analysis. Milic *et al.* addressed this by employing hydrophilic interaction liquid chromatography (HILIC) coupled to electrospray ionization (ESI)-MS/MS, which successfully identified peptide modifications resulting from adduction of oxidized 1-palmitoyl-2-linoleoyl-sn-glycerophosphatidylcholine, including Schiff adducts (Milic et al., 2015b). However, this method did not allow positional isomers (discriminate the exact site of adduction when the identified peptide contained multiple lipoxidation targets) to be identified. Using PONPC mixed with model peptides corresponding to the amphipathic β1 sheet sequence of apolipoprotein B-100 and traveling wave ion mobility spectrometry-MS, a technique orthogonal to HILIC and capable of separating isomeric peptide–lipid adducts, sites of adduction of PONPC via Schiff base formation could precisely be identified (Milic et al., 2015a). The use of such methods, in parallel with stabilization of Schiff adducts by reduction, could lead to a better detection of PONPC-PTEN adducts.

Although the attempt to detect PONPC adducts on PTEN was unsuccessful, the identification of numerous HHE modifications on PTEN-V5-His and the structural changes that it could undergo following treatment with PONPC suggested that both of these oxidized lipids could disrupt physiological PTEN function *in cellulo*. Evidence of lipoxidation of endogenous PTEN, would be necessary to draw firm conclusions on the relationship between lipoxidation of PTEN and biological effects. Further enrichment of endogenous PTEN from cell lysates would certainly have yielded more abundant peptides to obtain a better coverage of PTEN's sequence in the LC-MS/MS analysis. This could be achieved by immunoprecipitation, which consists in capturing the target protein from a cell lysate onto a solid support, typically using a specific antibody against the target protein. After binding, unbound proteins are washed away, and the target protein is eluted and collected. Using this method with a specific antibody targeting PTEN, the purified endogenous PTEN could then be analysed, similarly to PTEN-V5-His, using in-gel digestion followed by LC-MS/MS analysis, or even in-solution digestion if the sample purity were adequate to avoid competing contaminant peptides that could suppress weaker signals from PTEN low-abundance

peptides. This enrichment approach would allow more sensitive LC-MS/MS analysis, thereby increasing the likelihood of detecting modifications that might occur as a result of treatments with oxidized lipids such as HHE and PONPC. This was shown to be efficient in enriching PTEN from cell lysates, followed by MS analysis. This method was found to allow both quantification and detection of post-translational modifications of low abundance proteins, including PTEN (Patel et al., 2014), suggesting that it could be successful in detecting lipoxidation of endogenous PTEN. Smith performed immunoprecipitation of PTEN from untreated and acrolein-treated HCT116 and MCF-7 cells lysates in an attempt to detect modification of endogenous PTEN but the results were limited, providing no evidence of lipoxidation of the endogenous PTEN (Smith, 2022). Nonetheless, the results presented in this chapter provided useful insights into possible mechanisms by which PTEN could be altered, and future work would involve optimizing an immunoprecipitation protocol for enrichment of endogenous PTEN to confirm the possibility for HHE and PONPC to modify the protein *in cellulo*, providing more understanding of the molecular mechanisms involved in biological effects of these oxidized lipids.

Chapter 7 – General Discussion

7.1. Knowledge Gaps and Key Findings

Despite the growing recognition of the bioactivity of lipid peroxidation products (LPPs) such as HHE and PONPC, their specific effects on PTEN activity, localization and downstream signalling pathways are not fully understood. While previous studies have established that reactive aldehydes like 15d-PGJ_2, Δ12-PGJ_2, HNE or acrolein could modify PTEN leading to altered function and signalling (Covey et al., 2010, Shearn et al., 2011a, Shearn et al., 2013, Shearn et al., 2011b, Smith, 2022, Suh et al., 2018), these aldehydes only represent a few reactive LPPs amongst a wide variety (Afonso and Spickett, 2019). The potential for modifications by HHE and PONPC had not been explored previously. Given the structural similarity between HHE and HNE, it was hypothesized that HHE could impact PTEN function similarly. Most importantly, PONPC is a truncated oxidized phospholipid, a class of LPPs that had never been investigated in terms of effects on PTEN and its signalling pathway, despite its recognized biological activity and potential to affect cellular signalling pathways (Stamenkovic et al., 2021). PTEN regulates the PI3K/Akt signalling pathway by converting PIP3 to PIP2 (Georgescu et al., 1999, Walker et al., 2004, Denning et al., 2007). The extent to which LPPs interfere with PTEN's regulatory role in this pathway is not well understood. Given that dysregulation of the PI3K/Akt pathway is a hallmark of many cancers (Mundi et al., 2016, Osaki et al., 2004), elucidating how HHE and PONPC impact PTEN's ability to control Akt phosphorylation in different cancer cell lines, such as HCT116 and MCF-7 cells, could provide valuable insights into cancer biology and lead to new therapeutic strategies targeting oxidative stress and lipid peroxidation in tumour progression. Therefore, investigating the interplay between HHE, PONPC, PTEN, and Akt is crucial for filling this gap in the current literature and developing a more comprehensive understanding of the role of oxidized lipids in PTEN-related disorders. Additionally, the ability of LPPs to modify the subcellular localization of PTEN remained unexplored, while PTEN's localization is essential for its function (Denning et al., 2007, Gil et al., 2006, Gil et al., 2015, Stumpf et al., 2016). Some of the key residues regulating PTEN's function and subcellular localization are nucleophilic residues that are potential targets of the electrophilic LPPs, making the investigation of the effects of LPPs essential to the understanding of the redox regulation of PTEN and its signalling pathway.

Efforts to identify PTEN adduction by LPPs have so far focused on HNE and acrolein. Studies by Shearn *et al.* and Smith used a bottom-up proteomics approach to detect specific

sites of adduction on PTEN sequence, detecting multiple cysteine and lysine modifications on PTEN (Shearn et al., 2013, Smith, 2022). These studies provided strong evidence that HNE and acrolein could covalently modify PTEN and alter its function and structure, which could be related to the biological effects of these LPPs observed *in cellulo*. However, similar studies have not been conducted for HHE and PONPC, despite their structural and functional relevance. The current study aimed to fill this gap by investigating whether HHE and PONPC could modify PTEN at key residues, potentially altering its phosphatase activity, localization, and with downstream signalling pathways. While elucidation of adduction sites using recombinant PTEN is usually used and convenient, it may not fully reflect the reactions occurring *in cellulo* or *in vivo*, where regulatory mechanisms control lipid and oxidized lipid fate (Liu and Czaja, 2012, Ding et al., 2021, Karasawa, 2006, Chakraborti, 2003). Pathways within cells involved in lipid metabolism and detoxification may influence the extent of modification of PTEN by LPPs. Therefore, efforts were made in the current study to detect HHE- and PONPC-adduction on endogenous PTEN from MCF-7 cells to confirm whether modification of PTEN could occur in physiological conditions and identify possible critical residues targeted.

In the current study, a functional recombinant human PTEN (PTEN-V5-His) allowed confirmation that both HHE and PONPC could impair PTEN phosphatase activity *in vitro* in a concentration- and time-dependent manner. This decrease in PTEN-V5-His phosphatase activity correlated with a concentration- and time-dependent aggregation of the protein *in vitro*. This was particularly true for HHE as the levels of aggregation closely matched the degree of inhibition of PTEN-V5-His phosphatase activity, while PONPC effects seemed to be only partially correlated with aggregation of the protein, suggesting that it could lead to direct inhibition of PTEN's function.

In cells, HHE and PONPC seemed to modify levels of phosphorylation of Akt while not modifying PTEN expression levels significantly. The modification of p-Akt levels did not co-occur with modification of total Akt expression levels in cells treated with HHE, suggesting that p-Akt levels would correlate with the activation state of the PI3K/Akt pathway. On the other hand, PONPC seemed to lead to Akt degradation after prolonged exposure of HCT116 and MCF-7 cells, although more replicates would be necessary to draw firm conclusions. This suggested that increasing p-Akt levels in these conditions would not necessarily correlate with an increase in activation of the pathway but a decrease in p-Akt levels would strongly suggest a repression of the pathway. The analysis of co-localization of PTEN with the nucleus and cellular membranes suggested that HHE or PONPC, at high concentrations, could lead to accumulation of PTEN in the nucleus or at the membrane, respectively.

LC-MS/MS analysis of PTEN-V5-His identified 16 specific sites of HHE adduction on PTEN. Schiff base adducts were also detected but were suspected to be false positives. Although no specific PONPC adducts were identified, the SDS-PAGE results suggested that PTEN was modified by PONPC, as evidenced by a “smear” toward higher molecular weights. This analysis was attempted for endogenous PTEN from untreated and HHE- and PONPC-treated MCF-7 cells. However, the low abundance of endogenous PTEN in MCF-7 cells made it difficult to detect adducts *in cellulo*, highlighting the need for protein enrichment strategies in future studies. Nonetheless, these findings suggested that HHE and PONPC could significantly affect PTEN function through aggregation and chemical modification, contributing to altered cellular signalling.

7.2. Expanding the Understanding of PTEN Modulation by Lipid Peroxidation Products

In vitro, HHE and PONPC were shown to inhibit PTEN phosphatase activity. Significant decreases in PTEN activity could be observed from molar ratios as low as 1:1 (19.2 µM) and 5:1 (96 µM) (treatment:PTEN-V5-His) for PONPC and HHE, respectively. LPPs physiological concentrations can vary drastically depending on the tissue, diet, or specific pathological conditions related to increased oxidative stress such as inflammation or cancer. For instance, the intra-aortic concentrations of HHE in control C57BL/6 mice (reflecting physiological concentrations) were ~0.06 nmol/mg tissue, while it increased to 0.2 nmol/mg tissue in mice fed a fish-oil diet rich in unsaturated fatty acids (Ishikado et al., 2013). Assuming that the density of these aortas were 1.095 g/cm^3 (Yokawa et al., 2017), the corresponding concentrations of HHE in control and fish oil-fed mice would be 65 µM and 220 µM, respectively, suggesting that physiological levels of HHE could be in the micromolar range. For PONPC, physiological levels were found to be in the nanomolar range (Kimura et al., 2012) and levels can be significantly and rapidly increased in oxidative stress conditions (Sasabe et al., 2014). Concentrations of LPPs might be high in specific tissues like the heart, kidney, liver, brain and retina as these tissues generally have higher proportions of polyunsaturated phospholipids (Choi et al., 2018, Schnebelen et al., 2009).

Although the concentration of PTEN in HCT116 cells is unknown, Ibrahim *et al*. quantified the expression of PTEN in MCF-7 cells, which was found at a ratio of 0.56 fmol/µg (or nmol/g) of total proteins (Ibrahim et al., 2021). Considering that cells generally contain 200-300 g/L total proteins (Wiśniewski et al., 2014), the concentration of PTEN would be equivalent to 112 to 168 nM in MCF-7 cells. While the physiological levels of PONPC (nanomolar range) would lead to lower molar ratios (most likely to be equal or less than 1:1) in cells than those effective in reducing PTEN activity *in vitro*, HHE concentrations

(micromolar range) could be much higher than those of PTEN, fitting in the range of molar ratios effective in inhibiting PTEN function in cells. As HNE and acrolein were found to significantly reduce PTEN phosphatase activity *in vitro* at similar ratios (1:1 for HNE (Shearn et al., 2011b) and 2:1 for acrolein (Smith, 2022)), it may suggest that LPPs, in general, could inhibit PTEN function at a nanomolar to micromolar range of concentrations. This seemed plausible for acute exposure to LPPs with treatment of recombinant PTEN for 10 minutes to 4 hours with acrolein (Smith, 2022), 30 minutes for HNE (Shearn et al., 2011b) and 30 minutes to 2 hours for HHE and PONPC in this current study. As the inhibition of PTEN by HHE and PONPC was found to be time-dependent, it could also be possible for LPPs to inhibit PTEN at lower concentrations in cases of chronic exposure.

HHE-induced inhibition of PTEN function seemed to be mainly related to aggregation of PTEN-V5-His *in vitro* while PONPC-induced inhibition of PTEN phosphatase activity seemed to be partially caused by aggregation but also by direct inhibition. PTEN aggregation was not observed *in cellulo*. Indeed, western blotting of PTEN in HHE-treated HCT116 and MCF-7 cell lysates did not show bands additional to the monomeric PTEN. Cells have mechanisms to prevent aggregation of misfolded proteins, including action of chaperone proteins, which help refold misfolded proteins to prevent aggregation but also facilitate disaggregation of protein clumps for refolding or degradation (Markossian and Kurganov, 2004), or degradation through the proteasome or autophagy (Goldberg, 2003, Voss and Grune, 2007). Considering that PTEN expression levels did not seem to be significantly affected by treatments of HCT116 and MCF-7 cells with HHE or PONPC, it may be possible for PTEN to remain in cells as a LPP-modified inactive protein without aggregation, although degradation and quick turnover cannot be excluded. Evidence of HHE- and PONPC-modified endogenous PTEN in mammalian cells would be necessary to conclude definitely, which could not be achieved in the current study. However, the existence of such LPP-modified PTEN pools in mammalian cells was suggested by the detection of increased PTEN presenting carbonyls at the expected molecular weight for PTEN after treatment of HepG2 cells with 100 µM HNE for 1 hour (Shearn et al., 2011b) and MCF-7 cells with 10 µM Δ12-PGJ_2 or HNE for 30 minutes (Covey et al., 2010). This further suggested that the modified PTEN was not degraded in cells and, as the mechanisms of PTEN modification by these LPPs seemed similar to what could be observed for HHE and PONPC, it could be true for HHE- and PONPC-modified PTEN as well.

Although the identification of PONPC sites of adduction appeared to be challenging, most likely due to the instability of Schiff base formation or the possibility of PONPC degradation making its detection using MS strategies difficult, as discussed in Chapter 6, the identification of specific HHE sites of adduction on PTEN sequence was a major finding,

allowing information to be obtained on the effects of this LPP on PTEN function and structure. Amongst the identified residues modified by HHE, a few were of particular interest regarding the effects that their chemical modification could exhibit. Lys6 was found to be a key residue in membrane binding as, upon anchorage of the PBD (residues 1-14), Lys6 could interact with the phosphate group of 1,2-dioleoyl-sn-glycero-3-phosphocholine (Jang et al., 2021, Campbell et al., 2003). The identification of this modification *in vitro* could therefore correlate with an inhibition of the membrane binding of PTEN *in cellulo*. However, no significant decrease in membrane localization of PTEN was observed in the immunofluorescence work performed in the current study. Modification of Lys6 *in vitro* was only identified at the highest concentration of treatment (20:1 HHE:PTEN-V5-His molar ratio, corresponding to 384 µM), which was not physiologically relevant and >7-fold higher than the highest concentration used on MCF-7 cells. It could not be excluded that, as discussed previously, this residue could be modified *in cellulo* at lower concentrations after chronic exposure to HHE, potentially modifying PTEN membrane association. Cys71 is a well-known regulator of PTEN function due to its ability to form disulfide bonds with the catalytic Cys124 to decrease PTEN phosphatase activity (Lee et al., 2002). Moreover, its location at the active site implied that its adduction could have drastic effects on PTEN function. This was particularly important as the modification of Cys71 was one of the most frequently observed *in vitro*, suggesting a high sensitivity to LPPs. On the other hand, Cys136 lipoxidation has already been shown to be involved in inhibition of PTEN phosphatase activity and subsequent activation of the PI3K/Akt pathway as modification of this residue by 15-deoxy-Δ12-PGJ_2 was observed by MS analysis of both recombinant PTEN and endogenous PTEN from treated-MCF-7 cells (Suh et al., 2018). The detection of HHE-modified Cys136 with loss of phosphatase activity in the current study perfectly corroborated the findings of Suh *et al*. Finally, Lys313 and Lys349 are known to be methylated to down-regulate PTEN activity, increasing PI3K/Akt signalling (Nakakido et al., 2015) and decreasing PTEN-mediated DNA repair (Zhang et al., 2019). Lipoxidation of these residues could mimic the effects of methylation, especially with short-chain LPPs, and notably HHE in the case of the current study could lead to such effects via lipoxidation of Lys313 and Lys349. Hence, the biological effects of HHE on PTEN are most likely to be linked to its adduction on one or several of these key residues, regulating PTEN canonical and non-canonical functions as well as its membrane binding capacity but the relationship between PTEN lipoxidation and nuclear accumulation remains unclear. It seems reasonable to hypothesize that this could be true for PONPC as well but applying a different methodology than in the current study would be necessary to specifically identify sites of adduction of PONPC on PTEN, as discussed in Chapter 6.

For the first time, evidence that LPPs can influence PTEN subcellular localization was found, although at high concentrations. HHE could induce nuclear accumulation of PTEN whilst PONPC could retain PTEN at the cellular membranes. However, whether or not PTEN was still active at these sites was not determined. Nuclear localization of PTEN is regulated in various ways. NLS-like sequences (residues 265-269 (KKDK) together with residues 233-237 (RREDK) or 159-164 (RTRDKK)) allow Ca^{2+}-dependent nuclear import by interaction with the major vault protein (Chung et al., 2005, Minaguchi et al., 2006, Yu et al., 2002). A short N-terminal sequence (residues 20-25 (GFDLDL)) was found to be essential for PTEN cytoplasmic localization and mutations of these residues led to nuclear accumulation (Denning et al., 2007). Furthermore, PTMs such as phosphorylation, ubiquitination and SUMOylation participate in the regulation of nuclear levels of PTEN. Mono-ubiquitination of Lys13 and Lys289 (Trotman et al., 2007) and SUMOylation of Lys254 and Lys266 (Huang et al., 2012) promote nuclear accumulation. Most of these involve basic residues that could be targeted by LPPs. Amongst them, only Lys164 was identified as modified by HHE *in vitro*. If it were modified *in cellulo*, it could negatively affect PTEN nuclear import. However, there is no evidence that Lys164 alone is involved in PTEN nuclear transport as only mutation of Arg161 and Lys163 within the NLS-like sequence 159-164 (RTRDKK) were shown to decrease ability for PTEN to localize in the nucleus (Chung et al., 2005). The absence of adduction sites of HHE on PTEN sequence corresponding to residues regulating PTEN nuclear import corroborated the possibility of PTEN nuclear accumulation observed in HHE-treated MCF-7 cells as nuclear import processes were most likely not altered. However, it is still questionable whether the localization to the nucleus of PTEN following HHE treatments could be due to a response to DNA damage as discussed in Chapter 4.

For PONPC, the observation of accumulation of PTEN at the membranes fit with the hypothesis that PONPC could trap PTEN at the membrane by covalent binding as described by the lipid whisker model, which suggests that the addition of a polar oxygen atom following peroxidation of phospholipids reorients the polar acyl chain; instead of remaining buried within the membrane bilayer, it protrudes into the aqueous compartment (Greenberg et al., 2008). Nonetheless, to validate this hypothesis, it would be essential to confirm adduction of PONPC to PTEN using a different method, as discussed in Chapter 6, provide evidence that PONPC itself is retained in the membrane in a conformation suiting the lipid whisker model and that PTEN covalently interacts with it. To achieve this, a fluorescence resonance energy transfer (FRET)-based method could be useful. FRET is a physical process that depends on distance, where energy is transferred from an excited donor fluorophore to an acceptor fluorophore through long-range dipole-dipole interactions. Excitation of the fluorescent donor allows emission at a wavelength that corresponds to the excitation spectrum of the

fluorescent acceptor, which can, in turn, emit light. FRET is highly sensitive to molecular proximity, capable of measuring distances in the angstrom range (10–100 Å) and FRET efficiency decreases with the inverse sixth power of the distance between molecules (Sekar and Periasamy, 2003). In mammalian cells, expressing a tagged PTEN with a fluorescent acceptor and treating with LPPs conjugated to a fluorescent donor would enable visualization of the localization of both PTEN and LPPs as well as the interactions between them, and could be performed in live imaging, providing valuable insights into the dynamics, localization, abundance and stability of LPP-PTEN adducts *in cellulo*.

The differential localization of PTEN between HHE- and PONPC-treated was interesting as this showed that different classes of LPPs can affect PTEN differently. While the evidence of LPP-modified PTEN available in the literature all suggested similar mechanisms amongst the oxidized prostaglandins and short-chain α,β-unsaturated aldehydes (Smith, 2022, Shearn et al., 2013, Covey et al., 2010, Covey et al., 2007, Shearn et al., 2011b, Suh et al., 2018), the current study provided more insights into variations of effects. Although cellular processes might be similarly affected (inhibition of PTEN function and increase in Akt signalling, notably), the mechanisms by which they influence these mechanisms could differ and the effects on cellular processes that were not investigated in the context of lipoxidation of PTEN, like the non-canonical and nuclear functions of PTEN, could also vary.

7.3. Effects of HHE and PONPC on Cell Signalling: Consequences of PTEN Lipoxidation?

It is difficult to directly translate effects of HHE and PONPC on PTEN to a cellular context. Indeed, PTEN is not the only protein undergoing lipoxidation in cells treated with LPPs (Tanito et al., 2005, Vila et al., 2008); HHE and PONPC most likely have a wide range of targets, including proteins, phospholipids and DNA. This was illustrated by the decrease in cell viability observed using the MTT assay after treatment of HCT116 and MCF-7 cells with HHE and PONPC. If only PTEN were modified and the effect of lipoxidation of PTEN *in cellulo* were the same than *in vitro* (inhibition of its phosphatase activity), an increase in cell viability would be expected as PTEN inhibition leads to cell proliferation and survival (Sun et al., 1999). Therefore, other cellular process must have been affected by exposure of HCT116 and MCF-7 cells to HHE, particularly as it showed high toxicity for high concentrations and exposure times, and PONPC. Although the MTT assay is a method generally accepted to reflect cell viability, it is not a direct measurement of cell viability. Indeed, the MTT reagent (3-(4,5-dimethylthiazol-2-yl)-2,5-diphenyl-2H-tetrazolium bromide) is reduced in cells by oxidoreductase and dehydrogenase enzymes as well as electron donors such as NAD(P)H to form water-insoluble purple formazan. Therefore, MTT assays

measure metabolic and mitochondrial activity and, by extension, cell viability because it is proportional to these processes (Ghasemi et al., 2021). LPPs, in particular HHE in the context of the current study, could also affect metabolic and mitochondrial proteins, leading to direct interference with the assay.

Focusing on the PI3K/Akt pathway, prolonged HHE treatment in HCT116 cells seemed to increase phosphorylation of Akt at Ser473 while decreasing it at Thr308 in a concentration-dependent manner, a pattern also observed in MCF-7 cells, although the effect was dynamic, with decreased phosphorylation at both sites after 30 minutes of incubation. However, PONPC treatment seemed to result in increased phosphorylation of both Akt residues (Ser473 and Thr308) in HCT116 cells in a concentration- and time-dependent manner, whereas it was more difficult to observe a clear trend in MCF-7 cells. Additionally, these modifications of phospho-Akt levels were not related to a modification of PTEN levels as they seemed to remain stable across all conditions. Similarly, Akt levels were not co-occurring with a modification of total Akt levels in either cell lines after treatment with HHE, suggesting that the observed increases (and in some cases decreases) in phospho-Akt levels meant that the PI3K/Akt pathway was generally activated with HHE in a concentration- and time-dependent manner. The activation of the pathway could be explained by an inhibition of PTEN by HHE, as it was demonstrated by the inhibition of the recombinant PTEN-V5-His following HHE and PONPC treatments and consistent with the high susceptibility for Cys71 to modification by HHE, or could also be related to the observed increase in nuclear localization of PTEN at high concentrations of PTEN, which corresponded to the concentration leading to the most activation (50 µM). Indeed, nuclear PTEN does not contribute to the inhibition of Akt phosphorylation to the same extent as membrane-associated PTEN (Trotman et al., 2007), which could explain its activation following HHE treatments. On the other hand, PONPC seemed to decrease total Akt levels in HCT116 and MCF-7 cells after 2 and 4 hours of exposure but not 30 min, which suggested that the observed increase in phosphorylated Akt was unrelated to activation of the pathway. Interestingly, high concentrations of PONPC for 2 hours in MCF-7 cells appeared to lead to membrane localization of PTEN. If PTEN involved in the PONPC-mediated membrane-association was functional, this would most likely lead to an inhibition of Akt phosphorylation, which was generally not observed in HCT116 and MCF-7 cells, consistent with the *in vitro* inhibition of PTEN by PONPC. However, the apparent decrease in Akt levels following PONPC treatment of HCT116 and MCF-7 cells would need to be replicated to firmly determine its effect on the PI3K/Akt pathway. Most importantly, as the modifications observed were only on recombinant PTEN *in vitro*, it is necessary to confirm

adduction to endogenous PTEN to demonstrate conclusively that the effects seen were the consequence of PTEN lipoxidation.

An interesting finding regarding levels of phosphorylation of the Ser473 and Thr308 was that they could be separately regulated. As described above, while phosphorylation of Ser473 increased in a time- and concentration-dependent manner with HHE treatments in HCT116 cells, the same was not true for phosphorylation of Thr308. Akt Thr308 is phosphorylated by PDK1; the pleckstrin homology (PH) domains of both PDK1 and Akt bind to PIP3, enabling their co-localization, which allows PDK1 to phosphorylate Akt (Bozulic and Hemmings, 2009, DiNitto and Lambright, 2006). The phosphorylation of Ser473 increases Akt kinase activity and allows reactivity towards additional substrates (Alessi et al., 1996, Guertin et al., 2006) and is catalysed by mTORC2 and DNA-PK (Guertin et al., 2006, Feng et al., 2004). The functions of these phosphorylation sites were found to be distinct and non-overlapping by mutational analysis of Ser473 or Thr308 based on the transformation to an oncogenic phenotype and phosphorylation of downstream targets of Akt (Hart and Vogt, 2011). Therefore, the fine tuning of phosphorylation levels of Ser473 and Thr308 separately by LPPs could lead to different biological effects. This also suggested that PTEN was not necessarily the only protein affected by LPPs in the PI3K/Akt pathway. The above-mentioned kinases as well as the phosphatases involved in regulation, known as PHLPP and CSTP1, phosphatases dephosphorylating p-Akt (S473) (Gao et al., 2005, Zhuo et al., 2013), as well as PP2A, a phosphatase dephosphorylating p-Akt Thr308 (Kuo et al., 2008) could also be targets of LPPs, but also any effector upstream of Akt influencing its phosphorylation state. A comprehensive adductomics and functional analysis of the pathway would allow a complete understanding of the mechanisms by which Akt phosphorylation is regulated by LPPs. Additionally, the effects of HHE and PONPC on Akt phosphorylation seemed to vary between HCT116 and MCF-7 cells, suggesting that this regulation could be cell type-dependent.

7.4. Future Directions

Questions remain to be answered to draw a full picture of the mechanisms by which LPPs can influence PTEN function and PI3K cell signalling. Indeed, the sites of adduction of PONPC on PTEN sequence could not be identified and there was no evidence of adduction of PTEN by either HHE or PONPC *in cellulo*. The latter is certainly the most critical to be able to correlate effects observed *in vitro* to biological effects in cells after exposure to LPPs and specific identification of adduction sites could lead to the elucidation of the mechanism of regulation of phospho-Akt. As discussed in Chapter 6, this would require further enrichment of PTEN from cell lysates, which has successfully been achieved in other

studies. Nonetheless, an analysis of the adductome in LPP-treated cells could provide insights into possible other targets of lipoxidation in cells that could be relevant to the understanding of the regulation of Akt phosphorylation observed in HCT116 and MCF-7 cells. This is generally challenged by the relatively low abundance of most signalling proteins (Millioni et al., 2011). As antibodies targeting HHE adducts are commercially available, it could be interesting to investigate this using western blotting of lysates from HHE-treated mammalian cells or even on immunoprecipitated PTEN after such treatments. For PONPC, it could be more challenging as no specific anti-PONPC adduct antibody is available. In this case, the use of fluorescently labelled PONPC in treatments of cells and a simple analysis by SDS-PAGE with a fluorescence gel scanner could provide information on the PONPC adductome. Treatment of cells with fluorescently labelled LPPs could also allow real-time visualisation of the distribution of the LPP *in cellulo*. Indeed, the current study was limited by the absence of evidence of cellular uptake of PONPC or HHE in our experimental procedures. Mass spectrometry analysis of membrane extracts from HHE- and PONPC-treated HCT116 and MCF-7 cells would have been beneficial in confirming the cell uptake of these treatments. It was most likely that they could interact with cells as biological effects could be observed from treatments of HCT116 and MCF-7 cells but no specific data supported the internalization of these LPPs in cells. This is particularly important as the localization of the oxidized lipids would give essential information on their potential biological consequences, notably the localization of PONPC in the membrane to validate the lipid whisker model, as well as determining whether the accumulation of PTEN in the nucleus of MCF-7 cells after HHE treatment is correlated with the presence of HHE in the nucleus. The FRET-based assay discussed previously could be of great interest to identify the localization, but also the proportion, of LPP-PTEN interactions. Additionally, considering that HHE could lead to accumulation of PTEN in the nucleus, it would be of interest to investigate PTEN's non-canonical functions, especially related to DNA damage, as most of the studies to date have focused on the PI3K/Akt pathway and β-catenin signalling.

7.5. Final Conclusions

In conclusion, the current study reported, for the first time, effects of HHE and PONPC on PTEN and its downstream signalling at physiological concentrations. PTEN could be covalently modified by HHE on multiple cysteine, lysine and histidine residues. Although specific PONPC adducts could not be identified, it was suggested that PONPC could also covalently bind nucleophilic residues on PTEN sequence. HHE and PONPC both led to the inhibition of PTEN phosphatase activity *in vitro,* which could potentially be the result of lipoxidation of Cys71 or Cys136 and aggregation. Furthermore, this PTEN inhibition could be correlated with the general increase in Akt phosphorylation observed in preliminary data *in*

cellulo after treatment of HCT116 and MCF-7 cells with HHE and PONPC. These data corroborated previous investigations with other LPPs. As PONPC is part of a family of LPPs (truncated phospholipid) that had never been studied in the context of PTEN inhibition and PI3K/Akt pathway activation, the current study provided stronger generalization that LPPs were important modulators of the PI3K/Akt pathway in a PTEN-dependent manner. Last, the effects of LPPs on subcellular localization of PTEN, which had never been studied, were reported; HHE and PONPC, at high concentrations, could lead to accumulation of PTEN in the nucleus or at the membrane, respectively. This suggested that although the biological effects on the PI3K/Akt pathway seemed similar between the two LPPs, the mechanisms by which this was influenced could differ. Future studies need to examine other proteins involved in the pathway in order to draw a full picture of the effects of LPPs on cell signalling.

References

ADEMOWO, O. S., SHARMA, P., COCKWELL, P., REIS, A., CHAPPLE, I. L., GRIFFITHS, H. R. & DIAS, I. H. K. 2020. Distribution of plasma oxidised phosphatidylcholines in chronic kidney disease and periodontitis as a co-morbidity. *Free Radic Biol Med,* 146**,** 130-138.

ADEY, N. B., HUANG, L., ORMONDE, P. A., BAUMGARD, M. L., PERO, R., BYREDDY, D. V., TAVTIGIAN, S. V. & BARTEL, P. L. 2000. Threonine phosphorylation of the MMAC1/PTEN PDZ binding domain both inhibits and stimulates PDZ binding. *Cancer Res,* 60**,** 35-7.

AFONSO, C. B., SOUSA, B. C., PITT, A. R. & SPICKETT, C. M. 2018. A mass spectrometry approach for the identification and localization of small aldehyde modifications of proteins. *Arch Biochem Biophys,* 646**,** 38-45.

AFONSO, C. B. & SPICKETT, C. M. 2019. Lipoproteins as targets and markers of lipoxidation. *Redox Biol,* 23**,** 101066.

AHMED, S. F., DEB, S., PAUL, I., CHATTERJEE, A., MANDAL, T., CHATTERJEE, U. & GHOSH, M. K. 2012. The chaperone-assisted E3 ligase C terminus of Hsc70-interacting protein (CHIP) targets PTEN for proteasomal degradation. *J Biol Chem,* 287**,** 15996-6006.

AL-KHOURI, A. M., MA, Y., TOGO, S. H., WILLIAMS, S. & MUSTELIN, T. 2005. Cooperative phosphorylation of the tumor suppressor phosphatase and tensin homologue (PTEN) by casein kinases and glycogen synthase kinase 3beta. *J Biol Chem,* 280**,** 35195-202.

ALBERTS, B., JOHNSON, A., LEWIS, J., WALTER, P., RAFF, M. & ROBERTS, K. 2002. *Molecular Biology of the Cell 4th Edition: International Student Edition*, Routledge.

ALDINI, G., DOMINGUES, M. R., SPICKETT, C. M., DOMINGUES, P., ALTOMARE, A., SANCHEZ-GOMEZ, F. J., OESTE, C. L. & PEREZ-SALA, D. 2015a. Protein lipoxidation: Detection strategies and challenges. *Redox Biol,* 5**,** 253-266.

ALDINI, G., DOMINGUES, M. R., SPICKETT, C. M., DOMINGUES, P., ALTOMARE, A., SÁNCHEZ-GÓMEZ, F. J., OESTE, C. L. & PÉREZ-SALA, D. 2015b. Protein lipoxidation: Detection strategies and challenges. *Redox Biology,* 5**,** 253-266.

ALESSI, D. R., ANDJELKOVIC, M., CAUDWELL, B., CRON, P., MORRICE, N., COHEN, P. & HEMMINGS, B. A. 1996. Mechanism of activation of protein kinase B by insulin and IGF-1. *The EMBO Journal,* 15.

ALI, I. U., SCHRIML, L. M. & DEAN, M. 1999. Mutational spectra of PTEN/MMAC1 gene: a tumor suppressor with lipid phosphatase activity. *J Natl Cancer Inst,* 91**,** 1922-32.

ALIMONTI, A., CARRACEDO, A., CLOHESSY, J. G., TROTMAN, L. C., NARDELLA, C., EGIA, A., SALMENA, L., SAMPIERI, K., HAVEMAN, W. J., BROGI, E., RICHARDSON, A. L., ZHANG, J. & PANDOLFI, P. P. 2010. Subtle variations in Pten dose determine cancer susceptibility. *Nat Genet,* 42**,** 454-8.

ALLEN, R. D., SCHROEDER, C. C. & FOK, A. K. 1989. Intracellular binding of wheat germ agglutinin by Golgi complexes, phagosomes, and lysosomes of Paramecium multimicronucleatum. *J Histochem Cytochem,* 37**,** 195-202.

ALTSCHUL, S. F., MADDEN, T. L., SCHÄFFER, A. A., ZHANG, J., ZHANG, Z., MILLER, W. & LIPMAN, D. J. 1997. Gapped BLAST and PSI-BLAST: a new generation of protein database search programs. *Nucleic Acids Res,* 25**,** 3389-402.

ALTSCHUL, S. F., WOOTTON, J. C., GERTZ, E. M., AGARWALA, R., MORGULIS, A., SCHÄFFER, A. A. & YU, Y. K. 2005. Protein database searches using compositionally adjusted substitution matrices. *Febs j,* 272**,** 5101-9.

AMODIO, N., SCRIMA, M., PALAIA, L., SALMAN, A. N., QUINTIERO, A., FRANCO, R., BOTTI, G., PIROZZI, P., ROCCO, G., DE ROSA, N. & VIGLIETTO, G. 2010. Oncogenic role of the E3 ubiquitin ligase NEDD4-1, a PTEN negative regulator, in non-small-cell lung carcinomas. *Am J Pathol,* 177**,** 2622-34.

ANDRES-PONS, A., RODRIGUEZ-ESCUDERO, I., GIL, A., BLANCO, A., VEGA, A., MOLINA, M., PULIDO, R. & CID, V. J. 2007. In vivo functional analysis of the counterbalance of hyperactive phosphatidylinositol 3-kinase p110 catalytic oncoproteins by the tumor suppressor PTEN. *Cancer Res,* 67**,** 9731-9.

ARORA, N. & GHOSH, S. S. 2016. Functional characterizations of interactive recombinant PTEN–silica nanoparticles for potential biomedical applications. *RSC Advances,* 6**,** 114944-114954.

ASHRAFIZADEH, M., ZARRABI, A., SAMARGHANDIAN, S. & NAJAFI, M. 2020. PTEN: What we know of the function and regulation of this onco-suppressor factor in bladder cancer? *Eur J Pharmacol,* 881**,** 173226.

AU, W. H., MILLER-FLEMING, L., SANCHEZ-MARTINEZ, A., LEE, J. A., TWYNING, M. J., PRAG, H. A., RAIK, L., ALLEN, S. P., SHAW, P. J., FERRAIUOLO, L., MORTIBOYS, H. & WHITWORTH, A. J. 2024. Activation of the Keap1/Nrf2 pathway suppresses mitochondrial dysfunction, oxidative stress, and motor phenotypes in C9orf72 ALS/FTD models. *Life Sci Alliance,* 7.

AUNE, T. E. & AACHMANN, F. L. 2010. Methodologies to increase the transformation efficiencies and the range of bacteria that can be transformed. *Appl Microbiol Biotechnol,* 85**,** 1301-13.

AWADA, M., SOULAGE, C. O., MEYNIER, A., DEBARD, C., PLAISANCIE, P., BENOIT, B., PICARD, G., LOIZON, E., CHAUVIN, M. A., ESTIENNE, M., PERETTI, N., GUICHARDANT, M., LAGARDE, M., GENOT, C. & MICHALSKI, M. C. 2012. Dietary oxidized n-3 PUFA induce oxidative stress and inflammation: role of intestinal absorption of 4-HHE and reactivity in intestinal cells. *J Lipid Res,* 53**,** 2069-2080.

AYALA, A., MUÑOZ, M. F. & ARGÜELLES, S. 2014. Lipid peroxidation: production, metabolism, and signaling mechanisms of malondialdehyde and 4-hydroxy-2-nonenal. *Oxid Med Cell Longev,* 2014**,** 360438.

BACOT, S., BERNOUD-HUBAC, N., BADDAS, N., CHANTEGREL, B., DESHAYES, C., DOUTHEAU, A., LAGARDE, M. & GUICHARDANT, M. 2003. Covalent binding of hydroxy-alkenals 4-HDDE, 4-HHE, and 4-HNE to ethanolamine phospholipid subclasses. *J Lipid Res,* 44**,** 917-26.

BAE, E. H., CHO, S., JOO, S. Y., MA, S. K., KIM, S. H., LEE, J. & KIM, S. W. 2011. 4-Hydroxy-2-hexenal-induced apoptosis in human renal proximal tubular epithelial cells. *Nephrol Dial Transplant,* 26**,** 3866-73.

BAE, E. H., JOO, S. Y., MA, S. K., LEE, J. & KIM, S. W. 2016. Resveratrol attenuates 4-hydroxy-2-hexenal-induced oxidative stress in mouse cortical collecting duct cells. *Korean J Physiol Pharmacol,* 20**,** 229-36.

BAFFI, T. R., LORDÉN, G., WOZNIAK, J. M., FEICHTNER, A., YEUNG, W., KORNEV, A. P., KING, C. C., DEL RIO, J. C., LIMAYE, A. J., BOGOMOLOVAS, J., GOULD, C. M., CHEN, J., KENNEDY, E. J., KANNAN, N., GONZALEZ, D. J., STEFAN, E., TAYLOR, S. S. & NEWTON, A. C. 2021. mTORC2 controls the activity of PKC and Akt by phosphorylating a conserved TOR interaction motif. *Sci Signal,* 14.

BAGHBAN, R., FARAJNIA, S., RAJABIBAZL, M., GHASEMI, Y., MAFI, A., HOSEINPOOR, R., RAHBARNIA, L. & ARIA, M. 2019. Yeast Expression Systems: Overview and Recent Advances. *Mol Biotechnol,* 61**,** 365-384.

BAI, D., UENO, L. & VOGT, P. K. 2009. Akt-mediated regulation of NFkappaB and the essentialness of NFkappaB for the oncogenicity of PI3K and Akt. *Int J Cancer,* 125**,** 2863-70.

BAKER, L. M., BAKER, P. R., GOLIN-BISELLO, F., SCHOPFER, F. J., FINK, M., WOODCOCK, S. R., BRANCHAUD, B. P., RADI, R. & FREEMAN, B. A. 2007. Nitro-fatty acid reaction with glutathione and cysteine. Kinetic analysis of thiol alkylation by a Michael addition reaction. *J Biol Chem,* 282**,** 31085-93.

BALDIN, V., LUKAS, J., MARCOTE, M. J., PAGANO, M. & DRAETTA, G. 1993. Cyclin D1 is a nuclear protein required for cell cycle progression in G1. *Genes Dev,* 7**,** 812-21.

BANDYOPADHYAY, B., DAS GUPTA, T., ROY, D. & DAS GUPTA, S. K. 2012. DnaK dependence of the mycobacterial stress-responsive regulator HspR is mediated through its hydrophobic C-terminal tail. *J Bacteriol,* 194**,** 4688-97.

BARRERA, G., PIZZIMENTI, S., DAGA, M., DIANZANI, C., ARCARO, A., CETRANGOLO, G. P., GIORDANO, G., CUCCI, M. A., GRAF, M. & GENTILE, F. 2018. Lipid Peroxidation-Derived Aldehydes, 4-Hydroxynonenal and Malondialdehyde in Aging-Related Disorders. *Antioxidants (Basel),* 7.

BASSI, C., HO, J., SRIKUMAR, T., DOWLING, R. J., GORRINI, C., MILLER, S. J., MAK, T. W., NEEL, B. G., RAUGHT, B. & STAMBOLIC, V. 2013. Nuclear PTEN controls DNA repair and sensitivity to genotoxic stress. *Science,* 341**,** 395-9.

BEAUCHAMP, B. B. & RICHARDSON, C. C. 1988. A unique deoxyguanosine triphosphatase is responsible for the optA1 phenotype of Escherichia coli. *Proc Natl Acad Sci U S A,* 85**,** 2563-7.

BEN-SAHRA, I. & MANNING, B. D. 2017. mTORC1 signaling and the metabolic control of cell growth. *Curr Opin Cell Biol,* 45**,** 72-82.

BENITA, Y., KIKUCHI, H., SMITH, A. D., ZHANG, M. Q., CHUNG, D. C. & XAVIER, R. J. 2009. An integrative genomics approach identifies Hypoxia Inducible Factor-1 (HIF-1)-target genes that form the core response to hypoxia. *Nucleic Acids Research,* 37**,** 4587-4602.

BESSON, A., ROBBINS, S. M. & YONG, V. W. 1999. PTEN/MMAC1/TEP1 in signal transduction and tumorigenesis. *Eur J Biochem,* 263**,** 605-11.

BHASKAR, P. T. & HAY, N. 2007. The Two TORCs and Akt. *Developmental Cell,* 12**,** 487-502.

BILLMAN, J. H. & DIESING, A. C. 1957. Reduction of Schiff Bases with Sodium Borohydride. *The Journal of Organic Chemistry,* 22**,** 1068-1070.

BLUMENTHAL, G. M. & DENNIS, P. A. 2008. PTEN hamartoma tumor syndromes. *European Journal of Human Genetics,* 16**,** 1289-1300.

BOLANOS-GARCIA, V. M. & DAVIES, O. R. 2006. Structural analysis and classification of native proteins from E. coli commonly co-purified by immobilised metal affinity chromatography. *Biochim Biophys Acta,* 1760**,** 1304-13.

BOLTE, S. & CORDELIERES, F. P. 2006. A guided tour into subcellular colocalization analysis in light microscopy. *J Microsc,* 224**,** 213-32.

BONDA, D. J., WANG, X., PERRY, G., NUNOMURA, A., TABATON, M., ZHU, X. & SMITH, M. A. 2010. Oxidative stress in Alzheimer disease: A possibility for prevention. *Neuropharmacology,* 59**,** 290-294.

BONONI, A., BONORA, M., MARCHI, S., MISSIROLI, S., POLETTI, F., GIORGI, C., PANDOLFI, P. P. & PINTON, P. 2013. Identification of PTEN at the ER and MAMs and its regulation of Ca(2+) signaling and apoptosis in a protein phosphatase-dependent manner. *Cell Death Differ,* 20**,** 1631-43.

BONONI, A. & PINTON, P. 2015. Study of PTEN subcellular localization. *Methods,* 77-78**,** 92-103.

BORNHORST, J. A. & FALKE, J. J. 2000. Purification of proteins using polyhistidine affinity tags. *Methods Enzymol,* 326**,** 245-54.

BOZULIC, L. & HEMMINGS, B. A. 2009. PIKKing on PKB: regulation of PKB activity by phosphorylation. *Current opinion in cell biology,* 21 2**,** 256-61.

BRADLEY, M. A., XIONG-FISTER, S., MARKESBERY, W. R. & LOVELL, M. A. 2012. Elevated 4-hydroxyhexenal in Alzheimer's disease (AD) progression. *Neurobiol Aging,* 33**,** 1034-44.

BRAMBILLA, G., SCIABA, L., FAGGIN, P., MAURA, A., MARINARI, U. M., FERRO, M. & ESTERBAUER, H. 1986. Cytotoxicity, DNA fragmentation and sister-chromatid exchange in Chinese hamster ovary cells exposed to the lipid peroxidation product 4-hydroxynonenal and homologous aldehydes. *Mutat Res,* 171**,** 169-76.

BRIERCHECK, E. L., TROTTA, R., CHEN, L., HARTLAGE, A. S., COLE, J. P., COLE, T. D., MAO, C., BANERJEE, P. P., HSU, H. T., MACE, E. M., CIARLARIELLO, D., MUNDY-BOSSE, B. L., GARCIA-CAO, I., SCOVILLE, S. D., YU, L., PILARSKI, R., CARSON, W. E., 3RD, LEONE, G., PANDOLFI, P. P., YU, J., ORANGE, J. S. & CALIGIURI, M. A. 2015. PTEN is a negative regulator of NK cell cytolytic function. *J Immunol,* 194**,** 1832-40.

BURTON, G. J. & JAUNIAUX, E. 2011. Oxidative stress. *Best Pract Res Clin Obstet Gynaecol,* 25**,** 287-99.

CAMARILLO, J. M., ROSE, K. L., GALLIGAN, J. J., XU, S. & MARNETT, L. J. 2016. Covalent Modification of CDK2 by 4-Hydroxynonenal as a Mechanism of Inhibition of Cell Cycle Progression. *Chem Res Toxicol,* 29**,** 323-32.

CAMPBELL, R. B., LIU, F. & ROSS, A. H. 2003. Allosteric activation of PTEN phosphatase by phosphatidylinositol 4,5-bisphosphate. *J Biol Chem,* 278**,** 33617-20.

CARBONE, A., FIORETTI, F. M., FUCCI, L., AUSIO, J. & PISCOPO, M. 2012. High efficiency method to obtain supercoiled DNA with a commercial plasmid purification kit. *Acta Biochim Pol,* 59**,** 275-8.

CASSIDY, L., KAULICH, P. T., MAASS, S., BARTEL, J., BECHER, D. & THOLEY, A. 2021. Bottom-up and top-down proteomic approaches for the identification, characterization, and quantification of the low molecular weight proteome with focus on short open reading frame-encoded peptides. *Proteomics***,** e2100008.

CERNUDA-MOROLLÓN, E., PINEDA-MOLINA, E., CAÑADA, F. J. & PÉREZ-SALA, D. 2001. 15-Deoxy-Delta 12,14-prostaglandin J2 inhibition of NF-kappaB-DNA binding through covalent modification of the p50 subunit. *J Biol Chem,* 276**,** 35530-6.

CHAKRABORTI, S. 2003. Phospholipase A2 isoforms: A perspective. *Cellular Signalling,* 15**,** 637-665.

CHANG, C. J., MULHOLLAND, D. J., VALAMEHR, B., MOSESSIAN, S., SELLERS, W. R. & WU, H. 2008. PTEN nuclear localization is regulated by oxidative stress and mediates p53-dependent tumor suppression. *Mol Cell Biol,* 28**,** 3281-9.

CHAUVET, J. & ACHER, R. 1971. Tryptic cleavage of homoarginyl bonds in the oxidized guanidinated derivative of a bovine trypsin inhibitor (Kunitz inhibitor). *FEBS Letters,* 18**,** 265-267.

CHAVEZ, J. D., WU, J., BISSON, W. & MAIER, C. S. 2011. Site-specific proteomic analysis of lipoxidation adducts in cardiac mitochondria reveals chemical diversity of 2-alkenal adduction. *J Proteomics,* 74**,** 2417-29.

CHAZOTTE, B. 2011. Labeling membrane glycoproteins or glycolipids with fluorescent wheat germ agglutinin. *Cold Spring Harb Protoc,* 2011**,** pdb.prot5623.

CHEN, R. 2012. Bacterial expression systems for recombinant protein production: E. coli and beyond. *Biotechnol Adv,* 30**,** 1102-7.

CHEN, Z., DEMPSEY, D. R., THOMAS, S. N., HAYWARD, D., BOLDUC, D. M. & COLE, P. A. 2016. Molecular Features of Phosphatase and Tensin Homolog (PTEN) Regulation by C-terminal Phosphorylation. *J Biol Chem,* 291**,** 14160-14169.

CHEN, Z. H., ZHU, M., YANG, J., LIANG, H., HE, J., HE, S., WANG, P., KANG, X., MCNUTT, M. A., YIN, Y. & SHEN, W. H. 2014. PTEN interacts with histone H1 and controls chromatin condensation. *Cell Rep,* 8**,** 2003-2014.

CHIBAYA, L., KARIM, B., ZHANG, H. & JONES, S. N. 2021. Mdm2 phosphorylation by Akt regulates the p53 response to oxidative stress to promote cell proliferation and tumorigenesis. *Proc Natl Acad Sci U S A,* 118.

CHIURCHIÙ, V. & MACCARRONE, M. 2011. Chronic Inflammatory Disorders and Their Redox Control: From Molecular Mechanisms to Therapeutic Opportunities. *Antioxidants & Redox Signaling,* 15**,** 2605-2641.

CHO, S. H., LEE, C. H., AHN, Y., KIM, H., KIM, H., AHN, C. Y., YANG, K. S. & LEE, S. R. 2004. Redox regulation of PTEN and protein tyrosine phosphatases in H(2)O(2) mediated cell signaling. *FEBS Lett,* 560**,** 7-13.

CHOI, B. H., CHEN, Y. & DAI, W. 2013. Chromatin PTEN is involved in DNA damage response partly through regulating Rad52 sumoylation. *Cell Cycle,* 12**,** 3442-7.

CHOI, J., YIN, T., SHINOZAKI, K., LAMPE, J. W., STEVENS, J. F., BECKER, L. B. & KIM, J. 2018. Comprehensive analysis of phospholipids in the brain, heart, kidney, and liver: brain phospholipids are least enriched with polyunsaturated fatty acids. *Molecular and Cellular Biochemistry,* 442**,** 187-201.

CHOW, J. T. & SALMENA, L. 2020. Recent advances in PTEN signalling axes in cancer. *Fac Rev,* 9**,** 31.

CHOW, J. Y., BAN, M., WU, H. L., NGUYEN, F., HUANG, M., CHUNG, H., DONG, H. & CARETHERS, J. M. 2010. TGF-beta downregulates PTEN via activation of NF-kappaB in pancreatic cancer cells. *Am J Physiol Gastrointest Liver Physiol,* 298**,** G275-82.

CHOW, J. Y., CABRAL, J. A., CHANG, J. & CARETHERS, J. M. 2008a. TGFbeta modulates PTEN expression independently of SMAD signaling for growth proliferation in colon cancer cells. *Cancer Biol Ther,* 7**,** 1694-9.

CHOW, J. Y., DONG, H., QUACH, K. T., VAN NGUYEN, P. N., CHEN, K. & CARETHERS, J. M. 2008b. TGF-beta mediates PTEN suppression and cell motility through calcium-dependent PKC-alpha activation in pancreatic cancer cells. *Am J Physiol Gastrointest Liver Physiol,* 294**,** G899-905.

CHRISTINE, A., PARK, M. K., SONG, S. J. & SONG, M. S. 2022. The equilibrium of tumor suppression: DUBs as active regulators of PTEN. *Experimental & Molecular Medicine,* 54**,** 1814-1821.

CHUNG, J.-H. & ENG, C. 2005. Nuclear-Cytoplasmic Partitioning of Phosphatase and Tensin Homologue Deleted on Chromosome 10 (PTEN) Differentially Regulates the Cell Cycle and Apoptosis. *Cancer Research,* 65**,** 8096-8100.

CHUNG, J.-H., GINN-PEASE, M. E. & ENG, C. 2005. Phosphatase and Tensin Homologue Deleted on Chromosome 10 (PTEN) Has Nuclear Localization Signal–Like Sequences for Nuclear Import Mediated by Major Vault Protein. *Cancer Research,* 65**,** 4108-4116.

CLAES, F., MARITSCHNEGG, E., DE BAETS, G., SIEKIERSKA, A., RUBIO, M. S., RAMAKERS, M., MICHIELS, E., DE SMET, F., DEPREEUW, J., VERGOTE, I., VANDERSTICHELE, A., VAN DEN BROECK, A., OLBRECHT, S., HERMANS, E., AMANT, F., LAMBRECHTS, D., NILSSON, K. P. R., ROUSSEAU, F. & SCHYMKOWITZ, J. 2020. The tumor suppressor protein PTEN undergoes amyloid-like aggregation in tumor cells. *bioRxiv***,** 2020.11.30.402115.

COLZANI, M., ALDINI, G. & CARINI, M. 2013. Mass spectrometric approaches for the identification and quantification of reactive carbonyl species protein adducts. *J Proteomics,* 92**,** 28-50.

COMELLI, M., PRETIS, I., BUSO, A. & MAVELLI, I. 2018. Mitochondrial energy metabolism and signalling in human glioblastoma cell lines with different PTEN gene status. *J Bioenerg Biomembr,* 50**,** 33-52.

CONNOR, K. M., SUBBARAM, S., REGAN, K. J., NELSON, K. K., MAZURKIEWICZ, J. E., BARTHOLOMEW, P. J., APLIN, A. E., TAI, Y. T., AGUIRRE-GHISO, J., FLORES, S. C. & MELENDEZ, J. A. 2005. Mitochondrial H2O2 regulates the angiogenic phenotype via PTEN oxidation. *J Biol Chem,* 280**,** 16916-24.

COTTER, L., OZÇELIK, M., JACOB, C., PEREIRA, J. A., LOCHER, V., BAUMANN, R., RELVAS, J. B., SUTER, U. & TRICAUD, N. 2010. Dlg1-PTEN interaction regulates myelin thickness to prevent damaging peripheral nerve overmyelination. *Science,* 328**,** 1415-8.

COVEY, T. M., EDES, K., COOMBS, G. S., VIRSHUP, D. M. & FITZPATRICK, F. A. 2010. Alkylation of the tumor suppressor PTEN activates Akt and beta-catenin signaling: a mechanism linking inflammation and oxidative stress with cancer. *PLoS One,* 5**,** e13545.

COVEY, T. M., EDES, K. & FITZPATRICK, F. A. 2007. Akt activation by arachidonic acid metabolism occurs via oxidation and inactivation of PTEN tumor suppressor. *Oncogene,* 26**,** 5784-92.

COX, B. & EMILI, A. 2006. Tissue subcellular fractionation and protein extraction for use in mass-spectrometry-based proteomics. *Nat Protoc,* 1**,** 1872-8.

CRISTOBAL, A., MARINO, F., POST, H., VAN DEN TOORN, H. W. P., MOHAMMED, S. & HECK, A. J. R. 2017. Toward an Optimized Workflow for Middle-Down Proteomics. *Analytical Chemistry,* 89**,** 3318-3325.

CROSS, D. A. E., ALESSI, D. R., COHEN, P., ANDJELKOVICH, M. & HEMMINGS, B. A. 1995. Inhibition of glycogen synthase kinase-3 by insulin mediated by protein kinase B. *Nature,* 378**,** 785-789.

DAN, H. C., COOPER, M. J., COGSWELL, P. C., DUNCAN, J. A., TING, J. P. & BALDWIN, A. S. 2008. Akt-dependent regulation of NF-{kappa}B is controlled by mTOR and Raptor in association with IKK. *Genes Dev,* 22**,** 1490-500.

DANTAS, L. S., INAGUE, A., CHAVES-FILHO, A. B. & MIYAMOTO, S. 2020. Mass spectrometry dataset on apo-SOD1 modifications induced by lipid aldehydes. *Data in Brief,* 31**,** 105850.

DAS, S., DIXON, J. E. & CHO, W. 2003. Membrane-binding and activation mechanism of PTEN. *Proc Natl Acad Sci U S A,* 100**,** 7491-6.

DATTA, S. R., DUDEK, H., TAO, X., MASTERS, S., FU, H., GOTOH, Y. & GREENBERG, M. E. 1997. Akt Phosphorylation of BAD Couples Survival Signals to the Cell-Intrinsic Death Machinery. *Cell,* 91**,** 231-241.

DAVIES, S. S., MAY-ZHANG, L. S., BOUTAUD, O., AMARNATH, V., KIRABO, A. & HARRISON, D. G. 2020. Isolevuglandins as mediators of disease and the development of dicarbonyl scavengers as pharmaceutical interventions. *Pharmacol Ther,* 205**,** 107418.

DAWSON, J. E., SMITH, I. N., MARTIN, W., KHAN, K., CHENG, F. & ENG, C. 2022. Shape shifting: The multiple conformational substates of the PTEN N-terminal PIP(2) -binding domain. *Protein Sci,* 31**,** e4308.

DEMAIN, A. L. & VAISHNAV, P. 2009. Production of recombinant proteins by microbes and higher organisms. *Biotechnol Adv,* 27**,** 297-306.

DEMPSEY, D. R. & COLE, P. A. 2018. Protein Chemical Approaches to Understanding PTEN Lipid Phosphatase Regulation. *Methods Enzymol,* 607**,** 405-422.

DEMPSEY, D. R., VIENNET, T., IWASE, R., PARK, E., HENRIQUEZ, S., CHEN, Z., JELIAZKOV, J. R., PALANSKI, B. A., PHAN, K. L., COOTE, P., GRAY, J. J., ECK, M. J., GABELLI, S. B., ARTHANARI, H. & COLE, P. A. 2021. The structural basis of PTEN regulation by multi-site phosphorylation. *Nat Struct Mol Biol,* 28**,** 858-868.

DENLEY, A., GYMNOPOULOS, M., KANG, S., MITCHELL, C. & VOGT, P. K. 2009. Requirement of phosphatidylinositol(3,4,5)trisphosphate in phosphatidylinositol 3-kinase-induced oncogenic transformation. *Mol Cancer Res,* 7**,** 1132-8.

DENNING, G., JEAN-JOSEPH, B., PRINCE, C., DURDEN, D. L. & VOGT, P. K. 2007. A short N-terminal sequence of PTEN controls cytoplasmic localization and is required for suppression of cell growth. *Oncogene,* 26**,** 3930-40.

DEY, N., CROSSWELL, H. E., DE, P., PARSONS, R., PENG, Q., SU, J. D. & DURDEN, D. L. 2008. The protein phosphatase activity of PTEN regulates SRC family kinases and controls glioma migration. *Cancer Res,* 68**,** 1862-71.

DI MEO, S., REED, T. T., VENDITTI, P. & VICTOR, V. M. 2016. Role of ROS and RNS Sources in Physiological and Pathological Conditions. *Oxid Med Cell Longev,* 2016**,** 1245049.

DING, H., FAZELINIA, H., SPRUCE, L. A., WEISS, D. A., ZDERIC, S. A. & SEEHOLZER, S. H. 2020. Urine Proteomics: Evaluation of Different Sample Preparation Workflows for Quantitative, Reproducible, and Improved Depth of Analysis. *Journal of Proteome Research,* 19**,** 1857-1862.

DING, L., SUN, W., BALAZ, M., HE, A., KLUG, M., WIELAND, S., CAIAZZO, R., RAVERDY, V., PATTOU, F., LEFEBVRE, P., LODHI, I. J., STAELS, B., HEIM, M. & WOLFRUM, C. 2021. Peroxisomal β-oxidation acts as a sensor for intracellular fatty acids and regulates lipolysis. *Nature Metabolism,* 3**,** 1648-1661.

DINITTO, J. P. & LAMBRIGHT, D. G. 2006. Membrane and juxtamembrane targeting by PH and PTB domains. *Biochimica et biophysica acta,* 1761 8**,** 850-67.

DINKOVA-KOSTOVA, A. T., HOLTZCLAW, W. D., COLE, R. N., ITOH, K., WAKABAYASHI, N., KATOH, Y., YAMAMOTO, M. & TALALAY, P. 2002. Direct evidence that sulfhydryl groups of Keap1 are the sensors regulating induction of phase 2 enzymes that protect against carcinogens and oxidants. *Proc Natl Acad Sci U S A,* 99**,** 11908-13.

DUNN, K. W., KAMOCKA, M. M. & MCDONALD, J. H. 2011. A practical guide to evaluating colocalization in biological microscopy. *Am J Physiol Cell Physiol,* 300**,** C723-42.

ECKL, P. M., ORTNER, A. & ESTERBAUER, H. 1993. Genotoxic properties of 4-hydroxyalkenals and analogous aldehydes. *Mutat Res,* 290**,** 183-92.

ELLIOTT, A. D. 2020. Confocal Microscopy: Principles and Modern Practices. *Curr Protoc Cytom,* 92**,** e68.

EMANUELE JR, J. J., JIN, H., JACOBSON, B. L., CHANG, C. Y., EINSPAHR, H. M. & VILLAFRANCA, J. J. 1996. Kinetic and crystallographic studies of Escherichia coli UDP-N-acetylmuramate:L-alanine ligase. *Protein Science,* 5**,** 2566-2574.

ENDO, Y. & SAWASAKI, T. 2006. Cell-free expression systems for eukaryotic protein production. *Curr Opin Biotechnol,* 17**,** 373-80.

ESTERBAUER, H., SCHAUR, R. J. & ZOLLNER, H. 1991. Chemistry and biochemistry of 4-hydroxynonenal, malonaldehyde and related aldehydes. *Free Radic Biol Med,* 11**,** 81-128.

FARRE, J.-C., SHIRAHAMA-NODA, K., ZHANG, L., BOOHER, K. & SUBRAMANI, S. 2007. Localization of Proteins and Organelles Using Fluorescence Microscopy. *In:* CREGG, J. M. (ed.) *Pichia Protocols.* Totowa, NJ: Humana Press.

FENG, J., LIANG, J., LI, J., LI, Y., LIANG, H., ZHAO, X., MCNUTT, M. A. & YIN, Y. 2015. PTEN Controls the DNA Replication Process through MCM2 in Response to Replicative Stress. *Cell Rep,* 13**,** 1295-1303.

FENG, J., PARK, J., CRON, P., HESS, D. & HEMMINGS, B. A. 2004. Identification of a PKB/Akt Hydrophobic Motif Ser-473 Kinase as DNA-dependent Protein Kinase*♦. *Journal of Biological Chemistry,* 279**,** 41189 - 41196.

FENTON, W. A. & HORWICH, A. L. 1997. GroEL-mediated protein folding. *Protein Sci,* 6**,** 743-60.

FERNANDEZ-ACERO, T., BERTALMIO, E., LUNA, S., MINGO, J., BRAVO-PLAZA, I., RODRIGUEZ-ESCUDERO, I., MOLINA, M., PULIDO, R. & CID, V. J. 2019. Expression of Human PTEN-L in a Yeast Heterologous Model Unveils Specific N-Terminal Motifs Controlling PTEN-L Subcellular Localization and Function. *Cells,* 8.

FINE, B., HODAKOSKI, C., KOUJAK, S., SU, T., SAAL, L. H., MAURER, M., HOPKINS, B., KENIRY, M., SULIS, M. L., MENSE, S., HIBSHOOSH, H. & PARSONS, R. 2009. Activation of the PI3K pathway in cancer through inhibition of PTEN by exchange factor P-REX2a. *Science,* 325**,** 1261-5.

FORDE, J. E. & DALE, T. C. 2007. Glycogen synthase kinase 3: A key regulator of cellular fate. *Cellular and Molecular Life Sciences,* 64**,** 1930-1944.

FORMAN, H. J., TORRES, M. & FUKUTO, J. 2002. Redox signaling. *Mol Cell Biochem,* 234-235**,** 49-62.

FORMAN, H. J., URSINI, F. & MAIORINO, M. 2014. An overview of mechanisms of redox signaling. *J Mol Cell Cardiol,* 73**,** 2-9.

FORNELLI, L., AYOUB, D., AIZIKOV, K., BECK, A. & TSYBIN, Y. O. 2014. Middle-Down Analysis of Monoclonal Antibodies with Electron Transfer Dissociation Orbitrap Fourier Transform Mass Spectrometry. *Analytical Chemistry,* 86**,** 3005-3012.

FOURQUET, S., GUEROIS, R., BIARD, D. & TOLEDANO, M. B. 2010. Activation of NRF2 by nitrosative agents and H2O2 involves KEAP1 disulfide formation. *J Biol Chem,* 285**,** 8463-71.

FRITZ, K. S., GALLIGAN, J. J., SMATHERS, R. L., ROEDE, J. R., SHEARN, C. T., REIGAN, P. & PETERSEN, D. R. 2011. 4-Hydroxynonenal inhibits SIRT3 via thiol-specific modification. *Chem Res Toxicol,* 24**,** 651-62.

FRITZ, K. S., KELLERSBERGER, K. A., GOMEZ, J. D. & PETERSEN, D. R. 2012. 4-HNE adduct stability characterized by collision-induced dissociation and electron transfer dissociation mass spectrometry. *Chemical research in toxicology,* 25 4**,** 965-70.

FUMAROLA, C., BONELLI, M. A., PETRONINI, P. G. & ALFIERI, R. R. 2014. Targeting PI3K/AKT/mTOR pathway in non small cell lung cancer. *Biochem Pharmacol,* 90**,** 197-207.

FURUKAWA, M. & XIONG, Y. 2005. BTB protein Keap1 targets antioxidant transcription factor Nrf2 for ubiquitination by the Cullin 3-Roc1 ligase. *Mol Cell Biol,* 25**,** 162-71.

GAMBARDELLA, G., CATTANI, G., BOCEDI, A. & RICCI, G. 2020. New Factors Enhancing the Reactivity of Cysteines in Molten Globule-Like Structures. *Int J Mol Sci,* 21.

GAO, F., HUANG, W., ZHANG, Y., TANG, S., ZHENG, L., MA, F., WANG, Y., TANG, H. & LI, X. 2015. Hes1 promotes cell proliferation and migration by activating Bmi-1 and PTEN/Akt/GSK3β pathway in human colon cancer. *Oncotarget,* 6.

GAO, T., FURNARI, F. & NEWTON, A. C. 2005. PHLPP: a phosphatase that directly dephosphorylates Akt, promotes apoptosis, and suppresses tumor growth. *Mol Cell,* 18**,** 13-24.

GARCIA, B. A. 2010. What does the future hold for top down mass spectrometry? *Journal of the American Society for Mass Spectrometry,* 21**,** 193-202.

GAUTHIER, D. J. & LAZURE, C. 2008. Complementary methods to assist subcellular fractionation in organellar proteomics. *Expert Rev Proteomics,* 5**,** 603-17.

GELADOPOULOS, T. P., SOTIROUDIS, T. G. & EVANGELOPOULOS, A. E. 1991. A malachite green colorimetric assay for protein phosphatase activity. *Anal Biochem,* 192**,** 112-6.

GEORGESCU, M. M. 2010. PTEN Tumor Suppressor Network in PI3K-Akt Pathway Control. *Genes Cancer,* 1**,** 1170-7.

GEORGESCU, M. M., KIRSCH, K. H., AKAGI, T., SHISHIDO, T. & HANAFUSA, H. 1999. The tumor-suppressor activity of PTEN is regulated by its carboxyl-terminal region. *Proc Natl Acad Sci U S A,* 96**,** 10182-7.

GERSZON, J. & RODACKA, A. 2018. Oxidatively modified glyceraldehyde-3-phosphate dehydrogenase in neurodegenerative processes and the role of low molecular weight compounds in counteracting its aggregation and nuclear translocation. *Ageing Research Reviews,* 48**,** 21-31.

GHASEMI, M., TURNBULL, T., SEBASTIAN, S. & KEMPSON, I. 2021. The MTT Assay: Utility, Limitations, Pitfalls, and Interpretation in Bulk and Single-Cell Analysis. *Int J Mol Sci,* 22.

GHOSH, R., GILDA, J. E. & GOMES, A. V. 2014. The necessity of and strategies for improving confidence in the accuracy of western blots. *Expert Rev Proteomics,* 11**,** 549-60.

GIL, A., ANDRES-PONS, A., FERNANDEZ, E., VALIENTE, M., TORRES, J., CERVERA, J. & PULIDO, R. 2006. Nuclear localization of PTEN by a Ran-dependent mechanism enhances apoptosis: Involvement of an N-terminal nuclear localization domain and multiple nuclear exclusion motifs. *Mol Biol Cell,* 17**,** 4002-13.

GIL, A., LOPEZ, J. I. & PULIDO, R. 2016. Assessing PTEN Subcellular Localization. *Methods Mol Biol,* 1388**,** 169-86.

GIL, A., RODRIGUEZ-ESCUDERO, I., STUMPF, M., MOLINA, M., CID, V. J. & PULIDO, R. 2015. A functional dissection of PTEN N-terminus: implications in PTEN subcellular targeting and tumor suppressor activity. *PLoS One,* 10**,** e0119287.

GIMM, O., PERREN, A., WENG, L. P., MARSH, D. J., YEH, J. J., ZIEBOLD, U., GIL, E., HINZE, R., DELBRIDGE, L., LEES, J. A., MUTTER, G. L., ROBINSON, B. G., KOMMINOTH, P., DRALLE, H. & ENG, C. 2000. Differential nuclear and cytoplasmic expression of PTEN in normal thyroid tissue, and benign and malignant epithelial thyroid tumors. *Am J Pathol,* 156**,** 1693-700.

GINN-PEASE, M. E. & ENG, C. 2003. Increased nuclear phosphatase and tensin homologue deleted on chromosome 10 is associated with G0-G1 in MCF-7 cells. *Cancer Res,* 63**,** 282-6.

GIUSTARINI, D., DALLE-DONNE, I., TSIKAS, D. & ROSSI, R. 2009. Oxidative stress and human diseases: Origin, link, measurement, mechanisms, and biomarkers. *Crit Rev Clin Lab Sci,* 46**,** 241-81.

GOLDBERG, A. L. 2003. Protein degradation and protection against misfolded or damaged proteins. *Nature,* 426**,** 895-899.

GONG, L., GOVAN, J. M., EVANS, E. B., DAI, H., WANG, E., LEE, S. W., LIN, H. K., LAZAR, A. J., MILLS, G. B. & LIN, S. Y. 2015. Nuclear PTEN tumor-suppressor functions through maintaining heterochromatin structure. *Cell Cycle,* 14**,** 2323-32.

GONZÁLEZ-SANTAMARÍA, J., CAMPAGNA, M., ORTEGA-MOLINA, A., MARCOS-VILLAR, L., DE LA CRUZ-HERRERA, C. F., GONZÁLEZ, D., GALLEGO, P., LOPITZ-OTSOA, F., ESTEBAN, M., RODRÍGUEZ, M. S., SERRANO, M. & RIVAS, C. 2012. Regulation of the tumor suppressor PTEN by SUMO. *Cell Death & Disease,* 3**,** e393-e393.

GREENBERG, M. E., LI, X. M., GUGIU, B. G., GU, X., QIN, J., SALOMON, R. G. & HAZEN, S. L. 2008. The lipid whisker model of the structure of oxidized cell membranes. *J Biol Chem,* 283**,** 2385-96.

GU, J., TAMURA, M. & YAMADA, K. M. 1998. Tumor suppressor PTEN inhibits integrin- and growth factor-mediated mitogen-activated protein (MAP) kinase signaling pathways. *J Cell Biol,* 143**,** 1375-83.

GUERAUD, F., ATALAY, M., BRESGEN, N., CIPAK, A., ECKL, P. M., HUC, L., JOUANIN, I., SIEMS, W. & UCHIDA, K. 2010. Chemistry and biochemistry of lipid peroxidation products. *Free Radic Res,* 44**,** 1098-124.

GUERTIN, D. A., STEVENS, D. M., THOREEN, C. C., BURDS, A. A., KALAANY, N. Y., MOFFAT, J., BROWN, M., FITZGERALD, K. J. & SABATINI, D. M. 2006. Ablation in mice of the mTORC components raptor, rictor, or mLST8 reveals that mTORC2 is required for signaling to Akt-FOXO and PKCalpha, but not S6K1. *Developmental cell,* 11 6**,** 859-71.

HAAS-KOGAN, D., SHALEV, N., WONG, M., MILLS, G., YOUNT, G. & STOKOE, D. 1998. Protein kinase B (PKB/Akt) activity is elevated in glioblastoma cells due to mutation of the tumor suppressor PTEN/MMAC. *Current biology : CB,* 8**,** 1195-1198.

HARAYAMA, T. & RIEZMAN, H. 2018. Understanding the diversity of membrane lipid composition. *Nat Rev Mol Cell Biol,* 19**,** 281-296.

HARPER, S. & SPEICHER, D. W. 2011. Purification of proteins fused to glutathione S-transferase. *Methods Mol Biol,* 681**,** 259-80.

HARRIS, B. Z. & LIM, W. A. 2001. Mechanism and role of PDZ domains in signaling complex assembly. *J Cell Sci,* 114**,** 3219-31.

HARRISON, A. G. 2012. Pathways for Water Loss from Doubly Protonated Peptides Containing Serine or Threonine. *Journal of the American Society for Mass Spectrometry,* 23**,** 116-123.

HARRISON, K. A. & MURPHY, R. C. 1995. Isoleukotrienes are biologically active free radical products of lipid peroxidation. *J Biol Chem,* 270**,** 17273-8.

HART, J. R. & VOGT, P. K. 2011. Phosphorylation of AKT: a Mutational Analysis. *Oncotarget,* 2**,** 467 - 476.

HAUCK, A. K., ZHOU, T., HAHN, W., PETEGROSSO, R., KUANG, R., CHEN, Y. & BERNLOHR, D. A. 2018. Obesity-induced protein carbonylation in murine adipose tissue regulates the DNA-binding domain of nuclear zinc finger proteins. *J Biol Chem,* 293**,** 13464-13476.

HE, J., ZHANG, Z., OUYANG, M., YANG, F., HAO, H., LAMB, K. L., YANG, J., YIN, Y. & SHEN, W. H. 2016. PTEN regulates EG5 to control spindle architecture and chromosome congression during mitosis. *Nat Commun,* 7**,** 12355.

HE, L., FAN, C., KAPOOR, A., INGRAM, A. J., RYBAK, A. P., AUSTIN, R. C., DICKHOUT, J., CUTZ, J.-C., SCHOLEY, J. & TANG, D. 2011. α-Mannosidase 2C1 attenuates PTEN function in prostate cancer cells. *Nature Communications,* 2**,** 307.

HE, L., INGRAM, A., RYBAK, A. P. & TANG, D. 2010. Shank-interacting protein-like 1 promotes tumorigenesis via PTEN inhibition in human tumor cells. *J Clin Invest,* 120**,** 2094-108.

HEINRICH, F., CHAKRAVARTHY, S., NANDA, H., PAPA, A., PANDOLFI, P. P., ROSS, A. H., HARISHCHANDRA, R. K., GERICKE, A. & LOSCHE, M. 2015. The PTEN Tumor Suppressor Forms Homodimers in Solution. *Structure,* 23**,** 1952-1957.

HEMMINGS, B. A. & RESTUCCIA, D. F. 2012. PI3K-PKB/Akt pathway. *Cold Spring Harb Perspect Biol,* 4**,** a011189.

HETTINGER, K., VIKHANSKAYA, F., POH, M. K., LEE, M. K., DE BELLE, I., ZHANG, J. T., REDDY, S. A. & SABAPATHY, K. 2007. c-Jun promotes cellular survival by suppression of PTEN. *Cell Death Differ,* 14**,** 218-29.

HODAKOSKI, C., HOPKINS, B. D., BARROWS, D., MENSE, S. M., KENIRY, M., ANDERSON, K. E., KERN, P. A., HAWKINS, P. T., STEPHENS, L. R. & PARSONS, R. 2014. Regulation of PTEN inhibition by the pleckstrin homology domain of P-REX2 during insulin signaling and glucose homeostasis. *Proc Natl Acad Sci U S A,* 111**,** 155-60.

HOESEL, B. & SCHMID, J. A. 2013. The complexity of NF-κB signaling in inflammation and cancer. *Molecular Cancer,* 12**,** 86.

HOFF, H. F., O'NEIL, J., WU, Z., HOPPE, G. & SALOMON, R. L. 2003. Phospholipid hydroxyalkenals: biological and chemical properties of specific oxidized lipids present in atherosclerotic lesions. *Arterioscler Thromb Vasc Biol,* 23**,** 275-82.

HONG, L., LAI, M., CHEN, M., XIE, C., LIAO, R., KANG, Y. J., XIAO, C., HU, W. Y., HAN, J. & SUN, P. 2010. The miR-17-92 cluster of microRNAs confers tumorigenicity by inhibiting oncogene-induced senescence. *Cancer Res,* 70**,** 8547-57.

HONG, S. W., MOON, J. H., KIM, J. S., SHIN, J. S., JUNG, K. A., LEE, W. K., JEONG, S. Y., HWANG, J. J., LEE, S. J., SUH, Y. A., KIM, I., NAM, K. Y., HAN, S., KIM, J. E., KIM, K. P., HONG, Y. S., LEE, J. L., LEE, W. J., CHOI, E. K., LEE, J. S., JIN, D. H. & KIM, T. W. 2014. p34 is a novel regulator of the oncogenic behavior of NEDD4-1 and PTEN. *Cell Death Differ,* 21**,** 146-60.

HOPKINS, B. D., FINE, B., STEINBACH, N., DENDY, M., RAPP, Z., SHAW, J., PAPPAS, K., YU, J. S., HODAKOSKI, C., MENSE, S., KLEIN, J., PEGNO, S., SULIS, M. L., GOLDSTEIN, H., AMENDOLARA, B., LEI, L., MAURER, M., BRUCE, J., CANOLL, P., HIBSHOOSH, H. & PARSONS, R. 2013. A secreted PTEN phosphatase that enters cells to alter signaling and survival. *Science,* 341**,** 399-402.

HOU, B., XU, S., XU, Y., GAO, Q., ZHANG, C., LIU, L., YANG, H., JIANG, X. & CHE, Y. 2019. Grb2 binds to PTEN and regulates its nuclear translocation to maintain the genomic stability in DNA damage response. *Cell Death Dis,* 10**,** 546.

HOWITT, J., LACKOVIC, J., LOW, L. H., NAGUIB, A., MACINTYRE, A., GOH, C. P., CALLAWAY, J. K., HAMMOND, V., THOMAS, T., DIXON, M., PUTZ, U., SILKE, J., BARTLETT, P., YANG, B., KUMAR, S., TROTMAN, L. C. & TAN, S. S. 2012. Ndfip1 regulates nuclear Pten import in vivo to promote neuronal survival following cerebral ischemia. *J Cell Biol,* 196**,** 29-36.

HOWITT, J., LOW, L. H., PUTZ, U., DOAN, A., LACKOVIC, J., GOH, C. P., GUNNERSEN, J., SILKE, J. & TAN, S. S. 2015. Ndfip1 represses cell proliferation by controlling Pten localization and signaling specificity. *J Mol Cell Biol,* 7**,** 119-31.

HSU, F. F. & TURK, J. 2001. Structural determination of glycosphingolipids as lithiated adducts by electrospray ionization mass spectrometry using low-energy collisional-activated dissociation on a triple stage quadrupole instrument. *J Am Soc Mass Spectrom,* 12**,** 61-79.

HSU, F. F. & TURK, J. 2003. Electrospray ionization/tandem quadrupole mass spectrometric studies on phosphatidylcholines: the fragmentation processes. *J Am Soc Mass Spectrom,* 14**,** 352-63.

HUANG, J., YAN, J., ZHANG, J., ZHU, S., WANG, Y., SHI, T., ZHU, C., CHEN, C., LIU, X., CHENG, J., MUSTELIN, T., FENG, G. S., CHEN, G. & YU, J. 2012. SUMO1 modification of PTEN regulates tumorigenesis by controlling its association with the plasma membrane. *Nat Commun,* 3**,** 911.

IBRAHIM, S., LAN, C., CHABOT, C., MITSA, G., BUCHANAN, M., AGUILAR-MAHECHA, A., ELCHEBLY, M., POETZ, O., SPATZ, A., BASIK, M., BATIST, G., ZAHEDI, R. P. & BORCHERS, C. H. 2021. Precise Quantitation of PTEN by Immuno-MRM: A Tool To Resolve the Breast Cancer Biomarker Controversy. *Anal Chem,* 93**,** 10816-10824.

IHA, K., TSURUSAWA, N., TSAI, H.-Y., LIN, M.-W., SONODA, H., WATABE, S., YOSHIMURA, T. & ITO, E. 2022. Ultrasensitive ELISA detection of proteins in separated lumen and membrane fractions of cancer cell exosomes. *Analytical Biochemistry,* 654**,** 114831.

IKENOUE, T., INOKI, K., ZHAO, B. & GUAN, K. L. 2008. PTEN acetylation modulates its interaction with PDZ domain. *Cancer Res,* 68**,** 6908-12.

IM, K., MARENINOV, S., DIAZ, M. F. P. & YONG, W. H. 2019. An Introduction to Performing Immunofluorescence Staining. *Methods Mol Biol,* 1897**,** 299-311.

ISHIHAMA, Y., ODA, Y., TABATA, T., SATO, T., NAGASU, T., RAPPSILBER, J. & MANN, M. 2005. Exponentially Modified Protein Abundance Index (emPAI) for Estimation of Absolute Protein Amount in Proteomics by the Number of Sequenced Peptides per Protein*S. *Molecular & Cellular Proteomics,* 4**,** 1265-1272.

ISHII, T., YAMADA, T., MORI, T., KUMAZAWA, S., UCHIDA, K. & NAKAYAMA, T. 2007. Characterization of acrolein-induced protein cross-links. *Free Radical Research,* 41**,** 1253-1260.

ISHIKADO, A., MORINO, K., NISHIO, Y., NAKAGAWA, F., MUKOSE, A., SONO, Y., YOSHIOKA, N., KONDO, K., SEKINE, O., YOSHIZAKI, T., UGI, S., UZU, T., KAWAI, H., MAKINO, T., OKAMURA,

T., YAMAMOTO, M., KASHIWAGI, A. & MAEGAWA, H. 2013. 4-Hydroxy hexenal derived from docosahexaenoic acid protects endothelial cells via Nrf2 activation. *PLoS One,* 8**,** e69415.

ISHIKADO, A., NISHIO, Y., MORINO, K., UGI, S., KONDO, H., MAKINO, T., KASHIWAGI, A. & MAEGAWA, H. 2010. Low concentration of 4-hydroxy hexenal increases heme oxygenase-1 expression through activation of Nrf2 and antioxidative activity in vascular endothelial cells. *Biochem Biophys Res Commun,* 402**,** 99-104.

ITAKURA, K., HIROSE, T., CREA, R., RIGGS, A. D., HEYNEKER, H. L., BOLIVAR, F. & BOYER, H. W. 1977. Expression in Escherichia coli of a chemically synthesized gene for the hormone somatostatin. *Science,* 198**,** 1056-63.

JAAKKOLA, P., MOLE, D. R., TIAN, Y.-M., WILSON, M. I., GIELBERT, J., GASKELL, S. J., KRIEGSHEIM, A. V., HEBESTREIT, H. F., MUKHERJI, M. & SCHOFIELD, C. J. 2001. Targeting of HIF-α to the von Hippel-Lindau ubiquitylation complex by O2-regulated prolyl hydroxylation. *Science,* 292**,** 468-472.

JANG, H., SMITH, I. N., ENG, C. & NUSSINOV, R. 2021. The mechanism of full activation of tumor suppressor PTEN at the phosphoinositide-enriched membrane. *iScience,* 24**,** 102438.

JANG, H. D., NOH, J. Y., SHIN, J. H., LIN, J. J. & LEE, S. Y. 2013. PTEN regulation by the Akt/GSK-3β axis during RANKL signaling. *Bone,* 55**,** 126-31.

JE, J. H., LEE, J. Y., JUNG, K. J., SUNG, B., GO, E. K., YU, B. P. & CHUNG, H. Y. 2004. NF-kappaB activation mechanism of 4-hydroxyhexenal via NIK/IKK and p38 MAPK pathway. *FEBS Lett,* 566**,** 183-9.

JI, C., KOZAK, K. R. & MARNETT, L. J. 2001. IkappaB kinase, a molecular target for inhibition by 4-hydroxy-2-nonenal. *J Biol Chem,* 276**,** 18223-8.

JIA, B. & JEON, C. O. 2016. High-throughput recombinant protein expression in Escherichia coli: current status and future perspectives. *Open Biol,* 6.

JIN, H. Y., ODA, H., LAI, M., SKALSKY, R. L., BETHEL, K., SHEPHERD, J., KANG, S. G., LIU, W. H., SABOURI-GHOMI, M., CULLEN, B. R., RAJEWSKY, K. & XIAO, C. 2013. MicroRNA-17~92 plays a causative role in lymphomagenesis by coordinating multiple oncogenic pathways. *Embo j,* 32**,** 2377-91.

JOHNSTON, S. B. & RAINES, R. T. 2015a. Catalysis by the tumor-suppressor enzymes PTEN and PTEN-L. *PLoS One,* 10**,** e0116898.

JOHNSTON, S. B. & RAINES, R. T. 2015b. Conformational stability and catalytic activity of PTEN variants linked to cancers and autism spectrum disorders. *Biochemistry,* 54**,** 1576-82.

KALAMORZ, F., REICHENBACH, B., MÄRZ, W., RAK, B. & GÖRKE, B. 2007. Feedback control of glucosamine-6-phosphate synthase GlmS expression depends on the small RNA GlmZ and involves the novel protein YhbJ in Escherichia coli. *Molecular Microbiology,* 65**,** 1518-1533.

KANG, X., SONG, C., DU, X., ZHANG, C., LIU, Y., LIANG, L., HE, J., LAMB, K., SHEN, W. H. & YIN, Y. 2015. PTEN stabilizes TOP2A and regulates the DNA decatenation. *Sci Rep,* 5**,** 17873.

KAPPHAHN, R. J., BIGELOW, E. J. & FERRINGTON, D. A. 2007. Age-dependent inhibition of proteasome chymotrypsin-like activity in the retina. *Exp Eye Res,* 84**,** 646-54.

KARASAWA, K. 2006. Clinical aspects of plasma platelet-activating factor-acetylhydrolase. *Biochimica et Biophysica Acta - Molecular and Cell Biology of Lipids,* 1761**,** 1359-1372.

KARISCH, R. & NEEL, B. G. 2013. Methods to monitor classical protein-tyrosine phosphatase oxidation. *Febs j,* 280**,** 459-75.

KARKI, P. & BIRUKOV, K. G. 2020. Oxidized Phospholipids in Healthy and Diseased Lung Endothelium. *Cells,* 9.

KARKI, P., ZHANG, C. O., PROMNARES, K., LI, Y., KE, Y., BIRUKOVA, A. A. & BIRUKOV, K. G. 2023. Truncated oxidized phospholipids exacerbate endothelial dysfunction and lung injury caused by bacterial pathogens. *Cell Signal,* 109**,** 110804.

KARPIEVITCH, Y. V., POLPITIYA, A. D., ANDERSON, G. A., SMITH, R. D. & DABNEY, A. R. 2010. Liquid Chromatography Mass Spectrometry-Based Proteomics: Biological and Technological Aspects. *Ann Appl Stat,* 4**,** 1797-1823.

KATO, T., YAMADA, T., NAKAMURA, H., IGARASHI, A., ANDERS, R. A., SESAKI, H. & IIJIMA, M. 2020. The Loss of Nuclear PTEN Increases Tumorigenesis in a Preclinical Mouse Model for Hepatocellular Carcinoma. *iScience,* 23**,** 101548.

KAUR, M. & COLE, M. D. 2013. MYC Acts via the PTEN Tumor Suppressor to Elicit Autoregulation and Genome-Wide Gene Repression by Activation of the Ezh2 Methyltransferase. *Cancer Research,* 73**,** 695-705.

KE, Y., KARKI, P., KIM, J., SON, S., BERDYSHEV, E., BOCHKOV, V. N., BIRUKOVA, A. A. & BIRUKOV, K. G. 2019. Elevated truncated oxidized phospholipids as a factor exacerbating ALI in the aging lungs. *FASEB J,* 33**,** 3887-3900.

KE, Y., KARKI, P., LI, Y., PROMNARES, K., ZHANG, C. O., EGGERMAN, T. L., BOCHAROV, A. V., BIRUKOVA, A. A. & BIRUKOV, K. G. 2023. Aging-Related Accumulation of Truncated Oxidized Phospholipids Augments Infectious Lung Injury and Endothelial Dysfunction via Cluster of Differentiation 36-Dependent Mechanism. *Cells,* 12.

KEIL, P. D. B. Specificity of Proteolysis. Springer Berlin Heidelberg, 1992.

KIM, D. H., KIM, E. H., NA, H. K., SUN, Y. & SURH, Y. J. 2010a. 15-Deoxy-Delta(12,14)-prostaglandin J(2) stabilizes, but functionally inactivates p53 by binding to the cysteine 277 residue. *Oncogene,* 29**,** 2560-76.

KIM, S.-J., JUNG, H.-J. & LIM, C.-J. 2013. Reactive Oxygen Species-Dependent Down-Regulation of Tumor Suppressor Genes PTEN, USP28, DRAM, TIGAR, and CYLD Under Oxidative Stress. *Biochemical Genetics,* 51**,** 901-915.

KIM, Y., CHAY, K. O., KIM, I., SONG, Y. B., KIM, T. Y., HAN, S. J., AHN, Y., CHO, S. H., HOE, K. L., AHN, B. W., HUH, W. K. & LEE, S. R. 2011. Redox regulation of the tumor suppressor PTEN by glutaredoxin 5 and Ycp4. *Biochem Biophys Res Commun,* 407**,** 175-80.

KIM, Y., SONG, Y. B., KIM, T. Y., KIM, I., HAN, S. J., AHN, Y., CHO, S. H., CHOI, C. Y., CHAY, K. O., YANG, S. Y., AHN, B. W., HUH, W. K. & LEE, S. R. 2010b. Redox regulation of the tumor suppressor PTEN by glutathione. *FEBS Lett,* 584**,** 3550-6.

KIMBROUGH-ALLAH, M. N., MILLENA, A. C. & KHAN, S. A. 2018. Differential role of PTEN in transforming growth factor beta (TGF-beta) effects on proliferation and migration in prostate cancer cells. *Prostate,* 78**,** 377-389.

KIMURA, T., SHIBATA, Y., YAMAUCHI, K., IGARASHI, A., INOUE, S., ABE, S., FUJITA, K., UOSAKI, Y. & KUBOTA, I. 2012. Oxidized Phospholipid, 1-Palmitoyl-2-(9'-Oxo-Nonanoyl)-Glycerophosphocholine (PON-GPC), Produced in the Lung Due to Cigarette Smoking, Impairs Immune Function in Macrophages. *Lung,* 190**,** 169-182.

KOH, M. Y., SPIVAK-KROIZMAN, T. R. & POWIS, G. 2008. HIF-1 regulation: not so easy come, easy go. *Trends in Biochemical Sciences,* 33**,** 526-534.

KOTELEVETS, L., VAN HENGEL, J., BRUYNEEL, E., MAREEL, M., VAN ROY, F. & CHASTRE, E. 2001. The lipid phosphatase activity of PTEN is critical for stabilizing intercellular junctions and reverting invasiveness. *J Cell Biol,* 155**,** 1129-35.

KOTELEVETS, L., VAN HENGEL, J., BRUYNEEL, E., MAREEL, M., VAN ROY, F. & CHASTRE, E. 2005. Implication of the MAGI-1b/PTEN signalosome in stabilization of adherens junctions and suppression of invasiveness. *Faseb j,* 19**,** 115-7.

KOUL, D., JASSER, S. A., LU, Y., DAVIES, M. A., SHEN, R., SHI, Y., MILLS, G. B. & YUNG, W. K. 2002. Motif analysis of the tumor suppressor gene MMAC/PTEN identifies tyrosines critical for tumor suppression and lipid phosphatase activity. *Oncogene,* 21**,** 2357-64.

KUO, Y. C., HUANG, K. Y., YANG, C. H., YANG, Y. S., LEE, W. Y. & CHIANG, C. W. 2008. Regulation of phosphorylation of Thr-308 of Akt, cell proliferation, and survival by the B55alpha regulatory subunit targeting of the protein phosphatase 2A holoenzyme to Akt. *J Biol Chem,* 283**,** 1882-92.

KWAK, Y. D., MA, T., DIAO, S., ZHANG, X., CHEN, Y., HSU, J., LIPTON, S. A., MASLIAH, E., XU, H. & LIAO, F. F. 2010. NO signaling and S-nitrosylation regulate PTEN inhibition in neurodegeneration. *Mol Neurodegener,* 5**,** 49.

LANDETA, C., BOYD, D. & BECKWITH, J. 2018. Disulfide bond formation in prokaryotes. *Nat Microbiol,* 3**,** 270-280.

LAURORA, S., TAMAGNO, E., BRIATORE, F., BARDINI, P., PIZZIMENTI, S., TOALDO, C., REFFO, P., COSTELLI, P., DIANZANI, M. U., DANNI, O. & BARRERA, G. 2005. 4-Hydroxynonenal modulation of p53 family gene expression in the SK-N-BE neuroblastoma cell line. *Free Radical Biology and Medicine,* 38**,** 215-225.

LEE, D. Y., LEE, S. Y., YUN, S. H., JEONG, J. W., KIM, J. H., KIM, H. W., CHOI, J. S., KIM, G. D., JOO, S. T., CHOI, I. & HUR, S. J. 2022. Review of the Current Research on Fetal Bovine Serum and the Development of Cultured Meat. *Food Sci Anim Resour,* 42**,** 775-799.

LEE, J. O., YANG, H., GEORGESCU, M. M., DI CRISTOFANO, A., MAEHAMA, T., SHI, Y., DIXON, J. E., PANDOLFI, P. & PAVLETICH, N. P. 1999. Crystal structure of the PTEN tumor suppressor: implications for its phosphoinositide phosphatase activity and membrane association. *Cell,* 99**,** 323-34.

LEE, J. Y., JE, J. H., JUNG, K. J., YU, B. P. & CHUNG, H. Y. 2004a. Induction of endothelial iNOS by 4-hydroxyhexenal through NF-kappaB activation. *Free Radic Biol Med,* 37**,** 539-48.

LEE, J. Y., JE, J. H., KIM, D. H., CHUNG, S. W., ZOU, Y., KIM, N. D., AE YOO, M., SUCK BAIK, H., YU, B. P. & CHUNG, H. Y. 2004b. Induction of endothelial apoptosis by 4-hydroxyhexenal. *Eur J Biochem,* 271**,** 1339-47.

LEE, M. S., JEONG, M. H., LEE, H. W., HAN, H. J., KO, A., HEWITT, S. M., KIM, J. H., CHUN, K. H., CHUNG, J. Y., LEE, C., CHO, H. & SONG, J. 2015. PI3K/AKT activation induces PTEN ubiquitination and destabilization accelerating tumourigenesis. *Nat Commun,* 6**,** 7769.

LEE, S. R., YANG, K. S., KWON, J., LEE, C., JEONG, W. & RHEE, S. G. 2002. Reversible inactivation of the tumor suppressor PTEN by H2O2. *J Biol Chem,* 277**,** 20336-42.

LESLIE, N. R., BENNETT, D., LINDSAY, Y. E., STEWART, H., GRAY, A. & DOWNES, C. P. 2003. Redox regulation of PI 3-kinase signalling via inactivation of PTEN. *EMBO J,* 22**,** 5501-10.

LESLIE, N. R., KRIPLANI, N., HERMIDA, M. A., ALVAREZ-GARCIA, V. & WISE, H. M. 2016. The PTEN protein: cellular localization and post-translational regulation. *Biochem Soc Trans,* 44**,** 273-8.

LI, C., CHENG, L., WU, H., HE, P., ZHANG, Y., YANG, Y., CHEN, J. & CHEN, M. 2018a. Activation of the KEAP1-NRF2-ARE signaling pathway reduces oxidative stress in Hep2 cells. *Mol Med Rep,* 18**,** 2541-2550.

LI, D. M. & SUN, H. 1997. TEP1, encoded by a candidate tumor suppressor locus, is a novel protein tyrosine phosphatase regulated by transforming growth factor beta. *Cancer Res,* 57**,** 2124-9.

LI, G., YANG, J., YANG, C., ZHU, M., JIN, Y., MCNUTT, M. A. & YIN, Y. 2018b. PTENalpha regulates mitophagy and maintains mitochondrial quality control. *Autophagy,* 14**,** 1742-1760.

LI, J., YEN, C., LIAW, D., PODSYPANINA, K., BOSE, S., WANG, S. I., PUC, J., MILIARESIS, C., RODGERS, L., MCCOMBIE, R., BIGNER, S. H., GIOVANELLA, B. C., ITTMANN, M., TYCKO, B., HIBSHOOSH, H., WIGLER, M. H. & PARSONS, R. 1997. PTEN, a putative protein tyrosine phosphatase gene mutated in human brain, breast, and prostate cancer. *Science,* 275**,** 1943-7.

LI, M. & ZHANG, P. 2009. The function of APC/CCdh1 in cell cycle and beyond. *Cell Division,* 4**,** 2.

LI, Y., LOW, L. H., PUTZ, U., GOH, C. P., TAN, S. S. & HOWITT, J. 2014. Rab5 and Ndfip1 are involved in Pten ubiquitination and nuclear trafficking. *Traffic,* 15**,** 749-61.

LI, Z., DONG, X., WANG, Z., LIU, W., DENG, N., DING, Y., TANG, L., HLA, T., ZENG, R., LI, L. & WU, D. 2005. Regulation of PTEN by Rho small GTPases. *Nat Cell Biol,* 7**,** 399-404.

LIANG, H., CHEN, X., YIN, Q., RUAN, D., ZHAO, X., ZHANG, C., MCNUTT, M. A. & YIN, Y. 2017. PTENbeta is an alternatively translated isoform of PTEN that regulates rDNA transcription. *Nat Commun,* 8**,** 14771.

LIAW, D., MARSH, D. J., LI, J., DAHIA, P. L., WANG, S. I., ZHENG, Z., BOSE, S., CALL, K. M., TSOU, H. C., PEACOCKE, M., ENG, C. & PARSONS, R. 1997. Germline mutations of the PTEN gene in Cowden disease, an inherited breast and thyroid cancer syndrome. *Nat Genet,* 16**,** 64-7.

LIBEREK, K., MARSZALEK, J., ANG, D., GEORGOPOULOS, C. & ZYLICZ, M. 1991. Escherichia coli DnaJ and GrpE heat shock proteins jointly stimulate ATPase activity of DnaK. *Proc Natl Acad Sci U S A,* 88**,** 2874-8.

LIGER, D., MASSON, A., BLANOT, D., VAN HEIJENOORT, J. & PARQUET, C. 2005. Over-production, Purification and Properties of the Uridine-diphosphate-N -Acetylmuramate: l-alanine Ligase from Escherichia coli. *European Journal of Biochemistry,* 230**,** 80-87.

LIN, D., LEE, H.-G., LIU, Q., PERRY, G., SMITH, M. A. & SAYRE, L. M. 2005a. 4-Oxo-2-nonenal is both more neurotoxic and more protein reactive than 4-hydroxy-2-nonenal. *Chemical research in toxicology,* 18 8**,** 1219-31.

LIN, D., LEE, H. G., LIU, Q., PERRY, G., SMITH, M. A. & SAYRE, L. M. 2005b. 4-Oxo-2-nonenal is both more neurotoxic and more protein reactive than 4-hydroxy-2-nonenal. *Chem Res Toxicol,* 18**,** 1219-31.

LIN, R., XIA, S., SHAN, C., CHEN, D., LIU, Y., GAO, X., WANG, M., KANG, H. B., PAN, Y., LIU, S., CHUNG, Y. R., ABDEL-WAHAB, O., MERGHOUB, T., ROSSI, M., KUDCHADKAR, R. R., LAWSON, D. H., KHURI, F. R., LONIAL, S. & CHEN, J. 2018. The Dietary Supplement Chondroitin-4-Sulfate Exhibits Oncogene-Specific Pro-tumor Effects on BRAF V600E Melanoma Cells. *Mol Cell,* 69**,** 923-937 e8.

LINGAPPAN, K. 2018. NF-κB in oxidative stress. *Current Opinion in Toxicology,* 7**,** 81-86.

LIU, F., WAGNER, S., CAMPBELL, R. B., NICKERSON, J. A., SCHIFFER, C. A. & ROSS, A. H. 2005a. PTEN enters the nucleus by diffusion. *J Cell Biochem,* 96**,** 221-34.

LIU, J., LI, W., CHEN, R. & MCINTYRE, T. M. 2013. Circulating biologically active oxidized phospholipids show on-going and increased oxidative stress in older male mice. *Redox Biol,* 1**,** 110-4.

LIU, J. L., MAO, Z., LAFORTUNE, T. A., ALONSO, M. M., GALLICK, G. E., FUEYO, J. & YUNG, W. K. 2007. Cell cycle-dependent nuclear export of phosphatase and tensin homologue tumor suppressor is regulated by the phosphoinositide-3-kinase signaling cascade. *Cancer Res,* 67**,** 11054-63.

LIU, J. L., SHENG, X., HORTOBAGYI, Z. K., MAO, Z., GALLICK, G. E. & YUNG, W. K. 2005b. Nuclear PTEN-mediated growth suppression is independent of Akt down-regulation. *Mol Cell Biol,* 25**,** 6211-24.

LIU, K. & CZAJA, M. J. 2012. Regulation of lipid stores and metabolism by lipophagy. *Cell Death and Differentiation,* 20**,** 3-11.

LOIDL-STAHLHOFEN, A., HANNEMANN, K. & SPITELLER, G. 1994. Generation of alpha-hydroxyaldehydic compounds in the course of lipid peroxidation. *Biochim Biophys Acta,* 1213**,** 140-8.

LOPACHIN, R. M., GAVIN, T., PETERSEN, D. R. & BARBER, D. S. 2009. Molecular Mechanisms of 4-Hydroxy-2-nonenal and Acrolein Toxicity: Nucleophilic Targets and Adduct Formation. *Chemical Research in Toxicology,* 22**,** 1499-1508.

LOVELL, M. A., BRADLEY, M. A. & FISTER, S. X. 2012. 4-Hydroxyhexenal (HHE) impairs glutamate transport in astrocyte cultures. *J Alzheimers Dis,* 32**,** 139-46.

LU, J., WU, T., ZHANG, B., LIU, S., SONG, W., QIAO, J. & RUAN, H. 2021. Types of nuclear localization signals and mechanisms of protein import into the nucleus. *Cell Communication and Signaling,* 19**,** 60.

LUCENA-AGUILAR, G., SANCHEZ-LOPEZ, A. M., BARBERAN-ACEITUNO, C., CARRILLO-AVILA, J. A., LOPEZ-GUERRERO, J. A. & AGUILAR-QUESADA, R. 2016. DNA Source Selection for Downstream Applications Based on DNA Quality Indicators Analysis. *Biopreserv Biobank,* 14**,** 264-70.

LUCIANO, J., FOULQUIER, E., FANTINO, J. R., GALINIER, A. & POMPEO, F. 2009. Characterization of YvcJ, a conserved P-loop-containing protein, and its implication in competence in Bacillus subtilis. *J Bacteriol,* 191**,** 1556-64.

LUDWIG, K. R., SCHROLL, M. M. & HUMMON, A. B. 2018. Comparison of In-Solution, FASP, and S-Trap Based Digestion Methods for Bottom-Up Proteomic Studies. *Journal of Proteome Research,* 17**,** 2480-2490.

LYNCH, E. D., OSTERMEYER, E. A., LEE, M. K., ARENA, J. F., JI, H., DANN, J., SWISSHELM, K., SUCHARD, D., MACLEOD, P. M., KVINNSLAND, S., GJERTSEN, B. T., HEIMDAL, K., LUBS, H., MOLLER, P. & KING, M. C. 1997. Inherited mutations in PTEN that are associated with breast cancer, cowden disease, and juvenile polyposis. *Am J Hum Genet,* 61**,** 1254-60.

MA, J., BENITEZ, J. A., LI, J., MIKI, S., PONTE DE ALBUQUERQUE, C., GALATRO, T., ORELLANA, L., ZANCA, C., REED, R., BOYER, A., KOGA, T., VARKI, N. M., FENTON, T. R., NAGAHASHI MARIE, S. K., LINDAHL, E., GAHMAN, T. C., SHIAU, A. K., ZHOU, H., DEGROOT, J., SULMAN, E. P., CAVENEE, W. K., KOLODNER, R. D., CHEN, C. C. & FURNARI, F. B. 2019. Inhibition of Nuclear PTEN Tyrosine Phosphorylation Enhances Glioma Radiation Sensitivity through Attenuated DNA Repair. *Cancer Cell,* 35**,** 504-518.e7.

MA, Q. 2013. Role of nrf2 in oxidative stress and toxicity. *Annu Rev Pharmacol Toxicol,* 53**,** 401-26.

MADAN, D., LIN, Z. & RYE, H. S. 2008. Triggering protein folding within the GroEL-GroES complex. *J Biol Chem,* 283**,** 32003-13.

MADDIKA, S., KAVELA, S., RANI, N., PALICHARLA, V. R., POKORNY, J. L., SARKARIA, J. N. & CHEN, J. 2011. WWP2 is an E3 ubiquitin ligase for PTEN. *Nat Cell Biol,* 13**,** 728-33.

MAEHAMA, T. & DIXON, J. E. 1998. The tumor suppressor, PTEN/MMAC1, dephosphorylates the lipid second messenger, phosphatidylinositol 3,4,5-trisphosphate. *J Biol Chem,* 273**,** 13375-8.

MAEHAMA, T., TAYLOR, G. S. & DIXON, J. E. 2001. PTEN and Myotubularin: Novel Phosphoinositide Phosphatases. *Annual Review of Biochemistry,* 70**,** 247-279.

MAEHAMA, T., TAYLOR, G. S., SLAMA, J. T. & DIXON, J. E. 2000. A sensitive assay for phosphoinositide phosphatases. *Anal Biochem,* 279**,** 248-50.

MAIER, C. S., CHAVEZ, J., WANG, J. & WU, J. 2010. Chapter 16 - Protein Adducts of Aldehydic Lipid Peroxidation Products: Identification and Characterization of Protein Adducts Using an Aldehyde/Keto-Reactive Probe in Combination with Mass Spectrometry. *In:* CADENAS, E. & PACKER, L. (eds.) *Methods in Enzymology.* Academic Press.

MAK, L. H. & WOSCHOLSKI, R. 2015. Targeting PTEN using small molecule inhibitors. *Methods,* 77-78**,** 63-8.

MALANEY, P., PATHAK, R. R., XUE, B., UVERSKY, V. N. & DAVÉ, V. 2013. Intrinsic disorder in PTEN and its interactome confers structural plasticity and functional versatility. *Sci Rep,* 3**,** 2035.

MANDERS, E. M. M., VERBEEK, F. J. & ATEN, J. A. 1993. Measurement of co-localization of objects in dual-colour confocal images. *J Microsc,* 169**,** 375-382.

MANGLA, N., SINGH, R. & AGARWAL, N. 2023. HtpG Is a Metal-Dependent Chaperone Which Assists the DnaK/DnaJ/GrpE Chaperone System of Mycobacterium tuberculosis via Direct Association with DnaJ2. *Microbiology Spectrum,* 11**,** e00312-23.

MANNING, B. D. & TOKER, A. 2017. AKT/PKB Signaling: Navigating the Network. *Cell,* 169**,** 381-405.

MAREI, H. E., ALTHANI, A., AFIFI, N., HASAN, A., CACECI, T., POZZOLI, G., MORRIONE, A., GIORDANO, A. & CENCIARELLI, C. 2021. p53 signaling in cancer progression and therapy. *Cancer Cell International,* 21**,** 703.

MARINO, S. M. 2014. Protein Flexibility and Cysteine Reactivity: Influence of Mobility on the H-Bond Network and Effects on pKa Prediction. *The Protein Journal,* 33**,** 323-336.

MARKOSSIAN, K. A. & KURGANOV, B. I. 2004. Protein Folding, Misfolding, and Aggregation. Formation of Inclusion Bodies and Aggresomes. *Biochemistry (Moscow),* 69**,** 971-984.

MARTIN-SIERRA, C., LARANJEIRA, P., DOMINGUES, M. R. & PAIVA, A. 2019. Lipoxidation and cancer immunity. *Redox Biol,* 23**,** 101103.

MARTYNIUK, C. J., FANG, B., KOOMEN, J. M., GAVIN, T., ZHANG, L., BARBER, D. S. & LOPACHIN, R. M. 2011. Molecular mechanism of glyceraldehyde-3-phosphate dehydrogenase inactivation by alpha,beta-unsaturated carbonyl derivatives. *Chem Res Toxicol,* 24**,** 2302-11.

MASSON, G. R., PERISIC, O., BURKE, J. E. & WILLIAMS, R. L. 2016. The intrinsically disordered tails of PTEN and PTEN-L have distinct roles in regulating substrate specificity and membrane activity. *Biochem J,* 473**,** 135-44.

MATSUOKA, S., SHIBATA, T. & UEDA, M. 2013. Asymmetric PTEN distribution regulated by spatial heterogeneity in membrane-binding state transitions. *PLoS Comput Biol,* 9**,** e1002862.

MAYO, L. D. & DONNER, D. B. 2001. A phosphatidylinositol 3-kinase/Akt pathway promotes translocation of Mdm2 from the cytoplasm to the nucleus. *Proc Natl Acad Sci U S A,* 98**,** 11598-603.

MCCARTY, J. S. & WALKER, G. C. 1991. DnaK as a thermometer: threonine-199 is site of autophosphorylation and is critical for ATPase activity. *Proc Natl Acad Sci U S A,* 88**,** 9513-7.

MCELHANON, K. E., BOSE, C., SHARMA, R., WU, L., AWASTHI, Y. C. & SINGH, S. P. 2013. Gsta4 Null Mouse Embryonic Fibroblasts Exhibit Enhanced Sensitivity to Oxidants: Role of 4-Hydroxynonenal in Oxidant Toxicity. *Open J Apoptosis,* 2.

MCKENZIE, E. A. & ABBOTT, W. M. 2018. Expression of recombinant proteins in insect and mammalian cells. *Methods,* 147**,** 40-49.

MEFTAHI, G. H., BAHARI, Z., ZAREI MAHMOUDABADI, A., IMAN, M. & JANGRAVI, Z. 2021. Applications of western blot technique: From bench to bedside. *Biochemistry and Molecular Biology Education,* 49**,** 509-517.

MEHENNI, H., LIN-MARQ, N., BUCHET-POYAU, K., REYMOND, A., COLLART, M. A., PICARD, D. & ANTONARAKIS, S. E. 2005. LKB1 interacts with and phosphorylates PTEN: a functional link between two proteins involved in cancer predisposing syndromes. *Hum Mol Genet,* 14**,** 2209-19.

MICHAELSON, D. & PHILIPS, M. 2006. The use of GFP to localize Rho GTPases in living cells. *Methods Enzymol,* 406**,** 296-315.

MIGHELL, T. L., EVANS-DUTSON, S. & O'ROAK, B. J. 2018. A Saturation Mutagenesis Approach to Understanding PTEN Lipid Phosphatase Activity and Genotype-Phenotype Relationships. *Am J Hum Genet,* 102**,** 943-955.

MILIC, I., FEDOROVA, M., TEUBER, K., SCHILLER, J. & HOFFMANN, R. 2012. Characterization of oxidation products from 1-palmitoyl-2-linoleoyl-sn-glycerophosphatidylcholine in aqueous solutions and their reactions with cysteine, histidine and lysine residues. *Chem Phys Lipids,* 165**,** 186-96.

MILIC, I., KIPPING, M., HOFFMANN, R. & FEDOROVA, M. 2015a. Separation and characterization of oxidized isomeric lipid–peptide adducts by ion mobility mass spectrometry. *Journal of Mass Spectrometry,* 50**,** 1386-1392.

MILIC, I., MELO, T., DOMINGUES, M. R., DOMINGUES, P. & FEDOROVA, M. 2015b. Heterogeneity of peptide adducts with carbonylated lipid peroxidation products. *Journal of mass spectrometry : JMS,* 50 3**,** 603-12.

MILLER, R. M., IBRAHIM, K. & SMITH, L. M. 2021. ProteaseGuru: A Tool for Protease Selection in Bottom-Up Proteomics. *Journal of Proteome Research,* 20**,** 1936-1942.

MILLIONI, R., TOLIN, S., PURICELLI, L., SBRIGNADELLO, S., FADINI, G. P., TESSARI, P. & ARRIGONI, G. 2011. High Abundance Proteins Depletion vs Low Abundance Proteins Enrichment: Comparison of Methods to Reduce the Plasma Proteome Complexity. *PLoS ONE,* 6.

MINAGUCHI, T., WAITE, K. A. & ENG, C. 2006. Nuclear localization of PTEN is regulated by Ca(2+) through a tyrosil phosphorylation-independent conformational modification in major vault protein. *Cancer Res,* 66**,** 11677-82.

MOHD FAUZI, N. & SPICKETT, C. M. 2015. Lipid Oxidation. *In:* ROBERTS, S. M., KEHRER, J. P. & KLOTZ, L.-O. (eds.) *Studies on Experimental Toxicology and Pharmacology.* Cham: Springer International Publishing.

MOL, M., DEGANI, G., COPPA, C., BARON, G., POPOLO, L., CARINI, M., ALDINI, G., VISTOLI, G. & ALTOMARE, A. 2019. Advanced lipoxidation end products (ALEs) as RAGE binders: Mass

spectrometric and computational studies to explain the reasons why. *Redox Biol,* 23**,** 101083.

MONTINE, T. J., NEELY, M. D., QUINN, J. F., BEAL, M. F., MARKESBERY, W. R., ROBERTS, L. J. & MORROW, J. D. 2002. Lipid peroxidation in aging brain and Alzheimer's disease. *Free Radic Biol Med,* 33**,** 620-6.

MORROW, J. D., AWAD, J. A., KATO, T., TAKAHASHI, K., BADR, K. F., ROBERTS, L. J., 2ND & BURK, R. F. 1992. Formation of novel non-cyclooxygenase-derived prostanoids (F2-isoprostanes) in carbon tetrachloride hepatotoxicity. An animal model of lipid peroxidation. *J Clin Invest,* 90**,** 2502-7.

MOSESSIAN, S., AVLIYAKULOV, N. K., MULHOLLAND, D. J., BOONTHEUNG, P., LOO, J. A. & WU, H. 2009. Analysis of PTEN complex assembly and identification of heterogeneous nuclear ribonucleoprotein C as a component of the PTEN-associated complex. *J Biol Chem,* 284**,** 30159-66.

MOUMTZI, A., TRENKER, M., FLICKER, K., ZENZMAIER, E., SAF, R. & HERMETTER, A. 2007. Import and fate of fluorescent analogs of oxidized phospholipids in vascular smooth muscle cells. *J Lipid Res,* 48**,** 565-82.

MUKHERJEE, R., VANAJA, K. G., BOYER, J. A., GADAL, S., SOLOMON, H., CHANDARLAPATY, S., LEVCHENKO, A. & ROSEN, N. 2021. Regulation of PTEN translation by PI3K signaling maintains pathway homeostasis. *Mol Cell,* 81**,** 708-723 e5.

MUKHERJEE, S., DUTTA, A. & CHAKRABORTY, A. 2022. The interaction of oxidative stress with MAPK, PI3/AKT, NF-κB, and DNA damage kinases influences the fate of γ-radiation-induced bystander cells. *Arch Biochem Biophys,* 725**,** 109302.

MUND, T. & PELHAM, H. R. 2010. Regulation of PTEN/Akt and MAP kinase signaling pathways by the ubiquitin ligase activators Ndfip1 and Ndfip2. *Proc Natl Acad Sci U S A,* 107**,** 11429-34.

MUNDI, P. S., SACHDEV, J. C., MCCOURT, C. K. & KALINSKY, K. 2016. AKT in cancer: new molecular insights and advances in drug development. *British Journal of Clinical Pharmacology,* 82**,** 943 - 956.

MURAKAMI, M. & ISHIDA, N. 2017. β-Scission of Alkoxy Radicals in Synthetic Transformations. *Chemistry Letters,* 46**,** 1692-1700.

MYERS, M. P., PASS, I., BATTY, I. H., VAN DER KAAY, J., STOLAROV, J. P., HEMMINGS, B. A., WIGLER, M. H., DOWNES, C. P. & TONKS, N. K. 1998. The lipid phosphatase activity of PTEN is critical for its tumor supressor function. *Proc Natl Acad Sci U S A,* 95**,** 13513-8.

MYERS, M. P., STOLAROV, J. P., ENG, C., LI, J., WANG, S. I., WIGLER, M. H., PARSONS, R. & TONKS, N. K. 1997. P-TEN, the tumor suppressor from human chromosome 10q23, is a dual-specificity phosphatase. *Proc Natl Acad Sci U S A,* 94**,** 9052-7.

NADEAU, K., DAS, A. & WALSH, C. T. 1993. Hsp90 chaperonins possess ATPase activity and bind heat shock transcription factors and peptidyl prolyl isomerases. *J Biol Chem,* 268**,** 1479-87.

NAKAGAWA, F., MORINO, K., UGI, S., ISHIKADO, A., KONDO, K., SATO, D., KONNO, S., NEMOTO, K., KUSUNOKI, C., SEKINE, O., SUNAGAWA, A., KAWAMURA, M., INOUE, N., NISHIO, Y. & MAEGAWA, H. 2014. 4-Hydroxy hexenal derived from dietary n-3 polyunsaturated fatty acids induces anti-oxidative enzyme heme oxygenase-1 in multiple organs. *Biochem Biophys Res Commun,* 443**,** 991-6.

NAKAHATA, S., ICHIKAWA, T., MANEESAAY, P., SAITO, Y., NAGAI, K., TAMURA, T., MANACHAI, N., YAMAKAWA, N., HAMASAKI, M., KITABAYASHI, I., ARAI, Y., KANAI, Y., TAKI, T., ABE, T., KIYONARI, H., SHIMODA, K., OHSHIMA, K., HORII, A., SHIMA, H., TANIWAKI, M., YAMAGUCHI, R. & MORISHITA, K. 2014. Loss of NDRG2 expression activates PI3K-AKT signalling via PTEN phosphorylation in ATLL and other cancers. *Nat Commun,* 5**,** 3393.

NAKAKIDO, M., DENG, Z., SUZUKI, T., DOHMAE, N., NAKAMURA, Y. & HAMAMOTO, R. 2015. Dysregulation of AKT Pathway by SMYD2-Mediated Lysine Methylation on PTEN. *Neoplasia,* 17**,** 367-73.

NAKAMURA, M., TOMITORI, H., SUZUKI, T., SAKAMOTO, A., TERUI, Y., SAIKI, R., DOHMAE, N., IGARASHI, K. & KASHIWAGI, K. 2013. Inactivation of GAPDH as one mechanism of acrolein toxicity. *Biochem Biophys Res Commun,* 430**,** 1265-71.

NGUYEN, H. N., AFKARI, Y., SENOO, H., SESAKI, H., DEVREOTES, P. N. & IIJIMA, M. 2014. Mechanism of human PTEN localization revealed by heterologous expression in Dictyostelium. *Oncogene,* 33**,** 5688-96.

NGUYEN, H. N., YANG, J. M., MIYAMOTO, T., ITOH, K., RHO, E., ZHANG, Q., INOUE, T., DEVREOTES, P. N., SESAKI, H. & IIJIMA, M. 2015. Opening the conformation is a master switch for the dual localization and phosphatase activity of PTEN. *Sci Rep,* 5**,** 12600.

NIEVA, J., SHAFTON, A., ALTOBELL, L. J., 3RD, TRIPURANENI, S., ROGEL, J. K., WENTWORTH, A. D., LERNER, R. A. & WENTWORTH, P., JR. 2008. Lipid-derived aldehydes accelerate light chain amyloid and amorphous aggregation. *Biochemistry,* 47**,** 7695-705.

NUMAJIRI, N., TAKASAWA, K., NISHIYA, T., TANAKA, H., OHNO, K., HAYAKAWA, W., ASADA, M., MATSUDA, H., AZUMI, K., KAMATA, H., NAKAMURA, T., HARA, H., MINAMI, M., LIPTON, S. A. & UEHARA, T. 2011. On-off system for PI3-kinase-Akt signaling through S-nitrosylation of phosphatase with sequence homology to tensin (PTEN). *Proc Natl Acad Sci U S A,* 108**,** 10349-54.

NUSSINOV, R., ZHANG, M., TSAI, C. J. & JANG, H. 2021. Phosphorylation and Driver Mutations in PI3Kα and PTEN Autoinhibition. *Mol Cancer Res,* 19**,** 543-548.

O'HAIR, R. A. J. & REID, G. E. 1998. Does side chain water loss from protonated threonine yield N-protonated dehydroamino-2-butyric acid? *Rapid Communications in Mass Spectrometry,* 12**,** 999-1002.

OHSE, M., KAWADE, K. & KUSAOKE, H. 1997. Effects of DNA topology on transformation efficiency of Bacillus subtilis ISW1214 by electroporation. *Biosci Biotechnol Biochem,* 61**,** 1019-21.

OKUMURA, K., MENDOZA, M., BACHOO, R. M., DEPINHO, R. A., CAVENEE, W. K. & FURNARI, F. B. 2006. PCAF modulates PTEN activity. *J Biol Chem,* 281**,** 26562-8.

OLIVA, J. L., PÉREZ-SALA, D., CASTRILLO, A., MARTÍNEZ, N., CAÑADA, F. J., BOSCÁ, L. & ROJAS, J. M. 2003. The cyclopentenone 15-deoxy-delta 12,14-prostaglandin J2 binds to and activates H-Ras. *Proc Natl Acad Sci U S A,* 100**,** 4772-7.

OSAKI, M., OSHIMURA, M. & ITO, H. 2004. PI3K-Akt pathway: Its functions and alterations in human cancer. *Apoptosis,* 9**,** 667-676.

PALUMBO, E., ZHAO, B., XUE, B., UVERSKY, V. N. & DAVÉ, V. 2020. Analyzing aggregation propensities of clinically relevant PTEN mutants: a new culprit in pathogenesis of cancer and other PTENopathies. *J Biomol Struct Dyn,* 38**,** 2253-2266.

PANDAY, A., SAHOO, M. K., OSORIO, D. & BATRA, S. 2015. NADPH oxidases: an overview from structure to innate immunity-associated pathologies. *Cellular & Molecular Immunology,* 12**,** 5-23.

PANDE, A. H., KAR, S. & TRIPATHY, R. K. 2010. Oxidatively modified fatty acyl chain determines physicochemical properties of aggregates of oxidized phospholipids. *Biochimica et Biophysica Acta (BBA) - Biomembranes,* 1798**,** 442-452.

PAPA, A., WAN, L., BONORA, M., SALMENA, L., SONG, M. S., HOBBS, R. M., LUNARDI, A., WEBSTER, K., NG, C., NEWTON, R. H., KNOBLAUCH, N., GUARNERIO, J., ITO, K., TURKA, L. A., BECK, A. H., PINTON, P., BRONSON, R. T., WEI, W. & PANDOLFI, P. P. 2014. Cancer-associated PTEN mutants act in a dominant-negative manner to suppress PTEN protein function. *Cell,* 157**,** 595-610.

PATEL, B., MEIER, S., OPPERMAN, K., HANEY, P., KABOORD, B. & ROGERS, J. 2014. Abstract 1615: Enrichment of EGFR/PI3K/AKT/PTEN proteins using immunoprecipitation and analysis with mass spectrometry-based proteomics. *Cancer Research,* 74**,** 1615-1615.

PATEL, L., PASS, I., COXON, P., DOWNES, C. P., SMITH, S. A. & MACPHEE, C. H. 2001. Tumor suppressor and anti-inflammatory actions of PPARgamma agonists are mediated via upregulation of PTEN. *Curr Biol,* 11**,** 764-8.

PATINEN, T., ADINOLFI, S., CORTES, C. C., HARKONEN, J., JAWAHAR DEEN, A. & LEVONEN, A. L. 2019. Regulation of stress signaling pathways by protein lipoxidation. *Redox Biol,* 23**,** 101114.

PAVELKA, M., NEUMÜLLER, J. & ELLINGER, A. 2008. Retrograde traffic in the biosynthetic-secretory route. *Histochem Cell Biol,* 129**,** 277-88.

PERREN, A., KOMMINOTH, P., SAREMASLANI, P., MATTER, C., FEURER, S., LEES, J. A., HEITZ, P. U. & ENG, C. 2000. Mutation and expression analyses reveal differential subcellular compartmentalization of PTEN in endocrine pancreatic tumors compared to normal islet cells. *Am J Pathol,* 157**,** 1097-103.

PERRY, E. A., CASTELLANI, R. J., MOREIRA, P. I., NUNOMURA, A., LUI, Q., HARRIS, P. L., SAYRE, L. M., SZWEDA, P. A., SZWEDA, L. I., ZHU, X., SMITH, M. A. & PERRY, G. 2013. Neurofilaments are the major neuronal target of hydroxynonenal-mediated protein cross-links. *Free Radic Res,* 47**,** 507-10.

PIGUET, A. C. & DUFOUR, J. F. 2011. PI(3)K/PTEN/AKT pathway. *J Hepatol,* 54**,** 1317-9.

PILLON, N. J., SOULERE, L., VELLA, R. E., CROZE, M., CARE, B. R., SOULA, H. A., DOUTHEAU, A., LAGARDE, M. & SOULAGE, C. O. 2010. Quantitative structure-activity relationship for 4-hydroxy-2-alkenal induced cytotoxicity in L6 muscle cells. *Chem Biol Interact,* 188**,** 171-80.

PILLON, N. J., VELLA, R. E., SOULEERE, L., BECCHI, M., LAGARDE, M. & SOULAGE, C. O. 2011. Structural and functional changes in human insulin induced by the lipid peroxidation byproducts 4-hydroxy-2-nonenal and 4-hydroxy-2-hexenal. *Chem Res Toxicol,* 24**,** 752-62.

PIZZINO, G., IRRERA, N., CUCINOTTA, M., PALLIO, G., MANNINO, F., ARCORACI, V., SQUADRITO, F., ALTAVILLA, D. & BITTO, A. 2017. Oxidative Stress: Harms and Benefits for Human Health. *Oxid Med Cell Longev,* 2017**,** 8416763.

POLI, G., DIANZANI, M. U., CHEESEMAN, K. H., SLATER, T. F., LANG, J. & ESTERBAUER, H. 1985. Separation and characterization of the aldehydic products of lipid peroxidation stimulated by carbon tetrachloride or ADP-iron in isolated rat hepatocytes and rat liver microsomal suspensions. *Biochem J,* 227**,** 629-38.

PORTER, N. A. 1984. Chemistry of lipid peroxidation. *Methods Enzymol,* 105**,** 273-82.

PORTER, N. A., CALDWELL, S. E. & MILLS, K. A. 1995. Mechanisms of free radical oxidation of unsaturated lipids. *Lipids,* 30**,** 277-90.

PRYOR, W. A. & PORTER, N. A. 1990. Suggested mechanisms for the production of 4-hydroxy-2-nonenal from the autoxidation of polyunsaturated fatty acids. *Free Radic Biol Med,* 8**,** 541-3.

RADU, A., NEUBAUER, V., AKAGI, T., HANAFUSA, H. & GEORGESCU, M. M. 2003. PTEN induces cell cycle arrest by decreasing the level and nuclear localization of cyclin D1. *Mol Cell Biol,* 23**,** 6139-49.

RAHAL, A., KUMAR, A., SINGH, V., YADAV, B., TIWARI, R., CHAKRABORTY, S. & DHAMA, K. 2014. Oxidative stress, prooxidants, and antioxidants: the interplay. *Biomed Res Int,* 2014**,** 761264.

RAHDAR, M., INOUE, T., MEYER, T., ZHANG, J., VAZQUEZ, F. & DEVREOTES, P. N. 2009. A phosphorylation-dependent intramolecular interaction regulates the membrane association and activity of the tumor suppressor PTEN. *Proc Natl Acad Sci U S A,* 106**,** 480-5.

RAHIMZADEH, M., SADEGHIZADEH, M., NAJAFI, F., ARAB, S. & MOBASHERI, H. 2016. Impact of heat shock step on bacterial transformation efficiency. *Mol Biol Res Commun,* 5**,** 257-261.

RAMACHANDRAN, S., RAMI, B. R. & UDGAONKAR, J. B. 2000. Measurements of cysteine reactivity during protein unfolding suggest the presence of competing pathways11Edited by C. R. Matthews. *Journal of Molecular Biology,* 297**,** 733-745.

RAMASWAMY, S., NAKAMURA, N., VAZQUEZ, F., BATT, D. B., PERERA, S., ROBERTS, T. M. & SELLERS, W. R. 1999. Regulation of G1 progression by the PTEN tumor suppressor protein is linked to inhibition of the phosphatidylinositol 3-kinase/Akt pathway. *Proc Natl Acad Sci U S A,* 96**,** 2110-5.

RAUNIYAR, N. & PROKAI, L. 2009. Detection and identification of 4-hydroxy-2-nonenal Schiff-base adducts along with products of Michael addition using data-dependent neutral loss-driven

MS3 acquisition: method evaluation through an in vitro study on cytochrome c oxidase modifications. *Proteomics,* 9**,** 5188-93.

RAVANDI, A., KUKSIS, A., SHAIKH, N. & JACKOWSKI, G. 1997. Preparation of Schiff base adducts of phosphatidylcholine core aldehydes and aminophospholipids, amino acids, and myoglobin. *Lipids,* 32**,** 989-1001.

RAYNAL, B., LENORMAND, P., BARON, B., HOOS, S. & ENGLAND, P. 2014. Quality assessment and optimization of purified protein samples: why and how? *Microb Cell Fact,* 13**,** 180.

RECHSTEINER, M. & ROGERS, S. W. 1996. PEST sequences and regulation by proteolysis. *Trends Biochem Sci,* 21**,** 267-71.

REDFERN, R. E., REDFERN, D., FURGASON, M. L., MUNSON, M., ROSS, A. H. & GERICKE, A. 2008. PTEN phosphatase selectively binds phosphoinositides and undergoes structural changes. *Biochemistry,* 47**,** 2162-71.

REIS, A., DOMINGUES, M. R., AMADO, F. M., FERRER-CORREIA, A. J. & DOMINGUES, P. 2007. Radical peroxidation of palmitoyl-lineloyl-glycerophosphocholine liposomes: Identification of long-chain oxidised products by liquid chromatography-tandem mass spectrometry. *J Chromatogr B Analyt Technol Biomed Life Sci,* 855**,** 186-99.

REIS, A., DOMINGUES, P., FERRER-CORREIA, A. J. & DOMINGUES, M. R. 2006. Peptide-phospholipid cross-linking reactions: identification of leucine enkephalin-alka(e)nal-glycerophosphatidylcholine adducts by tandem mass spectrometry. *J Am Soc Mass Spectrom,* 17**,** 657-60.

REIS, A. & SPICKETT, C. M. 2012. Chemistry of phospholipid oxidation. *Biochim Biophys Acta,* 1818**,** 2374-87.

RENEDO, M., GAYARRE, J., GARCÍA-DOMÍNGUEZ, C. A., PÉREZ-RODRÍGUEZ, A., PRIETO, A., CAÑADA, F. J., ROJAS, J. M. & PÉREZ-SALA, D. 2007. Modification and activation of Ras proteins by electrophilic prostanoids with different structure are site-selective. *Biochemistry,* 46**,** 6607-16.

REUTER, S., GUPTA, S. C., CHATURVEDI, M. M. & AGGARWAL, B. B. 2010. Oxidative stress, inflammation, and cancer: how are they linked? *Free radical biology & medicine,* 49 11**,** 1603-16.

REZATABAR, S., KARIMIAN, A., RAMESHKNIA, V., PARSIAN, H., MAJIDINIA, M., KOPI, T. A., BISHAYEE, A., SADEGHINIA, A., YOUSEFI, M., MONIRIALAMDARI, M. & YOUSEFI, B. 2019. RAS/MAPK signaling functions in oxidative stress, DNA damage response and cancer progression. *J Cell Physiol,* 234**,** 14951-14965.

RIQUELME, S. A., HOPKINS, B. D., WOLFE, A. L., DIMANGO, E., KITUR, K., PARSONS, R. & PRINCE, A. 2017. Cystic Fibrosis Transmembrane Conductance Regulator Attaches Tumor Suppressor PTEN to the Membrane and Promotes Anti Pseudomonas aeruginosa Immunity. *Immunity,* 47**,** 1169-1181 e7.

ROBERTS, L. J., 2ND & MORROW, J. D. 1997. The generation and actions of isoprostanes. *Biochim Biophys Acta,* 1345**,** 121-35.

RODRIGUEZ-ESCUDERO, I., ROELANTS, F. M., THORNER, J., NOMBELA, C., MOLINA, M. & CID, V. J. 2005. Reconstitution of the mammalian PI3K/PTEN/Akt pathway in yeast. *Biochem J,* 390**,** 613-23.

ROSANO, G. L. & CECCARELLI, E. A. 2014. Recombinant protein expression in Escherichia coli: advances and challenges. *Front Microbiol,* 5**,** 172.

SAKAMOTO, S., PUTALUN, W., VIMOLMANGKANG, S., PHOOLCHAROEN, W., SHOYAMA, Y., TANAKA, H. & MORIMOTO, S. 2018. Enzyme-linked immunosorbent assay for the quantitative/qualitative analysis of plant secondary metabolites. *J Nat Med,* 72**,** 32-42.

SALOMON, R. G. 2005a. Distinguishing levuglandins produced through the cyclooxygenase and isoprostane pathways. *Chem Phys Lipids,* 134**,** 1-20.

SALOMON, R. G. 2005b. Levuglandins and isolevuglandins: stealthy toxins of oxidative injury. *Antioxid Redox Signal,* 7**,** 185-201.

SALOMON, R. G., SUBBANAGOUNDER, G., SINGH, U., O'NEIL, J. & HOFF, H. F. 1997. Oxidation of low-density lipoproteins produces levuglandin-protein adducts. *Chem Res Toxicol,* 10**,** 750-9.

SAMY, T. S. A., KAPPEN, L. S. & GOLDBERG, I. H. 1980. Reversible modification of arginine residues in neocarzinostatin. Isolation of a biologically active 89-residue fragment from the tryptic hydrolysate. *The Journal of biological chemistry,* 255 8**,** 3420-6.

SANCHEZ-GOMEZ, F. J., DIEZ-DACAL, B., PAJARES, M. A., LLORCA, O. & PEREZ-SALA, D. 2010. Cyclopentenone prostaglandins with dienone structure promote cross-linking of the chemoresistance-inducing enzyme glutathione transferase P1-1. *Mol Pharmacol,* 78**,** 723-33.

SANDERSON, M. J., SMITH, I., PARKER, I. & BOOTMAN, M. D. 2014. Fluorescence microscopy. *Cold Spring Harb Protoc,* 2014**,** pdb.top071795.

SANI, U. M., NA'IBI, H. U. & DAILAMI, S. A. 2018. In vitro antimicrobial and antioxidant studies on N-(2- hydroxylbenzylidene) pyridine -2-amine and its M(II) complexes. *Nigerian Journal of Basic and Applied Sciences*.

SARASWAT, M., MUSANTE, L., RAVIDA, A., SHORTT, B., BYRNE, B. & HOLTHOFER, H. 2013. Preparative purification of recombinant proteins: current status and future trends. *Biomed Res Int,* 2013**,** 312709.

SASABE, N., KEYAMURA, Y., OBAMA, T., INOUE, N., MASUKO, Y., IGARASHI, Y., AIUCHI, T., KATO, R., YAMAGUCHI, T., KUWATA, H., IWAMOTO, S., MIYAZAKI, A., HARA, S., YOSHIKAWA, T. & ITABE, H. 2014. Time course-changes in phosphatidylcholine profile during oxidative modification of low-density lipoprotein. *Lipids Health Dis,* 13**,** 48.

SAUERLAND, M. B. & DAVIES, M. J. 2022. Electrophile versus oxidant modification of cysteine residues: Kinetics as a key driver of protein modification. *Arch Biochem Biophys,* 727**,** 109344.

SAUERLAND, M. B., HELM, C., LORENTZEN, L. G., MANANDHAR, A., ULVEN, T., GAMON, L. F. & DAVIES, M. J. 2023. Identification of galectin-1 and other cellular targets of alpha,beta-unsaturated carbonyl compounds, including dimethylfumarate, by use of click-chemistry probes. *Redox Biology,* 59**,** 102560.

SAVITSKI, M. M., KJELDSEN, F., NIELSEN, M. L. & ZUBAREV, R. A. 2007. Relative Specificities of Water and Ammonia Losses from Backbone Fragments in Collision-Activated Dissociation. *Journal of Proteome Research,* 6**,** 2669-2673.

SCHARF, B., CLEMENT, C. C., YODMUANG, S., URBANSKA, A. M., SUADICANI, S. O., APHKHAZAVA, D., THI, M. M., PERINO, G., HARDIN, J. A., COBELLI, N., VUNJAK-NOVAKOVIC, G. & SANTAMBROGIO, L. 2013. Age-related carbonylation of fibrocartilage structural proteins drives tissue degenerative modification. *Chem Biol,* 20**,** 922-34.

SCHNEBELEN, C., VIAU, S., GRÉGOIRE, S., JOFFRE, C., CREUZOT-GARCHER, C. P., BRON, A. M., BRETILLON, L. & ACAR, N. 2009. Nutrition for the Eye: Different Susceptibility of the Retina and the Lacrimal Gland to Dietary Omega-6 and Omega-3 Polyunsaturated Fatty Acid Incorporation. *Ophthalmic Research,* 41**,** 216-224.

SCHOPFER, F. J., COLE, M. P., GROEGER, A. L., CHEN, C. S., KHOO, N. K., WOODCOCK, S. R., GOLIN-BISELLO, F., MOTANYA, U. N., LI, Y., ZHANG, J., GARCIA-BARRIO, M. T., RUDOLPH, T. K., RUDOLPH, V., BONACCI, G., BAKER, P. R., XU, H. E., BATTHYANY, C. I., CHEN, Y. E., HALLIS, T. M. & FREEMAN, B. A. 2010. Covalent peroxisome proliferator-activated receptor gamma adduction by nitro-fatty acids: selective ligand activity and anti-diabetic signaling actions. *J Biol Chem,* 285**,** 12321-33.

SCHUTZ, A., BERNHARD, F., BERROW, N., BUYEL, J. F., FERREIRA-DA-SILVA, F., HAUSTRAETE, J., VAN DEN HEUVEL, J., HOFFMANN, J. E., DE MARCO, A., PELEG, Y., SUPPMANN, S., UNGER, T., VANHOUCKE, M., WITT, S. & REMANS, K. 2023. A concise guide to choosing suitable gene expression systems for recombinant protein production. *STAR Protoc,* 4**,** 102572.

SEKAR, R. B. & PERIASAMY, A. 2003. Fluorescence resonance energy transfer (FRET) microscopy imaging of live cell protein localizations. *J Cell Biol,* 160**,** 629-33.

SETO, A., KAWANISHI, M., MATSUDA, S., OGAWA, K. & MIYOSHI, I. 1988a. Adult T cell leukemia-like disease experimentally induced in rabbits. *Jpn J Cancer Res,* 79**,** 335-41.

SETO, D., BHATNAGAR, S. K. & BESSMAN, M. J. 1988b. The purification and properties of deoxyguanosine triphosphate triphosphohydrolase from Escherichia coli. *J Biol Chem,* 263**,** 1494-9.

SHEARN, C. T., FRITZ, K. S., REIGAN, P. & PETERSEN, D. R. 2011a. Modification of Akt2 by 4-hydroxynonenal inhibits insulin-dependent Akt signaling in HepG2 cells. *Biochemistry,* 50**,** 3984-96.

SHEARN, C. T., SMATHERS, R. L., BACKOS, D. S., REIGAN, P., ORLICKY, D. J. & PETERSEN, D. R. 2013. Increased carbonylation of the lipid phosphatase PTEN contributes to Akt2 activation in a murine model of early alcohol-induced steatosis. *Free Radic Biol Med,* 65**,** 680-692.

SHEARN, C. T., SMATHERS, R. L., STEWART, B. J., FRITZ, K. S., GALLIGAN, J. J., HAIL, N., JR. & PETERSEN, D. R. 2011b. Phosphatase and tensin homolog deleted on chromosome 10 (PTEN) inhibition by 4-hydroxynonenal leads to increased Akt activation in hepatocytes. *Mol Pharmacol,* 79**,** 941-52.

SHEN, W. H., BALAJEE, A. S., WANG, J., WU, H., ENG, C., PANDOLFI, P. P. & YIN, Y. 2007. Essential role for nuclear PTEN in maintaining chromosomal integrity. *Cell,* 128**,** 157-70.

SHEN, Y. H., ZHANG, L., GAN, Y., WANG, X., WANG, J., LEMAIRE, S. A., COSELLI, J. S. & WANG, X. L. 2006. Up-regulation of PTEN (phosphatase and tensin homolog deleted on chromosome ten) mediates p38 MAPK stress signal-induced inhibition of insulin signaling. A cross-talk between stress signaling and insulin signaling in resistin-treated human endothelial cells. *J Biol Chem,* 281**,** 7727-36.

SHENOY, S. S., NANDA, H. & LOSCHE, M. 2012. Membrane association of the PTEN tumor suppressor: electrostatic interaction with phosphatidylserine-containing bilayers and regulatory role of the C-terminal tail. *J Struct Biol,* 180**,** 394-408.

SHI, T., VAN SOEST, D. M. K., POLDERMAN, P. E., BURGERING, B. M. T. & DANSEN, T. B. 2021. DNA damage and oxidant stress activate p53 through differential upstream signaling pathways. *Free Radical Biology and Medicine,* 172**,** 298-311.

SHI, Y., PALUCH, B. E., WANG, X. & JIANG, X. 2012. PTEN at a glance. *J Cell Sci,* 125**,** 4687-92.

SHIBATA, T., IIO, K., KAWAI, Y., SHIBATA, N., KAWAGUCHI, M., TOI, S., KOBAYASHI, M., KOBAYASHI, M., YAMAMOTO, K. & UCHIDA, K. 2006. Identification of a lipid peroxidation product as a potential trigger of the p53 pathway. *J Biol Chem,* 281**,** 1196-204.

SHIBATA, T., SHIMIZU, K., HIRANO, K., NAKASHIMA, F., KIKUCHI, R., MATSUSHITA, T. & UCHIDA, K. 2017. Adductome-based identification of biomarkers for lipid peroxidation. *Journal of Biological Chemistry,* 292**,** 8223-8235.

SHIBATA, T. & UCHIDA, K. 2019. Protein adductomics: A comprehensive analysis of protein modifications by electrophiles. *Free Radic Biol Med,* 144**,** 218-222.

SHIRAKI, T., KAMIYA, N., SHIKI, S., KODAMA, T. S., KAKIZUKA, A. & JINGAMI, H. 2005. Alpha,beta-unsaturated ketone is a core moiety of natural ligands for covalent binding to peroxisome proliferator-activated receptor gamma. *J Biol Chem,* 280**,** 14145-53.

SHRINGARPURE, R., GRUNE, T., SITTE, N. & DAVIES, K. J. 2000. 4-Hydroxynonenal-modified amyloid-beta peptide inhibits the proteasome: possible importance in Alzheimer's disease. *Cell Mol Life Sci,* 57**,** 1802-9.

SIDOLI, S., LIN, S., KARCH, K. R. & GARCIA, B. A. 2015. Bottom-Up and Middle-Down Proteomics Have Comparable Accuracies in Defining Histone Post-Translational Modification Relative Abundance and Stoichiometry. *Analytical Chemistry,* 87**,** 3129-3133.

SILVA, A., YUNES, J. A., CARDOSO, B. A., MARTINS, L. R., JOTTA, P. Y., ABECASIS, M., NOWILL, A. E., LESLIE, N. R., CARDOSO, A. A. & BARATA, J. T. 2008. PTEN posttranslational inactivation and hyperactivation of the PI3K/Akt pathway sustain primary T cell leukemia viability. *J Clin Invest,* 118**,** 3762-74.

SINHA, A., SALEH, A., ENDERSBY, R., YUAN, S. H., CHOKSHI, C. R., BROWN, K. R., KUZIO, B., KAUPPINEN, T., SINGH, S. K., BAKER, S. J., MCKINNON, P. J. & KATYAL, S. 2020. RAD51-Mediated DNA Homologous Recombination Is Independent of PTEN Mutational Status. *Cancers (Basel),* 12.

SKULJ, S., VAZDAR, K., MARGETIC, D. & VAZDAR, M. 2019. Revisited Mechanism of Reaction between a Model Lysine Amino Acid Side Chain and 4-Hydroxynonenal in Different Solvent Environments. *J Org Chem,* 84**,** 526-535.

SMITH, S. L. 2022. *The Biological Role of Redox Signalling by the Tumour Suppressor PTEN.* PHD, Aston University.

SOLATI, Z., SURENDRAN, A., EDEL, A., ROZNIK, M., ALLEN, D. & RAVANDI, A. 2021. Increase in Plasma Oxidized Phosphatidylcholines (OxPCs) in Patients Presenting With ST-Elevation Myocardial Infarction (STEMI). *Front Med (Lausanne),* 8**,** 716944.

SONG, M. S., CARRACEDO, A., SALMENA, L., SONG, S. J., EGIA, A., MALUMBRES, M. & PANDOLFI, P. P. 2011. Nuclear PTEN regulates the APC-CDH1 tumor-suppressive complex in a phosphatase-independent manner. *Cell,* 144**,** 187-99.

SONG, M. S., SALMENA, L., CARRACEDO, A., EGIA, A., LO-COCO, F., TERUYA-FELDSTEIN, J. & PANDOLFI, P. P. 2008. The deubiquitinylation and localization of PTEN are regulated by a HAUSP-PML network. *Nature,* 455**,** 813-7.

SOULAGE, C. O., PELLETIER, C. C., FLORENS, N., LEMOINE, S., DUBOURG, L., JUILLARD, L. & GUEBRE-EGZIABHER, F. 2020. Two Toxic Lipid Aldehydes, 4-hydroxy-2-hexenal (4-HHE) and 4-hydroxy-2-nonenal (4-HNE), Accumulate in Patients with Chronic Kidney Disease. *Toxins (Basel),* 12.

SOULAGE, C. O., SARDON PUIG, L., SOULERE, L., ZARROUKI, B., GUICHARDANT, M., LAGARDE, M. & PILLON, N. J. 2018. Skeletal muscle insulin resistance is induced by 4-hydroxy-2-hexenal, a by-product of n-3 fatty acid peroxidation. *Diabetologia,* 61**,** 688-699.

SOUSA, B. C., AHMED, T., DANN, W. L., ASHMAN, J., GUY, A., DURAND, T., PITT, A. R. & SPICKETT, C. M. 2019. Short-chain lipid peroxidation products form covalent adducts with pyruvate kinase and inhibit its activity in vitro and in breast cancer cells. *Free Radic Biol Med,* 144**,** 223-233.

SOUSA, B. C., PITT, A. R. & SPICKETT, C. M. 2017. Chemistry and analysis of HNE and other prominent carbonyl-containing lipid oxidation compounds. *Free Radic Biol Med,* 111**,** 294-308.

SPICKETT, C. M. 2013. The lipid peroxidation product 4-hydroxy-2-nonenal: Advances in chemistry and analysis. *Redox Biol,* 1**,** 145-52.

SPICKETT, C. M. & PITT, A. R. 2020. Modification of proteins by reactive lipid oxidation products and biochemical effects of lipoxidation. *Essays Biochem,* 64**,** 19-31.

SPINELLI, L. & LESLIE, N. R. 2015. Assaying PTEN catalysis in vitro. *Methods,* 77-78**,** 51-7.

SRIVASTAVA, S., SINHA, R. & ROY, D. 2004. Toxicological effects of malachite green. *Aquat Toxicol,* 66**,** 319-29.

STADLER, C., REXHEPAJ, E., SINGAN, V. R., MURPHY, R. F., PEPPERKOK, R., UHLÉN, M., SIMPSON, J. C. & LUNDBERG, E. 2013. Immunofluorescence and fluorescent-protein tagging show high correlation for protein localization in mammalian cells. *Nature Methods,* 10**,** 315-323.

STAMBOLIC, V., MACPHERSON, D., SAS, D., LIN, Y., SNOW, B., JANG, Y., BENCHIMOL, S. & MAK, T. W. 2001. Regulation of PTEN transcription by p53. *Mol Cell,* 8**,** 317-25.

STAMBOLIC, V., SUZUKI, A., DE LA POMPA, J. L., BROTHERS, G. M., MIRTSOS, C., SASAKI, T., RULAND, J., PENNINGER, J. M., SIDEROVSKI, D. P. & MAK, T. W. 1998. Negative regulation of PKB/Akt-dependent cell survival by the tumor suppressor PTEN. *Cell,* 95**,** 29-39.

STAMENKOVIC, A., O'HARA, K. A., NELSON, D. C., MADDAFORD, T. G., EDEL, A. L., MADDAFORD, G., DIBROV, E., AGHANOORI, M., KIRSHENBAUM, L. A., FERNYHOUGH, P., ALIANI, M., PIERCE, G. N. & RAVANDI, A. 2021. Oxidized phosphatidylcholines trigger ferroptosis in cardiomyocytes during ischemia-reperfusion injury. *Am J Physiol Heart Circ Physiol,* 320**,** H1170-H1184.

STECK, P. A., PERSHOUSE, M. A., JASSER, S. A., YUNG, W. K., LIN, H., LIGON, A. H., LANGFORD, L. A., BAUMGARD, M. L., HATTIER, T., DAVIS, T., FRYE, C., HU, R., SWEDLUND, B., TENG, D. H. &

TAVTIGIAN, S. V. 1997. Identification of a candidate tumour suppressor gene, MMAC1, at chromosome 10q23.3 that is mutated in multiple advanced cancers. *Nat Genet,* 15**,** 356-62.

STEMMER, U. & HERMETTER, A. 2012. Protein modification by aldehydophospholipids and its functional consequences. *Biochim Biophys Acta,* 1818**,** 2436-45.

STEWART, G. S., WANG, B., BIGNELL, C. R., TAYLOR, A. M. R. & ELLEDGE, S. J. 2003. MDC1 is a mediator of the mammalian DNA damage checkpoint. *Nature,* 421**,** 961-966.

STRAUS, D. S., PASCUAL, G., LI, M., WELCH, J. S., RICOTE, M., HSIANG, C. H., SENGCHANTHALANGSY, L. L., GHOSH, G. & GLASS, C. K. 2000. 15-deoxy-delta 12,14-prostaglandin J2 inhibits multiple steps in the NF-kappa B signaling pathway. *Proc Natl Acad Sci U S A,* 97**,** 4844-9.

STUMPF, M., BLOKZIJL-FRANKE, S. & DEN HERTOG, J. 2016. Fine-Tuning of Pten Localization and Phosphatase Activity Is Essential for Zebrafish Angiogenesis. *PLoS ONE,* 11.

SU, L.-J., ZHANG, J.-H., GOMEZ, H., MURUGAN, R., HONG, X., XU, D., JIANG, F. & PENG, Z.-Y. 2019. Reactive Oxygen Species-Induced Lipid Peroxidation in Apoptosis, Autophagy, and Ferroptosis. *Oxidative Medicine and Cellular Longevity,* 2019**,** 5080843.

SUBAUSTE, M. C., NALBANT, P., ADAMSON, E. D. & HAHN, K. M. 2005. Vinculin controls PTEN protein level by maintaining the interaction of the adherens junction protein beta-catenin with the scaffolding protein MAGI-2. *J Biol Chem,* 280**,** 5676-81.

SUBBANAGOUNDER, G., LEITINGER, N., SCHWENKE, D. C., WONG, J. W., LEE, H., RIZZA, C., WATSON, A. D., FAULL, K. F., FOGELMAN, A. M. & BERLINER, J. A. 2000. Determinants of bioactivity of oxidized phospholipids. Specific oxidized fatty acyl groups at the sn-2 position. *Arterioscler Thromb Vasc Biol,* 20**,** 2248-54.

SUH, J., KIM, D. H., KIM, E. H., PARK, S. A., PARK, J. M., JANG, J. H., KIM, S. J., NA, H. K., KIM, N. D., KIM, N. J., SUH, Y. G. & SURH, Y. J. 2018. 15-Deoxy-Delta(12,14)-prostaglandin J2 activates PI3K-Akt signaling in human breast cancer cells through covalent modification of the tumor suppressor PTEN at cysteine 136. *Cancer Lett,* 424**,** 30-45.

SUN, H., LESCHE, R., LI, D.-M., LILIENTAL, J., ZHANG, H., GAO, J., GAVRILOVA, N., MUELLER, B., LIU, X. & WU, H. 1999. PTEN modulates cell cycle progression and cell survival by regulating phosphatidylinositol 3,4,5,-trisphosphate and Akt/protein kinase B signaling pathway. *Proceedings of the National Academy of Sciences of the United States of America,* 96 11**,** 6199-204.

SUN, X., OU, Z., CHEN, R., NIU, X., CHEN, D., KANG, R. & TANG, D. 2016. Activation of the p62-Keap1-NRF2 pathway protects against ferroptosis in hepatocellular carcinoma cells. *Hepatology,* 63**,** 173-84.

SUN, Z., XIAO, W., LI, N., CHANG, L., XU, P. & LI, Y. 2023. Large-Scale Profiling of Unexpected Tryptic Cleaved Sites at Ubiquitinated Lysines. *Journal of Proteome Research,* 22**,** 1245-1254.

TAKAHASHI, Y., MORALES, F. C., KREIMANN, E. L. & GEORGESCU, M. M. 2006. PTEN tumor suppressor associates with NHERF proteins to attenuate PDGF receptor signaling. *EMBO J,* 25**,** 910-20.

TAN, A., ZIEGLER, A., STEINBAUER, B. & SEELIG, J. 2002. Thermodynamics of Sodium Dodecyl Sulfate Partitioning into Lipid Membranes. *Biophysical Journal,* 83**,** 1547-1556.

TAN, P. L., SHAVLAKADZE, T., GROUNDS, M. D. & ARTHUR, P. G. 2015. Differential thiol oxidation of the signaling proteins Akt, PTEN or PP2A determines whether Akt phosphorylation is enhanced or inhibited by oxidative stress in C2C12 myotubes derived from skeletal muscle. *Int J Biochem Cell Biol,* 62**,** 72-9.

TANAKA, T., MIZUKOSHI, T., SASAKI, K., KOHDA, D. & MASAI, H. 2007. Escherichia coli PriA protein, two modes of DNA binding and activation of ATP hydrolysis. *J Biol Chem,* 282**,** 19917-27.

TANAKA, T., TANIYAMA, C., ARAI, K.-I. & MASAI, H. 2003. ATPase/helicase motif mutants of Escherichia coli PriA protein essential for recombination-dependent DNA replication. *Genes to Cells,* 8**,** 251-261.

TANITO, M., ELLIOTT, M. H., KOTAKE, Y. & ANDERSON, R. E. 2005. Protein modifications by 4-hydroxynonenal and 4-hydroxyhexenal in light-exposed rat retina. *Invest Ophthalmol Vis Sci,* 46**,** 3859-68.

TERPE, K. 2006. Overview of bacterial expression systems for heterologous protein production: from molecular and biochemical fundamentals to commercial systems. *Appl Microbiol Biotechnol,* 72**,** 211-22.

TERRIEN, E., CHAFFOTTE, A., LAFAGE, M., KHAN, Z., PRÉHAUD, C., CORDIER, F., SIMENEL, C., DELEPIERRE, M., BUC, H., LAFON, M. & WOLFF, N. 2012. Interference with the PTEN-MAST2 interaction by a viral protein leads to cellular relocalization of PTEN. *Sci Signal,* 5**,** ra58.

THORPE, L. M., YUZUGULLU, H. & ZHAO, J. J. 2015. PI3K in cancer: divergent roles of isoforms, modes of activation and therapeutic targeting. *Nat Rev Cancer,* 15**,** 7-24.

TIMUCIN, A. C. & BASAGA, H. 2017. Pro-apoptotic effects of lipid oxidation products: HNE at the crossroads of NF-κB pathway and anti-apoptotic Bcl-2. *Free Radical Biology and Medicine,* 111**,** 209-218.

TOBY, T. K., FORNELLI, L. & KELLEHER, N. L. 2016. Progress in Top-Down Proteomics and the Analysis of Proteoforms. *Annual Review of Analytical Chemistry,* 9**,** 499-519.

TORRES, J. & PULIDO, R. 2001. The tumor suppressor PTEN is phosphorylated by the protein kinase CK2 at its C terminus. Implications for PTEN stability to proteasome-mediated degradation. *J Biol Chem,* 276**,** 993-8.

TOSSOUNIAN, M.-A., ZHAO, Y., YU, B. Y. K., MARKEY, S. A., MALANCHUK, O., ZHU, Y., CAIN, A. & GOUT, I. 2024. Low-molecular-weight thiol transferases in redox regulation and antioxidant defence. *Redox Biology,* 71**,** 103094.

TROTMAN, L. C., WANG, X., ALIMONTI, A., CHEN, Z., TERUYA-FELDSTEIN, J., YANG, H., PAVLETICH, N. P., CARVER, B. S., CORDON-CARDO, C., ERDJUMENT-BROMAGE, H., TEMPST, P., CHI, S. G., KIM, H. J., MISTELI, T., JIANG, X. & PANDOLFI, P. P. 2007. Ubiquitination regulates PTEN nuclear import and tumor suppression. *Cell,* 128**,** 141-56.

TSUCHIYA, Y., YAMAGUCHI, M., CHIKUMA, T. & HOJO, H. 2005. Degradation of glyceraldehyde-3-phosphate dehydrogenase triggered by 4-hydroxy-2-nonenal and 4-hydroxy-2-hexenal. *Arch Biochem Biophys,* 438**,** 217-22.

TU, W., WANG, H., LI, S., LIU, Q. & SHA, H. 2019. The Anti-Inflammatory and Anti-Oxidant Mechanisms of the Keap1/Nrf2/ARE Signaling Pathway in Chronic Diseases. *Aging Dis,* 10**,** 637-651.

URH, M., SIMPSON, D. & ZHAO, K. 2009. Affinity chromatography: general methods. *Methods Enzymol,* 463**,** 417-38.

VADLAKONDA, L., DASH, A., PASUPULETI, M., ANIL KUMAR, K. & REDDANNA, P. 2013. The Paradox of Akt-mTOR Interactions. *Front Oncol,* 3**,** 165.

VAN THEMSCHE, C., LEBLANC, V., PARENT, S. & ASSELIN, E. 2009. X-linked inhibitor of apoptosis protein (XIAP) regulates PTEN ubiquitination, content, and compartmentalization. *J Biol Chem,* 284**,** 20462-6.

VASIL'EV, Y. V., TZENG, S. C., HUANG, L. & MAIER, C. S. 2014. Protein modifications by electrophilic lipoxidation products: adduct formation, chemical strategies and tandem mass spectrometry for their detection and identification. *Mass Spectrom Rev,* 33**,** 157-82.

VAZQUEZ, F., GROSSMAN, S. R., TAKAHASHI, Y., ROKAS, M. V., NAKAMURA, N. & SELLERS, W. R. 2001. Phosphorylation of the PTEN tail acts as an inhibitory switch by preventing its recruitment into a protein complex. *J Biol Chem,* 276**,** 48627-30.

VAZQUEZ, F., RAMASWAMY, S., NAKAMURA, N. & SELLERS, W. R. 2000. Phosphorylation of the PTEN tail regulates protein stability and function. *Mol Cell Biol,* 20**,** 5010-8.

VERRASTRO, I., TVEEN-JENSEN, K., SPICKETT, C. M. & PITT, A. R. 2018. The effect of HOCl-induced modifications on phosphatase and tensin homologue (PTEN) structure and function. *Free Radic Res,* 52**,** 232-247.

VERRASTRO, I., TVEEN-JENSEN, K., WOSCHOLSKI, R., SPICKETT, C. M. & PITT, A. R. 2016. Reversible oxidation of phosphatase and tensin homolog (PTEN) alters its interactions with signaling and regulatory proteins. *Free Radic Biol Med,* 90**,** 24-34.

VIEDMA-POYATOS, A., GONZALEZ-JIMENEZ, P., LANGLOIS, O., COMPANY-MARIN, I., SPICKETT, C. M. & PEREZ-SALA, D. 2021. Protein Lipoxidation: Basic Concepts and Emerging Roles. *Antioxidants (Basel),* 10.

VILA, A., TALLMAN, K. A., JACOBS, A. T., LIEBLER, D. C., PORTER, N. A. & MARNETT, L. J. 2008. Identification of Protein Targets of 4-Hydroxynonenal Using Click Chemistry for ex Vivo Biotinylation of Azido and Alkynyl Derivatives. *Chemical Research in Toxicology,* 21**,** 432-444.

VIRMANI, R., SINGH, Y. & HASIJA, Y. 2018. GroEL Mediates Folding of Bacillus anthracis Serine/Threonine Protein Kinase, PrkC. *Indian J Microbiol,* 58**,** 520-524.

VIROLLE, T., ADAMSON, E. D., BARON, V., BIRLE, D., MERCOLA, D., MUSTELIN, T. & DE BELLE, I. 2001. The Egr-1 transcription factor directly activates PTEN during irradiation-induced signalling. *Nature Cell Biology,* 3**,** 1124-1128.

VLADYKOVSKAYA, E., SITHU, S. D., HABERZETTL, P., WICKRAMASINGHE, N. S., MERCHANT, M. L., HILL, B. G., MCCRACKEN, J., AGARWAL, A., DOUGHERTY, S., GORDON, S. A., SCHUSCHKE, D. A., BARSKI, O. A., O'TOOLE, T., D'SOUZA, S. E., BHATNAGAR, A. & SRIVASTAVA, S. 2012. Lipid peroxidation product 4-hydroxy-trans-2-nonenal causes endothelial activation by inducing endoplasmic reticulum stress. *J Biol Chem,* 287**,** 11398-409.

VOITKUN, V. & ZHITKOVICH, A. 1999. Analysis of DNA-protein crosslinking activity of malondialdehyde in vitro. *Mutat Res,* 424**,** 97-106.

VOSS, P. & GRUNE, T. 2007. The nuclear proteasome and the degradation of oxidatively damaged proteins. *Amino Acids,* 32**,** 527-534.

WAKABAYASHI, N., DINKOVA-KOSTOVA, A. T., HOLTZCLAW, W. D., KANG, M. I., KOBAYASHI, A., YAMAMOTO, M., KENSLER, T. W. & TALALAY, P. 2004. Protection against electrophile and oxidant stress by induction of the phase 2 response: fate of cysteines of the Keap1 sensor modified by inducers. *Proc Natl Acad Sci U S A,* 101**,** 2040-5.

WALKER, S. M., LESLIE, N. R., PERERA, N. M., BATTY, I. H. & DOWNES, C. P. 2004. The tumour-suppressor function of PTEN requires an N-terminal lipid-binding motif. *Biochem J,* 379**,** 301-7.

WANG, J. & LINDAHL, T. 2016. Maintenance of Genome Stability. *Genomics Proteomics Bioinformatics,* 14**,** 119-121.

WANG, X., TROTMAN, L. C., KOPPIE, T., ALIMONTI, A., CHEN, Z., GAO, Z., WANG, J., ERDJUMENT-BROMAGE, H., TEMPST, P., CORDON-CARDO, C., PANDOLFI, P. P. & JIANG, X. 2007. NEDD4-1 is a proto-oncogenic ubiquitin ligase for PTEN. *Cell,* 128**,** 129-39.

WEERAPANA, E., WANG, C., SIMON, G. M., RICHTER, F., KHARE, S., DILLON, M. B. D., BACHOVCHIN, D. A., MOWEN, K., BAKER, D. & CRAVATT, B. F. 2010. Quantitative reactivity profiling predicts functional cysteines in proteomes. *Nature,* 468**,** 790-795.

WEI, Y., STEC, B., REDFIELD, A. G., WEERAPANA, E. & ROBERTS, M. F. 2015. Phospholipid-binding sites of phosphatase and tensin homolog (PTEN): exploring the mechanism of phosphatidylinositol 4,5-bisphosphate activation. *J Biol Chem,* 290**,** 1592-606.

WINTER, C. K., SEGALL, H. J. & HADDON, W. F. 1986. Formation of cyclic adducts of deoxyguanosine with the aldehydes trans-4-hydroxy-2-hexenal and trans-4-hydroxy-2-nonenal in vitro. *Cancer Res,* 46**,** 5682-6.

WIŚNIEWSKI, J. R., HEIN, M. Y., COX, J. & MANN, M. 2014. A “Proteomic Ruler” for Protein Copy Number and Concentration Estimation without Spike-in Standards*. *Molecular & Cellular Proteomics,* 13**,** 3497-3506.

WU, Q., YUAN, H., ZHANG, L. & ZHANG, Y. 2012. Recent advances on multidimensional liquid chromatography–mass spectrometry for proteomics: From qualitative to quantitative analysis—A review. *Analytica Chimica Acta,* 731**,** 1-10.

WU, Y., DOWBENKO, D., SPENCER, S., LAURA, R., LEE, J., GU, Q. & LASKY, L. A. 2000. Interaction of the tumor suppressor PTEN/MMAC with a PDZ domain of MAGI3, a novel membrane-associated guanylate kinase. *J Biol Chem,* 275**,** 21477-85.

WU, Y., ZHOU, H., WU, K., LEE, S., LI, R. & LIU, X. 2014. PTEN phosphorylation and nuclear export mediate free fatty acid-induced oxidative stress. *Antioxid Redox Signal,* 20**,** 1382-95.

XIA, D., SRINIVAS, H., AHN, Y. H., SETHI, G., SHENG, X., YUNG, W. K., XIA, Q., CHIAO, P. J., KIM, H., BROWN, P. H., WISTUBA, II, AGGARWAL, B. B. & KURIE, J. M. 2007. Mitogen-activated protein kinase kinase-4 promotes cell survival by decreasing PTEN expression through an NF kappa B-dependent pathway. *J Biol Chem,* 282**,** 3507-19.

XIAO, Y., YEONG CHIT CHIA, J., GAJEWSKI, J. E., SIO SENG LIO, D., MULHERN, T. D., ZHU, H. J., NANDURKAR, H. & CHENG, H. C. 2007. PTEN catalysis of phospholipid dephosphorylation reaction follows a two-step mechanism in which the conserved aspartate-92 does not function as the general acid--mechanistic analysis of a familial Cowden disease-associated PTEN mutation. *Cell Signal,* 19**,** 1434-45.

YAMANO, S., DAI, J. & MOURSI, A. M. 2010. Comparison of transfection efficiency of nonviral gene transfer reagents. *Mol Biotechnol,* 46**,** 287-300.

YAN, W., HWANG, D. & AEBERSOLD, R. 2008. Quantitative proteomic analysis to profile dynamic changes in the spatial distribution of cellular proteins. *Methods Mol Biol,* 432**,** 389-401.

YANG, B., LI, R., MICHAEL GREENLIEF, C., FRITSCHE, K. L., GU, Z., CUI, J., LEE, J. C., BEVERSDORF, D. Q. & SUN, G. Y. 2018a. Unveiling anti-oxidative and anti-inflammatory effects of docosahexaenoic acid and its lipid peroxidation product on lipopolysaccharide-stimulated BV-2 microglial cells. *J Neuroinflammation,* 15**,** 202.

YANG, J., NIE, J., MA, X., WEI, Y., PENG, Y. & WEI, X. 2019. Targeting PI3K in cancer: mechanisms and advances in clinical trials. *Molecular Cancer,* 18**,** 26.

YANG, Y., ANDERSON, E. & ZHANG, S. 2018b. Evaluation of six sample preparation procedures for qualitative and quantitative proteomics analysis of milk fat globule membrane. *ELECTROPHORESIS,* 39**,** 2332-2339.

YASUI, M., MATSUOKA, S. & UEDA, M. 2014. PTEN Hopping on the Cell Membrane Is Regulated via a Positively-Charged C2 Domain. *PLOS Computational Biology,* 10**,** e1003817.

YEANG, C., HASANALLY, D., QUE, X., HUNG, M. Y., STAMENKOVIC, A., CHAN, D., CHAUDHARY, R., MARGULETS, V., EDEL, A. L., HOSHIJIMA, M., GU, Y., BRADFORD, W., DALTON, N., MIU, P., CHEUNG, D. Y., JASSAL, D. S., PIERCE, G. N., PETERSON, K. L., KIRSHENBAUM, L. A., WITZTUM, J. L., TSIMIKAS, S. & RAVANDI, A. 2019. Reduction of myocardial ischaemia-reperfusion injury by inactivating oxidized phospholipids. *Cardiovasc Res,* 115**,** 179-189.

YIM, E. K., PENG, G., DAI, H., HU, R., LI, K., LU, Y., MILLS, G. B., MERIC-BERNSTAM, F., HENNESSY, B. T., CRAVEN, R. J. & LIN, S. Y. 2009. Rak functions as a tumor suppressor by regulating PTEN protein stability and function. *Cancer Cell,* 15**,** 304-14.

YIN, H., XU, L. & PORTER, N. A. 2011. Free radical lipid peroxidation: mechanisms and analysis. *Chem Rev,* 111**,** 5944-72.

YOKAWA, K., TSUKUBE, T., YAGI, N., HOSHINO, M., NAKASHIMA, Y., NAKAGAWA, K. & OKITA, Y. 2017. Abstract 490: Quantitative and Dynamic Measurements of Aortic Wall of Acute Type-A Aortic Dissection With X-Ray Phase-Contrast Tomography. *Arteriosclerosis, Thrombosis, and Vascular Biology,* 37**,** A490-A490.

YOSHIDA, N. & SATO, M. 2009. Plasmid uptake by bacteria: a comparison of methods and efficiencies. *Appl Microbiol Biotechnol,* 83**,** 791-8.

YOSHIDA, Y., SAITO, Y., HAYAKAWA, M., HABUCHI, Y., IMAI, Y., SAWAI, Y. & NIKI, E. 2007. Levels of lipid peroxidation in human plasma and erythrocytes: comparison between fatty acids and cholesterol. *Lipids,* 42**,** 439-49.

YOUNG, C. L., BRITTON, Z. T. & ROBINSON, A. S. 2012. Recombinant protein expression and purification: a comprehensive review of affinity tags and microbial applications. *Biotechnol J,* 7**,** 620-34.

YU, Q., ZHANG, R., LI, T., YANG, L., ZHOU, Z., HOU, L., WU, W., ZHAO, R., CHEN, X., YAO, Y., HUANG, S. & CHEN, L. 2023. Mitochondrial Hydrogen Peroxide Activates PTEN and Inactivates Akt Leading to Autophagy Inhibition-Dependent Cell Death in Neuronal Models of Parkinson's Disease. *Molecular Neurobiology,* 60**,** 3345-3364.

YU, Z., FOTOUHI-ARDAKANI, N., WU, L., MAOUI, M., WANG, S., BANVILLE, D. & SHEN, S. H. 2002. PTEN associates with the vault particles in HeLa cells. *J Biol Chem,* 277**,** 40247-52.

YUAN, L., LV, Y., LI, H., GAO, H., SONG, S., ZHANG, Y., XING, G., KONG, X., WANG, L., LI, Y., ZHOU, T., GAO, D., XIAO, Z.-X., YIN, Y., WEI, W., HE, F. & ZHANG, L. 2015. Deubiquitylase OTUD3 regulates PTEN stability and suppresses tumorigenesis. *Nature Cell Biology,* 17**,** 1169-1181.

YUSTE, R. 2005. Fluorescence microscopy today. *Nature Methods,* 2**,** 902-904.

ZHANG, C., MA, H. M., DONG, S. S., ZHANG, N., HE, P., GE, M. K., XIA, L., YU, J. X., XIA, Q., CHEN, G. Q. & SHEN, S. M. 2022. Furin extracellularly cleaves secreted PTENalpha/beta to generate C-terminal fragment with a tumor-suppressive role. *Cell Death Dis,* 13**,** 532.

ZHANG, D. D. & HANNINK, M. 2003. Distinct cysteine residues in Keap1 are required for Keap1-dependent ubiquitination of Nrf2 and for stabilization of Nrf2 by chemopreventive agents and oxidative stress. *Mol Cell Biol,* 23**,** 8137-51.

ZHANG, H. & GE, Y. 2011. Comprehensive Analysis of Protein Modifications by Top-Down Mass Spectrometry. *Circulation: Cardiovascular Genetics,* 4**,** 711-711.

ZHANG, J., LEE, Y. R., DANG, F., GAN, W., MENON, A. V., KATON, J. M., HSU, C. H., ASARA, J. M., TIBAREWAL, P., LESLIE, N. R., SHI, Y., PANDOLFI, P. P. & WEI, W. 2019. PTEN Methylation by NSD2 Controls Cellular Sensitivity to DNA Damage. *Cancer Discov,* 9**,** 1306-1323.

ZHANG, J., LI, M., LV, Y., GUO, S. & YANG, B. 2023. Protein aggregation impacts in vitro protein digestibility, peptide profiling and potential bioactive peptides of soymilk and dry-heated soybeans. *LWT,* 182**,** 114857.

ZHANG, J., ZHANG, P., WEI, Y., PIAO, H. L., WANG, W., MADDIKA, S., WANG, M., CHEN, D., SUN, Y., HUNG, M. C., CHEN, J. & MA, L. 2013. Deubiquitylation and stabilization of PTEN by USP13. *Nat Cell Biol,* 15**,** 1486-1494.

ZHANG, W. & LIU, H. T. 2002. MAPK signal pathways in the regulation of cell proliferation in mammalian cells. *Cell Research,* 12**,** 9-18.

ZHANG, X., TANG, N., HADDEN, T. J. & RISHI, A. K. 2011. Akt, FoxO and regulation of apoptosis. *Biochim Biophys Acta,* 1813**,** 1978-86.

ZHANG, X. C., PICCINI, A., MYERS, M. P., VAN AELST, L. & TONKS, N. K. 2012. Functional analysis of the protein phosphatase activity of PTEN. *Biochem J,* 444**,** 457-64.

ZHAO, J., CHEN, J., ZHU, H. & XIONG, Y. L. 2012. Mass spectrometric evidence of malonaldehyde and 4-hydroxynonenal adductions to radical-scavenging soy peptides. *J Agric Food Chem,* 60**,** 9727-36.

ZHAO, X., LI, G. & LIANG, S. 2013. Several affinity tags commonly used in chromatographic purification. *J Anal Methods Chem,* 2013**,** 581093.

ZHONG, Y. Q., WEI, J., FU, Y. R., SHAO, J., LIANG, Y. W., LIN, Y. H., LIU, J. & ZHU, Z. H. 2008. [Toxicity of cationic liposome Lipofectamine 2000 in human pancreatic cancer Capan-2 cells]. *Nan Fang Yi Ke Da Xue Xue Bao,* 28**,** 1981-4.

ZHUO, D. X., ZHANG, X. W., JIN, B., ZHANG, Z., XIE, B. S., WU, C. L., GONG, K. & MAO, Z. B. 2013. CSTP1, a novel protein phosphatase, blocks cell cycle, promotes cell apoptosis, and suppresses tumor growth of bladder cancer by directly dephosphorylating Akt at Ser473 site. *PLoS One,* 8**,** e65679.

ZORRILLA, S., MONICO, A., DUARTE, S., RIVAS, G., PEREZ-SALA, D. & PAJARES, M. A. 2019. Integrated approaches to unravel the impact of protein lipoxidation on macromolecular interactions. *Free Radic Biol Med,* 144**,** 203-217.

Supplementary Data

A

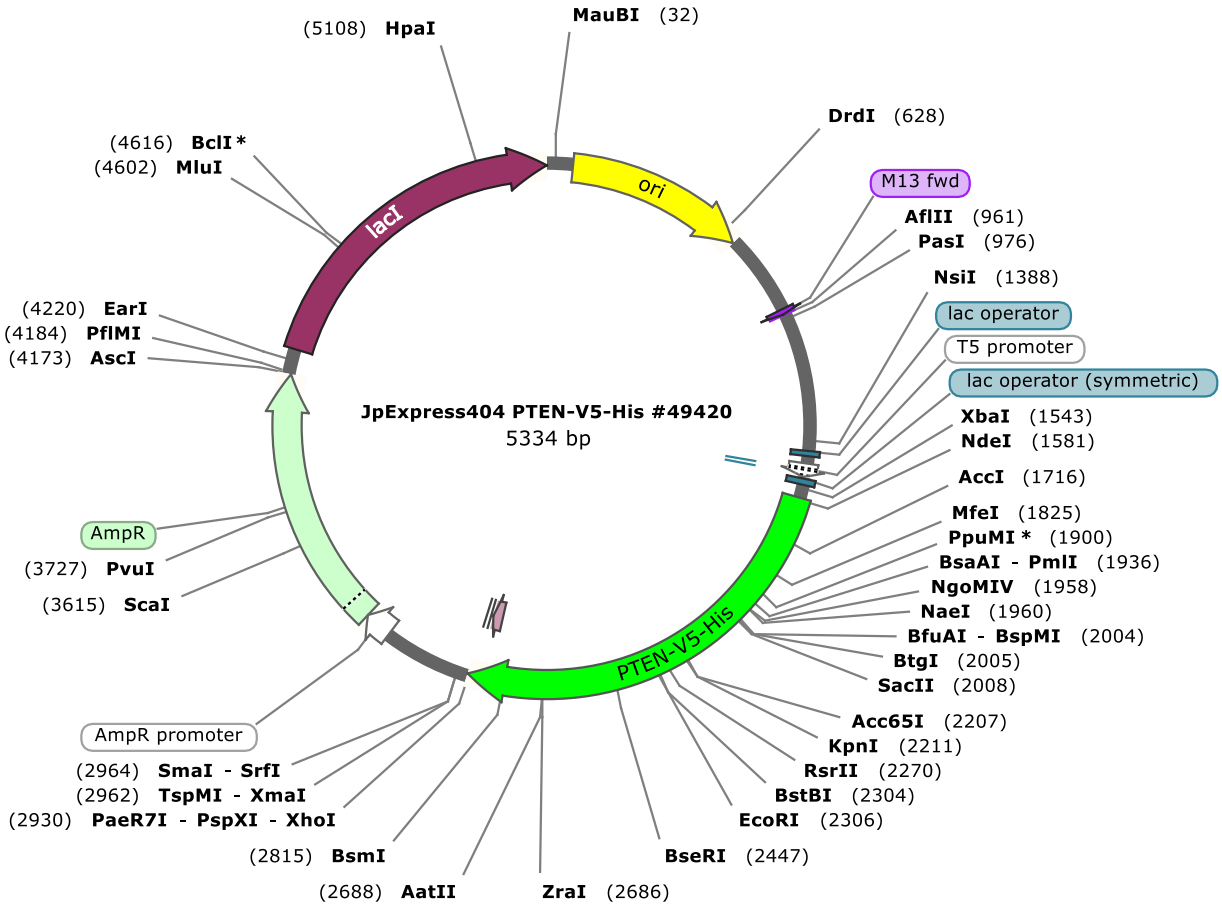

B

5’atgaccgcgattatcaaagagatcgtgtcccgtaacaagcgccgttatcaagaagatggctttgacctggacctgacctacatc
tacccgaacattatcgcgatgggttttccagccgagcgcctggagggcgtctaccgtaataacatcgatgatgtggttcgttttctgg
acagcaaacataagaaccattacaagatctataatctgtgcgccgagcgtcattatgacaccgcgaaattcaattgccgtgttgc
gcagtacccgttcgaggaccacaatccgccgcaactggaactgattaaaccgttctgcgaggacctggatcagtggctgtccga
ggacgacaaccacgtggccgcgattcactgtaaggccggcaaaggtcgtaccggcgtcatgatctgcgcgtacctgctgcacc
gcggtaagtttctgaaggcgcaagaagcgctggacttttacggcgaggtgcgtacccgcgacaaaaagggtgtcaccatcccg
agccaacgccgctatgtttactactacagctatttgctgaaaaaccacctggattatcgtcctgtcgccctgttgtttcacaagatgat
gtttgaaacgattccgatgttcagcggcggtacctgtaatccgcagttcgtcgtttgtcagctgaaggtgaagatctacagctctaat
agcggtccgacccgtcgcgaagataagtttatgtatttcgaattcccgcagccgctgccggtttgtggtgacatcaaggtggagttc
ttccataaacaaaacaagatgttgaagaaagataagatgttccatttttgggtcaacactttctttattccgggtccggaggagacta
gcgagaaagttgagaacggtagcctgtgcgatcaagaaatcgatagcatttgcagcatcgaacgtgcggataatgacaaaga
atatctggtcttgaccctgacgaaaaacgacctggacaaagcgaacaaagataaagcgaatcgctatttcagcccgaatttcaa

agttaagctgtactttaccaaaactgtggaggaaccgagcaatccggaggcgtctagctctaccagcgtgaccccggacgtcag
cgacaatgagccggaccactatcgttacagcgacacgaccgacagcgatcctgaaaatgaaccgtttgacgaagatcaacat
acgcagattaccaaggtgaaaggcaacagcgcggatattcagcattctggtggccgtagcagcttggaaggccctcgcttcga
gggtaagccgattccgaatccgctgctgggtctggatagcacgcgcacgggtcaccaccaccatcaccactaa 3’

C

MTAIIKEIVSRNKRRYQEDGFDLDLTYIYPNIIAMGFPAERLEGVYRNNIDDVVRFLDSKHKN
HYKIYNLCAERHYDTAKFNCRVAQYPFEDHNPPQLELIKPFCEDLDQWLSEDDNHVAAIHC
KAGKGRTGVMICAYLLHRGKFLKAQEALDFYGEVRTRDKKGVTIPSQRRYVYYYSYLLKNH
LDYRPVALLFHKMMFETIPMFSGGTCNPQFVVCQLKVKIYSSNSGPTRREDKFMYFEFPQP
LPVCGDIKVEFFHKQNKMLKKDKMFHFWVNTFFIPGPEETSEKVENGSLCDQEIDSICSIER
ADNDKEYLVLTLTKNDLDKANKDKANRYFSPNFKVKLYFTKTVEEPSNPEASSSTSVTPDVS
DNEPDHYRYSDTTDSDPENEPFDEDQHTQITKVKGNSADIQHSGGRSSLEGPRFEGKPIPN
PLLGLDSTRTGHHHHHH*

PTEN
Linkers
V5-tag
His-tag

Supplementary Figure 1. Map and insert sequence of the JpExpress404 PTEN-V5-His plasmid. Map (A), DNA sequence of the insert encoding for PTEN-V5-His (B) and translated sequence for PTEN-V5-His (black: PTEN protein sequence; orange: linker sequences; blue: epitope tag from simian virus 5 (V5) tag; purple: 6xHis-tag) (C). JpExpress404 PTEN was a gift from Ramon Parsons (Addgene plasmid #49420; http://n2t.net/addgene:49420; RRID:Addgene_49420) (Hopkins et al., 2013).

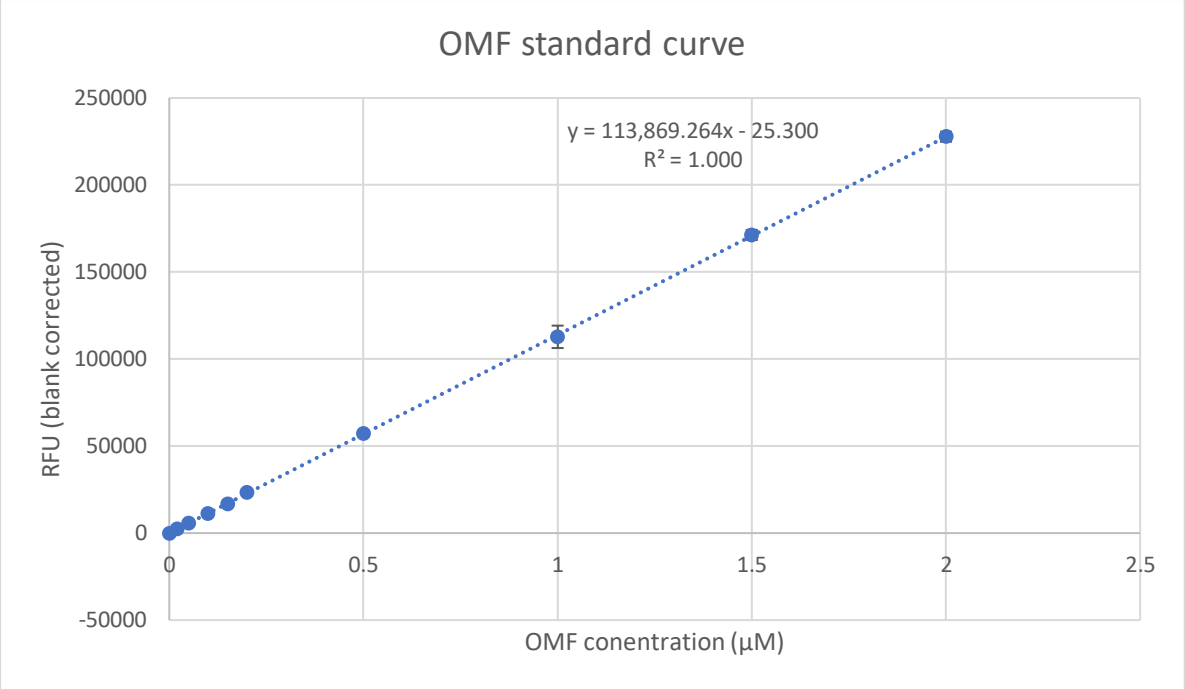

Supplementary Figure 2. OMF standard curve.
The OMF standard curve was prepared in triplicates in a black 96-well plate by diluting a 10 µM OMF stock solution in OMFP assay buffer to obtain concentrations of 0.1, 0.25, 0.5, 0.75, 1, 2.5, 5, 7.5 and 10 µM in 200 µL final volume per well and a triplicate of 200 µL per well of OMFP assay buffer without OMF was added to the plate as a blank. Gain adjustment was set to 90% of the fluorescence value of the highest standard concentration of OMF. The fluorescence was measured with 485 nm excitation (485BP1 filter) and 520 nm emission (EM520 filter) using 20 flashes/well after shaking at 300 rpm for 3 seconds and settling for 0.5 seconds. Values were adjusted to the blank.

A

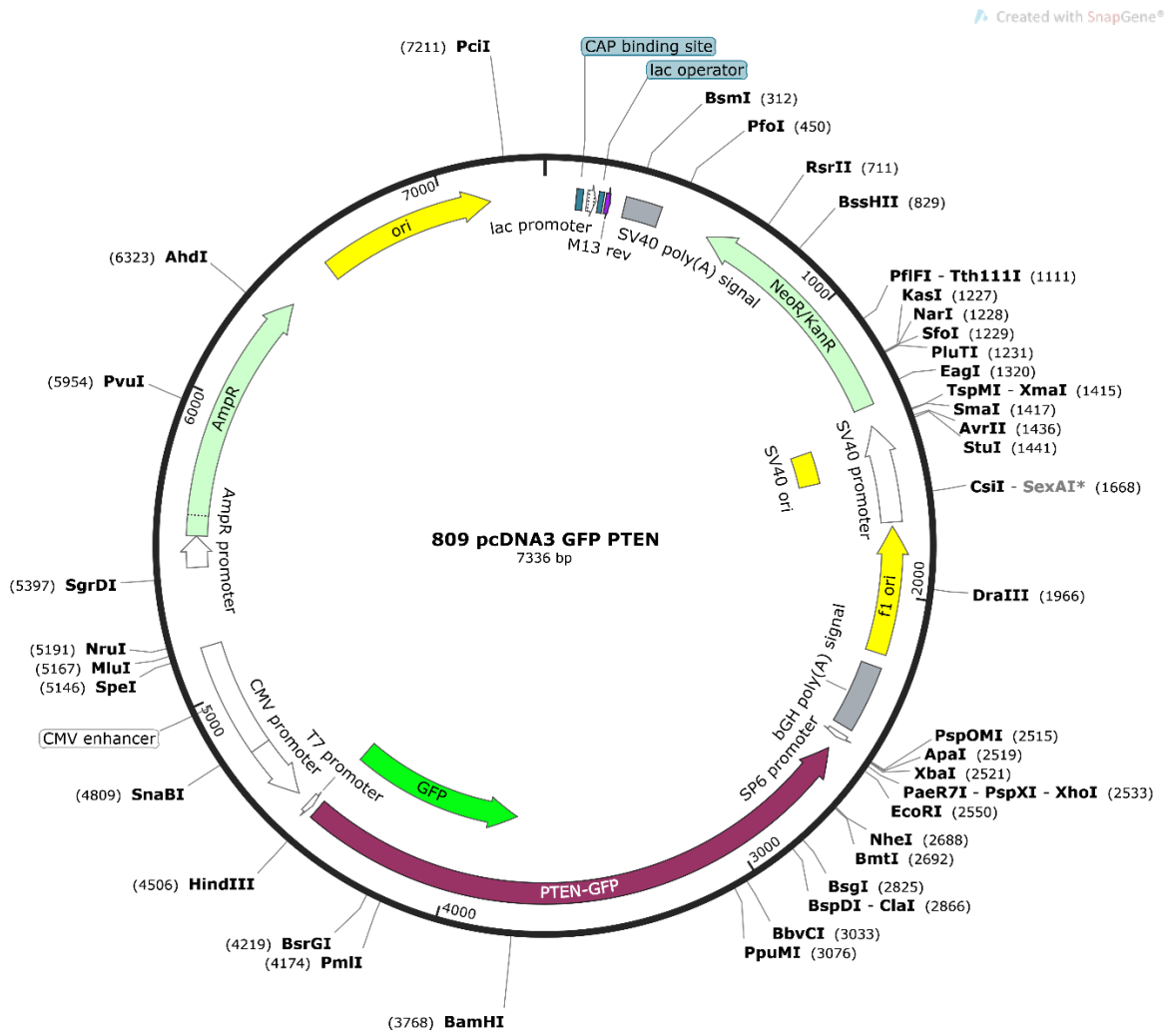

B

5’atgagtaaaggagaagaactcttcactggagttgtcccaattcttgttgaattagatggtgatgttaatgggcacaaattttctgtca
gtggagagggtgaaggtgatgcaacatacggaaaacttacccttaaatttatttgcactactggaaaactacctgttccatggcca
acacttgtcactactttcacttatggtgttcagtgcttttcaagatacccggatcatatgaaacggcatgacttttttcaagagtgccatg
cccgaaggttatgtacaggaaagaactatatttttcaaagatgacgggaactacaagacacgtgctgaagtcaagtttgaaggtg
ataccccttgttaatagaatcgagttaaaaggtattgattttaaagaagatggaaacattcttgggcacaaattggaatacaactata
actcacacaatgtatacatcatggcagacaaacaaaagaatggaatcaaagctaacttcaaaattagacacaacattgaagat
ggaagcgttcaactagcagaccattatcaacaaaatactccaattggcgatggccctgtccttttaccagacaaccattacctgtc
cacacaatctgccctttcgaaagatcccaacgaaaagagagaccacatggtccttcttgagtttgtaacagctgctgggattacac
atggcatggatgaactatacaaacagcagcttcagggatccatgacagccatcatcaaagagatcgttagcagaaacaaaag
gagatatcaagaggatggattcgacttagacttgacctatatttatccaaacattattgctatgggatttcctgcagaaagacttgaa
ggcgtatacaggaacaatattgatgatgtagtaaggtttttggattcaaagcataaaaaccattacaagatatacaatctttgtgctg

aaagacattatgacaccgccaaatttaattgcagagttgcacaatatccttttgaagaccataacccaccacagctagaacttatc
aaacccttttgtgaagatcttgaccaatggctaagtgaagatgacaatcatgttgcagcaattcactgtaaagctggaaagggac
gaactggtgtaatgatatgtgcatatttattacatcggggcaaatttttaaaggcacaagaggccctagatttctatggggaagtaa
ggaccagagacaaaaagggagtaactattcccagtcagaggcgctatgtgtattattatagctacctgttaaagaatcatctggat
tatagaccagtggcactgttgtttcacaagatgatgtttgaaactattccaatgttcagtggcggaacttgcaatcctcagtttgtggtc
tgccagctaaaggtgaagatatattcctccaattcaggacccacacgacgggaagacaagttcatgtactttgagttccctcagcc
gttacctgtgtgtggtgatatcaaagtagagttcttccacaaacagaacaagatgctaaaaaaggacaaaatgtttcacttttgggt
aaatacattcttcataccaggaccagaggaaacctcagaaaaagtagaaaatggaagtctatgtgatcaagaaatcgatagca
tttgcagtatagagcgtgcagataatgacaaggaatatctagtacttactttaacaaaaaatgatcttgacaaagcaaataaaga
caaagccaaccgatacttttctccaaattttaaggtgaagctgtacttcacaaaaacagtagaggagccgtcaaatccagaggct
agcagttcaacttctgtaacaccagatgttagtgacaatgaacctgatcattatagatattctgacaccactgactctgatccagag
aatgaacctttgatgaagatcagcatacacaaattacaaaagtctga 3’

C

MSKGEELFTGVVPILVELDGDVNGHKFSVSGEGEGDATYGKLTLKFICTTGKLPVPWPTLVT
TFTYGVQCFSRYPDHMKRHDFFKSAMPEGYVQERTIFFKDDGNYKTRAEVKFEGDTLVNRI
ELKGIDFKEDGNILGHKLEYNYNSHNVYIMADKQKNGIKANFKIRHNIEDGSVQLADHYQQN
TPIGDGPVLLPDNHYLSTQSALSKDPNEKRDHMVLLEFVTAAGITHGMDELYKQQLQGSMT
AIIKEIVSRNKRRYQEDGFDLDLTYIYPNIIAMGFPAERLEGVYRNNIDDVVRFLDSKHKNHYK
IYNLCAERHYDTAKFNCRVAQYPFEDHNPPQLELIKPFCEDLDQWLSEDDNHVAAIHCKAG
KGRTGVMICAYLLHRGKFLKAQEALDFYGEVRTRDKKGVTIPSQRRYVYYYSYLLKNHLDY
RPVALLFHKMMFETIPMFSGGTCNPQFVVCQLKVKIYSSNSGPTRREDKFMYFEFPQPLPV
CGDIKVEFFHKQNKMLKKDKMFHFWVNTFFIPGPEETSEKVENGSLCDQEIDSICSIERADN
DKEYLVLTLTKNDLDKANKDKANRYFSPNFKVKLYFTKTVEEPSNPEASSSTSVTPDVSDNE
PDHYRYSDTTDSDPENEPFDEDQHTQITKV*

GFP
Linker
PTEN

Supplementary Figure 3. Map and insert sequence of the pcDNA3 GFP-PTEN plasmid.
Map (A), DNA sequence of the insert encoding for GFP-PTEN (B) and translated sequence for GFP-PTEN (green: GFP protein sequence; orange: linker sequence; black: PTEN protein sequence) (C). 809 pcDNA3 GFP PTEN was a gift from William Sellers (Addgene plasmid # 10759 ; http://n2t.net/addgene:10759 ; RRID:Addgene_10759) (Vazquez et al., 2001).

Supplementary Table 1. Amino acid mass reference table.
Reproduced from https://www.matrixscience.com/help/aa_help.html.

The data in this table are for amino acid *residues*. To calculate the mass of a neutral peptide or protein, sum the residue masses plus the masses of the terminating groups (e.g. H at the N-terminus and OH at the C-terminus).

Residue	3-letter code	1-letter code	Mono-isotopic mass	Average mass	Structure
Alanine C_3H_5NO	Ala	A	71.037114	71.0779	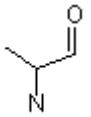
Arginine $C_6H_{12}N_4O$	Arg	R	156.101111	156.1857	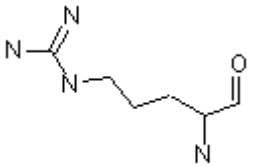
Asparagine $C_4H_6N_2O_2$	Asn	N	114.042927	114.1026	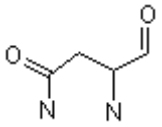
Aspartic acid $C_4H_5NO_3$	Asp	D	115.026943	115.0874	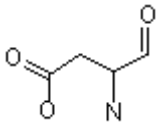
Cysteine C_3H_5NOS	Cys	C	103.009185	103.1429	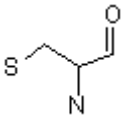
Glutamic acid $C_5H_7NO_3$	Glu	E	129.042593	129.114	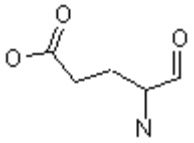
Glutamine $C_5H_8N_2O_2$	Gln	Q	128.058578	128.1292	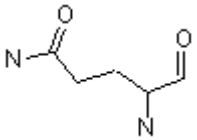
Glycine C_2H_3NO	Gly	G	57.021464	57.0513	
Histidine $C_6H_7N_3O$	His	H	137.058912	137.1393	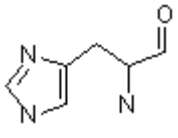

Isoleucine $C_6H_{11}NO$	Ile	I	113.084064	113.1576	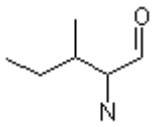
Leucine $C_6H_{11}NO$	Leu	L	113.084064	113.1576	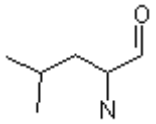
Lysine $C_6H_{12}N_2O$	Lys	K	128.094963	128.1723	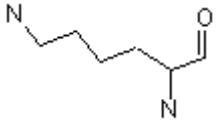
Methionine C_5H_9NOS	Met	M	131.040485	131.1961	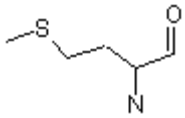
Phenylalanine C_9H_9NO	Phe	F	147.068414	147.1739	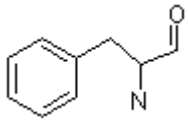
Proline C_5H_7NO	Pro	P	97.052764	97.1152	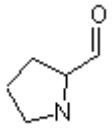
Serine $C_3H_5NO_2$	Ser	S	87.032028	87.0773	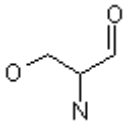
Threonine $C_4H_7NO_2$	Thr	T	101.047679	101.1039	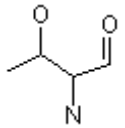
Selenocysteine C_3H_5NOSe	Sec	U	150.95363	150.0379	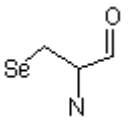
Tryptophan $C_{11}H_{10}N_2O$	Trp	W	186.079313	186.2099	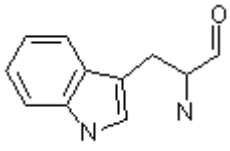
Tyrosine $C_9H_9NO_2$	Tyr	Y	163.06332	163.1733	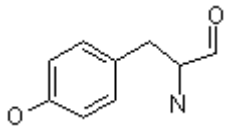
Valine C_5H_9NO	Val	V	99.068414	99.1311	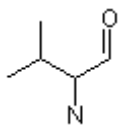

Supplementary Table 2. Representative raw data from Mascot identification of proteins in HHE- and PONPC-induced PTEN-V5-His aggregates.
Data represents one condition (molar ratio of 5:1 treatment:PTEN-V5-His for 2 hours at 37˚C) of one biological replicate. The data for PTEN was highlighted in red, showing high differences in detection of PTEN between HHE- and PONPC-induced PTEN-V5-His aggregates.

HHE (n3, sample aggregate HHE 2h:PTEN-V5-His 5:1)										
Database	Accession	Score	Mass	Sequence coverage	Num. of matches	Num. of significant matches	Num. of significant unique sequences	Num. of significant sequences	emPAI	Description
SwissProt	PTEN_CANLF	3214	47136	0.51	127	127	18	18	18.88	Phosphatidylinositol 3,4,5-trisphosphate 3-phosphatase and dual-specificity protein phosphatase PTEN OS=Canis lupus familiaris OX=9615 GN=PTEN PE=2 SV=1
SwissProt	ARNA_ECOBW	1337	74242	0.47	54	54	25	25	4.34	Bifunctional polymyxin resistance protein ArnA OS=Escherichia coli (strain K12 / MC4100 / BW2952) OX=595496 GN=arnA PE=3 SV=1
SwissProt	ALBU_BOVIN	1101	69248	0.37	39	39	21	21	2.67	Albumin OS=Bos taurus OX=9913 GN=ALB PE=1 SV=4
SwissProt	CH60_ECO24	867	57293	0.53	22	22	18	18	3.46	Chaperonin GroEL OS=Escherichia coli O139:H28 (strain E24377A / ETEC) OX=331111 GN=groEL PE=3 SV=1
SwissProt	ASTC_ECOBW	822	43638	0.51	24	24	13	13	3.34	Succinylornithine transaminase OS=Escherichia coli (strain K12 / MC4100 / BW2952) OX=595496 GN=astC PE=3 SV=1
SwissProt	TRYP_PIG	786	24394	0.42	32	32	7	7	3.01	Trypsin OS=Sus scrofa OX=9823 PE=1 SV=1
SwissProt	DNAK_ECOHS	577	69088	0.39	21	21	16	16	1.7	Chaperone protein DnaK OS=Escherichia coli O9:H4 (strain HS) OX=331112 GN=dnaK PE=3 SV=1
SwissProt	SLYD_ECOLI	362	20840	0.36	9	9	3	3	1.25	FKBP-type peptidyl-prolyl cis-trans isomerase SlyD OS=Escherichia coli (strain K12) OX=83333 GN=slyD PE=1 SV=1
SwissProt	RL2_ECO24	358	29842	0.37	19	19	8	8	3.79	Large ribosomal subunit protein uL2 OS=Escherichia coli O139:H28 (strain E24377A / ETEC) OX=331111 GN=rplB PE=3 SV=1
SwissProt	GLGA_ECOBW	334	52789	0.24	9	9	8	8	1.07	Glycogen synthase OS=Escherichia coli (strain K12 / MC4100 / BW2952) OX=595496 GN=glgA PE=3 SV=1
SwissProt	RSMI_ECOLI	325	31329	0.46	10	10	9	9	2.4	Ribosomal RNA small subunit methyltransferase I OS=Escherichia coli (strain K12) OX=83333 GN=rsmI PE=1 SV=1
SwissProt	RS3_ECO24	281	25967	0.26	8	8	4	4	0.92	Small ribosomal subunit protein uS3 OS=Escherichia coli O139:H28 (strain E24377A / ETEC) OX=331111 GN=rpsC PE=3 SV=1
SwissProt	EFTU1_ECO24	228	43256	0.23	9	9	7	7	0.99	Elongation factor Tu 1 OS=Escherichia coli O139:H28 (strain E24377A / ETEC) OX=331111 GN=tuf1 PE=3 SV=1
SwissProt	K2C1_HUMAN	196	65999	0.14	7	7	7	7	0.58	Keratin, type II cytoskeletal 1 OS=Homo sapiens OX=9606 GN=KRT1 PE=1 SV=6
SwissProt	FTSZ_ECOLI	160	40299	0.15	4	4	4	4	0.53	Cell division protein FtsZ OS=Escherichia coli (strain K12) OX=83333 GN=ftsZ PE=1 SV=1
SwissProt	RECA_ECOBW	148	37950	0.19	5	5	5	5	0.75	Protein RecA OS=Escherichia coli (strain K12 / MC4100 / BW2952) OX=595496 GN=recA PE=3 SV=1
SwissProt	XERD_ECOLI	140	34225	0.15	3	3	3	3	0.45	Tyrosine recombinase XerD OS=Escherichia coli (strain K12) OX=83333 GN=xerD PE=1 SV=1
SwissProt	GLPR_ECOLI	125	28030	0.15	3	3	3	3	0.57	Glycerol-3-phosphate regulon repressor OS=Escherichia coli (strain K12) OX=83333 GN=glpR PE=1 SV=1
SwissProt	CRP_ECOLI	124	23625	0.21	4	4	4	4	1.05	DNA-binding transcriptional dual regulator CRP OS=Escherichia coli (strain K12) OX=83333 GN=crp PE=1 SV=1
SwissProt	CASA1_BOVIN	116	24513	0.17	3	3	3	3	0.68	Alpha-S1-casein OS=Bos taurus OX=9913 GN=CSN1S1 PE=1 SV=2
SwissProt	LACB_BOVIN	102	19870	0.22	3	3	3	3	0.89	Beta-lactoglobulin OS=Bos taurus OX=9913 GN=LGB PE=1 SV=3
SwissProt	GLMS_ECOLI	100	66853	0.07	3	3	3	3	0.21	Glutamine--fructose-6-phosphate aminotransferase [isomerizing] OS=Escherichia coli (strain K12) OX=83333 GN=glmS PE=1 SV=4

SwissProt	BLUF_ECOLI	93	45266	0.09	4	4	4	4	0.46	Blue light- and temperature-regulated antirepressor BluF OS=Escherichia coli (strain K12) OX=83333 GN=bluF PE=1 SV=1
SwissProt	PHNO_ECOLI	92	16559	0.29	4	4	4	4	1.76	Aminoalkylphosphonate N-acetyltransferase OS=Escherichia coli (strain K12) OX=83333 GN=phnO PE=1 SV=1
SwissProt	RL15_ECO24	92	14957	0.24	3	3	3	3	1.31	Large ribosomal subunit protein uL15 OS=Escherichia coli O139:H28 (strain E24377A / ETEC) OX=331111 GN=rplO PE=3 SV=1
SwissProt	RS5_ECO24	85	17592	0.27	3	3	3	3	1.05	Small ribosomal subunit protein uS5 OS=Escherichia coli O139:H28 (strain E24377A / ETEC) OX=331111 GN=rpsE PE=3 SV=1
PONPC (n3, sample aggregate PONPC 2h:PTEN-V5-His 5:1)										
Database	Accession	Score	Mass	Sequence coverage	Num. of matches	Num. of significant matches	Num. of significant unique sequences	Num. of significant sequences	emPAI	Description
SwissProt	PTEN_CANLF	981	47706	0.47	27	27	14	14	2.93	Phosphatidylinositol 3,4,5-trisphosphate 3-phosphatase and dual-specificity protein phosphatase PTEN OS=Canis lupus familiaris OX=9615 GN=PTEN PE=2 SV=1
SwissProt	CH60_ECO24	753	57464	0.32	12	12	9	9	1.14	Chaperonin GroEL OS=Escherichia coli O139:H28 (strain E24377A / ETEC) OX=331111 GN=groEL PE=3 SV=1
SwissProt	ALBU_BOVIN	590	71244	0.37	19	19	19	19	2.21	Albumin OS=Bos taurus OX=9913 GN=ALB PE=1 SV=4
SwissProt	TRYP_PIG	462	25078	0.31	16	16	5	5	1.36	Trypsin OS=Sus scrofa OX=9823 PE=1 SV=1
SwissProt	ARNA_ECOBW	440	74869	0.27	18	18	16	16	1.55	Bifunctional polymyxin resistance protein ArnA OS=Escherichia coli (strain K12 / MC4100 / BW2952) OX=595496 GN=arnA PE=3 SV=1
SwissProt	GLMS_ECOLI	158	67081	0.09	3	3	3	3	0.22	Glutamine--fructose-6-phosphate aminotransferase [isomerizing] OS=Escherichia coli (strain K12) OX=83333 GN=glmS PE=1 SV=4
SwissProt	K2C1_HUMAN	150	66170	0.09	6	6	6	6	0.49	Keratin, type II cytoskeletal 1 OS=Homo sapiens OX=9606 GN=KRT1 PE=1 SV=6
SwissProt	CASA2_BOVIN	84	26173	0.14	3	3	3	3	0.64	Alpha-S2-casein OS=Bos taurus OX=9913 GN=CSN1S2 PE=1 SV=2
SwissProt	K1C10_CANLF	67	57847	0.04	3	3	3	3	0.25	Keratin, type I cytoskeletal 10 OS=Canis lupus familiaris OX=9615 GN=KRT10 PE=2 SV=1

A HHE-modified C218 (untreated PTEN-V5-His)

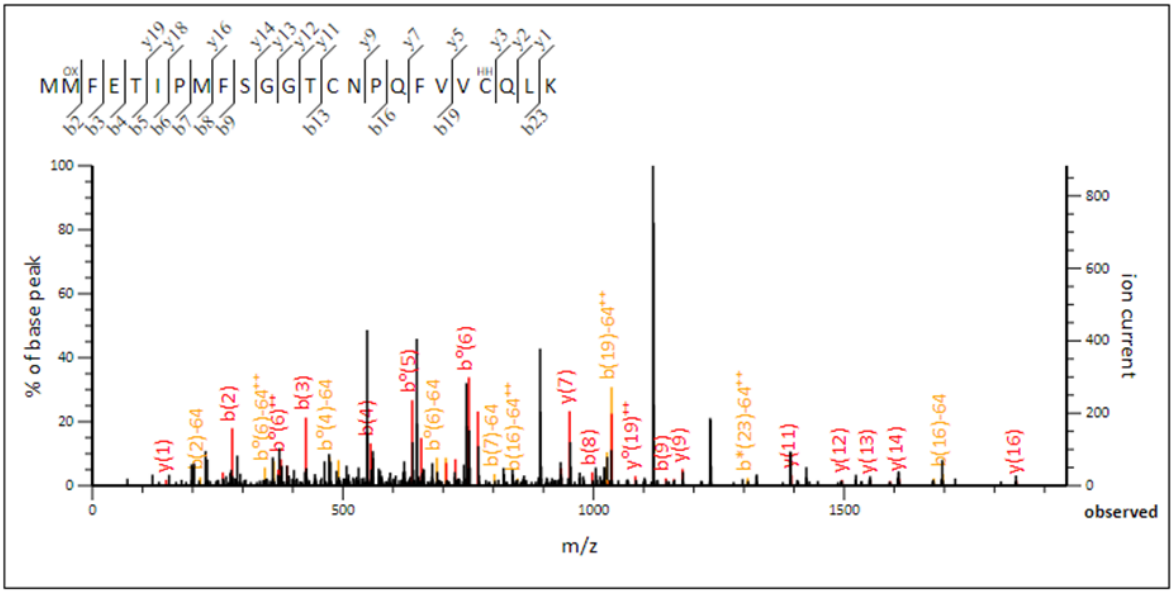

#	b	b^{++}	b*	b*$^{++}$	b^{0}	b^{0++}	Seq.	y	y^{++}	y*	y*$^{++}$	y^{0}	y^{0++}	#
1	132.0478	66.5275					M							24
2	*279.0832*	140.0452					M	2709.2795	1355.1434	2692.2530	1346.6301	2691.2689	1346.1381	23
3	*426.1516*	213.5794					F	2562.2441	1281.6257	2545.2176	1273.1124	2544.2335	1272.6204	22
4	*555.1942*	278.1007			537.1836	269.0954	E	2415.1757	1208.0915	2398.1491	1199.5782	2397.1651	1199.0862	21
5	*656.2418*	328.6246			638.2313	319.6193	T	2286.1331	1143.5702	2269.1065	1135.0569	2268.1225	1134.5649	20
6	*769.3259*	385.1666			751.3153	376.1613	I	2185.0854	1093.0463	2168.0589	1084.5331	2167.0749	1084.0411	19
7	866.3787	433.6930			848.3681	424.6877	P	2072.0014	1036.5043	2054.9748	1027.9910	2053.9908	1027.4990	18
8	*997.4192*	499.2132			979.4086	490.2079	M	1974.9486	987.9779	1957.9220	979.4647	1956.9380	978.9727	17
9	*1144.4876*	572.7474			1126.4770	563.7421	F	*1843.9081*	922.4577	1826.8816	913.9444	1825.8975	913.4524	16
10	1231.5196	616.2634			1213.5090	607.2582	S	*1696.8397*	848.9235	1679.8131	840.4102	1678.8291	839.9182	15
11	1288.5411	644.7742			1270.5305	635.7689	G	*1609.8077*	805.4075	1592.7811	796.8942	1591.7971	796.4022	14
12	1345.5625	673.2849			1327.5520	664.2796	G	*1552.7862*	776.8967	1535.7597	768.3835	1534.7756	767.8915	13
13	1446.6102	723.8087			1428.5996	714.8035	T	*1495.7647*	748.3860	1478.7382	739.8727	1477.7542	739.3807	12
14	1549.6194	775.3133			1531.6088	766.3081	C	*1394.7171*	697.8622	1377.6905	689.3489			11
15	1663.6623	832.3348	1646.6358	823.8215	1645.6518	823.3295	N	1291.7079	646.3576	1274.6813	637.8443			10
16	1760.7151	880.8612	1743.6885	872.3479	1742.7045	871.8559	P	*1177.6649*	589.3361	1160.6384	580.8228			9
17	1888.7737	944.8905	1871.7471	936.3772	1870.7631	935.8852	Q	1080.6122	540.8097	1063.5856	532.2965			8
18	2035.8421	1018.4247	2018.8155	1009.9114	2017.8315	1009.4194	F	*952.5536*	476.7804	935.5271	468.2672			7
19	2134.9105	1067.9589	2117.8839	1059.4456	2116.8999	1058.9536	V	805.4852	403.2462	788.4586	394.7330			6
20	2233.9789	1117.4931	2216.9524	1108.9798	2215.9683	1108.4878	V	*706.4168*	353.7120	689.3902	345.1988			5
21	2453.0718	1227.0395	2436.0453	1218.5263	2435.0613	1218.0343	C	607.3484	304.1778	590.3218	295.6645			4
22	2581.1304	1291.0688	2564.1038	1282.5556	2563.1198	1282.0636	Q	*388.2554*	194.6314	371.2289	186.1181			3
23	2694.2145	1347.6109	2677.1879	1339.0976	2676.2039	1338.6056	L	*260.1969*	130.6021	243.1703	122.0888			2
24							K	*147.1128*	74.0600	130.0863	65.5468			1

B HHE-modified C218 (HHE-treated PTEN-V5-His)

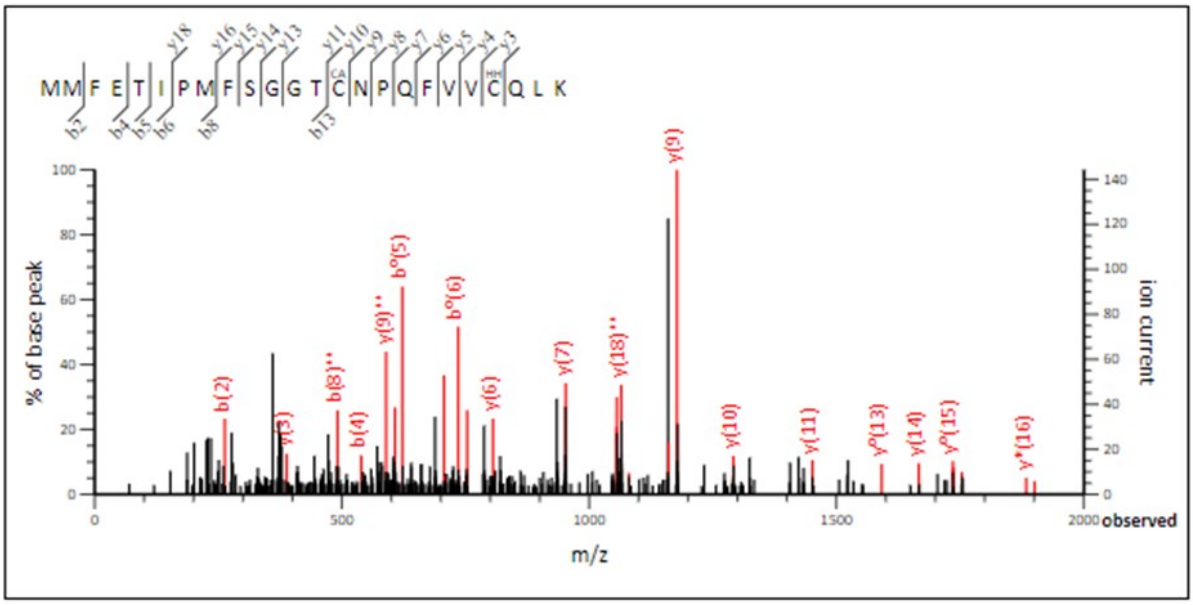

#	b	b^{++}	b*	b*$^{++}$	b^{0}	b^{0++}	Seq.	y	y^{++}	y*	y*$^{++}$	y^{0}	y^{0++}	#
1	132.0478	66.5275					M							24
2	**263.0882**	132.0478					M	2750.3061	1375.6567	2733.2795	1367.1434	2732.2955	1366.6514	23
3	410.1567	205.5820					F	2619.2656	1310.1364	2602.2390	1301.6231	2601.2550	1301.1311	22
4	**539.1993**	270.1033			521.1887	261.0980	E	2472.1972	1236.6022	2455.1706	1228.0889	2454.1866	1227.5969	21
5	640.2469	320.6271			622.2364	311.6218	T	2343.1546	1172.0809	2326.1280	1163.5676	2325.1440	1163.0756	20
6	**753.3310**	377.1691			735.3204	368.1639	I	2242.1069	1121.5571	2225.0803	1113.0438	2224.0963	1112.5518	19
7	850.3838	425.6955			832.3732	416.6902	P	2129.0228	**1065.0150**	2111.9963	1056.5018	2111.0123	1056.0098	18
8	981.4242	491.2158			963.4137	482.2105	M	2031.9701	1016.4887	2014.9435	1007.9754	2013.9595	1007.4834	17
9	1128.4927	564.7500			1110.4821	555.7447	F	***1900.9296***	950.9684	1883.9030	942.4551	1882.9190	941.9631	16
10	1215.5247	608.2660			1197.5141	599.2607	S	***1753.8612***	877.4342	1736.8346	868.9209	1735.8506	868.4289	15
11	1272.5462	636.7767			1254.5356	627.7714	G	***1666.8291***	833.9182	1649.8026	825.4049	1648.8186	824.9129	14
12	1329.5676	665.2874			1311.5571	656.2822	G	1609.8077	**805.4075**	1592.7811	796.8942	1591.7971	796.4022	13
13	1430.6153	715.8113			1412.6047	706.8060	T	1552.7862	776.8967	1535.7597	768.3835	1534.7756	767.8915	12
14	1590.6459	795.8266			1572.6354	786.8213	C	***1451.7385***	726.3729	1434.7120	717.8596			11
15	1704.6889	852.8481	1687.6623	844.3348	1686.6783	843.8428	N	***1291.7079***	646.3576	1274.6813	637.8443			10
16	1801.7416	901.3745	1784.7151	892.8612	1783.7311	892.3692	P	***1177.6649***	**589.3361**	1160.6384	580.8228			9
17	1929.8002	965.4037	1912.7737	956.8905	1911.7896	956.3985	Q	***1080.6122***	540.8097	1063.5856	532.2965			8
18	2076.8686	1038.9380	2059.8421	1030.4247	2058.8581	1029.9327	F	***952.5536***	476.7804	935.5271	468.2672			7
19	2175.9370	1088.4722	2158.9105	1079.9589	2157.9265	1079.4669	V	***805.4852***	403.2462	788.4586	394.7330			6
20	2275.0055	1138.0064	2257.9789	1129.4931	2256.9949	1129.0011	V	***706.4168***	353.7120	689.3902	345.1988			5
21	2494.0984	1247.5528	2477.0718	1239.0395	2476.0878	1238.5475	C	***607.3484***	304.1778	590.3218	295.6645			4
22	2622.1569	1311.5821	2605.1304	1303.0688	2604.1464	1302.5768	Q	***388.2554***	194.6314	371.2289	186.1181			3
23	2735.2410	1368.1241	2718.2145	1359.6109	2717.2304	1359.1189	L	260.1969	130.6021	243.1703	122.0888			2
24							K	147.1128	74.0600	130.0863	65.5468			1

Supplementary Figure 4. Representative Mascot peptide identification for false and true positive HHE modification of Cys218 in untreated-PTEN-V5-His and HHE-treated PTEN-V5-His samples.

A Mascot search identified peptide 198-221 (MMFETIPMFSGGTCNPQRVVCQLK) with an HHE Michael adduct on C218 in an untreated PTEN-V5-His sample (A) and an HHE-treated PTEN-V5-His sample (B). Panel (A) and (B) both display an upper pane with the fragmentation spectrum showing identified ions as peaks marked in red. The yellow peaks denote the loss of the side chain from oxidized methionine residues (-64 Da). The lower table presents the matched b and y ion coverage, with the matching ions shown in red. Bold italic red: the ion series contributed to the score of the peptide; bold red: the number of matches in the ion series is greater than would be expected by

chance; non-bold red: the number of matches in the ion series is no greater than would be expected by chance.

The peaks that were picked by Mascot for sequencing and identification of the HHE Michael adduct were not the peaks of highest intensity on the fragmentation spectrum, in opposition to the identification of the peptide in the HHE-treated PTEN-V5-His sample. Additionally, numerous peaks were assigned to b ions with a neutral loss of the side chains of the oxidized methionine (M199) and their intensity corresponded to the intensity of the identified b and y ions without neutral loss, which seemed unlikely, suggesting that the assignment was random. Although the b ion coverage was found to be better in the identification of the peptide in the untreated PTEN-V5-His than in the HHE-treated PTEN-V5-His sample, the relevance of the assignment of these ions could be questioned considering the above-mentioned limitations in the fragmentation spectrum of the peptide in the untreated PTEN-V5-His sample. However, the 75% coverage of y ions between y(1) and y(16) in both untreated and HHE-treated samples made it difficult to fully rule out the possibility of HHE-modification of the 198-221 peptide in the untreated PTEN-V5-his sample. An important piece of information in the fragmentation data of the peptide identified in the untreated PTEN-V5-His sample resided in the lack of detection of y(4), the first y ion including the putative HHE-modified C218 residue, which strongly suggested that this assignment could be incorrect. Additionally, the y ion coverage highly reduced between y(4) (for C218) and y(11) (for C211), with only every other y ion detected. This contrasted the data found for the peptide identified in the HHE-treated PTEN-V5-His sample, which picked both the y(4) and y(11) ions. This further suggested a misidentification of the HHE Michael adduct, which could more likely be on C211 than C218, if only substantial.

HHE-modified R378: False positive (C-terminal R)

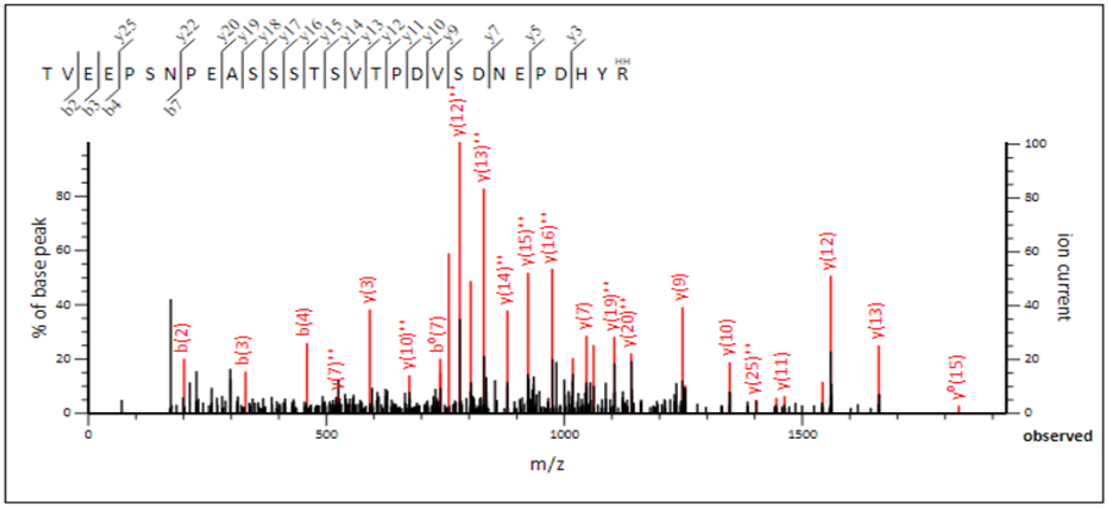

#	b	b^{++}	b*	b*$^{++}$	b^0	b^{0++}	Seq.	y	y^{++}	y*	y*$^{++}$	y^0	y^{0++}	#
1	102.0550	51.5311			84.0444	42.5258	T							29
2	**201.1234**	101.0653			183.1128	92.0600	V	3161.4029	1581.2051	3144.3764	1572.6918	3143.3924	1572.1998	28
3	**330.1660**	165.5866			312.1554	156.5813	E	3062.3345	1531.6709	3045.3080	1523.1576	3044.3239	1522.6656	27
4	**459.2086**	230.1079			441.1980	221.1026	E	2933.2919	1467.1496	2916.2654	1458.6363	2915.2813	1458.1443	26
5	556.2613	278.6343			538.2508	269.6290	P	2804.2493	***1402.6283***	2787.2228	1394.1150	2786.2388	1393.6230	25
6	643.2933	322.1503			625.2828	313.1450	S	2707.1966	1354.1019	2690.1700	1345.5886	2689.1860	1345.0966	24
7	**757.3363**	379.1718	740.3097	370.6585	739.3257	370.1665	N	2620.1645	1310.5859	2603.1380	1302.0726	2602.1540	1301.5806	23
8	854.3890	427.6982	837.3625	419.1849	836.3785	418.6929	P	2506.1216	***1253.5644***	2489.0950	1245.0512	2488.1110	1244.5592	22
9	983.4316	492.2195	966.4051	483.7062	965.4211	483.2142	E	2409.0688	1205.0381	2392.0423	1196.5248	2391.0583	1196.0328	21
10	1054.4687	527.7380	1037.4422	519.2247	1036.4582	518.7327	A	2280.0262	***1140.5168***	2262.9997	1132.0035	2262.0157	1131.5115	20
11	1141.5008	571.2540	1124.4742	562.7407	1123.4902	562.2487	S	2208.9891	***1104.9982***	2191.9626	1096.4849	2190.9786	1095.9929	19
12	1228.5328	614.7700	1211.5063	606.2568	1210.5222	605.7648	S	2121.9571	***1061.4822***	2104.9305	1052.9689	2103.9465	1052.4769	18
13	1315.5648	658.2861	1298.5383	649.7728	1297.5543	649.2808	S	2034.9251	***1017.9662***	2017.8985	1009.4529	2016.9145	1008.9609	17
14	1416.6125	708.8099	1399.5860	700.2966	1398.6019	699.8046	T	1947.8930	***974.4502***	1930.8665	965.9369	1929.8825	965.4449	16
15	1503.6445	752.3259	1486.6180	743.8126	1485.6340	743.3206	S	1846.8454	***923.9263***	1829.8188	915.4130	1828.8348	914.9210	15
16	1602.7130	801.8601	1585.6864	793.3468	1584.7024	792.8548	V	1759.8133	***880.4103***	1742.7868	871.8970	1741.8028	871.4050	14
17	1703.7606	852.3840	1686.7341	843.8707	1685.7501	843.3787	T	***1660.7449***	***830.8761***	1643.7184	822.3628	1642.7344	821.8708	13
18	1800.8134	900.9103	1783.7868	892.3971	1782.8028	891.9051	P	***1559.6972***	***780.3523***	1542.6707	771.8390	1541.6867	771.3470	12
19	1915.8403	958.4238	1898.8138	949.9105	1897.8298	949.4185	D	***1462.6445***	731.8259	1445.6179	723.3126	1444.6339	722.8206	11
20	2014.9088	1007.9580	1997.8822	999.4447	1996.8982	998.9527	V	***1347.6175***	***674.3124***	1330.5910	665.7991	1329.6070	665.3071	10
21	2101.9408	1051.4740	2084.9142	1042.9608	2083.9302	1042.4687	S	***1248.5491***	624.7782	1231.5226	616.2649	1230.5386	615.7729	9
22	2216.9677	1108.9875	2199.9412	1100.4742	2198.9572	1099.9822	D	1161.5171	581.2622	1144.4905	572.7489	1143.5065	572.2569	8
23	2331.0106	1166.0090	2313.9841	1157.4957	2313.0001	1157.0037	N	***1046.4901***	***523.7487***	1029.4636	515.2354	1028.4796	514.7434	7
24	2460.0532	1230.5303	2443.0267	1222.0170	2442.0427	1221.5250	E	932.4472	466.7272	915.4207	458.2140	914.4367	457.7220	6
25	2557.1060	1279.0566	2540.0795	1270.5434	2539.0954	1270.0514	P	***803.4046***	402.2060	786.3781	393.6927	785.3941	393.2007	5
26	2672.1329	1336.5701	2655.1064	1328.0568	2654.1224	1327.5648	D	706.3519	353.6796	689.3253	345.1663	688.3413	344.6743	4
27	2809.1919	1405.0996	2792.1653	1396.5863	2791.1813	1396.0943	H	***591.3249***	296.1661	574.2984	287.6528			3
28	2972.2552	1486.6312	2955.2286	1478.1180	2954.2446	1477.6260	Y	454.2660	227.6366	437.2395	219.1234			2
29							R	291.2027	146.1050	274.1761	137.5917			1

Supplementary Figure 5. Representative Mascot output for false positive identification of HHE modification on C-terminal R residues of the identified peptide 350-378 (TVEEPSNPEASSSTSVTPDVSDNEPDHYR).

A Mascot search identified the peptide 350-378 (TVEEPSNPEASSSTSVTPDVSDNEPDHYR) with an HHE Michael adduct on R378 in an HHE-treated PTEN-V5-His sample. An upper pane with the fragmentation spectrum showing identified ions as peaks marked in red and a lower table with the matched b and y ion coverage, with the matching ions shown in red are presented. Bold italic red: the ion series contributed to the score of the peptide; bold red: the number of matches in the ion series is greater than would be expected by chance; non-bold red: the number of matches in the ion series is no greater than would be expected by chance.

However, the y(1) and y(2) ions, which are C-terminal fragments that do not include His376 (R and YR, respectively), did not exhibit the expected +116.0837 Da mass shift. In contrast, fragments containing His376 did show this shift, suggesting that the HHE Michael adduct was incorrectly assigned to Arg378 and that His376 was the more likely the site of modification by HHE.

HHE-modified K221 (C-terminal K) and C218 from the same precursor ion: difficulty of assignment

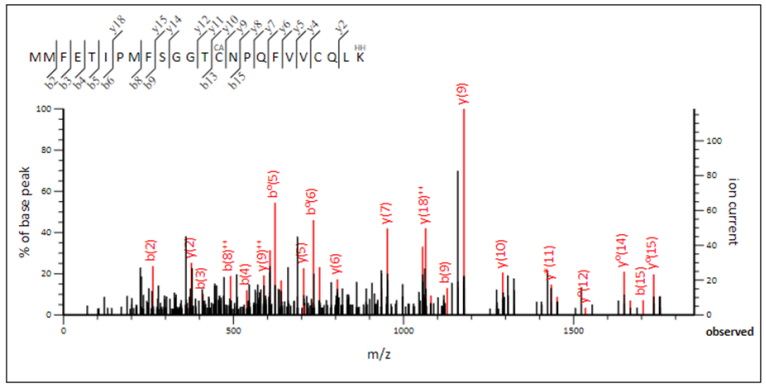

#	b	b^{++}	b*	b*$^{++}$	b^0	b^{0++}	Seq.	y	y^{++}	y*	y*$^{++}$	y^0	y^{0++}	#
1	132.0478	66.5275					M							24
2	***263.0882***	132.0478					M	2750.3061	1375.6567	2733.2795	1367.1434	2732.2955	1366.6514	23
3	***410.1567***	205.5820					F	2619.2656	1310.1364	2602.2390	1301.6231	2601.2550	1301.1311	22
4	***539.1993***	270.1033			521.1887	261.0980	E	2472.1972	1236.6022	2455.1706	1228.0889	2454.1866	1227.5969	21
5	***640.2469***	320.6271			622.2364	311.6218	T	2343.1546	1172.0809	2326.1280	1163.5676	2325.1440	1163.0756	20
6	***753.3310***	377.1691			735.3204	368.1639	I	2242.1069	1121.5571	2225.0803	1113.0438	2224.0963	1112.5518	19
7	850.3838	425.6955			832.3732	416.6902	P	2129.0228	1065.0150	2111.9963	1056.5018	2111.0123	1056.0098	18
8	981.4242	491.2158			963.4137	482.2105	M	2031.9701	1016.4887	2014.9435	1007.9754	2013.9595	1007.4834	17
9	***1128.4927***	564.7500			1110.4821	555.7447	F	1900.9296	950.9684	1883.9030	942.4551	1882.9190	941.9631	16
10	1215.5247	608.2660			1197.5141	599.2607	S	***1753.8612***	877.4342	1736.8346	868.9209	1735.8506	868.4289	15
11	1272.5462	636.7767			1254.5356	627.7714	G	***1666.8291***	833.9182	1649.8026	825.4049	1648.8186	824.9129	14
12	1329.5676	665.2874			1311.5571	656.2822	G	1609.8077	805.4075	1592.7811	796.8942	1591.7971	796.4022	13
13	1430.6153	715.8113			1412.6047	706.8060	T	1552.7862	776.8967	1535.7597	768.3835	1534.7756	767.8915	12
14	1590.6459	795.8266			1572.6354	786.8213	C	***1451.7385***	726.3729	1434.7120	717.8596			11
15	***1704.6889***	852.8481	1687.6623	844.3348	1686.6783	843.8428	N	***1291.7079***	646.3576	1274.6813	637.8443			10
16	1801.7416	901.3745	1784.7151	892.8612	1783.7311	892.3692	P	***1177.6649***	589.3361	1160.6384	580.8228			9
17	1929.8002	965.4037	1912.7737	956.8905	1911.7896	956.3985	Q	***1080.6122***	540.8097	1063.5856	532.2965			8
18	2076.8686	1038.9380	2059.8421	1030.4247	2058.8581	1029.9327	F	***952.5536***	476.7804	935.5271	468.2672			7
19	2175.9370	1088.4722	2158.9105	1079.9589	2157.9265	1079.4669	V	***805.4852***	403.2462	788.4586	394.7330			6
20	2275.0055	1138.0064	2257.9789	1129.4931	2256.9949	1129.0011	V	***706.4168***	353.7120	689.3902	345.1988			5
21	2378.0146	1189.5110	2360.9881	1180.9977	2360.0041	1180.5057	C	***607.3484***	304.1778	590.3218	295.6645			4
22	2506.0732	1253.5402	2489.0467	1245.0270	2488.0627	1244.5350	Q	504.3392	252.6732	487.3126	244.1600			3
23	2619.1573	1310.0823	2602.1307	1301.5690	2601.1467	1301.0770	L	***376.2806***	188.6439	359.2540	180.1307			2
24							K	***263.1965***	132.1019	246.1700	123.5886			1

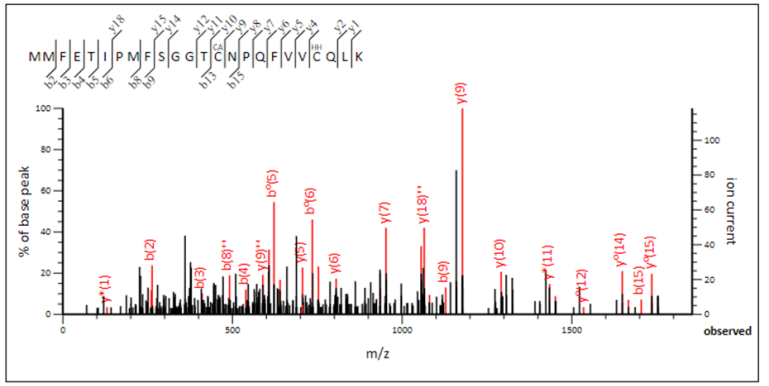

#	b	b^{++}	b*	b*$^{++}$	b^0	b^{0++}	Seq.	y	y^{++}	y*	y*$^{++}$	y^0	y^{0++}	#
1	132.0478	66.5275					M							24
2	***263.0882***	132.0478					M	2750.3061	1375.6567	2733.2795	1367.1434	2732.2955	1366.6514	23
3	***410.1567***	205.5820					F	2619.2656	1310.1364	2602.2390	1301.6231	2601.2550	1301.1311	22
4	***539.1993***	270.1033			521.1887	261.0980	E	2472.1972	1236.6022	2455.1706	1228.0889	2454.1866	1227.5969	21
5	***640.2469***	320.6271			622.2364	311.6218	T	2343.1546	1172.0809	2326.1280	1163.5676	2325.1440	1163.0756	20
6	***753.3310***	377.1691			735.3204	368.1639	I	2242.1069	1121.5571	2225.0803	1113.0438	2224.0963	1112.5518	19
7	850.3838	425.6955			832.3732	416.6902	P	2129.0228	1065.0150	2111.9963	1056.5018	2111.0123	1056.0098	18
8	981.4242	491.2158			963.4137	482.2105	M	2031.9701	1016.4887	2014.9435	1007.9754	2013.9595	1007.4834	17
9	***1128.4927***	564.7500			1110.4821	555.7447	F	1900.9296	950.9684	1883.9030	942.4551	1882.9190	941.9631	16
10	1215.5247	608.2660			1197.5141	599.2607	S	***1753.8612***	877.4342	1736.8346	868.9209	1735.8506	868.4289	15
11	1272.5462	636.7767			1254.5356	627.7714	G	***1666.8291***	833.9182	1649.8026	825.4049	1648.8186	824.9129	14
12	1329.5676	665.2874			1311.5571	656.2822	G	1609.8077	805.4075	1592.7811	796.8942	1591.7971	796.4022	13
13	1430.6153	715.8113			1412.6047	706.8060	T	1552.7862	776.8967	1535.7597	768.3835	1534.7756	767.8915	12
14	1590.6459	795.8266			1572.6354	786.8213	C	***1451.7385***	726.3729	1434.7120	717.8596			11
15	***1704.6889***	852.8481	1687.6623	844.3348	1686.6783	843.8428	N	***1291.7079***	646.3576	1274.6813	637.8443			10
16	1801.7416	901.3745	1784.7151	892.8612	1783.7311	892.3692	P	***1177.6649***	589.3361	1160.6384	580.8228			9
17	1929.8002	965.4037	1912.7737	956.8905	1911.7896	956.3985	Q	***1080.6122***	540.8097	1063.5856	532.2965			8
18	2076.8686	1038.9380	2059.8421	1030.4247	2058.8581	1029.9327	F	***952.5536***	476.7804	935.5271	468.2672			7
19	2175.9370	1088.4722	2158.9105	1079.9589	2157.9265	1079.4669	V	***805.4852***	403.2462	788.4586	394.7330			6
20	2275.0055	1138.0064	2257.9789	1129.4931	2256.9949	1129.0011	V	***706.4168***	353.7120	689.3902	345.1988			5
21	2494.0984	1247.5528	2477.0718	1239.0395	2476.0878	1238.5475	C	***607.3484***	304.1778	590.3218	295.6645			4
22	2622.1569	1311.5821	2605.1304	1303.0688	2604.1464	1302.5768	Q	388.2554	194.6314	371.2289	186.1181			3
23	2735.2410	1368.1241	2718.2145	1359.6109	2717.2304	1359.1189	L	***260.1969***	130.6021	243.1703	122.0888			2
24							K	147.1128	74.0600	130.0863	65.5468			1

Supplementary Figure 6. Representative Mascot output for false positive identification of HHE modification on C-terminal K residue of the identified peptide 198-221 (MMFETIPMFSGGTCNPQFVVCQLK).

A Mascot search identified the peptide 198-221 (MMFETIPMFSGGTCNPQFVVCQLK) with an HHE Michael adduct on K221 in an HHE-treated PTEN-V5-His sample. An upper pane with the fragmentation spectrum showing identified ions as peaks marked in red and a lower table with the matched b and y ion coverage, with the matching ions shown in red are presented. Bold italic red: the ion series contributed to the score of the peptide; bold red: the number of matches in the ion series is greater than would be expected by chance; non-bold red: the number of matches in the ion series is no greater than would be expected by chance.

The lack of C-terminal fragments suggested that Cys218 could be the actual site of modification. In this case, two fragments that did not include Cys218 (y(1) and y(2) for K and LK, respectively) showed a +116.0837 Da mass shift, although one of these fragments (y(2) corresponding to the LK fragment) was also detected without the mass shift, making it difficult to determine conclusively the exact site of HHE modification

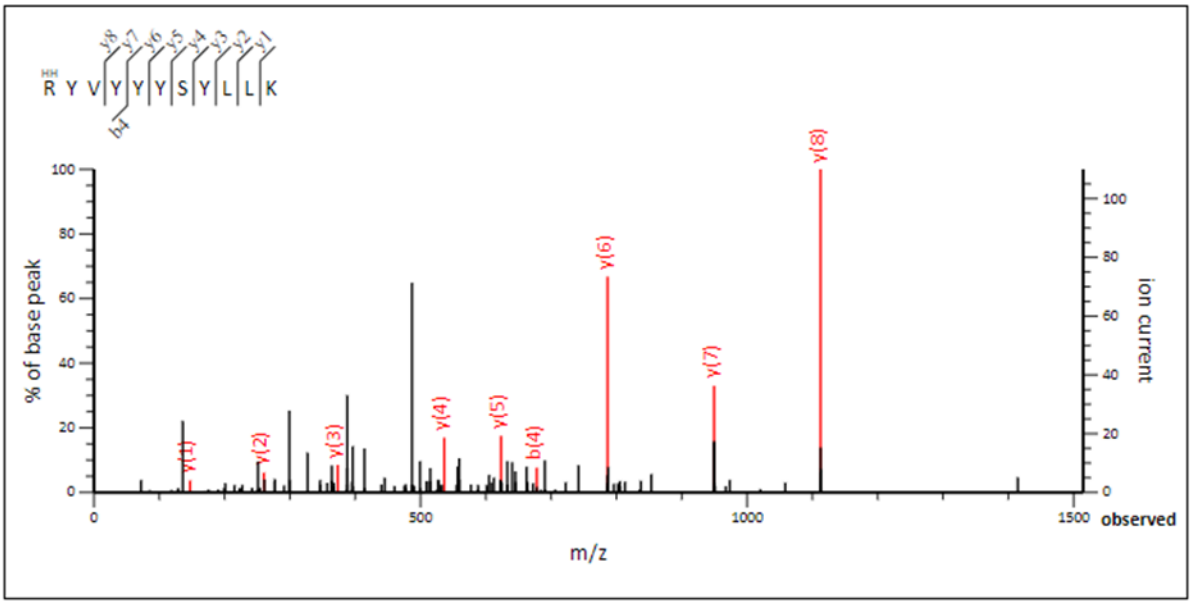

#	b	b^{++}	b*	b^{*++}	b^{0}	b^{0++}	Seq.	y	y^{++}	y*	y^{*++}	y^{0}	y^{0++}	#
1	253.1659	127.0866	236.1394	118.5733			R							11
2	416.2292	208.6183	399.2027	200.1050			Y	1374.6980	687.8526	1357.6715	679.3394	1356.6875	678.8474	10
3	515.2976	258.1525	498.2711	249.6392			V	1211.6347	606.3210	1194.6081	597.8077	1193.6241	597.3157	9
4	678.3610	339.6841	661.3344	331.1709			Y	***1112.5663***	556.7868	1095.5397	548.2735	1094.5557	547.7815	8
5	841.4243	421.2158	824.3978	412.7025			Y	***949.5029***	475.2551	932.4764	466.7418	931.4924	466.2498	7
6	1004.4876	502.7475	987.4611	494.2342			Y	***786.4396***	393.7234	769.4131	385.2102	768.4291	384.7182	6
7	1091.5197	546.2635	1074.4931	537.7502	1073.5091	537.2582	S	***623.3763***	312.1918	606.3497	303.6785	605.3657	303.1865	5
8	1254.5830	627.7951	1237.5564	619.2819	1236.5724	618.7899	Y	***536.3443***	268.6758	519.3177	260.1625			4
9	1367.6671	684.3372	1350.6405	675.8239	1349.6565	675.3319	L	***373.2809***	187.1441	356.2544	178.6308			3
10	1480.7511	740.8792	1463.7246	732.3659	1462.7406	731.8739	L	***260.1969***	130.6021	243.1703	122.0888			2
11							K	***147.1128***	74.0600	130.0863	65.5468			1

Supplementary Figure 7. Mascot peptide identification of Arg173 modified by HHE through Schiff base formation was classified as a false positive result.

A Mascot search identified the peptide 173-123 (RYVYYYSYLLK) with an HHE Schiff adduct on R173 in an HHE-treated PTEN-V5-His sample. An upper pane with the fragmentation spectrum showing identified ions as peaks marked in red and a lower table with the matched b and y ion coverage, with the matching ions shown in red, are presented. Bold italic red: the ion series contributed to the score of the peptide; bold red: the number of matches in the ion series is greater than would be expected by chance; non-bold red: the number of matches in the ion series is no greater than would be expected by chance.

There was a good coverage of y ions, leading to confidence in the peptide identification, but there was no coverage of the fragments containing the putative modification.

HHE-modified K254 (Schiff)

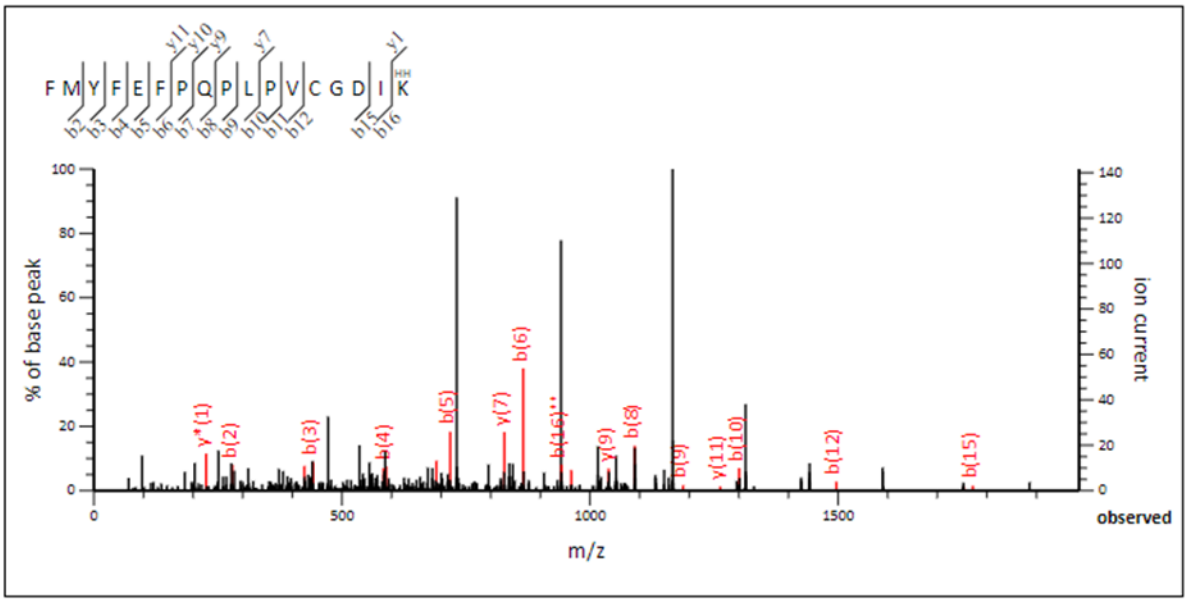

#	b	b^{++}	b*	b^{*++}	b^0	b^{0++}	Seq.	y	y^{++}	y*	y^{*++}	y^0	y^{0++}	#
1	148.0757	74.5415					F							17
2	*279.1162*	140.0617					M	1979.9646	990.4859	1962.9380	981.9726	1961.9540	981.4806	16
3	*442.1795*	221.5934					Y	1848.9241	924.9657	1831.8975	916.4524	1830.9135	915.9604	15
4	*589.2479*	295.1276					F	1685.8607	843.4340	1668.8342	834.9207	1667.8502	834.4287	14
5	*718.2905*	359.6489			700.2799	350.6436	E	1538.7923	769.8998	1521.7658	761.3865	1520.7818	760.8945	13
6	*865.3589*	433.1831			847.3484	424.1778	F	1409.7497	705.3785	1392.7232	696.8652	1391.7392	696.3732	12
7	*962.4117*	481.7095			944.4011	472.7042	P	**1262.6813**	631.8443	1245.6548	623.3310	1244.6708	622.8390	11
8	*1090.4703*	545.7388	1073.4437	537.2255	1072.4597	536.7335	Q	1165.6286	583.3179	1148.6020	574.8046	1147.6180	574.3126	10
9	*1187.5230*	594.2652	1170.4965	585.7519	1169.5125	585.2599	P	**1037.5700**	519.2886	1020.5434	510.7754	1019.5594	510.2833	9
10	*1300.6071*	650.8072	1283.5805	642.2939	1282.5965	641.8019	L	940.5172	470.7622	923.4907	462.2490	922.5067	461.7570	8
11	1397.6599	699.3336	1380.6333	690.8203	1379.6493	690.3283	P	**827.4332**	414.2202	810.4066	405.7069	809.4226	405.2149	7
12	*1496.7283*	748.8678	1479.7017	740.3545	1478.7177	739.8625	V	730.3804	365.6938	713.3538	357.1806	712.3698	356.6886	6
13	1599.7375	800.3724	1582.7109	791.8591	1581.7269	791.3671	C	631.3120	316.1596	614.2854	307.6464	613.3014	307.1543	5
14	1656.7589	828.8831	1639.7324	820.3698	1638.7484	819.8778	G	528.3028	264.6550	511.2762	256.1418	510.2922	255.6498	4
15	*1771.7859*	886.3966	1754.7593	877.8833	1753.7753	877.3913	D	471.2813	236.1443	454.2548	227.6310	453.2708	227.1390	3
16	1884.8699	942.9386	1867.8434	934.4253	1866.8594	933.9333	I	356.2544	178.6308	339.2278	170.1176			2
17							K	243.1703	122.0888	226.1438	113.5755			1

Supplementary Figure 8. Mascot peptide identification of Lys254 modified by HHE through Schiff base formation was classified as a false positive result.

A Mascot search identified the peptide 238-254 (FMYFEFPQPLPVCGDIK) with an HHE Schiff adduct on K254 in an HHE-treated PTEN-V5-His sample. An upper pane with the fragmentation spectrum showing identified ions as peaks marked in red and a lower table with the matched b and y ion coverage, with the matching ions shown in red, are presented. Bold italic red: the ion series contributed to the score of the peptide; bold red: the number of matches in the ion series is greater than would be expected by chance; non-bold red: the number of matches in the ion series is no greater than would be expected by chance.

The HHE Schiff adduct on Lys254 was also classified as false positive based on the lack of assignment of peaks of highest intensity in the fragmentation data and the fact that Lys254 was the C-terminal residue which trypsin cleaved successfully after and was not covered by y ions. In fact, the y ions coverage was limited to the identification of three fragment ions which were of little intensity and could have been noise rather than true fragment ions.

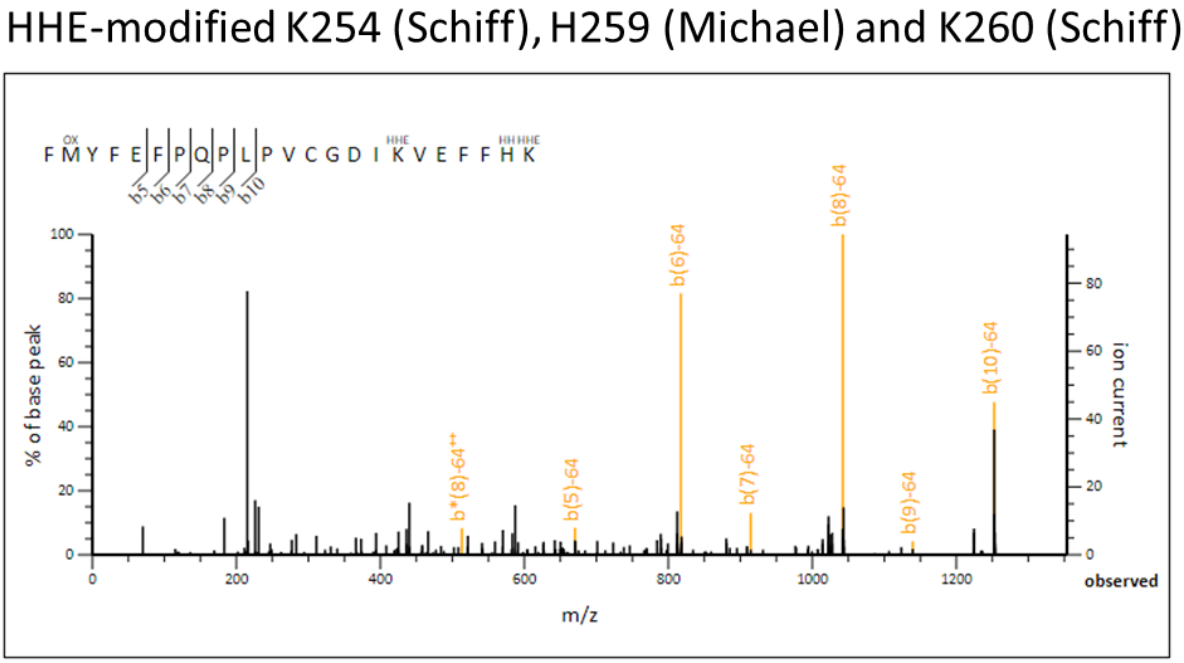

#	b	b^{++}	b*	b*$^{++}$	b^{0}	b^{0++}	Seq.	y	y^{++}	y*	y*$^{++}$	y^{0}	y^{0++}	#
1	148.0757	74.5415					F							23
2	231.1128	116.0600					M	2931.5041	1466.2557	2914.4776	1457.7424	2913.4936	1457.2504	22
3	394.1761	197.5917					Y	2848.4670	1424.7372	2831.4405	1416.2239	2830.4565	1415.7319	21
4	541.2445	271.1259					F	2685.4037	1343.2055	2668.3771	1334.6922	2667.3931	1334.2002	20
5	*670.2871*	335.6472			652.2766	326.6419	E	2538.3353	1269.6713	2521.3087	1261.1580	2520.3247	1260.6660	19
6	*817.3556*	409.1814			799.3450	400.1761	F	2409.2927	1205.1500	2392.2661	1196.6367	2391.2821	1196.1447	18
7	*914.4083*	457.7078			896.3978	448.7025	P	2262.2243	1131.6158	2245.1977	1123.1025	2244.2137	1122.6105	17
8	*1042.4669*	521.7371	1025.4403	513.2238	1024.4563	512.7318	Q	2165.1715	1083.0894	2148.1450	1074.5761	2147.1609	1074.0841	16
9	*1139.5197*	570.2635	1122.4931	561.7502	1121.5091	561.2582	P	2037.1129	1019.0601	2020.0864	1010.5468	2019.1024	1010.0548	15
10	*1252.6037*	626.8055	1235.5772	618.2922	1234.5932	617.8002	L	1940.0602	970.5337	1923.0336	962.0204	1922.0496	961.5284	14
11	1349.6565	675.3319	1332.6299	666.8186	1331.6459	666.3266	P	1826.9761	913.9917	1809.9496	905.4784	1808.9655	904.9864	13
12	1448.7249	724.8661	1431.6984	716.3528	1430.7143	715.8608	V	1729.9233	865.4653	1712.8968	856.9520	1711.9128	856.4600	12
13	1551.7341	776.3707	1534.7075	767.8574	1533.7235	767.3654	C	1630.8549	815.9311	1613.8284	807.4178	1612.8444	806.9258	11
14	1608.7556	804.8814	1591.7290	796.3681	1590.7450	795.8761	G	1527.8457	764.4265	1510.8192	755.9132	1509.8352	755.4212	10
15	1723.7825	862.3949	1706.7559	853.8816	1705.7719	853.3896	D	1470.8243	735.9158	1453.7977	727.4025	1452.8137	726.9105	9
16	1836.8666	918.9369	1819.8400	910.4236	1818.8560	909.9316	I	1355.7973	678.4023	1338.7708	669.8890	1337.7868	669.3970	8
17	2061.0190	1031.0132	2043.9925	1022.4999	2043.0085	1022.0079	K	1242.7133	621.8603	1225.6867	613.3470	1224.7027	612.8550	7
18	2160.0875	1080.5474	2143.0609	1072.0341	2142.0769	1071.5421	V	1018.5608	509.7840	1001.5342	501.2708	1000.5502	500.7788	6
19	2289.1300	1145.0687	2272.1035	1136.5554	2271.1195	1136.0634	E	919.4924	460.2498	902.4658	451.7366	901.4818	451.2445	5
20	2436.1985	1218.6029	2419.1719	1210.0896	2418.1879	1209.5976	F	790.4498	395.7285	773.4232	387.2153			4
21	2583.2669	1292.1371	2566.2403	1283.6238	2565.2563	1283.1318	F	643.3814	322.1943	626.3548	313.6811			3
22	2836.4095	1418.7084	2819.3830	1410.1951	2818.3989	1409.7031	H	496.3130	248.6601	479.2864	240.1468			2
23							K	243.1703	122.0888	226.1438	113.5755			1

Supplementary Figure 9. Mascot peptide identification of multiple modifications on a single peptide 238-260 (FMYFEFPQPLPVCGDIKVEFFHK) by HHE through Schiff base formation and Michael addition: a false positive.

A Mascot search identified the peptide 238-260 (FMYFEFPQPLPVCGDIKVEFFHK) with an HHE Schiff adduct on K254 and K260 along with HHE Michael adduction on H259 in an HHE-treated PTEN-V5-His sample. An upper pane with the fragmentation spectrum showing identified ions as peaks marked in red and a lower table with the matched b and y ion coverage, with the matching ions shown in red, are presented. Bold italic red: the ion series contributed to the score of the peptide; bold red: the number of matches in the ion series is greater than would be expected by chance; non-bold red: the number of matches in the ion series is no greater than would be expected by chance.

The peaks that were selected by Mascot for sequencing of the peptide 238-260 (FMYFEFPQPLPVCGDIKVEFFHK) were exclusively corresponding to fragments with a loss of

ammonium (-64 Da) and limited to 6 b ions and 2 y ions for a 23 amino acid-long peptide, which strongly suggested that this was a misidentification

Unreduced PONPC Schiff adduct K269: False positive

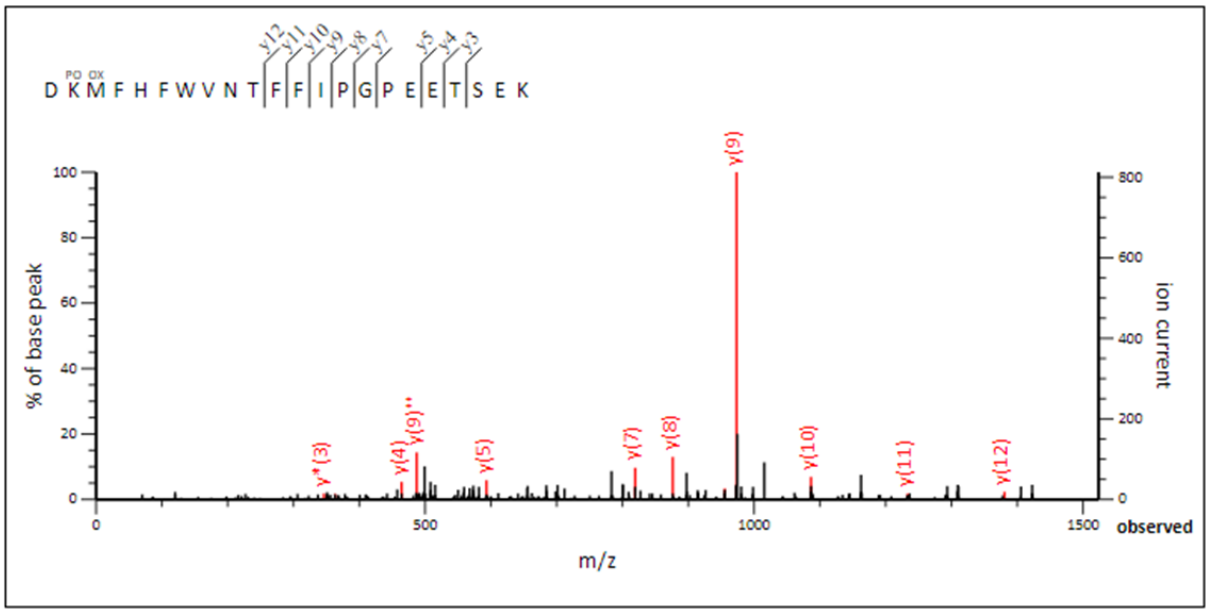

#	b	b^{++}	b*	b^{*++}	b^{0}	b^{0++}	Seq.	y	y^{++}	y*	y^{*++}	y^{0}	y^{0++}	#
1	116.0342	58.5207			98.0237	49.5155	D							22
2	875.5505	438.2789	858.5239	429.7656	857.5399	429.2736	K	3218.6539	1609.8306	3201.6274	1601.3173	3200.6434	1600.8253	21
3	1022.5859	511.7966	1005.5593	503.2833	1004.5753	502.7913	M	2459.1376	1230.0725	2442.1111	1221.5592	2441.1271	1221.0672	20
4	1169.6543	585.3308	1152.6278	576.8175	1151.6437	576.3255	F	2312.1022	1156.5548	2295.0757	1148.0415	2294.0917	1147.5495	19
5	1306.7132	653.8602	1289.6867	645.3470	1288.7026	644.8550	H	2165.0338	1083.0206	2148.0073	1074.5073	2147.0233	1074.0153	18
6	1453.7816	727.3945	1436.7551	718.8812	1435.7711	718.3892	F	2027.9749	1014.4911	2010.9484	1005.9778	2009.9644	1005.4858	17
7	1639.8609	820.4341	1622.8344	811.9208	1621.8504	811.4288	W	1880.9065	940.9569	1863.8800	932.4436	1862.8959	931.9516	16
8	1738.9294	869.9683	1721.9028	861.4550	1720.9188	860.9630	V	1694.8272	847.9172	1677.8006	839.4040	1676.8166	838.9120	15
9	1852.9723	926.9898	1835.9457	918.4765	1834.9617	917.9845	N	1595.7588	798.3830	1578.7322	789.8698	1577.7482	789.3777	14
10	1954.0200	977.5136	1936.9934	969.0003	1936.0094	968.5083	T	1481.7159	741.3616	1464.6893	732.8483	1463.7053	732.3563	13
11	2101.0884	1051.0478	2084.0618	1042.5346	2083.0778	1042.0425	F	*1380.6682*	690.8377	1363.6416	682.3245	1362.6576	681.8324	12
12	2248.1568	1124.5820	2231.1302	1116.0688	2230.1462	1115.5767	F	*1233.5998*	617.3035	1216.5732	608.7902	1215.5892	608.2982	11
13	2361.2409	1181.1241	2344.2143	1172.6108	2343.2303	1172.1188	I	*1086.5313*	543.7693	1069.5048	535.2560	1068.5208	534.7640	10
14	2458.2936	1229.6504	2441.2671	1221.1372	2440.2831	1220.6452	P	*973.4473*	487.2273	956.4207	478.7140	955.4367	478.2220	9
15	2515.3151	1258.1612	2498.2885	1249.6479	2497.3045	1249.1559	G	*876.3945*	438.7009	859.3680	430.1876	858.3840	429.6956	8
16	2612.3678	1306.6876	2595.3413	1298.1743	2594.3573	1297.6823	P	*819.3731*	410.1902	802.3465	401.6769	801.3625	401.1849	7
17	2741.4104	1371.2089	2724.3839	1362.6956	2723.3999	1362.2036	E	722.3203	361.6638	705.2937	353.1505	704.3097	352.6585	6
18	2870.4530	1435.7302	2853.4265	1427.2169	2852.4425	1426.7249	E	*593.2777*	297.1425	576.2511	288.6292	575.2671	288.1372	5
19	2971.5007	1486.2540	2954.4742	1477.7407	2953.4901	1477.2487	T	*464.2351*	232.6212	447.2086	224.1079	446.2245	223.6159	4
20	3058.5327	1529.7700	3041.5062	1521.2567	3040.5222	1520.7647	S	*363.1874*	182.0974	346.1609	173.5841	345.1769	173.0921	3
21	3187.5753	1594.2913	3170.5488	1585.7780	3169.5648	1585.2860	E	276.1554	138.5813	259.1288	130.0681	258.1448	129.5761	2
22							K	147.1128	74.0600	130.0863	65.5468			1

Supplementary Figure 10. False positive Mascot peptide identification of Lys269 residue modified by PONPC through Schiff base formation.

A Mascot search identified the peptide 268-289 (DKMFHFWVNTFFIPGPEETSEK) with a PONPC Schiff adduct on K269. An upper pane with the fragmentation spectrum showing identified ions as peaks marked in red and a lower table with the matched b and y ion coverage, with the matching ions shown in red, are presented. Bold italic red: the ion series contributed to the score of the peptide; bold red: the number of matches in the ion series is greater than would be expected by chance; non-bold red: the number of matches in the ion series is no greater than would be expected by chance.

The peptide spanning residues 268-289 (DKMFHFWVNTFFIPGPEETSEK) showed good y ion coverage between y(3) and y(12), which partially covered the sequence (FFIPGPEETS). However, the peaks assigned to these y ions were not the dominant peaks in the spectrum, questioning the reliability of these assignments. The lack of detected b ions meant that there was no confirmation of sequence coverage around Lys269, thereby strongly suggesting a false positive for the identification of the PONPC Schiff adduct at this position

A

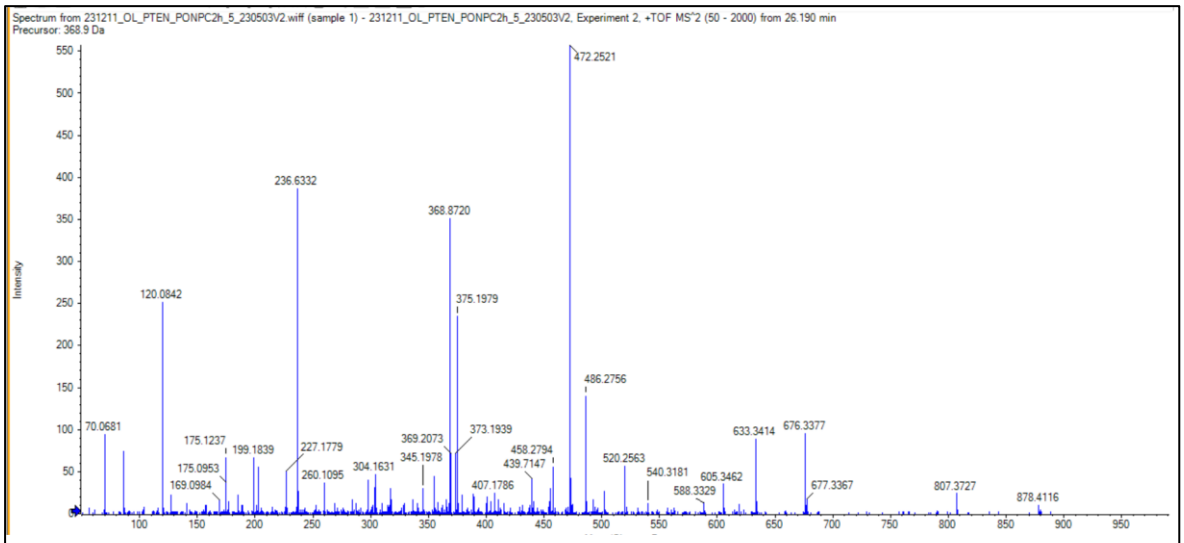

878.4116 (1) → 807.3727 (2) → 676.3377 (3) → 619.3134 (4) → 472.2521 (5) → 375.1979 (6) → 304.1631 (7) → 175.1237 (8)

- (1→2) = 71.0389 = A
- (2→3) = 131.0350 = M
- (3→4) = 57.0243 = G
- (4→5) = 147.0612 = F
- (5→6) = 97.0542 = P
- (6→7) = 71.0348 = A
- (7→8) = 129.0394 = E

B

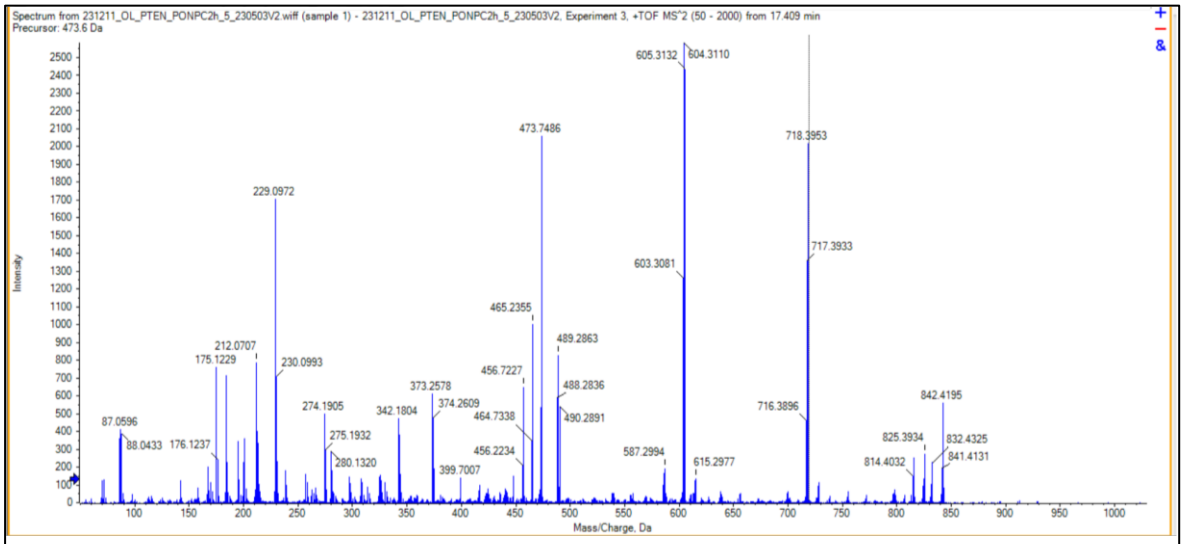

830.4229 (1) → 716.3896 (2) → 603.3081 (3) → 488.2836 (4) → 373.2578 (5) → 274.1905 (6) → 175.1229 (7)

- (1→2) = 114.0333 = N
- (2→3) = 113.0815 = I or L
- (3→4) = 115.0244 = D
- (4→5) = 115.0258 = D
- (5→6) = 99.0673 = V
- (6→7) = 99.0676 = V

C

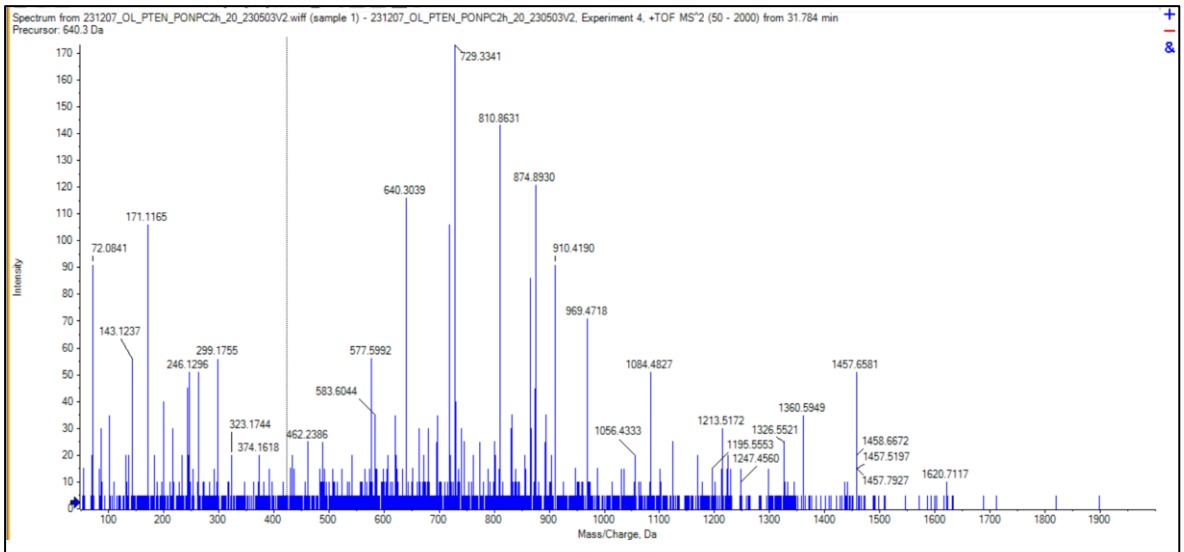

1457.6581 (1) → 1360.5949 (2) → 1213.5172 (3) → 1084.4827 (4) → 969.4718 (5) → 832.4132 (6) → 718.3736 (7) → 621.3213 (8)

- (1→2) = 97.0632 = P
- (2→3) = 147.0777 = F
- (3→4) = 129.0345 = E
- (4→5) = 115.0109 = D
- (5→6) = 137.0586 = H
- (6→7) = 114.0396 = N
- (7→8) = 97.0523 = P

D

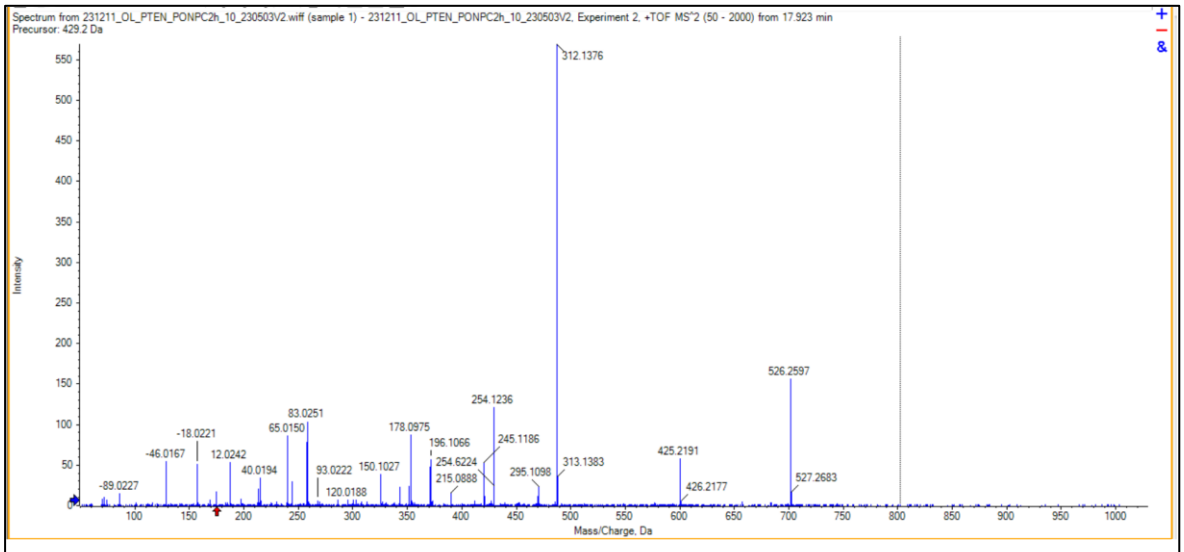

701.3846 (1) → 600.3440 (2) → 487.2625 (3) → 390.2137 (4) → 303.1827 (5) → 175.1249 (6)

- (1→2) = 101.0406 = T
- (2→3) = 113.0814 = I or L
- (3→4) = 97.0488 = P
- (4→5) = 87.0310 = S
- (5→6) = 128.0578 = Q

E

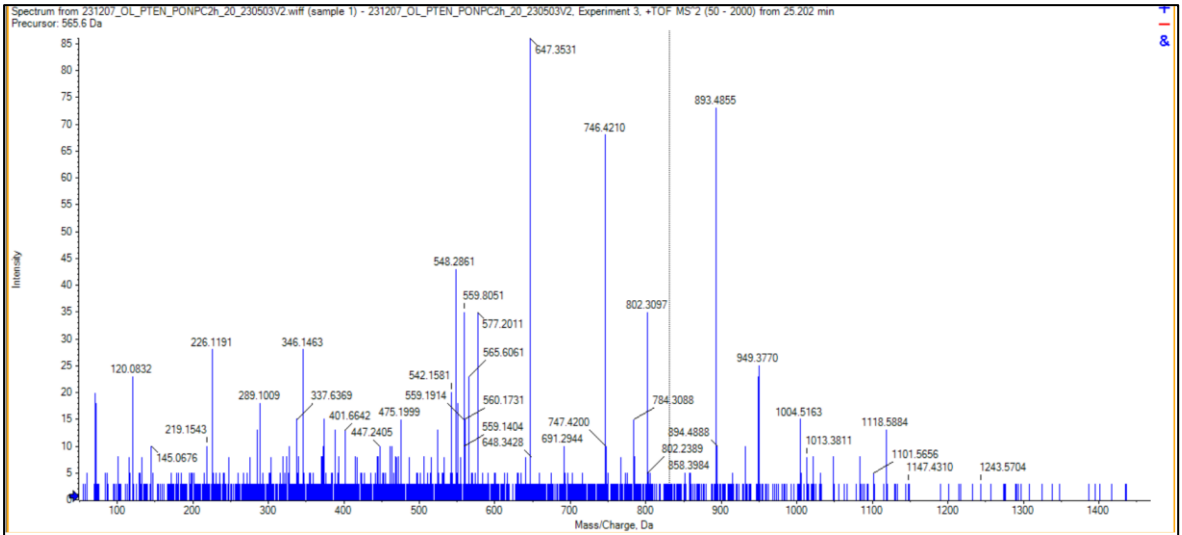

1118.5884 (1) → 1021.5335 (2) → 893.4855 (3) → 746.4210 (4) → 647.3531 (5) → 548.2861 (6)

- (1→2) = 97.0550 = P
- (2→3) = 128.0479 = Q
- (3→4) = 147.0646 = F
- (4→5) = 99.0678 = V
- (5→6) = 99.0671 = V

F

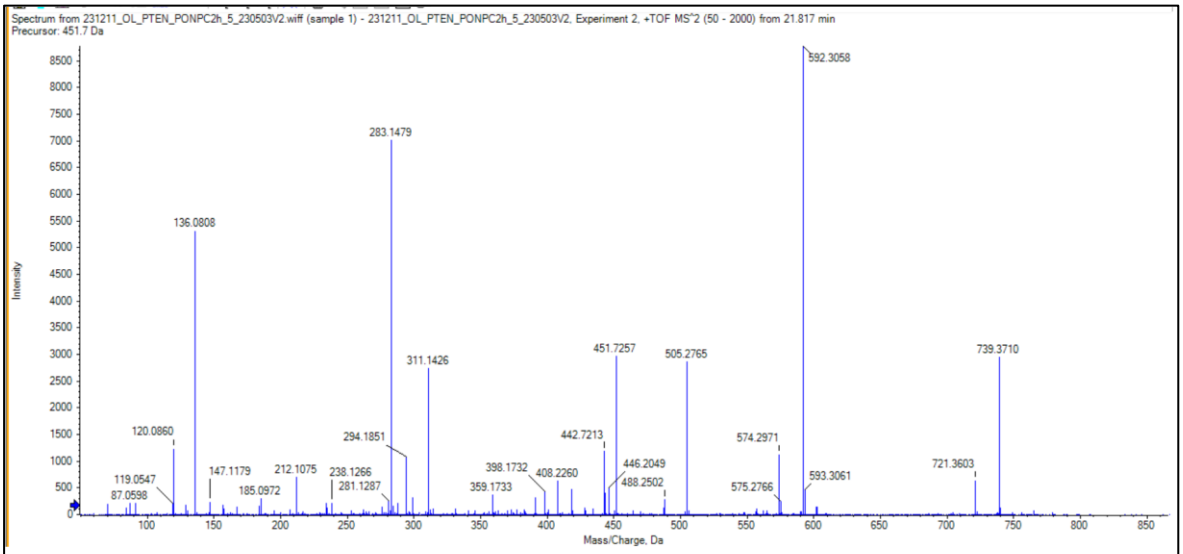

739.3710 (1) → 592.3058 (2) → 505.2765 (3) → 408.2260 (4) → 294.1851 (5)

- (1→2) = 147.0652 = F
- (2→3) = 87.0292 = S
- (3→4) = 97.0505 = P
- (4→5) = 114.0409 = N

Supplementary Figure 11. Representative *de novo* sequencing of PTEN peptides suspected to be modified by PONPC based on the identification of 184.07 Da ions corresponding to the mass of fragmented PONPC's phosphocholine group.

PTEN-V5-His was treated with PONPC at increasing molar ratios for 30 or 120 min at 37˚C. Resulting monomeric PTEN-V5-His and protein aggregates were analysed by LC-MS/MS following in-gel digestion using trypsin. Data from samples in which PTEN-V5-His was believed to be covalently modified by PONPC were manually analysed using the PeakView software (SCIEX, U.S.A.). This shows the MS/MS spectrum of the ions identified as peptides originating from PTEN-V5-His (peptides (A) 34-40 (AMGFPAE), (B) 49-54 (NIDDVV), (C) 89-95 (PFEDHNP), (D) 167-171 (TIPSQ), (E) 213-217 (PQFVV), and (F) 337-340 (FSPN)). The details of the *de novo* sequencing are shown below the corresponding spectra.